SCHOLARLY PUBLICATIONS

A CURRENT AWARENESS BULLETIN
OF RESEARCH OUTPUT

@DTU

(45th Edition)

SEPTEMBER 2016

BY: CENTRAL LIBRARY

DELHI TECHNOLOGICAL UNIVERSITY
(FORMERLY *DELHI COLLEGE OF ENGINEERING)*
GOVT. OF N.C.T. OF DELHI
SHAHBAD DAULATPUR, MAIN BAWANA ROAD
DELHI 110042

PREFACE

This is the **Forty fifth** Issue of Current Awareness Bulletin started by Delhi Technological University, Central Library. The aim of the bulletin is to compile, preserve and disseminate information published by the faculty, students and alumni for mutual benefits. The bulletin also aims to propagate the intellectual contribution of Delhi Technological University (DTU) as a whole to the academia.

The bulletin contains information resources available in the internet in the form of articles, reports, presentations published in international journals, websites, etc. by the faculty and students of DTU. The publications of faculty and student which are not covered in this bulletin may be because of the reason that the full text either was not accessible or could not be searched by the search engine used by the library for this purpose.

The learned faculty and students are requested to provide their uncovered publications to the library either through email or in CD, etc to make the bulletin more comprehensive.

This issue contains the information published during **September 2016**. The arrangement of the contents is alphabetical. The full text of the article which is either subscribed by the university or available in the web is provided in this bulletin.

Central Library

CONTENTS

1. A parametric study of a concentrating integral Storage solar water heater for domestic uses, Jaji Varghese, ***3.Samsher*** and ***3.K. Manjunath***, Department of Mechanical Engineering, DTU

2. ANAEROBIC TREATMENT OF DAIRY EFFLUENT- A STEP FOR ENERGY SAVING & GHG MITIGATION, ***3.Rakesh Mehrotra, 3.A Trivedi*** and ***3.1S. K. Mazumder***, Civil Engineering, DTU

3. Bismuth oxide nanorods based immunosensor for mycotoxin detection, Pratima R. Solanki ***3.Jay Singh,*** Applied Chemistry and Polymer Technology, Bharti Rupavali, Sachchidanand Tiwari, ***3.Bansi D.Malhotra,*** Biotechnology DTU

4. Canonic Realizations of Voltage-Controlled Floating Inductors Using CFOAs and Analog Multipliers, Raj Senani, ***3.Data Ram Bhaskar,*** Bhaskar, Munish Prasad Tripathi, Manoj Kumar Jain, Electrical Engineering, DTU

5. Comparative Energetic and Exergetic Analysis of R22, R438A and M1, Suneel Kumar Kalla, ***3.B.B. Arora*** and J.A. Usmani, Mechanical. Engineering, DTU

6. Computational Analysis and Predictive Cheminformatics Modeling of Small Molecule Inhibitors of Epigenetic Modifiers, Salma Jamal, ***3. Sonam Arora,*** Vinod Scaria***,*** Bio Technology, DTU

7. Development of surface functionalized ZnO-doped LiFePO4/C composites as alternative cathode material for lithium ion batteries, ***3.Rakesh Sarohaa, 3.Amrish K. Panwara***, Yogesh Sharmab, ***3.Pawan K. Tyagia***, and Sudipto Ghoshc, Applied Physics DTU

8. Effect of single wall carbon nanotube networks on gas sensorresponse and detection limit, Deepak Kumara, Poornendu Chaturvedia, Praveen Sahoa, Pika

Jhaa, Abhilasha Choukseya, ***8.1. Mohan Lal***, J.S.B.S. Rawata, R.P. Tandonb, P.K. Chaudhuryaa, Electrical Engineering, DTU

9. Effect Of ZnO Coating On Physicochemical Properties Of LiFePO4 Cathode Material For Lithium Ion Batteries, ***3.Rakesh Saroha***, ***3.Aditya Jain*** and ***3.A. K. Panwar,*** Applied Physics, DTU

10. Electrospun Sericin/PVA/Clay Nanofibrous Mats for Antimicrobial Air Filtration Mask, ***3.Roli Purwar***, ***3.K.Sai Goutham***, and ***3.Chandra Mohan Srivastava***, Applied Chemistry and Polymer Technology, DTU

11. EMPIRICAL ANALYSIS OF WORKFORCE DIVERSITY AND ITS MANAGEMENT IN TODAY'S IT ORGANIZATIONS, ***3.Dr. Shikha N. Khera*** and ***6. Karishma Gulati***, DSM, DTU

12. Estimation of Electrical Energy Generation from Anaerobic Digestion Technology ***7.Shubham Gupta*** and ***3.Prof. R. S. Mishra,*** Mechanical Engineering, DTU

13. Experimental Investigations of Performance and Emissions Characteristics of Kusum (Schleichera Oleosa) Biodiesel in a Multi-Cylinder Transportation Diesel Engine, Ashok Kumar Yadav, Mohd Emran Khan, ***3. Amit Pal*** and Alok Manas Dubey, Mechanical Engineering, DTU

14. Failure investigations of a first stage Ni based super alloy gas turbine blade, ***3. Sushila Rania, 3.Atul K Agrawalb*** and ***3.Vikas Rastogi,*** Mechanical, Production and Automobile Engineering, DTU

15. Hierarchical clustering of interval-valued intuitionistic fuzzy relations and its application to elicit criteria weights in MCDM problems, ***3.Mamata Sahu, 3.Anjana Gupta*** and Aparna Mehra, Applied Mathematics, DTU

16. Holographic dark energy in Brans-Dicke theory with logarithmic form of scalar field, ***3.C. P. Singh*** and ***3.Pankaj Kumar,*** Applied Mathematics, DTU

17. Influence of milling duration on micro structural, electrical, ferroelectric and piezo electric properties of Ba0.9Sr0.1Zr0.04Ti0.96O3 ceramic, ***3. Aditya Jain, 3.Amrish K. Panwar*** and A.K.Jha***,*** Applied Physics DTU

18. Investigation of temperature variations on analog/RF and linearity performance of stacked gate GEWE-SiNW MOSFET for improved device reliability, ***3.N. Gupta*** and ***3.R. Chaujar,*** Engineering Physics, DTU

19. Kirchhoff's laws from Tellegen's Theorem, ***3.1Vishnuvajjula Charan PRASAD,*** DTU

20. Micro Structural and Mechanical Behaviours of Nano-TiC-Reinforced AA6082 FSW Joints, ***3.Mohd Rashid***, ***3.N. Yuvraj*** and ***3.Shailesh Kumar Singh,*** Mechanical Engineering and***,*** Production Engineering***,*** DTU

21. Morphology control in the bulk heterojunction blend of inverted organic solar cell via co- solvent addition, ***3.Sarita S Nair*** and ***3.D Kumar,*** Applied Chemistry & Polymer Technology, DTU

22. MOS currentmodelogicexclusive-ORgateusingmulti-threshold triple-tail cells, ***3.Neeta Pandey, 3.KirtiGupta, 3.GarimaBhatia*** and ***3.BharatChoudhary,*** DTU

23. Nash Commitment for Energy Trading in Liberalized Power Market: a State of Art Review, ***3.Madan Mohan Tripathi,*** Anil Pandey, Amit Verma, K. G. Upadhyay, D. Chandra, Electrical Engineering, DTU

24. New agegraphic dark energy in Brans-Dicke theory with loga- rithmic form of scalar field***, 3.Pankaj Kumar*** and ***3. C. P. Singh,*** Applied Mathematics DTU

25. Numerical simulation of rear contact silicon solar cell with a novel front surface design for the suppression of interface recombination and improved absorption, ***3.Rahul Pandey*** and ***3.Rishu Chaujar,*** Engineering physics DTU

26. PROCESS OPTIMIZATION IN FERTILIZER MANUFACTURE INDUSTRY FOR ENVIRONMENTAL INTEGRATION, ***3.Arushi Gupta, 3.Geeta Singh*** and ***3.Anunay Gour,*** Environmental Engineering, DTU

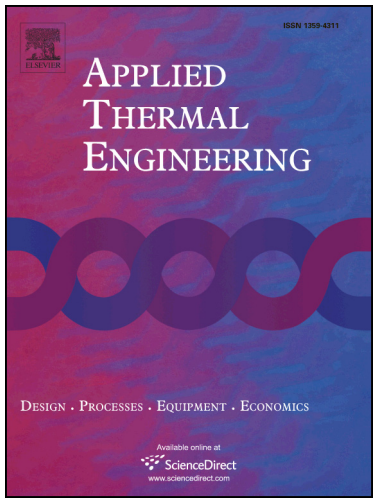
27. Re-expression of cell cycle markers in aged neurons and muscles: Whether cells should divide or die***?, 3.Renu Sharma, 3.Dhiraj Kumar, 3.Niraj Kumar Jha, 3.Saurabh Kumar Jha, 3.Rashmi K Ambasta*** and ***3.Pravir Kumar***, Molecular Neuroscience and Functional Genomics Laboratory, DTU

28. Signature of triply excited Li-like V states in ion–solid collisions, ***3.Gaurav Sharma***, K. Haris, ***3.G. Singh***, B. Kumarc, S. Karmakar, ***3.N.K.Puri***, Adya P. Mishra, PravinKumar, T.Nandi, DTU

29. Two degrees of freedom dc voltage controller of grid interfaced PV system with optimized gains, ***7.1. Ravi Nath*** Tripathi and Tsuyoshi Hanamoto, Power Systems, DTU

1. *Chancellor*
2. *Pro Vice Chancellor* — ***2.1.*** *Ex Pro Vice Chancellor*
3. *Faculty* — ***3.1.*** *Ex Faculty*
4. *Teaching-cum-Research Fellow*
5. *Alumni*
6. *Research Scholar* — ***6.1.*** *Ex Research Scholar*
7. *PG Scholar* — ***7.1.*** *Ex PG Scholar*
8. *Undergraduate Student* — ***8.1.*** *Ex Udergraduate Student*

Accepted Manuscript



Research Paper

A parametric study of a concentrating integral Storage solar water heater for domestic uses

Jaji Varghese, Samsher, K. Manjunath

PII: S1359-4311(16)31828-2
DOI: http://dx.doi.org/10.1016/j.applthermaleng.2016.09.127
Reference: ATE 9152

To appear in: *Applied Thermal Engineering*

Received Date: 4 June 2016
Revised Date: 10 August 2016
Accepted Date: 21 September 2016

Please cite this article as: J. Varghese, Samsher, K. Manjunath, A parametric study of a concentrating integral Storage solar water heater for domestic uses, *Applied Thermal Engineering* (2016), doi: http://dx.doi.org/10.1016/j.applthermaleng.2016.09.127

This is a PDF file of an unedited manuscript that has been accepted for publication. As a service to our customers we are providing this early version of the manuscript. The manuscript will undergo copyediting, typesetting, and review of the resulting proof before it is published in its final form. Please note that during the production process errors may be discovered which could affect the content, and all legal disclaimers that apply to the journal pertain.

ACCEPTED MANUSCRIPT

A parametric study of a concentrating integral Storage solar water heater for domestic uses

Jaji Varghese[1], Dr.Samsher[2], Dr.Manjunath.K[3]

[1](Department of Mechanical Engineering, Aryabhat Institute of Technology, Delhi, India),

[1]corresponding author: email:jajivarghese18@gmail.com

[2, 3](Department of Mechanical Engineering, Delhi Technological University, India)

Abstract

A parametric study of a concentrating integrated collector storage solar water heater was undertaken. The concentrator used was the Compound Parabolic Concentrator (CPC), an optical non-imaging device, a wider acceptance angle was used (64◦) so that only occasional tracking is needed making this suitable for household purposes. The reflective concentrator was supported on a wooden cradle which comprised the two parabolas of the compound parabolic concentrator. Unlike conventional CPC systems with a large number of smaller diameter tubes, here is a single larger diameter drum was positioned at the focus of the CPC. Experimental studies were carried out and the mean collector efficiency computed on the model with an air gap introduced in the side walls (arms of the CPC). The parametric study of the design by EES at solar noon was in good agreement with the collected experimental results. The maximum thermal efficiency of the collector was 38% and the maximum water temperature attained was 53°C.

Keywords – household, batch water heater, compound parabolic, solar water heater, air gap

1.0 Introduction

Integral or batch solar water heaters (BSWH) are well insulated weather-tight enclosures containing one or more tanks painted black. The enclosure has its south facing exposed to sun's rays fitted with clear glass or plastic, so as to allow the rays to enter directly on the tank and warms the "batch" of water within. It is generally tilted at an angle approximately equal to the geographic latitude of the site, so as to have a maximum incidence of solar radiation. The first batch heater was built around 1890 by Clarence Kemp, an ingenious Baltimore businessman. It brings down the cost of the system considerably due to the absence of a separate storage tank. Unlike

ACCEPTED MANUSCRIPT

conventional flat plate/evacuated tube collectors, the design is uncomplicated because batch heaters need no pumps, blowers, differential thermostats, or other externally powered devices. It is naturally circulated type operating under overhead tank pressure. The tank/drum is supported in an insulated wooden box and connected to the supply line with valves installed so that one can fill and drain the system as needed. The history and the technological advances made in integrated collector storage solar water heaters (ICSSWH) have been dealt in detail by Smith et al. [1]. In the Indian context, in spite of the efforts made by Ministry of Non-conventional Energy sources, (MNES), Indian Renewable development agency, (IREDA) and other Govt. & Private agencies the concept of Solar Water Heating for domestic purposes is not widely acceptable. Even the global status report published by REN21 (2010), depicting the average annual growth rates of renewable energy capacity, (2005-2010), the growth in solar water heating system is at standstill, (Year 2005- 16% & year 2010 also 16%) whereas there has been substantial growth in concentrated solar power (25% to 77%) and solar photovoltaic (49% to 72%). The reasons being high first-time capital and installation cost of FPC/ETC solar water heaters; although operating cost is negligible it requires close monitoring as operating cost increases with poor up keeping and maintenance.

The present work is an integration of this older concept of batch water heating with the modern trends in solar water heating technologies i.e. incorporating a concentrator in the design. So the design in principle is a BSWH with a concentrator. The concentrator, in this case, is a CPC reflector supported in a wooden cradle, backed with glass wool insulation. The SWH is designed to cater the need of a family of four. The cylindrical storage tank painted black is positioned at the focus of CPC so as to absorb maximum solar radiation. Since the focus of the study is for households although the use of TIM, PCM can enhance system efficiency but also adds to the cost, alternatively an air gap is introduced in the arms of CPC to enhance system performance. The use of CPC reflector reduces the thermal mass of system compared to an FPC and hence transient effects are also small. Also, the wider acceptance angle requires minimal tracking. In this paper, the parametric study of the collector is carried out and the performance of the proposed model is compared with a similar model but without an air gap. Under no withdrawal condition, the maximum temperature of 62 ^{o}C was attained. It is observed that the performance parameters obtained by this system are comparable to other ICSSWH systems but more lucrative especially in developing countries due to its simple design. A simple batch solar water heater was investigated by Akuffo and Jackson in Ghana [2]. The integrated storage-collector unit was a rectangular galvanised steel box with a total storage capacity of 90 L. This design achieved a maximum temperature of 45 °C by 4:30 pm and provided 30 °C water at 5:30 am the next day. A similar system was studied by Asif and Muneer, [3] except their rectangular integrated storage-collector unit incorporated fins to improve thermal performance and structural stability. The unit was made of stainless steel sheets painted matte black, with four stainless steel fins. When compared to a finless (plain) model, the finned integrated system was found to be more efficient. However, although it is true that the extended surfaces present higher characteristic length for convective heat transfer from the storage tank to water, obtaining higher daytime water temperature, it results in higher thermal losses in night time operation.

ACCEPTED MANUSCRIPT

To obtain higher operating temperature for longer time, Rakesh Kumar and Rosen [4] modified the plane rectangular absorber surface with corrugated surface thereby having more area exposed to solar radiation although they found the system efficiency reduced marginally. Kaushik et al. [5] worked on a batch solar water heater with triangular cross section and found that the system resulted in higher solar gain and leading to a higher water temperature at different flow rates in the winter season. To broaden the usefulness of integrated collector storage SWH system especially for overnight applications Kumar and Rosen investigated on storage tank with an extended storage unit [6] resulting in an enhanced performance of 5 %. A 3D CFD model was developed and studied for different depths of extended surfaces by Monia Chaabane, Hatem Mhiri, and Philippe Bournot, [7] supplemented this fact. Another integrated storage-collector design was investigated by Mohamad, [8] with the use of a thermal diode to prevent reverse circulation at night time. Mohamad found that the thermal diode yielded 10 % improvement in maintaining the water temperature overnight when compared to a prototype with no diode.

The success of any solar water heater system is envisaged only if it is capable of delivering hot water when needed and even during non-sunshine hours. The design, therefore, should incorporate these two important criteria, a good solar fraction and good heat retention. A good solar fraction can be obtained by improved optical efficiency and heat retention by proper insulation and good thermal storage. Many techniques have been evolved to have good heat retention. To minimize the heat losses apart from the use of good insulation, Chaurasia and John Twidell [9] carried out studies to measure overall loss coefficient with simple glass glazing and with the use of transparent insulation material (TIM). The effect of using TIM and varying its configuration within the collector has been studied by Reddy and Kaushika [10]. To minimize the nocturnal heat losses Shridhar and Reddy designed and developed a modified cuboid solar integrated-collector-storage (ICS) system with TIM [11]. Abdul Jabbar Khalifa et al. [12] suggested DSWH's system with a back layer of phase change material (PCM), which yielded increase in plate temperature and better heat storage during off-sunshine hours. Hailliot et al. [13] evaluated the potential of compressed expanded natural graphite (CENG) and phase change material (PCM) composites to improve the performance of solar domestic hot water (SDHW) systems. Smith et al. [14] proposed an ICS vessel with inner sleeve arrangement which showed improved thermal collection and heat retention capability and reduces heat loss up to 20 %. Stratification increases the performance of solar systems. When tanks are horizontally placed, they are usually less stratified than when they are vertical. Carrilleo and Cejudo [15] used TRNSYS software to study a model, an indirect solar domestic hot water system with horizontal storage and a mantle heat exchanger. Tank volume to collector area (V_t/A_c) ratio has also an important bearing on system performance for thermosyphon systems. Using TRNSYS simulation program, Sharaih and Lof [16] obtained optimum values for tank height and volume, which maximizes the annual solar fraction for temperatures ranging from 50-80◦C. The positioning of the auxiliary heater within the tank is also an important parameter thereby providing good thermal stratification. Shariah and Lof [17] made studies on the effects of an auxiliary heater on the annual performance of thermosyphon solar

ACCEPTED MANUSCRIPT

water heater simulated under variable operating conditions. Sabatellli et al. [18] computed collector efficiency using a three parameter model but adopted a methodology to find out the strong dependence of some uncertainties in the evaluation so as to judge the reliability of test procedure and its goodness toward fitness.

The introduction of a concentrator in a domestic solar water heating system is not yet commercialized but research studies have been carried out and model validation done with symmetrical and asymmetrical type of reflectors. To increase the optical efficiency extensive study on domestic use of solar water heaters with stationary concentrating reflectors has been performed by Tripanagnostopoulos and Yianoulis [19, 20], presenting a new concept on ICS systems. Helal et al. [21] designed an ICS solar water heater based on three parabolic sections. The performance of the system is modelled by a simulation program written in MATLAB programming language and the results compared with the symmetric and asymmetric CPC reflectors of Tripanagnostopoulos model. Senthilkumar and Yasodha [22] developed a three-dimensional compound parabolic concentrator, with the CPC reflectors fabricated as horizontal segments instead of vertical segments. Surface errors were thus reduced and optical efficiency increased. Lens walled CPC, a novel design by Yuehong Sua et al. [23] with large acceptance angle applied to PV applications can be incorporated in the ICS design. Thermal performance of CPC with large acceptance angle has been studied by Jaji Varghese et al. [24] with a mean daily efficiency of 37 % and maximum water temperature 60 ^{0}C attained. Performance study on an ICS with single tube involute reflector was done by Schmidt and Goetzberger [25]. Such reflector has an acceptance angle of 180°. This means that even diffuse light which is scattered by the transparent insulation material is completely reflected onto the absorber. A simple analytic technique for calculating the average number of reflections for radiation passing through a CPC was developed by Rabl, [26] and is useful for computing optical losses. In most practical applications, a CPC will be truncated because a large portion of the reflector area can be eliminated without seriously reducing the concentration. An improvement in CPC design has been suggested by Atul Jadhav et.al. [27], which brings down its height (truncated CPC) without much compromise in concentration ratio. To determine key parameters that have a greater influence on collector performance, the sensitivity analysis was carried out by Farghally et.al. [28]. In this work to study the dependence of thermal efficiency on the ratio of the temperature difference between collector inlet and ambient relative to global solar radiation was carried out on a PV/T collector. A procedure for estimating the payback period of residential SWH in terms of cost and effective energy savings over conventional heating fuels/electricity was established by Lin et al. [29], by undertaking a case study in southern Taiwan which can be handy for payback period calculations, especially for domestic solar collectors. The techno-economic analysis of an integrated storage solar water heater by Smith et al. [30] compared with SWH installations on domestic dwellings in the UK, showed that the total cost is sufficiently low to give payback periods that can compete with traditional forms of water heating. A 100 litres capacity SWH system is able to save about 1500 KWh of electricity annually in the residential sector, [31] and thus reduces about 1.5 tonnes of CO_2 emission load on the environment. Also, a system working on thermosyphon principle will have lower environmental impacts than evacuated tube designs. A study made by Benjamin Greening and

ACCEPTED MANUSCRIPT

Adisa Azapagic [32] on the life cycle environmental impacts of the two types of solar thermal systems used for domestic water heating, the flat plate and evacuated tube collectors suggest that the latter has higher environmental impacts due to the greater energy requirements for the production of the evacuated tube collector system. Manufacturing is the main contributor which accounts for (60%) to the environmental impacts. In comparison, this low cost integral solar water heater is simple in design and can be built with a minimum of carpentry and plumbing work.

2.0 Description of the system

The BSWH is designed for households, where the drum is sized to cater the needs of a family of four based on the normal consumption pattern. The drum should be able to withstand the overhead line pressure only as there is no separate circulation pump being natural circulation type. The wooden cradle (Fig.1) which not only supports the reflectors but is also an important entity to concentrate the insolation onto the receiver drum. Being part of the CPC concept, the aperture of the cradle should be such that it should have wider acceptance angle so that the SWH requires almost no tracking. The profile of the parabolic reflector is made in AUTOCAD and the printout obtained on a flex in 1:1 scale. The profile is then cut on a sheet metal with the help of a shearing machine. This template is then used to cut the plywood sheets. For the preparation of the wooden cradle two full sheets (8 ft x 4 ft) phenol bonded plywood are used. For obtaining the CPC profile, the template is superimposed on the plywood and cut made. Three such strips are cut and then interconnected by longitudinal strips. The skeleton of the wooden profile is then backed by supporting frame. The height of the cradle and its inclination should be such that it should not shadow the drum under any circumstance. The drum painted black (Fig.2) is so positioned on the wooden cradle that its periphery lies on the focus of the parabolic reflector, so as to intercept maximum reflected rays which fall on the focal axis.

The reflector is made of stainless steel of 18 gauge. The entire assembly is then housed in a wooden cradle (Phenol bonded plywood) and supported with circular clamps. The glass wool insulating material is used between the wooden cradle and stainless steel reflector. Non- return valve is fitted at the inlet line and air vent/pressure relief valve at the outlet line. Since the drum serves the dual purpose of absorber and storage tank, the drum cannot be insulated but thermal resistance is added by providing insulation on the front, bottom and side panels of the SWH. The choice of the glass covers, number and thickness can be done only after elaborate experimental analysis. As a thumb rule, one can begin with two glass covers. In the present design to minimize the heat losses from the side walls which constitute a major portion of the system compared to its frontal area, an additional thermal resistance is added by introducing an air gap as also shown in the cut-section, Fig.3 of the arm of CPC. The complete assembly, Fig.4 is installed on an open terrace, tilted at an angle of 28.58^0, the latitude of the location.

2.1 Design of CPC profile

ACCEPTED MANUSCRIPT

A two-dimensional CPC is mounted with its length parallel to the horizontal east-west direction and aperture plane sloping towards the south. The tracking requirement and the frequency of adjustments required depend on the concentration ratio. Since this collector is designed for households, one requires minimal or almost no tracking to facilitate minimum interference. Thus the CPC is designed for lower concentration ratio and wider acceptance angle. It is thus necessary to calculate the solar swing angle for the time period of the day for which collection is to be done. It may be noted that the solar swing angle is maximum on solstice days, i.e. June 21 and Dec 21.So firstly the solar swing angle is calculated (Appendix. A) and values worked out from 8:00 hrs. to 17:00 hrs. as shown in parametric Table1.The minimum acceptance angle $2\theta_a$ required for the collector is equal to the solar swing angle and the concentration ratio

$$2\theta_a = \propto_v \quad (1)$$

and $$C = \frac{1}{sin_{\theta a}} \quad (2)$$

where θ_a is the half acceptance angle. From results obtained shown in Table.1, the concentration ratio may vary from 2 to 3. With known value of concentration ratio, other geometric parameters were obtained, for the geometry of CPC as shown in Fig.5. Now from geometry of CPC, concentration ratio,

$$C = \frac{W}{b} \quad (3)$$

where W is the plane opening of the aperture and b is the width represented by BC. [Ref. Fig.5]

In our case, it is the diameter of the drum which is positioned at the focus. Since drum is for a capacity of 100 litres, the suitable value for diameter which accounts to width 'b' is chosen and accordingly length of the drum is obtained. Now with known value of 'b' from the relation of concentration ratio, W is obtained and the length of collector calculated for aperture area $1m^2$. The height to aperture ratio given by the expression

$$\frac{H}{W} = \frac{1}{2}\left(1 + \frac{1}{sin\theta_a}\right) cos\theta_a, \text{ [A. Rabl], [26]} \quad (4)$$

the height of the profile is obtained.

The system design parameters are shown in Table 2.

3.0 Experimentation and performance analysis

For prediction of thermal performance of the collector the experiments were conducted under the clear sky at an open terrace of Aryabhat Institute of Technology, Delhi, as recommended by ISO 9458[2] for outdoor tests. The tank was charged at 11:00 hrs. and readings were taken at half hourly interval till 15: 00 hrs. The collector is facing due south with collector tilt at an angle of 28.58^0 equal to the latitude of the location. With no tracking or occasional tracking, it is customary to keep solar tilt equal to the latitude of location to get maximum sunshine hours. The solar insolation falling on the aperture is measured with the help of

ACCEPTED MANUSCRIPT

solar power meter [(Additional temperature included an error (+/- 0.38 W/m^2 / ° C from 25 ° C)].For surface temperature measurement of the drum, glass cover and front, bottom and side panels of the collector J-Type thermocouples are used. These thermocouples are suitably mounted and fixed with the help of aluminium tape. The output was obtained on a digital display temperature indicator via a selector switch. A total of thirteen thermocouples were used (with four fixed on drum, four inserted in air gap at arms of CPC, two at different points inside drum for water temperature and two on top of glass surface) and the last thermocouple was kept handy so to measure outer wall temperatures at different locations to obtain the average outer wall temperature. The output of the thermocouples is obtained on a digital display temperature indicator via a selector switch. The temperature of inlet and outlet water temperatures are measured by a scientific thermometer. The experimental setup is shown in Fig.6.

The parametric study of the collector was done by Energy equation solver EES. [33] The thermal performance of the collector was evaluated by computing the instantaneous efficiency of the collector by calculating the flux observed, heat loss and useful heat gain. It is convenient to express the heat lost from the collector in terms of overall heat transfer coefficient defined by the equation

$$q_i = U_l A_{ap} \left(T_{pm} - T_a\right) \quad (5)$$

where U_l is the overall heat transfer coefficient, A_{ap} effective area of absorber (drum) in m^2 and T_{pm}, T_a are mean plate (i.e. drum in this case) and ambient temperature respectively in ^{o} C. The heat lost from the collector is the sum of heat lost from the top, front, bottom and sides, and each expressed in terms of coefficients called top loss coefficient U_l, front loss coefficient U_f, bottom loss coefficient U_b and side loss coefficient U_s. Then overall heat transfer coefficient is

$$U_l = U_t + U_f + U_r + U_s + U_b \quad (6)$$

The performance analysis proceeds in a similar manner to that of a cylindrical parabolic collector. However for a compound parabolic collector, because of its large acceptance angle, a CPC absorbs both beam and diffuse radiation. The beam radiation falling on the aperture plane is $I_b R_b$ and diffuse radiation within the acceptance angle is [$I_b R_b + I_d$/C],

and so the expression for flux absorbed is

$$S = \left(I_b R_b + \frac{I_d}{C}\right) \tau \, \alpha \, \rho_e \quad (7)$$

where notations having their usual meaning and C is the concentration ratio.

In order to obtain the useful heat gain, proceeding on similar lines to that adopted for cylindrical collector, q_u is obtained from the energy balance equation and given by:

$$q_u = \left[S - \frac{U_l}{C}\left(T_{pm} - T_a\right)\right](W - D_o)L \quad (8)$$

where W and L are width and length of aperture plane in m and D_o outside diameter of the drum. The instantaneous efficiency is then given by

$$\eta_{it} = \frac{q_u}{A_p I_T} \quad (9)$$

ACCEPTED MANUSCRIPT

where A_p is the area of aperture in m^2.

3.1 Uncertainty Analysis

The measurands in the experiment are the solar insolation, the aperture area, and the temperature measurement by thermocouples. The uncertainties in the estimated parameter are very sensitive to measurement error of solar insolation (values obtained for both peak solar and maximum outlet temperature) and small for temperature measurement. So solar measurements were done with a larger accuracy level.

The aperture area $A_p = L * W$ in m^2 (10)

L= 1.4 m ± 0.001 m

W= 0.72 ± 0.001 m

The fractional uncertainty in area measurement $\frac{\omega_{Ap}}{A_p} = \sqrt{\left(\frac{\sigma L}{L}\right)^2 + \left(\frac{\sigma W}{W}\right)^2}$ = 1.56 x 10^{-3} (11)

Absolute uncertainty ω_{Ap} = 0.00157

A_p = 1.008 ± 0.00157 m^2

At peak solar insolation

Incident radiation I_T = 842 ± 5.7 W/m^2

Temperature measurement $(T_{pm} - T_a)$ = 15 ± 0.1 °C

Combined uncertainty ω_c = 0.00962

At maximum outlet water temperature

Incident radiation I_T = 485± 2.66 W/m^2

Temperature measurement $(T_{pm} - T_a)$ = 10 ± 0.1 °C

Combined uncertainty ω_c = 0.0115

The combined uncertainty and its influence on efficiency is shown in Table 3 and Table 4.

4.0 Performance evaluation and validation

The efficiency of a solar collector depends on many factors such as collector temperature, ambient temperature, insolation and mass flow rate of fluid. It is, therefore, important to specify the conditions in which the efficiency has been measured and calculated. In this case, the measured parameters are hovering around solar noon and with no water withdrawal from the tank. Using the energy balance equation to obtain thermal efficiency and the plots obtained satisfying the equation in the form

$$\eta_{it.}A_p = \frac{S}{I_T} - \frac{U_l}{C}\frac{(T_{pm} - T_a)}{I_T} \quad (12)$$

ACCEPTED MANUSCRIPT

The fact is that U_l is not always a constant but depends on the collector operating temperature and ambient conditions. As the heat loss coefficient varies non-linearly with the rise in collector temperature, the graph of efficiency vs $(T_{pm} - T_a)/ I_T$ represented as Collector performance parameter CP (in ◦C- m^2/W) should bend slightly downwards as the ratio increases. The magnitude of this effect may be quite small making straight line representation adequate. Thus the y-axis intercept would be flux absorbed and $\frac{U_l}{C}$ would be the slope of the line. To obtain the dependence of thermal efficiency on the ratio of temperature difference between collector mean temperature and ambient i.e. $(T_{pm} - T_{a)}$ relative to global solar radiation I_T, regression analysis was carried out on obtained data. The trend line is indicative of the fact that as CP increases efficiency decreases. (Fig. 7). Theoretical values of efficiency are higher for CP between 0.015 - 0.016 compared to experimental values. (Also seen in Fig. 8). For CP between 0.016 – 0.0175 the experimental values of efficiency cluster around almost 37 % – 37.5 % without much drop in efficiency. This is because of the presence of air gap. The air in the gap is heated up as day progresses and reduces the effective temperature difference between system and surrounding. So although I_T decreases after solar noon the efficiency values remains almost same. For theoretical analysis the introduction of the air gap is done as an added thermal resistance in the heat transfer circuit but experimental values reflect that the temperature of air has also an important bearing in suppressing the heat loss. Thus the results show that there is a slight increase in efficiency for CP between 0.019 – 0.02 in comparison to theoretical values.

5.0 Results and discussions

5.1 Parametric study

The variation of the solar intensity, useful heat gain, collector efficiency with time is shown in (Fig.8) and (Fig.9) both experimental and theoretical with a maximum outlet temperature of 53 ^{0}C attained at 1500 hrs. (Fig. 10). It is also seen that the theoretical and experimental values of various performance parameters complement each other. The solar intensity increases from 11.00 hours to 13.30 hours, reaching a maximum value of 842 W/m^2 at 13.30 hours. It has been observed that with air gap introduced at the arms of the CPC, even with the fall of solar insolation, there is a rise in temperature of outlet water, wherein the trend of increase in outlet temperature continues even after the drop in efficiency after 13:30 hrs. (Fig.10). It is also depicted in the diurnal curve, (Fig.11). This is because the air gap acts as a thermal barrier between absorber cum drum and outside ambient air.

5.2 Comparative study with a model without an air gap

A comparison with a similar model developed by the author [18], but without an air gap, it is observed that in contrast to the model with an air gap, the outlet temperature reduces with the decrease in solar insolation.

A few approximations are done for comparison in the analysis:

ACCEPTED MANUSCRIPT

(i) Since the objective of the study is the comparison between the two models, the heat stored within the walls of the drum is not considered also being the two collectors designed for the same capacity. Only the quantity of heat stored by water is used in the computation of mean collector efficiency.

(ii) The models have been tested at different locations and on different days, but for the comparative study, the readings when the mean solar radiation incident on the aperture plane on the two models is in close proximity has only been taken into consideration.

(iii) As both the models have low concentration ratio, optical losses have not been worked out for the analysis.

For calculation of the mean collector efficiency for the test duration computation is done using the formula

$$\eta_c = \frac{Q_{wd}}{Q_a} \quad (13)$$

Where Q_{wd} in Joules is the amount of heat quantity of stored water in the drum and Q_a is the solar energy incident on the aperture surface during the four hour duration of experimentation. If T_i is initial temperature of water at the time of charging at 11:00am and T_f is the temperature of water at 3:00 pm, then:

$Q_{wd} = m_w c_{pw}(T_i - T_f)$ where m_w is the mass of water in storage cum absorber drum in Kg (14)

The solar energy Q_a in joules intercepted by the aperture surface A_a is determined by the integration of the solar radiation intensity G(t) measured on the aperture plane;

$$Q_a = A_a \int_{t_i}^{t_f} G(t)dt \quad (15)$$

Now $\int_{t_i}^{t_f} G(t)dt = G_m$ *the* mean solar radiation for the time period from t_i (11:00am) to t_f (3:00 pm.)

Thus the mean collection efficiency $\eta_c = \frac{m_w c_{pw}(T_i - T_f)}{A_a * G_m * \Delta t}$ (16)

The results of the study has been depicted in Table 5.

It is observed that maximum temperature difference of water obtained with air gap is 29 ^{o}C and that obtained without air gap is 14 ^{o}C and the average percentage increase in collector efficiency is 24.6 % (on condition of no withdrawal) with an air gap introduced on the side arms of the CPC.

5.3 Thermal loss coefficient vs mean temperature difference ΔT i.e. ($T_{pm} - T_a$)

For these type of systems, the thermal losses are significant as no thermal insulation can be provided on the drum which is also the absorber. To overcome this problem the system has to be thermally insulated from outside. Both the models are well insulated by glass wool insulation on the bottom and side and backed by plywood. In addition in the discussed model an air gap has been introduced at the arms of the CPC which not only adds to the thermal resistance, but also the air gets heated up which reduces the temperature difference between the drum and surrounding. From the values of regression coefficients obtained, it seen that the average values of

ACCEPTED MANUSCRIPT

overall loss coefficient vary from 9-10 W/m^2-K as also obtained from heat loss calculations. The thermal loss coefficient per unit absorber area with and without air gap is shown in Fig.12.

5.4 Side loss coefficient with and without an air gap

Parametric study made on the model with and without an air gap has shown that there is a percentage reduction of heat loss from the side walls from 13.4 % to 52.5 % as ΔT increases from 14 ^{o}C to 26 ^{o}C. Initially when the temperature difference is lower and air in the gap is not heated up, heat losses are higher but as the day progresses and temperature in air gap increases, it acts as a thermal barrier between the drum and ambient air. Later the heat loss remains fairly constant. The side loss coefficient with air gap averages about 1.41 W/m^2-K and without an air gap was 2.81 W/m^2-K. Variation of the heat lost from the side walls in both cases is shown in Fig.13.

5.5 Effect of mass flow rate (average readings taken for time duration 12:30 hrs. to 16:30 hrs.) for 7 days

The effect of mass flow rate on outlet temperature on different days with solar insolation is shown in Fig.14.

5.5.1 Case 1 and case 6 (No- flow condition)

Higher the solar insolation, higher is the useful heat gain and higher the temperature of outlet water.

5.5.2 Case 3 and case 5 (Almost same outlet temperature in both cases)

In normal cases as flow rate increases, the maximum water temperature decreases although the system efficiency increases due to lower heat losses caused by lower operating temperature. But with this collector, it is seen that the variation in the outlet temperature of water is minimal, except for drastic variations in flow rate

5.5.3 Case 2 and case 5 (Almost same average solar insolation)

Here the marginal higher temperature of outlet water in case 2 is due to marginally higher system efficiency due to higher mass flow rate (from 16 kg/hr. to 18 kg/hr.), although the difference in temperature is not much significant.

5.5.4 Case 2 and case 7 (At very high mass flow rate)

Almost same average solar insolation but very high mass flow rate, there is significant drop in outlet temperature from 49.75 ^{o}C to 41.5 ^{o}C.

Thus, it can be concluded that the effect of mass flow rate is not much profound and for households, with normal consumption pattern, this system is capable of providing hot water with average temperatures ranging from 45 ^{o}C to 55 ^{o}C throughout the day, even late evenings.

5.6 Water temperature preservation

To obtain its wider acceptability in the domestic sector, the need is to improve the water temperature rise during the daily operation and water temperature preservation during the night. With the introduction of an air gap, the system is capable of delivering hot water at an average temperature of 45 ^{o}C- 55 ^{o}C throughout the day. To obtain the heat storage capability of the system, the temperature of

ACCEPTED MANUSCRIPT

outlet water just before dusk, was recorded and the system was left alone under no drain off condition and with no shield or top cover. The next day, the temperature of water at 6:00 am was recorded. Same methodology was adopted in both cases i.e. with air gap and without an air gap. It was found that in both the cases the average temperature difference between inlet and outlet water temperature was between 10 ^{o}C- 12 ^{o}C. This is indicative of the fact that few hours after the dusk, the heat lost from the side walls increases as the temperature in the air gap starts decreasing, mean temperature difference between the system and ambient increases and the air in the gap does not make any meaningful contribution to suppress heat loss. The system behaves more as that without an air gap. The heat preservation obtained was due to glass wool insulation provided at the sides and bottom of the collector. However in northern India, the temperature drop of air during night is relatively less and the system is capable of delivering reasonable hot water in the range of 28-30^{o}C early next morning.

The system efficiency is comparable to other systems despite the fact that nothing is provided to enhance the system performance like TIM, PCM etc. so as not to add to the cost. On comparison with an ICS system with and without TIM, the system efficiency without TIM is 11.1 % and that with TIM 38.1 %. The system efficiency of this design also averages close to 38 %. Also the maximum temperatures obtained are comparable to other systems in the range of 50 ^{o}C to 60 ^{o}C, but with this design the temperatures attained are prolonged for longer periods even with drop in solar insolation. The air in the gap attained maximum temperature of 66 ^{o}C (averaging above 60 ^{o}C), whereas the ambient temperature hovered between 36 ^{o}C – 38 ^{o}C. Thus the air in the gap at the arms of CPC acts as a thermal barrier between the system and ambient which improves heat retention and suppresses heat loss.

Conclusion

The present design is a batch solar water heater in principle but incorporated with a CPC reflector and with an air gap introduced at the arms of the CPC so as to suppress the heat loss from the side walls of the solar water heater. Parametric studies conducted on the model and comparative studies with a similar model but without an air gap has revealed that there is improvement in the collection efficiency. The maximum temperature difference of water obtained with and without an air gap are 29 ^{o}C and 14 ^{o}C respectively. The average percentage increase in collector efficiency is 24.6% (on condition of no withdrawal) with an air gap introduced on the side walls of the CPC. The effect of mass flow rate on the outlet temperature is less profound when compared to ICS's with plane surfaces and even with extended storage units. Under no flow condition, maximum temperature attained was 62^{o}C and tests conducted on a ten day trial, the system hot water delivery average temperature was 45 ^{o}C – 55 ^{o}C. The temperature of the water even after dusk did not drop below 42^{o}C which means that, this BSWH is capable of delivering hot water at fairly constant temperature throughout the day Thus this model is an amicable alternative to the conventional flat plate/ evacuated collectors as it cuts down the cost of separate storage tank and working on thermosyphon principle also eliminates cost of other auxiliaries.

ACCEPTED MANUSCRIPT

Appendix A

To calculate solar swing angle $\propto_v$ and flux absorbed

$$tan \propto_v = \frac{sin\emptyset sin\delta + cos\emptyset cos\delta}{sin\emptyset cos\delta cos\omega - cos\emptyset sin\delta} \quad \text{A.1}$$

Declination angle $\delta = 23.45\ sin\left[\frac{360}{365}(284+n)\right]$ A.2

ω Angular measurement of time equivalent to15° per hour measured from noon,

based on local apparent time (LAT)

ϕ is the latitude of location

Day length in hrs. $S_{max} = \frac{2}{15}cos^{-1}[-tan(\emptyset - \beta)tan\delta]$ A.3

For obtaining the parametric Table 1. Values taken are n= 355, ω= 1100 hrs.

and $\propto_v$ obtained is 37.24°

Half acceptance angle $\theta_a = sin^{-1}\left(\frac{1}{c}\right)$ where C is concentration ratio, C= 2.03 A.4

Average number of reflections

$$m = \frac{1}{2sin\theta_a}(1+C) - \frac{(1-sin\theta_a)(1+2sin\theta_a)}{2sin^2\theta_a} \quad \text{A.5}$$

$\rho_e = \rho^m$ where ρ is the reflectivity value for a single radiation.

Since the slope of the aperture is 28°, the angle made by the axis of CPC with horizontal is 62°,

thus the beam radiation having solar elevation angle between the limits $(62^o \pm \theta_a)$

i.e. between 91° and 33° would be accepted by collector. In this case the beam radiation is falling

between these limits.

The flux absorbed $S = \left[I_b R_b + \frac{I_d}{C}\right]\tau\alpha\rho_e$ A.6

ACCEPTED MANUSCRIPT

Nomenclature

A_p	Aperture surface area in m^2
A_{ap}	Effective area of absorber (drum) in m^2
c_{pw}	Specific heat of water in J/Kg-K
C	Concentration Ratio
CP	Collector performance parameter
D_o	Outside diameter of drum in m
G_m	Mean solar radiation for the time interval in W/m^2
G (t)	Solar radiation intensity in W/m^2
H	Height of solar water heater in m
I_T	Solar insolation on tilted plane in W/m^2
I_b	Beam radiation in W/m^2
I_d	Diffuse radiation in W/m^2
h_w	Wind heat transfer coefficient in W/m^2-K
h_i	Heatt transfer coefficient of air in air gap in W/m^2-K
L	Length of collector in m / Thickness of insulation in m
K	Thermal conductivity in W/m-K
m	Average number of reflections
m_w	Mass of water in storage cum absorber drum in kg
Q_a	The solar energy intercepted by the aperture surface in J
Q_{wd}	Amount of heat quantity of stored water in J
q_u	Useful heat gain in W
R	Thermal resistance in K/W
S	Flux absorbed in W/m^2
S_{max}	Day length in hrs.
T_i	Initial temperature of water in ºC at the time of charging 11:00 am
T_f	Mean final temperature of water at 3:00 pm in ºC

ACCEPTED MANUSCRIPT

t_i	Time of start of experiment	
t_f	Time at the finish of experiment	
Δt	The time interval between start and finish of experiment in seconds	
T_{pm}	Mean plate (drum) temperature in -^oC	
U_f	Front loss coefficient W/m^2-K	
U_b	Bottom loss coefficient W/m^2-K	
U_s	Side loss coefficient W/m^2- K	
U_l	Overall loss coefficient in W/m^2- K	
W	Aperture in m	
T_{a1}, Ta_2, Ta_3, Ta_4		Thermocouple probes inserted in air gap
T_{d1}, T_{d2}, T_{d3}, T_{d4}		Thermocouple probes located on drum
T_{g1}, T_{g2}		Thermocouple probes located on glass surface
T_{w1}, T_{w2}		Thermocouple probes inserted inside drum
T_w		Thermocouple probe for measuring outside wall temperature

Greek letters

δ	Declination angle
ρ_e	Effective reflectivity
ε_p	Emissivity of absorber surface for long wave radiation
ε_c	Emissivity of cover for long wave radiation
ω	Hour angle
θ_a	Half acceptance angle
ρ	Reflectivity of SS mirror finish
α_v	Solar swing angle
$(\tau\alpha)_b$	Transmissivity-absorbivity product for beam radiation
$(\tau\alpha)_d$	Transmissivity-absorbivity product for diffuse radiation
ΔT	Temperature difference between drum and ambient in ◦C
σ	Stefan Boltzmann constant W/m^2-K^4
η_{it}	Instantaneous thermal efficiency
η_c	Collector efficiency

ACCEPTED MANUSCRIPT

Subscripts

a	air gap
b	bottom of collector
f	front face of collector
p	plywood
r	rear face of collector
s	sides of collector
t	top or aperture surface
thf	Thermal resistance of front face
thr	Thermal resistance of rear face
thb	Thermal resistance of bottom face
ths	Thermal resistance of side face
w	glass wool

References

[1] M. Symth, P.C. Eames, B. Norton, *Integrated collector storage solar water heaters, Renewable and Sustainable Energy Reviews, Vol.10, (2006), pp.503-538.*

[2] F.O. Akuffo, A. Jackson, *Simulation studies on a compact solar water heater in the tropics, Solar & Wind Technology, Vol.5, (1998), pp.229-237.*

[3] M. Asif, T. Muneer, *Life cycle assessment of built-in-storage solar water heaters in Pakistan: Building Service Engineering Research and Technology, Vol.27, (2006), pp.63-69.*

[4] Rakesh Kumar, M.A Rosen, *Thermal performance* of i*ntegrated collector-storage solar water heater with corrugated absorber surface, Applied Thermal Engineering, Vol.30, (2010), pp.1764-1768.*

[5] S.C. Kaushik, Rakesh Kumar, H.P Garg, J. Prakash , *Transient analysis of a triangular built-in-storage solar water heater under winter conditions, Heat Recovery Systems and CHP, Vol.14, (1994), pp.337-341*

ACCEPTED MANUSCRIPT

447 [6] Rakesh Kumar, M.A Rosen, *Integrated collector-storage solar water heater with extended storage unit, Applied Thermal*
448 *Engineering, Vol.31, (2011), pp.348-354.*

449 [7] Monia Chaabane, Hatem Mhiri, Philippe Bournot, *Thermal performance* of i*ntegrated collector-storage solar water*
450 *heater(ICSSH) with a storage tank equipped with radial fins of rectangular profile, Heat and Mass Transfer, Vol.1, (2012, pp.1-8.*

451 [8] A. Mohamad, *A Storage domestic solar hot water system with a back layer of phase change material, Experimental Thermal and*
452 *Fluid Science, Vol.44, (2013), pp.174-81.*

453 [9] B.L. Chaurasia, John Twidell, *Collector cum storage solar water heater with and without transparent insulation material, Solar*
454 *Energy, Vol.70, No.5, (2001), pp.403–416.*

455 [10] K.S Reddy, N.D. Kaushika, *Comparative study of transparent insulation materials cover systems for integrated-collector-storage*
456 *solar water heaters, Solar Energy Materials & Solar Cells, Vol.58, (1999), pp.431-446.*

457 [11] A. Sridhar, K.S Reddy, *Transient analysis of modified cuboid solar integrated collector storage system, Applied Thermal*
458 *Engineering, Vol.27, (2007), pp.330–346.*

459 [12] N. Abdul Jabbar Khalifa, H. Kadhim Suffe, Mahmoud Sh. Mahmoud, *A Storage domestic solar hot water system with a back*
460 *layer of phase change material, Experimental Thermal and Fluid Science, Vol.44, (2013), pp.174-81.*

461 [13] D. Haillot, F. Nepveu, V.Goetz, X. Pya, M. Benabdelkarim, *High performance storage composite for the enhancement of solar*
462 *domestic hot water systems, Solar Energy, Vol.86, (2012), pp.64–77.*

463 [14] M. Symth, P.C. Eames, B. Norton, *A comparative performance rating for an integrated solar collector/storage vessel with inner*
464 *sleeves to increase heat retention, Solar Energy, Vol.66, (1999), pp.291– 303.*

465 [15] Carrilleo Andres. A. Cejudo Lopez. J .M, *TRNSY model of a thermosyphon solar domestic water heater with a horizontal store*
466 *and mantle heat exchanger, Solar Energy, Vol.72, No. 2, (2002), pp.89–98.*

467 [16] A.M Shariah, G. Lof, *The optimisation of the tank volume-to-collector area ratio for a thermosyphon solar water heater,*
468 *Renewable Energy, Vol.7, No.3, (1996), pp.289-300.*

469 [17] A.M Shariah, G. Lof, *Effects of Auxillary Heater on annual performance of thermosyphom SWH simulated under variable*
470 *operating conditions, Solar Energy Vol. 60, No.2, (1997), pp.19-126.*

471 [18] V. Sabatelli, D. Marona, G. Braccio, V. K. Sharma, *Efficiency test of solar collectors: Uncertainty in the estimation of regression*
472 *parameters and sensitivity analysis, Energy Conversion and Management, Vol.43, (2002), pp.2287-2295.*

ACCEPTED MANUSCRIPT

[19] M. Souliotis, P. Quinlan, M. Smyth, Y.Tripanagnostopoulos, *Heat retaining integrated collector storage solar water heater with asymmetric CPC reflector, Solar Energy, Vol.85, (2011), pp.2474–2487.*

[20] D. Souliotis Chemisana, Y.G Caouris, Y. Tripanagnostopoulos, *Experimental study of integrated collector storage solar water heaters, Renewable Energy, Vol.50, (2013), pp.1083-1094.*

[21] O. Helal, B. Chaouachi, S. Gabsi, *Design and thermal performance of an ICS solar water heater based on three parabolic sections, Solar Energy, Vol.85, (2011), pp.2421–2432.*

[22] S. Senthilkumar, N. Yasodha, *Design and Development of a Three Dimensional Compound Parabolic Concentrator and Study of Optical and Thermal performance, International Journal of Energy Science, Vol.2, 2012, pp.64-68.*

[23] Yuehong Sua, B. Saffa Riffat, Gang Peia, *Comparative study on annual solar energy collection of a novel lens-walled compound parabolic concentrator (lens-walled CPC), Sustainable Cities and Society, Vol.4, (2012), pp. 35– 40.*

[24] Jaji Varghese, K. Gajanan Awari, P. Mahendra Singh, *Experimental analysis of a distinct design of a batch solar water heater with integrated collector storage system, Thermal Science, Vol.11, (2007), No. 4, pp.135-142.*

[25] C. Schmidt, A. Goetzberger, *Single tube integrated collector storage systems with transparent insulation and involute reflector, Solar Energy, Vol.45, (1990), pp.93-100.*

[26] A. Rabl, *Optical and thermal properties of compound parabolic concentrators, Solar Energy, Vol.18, (1976), pp.497-500.*

[27] S. Atul Jadhav, Ajit Kumar Gundekar, P. Ramchandra, Jyeshraj Joshi, *Performance analysis of a novel cost effective CPC system, Energy Conversion and Management,Vol.66,(2013), pp.56-65.*

[28] H.M Farghally, N.M Ahmed, *Design and sensitivity analysis of photovoltaic/thermal solar collector, World academy of Science, Engineering and Tecnology,Vol.18,No.5(2014).*

[29] W .M. Lin, K.C Chang, K.M Chung, *Payback period of residential solar water heaters in Taiwan, Vol.41 (2015), pp.901-906.*

[30] M. Symth, P.C. Eames, B. Norton, *Techno-economic appraisal of an integrated collector/storage solar water heater, Renewable Energy, Vol.29 (2004), pp.1503 – 1514.*

[31] S. C. Kaushikand, K. R. Ranjan, *Energetic and Exergetic Performance Evaluation of Natural Circulation Solar Water Heating System, Applied Solar Energy, Vol.52 (2016), No. 1, pp.16–26.*

ACCEPTED MANUSCRIPT

[32] Benjamin Greening, Adisa Azapagic, *Domestic solar thermal water heating: A sustainable option for the UK, Renewable Energy Vol.63 (2014), pp.23-36.*

[33] Klein SA. Engineering equation solver, version 8.158. F Chart Software; 2008.

Captions of Figures, Tables and Appendix

Figures

Fig.1 Wooden Cradle

Fig.2 Absorber cum Storage Drum

Fig. 3 Sectional view of CPC

Fig.4 Complete Assembly of BSWH

Fig.5 Geometry of CPC

Fig.6 Experimental Setup

Fig.7 CP vs. η

Fig.8 Efficiency vs. Time (Theoretical and Experimental)

Fig.9 Variation of I_T and q_u vs Time

Fig. 10 Variation of incident solar insolation and outlet temperature with Time (Experimental)

Fig.11 Diurnal variation

Fig.12 Thermal loss coefficient with and without air gap

Fig.13 Heat loss from side walls of the CPC panel with and without air gap

Fig.14 Effect of mass flow rate

Tables

Table 1 Time vs. solar swing

Table 2 System Design Parameters

Table 3 Uncertainty Analysis

Table 4 Influence on efficiency

Table 5 Comparative Table

Appendix. A

ACCEPTED MANUSCRIPT

ACCEPTED MANUSCRIPT



Fig.1 Wooden Cradle



Fig.2 Absorber cum Storage Drum



Inside section of arm of CPC **Front view of the CPC**

Fig. 3



Complete Assembly of BSWH

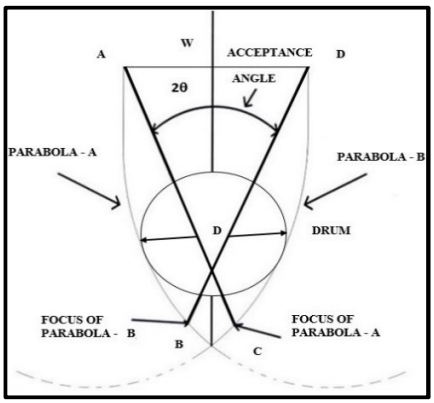


Fig.5 Geometry of CPC

Fig.4

ACCEPTED MANUSCRIPT

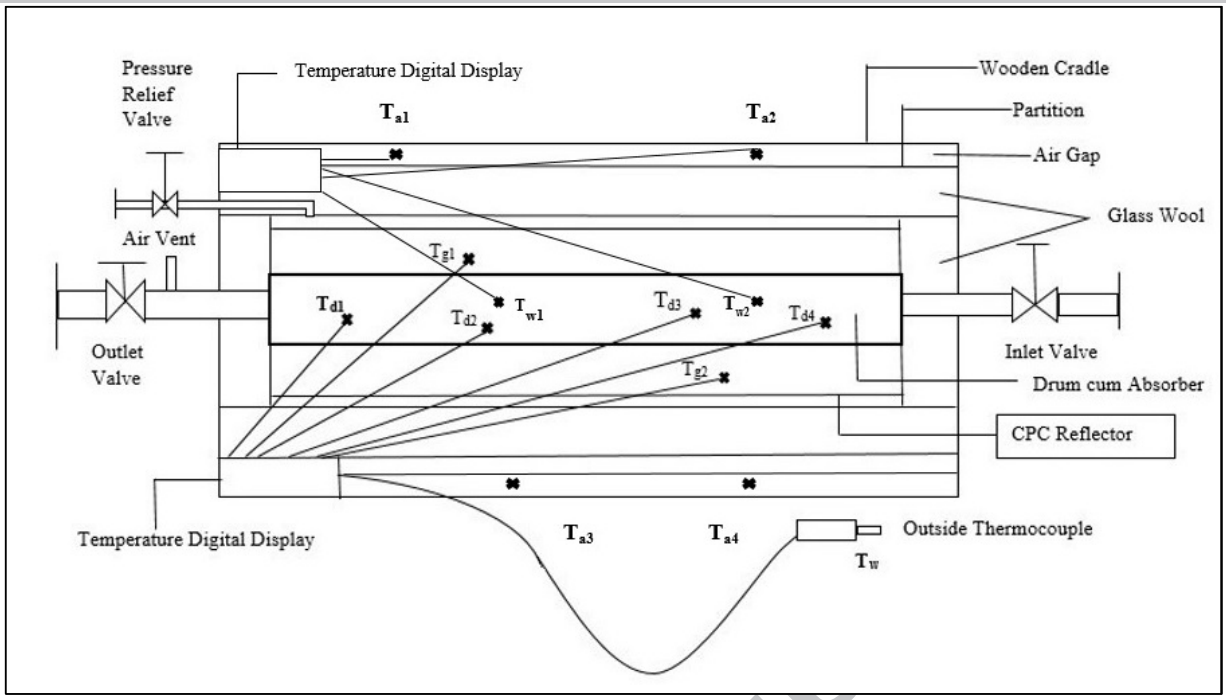


Fig.6 Experimental Setup

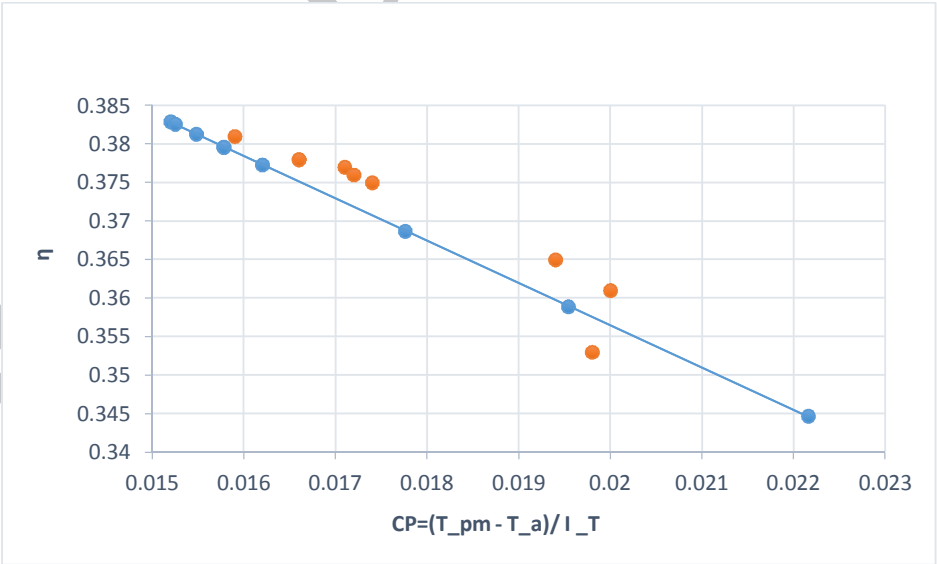


Fig. 7 CP vs η

ACCEPTED MANUSCRIPT

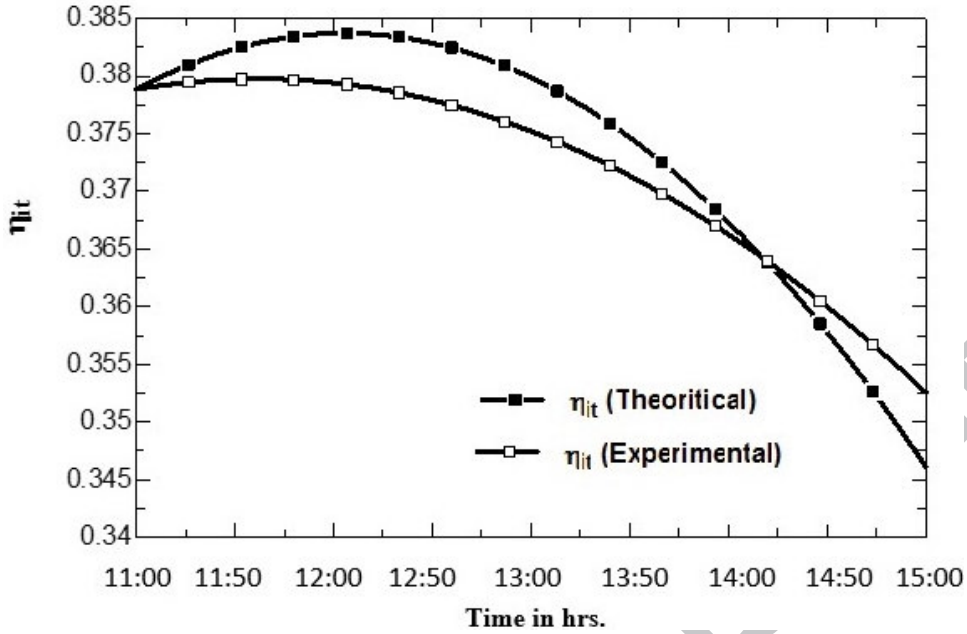


Fig. 8 Efficiency vs. Time (theoretical and Experimental)

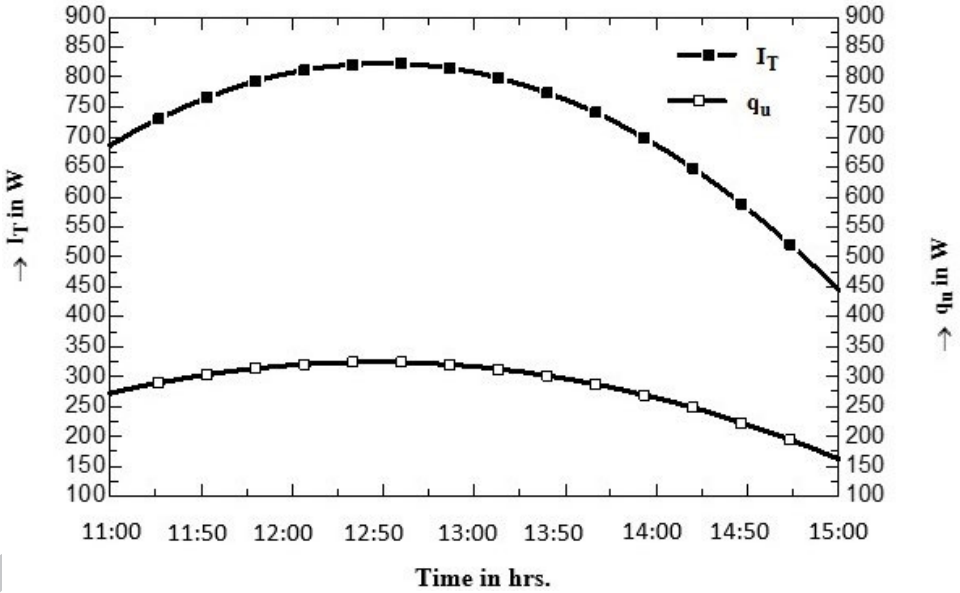


Fig.9 Variation of I_T and q_u vs Time (Experimental)

ACCEPTED MANUSCRIPT

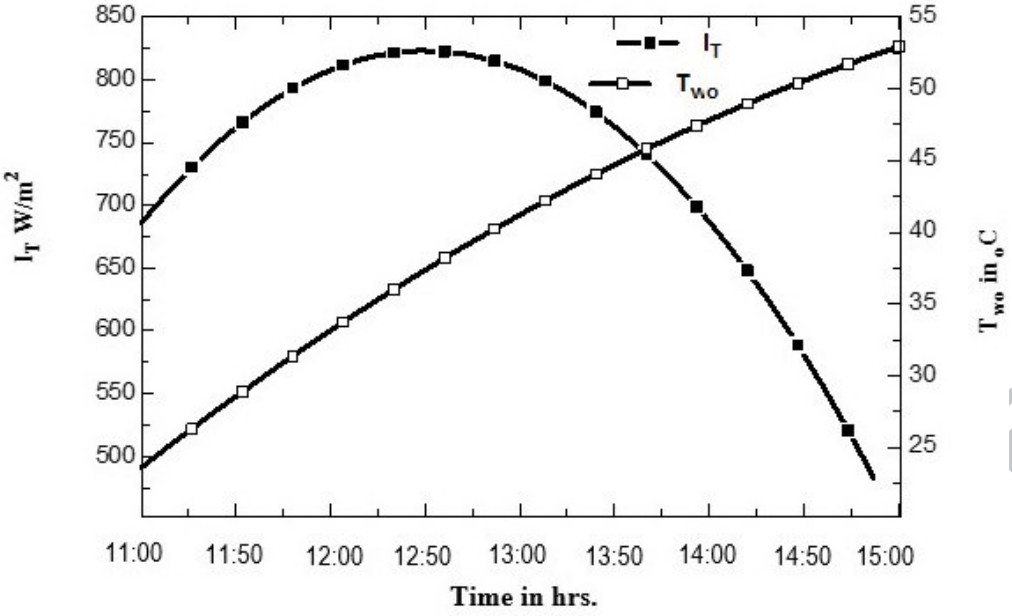


Fig. 10 Variation of incident solar insolation and outlet temperature with Time (Experimental)

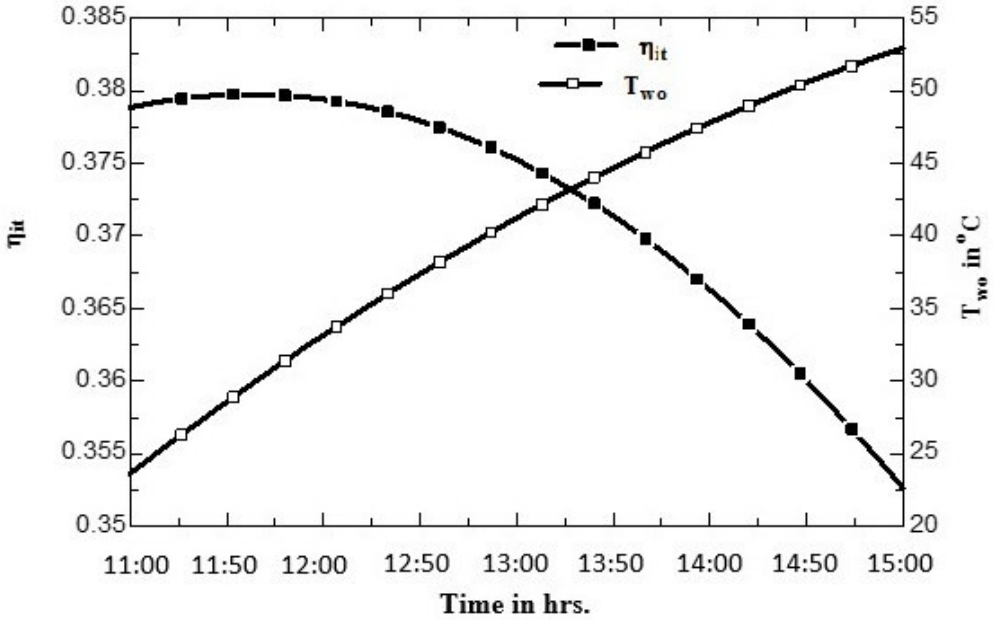
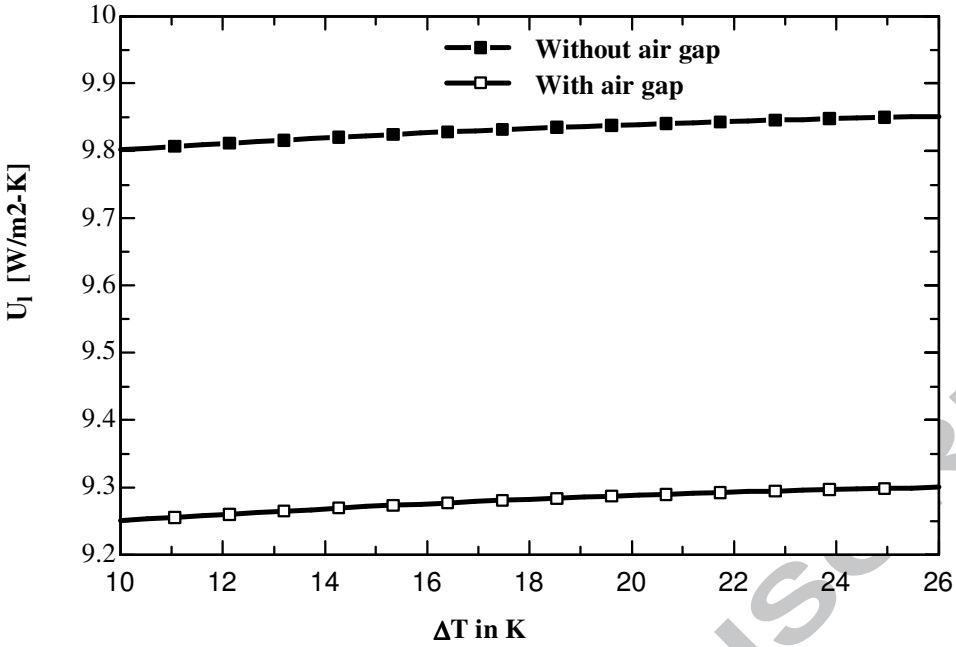
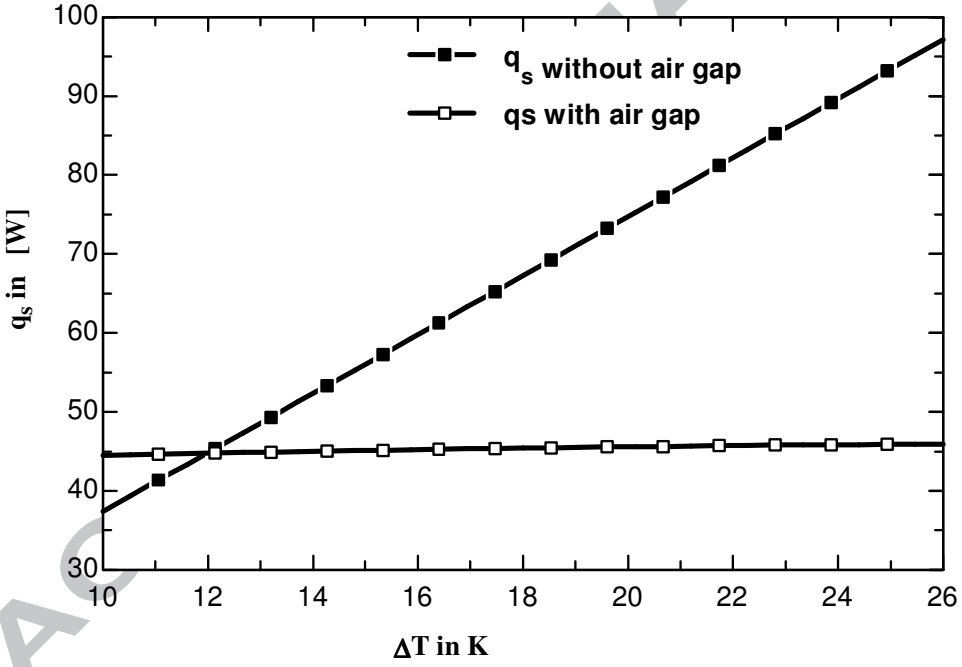


Fig.11 Diurnal variation

ACCEPTED MANUSCRIPT



560
561 **Fig 12. Thermal loss coefficient with and without air gap**
562
563



564
565 **Fig.13 Heat loss from side walls of the CPC panel with and without air gap**
566

ACCEPTED MANUSCRIPT

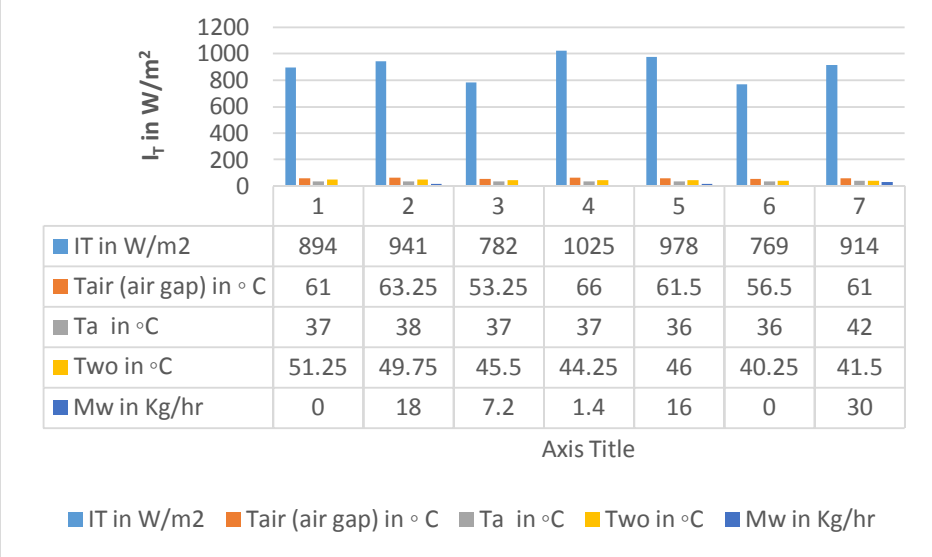


Fig.14 Effect of mass flow rate

1. 30/3/2016 (normal sunshine hrs.) Avg. wind speed 4.4 kmph
2. 31/3/2016 (normal sunshine hrs.) Avg. wind speed 3.2 kmph
3. 6/4/2016 (partial cloud) windy day, wind speed 7.5 kmph
4. 7/4/2016 (normal sunshine hrs.) Avg. wind speed 4.3 kmph
5. 8/4/2016 (normal sunshine hrs.) Avg. wind speed 3 kmph
6. 9/4/2016 (partial cloud) Avg. wind speed 6.7 kmph
7. 19/5/2016 (dust haze) Avg. wind speed 6.4 kmph

ACCEPTED MANUSCRIPT

ACCEPTED MANUSCRIPT

581

Table 1
Time vs. solar swing

Time in hrs.	Solar swing α_v in ◦(degrees)
8:00	20.48
9:00	29.89
10:00	34.81
11:00	37.24
12:00	37.97
13:00	37.24
14:00	34.81
15:00	29.89
16:00	20.48

582
583

Table 2
System Design Parameters

S.no	Component	Material	Specification	Dimension
1	**CPC Component**			
	Wooden cradle	Ply wood Phenol bonded	l x b x h in meters	1.4 m x 0.72m x0.91 m
	Reflector	Stainless steel (mirror finish)	Aperture area in m^2	1.008 m^2
		Gauge 28	Concentration Ratio	2.06
2	**Glass cover**	Clear Float glass	l x b in meters	1.4 x 0.72 m
			thickness in mm	4 mm
3	**Storage component**	MS 304 18 Gauge Coating- Black paint nonselective	Capacity in liters	100 litres
4	**Insulation**	Glass wool	Front and rear face in m^2	1.14 m^2
			Side wall in m^2	2.66 m^2
			Bottom side	1.68 m^2
5	**Air gap**		in mm	80 mm

Table 3
Uncertainty Analysis

ACCEPTED MANUSCRIPT

Time in hrs.	A_p in m^2	ω_{Ap}	$(T_{pm} - T_a)$ in ^oC	$\omega_{\delta T}$	I_T W/m^2	ω_{IT}	Combined uncertainty ω_c
13:30 (At Peak Solar)	1.008	± 0.001	15	± 0.1	842	± 5.7	0.00962
15:00 (Max. Outlet) Temp.	1.008	± 0.001	10	± 0.1	495	± 2.66	0.0115

Table 4
Influence on efficiency

Condition at	Error in %	Nominal value of η_c in %	$\omega_c\ \eta_c$
Peak Solar	2.50	37.60	± 0.36
Max outlet Temp	3.25	35.33	± 0.41

Table 5

Comparative Table

	Without air gap		With air gap	
Inlet Temp. of water	30 ^oC		24 ^oC	
Time	Temp. of outlet water T_{wo} in ^oC	collection efficiency η %	Temp. of outlet water T_{wo} in ^oC	collection efficiency η %
1 hr. prior to solar noon	43	24.67	38	38.10
At solar noon	44	29.70	47	37.54
At 3 pm	41	28.56	53	35.33

ACCEPTED MANUSCRIPT

- BSWH with a CPC reflector having a wider acceptance angle proposed.
- Additional thermal resistance added by introducing an air gap at the arms of CPC.
- Percentage reduction of heat loss from 13.4% to 52.5 % with provision of air gap.
- Mass flow rate effect less dominant, system delivers water between 45^{o}C to 55^{o}C.
- Best suited for domestic applications, an alternative to FPC/ETC SWH's.

ACCEPTED MANUSCRIPT

International Journal of Engineering Applied Sciences and Technology, 2016
Vol. 1, Issue 10, ISSN No. 2455-2143, Pages 5-8
Published Online August - September 2016 in IJEAST (http://www.ijeast.com)



ANAEROBIC TREATMENT OF DAIRY EFFLUENT- A STEP FOR ENERGY SAVING & GHG MITIGATION

Rakesh Mehrotra, A Trivedi
Dept. Of Civil Engineering,
Delhi Technological University,
Delhi-42

S. K. Mazumder
Former Professor,
Delhi College of Engineering,
Delhi

I. INTRODUCTION

India has emerged as one of the world's largest producer and fastest growing markets for milk and milk products with an annual growth of over 4-5%. As per FAO report (June 2016), India produced 146.3million tonnes of milk in 2014-15 fiscal, which comprised about 18-19% of global production. It is estimated that 148.15 million tonnes of milk will be produced in 2015-16 and a production of 155.2 million tonnes of milk in expected in 2016-17.India has a unique pattern of production, processing and marketing/consumption of milk, which is not comparable with any large milk producing country. Only a small part of milk produced in India is processed. The organized sector (large scale dairy plants) processes about 25-28 million tonnes annually, which is 18-20 per cent of the total production.(140)/ 3,800 LLPD of milk. According to NDDB and Crisil Research estimates, the country produces around **3,800 LLPD** of milk, accounting for a fifth of the global output. About 40 per cent of this is retained by producers (farmers) for household consumption; another 41 per cent share is with the unorganised segment. **Only 19 per cent** is procured, processed and sold through by organised dairies currently. **Organised sector is expected to grow to 25% of total production in** 2018-1050 LLPD of milk from 730 LLPD of milk.

(www.thehindubusinessline.com, 27 oct / 21 Dec 2015)
In the organized sector, there are over 1000 dairy plants in the cooperative, public and private sectors, registered with the Government of India and the State Governments. These plants are projected to process nearly 100 million litres of milk per day. (one single organization with brand AMUL has presently an aggregate national processing capacity of 28.0 million litres per day & expected to be 32 million litres per day by 2017). Most of the plants are in the co-operative or private sector. The processing capacity is expected to grow many fold through external investments in the future to cater to a large market in the Indian cities
The effluent is generated in dairy plant, from washing of cans/tankers, cleaning in place of process equipment(such as pasteurizers, separators, pipelines, chillers, vats, storage tank and silos, sachet filling machines),floor washings, spillages/leakages of milk/milk products, boiler blow down, softener regeneration water & bleed from the condenser etc.[1]
The volume and strength of the effluent generated in a dairy vary from plant to plant. The characteristics depend on the products and production level. Average characteristics as observed during the CPCB survey (1992)[2] are presented in the table 1

Table 1: combined wastewater characteristics of dairies.

Parameter	Milk Processing	Integrated Dairy
BOD_5	657-1,016	1,634-4,953
COD	1,341-2,195	3,800-8,631
SS	538-657	89-4,953
Nitrogen	50.25-126.2	96.32
pH	6.6-6.9	5.6-6.8
Oil and grease	-	280-2,207

- Note: all units are mg/l except pH.

It is estimated that the quantum of milk washed into the drain amounts to almost 2% of milk handled and the volume of wastewater generated is nearly 2 to 5 times of milk processed. Hence, Indian Dairies produce an aggregate 200-500 million litres of wastewater per day.

International Journal of Engineering Applied Sciences and Technology, 2016
Vol. 1, Issue 10, ISSN No. 2455-2143, Pages 5-8
Published Online August - September 2016 in IJEAST (http://www.ijeast.com)



The dairy plant waste water consists of highly biodegradable organic matter. Aerobic technologies of dairy waste treatment are the most commonly employed methods of treatment in India.[1]

It has been realized recently that anaerobic treatment offers several advantages over aerobic system in terms of energy, chemicals and sludge handling costs. High rate anaerobic systems are capable of removing 60-90% COD and have the advantage of capturing 80-90% of biochemical energy of organic matter in the form of biogas[4].

Energy being a scarce resource in India, therefore the energy analysis of waste water treatment system assumes great importance. In this study, comparisons have been made between aerobic & anaerobic treatment with a view to project the energy saving effected by adopting anaerobic process technology for treatment of dairy waste water in India & the resultant benefits in terms of GWP.

Due to high organic composition, dairy effluents are readily treated by biological process. The treatment process is determined by flow rate, waste strength and stream conditions. Methods used for treatment of dairy effluent include Physico-chemical treatment, Aerobic biological treatment such as Aerated lagoon, Conventional Activated Sludge Process, Extended Aeration, Trickling Filter, Oxidation Pond, Flocculating Algae-Bacterial System etc. ASP is the most common form of biological treatment employed for dairy effluent with COD removal efficiency of 90%. In aerobic systems the provision of oxygen for biochemical oxidation renders the system highly energy intensive.

Rapid advances in bioscience and recent developments in biochemical process engineering are having a substantial impact on the application of anaerobic biotechnology to waste treatment and energy production[5]. Anaerobic treatment units of following configurations have been successfully employed for treatment of dairy waste:

A. Anaerobic contact process

1. Upflow Anaerobic Sludge Blanket Process
2. Anaerobic Activated Sludge Process.
3. Anaerobic digester.

B. Submerged Media Anaerobic Bacteria

1. Anaerobic fixed film Bio-reactors (anaerobic filter)
2. Anaerobic Attached Film Expanded-Bed/ Fluidised-Bed Reactors.
3. Anaerobic Rotating Biological Contactor.

Anaerobic treatment alone does not suffice to reduce the BOD/COD to permissible levels. Therefore, additional Aerobic polishing is required before final disposal.

Table 2: Performance of Anaerobic attached growth bio-reactors on dairy waste

Type of Reactor	OLR Kg.COD/m^3d	Total COD removal, %	Waste strength g COD L^{-1}	Temp	Ref.
Anaerobic Attached Bed Bioreactors	<1.19	80	0.8-3.5	Ambient	6
Anaerobic Packed Bed Upflow Filter	1.348	88	1.203	35	7

Energy Considerations in Dairy wastewater treatment

Aerobic process are inherently energy intensive processes, whereas anaerobic processes are not only requiring lesser energy input but are capable of producing energy by way of biogas. Aerobic process for sewage treatment consume 12-15 kWh/person/year for Activated sludge process, 16-19 kWh/person/year for Oxidation ditch and 7-11 kWh/person/year for Trickling filter. Anaerobic process such as Anaerobic filter and Upflow Anaerobic Sludge Blanket Reactor require only 0.05 kWh/person/year.[8]

*There are however some practical aspect associated with Anaerobic treatment systems: COD removed as sludge- upto 30%, Gas recovery- > 23% COD and Methane remaining in the effluent- .028 M^3/ M^3 waste water.

Mathematical equations to predict the energy consumption in Anaerobic filter and Up-flow sludge blanket reactor are given.[9]

Energy input kWh/year:

Anaerobic Filter =1657.Q.H (i)

UASB = 1657.7Q $(S_s-1)(1-f_e)H_s$ (ii)

Assuming, pump efficiency = 0.8,

Efficiency of motor = 0.75

h = Head lost in Anaerobic filter in m.

H_s = height of sludge blanket in m.

f_e = Porosity of sludge blanket, Dimension less.

S_s = Specific gravity of sludge blanket, Dimension less.

Further the anaerobic waste treatment system have the advantage of capturing the biochemical energy of organic matter in the form of biogas (0.415 m^3 biogas/kg COD removed). The biogas thus produced can be utilized as a fuel for heating or it could be used effectively as a primary fuel source for reciprocating engines and gas turbines. The engine power can be applied to drive electric generator, compressor, pump etc. Gas can be also used to run dual-fuel engines and gas turbine for generating electricity for supplementary implant needs or for sale.

International Journal of Engineering Applied Sciences and Technology, 2016
Vol. 1, Issue 10, ISSN No. 2455-2143, Pages 5-8
Published Online August - September 2016 in IJEAST (http://www.ijeast.com)



II. CASE STUDY

In this case study, it is intended to find the energy budgeting of effluent treatment for the whole of the **organized Indian dairy industry**. Comparisons have been made between (i) proposed Anaerobic pre-treatment followed by Aerobic polishing and (ii) currently popular Extended Aeration-Activated Sludge process.

1. Study Basis:

Total Number of Dairies in India = appx 1000
Total capacity of Dairy plants = 100 MLD (in terms of volume of milk processed)
Assuming the volume of wastewater generated from the dairy processing plants is '2.404' times of volume of milk processed.
Wastewater generated from the plants = 240.415 MLD
Chemical Oxygen Demand of a typical dairy = 1500mg/l
Consider 80% of COD being consumed/ utilised for biochemical reactions to be accomplished in an anaerobic process.

Therefore, COD removed = 1200 mg/l
Total COD removed/day
= 240.415 MLD × 1200 × 10^{-6}
= 288.498 × 10^3 kg COD.

It is reported that one kg of COD is capable of producing 0.415 m^3 of biogas.
Therefore, quantity of biogas generated per day = 288.498 × 10^3 × 0.415 = **119727 m^3**
Calorific value of 1m^3 biogas = 6000 kcal. (The energy equivalent of biogas = 6.978 kWh)

2. Energy saving and cost benefits:

(I) Saving due to recovery of Biogas as a bye product in Anaerobic treatment and its utilisation.

Thus, the total energy available from biogas = 11,9727 × 6.978
= **8.355 lakh kWh/d**

(a) The thermal energy can be transferred by a heat exchanger @ 75% efficiency = 8.355 × 0.75
= 6.266 lac kWh/d

Thermal energy is required for various heating requirements in Dairy plants, so it can act as a light diesel oil (LDO) substitute (calorific value of LDO = 10,700 kcal)
Fuel equivalent in terms of LDO = 67136.64kg
Cost of LDO @ Rs.40/-kg = Rs. 2685465.6/-
Alternatively, if the biogas produced is used for the generation of electricity in a duel- fuel engine:

(b) Electrical energy generated by a duel fuel engine operating @34% efficiency = 8.355 × 0.34
= 2.841 lac kWh/d

(II) Energy demand for treatment of effluent:

It is roughly estimated that energy demand for option :

A. With Anaerobic –Aerobic process = 17hp(EM)/MLD of waste being treated.
B. With Aerobic treatment process = 100 hp(EM)/MLD of waste being treated

Therefore, saving due to implementation of proposed Anaerobic-Aerobic treatment process = 83hp(EM)/ MLD
Therefore, energy saving in treating total waste generated by Indian milk processing industry (B-A) = 240.415 × 83
= 19955 hp(EM)/d
= 359180 kWh/d
= 3.59 lac kWh/d
Therefore, the aggregate energy saving in all 1000 Indian dairies by Anaerobic- Aerobic processs is **3.59 lac kWh/d**
If electricity price @ Rs 6/- per unit
Saving in electricity bill = **Rs.21,54,000/d**
Hence the total conservation of electrical energy by adopting Anaerobic treatment of dairy waste = 3.59+2.841
= **6.431 lac kWh/d**
Considering the price of electricity @ Rs.6/-per unit (kWh) and the contribution of fuel to the total cost of electicity generation taken as 50% of the total generation cost.
Therefore, contribution of bye product biogas for electricity generation
= **Rs.8, 52,300/- per day**
= Rs. 311 million/yr.
Annual O&M cost (assumed) = Annual cost of electricity × 1.2
For (A) 17hp×0.75×240.415×24×365×1.2×6 = Appx. **Rs. 53.77 million**
(B)100hp×0.75×240.415×24×365×1.2×6 = Appx. **Rs. 316.3 million**
Difference in Annual O&M = **Rs. 262.43 million**

3. Annualised cost:

Capital cost
(A) Anaerobic- Aerobic Process = **Rs.8789.2 million**
(B) Aerobic process = **Rs.6358.8 million**
Difference in capital cost = Rs. 2430.4 million
Assuming an interest rate @ 12% & inflation rate @ 6% for design period of 20 yrs & taking 5% salvage on replacement.
Annualised capital cost = Cap. Cost×crf (6%-20yrs) – (0.05) cap.cost×sfdf (6%-20yrs)
(Note : crf = capital-recovery factor, sfdf= sinking-fund deposit factor)
Therefore, annualized capital cost
(A) Rs 755 million
(B) Rs 549 million
Total annual cost (without considering energy recovery from biogas) = Annualised capital cost + Annualised O&M cost
(A) 755**million** + 53 million **= Rs.808.8 million**
(B) 546 **million** + 316.3 million **= Rs.862.3million**

International Journal of Engineering Applied Sciences and Technology, 2016
Vol. 1, Issue 10, ISSN No. 2455-2143, Pages 5-8
Published Online August - September 2016 in IJEAST (http://www.ijeast.com)



Therefore, annual gain by adopting(A) compared to (B)- **Rs 53.5 million & Option A is a better economic choice.**

Diff. in cost on O&M+ electricity generation/yr(from recovered Biogas) for A = Rs. **262.43 million+ 311 million**= Rs. 573.43 million

Therefore, by an extra capital expenditure of Rs. 2430.4 million on Anaerobic-Aerobic technology, we get an additional saving of Rs.573.43 million annually on recurring cost. Therefore, pay back on investment can be achieved in 4.3 years only.

III. CONCLUSIONS

The following conclusions are drawn from the above case study:

1. Saving on energy demand in comparison with activated sludge process = **3.59 lac kWh/d**
2. Energy gain due to recovery of Biogas as a bye product = 8.355 lac kWh/d equivalent as calorific value. Biogas can be directly used for raising steam/ heating required in the Dairy plant , thus saving fossil fuel.
3. Total conservation of energy in Indian Dairy Processing Industry = (**3.59 + 6.266) lac kWh/d** = 9.856 **lac kWh/d.**

It is found that by adopting combined Anaerobic-Aerobic treatment at additional capital investment of Rs. 2430.4 million yields annual cost benefits of Rs. 573.43 million./yr and pay back on investment can be achieved in a short span of 4.3yrs. Implementation of such treatment process with gas recovery, while controlling pollution can result in energy conservation for the nation.

IV. REFERENCES

1. CII, (2009). *Indian Dairying: Challenges and Opportunities.* Background Paper.Conference on "Indian Dairy Industry" organized by Confederation of Indian Industries at N.D.R.I., Karnal on 22nd Oct., 2009.
2. Arvanitoyannis I.S(2008) waste management for the food industry, Elsevier academic press, Amsterdam
3. Comprehensive Industry Document Dairy Industry, Central Pollution Control Board ,Delhi. Sept.1993.
4. Owen, William.F.,(1982) Energy in Wastewater Treatment, Prentice-Hall, Inc., Englewood Cliffs, New Jersey, pp. 199-240, 259-263.
5. Switzenbaum, S., Scott C.Dankin,(1981) Anaerobic Expanded Bed Treatment of Whey, Proceedings of 36th Purdue Industrial Waste conference, Purdue University, pp. 414-424.
6. Sammaiah,P., Sastry, C.A. and Murthy, D.V.S.,(1991a). Dairy Waste Water Treatment using Anaerobic contact Filter, Indian Journal of Environmental Protection, Vol-11, No.6, pp418-424.
7. Taori, K.B., Dhabadgonkar, K. and Raman, V.,(1983) Dairy waste treatment by Anaerobic Packed Bed Upflow filter. IAWPC Tech. Annual, X, pp.21-29
8. Arceivala, S. J. and Asolekar, S. R. (2006)" Wastewater Treatment for Pollution Control" (3rd Edition), McGraw Hill Education (India) Pvt. Ltd., New Delhi
9. Anaerobic Technology for Domestic Waste water Treatment, Ch.7, pp.4-5, ISTE Summer School, June 1991, Deptt. Of Civil Engg., MNR Engg. College, Allahabad.
10. Amritkar, S.R., Introduction of Anaerobic Pretreatment in Treating dairy Effluents- A positive Step towards Conservation and Co-Generation of energy, 3rd International conference-Appropriate Waste Management technologies for developing countries, Nagpur, Feb. 1995 vol.1 pp. 127-132

Materials Science and Engineering C 70 (2017) 564–571

Contents lists available at ScienceDirect

Materials Science and Engineering C

journal homepage: www.elsevier.com/locate/msec

Bismuth oxide nanorods based immunosensor for mycotoxin detection

Pratima R. Solanki [a,b,*], Jay Singh [a,c], Bharti Rupavali [a], Sachchidanand Tiwari [b], Bansi D. Malhotra [a,d,*]

[a] DST Centre for Biomolecular Electronics, CSIR-National Physical Laboratory, K.S. Krishnan Marg, New Delhi, India
[b] Special Centre for Nano Sciences, Jawaharlal Nehru University, New Delhi 110067, India
[c] Department of Applied Chemistry and Polymer Technology, Delhi Technological University, Shahbad Daulatpur, Main Bawana Road, Delhi 110042, India
[d] Department of Biotechnology, Delhi Technological University, Shahbad Daulatpur, Main Bawana Road, Delhi 110042, India

ARTICLE INFO

Article history:
Received 15 June 2016
Received in revised form 19 August 2016
Accepted 12 September 2016
Available online 13 September 2016

Keywords:
Bismuth oxide nanorods (nBi_2O_3)
Aflatoxin B1
Immunosensor
Electrochemical studies

ABSTRACT

We report results of the studies relating to fabrication of an efficient immunosensor based on bismuth oxide nanorods (nBi_2O_3), electrophoretically deposited onto indium-tin-oxide (ITO) coated glass substrate. This immunosensor was fabricated by immobilization of anti-aflatoxin monoclonal antibodies (Ab-AFB1) and bovine serum albumin (BSA) for aflatoxin B1 detection. The structural and morphological studies of n-Bi_2O_3 have been carried out by XRD, UV–vis spectrophotometer; SEM, AFM and FTIR. It was found that the nBi_2O_3 provided improved sensing characteristics to the electrode interface in terms of electroactive surface area, diffusion coefficient, charge transfer rate constant and electron transfer kinetics. The results of electrochemical response studies of this BSA/Ab-AFB1/nBi_2O_3/ITO immunosensor revealed good linearity in the range of 1–70 ng dL^{-1} with low detection limit of 8.715 ng/dL, improved sensitivity of 1.132 μA/(ng/dL cm^{-2}), regression coefficient R^2 of 0.918 and reproducibility of >11 times. The association constant for the BSA/Ab-AFB1/nBi_2O_3/ITO immunosensor was determined as 7.318 ng/dL.

© 2016 Elsevier B.V. All rights reserved.

1. Introduction

The nanostructured metal oxides have recently aroused much attention of researchers actively engaged in different scientific disciplines including materials science, bioscience and nanotechnology due to their interesting properties and potential applications [1,2]. In the past decade, several researches on the synthesis of low-dimensional nanostructures are underway [3,4]. Their attractive properties and a wide range of applications have been attributed to their interesting structures. Bismuth and its compounds are fascinating to scientists due to their unique structures and properties [5] such as highly anisotropic Fermi surface, high refractive index, dielectric permittivity and low carrier densities [6,7]. Therefore, it has been widely used for the development of solid oxide fuel cells, gas sensors, photoelectric materials, high temperature superconductor materials, catalysts, functional ceramics [8–11]. Recently, 1D metal oxides have been found to display high surface basicity, fast oxygen ion mobility, efficient charge transfer ability and interesting catalytic properties [12,13]. These properties have been predicted to be useful for investigating the effect of both dimensionality and size on physical properties, and also for application in nanodevices [3]. Bismuth oxide (Bi_2O_3) based compounds are known to be better solid electrolytes than those of zirconia since the face-centred cubic (fcc) Bi_2O_3 has been found to exhibit the highest ion conductivity of all oxide ion conductors.

Bi_2O_3 is one of the important metal oxides since it plays a significant role in modern solid-state technology due to its peculiar properties such as wide band gap, high refractive index, high dielectric permittivity, high oxygen conductivity, resistivity, photoconductivity and photoluminescence, etc. Its excellent properties have been found to have a variety of applications such as catalysts, optical coatings [14], photovoltaic cells, microwave integrated circuits, fuel cells [15], nanoenergetic gas generator [16] and in the fabrication of sensors [17,18]. Moreover, they have been predicted to provide a favorable environment for the biomolecules adsorption, nontoxicity, chemical inertness, biocompatibility, greater surface free energy, and good electrochemical stability, etc. [19,20]. Recently, Bi_2O_3 film has been utilized for the detection of phenolic compounds using amperometric biosensors [21]. A composite of Bi_2O_3 with chitosan has been used for the fabrication of an electrochemical DNA biosensor [18]. Ding et al. have fabricated a nano-Bi_2Ox electrode for glucose detection by amperometric technique [19]. A nanocomposite of Bi_2O_3-multi walled carbon nanotubes (MWCNTs) onto glassy carbon electrode (GCE) has utilized for hydrogen peroxide detection [20]. A lithium doped bismuth oxide - MWCNTs modified GCE has found application in monitoring electrocatalytical behavior of ascorbic acid [22,23].

The contamination of food by mycotoxins is currently a matter of great concern, as these are responsible for many diseases [24,25]. Worldwide, about 25% of crops are annually affected by toxigenic fungi. Thus, mycotoxins have become a part of the food chain. High levels of mycotoxins in the diet can cause adverse acute and chronic effects on humans and animals. These may particularly affect liver, kidney,

* Corresponding authors at: DST Centre for Biomolecular Electronics, CSIR-National Physical Laboratory, K.S. Krishnan Marg, New Delhi, India.
E-mail addresses: pratimarsolanki@gmail.com (P.R. Solanki), bansi.malhotra@gmail.com (B.D. Malhotra).

http://dx.doi.org/10.1016/j.msec.2016.09.027
0928-4931/© 2016 Elsevier B.V. All rights reserved.

nervous system, endocrine and immune systems [26]. Aflatoxin B1 (AFB1) is one of the most potent toxic substances as compared to other types of aflatoxins i.e. B_2, B_3, G_1 and G_2 that occur naturally. AFB1 is known to be carcinogenic, mutagenic, immunosuppressive agents that are a group of closely related mycotoxins produced by fungi *Aspergillus flavus* and *A. parasites* in fruit, vegetable and food product [27]. The aflatoxins may cause contamination of nuts (almonds, walnuts), cereals (rice, wheat, maize) and oilseeds (soybean and peanuts). Some of the conventional methods currently being used for mycotoxins detection include thin layer chromatography liquid chromatography, high-performance liquid chromatography, immune-chromatography, enzyme-linked immunosorbent assay [28,29]. These techniques are time consuming, expensive, and require high skilled manpower, sometimes may give unreliable results for food and biological samples due to the difficulty in obtaining a clear solution for analysis. Thus, there is an urgent need for the development of reliable, rapid, quick and sensitive method for detection of aflatoxins. Kalita et al. have fabricated ring like nickel nanoparticles (RnNi) NPs of 10–20 nm through pulsed laser ablation method for an electrochemical immunosensor for AFB1 detection. This bioelectrode shows the linearity as 5–100 ng dL^{-1}, sensitivity of 0.59 μA/ng dL^{-1} with detection limit of 32.7 ng dL^{-1} [30]. Singh et al. used samarium oxide nanorods modified ITO electrode for the co-immobilization of Ab-AFB1. This fabricated immunoelectrode (BSA/Ab-AFB_1/n-Sm_2O_3/ITO) showed the detection of AFB1 in a range of 10–700 pg mL^{-1} with sensitivity and detection limit of 48.39 μA pg^{-1} mL^{-1} cm^{-2} and 57.82 pg mL^{-1} cm^{-1}, respectively [31]. The microelectrode was fabricated using 2-aminoethane thiol (AET) on Au electrode and used for fabrication of immunosensor by self assembling of horseradish peroxidase (HRP) and AFB1 antibody molecules for AFB1 detection [32]. The linear range was found to be from 0.5 to 10 ng mL^{-1} with a relatively low detection limit of 0.1 ng mL^{-1}. Glassy carbon electrode (GCE) consisting of chitosan/Au nanoparticle/anti-AFB_1, and a Fe_3O_4 magnetic core with a gold shell functionalized with 3-((2-mercaptoethylimino) methyl) benzene-1,2-diol for the detection of AFB1 [33]. This immunoelectrode revealed the detect range of 0.6–110 ng mL^{-1} with a detection limit of 0.2 ng mL^{-1} for AFB1. Polythionine (PTH)/AuNP modified GCE based electrochemical immunosensor exhibited a linear range of 0.6–2.4 ng mL^{-1} AFB1 and a limit of detection of 0.07 ng mL^{-1} AFB1 for the determination of aflatoxin B1 [34].

We report results of studies relating to the preparation of Bi_2O_3 nanorods *via* sol-gel method for development of an immunosensor for aflatoxin AFB1 detection. It is shown that the Ab-AFB1/nBi_2O_3/ITO bioelectrode exhibits improved sensitivity, low detection limit and wide detection range (Table 1).

2. Materials and methods

2.1. Materials

Bismuth nitrate [$Bi(NO_3)_3 \cdot 5H_2O$], polyethylene glycol (PEG), nitric acid (HNO_3) were purchased from MERCK (New Delhi, India). Aflatoxin B1 (AFB1), anti-aflatoxin B1 mouse monoclonal antibodies (Ab-AFB1) and bovine serum albumin (BSA, 98%) were procured from Sigma-Aldrich (USA). All other chemicals were of analytical grade and used without further purification. The indium-tin-oxide (ITO) coated glass (Balzers) sheet of resistance 15 W/cm was used as substrate for deposition of the desired nanocomposite that worked as the working electrode. All solutions in these studies were prepared using deionized water of resistivity of not less than 18 MΩ taken from a Milli-Q water purification system (Milli-Q, USA).

2.2. Preparation of antibody aflatoxin B1 (Ab-AFB1) and bovine serum albumin (BSA) solutions

The stock solution of AFB1 was freshly prepared in phosphate buffer (50 mM, pH 7.0) with 10% methanol and aliquoted in different working concentrations (1–70 ng dL^{-1}). Ab-AFB1 was prepared in phosphate buffer (50 mM, pH 7.0) prior to being used. 0.15 M sodium azide (NaN_3) was added into both these solutions as a preservative and stored at −20 °C when not in use. The bovine serum albumin (BSA, 98%) was freshly prepared (2 mg mL^{-1}) in phosphate buffer (50 mM, pH 7.0) and used as blocking agent for non-specific binding sites.

2.3. Synthesis of Bi_2O_3 nanorods

In a typical procedure, 0.05 mol $Bi(NO_3)_3$ was dissolved into 30 mL of 0.05 mol/L HNO_3 to get transparent Bi^{3+} acidic solution. 20 mL polyethylene glycol (PEG-600) was added drop wise as a dispersant to the above solution and magnetically stirred for 2 h at room temperature. 50 mL of NaOH (4 mol) aqueous solutions was quickly poured into it under vigorous stirring resulting in a yellow solution. The resultant yellow solution was stirred at 90 °C for 2 h. Then it was filtered and washed with deionized water and ethanol for 5–10 times. The precipitation was dried at 70 °C for 12 h in vacuum drier to obtain faint yellow Bi_2O_3 nanorods.

2.4. Preparation of nBi_2O_3 films by electrophoretic deposition

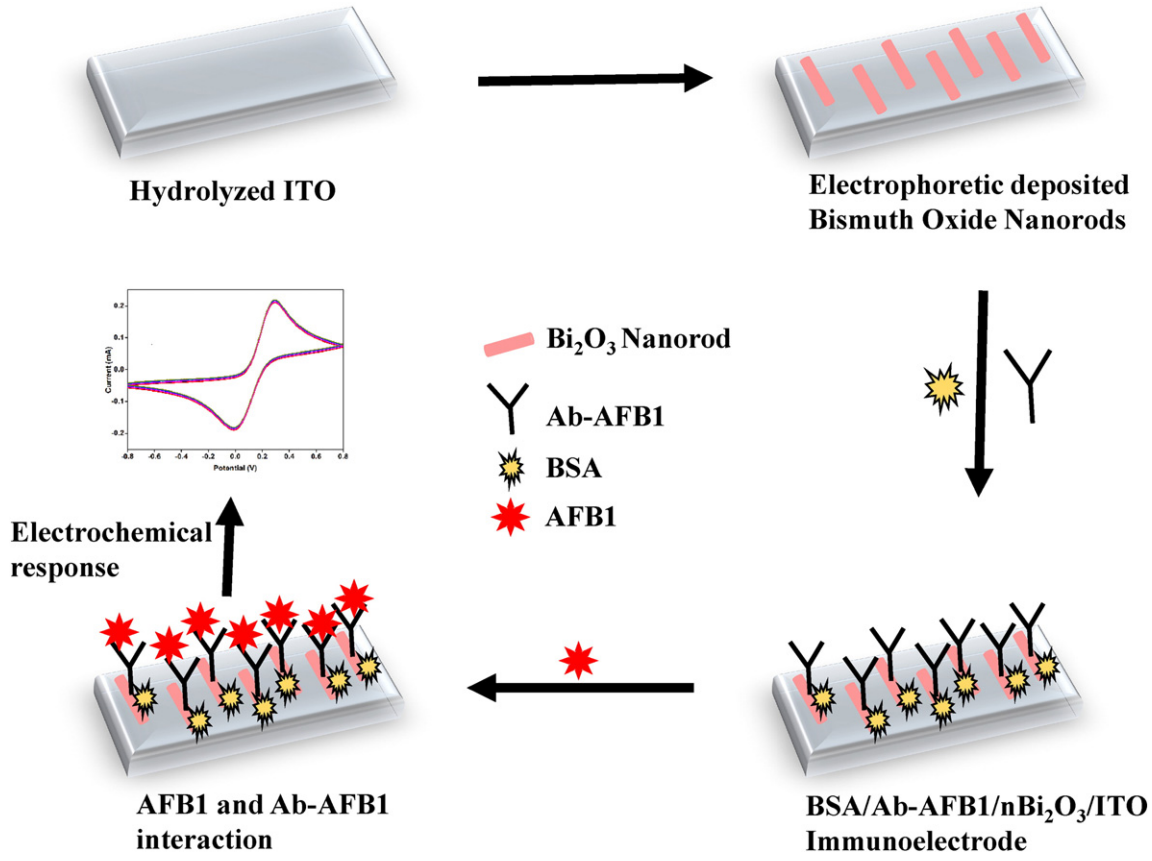
Electrophoretic deposition (EPD) was carried out by using a DC battery (BioRad, Model 200/2.0). Prior to deposition of nBi_2O_3 onto ITO substrate, uniform suspension of known amount of nBi_2O_3 (10 mg) was prepared in de-ionized water (1 mg mL^{-1}) through vigorous stirring followed by sonication for about 1 h. During EPD, a platinum foil (1 cm × 2 cm) was used as the anode and a hydrolyzed ITO coated glass plate as cathode. The two electrodes, placed parallel to each other with separation of 1 cm, were dipped in the nBi_2O_3 colloidal suspension. The colloidal suspension solution consisted of positively charged nBi_2O_3 nanoparticles. Since ITO plates were hydrolyzed, OH group were present on its surface. The optimized condition for EPD of Bi_2O_3 nanorods onto ITO plates was obtained as 10 V for 20 s as the nBi_2O_3 film exhibits maximum amperometric current at this condition. During the process positively charged Bi_2O_3 nanorods were attracted with OH group present on ITO surface *via* electrostatic interaction. Thus nBi_2O_3 (0.25 cm^2) was deposited onto ITO plate. This nBi_2O_3/ITO electrode was washed with deionized water followed by ethanol to remove any unbound particles and dried at room temperature (25 °C) for 12 h.

2.5. Fabrication of immunoelectrode

The optimal amount of freshly prepared solution (10 μL) of Ab-AFB1 was uniformly spread onto the desired nBi_2O_3/ITO electrode surface and

Table 1
Characteristics of the BSA/Ab-AFB1/nBi_2O_3/ITO immunoelectrode along with those reported in the literature for aflatoxin B1 detection, with their important parameters.

Bioelectrode	Detection method	Sensitivity	Limit of detection	Detection range	Stability (days)	Ref.
RnNi-film/ITO	Electrochemical	0.59 μA/ng dL^{-1}	32.7 ng dL^{-1}	5–100 ng dL^{-1}	60	[30]
BSA/anti-AFB1/MWCNTs/ITO	Electrochemical	95.2 mA ng/mL cm^{-2}	0.08 ng mL^{-1}	0.25–1.375 ng mL^{-1}	45	[31]
BSA-anti-AFB1/Au NPs	Conductometric	–	10.1 ng mL^{-1}	0.5–10 ng mL^{-1}	12	[32]
GCE/chitosan/AuNP/aAFB1	Electrochemical	–	0.2 ng mL^{-1}	0.6–110 ng mL^{-1}	–	[33]
PTH/AuNP/GCE	Electrochemical	–	0.07 ng mL^{-1}	0.6–2.4 ng mL^{-1}	–	[34]
BSA/Ab-AFB1/nBi_2 O_3/ITO	Electrochemical	1.132 μA ng/dL cm^{-2}	8.72 ng dL^{-1}	1–70 ng dL^{-1}	15	Present work



Scheme 1. Schematic representation of fabrication of the Ab-AFB1/nBi_2O_3/ITO immunosensor.

kept undisturbed in a humid chamber for about 12 h at 25 °C. The Ab-AFB1/nBi_2O_3/ITO bioelectrode was washed thoroughly with phosphate buffer (50 mM, pH 7.0) to remove any unbound antibodies followed by drying at room temperature (25 °C). The non-specific binding sites of the modified Ab-AFB1/nBi_2O_3/ITO bioelectrode were blocked by using bovine serum albumin (BSA, 98%). 10 μL freshly prepared BSA solution (1 mg mL^{-1}) was uniformly spread over Ab-AFB1/nBi_2O_3/ITO bioelectrode and kept overnight in a humid chamber at room temperature (25 °C) followed by washing with phosphate buffer (50 mM, pH 7.0) to remove any unbound biomolecules. The optimal amount of Ab-AFB1 (10 μL) and BSA (10 μL) to obtain the maximum magnitude of current response in PBS (50 mM, pH 6.0, 0.9% NaCl) containing $[Fe(CN)_6]^{3-/4-}$ (5 mM) at 20 mV/s scan rate using CV technique. This fabricated Ab-AFB1/nBi_2O_3/ITO bioelectrode was dried and was further used for characterization and AFB1 detection.

Scheme 1 shows the stepwise fabrication of the Ab-AFB1/nBi_2O_3/ITO bioelectrode along with the interaction between AFB1 and Ab-AFB1 on the nBi_2O_3/ITO electrode surface. The nBi_2O_3 carries positive charge and Fac part (COO^- group) of Ab-AFB1 is negative charge which could bind electrostatically onto nBi_2O_3/ITO surface. The adsorption of Ab-AFB1 on the nBi_2O_3/ITO retains their bioactivity due to their biocompatibility.

2.6. Characterizations techniques

The structure, shape and crystallite size of synthesized nBi_2O_3 nanoparticles were investigated using X-ray diffraction (XRD), Rigaku D/Max 2200 diffractometer with CuKα radiation 10 at λ = 1.5406 Å. FT-IR spectra of the electrode was recorded with FTIR spectrophotometer (PerkinElmer, Spectrum BX II). Transmission electron microscopy (TEM) studies were carried with JEOL JEM-2200 FS (Japan). The surface morphological studies of Ab-AFB1/nBi_2O_3/ITO bioelectrode and BSA/Ab-AFB1/nBi_2O_3/ITO immunosensor were investigated using atomic force microscopy (AFM, Model Vicco 440, Nanoscope) and Scanning Electron Microscopy (SEM, Zeiss, EVO, 40). The cyclic voltammetry (CV), differential pulse voltammetry (DPV) and electrochemical impedance spectroscopy (EIS) measurements were recorded on an Autolab Potentiostat/Galvanostat (Eco Chemie, The Netherlands). The electrochemical measurements were conducted on a three-electrode system with BSA/Ab-AFB1/nBi_2O_3/ITO immunoelectrode as the working electrode, a platinum (Pt) wire as the counter electrode, and saturated Ag/AgCl electrode as a reference electrode in phosphate buffer saline (PBS, 50 mM, pH 6.0, 0.9% NaCl) containing 5 mM $[Fe(CN)_6]^{3-/4-}$ as a mediator.

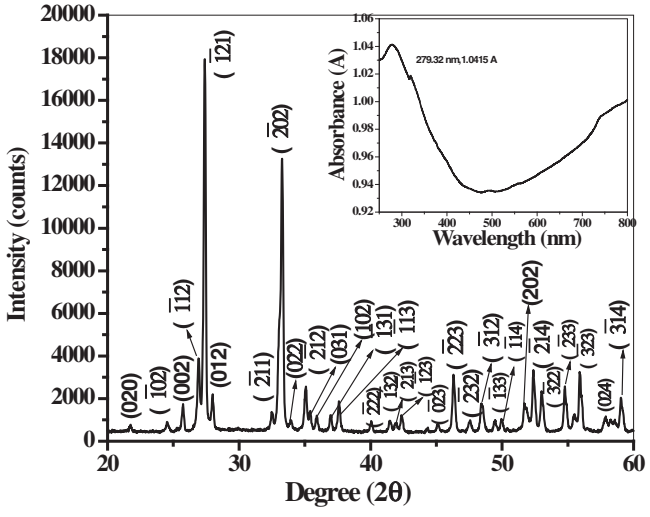
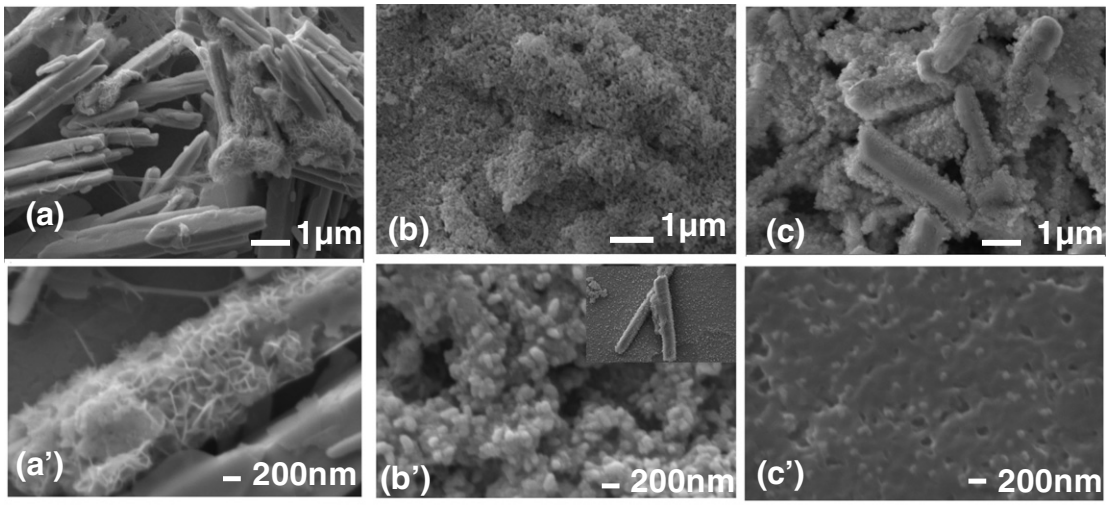


Fig. 1. X-ray diffraction pattern of nanostructured Bi_2O_3. Inset shows UV–vis spectrum of Bi_2O_3 nanoparticles.

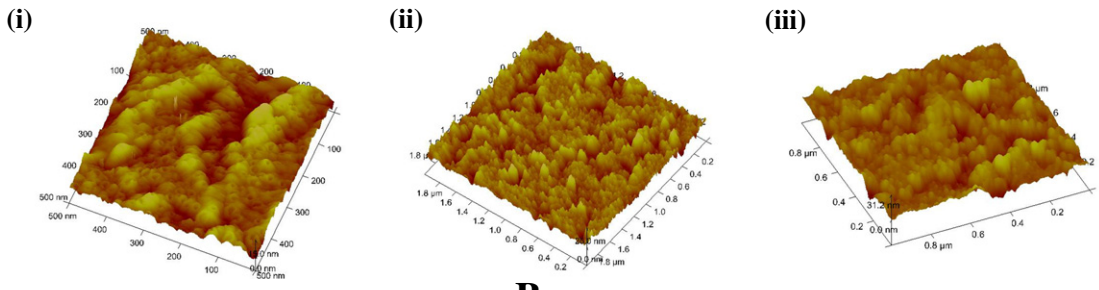
3. Results and discussions

3.1. Structural and morphological studies

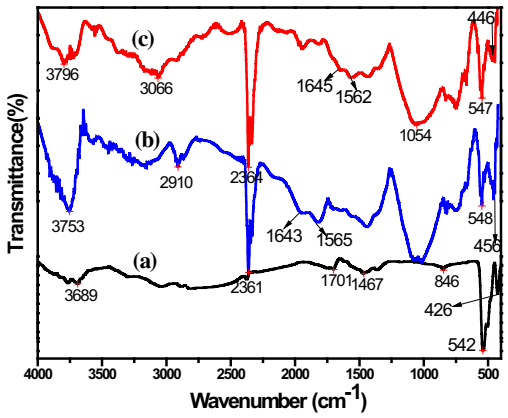
The X-ray diffraction pattern obtained for the synthesized product is shown in Fig. 1. All the diffraction peaks could be indexed to single phase of monoclinic Bi_2O_3 (α-Bi_2O_3). The calculated lattice constants (a = 5.849 Å, b = 8.169 Å, and c = 7.511 Å) are in good agreement with the standard values of a = 5.848 Å, b = 8.166 Å, and c = 7.510 Å (JCPDS 27-0053) that confirm the formation of crystalline structure. The XRD pattern shows reflection planes in (002), (−112), (−202), (−212), (−232), (−214), (−323) and (400). No peak



A



B



C

Fig. 2. (A): SEM image of (a) nBi_2O_3/ITO electrode, (a′) extended image of (a); (b) Ab-AFB1/nBi_2O_3/ITO bioelectrode, (b) extended image of (b), (c) BSA/Ab-AFB1/nBi_2O_3/ITO immunoelectrode (c′) extended image of (c). (B): AFM image of (i) nBi_2O_3/ITO, (ii) Ab-AFB1/nBi_2O_3/ITO bioelectrode, (iii) BSA/Ab-AFB1/nBi_2O_3/ITO immunoelectrode. (C): FTIR spectra of (a) nBi_2O_3/ITO electrode, (b) Ab-AFB1/nBi_2O_3/ITO bioelectrode (c) BSA/Ab-AFB1/nBi_2O_3/ITO immunoelectrode.

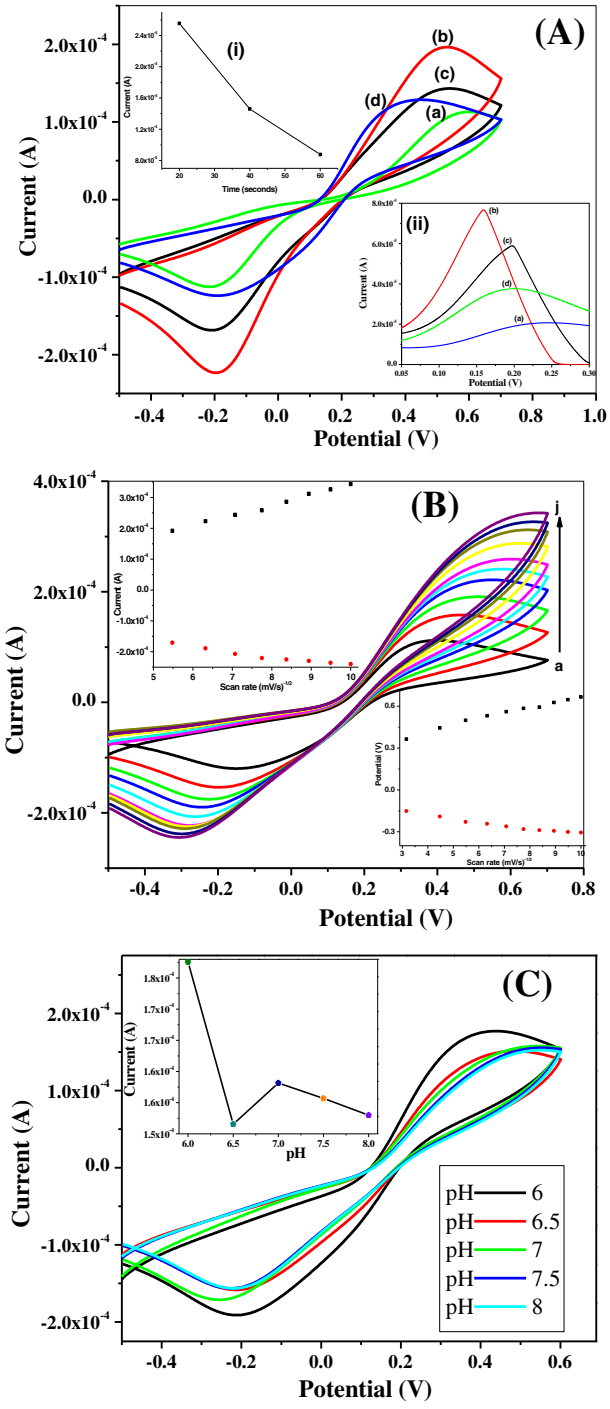


Fig. 3. (A): Cyclic voltammogram (CV) obtained for (a) bare ITO electrode (b) nBi_2O_3/ITO electrode (c) Ab-AFB1/nBi_2O_3/ITO bioelectrode (d) BSA/Ab-AFB1/nBi_2O_3/ITO immunoelectrode. Inset (i) shows the optimization of time for nBi_2O_3 film deposited onto ITO surface. Inset (ii) shows the DPV of (a) bare ITO electrode, (b) nBi_2O_3/ITO electrode, (c) Ab-AFB1/nBi_2O_3/ITO bioelectrode, (d) BSA/Ab-AFB1/nBi_2O_3/ITO immunoelectrode. (B): CV of BSA/Ab-AFB1/nBi_2O_3/ITO immunoelectrode as a function of scan rate. The inset shows the linearity of the oxidation and reduction peak currents. (C): CV of BSA/Ab-AFB1/nBi_2O_3/ITO immunoelectrode as a function of pH varies from 6.0–8.0. Inset shows the plot between oxidation current and pH valve.

corresponding to any impurity was detected, suggesting single crystalline nature of Bi_2O_3. The average crystallite size found to be as ~55 nm was calculated by the Scherrer formula as shown below (Eq. (1)).

$$D = \frac{0.9\lambda}{\beta \cos\theta} \quad (1)$$

where, D is the crystallite size in Å, β is the full width at half maxima (FWHM) of the diffraction peaks, θ is the glancing angle and (λ = 1.54060 Å) is the wavelength of X-ray.

The UV–visible spectrum shows a strong absorption peak at 279 nm which corresponds to the Bi^{3+} in Bi_2O_3 as compared to bulk (~320) nm [35] (inset Fig. 1). This result shows a blue shift ~41 nm indicating the formation of the nanostructured Bi_2O_3. The absorption of a photon, leading to excitation of an electron from the valence band to the conduction band in the semiconductor, is referred to as band gap energy (Eg). Compared to polycrystalline material, the nanoparticles often show a shift of the band gap energy (Eg) towards higher value due to decrease in the size of the particle. The blue shift of 24–26 nm of the absorption band is observed in the absorption spectra. This is due to the fact that the nanostructures are laterally quantum confined and occupy energy levels that are different from the traditional continuum of energy levels or bands found in a bulk material.

The surface morphological studies of nBi_2O_3/ITO film, Ab-AFB1/nBi_2O_3/ITO bioelectrode and BSA/Ab-AFB1/nBi_2O_3/ITO immunosensor investigated using SEM are shown in Fig. 2A(a–c; a′–c′), respectively. SEM image (a) of nBi_2O_3/ITO clearly reveals uniform distribution of 1D nanostructure (nanorods ID) that provides a fibrous morphology due to electrophoretic deposition of nBi_2O_3 on ITO plates. The bundles of nanorods observed with different size provide rough provide high surface-to-volume ratio resulting in enhanced loading of antibodies. Image (a′) shows that the single nanorods have a fibrous morphology. The image (b) exhibits that the antibodies Ab-AFB1 are fully covered with the nanorods in the form of small granular structure that confirms the immobilization of antibodies onto the nBi_2O_3/ITO electrodes. The image (b′) clearly shows that the individual nanorod can be used to load higher amount of Ab-AFB1. However, after the immobilization of BSA onto the Ab-AFB1/nBi_2O_3/ITO bioelectrode [image (c, c′)] results in the increased granules size of the Ab-AFB1 immobilized nanorods indicating blocking of the non-specific sites. This confirms the immobilization of BSA onto Ab-AFB1/nBi_2O_3/ITO bioelectrode.

The morphological studies of nBi_2O_3/ITO film, Ab-AFB1/nBi_2O_3/ITO bioelectrode and BSA/Ab-AFB1/nBi_2O_3/ITO immunosensor were investigated using atomic force microscopy (AFM), respectively [Fig. 2B]. The AFM image of nBi_2O_3/ITO revealed that the nanorods were open on the top surface indicating nanoporous morphology [image (a)]. After the immobilization of antibodies Ab-AFB1 onto the nBi_2O_3/ITO films, the nanoporous morphology changed to granular form [image (b)] indicating immobilization of Ab-AFB1 onto the nBi_2O_3/ITO electrodes. This could be assigned to electrostatic interaction between the positive charge of matrix nBi_2O_3/ITO electrode and the negative charge of carboxyl group of antibody AFB1. The AFM image (c) showed that the surface morphology of Ab-AFB1/nBi_2O_3/ITO bioelectrode changed after the immobilization of BSA. As compared to the nBi_2O_3 film, the average peak height (Rpm) decreased after immobilization of Ab-AFB1 (4.59 nm) onto nBi_2O_3/ITO surface (7.28 nm) and increased after the immobilization of BSA (4.94 nm). The variation of the peak-to-valley height (R_{max}) measured as 61.3 nm for nBi_2O_3/ITO electrode decreased to 36.7 nm for Ab-AFB1/nBi_2O_3/ITO bioelectrode, then further decreased to 31.8 nm for the BSA/Ab-AFB1/nBi_2O_3/ITO immunosensor.

The FTIR spectrum obtained for the synthesized Bi_2O_3 nanorods in the range of 400–4000 cm^{-1} is shown in Fig. 2C (a). Four characteristic bands can be clearly seen from Fig. 2C (a), in which the broad band at 3689 cm^{-1} corresponds to the stretching vibration of OH, while the band appearing at 1701 cm^{-1} and 1467 cm^{-1} represents the stretching mode of absorbed H_2O. In addition, the band located at 1350 cm^{-1} can be ascribed to the bending vibration of NO_3^-, this suggests that the as-synthesized BiOx contains a large amount of NO_3^- groups that are crucial for further surface functionalization and coating by any other functional groups. The band 846 cm^{-1} is due to Bi—O—Bi and band at 542 and 426 cm^{-1} are attributed to the stretching mode of Bi—O metal oxide bond. The additional bands at 2365 and 1014 cm^{-1} for nBi_2O_3/ITO

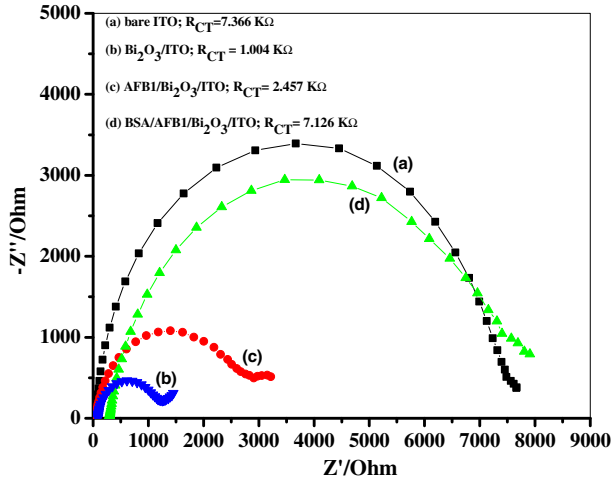


Fig. 4. EIS of (a) bare ITO electrode, (b) nBi_2O_3/ITO electrode, (c) Ab-AFB1/nBi_2O_3/ITO bioelectrode, (d) BSA/Ab-AFB1/nBi_2O_3/ITO immunoelectrode.

film were attributed to the carbonate and sulphate impurity present during the film formation. The antibody Ab-AFB1 conjugated in nBi_2O_3/ITO electrode Fig. 2C (b) resulted in the increase in carbonyl absorption at 1643 cm^{-1} and the broad strong band observed at 3753 cm^{-1}. However, after immobilization of antibodies, the characteristic peaks containing NH_3^+ of amide I band appeared at 1643 cm^{-1} and NH bending of amide II band at 1565 cm^{-1} indicating immobilization of antibodies onto Bi_2O_3/ITO film. The metal band (M-O) stretching of Ab-AFB1/Bi_2O_3/ITO immunoelectrode increased in comparison to nBi_2O_3/ITO film indicating the presence of electrostatic interaction. The spectra of BSA/Ab-AFB1/nBi_2O_3/ITO immunoelectrode [Fig. 2C (c)] shows lowering of wave number value in compression to that of Ab-AFB1/nBi_2O_3/ITO immunoelectrode due to deactivation at the binding sites of Ab-AFB1.

3.2. Electrochemical studies

The cyclic voltammograms (CV) obtained for various nBi_2O_3 based electrodes in phosphate buffer (50 mM, pH 6.0, 0.9% NaCl) containing $[Fe(CN)_6]^{3-/4-}$ at a scan rate of 20 mV/s are shown in Fig. 3A. It can be seen that the anodic potential (Fig. 4) shifted towards the higher current and the cathodic peak potential shifts in the reverse direction. In case of the nBi_2O_3/ITO electrode (curve b), the magnitude of peak current is increased as compare to ITO electrode (curve a). This suggests that electrophoretically deposited nBi_2O_3/ITO electrode promotes fast electron transfer due to the formation of a continuous array of Bi_2O_3 nanoparticles throughout the electrophoretic network at the electrode. Moreover, the value of the peak current is decreased after the immobilization of Ab-AFB1 onto the nBi_2O_3/ITO electrode (curve c). This may be attributed to the available non-binding sites onto Ab-AFB1 and nBi_2O_3/ITO electrode that play an important role in deaccelerating electron transfer between Ab-AFB1 and the nBi_2O_3/ITO electrode. Further, the magnitude of current is decreased after the immobilization of BSA (curve d) revealing that the blocking of non-binding sites of Ab-AFB1 hinders electron transfer between medium and electrode, indicating the immobilization of BSA onto the Ab-AFB1/nBi_2O_3/ITO bioelectrode. The optimization time for film deposition [inset Fig. 3A(i)] was found to be as 20 s indicating that Bi_2O_3 was highly charged and it moved faster towards ITO electrode.

The differential pulse voltammograms (DPV) obtained for the ITO electrode (curve a), nBi_2O_3/ITO electrode (curve b), Ab-AFB1/nBi_2O_3/ITO bioelectrode (curve c), BSA/Ab-AFB1/nBi_2O_3/ITO immunosensor (curve d) are shown in Fig. 3A [inset (ii)]. The DPV studies showed similar response as those of the CV studies. The magnitude of anodic peak current of ITO was the lowest (curve a). It increased after nBi_2O_3 was electrophoretically deposited onto ITO surface (curve b). The anodic peak current decreased after immobilization of Ab-AFB1 onto nBi_2O_3/ITO electrode (curve c). It decreased further on immobilization of BSA onto Ab-AFB1/nBi_2O_3/ITO bioelectrode (curve d).

The CV of the BSA/Ab-AFB1/nBi_2O_3/ITO immunosensor obtained as a function of scan rate varying from 10 to 100 mV/s is shown in Fig. 3B. It was found that the potential and the magnitude of currents were dependent on scan rate. The magnitudes of both anodic (Epa) and cathodic (Epc) peak currents and potential peak shift ($\Delta Ep = Epa - Epc$) increased linearly with the scan rate suggesting that the electrode reaction was a diffusion controlled process. It was also observed that the peak height varied directly with the sweep rate (with linear regression coefficient 0.918), indicating improved electrocatalytic behavior. Thus this nBi_2O_3/ITO can be used for the immobilization of Ab-AFB1 providing sufficient accessibility to electrons to shuttle between the antibody and the electrode. The surface concentration of the BSA/Ab-AFB1/nBi_2O_3/ITO immunosensor was estimated from the plot of current versus potential (CV) using Brown-Anson model that is based on the following equation:

$$Ip = \frac{n^2 F^2 I^* AV}{4RT} \quad (2)$$

where n is the number of electrons transferred (1), F is the Faraday constant (96,485 C/mol), I^* is the surface concentration of the BSA/Ab-AFB1/nBi_2O_3/ITO immunosensor (mol cm^{-2}), A is the surface area of the electrode (0.25 cm^2), V is the scan rate (20 mV/s), R is the gas constant (8.314 J mol^{-1} K^{-1}) and T is the room temperature (300 K). The surface concentration of nBi_2O_3/ITO was calculated as 4.22×10^{-11} mol/cm^2 which decreases to 3.08×10^{-11} mol/cm^2 for Ab-AFB1/nBi_2O_3/ITO bioelectrode and further decreased to 2.77×10^{-11} mol/cm^2 for BSA/Ab-AFB1/nBi_2O_3/ITO immunosensor.

3.3. Effect of pH

The effect of pH value on the performance of the biosensor is of great importance, because the activity of the immobilized antibody is pH dependent. The effect of pH (ranging from 6 to 8) onto BSA/Ab-AFB1/nBi_2O_3/ITO immunosensor was investigated using CV technique in PBS (50 mM 0.9% NaCl) containing $[Fe(CN)_6]^{3-/4-}$ at scan rate of 20 mV/s (Fig. 3C). It was found that magnitude of the peak current decreased and the peak potential shifted towards higher potential on increasing the pH. This could be due to decrease in the concentration of positively charged moieties present onto nBi_2O_3 matrix as pH of PBS approaches towards its isoelectric point resulting in decreased interaction between redox ions $[Fe(CN)_6^{3-/4-}]$ onto nBi_2O_3 surface. This resulted in increased hindrance in electron transport between the medium and electrode leading to decreased value of electrochemical signal at elevated pH. In the case of BSA/Ab-AFB1/nBi_2O_3/ITO immunosensor, magnitude of change in current response was higher at pH 6 and decreased from 6.0 to 6.5 (Fig. 3C). This result suggested that BSA/Ab-AFB1/nBi_2O_3/ITO immunosensor could be used at pH 6.0 for aflatoxin B1 detection. Moreover, it appeared that higher pH was responsible for desorption of the biomolecule, and the current response decreased by ~19% at pH < 8.0. Thus all the experiments were conducted at pH 6.0. The results of electrochemical measurements conducted in triplet sets under identical conditions revealed good reproducibility. Thus pH 6.0 was selected for the subsequent experiments.

3.4. Electrochemical impedance spectra

The EIS of bare ITO electrode, nBi_2O_3/ITO electrode, Ab-AFB1/nBi_2O_3/ITO bioelectrodes and BSA/Ab-AFB1/nBi_2O_3/ITO immunosensor in PBS

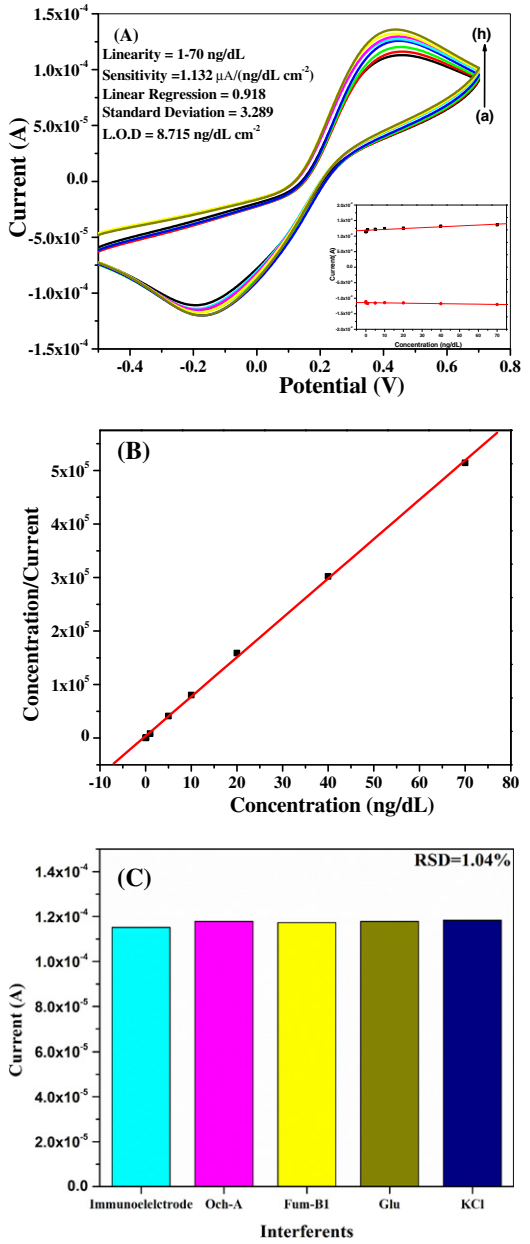


Fig. 5. (A): Electrochemical response studies of the BSA/Ab-AFB1/nBi_2O_3/ITO immunoelectrode as a function of aflatoxin B1 concentration using CV. Inset shows the linear fit curve of sensitivity of BSA/Ab-AFB1/nBi_2O_3/ITO immunoelectrode. (B): Hanes plot between the substrate concentration and substrate concentration/current obtain from previous figure [Fig. 5A]. (C): Selectivity studies of BSA/Ab-AFB1/nBi_2O_3/ITO immunoelectrode.

containing $[Fe(CN)_6]^{3-/4-}$ in the frequency range, 0.00–10^7 Hz was studied by monitoring charge transfer resistance (R_{CT}) at the electrode and electrolyte interface (Fig. 4). In the EIS, the semicircle part corresponds to electron-transfer limited process and its diameter is equal to the electron transfer resistance, R_{CT} that controls electron transfer kinetics of the redox probe at the electrode interface [36]. It can be seen from the Nyquist plots that semicircle of the nBi_2O_3/ITO electrode (R_{CT} = 1.005 KΩ; curve b) is smaller than that of the bare ITO electrode (R_{CT} = 7.366 KΩ; curve a). This suggested that nBi_2O_3 resulted in improved conductivity of the electrode. Further, the R_{CT} value increased after the immobilization of Ab-AFB1 onto the nBi_2O_3/ITO electrode (curve c) indicating that non-binding sites on Ab-AFB1 perhaps facilitated electron transfer between the Ab-AFB1/nBi_2O_3/ITO bioelectrode and electrolyte. Moreover, R_{CT} increased after immobilization of BSA onto the Ab-AFB1/nBi_2O_3/ITO bioelectrode (curve d), revealing hindrance in electron communication between the BSA/Ab-AFB1/nBi_2O_3/ITO immunosensor and electrode. Thus, R_{CT} value was obtained in the sequence: R_{CT} (curve b) < R_{CT} (curve c) < R_{CT} (curve d) < R_{CT} (curve a). The value of R_{CT} is dependent on electrochemical reaction time constant, τ (τ = $1/2\pi f_{max}$ = Rp·CdL, where f_{max} is the frequency at which maximum Z'' is obtained, Rp is the polarization resistance and CdL is the double layer capacitance).

3.5. Electrochemical response studies

The electrochemical response of the BSA/Ab-AFB1/nBi_2O_3/ITO immunosensor was investigated as a function of aflatoxin B1 concentration (0.125–70 ng dL^{-1}) using the CV techniques [Fig. 5A]. The magnitude of current was found to increase on addition of aflatoxin B1. This was attributed to the formation of an antigen-antibody complex between aflatoxin B1 and Ab-AFB1 on the electrode surface that acted as an electron transfer accelerating layer for transfer of electrons. The BSA/Ab-AFB1/nBi_2O_3/ITO immunosensor exhibited good linearity in the range of 1–70 ng dL^{-1} with low detection limit of 8.715 ng/dL cm^{-2}, linear regression coefficient R^2 of 0.918 and reproducibility of >11 times. The sensitivity of the BSA/Ab-AFB1/nBi_2O_3/ITO immunosensor calculated from the slope of curve was found to be 1.132 μA/(ng dL^{-1} cm^{-2}). The standard deviation from the linear regression analysis for the bioelectrode was found to be 3.289 μA. Fig. 5B shows the Hanes plot between the substrate concentration and substrate concentration/current obtained from Fig. 5A. The association constant (K_a) for the BSA/Ab-AFB1/nBi_2O_3/ITO immunosensor, estimated by Hanes plot i.e. graph between [substrate concentration] and [substrate concentration/current] [Fig. 5B] was found to be as 7.318 ng dL^{-1}. The value of K_a is known to depend on various factors such as matrix and the method of immobilization of antibodies that could bring different conformational changes in the antibody structure. The small K_a value indicates that increased affinity of BSA/Ab-AFB1/nBi_2O_3/ITO immunosensor can be attributed to favorable conformation of Ab-AFB1 and higher loading onto nBi_2O_3/ITO electrode surface.

The reproducibility of the proposed BSA/Ab-AFB1/nBi_2O_3/ITO immunosensor was estimated by repetitive measurement of current response with 25 ng dL^{-1} standard AFB1 solutions in PBS. The results obtained in five repeated measurements show an RSD of 2–3%, indicating that the obtained data are reproducible.

The selectivity test of BSA/Ab-AFB1/nBi_2O_3/ITO immunoelectrode was performed with the mycotoxins [Ochratoxin A (Och A), Fumonisin B1 (Fum B1)], glucose (Glu) and potassium chloride (KCl), which are generally present in milk. The interferent solutions were of normal concentrations: Och A (7 mg mL^{-1}); Fum B1 (8.38 mM); Glu (1 ng mL^{-1}) and KCl (100 pg mL^{-1}) was used [Fig. 5C]. The electrochemical behavior of BSA/Ab-AFB1/nBi_2O_3/ITO immunoelectrode was monitored in the presence of these interferents under similar condition using CV technique. It was found that there was not much change in magnitude of current in the presence of these interferents. We observed a low relative standard deviation (RSD) of 1.04%, indicating negligible interferents with other analytes, indicating that the fabricated BSA/Ab-AFB1/nBi_2O_3/ITO immunoelectrode was highly selective for aflatoxin B1 detection.

The storage stability of this BSA/Ab-AFB1/nBi_2O_3/ITO immunoelectrode was investigated by observing the current response at a regular interval of 5 days for 45 days with 25 ng mL^{-1} concentration of AFB1. The results of these studies revealed no significant decrease in the current (within 5%) after 45 days, indicating excellent storage stability.

4. Conclusions

The electrophoretically derived nanostructured nBi_2O_3 film has been used to fabricate an Ab-AFB1 based immunosensors for aflatoxin B1detection. It has been shown that the presence of nBi_2O_3 results in a

favorable environment with increased electroactive surface. The fabricated BSA/Ab-AFB1/nBi_2O_3/ITO immunoelectrode shows remarkably enhanced sensitivity and selectivity for aflatoxin B1. This immunosensor shows relatively rapid response (15 s), high sensitivity 1.132 μA/(ng/dL cm^{-2}), broad linear range (1–70 ng/dL), low detection limit (8.715 ng/dL), linear regression coefficient 0.918, good reproducibility and long term stability. The wide detection range and high sensitivity has been assigned to the amplification of the magnitude of current response since Bi_2O_3 nanoparticles with good biocompatibility maintain the biological activity of the antibody and improve the electron transfer between analyte (aflatoxin B1) and BSA/Ab-AFB1/nBi_2O_3/ITO immunoelectrode surface. The low value of association constant (K_a) of 0.234 nM indicates high antibody affinity of Ab-AFB1 to aflatoxin B1. The results clearly suggest that nBi_2O_3/ITO electrode provides an attractive matrix for effective immobilization of antibodies for fabricating of third generation biosensors and bioelectronics devices. The unique properties of nBi_2O_3 and the ease of nBi_2O_3 nanostructure fabrication make this material extremely interesting for biosensor applications.

Acknowledgements

We thank Director, CSIR-National Physical Laboratory, New Delhi for providing the facilities. PRS is grateful to the Department of Science and Technology (DST), India for Young Scientist Award. JS acknowledges Department of Science and Technology, New Delhi, India for the INSPIRE Faculty award [IFA-13-CH-105].

References

[1] P.R. Solanki, A. Kaushik, V.V. Agrawal, B.D. Malhotra, NPG Asia Mater. 3 (2011) 17–24.
[2] A.P.F. Turner, Chem. Soc. Rev. 42 (2013) 3184–3196.
[3] P.R. Solanki, M.A. Ali., V.V. Agrawal, A.K. Srivastava, R.K. Kotnala, B.D. Malhotra, RSC Adv. 3 (2013) 16060–16067.
[4] Y.T. Chen, R. Gong, W. Zhang, X.Q. Xu, Y.Q. Fan, W.S. Liu, Mater. Lett. 59 (2005) 909–911.
[5] W.G. Lu, Y. Ding, Y.X. Chen, Z.L. Wang, J.Y. Fang, J. Am. Chem. Soc. 127 (2005) 10112–10116.
[6] Y.M. Lin, S.B. Cronin, J.Y. Ying, M.S. Dresselhaus, J.P. Heremans, Appl. Phys. Lett. 76 (2000) 3944.
[7] L. Leontie, M. Caraman, M. Delibas, G.I. Rusu, Mater. Res. Bull. 36 (2001) 1629–1637.
[8] M. Gotic, S. Popovic, S. Music, Mater. Lett. 61 (2007) 709–714.
[9] N.V. Skorodumova, A.K. Jonsson, M. Herranen, M. Stromme, G.A. Niklasson, B. Johansson, S.I. Simak, Appl. Phys. Lett. 86 (2005) 241910.
[10] L.S. Zhang, W.Z. Wang, J. Yang, Z.G. Chen, W.Q. Zhang, L. Zhou, S.W. Liu, Appl. Catal. A Gen. 308 (2006) 105–110.
[11] T.P. Gujar, V.R. Shinde, C.D. Lokhande, S.H. Han, J. Power Sources 161 (2006) 1479–1485.
[12] Y.B. He, G.R. Li, Z.L. Wang, C.Y. Su, Y.X. Tong, Energy Environ. Sci. 4 (2011) 1288–1292.
[13] N. Soltanzadeh, A. Morsali, Ultrason. Sonochem. 17 (2010) 139–144.
[14] M. Schuisky, A. Hdrsta, Chem. Vap. Depos. 2 (9) (1996) 235–238.
[15] N. Jiang, E.D. Wachsman, J. Am. Ceram. Soc. 82 (11) (1999) 3057–3064.
[16] K.S. Martirosyan, L. Wang, A. Vicent, D. Luss, Nanotechnology 20 (2009) 405609.
[17] M. Khairy, R.O. Kadara, D.K. Kampouris, C.E. Banks, Electroanalysis 22 (2010) 1455–1459.
[18] S. Taufik, N.A. Yusof, T.W. Tee, Ramli, Int. J. Electrochem. Sci. 6 (2011) 1880–1891.
[19] S.N. Ding, D. Shan, H.G. Xue, S. Cosnier, Bioelectrochemistry 79 (2010) 218–222.
[20] A.P. Periasamy, S. Yang, S.M. Chen, Talanta 87 (2011) 15–23.
[21] D. Shan, J. Zhang, H.G. Xue, Y.C. Zhang, S. Cosnier, S.N. Ding, Biosens. Bioelectron. 24 (2009) 3671–3676.
[22] M. Zidan, T.W. Tee, A.H. Abdullah, Z. Zainal, G.J. Kheng, Int. J. Electrochem. Sci. 6 (2011) 279–288.
[23] R. Liman, Chemosphere 93 (2) (2013) 269–273.
[24] J.L. Richard, Int. J. Food Microbiol. 119 (1) (2007) 3–10.
[25] B.D. Malhotra, S. Srivastava, M.A. Ali, C. Singh, Appl. Biochem. Biotechnol. 174 (3) (2014) 880–896.
[26] K.I. Cigic, H. Prosen, Int. J. Mol. Sci. 10 (1) (2009) 62–115.
[27] S.J. Daly, G.J. Keating, P.P. Dillon, B.M. Manning, R. O'Kennedy, H.A. Lee, M.R.A. Morgan, J. Agric, Food Chem. 48 (2000) 5097–5104.
[28] C.M. Maragos, V.S. Thompson, Nat. Toxins 7 (1999) 371–376.
[29] P.R. Solanki, A. Kaushik, T. Manaka, M.K. Pandey, M. Iwamoto, V.V. Agrawal, B.D. Malhotra, Nanoscale 2 (2010) 2811–2817.
[30] P. Kalita, J. Singh, M.K. Singh, P.R. Solanki, G. Sumana, B.D. Malhotra, Appl. Phys. Lett. 100 (2012) 093702.
[31] J. Singh, A. Roychoudhury, M. Srivastava, P.R. Solanki, D.W. Lee, S.H. Lee, B.D. Malhotra, J. Mater. Chem. B 1 (2013) 4493–4503.
[32] Y. Liu, Z. Qin, X. Wu, H. Jiang, Biochem. Eng. J. 32 (2006) 211–217.
[33] L. Masoomi, O. Sadeghi, M.H. Banitaba, A. Shahrjerdi, S.S.H. Davarani, Sensors Actuators B 177 (2013) 1122–1127.
[34] J.H.O. Owino, O.A. Arotiba, N. Hendricks, E.A. Songa, N. Jahed, T.T. Waryo, et al., Sensors 8 (2008) 8262–8274.
[35] M. Peng, L. Wondraczek, J. Mater. Chem. 19 (2009) 627–630.
[36] M.A. Ali, S. Srivastava, P.R. Solanki, V. Reddy, V.V. Agrawal, C.G. Kim, R. John, B.D. Malhotra, Sci. Rep. 3 (2013) 2661.

Scientific Research Publishing

Circuits and Systems, 2016, 7, 3617-3625
http://www.scirp.org/journal/cs
ISSN Online: 2153-1293
ISSN Print: 2153-1285

Canonic Realizations of Voltage-Controlled Floating Inductors Using CFOAs and Analog Multipliers

Raj Senani[1*], Data Ram Bhaskar[2,3], Munish Prasad Tripathi[4], Manoj Kumar Jain[5]

[1]Division of Electronics and Communication Engineering, Netaji Subhas Institute of Technology, New Delhi, India
[2]Department of Electronics and Communication Engineering, Faculty of Engineering and Technology, Jamia Millia Islamia, New Delhi, India
[3]Department of Electrical Engineering, Delhi Technological University, New Delhi, India
[4]Department of Electronics and Communication Engineering, National Institute of Technology, Ashok Rajpath, Bihar, India
[5]Department of Electronics Engineering, Institute of Engineering and Technology, Lucknow, India
Email: *senani@ieee.org, drbset@yahoo.com, munishprasadtripathi@rediffmail.com, mkjain71@gmail.com

How to cite this paper: Senani, R., Bhaskar, D.R., Tripathi, M.P. and Jain, M.K. (2016) Canonic Realizations of Voltage-Controlled Floating Inductors Using CFOAs and Analog Multipliers. *Circuits and Systems*, **7**, 3617-3625.
http://dx.doi.org/10.4236/cs.2016.711306

Received: May 11, 2016
Accepted: May 26, 2016
Published: September 8, 2016

Copyright © 2016 by authors and Scientific Research Publishing Inc.
This work is licensed under the Creative Commons Attribution International License (CC BY 4.0).
http://creativecommons.org/licenses/by/4.0/

Open Access

Abstract

New voltage-controlled floating inductors employing CFOAs and an analog multiplier have been presented which have the attractive features of using a canonic number of passive components (only two resistors and a capacitor) and not requiring any component-matching conditions and design constraints for the intended type of inductance realization. The workability and applications of the new circuits have been demonstrated by SPICE simulation and hardware experimental results based upon AD844-type CFOAs and AD633-type/MPY534 type analog multipliers.

Keywords

Voltage Controlled Inductors, Floating Inductors, Inductance Simulation, Current Feedback Op-Amps, Analog Multipliers, Analog Circuits

1. Introduction

Voltage-controlled-resistors and a variety of other voltage-controlled impedances are useful elements in the realization of electronically-controllable filters and oscillators and have been investigated in past using a variety of active elements such as op-amps, operational transconductance amplifiers, operational mirrored amplifiers, current conveyors and current feedback op-amps, for instance, see [1]-[13] and the references cited therein.

A recent paper [14] published in this Journal has presented two configurations for realizing voltage-controlled floating inductance (VC-FI) realization using thee/four Current feedback op-amps (CFOA) along with an analog multiplier. The first circuit of [14] employs four CFOAs, three resistors, a grounded capacitor and an analog multiplier and has been shown[1] to realize lossless VC-FI providing inductance value proportional to an external control voltage V_c. On the other hand, the second circuit of [14] employs one multiplier and as many passive components as in the former circuit, but uses one less CFOA to realize a lossless VC-FI inversely proportional to V_c. The circuits proposed in [14] however, suffer from two drawbacks: (i) employment of *non-canonic* number of resistors (three) and (ii) requirement of certain conditions/constraints to realize the intended type of FIs.

The purpose of this article is to present four new circuits which, in contrast to the circuits of [14] quoted above, employ a *canonic* number of resistors (only two) and, unlike the quoted circuits of [14], do not require any component-matching/realization conditions.

2. Canonic Realizations of Lossless Voltage-Controlled Floating Inductors

The proposed circuits, which employ canonic number of only two resistors and a grounded capacitor (GC) for realizing lossless VC-FIs, are shown in **Figure 1** and **Figure 2** respectively. The proposed circuits are obtained by appropriate embedding[2] of an analog divider (as in the circuits of **Figure 1**) and analog multiplier (as in the circuits of **Figure 2**) into appropriate lossless floating inductance circuits [17] [18]. By a straight forward analysis, assuming the CFOAs to be characterized by $i_y = 0$, $v_x = v_y$, $i_z = i_x$

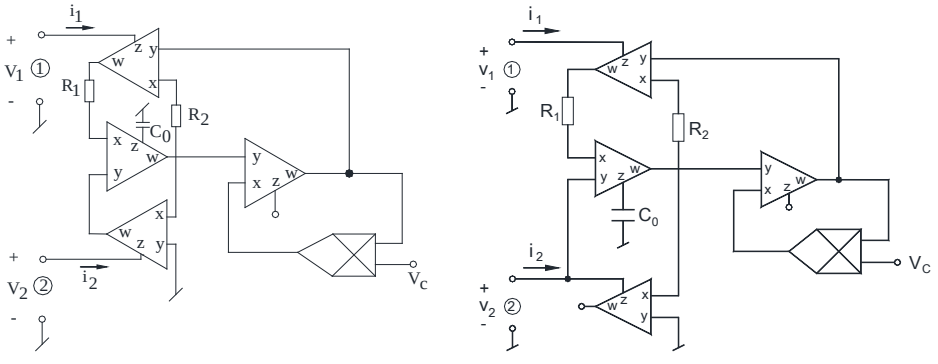


Figure 1. Proposed circuits for realizing VC-FI proportional to VC.

[1]For the correction of some discrepancies in the analysis in the quoted circuits of [14] and an anomaly in the citation of an earlier work therein, see Appendix 1.

[2]The techniques of embedding analog dividers and analog multipliers (as in the circuits of **Figure 1**, **Figure 2** and **Figure 5** here which have their origin in the earlier works of [15]-[18]) to create op-amp-AM-based voltage-controlled-resistors have been taught by the first author (RS) in the course on Linear Integrated Circuits since 1990 and these *unpublished* ideas have been adopted by and circulated amongst the academic fraternity at numerous institutions freely.

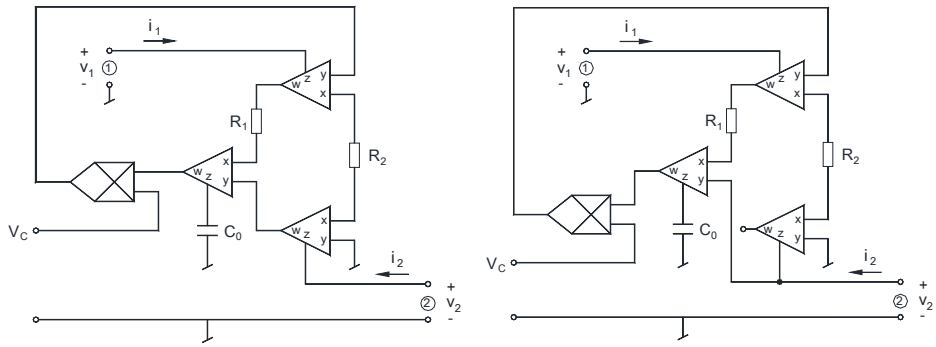


Figure 2. Proposed circuits for realizing VC-FI inversely proportional to VC.

and $v_w = v_z$, both the circuits of **Figure 1** are found to be characterized by the following short-circuit admittance matrix:

$$\begin{bmatrix} i_1 \\ i_2 \end{bmatrix} = \left(\frac{V_{ref}}{V_c} \right) \left(\frac{1}{sC_0R_1R_2} \right) \begin{bmatrix} 1 & -1 \\ -1 & 1 \end{bmatrix} \begin{bmatrix} v_1 \\ v_2 \end{bmatrix} \tag{1}$$

Thus, the circuits realize an equivalent floating inductance $L_{eq} = C_0R_1R_2\left(V_c/V_{ref}\right)$. Note that, in contrast to the circuit of **Figure 2(a)** of [14] which requires matching of two resistors therein namely, $R_2 = R_3$ to realize the intended type of VC-FI, the circuits of **Figure 1** here do not require any design constraints/conditions to be fulfilled to realize a VC-FI.

Consider now the circuits of **Figure 2**. By straight forward analysis, these two circuits are characterized by the following equation:

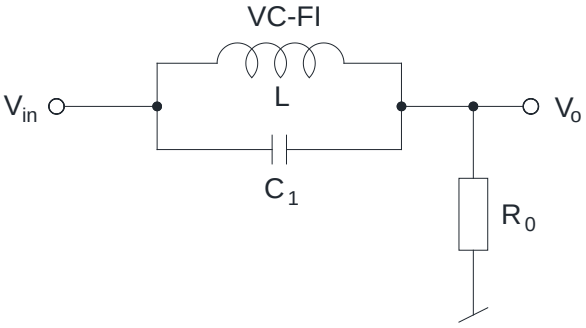
$$\begin{bmatrix} i_1 \\ i_2 \end{bmatrix} = \left(\frac{V_c}{V_{ref}} \right) \left(\frac{1}{sC_0R_1R_2} \right) \begin{bmatrix} 1 & -1 \\ -1 & 1 \end{bmatrix} \begin{bmatrix} v_1 \\ v_2 \end{bmatrix} \tag{2}$$

These circuits, therefore, realize an equivalent VC-FI of value $L_{eq} = C_0R_1R_2\left(V_{ref}/V_c\right)$. In this case also, it must be pointed out that while the circuit of **Figure 3(a)** of [14] requires two conditions namely $R_2 \gg R_1$ and $\left(R_1 + R_2 = R_3\right)$, no such conditions or constraints are needed in the new proposed circuits of **Figure 2**.

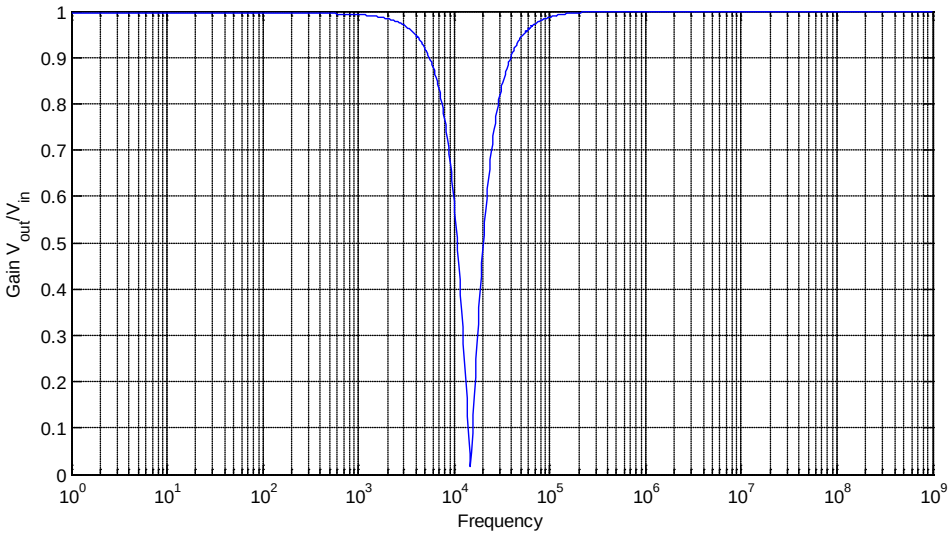
Lastly, it must also be noticed that in contrast to the circuits of **Figure 2(a)** and **Figure 3(a)** of [14] both of which require three resistors, the proposed new circuits require a bare minimum of only two resistors!

3. Applications of the Proposed VC-FIs, SPICE Simulation and Experimental Results

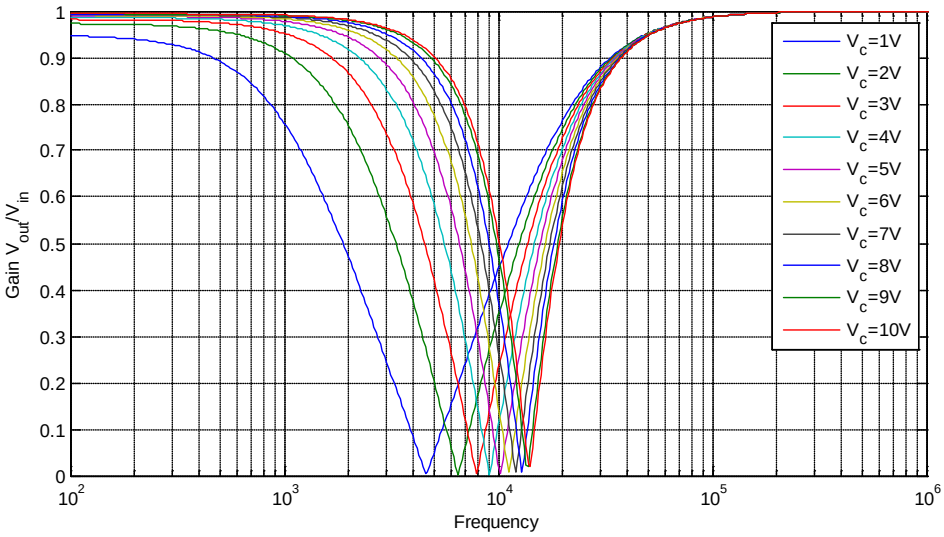
To check the workability of the proposed circuits, all the VC-FIs were tested by utilizing them in the realization of a second-order voltage-controllable notch filter as shown in **Figure 3(a)**. The frequency response of the notch filter employing the VC-FI of **Figure 1(a)** and designed to obtain a notch frequency of 15.9 kHz is shown in **Figure 3(b)**. **Figure 3(c)** shows the variability of the notch frequency with respect to the control voltage V_c for the notch filter when it was realized by using the VC-FI of **Figure 2(a)**.



(a)



(b)



(c)

Figure 3. SPICE simulation results: (a) A voltage-controllable notch filter; (b) Frequency response of the notch filter realized by using the VC-FI of **Figure 1(a)**; and (c) Variation of notch frequency with control voltage (V_c) with the notch filter realized using the VC-FI of **Figure 2(a)**.

In the simulations, AD844 type CFOAs were used which were biased with ±12 V DC power supplies. The simulation results of **Figure 3(b)** and **Figure 3(c)** are seen to be in close agreement with the theoretical results.

For verifying the practical validity of the proposed VC-FI formulations, we present here the results of the hardware implementation of a voltage-controlled band reject filter (shown in **Figure 4(a)**) wherein the VC-FI was implemented with the configuration of **Figure 2(b)**. AD844 type CFOAs biased with ±12 volts and MPY534 type analog multipliers biased with ±12 V were used along with the following component values: R_1 = 1 k Ω, R_2 = 1 k Ω, C_1 = 1.0 nF, R_0 = 680 Ω to obtain f_0 = 5.2 kHz and bandwidth = 5.58 kHz. V_c was varied from 1 to 10 volts to vary the center frequency. An exemplary frequency response for V_c = 1 volt is shown in **Figure 4(b)** whereas the variability of f_0 with respect to V_c has been shown in **Figure 4(c)**.

The SPICE simulation results of **Figure 3** and the experimental results of **Figure 4**, thus, confirm the feasibility of the proposed formulations.

4. Concluding Remarks

Four new lossless VC-FIs are introduced which employ a canonical number of passive components (namely, only one GC and two resistors) and realize the intended type of floating inductances without any conditions/design constraints. This is in contrast to the recently reported circuits of [14] for the same purposes which suffer from the drawback of employing a non-canonical number of resistors (three) and requirement of component matching/design constraint to be fulfilled.

The workability of the new circuits as VC-FIs and the variability of the inductance value through an external control voltage V_c were demonstrated by SPICE simulation results of a notch filter, as well as through experimental results of another voltage-controlled notch filter.

It is expected that the proposed new circuits may find applications in situations requiring voltage-controlled inductors.

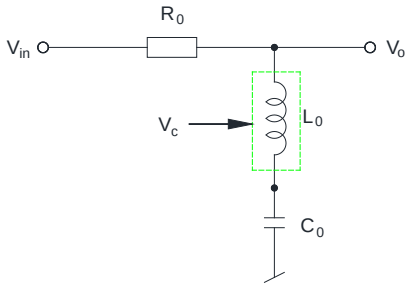
Lastly, it may be mentioned that the realization of many other grounded/floating, positive/negative and generalized linear voltage controlled impedances, based upon the ideas contained in [15]-[18] are possible; for instance, see the two configurations of **Figure 5** both of which realize VC-floating generalized impedance converters/inverters having equivalent floating impedance values given by:

$$Z_{1-2} = \left(\frac{V_{ref}}{V_c}\right)\frac{Z_1 Z_3 Z_5}{Z_2 Z_4} \tag{3}$$

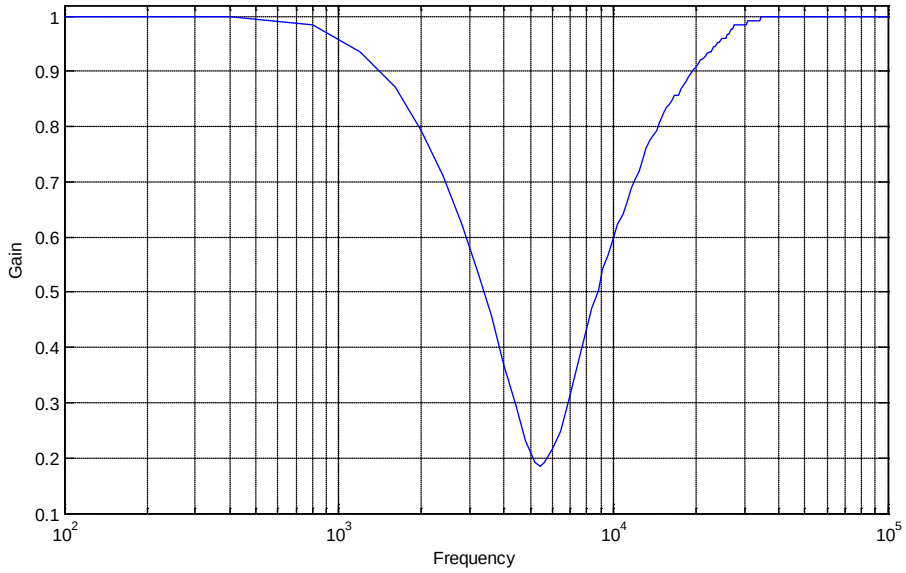
and

$$Z_{1-2} = \left(\frac{V_c}{V_{ref}}\right)\frac{Z_1 Z_3 Z_5}{Z_2 Z_4} \tag{4}$$

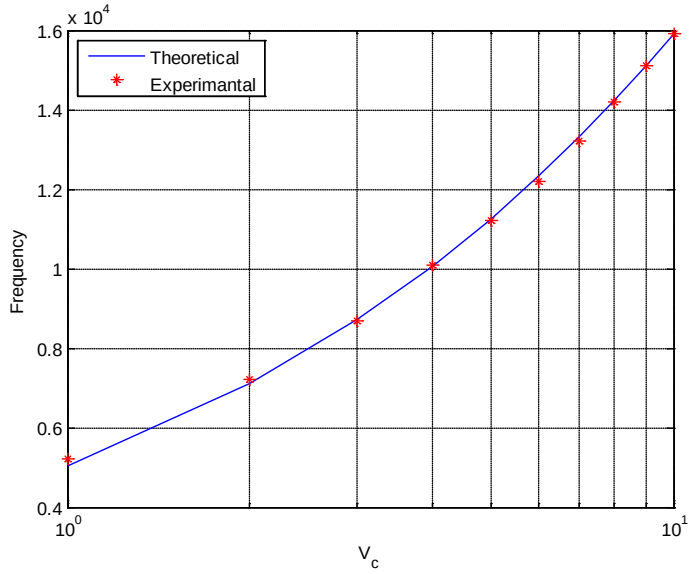
respectively. The circuits of **Figure 1** and **Figure 2** can also be generalized similarly by replacing R_1, R_2 and C_0 by impedances Z_1, Z_2 and Z_3 respectively.



(a)



(b)



(c)

Figure 4. Experimental results of (a) the band reject filter using the VC-FI of **Figure 2(b)**; (b) experimentaly measured frequency response; (c) variation of the centre frequency with the controlled voltage.

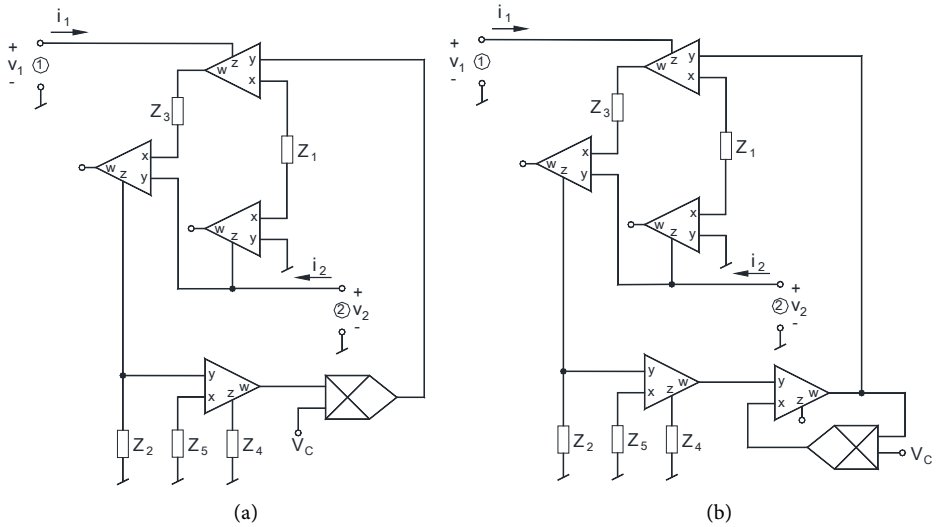


Figure 5. Two exemplary circuits realizing voltage-controlled floating generalized *impedance inverters/converters*.

Furthermore, the negative floating impedances are realizable from the configurations of **Figure 1**, **Figure 2** and **Figure 5**, by the simple artifice of interchanging some connections in the manner outlined earlier in [16] and [18], while various types of grounded positive/negative voltage controlled impedances are realizable by shorting port 2 to ground (thereby also leading to a reduced number of CFOAs in each case).

References

[1] Nay, K.W. and Budak, A. (1983) A Voltage-Controlled Resistance with Wide Dynamic Range and No Distortion. *IEEE Transactions on Circuits and Systems*, **30**, 770-772. http://dx.doi.org/10.1109/TCS.1983.1085290

[2] Nay, K.W. and Budak, A. (1985) A Variable Negative Resistance. *IEEE Transactions on Circuits and Systems,* **32**, 1193-1194. http://dx.doi.org/10.1109/TCS.1985.1085637

[3] Senani, R. and Bhaskar, D.R. (1991) Realization of Voltage-Controlled Impedances. *IEEE Trans. Circuits and Systems*, **38**, 1081-1086; 162. http://dx.doi.org/10.1109/31.83879

[4] Senani, R. and Bhaskar, D.R. (1992) A simple Configuration for Realizing Voltage-Controlled Impedances. *IEEE Transactions on Circuits and Systems*, **39**, 52-59. http://dx.doi.org/10.1109/81.109244

[5] Senani, R. and Bhaskar, D.R. (1994) Versatile Voltage-Controlled Impedance Configuration. *IEE Proceedings—Circuits, Devices and Systems*, **141**, 414-416. http://dx.doi.org/10.1049/ip-cds:19941296

[6] Senani, R. (1995) Universal Linear Voltage-Controlled Impedance Configuration. *IEE Proceedings—Circuits, Devices and Systems*, **142**, 208. http://dx.doi.org/10.1049/ip-cds:19951944

[7] Ndjountche, T. (1996) Linear Voltage-Controlled Impedance Architecture. *Electronics Letters,* **32**, 1528-1529. http://dx.doi.org/10.1049/el:19961020

[8] Leuciuc, A. and Goras, L. (1998) New General Immittance Converter JFET Voltage-Controlled Impedances and Their Applications to Controlled Biquads Synthesis. *IEEE Transactions on Circuits and Systems*, **45**, 678-682. http://dx.doi.org/10.1109/81.678494

[9] Senani, R. (1994) Realisation of Linear Voltage-Controlled Resistance in Floating Form. *Electronics Letters*, **30**, 1909-1911. http://dx.doi.org/10.1049/el:19941313

[10] Senani, R. (1995) Floating GNIC/GNII Configuration Realized with Only a Single OMA. *Electronics Letters*, **31**, 423-424. http://dx.doi.org/10.1049/el:19950287

[11] Ndjountche, T., Unbehauen, R. and Luo, F.L. (1999) Electronically Tunable Generalized Impedance Converter Structures. *International Journal of Circuit Theory and Applications*, **27**, 517-522. http://dx.doi.org/10.1002/(SICI)1097-007X(199909/10)27:5<517::AID-CTA76>3.0.CO;2-Y

[12] Maundy, B., Gift, S. and Aronhime, P. (2008) Practical Voltage/ Current Controlled Grounded Resistor with Dynamic Range Extension. *IET Circuits, Devices & Systems*, **2**, 201-206. http://dx.doi.org/10.1049/iet-cds:20070164

[13] Senani, R. and Bhaskar, D.R. (2008) Comment: Practical Voltage/Current Controlled Grounded Resistor with Dynamic Range Extension. *IET Circuits, Devices & Systems*, **2**, 465-466. http://dx.doi.org/10.1049/iet-cds:20080211

[14] Sinha, P.K., Sharma, N. and Mishra, R. (2015) A Configuration for Realizing Voltage Controlled Floating Inductance and Its Application. *Circuits and Systems*, **6**, 189-199. http://dx.doi.org/10.4236/cs.2015.69020

[15] Senani, R., Bhaskar, D.R., Singh, A.K. and Singh, V.K. (2013) Current Feedback Operational Amplifiers and Their Applications. Springer Science+ Business Media, New York, Ch. 3 Section 3.1 Introduction; First Sentence, 49.

[16] Senani, R., Bhaskar, D.R., Gupta, S.S. and Singh, V.K. (2009) A Configuration for Realizing Floating, Linear, Voltage-Controlled Resistance, Inductance and FDNC Elements. *International Journal of Circuit Theory and Applications*, **37**, 709-719. http://dx.doi.org/10.1002/cta.510

[17] Chang, C.M. and Hwang, C.S. (1995) Comment on "Voltage-Mode Notch, Low Pass and Band Pass Filter Using Current-Feedback Amplifiers". *Electronics Letters*, **31**, 246. http://dx.doi.org/10.1049/el:19950168

[18] Senani, R. (1998) Realization of a Class of Analog Signal Processing/Signal Generation Circuits: Novel Configurations Using Current Feedback Op-Amps. *Frequenz*, **52**, 196-206. http://dx.doi.org/10.1515/FREQ.1998.52.9-10.196

[19] Mitra, S.K. (1969) Analysis and Synthesis of Linear Active Networks. John Wiley & Sons Inc., New York, 495.

[20] Rikoski, R.A. and Choudhry, A. (1976) Mutator Realized Inductance. *Proceedings of the IEEE*, **64**, 1012-1013. http://dx.doi.org/10.1109/PROC.1976.10256

[21] Dutta Roy, S.C. (2016) A Unified Theory of Op-Amp Sinusoidal Oscillators Using Reactive π and T Networks in the Feedback Path. *IETE Journal of Education*, 90-95. http://dx.doi.org/10.1080/09747338.2016.1180962

Appendix 1: Some Appraisals

In the context of the analysis and citations of references in [14], the following are worth pointing out for the benefit of the readers of this Journal.

1) The analysis of Section 2 at pages 192-193 of [14] is clumsy. It is well-known (for instance, see [19] [20]) that a 2-port representing floating impedance Z_{eq} is correctly characterized by either the following y-matrix [19]:

$$\begin{bmatrix} i_1 \\ i_2 \end{bmatrix} = \left(\frac{1}{Z_{eq}} \right) \begin{bmatrix} 1 & -1 \\ -1 & 1 \end{bmatrix} \begin{bmatrix} v_1 \\ v_2 \end{bmatrix}$$

or *equivalently*, by the following transmission matrix [20]:

$$\begin{bmatrix} v_1 \\ i_1 \end{bmatrix} = \begin{bmatrix} 1 & Z_{eq} \\ 0 & 1 \end{bmatrix} \begin{bmatrix} v_2 \\ -i_2 \end{bmatrix}$$

Thus, a straight forward analysis of the circuit of **Figure 2(a)** of [14] yield its correct y-matrix as:

$$\begin{bmatrix} i_1 \\ i_2 \end{bmatrix} = \left(\frac{V_{ref}}{V_c} \right) \left(\frac{1}{sCR_1} \right) \begin{bmatrix} 1/R_2 & -1/R_2 \\ -1/R_3 & 1/R_3 \end{bmatrix} \begin{bmatrix} v_1 \\ v_2 \end{bmatrix}$$

Therefore, the circuit of **Figure 2(a)** of [14] will realize a lossless VC-FI subject to fulfillment of the condition $R_2 = R_3$.

On the other hand, the circuit of **Figure 3(a)** of [14] has a similar y-matrix with $L_{eq} = CR_1R_3V_{ref}/V_c$ the condition of realization being $R_1 = R_2$. Therefore, the conditions $R_2 \gg R_1$ and $(R_1 + R_2) = R_3$ as given by the authors at page 193 of [14] for their circuit of **Figure 3(a)** are unnecessary.

2) While comparing their propositions of **Figure 2(a)** and **Figure 3(a)**, the authors of [14] have cited an *unpublished work*[3] as reference 17, which is extremely surprising since this unpublished reference is not an open literature and was, therefore, definitely not available to the authors of [14]. In fact, this unpublished work[3] was quoted in the acknowledgement of reference [16] of this communication as reference 26. It is, therefore, obvious that the authors of the quoted paper [14] could have known the existence of this unpublished work (quoted as reference 17 in their paper [14]) only from the published paper [16] which curiously has not been cited by them! In view of this, reference 17 of [14] in fact, should be reference [16] of the present paper.

3) Making a Hartley oscillator using an ideal op-amp is anomalous since inductor L_1, due to being connected directly from the output of the ideal op-amp to ground, will not appear in any open loop transfer function (or loop gain) or the characteristic equation of the circuit. A resolution to this anomaly has recently been provided in [21].

[3]Senani, R, Novel linear voltage controlled floating-impedance configurations. ELL/96/53450, dated25 November 1996, *unpublished.* The above unpublished work was cited as reference 26 in [16].

Scientific Research Publishing

Submit or recommend next manuscript to SCIRP and we will provide best service for you:

Accepting pre-submission inquiries through Email, Facebook, LinkedIn, Twitter, etc.
A wide selection of journals (inclusive of 9 subjects, more than 200 journals)
Providing 24-hour high-quality service
User-friendly online submission system
Fair and swift peer-review system
Efficient typesetting and proofreading procedure
Display of the result of downloads and visits, as well as the number of cited articles
Maximum dissemination of your research work

Submit your manuscript at: http://papersubmission.scirp.org/
Or contact cs@scirp.org

ResearchGate

See discussions, stats, and author profiles for this publication at: https://www.researchgate.net/publication/305930123

Comparative Energetic and Exergetic Analysis of R22, R438A and M1

Article *in* International Journal of Applied Engineering Research · August 2016

CITATIONS
0

READS
32

3 authors, including:



Suneel K Kalla
IMS Engineering College
6 PUBLICATIONS **0** CITATIONS
SEE PROFILE



B B Arora
Delhi Technological University
29 PUBLICATIONS **30** CITATIONS
SEE PROFILE

All in-text references underlined in blue are linked to publications on ResearchGate, letting you access and read them immediately.

Available from: Suneel K Kalla
Retrieved on: 25 September 2016

International Journal of Applied Engineering Research, ISSN 0973-4562 Vol. 10 No.94 (2015)
© Research India Publications; http/www.ripublication.com/ijaer.htm

Comparative Energetic and Exergetic Analysis of R22, R438A and M1

Suneel Kumar Kalla
Deptt. Of Mech. Engg.,
JamiaMilliaIslamia
New Delhi, India
skkalla@yahoo.com

B.B. Arora
Deptt. Of Mech. Engg.,
Delhi Technological University
New Delhi,India
prof_bbar@yahoo.com

J.A. Usmani
Deptt. Of Mech. Engg.,
JamiaMilliaIslamia
New Delhi, India
jausmani@yahoo.com

***Abstract*—Theaim of this paper is to determine which refrigerant among R438A and M1 (R32/R125/R600a) is a better alternative to R22. For this purpose both energy as well as exergy analyses have been performed using NIST Cycle-D program for vapour compression refrigeration cycle design. The results show that energetic as well as exergetic efficiency of R438A is higher than M1 and thus it is a better option to replace R22.**

Keywords—Refrigerant; energy; exergy;Cycle-D; Vapour compression

I. INTRODUCTION

HCFC (hydrochloroflurocarbon) R22 being an ozone depleting substance has to be replaced by an environment friendly refrigerant by 2040 in developing countries including India as per Montreal protocol. At the same the new alternative should have low GWP (Global Warming Potential) in line with Kyoto protocol. Alternative refrigerants to R22 can be classified into four categories: first category being HFCs (hydrofluorocarbons) like R407C and R410A; second category is HCs (hydrocarbons) like R290 (propane) and R1270 (propylene); third category is refrigerant mixtures like R422A (R125/R134a/R600a) and R417A (R125/R134a/R600); fourth category comprises refrigerants like ammonia and carbon dioxide. The drawback with HFC R410A is that it has lower critical temperature, which curtails its use in vapour compression systems that work at higher condenser temperatures. In case of R407C, we have to switch over topolyol ester (POE) lubricant and propane is flammable. The carbon dioxide systems consume high power and cooling effect is lower at high temperatures. NH_3 has high toxicity. Therefore till today we do not have an alternative refrigerant that could substitute R22.

Park et al. [1]in an experimental study tested the thermodynamic performance of R433A (composed of 30% propylene and 70% propane) to act as a substitute for R22 in air-conditioners. They observed that the coefficient of performanceof R433A is 4.9–7.6% higher whereas the capacity of R433A is 1.0–5.5% lower. The compressor outlet temperature of R433A is 22.6–27.9º C lower. At the same time the charge required for R433A is 57.0–57.7% lower. In a similar study, Park et al. [2] also tested the performance of R432A in a heat pump and observed that the coefficient of performance of R432A is 8.5–8.7% higher than that of R22 whereas the capacity of R432A is 1.9–6.4% higher than that of R22. The compressor outlet temperature of R432A is 14.1–17.3 ºC lower than that of R22. At the same time the requirement of charge for R432A is 50% lower than that of R22 which can be attributed to its low density. Cleland et al. [3]conducted experimental studies on an on-farm milk cooling working with Care-50[a mixture of propane (R-290) and ethane (R-170)] as an alternative to R22. They concluded that Care-50 consumed lesser energy by 6–8%, and at the same time had cooling capacity comparable to R22. Because of the fact that hydrocarbons require smaller charges, they meet the safety standards adequately. Allgood& Lawson [4] experimented with R438A in existing refrigeration & air conditioning systems and reported that compared to R22, similar cooling performance & energy efficiency were achieved. Lower discharge temperature and similar evaporator & condenser pressure were observed with no change of lubricant during retrofit. BOCK Compressors [5] tested R422D (MO29), R417A (MO59) and R438A (MO99) in their compressors and found that among the three alternative refrigerants, the compression temperature was the least for R417A; R438A had the highest cooling effectand R417A had the highest energy efficiency, s compared to R22. Lopez [6]observed that R434A is the best alternative refrigerant for air conditioning applications. He advocatedusingR434A with adjustable expansion devices so that correct superheat could be set. Cabello et al. [7]did experimental study on single-stage vapour compression refrigeration plant using drop-in fluids R417B and R422A and long-term substitute R404A. They concluded that by using an internal heat exchanger, the drop-in fluids give an energy performance which is comparable to that of R22, particularly in the case of R417B. Ramu et al. [8]analysed a new blendR32/R125/R600a (in the ratio of 0.4:0.4:0.2, by mass) as a substitute to R22 in an air conditioner. They concluded that VCC of new refrigerant blend is nearer to R22 and coefficient of performance of the mixture was lower by about 16-20%. The compressor outlet

temperature of the new refrigerant blend was 6-11ºC lower whereas TEWI of new refrigerant blend was reported to be higher than that of R22 by about 20%. Dalkilic et al. [9] theoretically analysed the performance of various alternative refrigerants in a shell and tube condenser at an evaporating temp of -10 °C and a condensing temperature of 35 to 55°C.They concluded that the refrigerant blend of R290/R600, R152a/R125/R32 and R32/R134a were most suitable among the chosen refrigerants to act as alternatives.

To the authors' knowledge, there is no specific work reported on the energy and exergy performance comparison of R438A and R32/R125/R600a mixture (referred to as M1 in this study) as a substitute to R22 in air conditioners. The main objective of this paper is to investigate which of these two refrigerant blends can be a potential alternative to R22 both energetically as well as exergetically.

II. SIMULATION

Cycle-D from NIST is the simulation software used for energy analysis of the vapour compression refrigeration cycle utilized in air conditioning. Fig.1 shows the simplified diagram of a vapour compression refrigeration system with liquid line suction line heat exchanger. Fig. 2 depicts the corresponding pressure-enthalpy diagram of the cycle. Table I summarizes the working conditions of the air conditioning system.

Coefficient of performance (COP), which is a measure of performance of refrigeration cycles according to first law, is computed as

$$COP = \frac{\dot{Q}_e}{\dot{W}_{comp}} \quad (1)$$

where $\dot{Q}_e$ is the net refrigeration effect produced and $\dot{W}_{comp}$ is the work interaction.

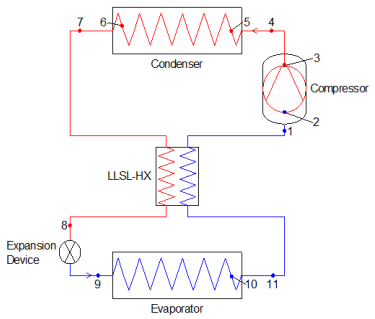


Fig. 1. Schematic of vapour compression refrigeration system.

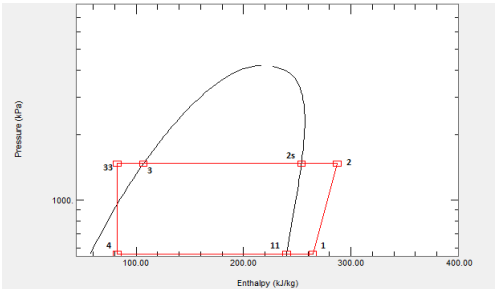


Fig. 2. Pressure enthalpy diagram of vapour compression refrigeration cycle.

III. EXERGY ANALYSIS

Energy analysis is based on the first law of thermodynamics. It provides us with a quantitative analysis. As compared to this qualitative analysis is possible with exergy analysis which is based on the second law of thermodynamics. It aids us in identifying the component which is having the highest irreversibility so that it can be improved.

Exergy balance as applied to a control volume for a steady stateprocess is given by[10].

$$\dot{ED}_i = \Sigma (\dot{me}_x)_{in} - \Sigma (\dot{me}_x)_{out} + [\Sigma(\dot{Q}\left(1 - \frac{T_O}{T}\right)_{in} - \Sigma\left(\dot{Q}\left(1 - \frac{T_O}{T}\right)_{out}\right] \pm \Sigma\dot{W} (2)$$

where $\dot{ED}_i$is thethe rate of exergy destruction in the process, $m_i$is the mass flow rate of refrigerant, T is the temperature at which heat transfer Q is happening, $T_0$is the dead state temperature, $h_x$is the specific enthalpy at state point x, $s_x$is the specific enthalpy at state point x and W is the work interaction.Different state points are depicted in Fig. 2.

Exergy destruction in Evaporator:

$$\dot{ED}_e = \dot{E}_{x_4} + \dot{Q}_e\left(1 - \frac{T_0}{T_r}\right) - \dot{E}_{x_{11}} = \dot{m}_r(h_4 - T_0\, s_4) + \dot{Q}_e\left(1 - \frac{T_0}{T_r}\right) - \dot{m}_r(h_{11} - T_0\, s_{11}) (3)$$

Exergy destruction in Compressor:

$$\dot{ED}_{comp} = \dot{E}_{x_1} + \dot{W}_{comp} - \dot{E}_{x_2} = \dot{m}_r\left(T_0(s_2 - s_1)\right) (4)$$

Exergy destruction in Condenser:

$$\dot{ED}_c = \dot{E}_{x_2} - \dot{E}_{x_3} = \dot{m}_r(h_2 - T_0 s_2) - \dot{m}_r(h_3 - T_0 s_3) (5)$$

Exergy destruction in Throttle valve:

$$\dot{ED}_t = \dot{E}_{x_{33}} - \dot{E}_{x_4} = \dot{m}_r(h_{33} - T_0 s_3) - \dot{m}_r(h_4 - T_0 s_4) = \dot{m}_r\left(T_0(s_4 - s_{33})\right) (6)$$

Exergy destruction in Liquid line vapour line heat exchanger:

$$\dot{ED}_{lvhe} = \dot{E}_{x_3} - \dot{E}_{x_{33}} + \dot{E}_{x_{11}} - \dot{E}_{x_1} = \dot{m}_r((h_3 - h_{33} + h_{11} - h_1) - T_0((s_3 - s_{33} + s_1 - s_{11})) \quad (7)$$

Total exergy destruction is given by:

$$\Sigma\dot{ED}_i = \dot{ED}_e + \dot{ED}_{comp} + \dot{ED}_c + \dot{ED}_t + \dot{ED}_{lvhe} (8)$$

Exergetic efficiency is

$$\eta_{ex} = \frac{|\dot{Q}_e\left(1 - \frac{T_0}{T_r}\right)|}{\dot{W}_{comp}} \quad (9)$$

IV. RESULTS

Fig. 3depicts the change in coefficient of performance (COP) of the three refrigerants with respect to evaporating temperature at three condenser temperatures i.e. 30°, 40° and 50°C at heat exchanger effectiveness of 0.5. It is seen that COP increases as the evaporating temperature is increased and it reduces as the condensing temperature increases. The increasein COP is steeper at higher evaporating temperatures and lower condenser temperatures. In addition it is observed that that COP of R438A is nearer to R22 than M1 at all evaporating as well as condensing temperatures. At 40°C condenser temperature and -30°C evaporator temperature R438A is having 7.7 % lower COP than R22 whereas at 10°C it is 9.5% lower.

TABLE I. WORKING CONDITIONS OF THE AIR CONDITIONING SYSTEM.

PARAMETER	VALUE/RANGE
REFERENCE TEMPERATURE (T_0)	298K
REFERENCE PRESSURE (P_0)	100KPA
REFRIGERATION CAPACITY (Q_{EV})	5.25KW
EVAPORATOR TEMPERATURE RANGE (T_R)	243-283K
CONDENSER TEMPERATURE (T_{COND})	323K
COMPRESSOR ISENTROPIC EFFICIENCY	85%
COMPRESSOR VOLUMETRIC EFFICIENCY	68%
ELECTRIC MOTOR EFFICIENCY	70%

Fig. 4 shows the change in total exergy destruction of the three refrigerants with respect to evaporating temperature at three condensing temperatures i.e. 30°, 40° and 50°C at heat exchanger effectiveness of 0.5. It is seen that exergy destruction reduces as the evaporator temperature increases and it increases as the condenser temperature increases. The decrease in exergy destruction is steeper at lower evaporating temperatures and higher condenser temperatures. Additionally it is observed that exergy destruction of R438A is nearer to R22 than M1 at all evaporator as well as condenser temperatures. At 40°C condenser temperature and -30°C evaporator temperature R438A is having 15.3 % greaterexergy destruction than R22 whereas at 10°C it is 15.5% greater.

Fig. 5 shows the change inexergy efficiency of the three refrigerants with respect to evaporating temperature at three condensing temperatures i.e. 30°, 40° and 50°C at heat exchanger effectiveness of 0.5. It is seen that exergy efficiency reduces with increase in the evaporator temperature as well as with the increase in condenser temperature. The reduction in exergy efficiency is sharper athigher evaporating temperatures. Also, it is seen that exergy efficiency of R438A is closer to R22 than M1 at all evaporator as well as condenser temperatures. At 40°C condenser temperature and -30°C evaporator temperature R438A is having 7.7 % lower exergy efficiency than R22 whereas at 10°C it is 9.5% lower.

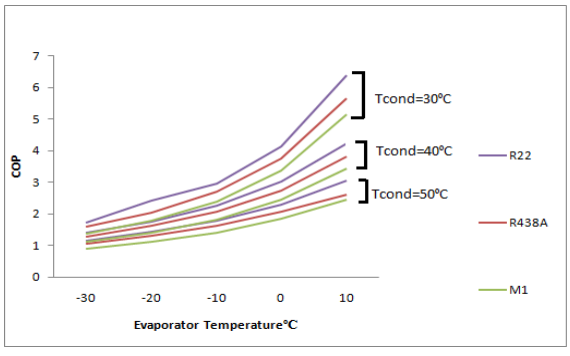


Fig. 3.Variation of COP with evaporator temperature and condenser temperature at heat exchanger effectivenessof 0.5.

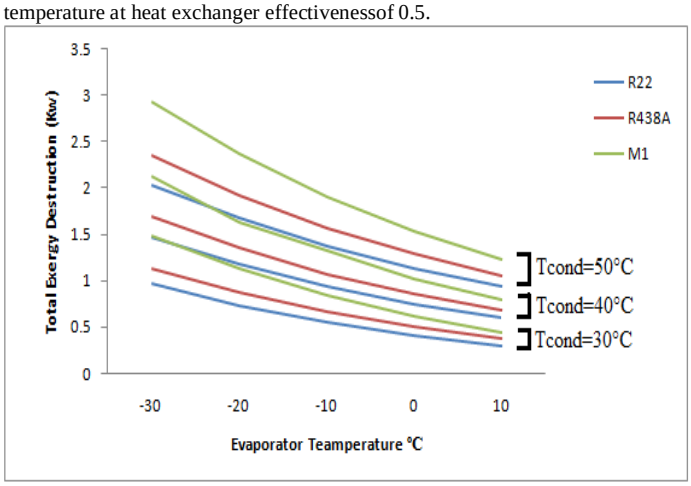


Fig.4. Variation of Total Exergy destruction with evaporatortemperature and condenser temperature at heat exchanger effectiveness of 0.5.

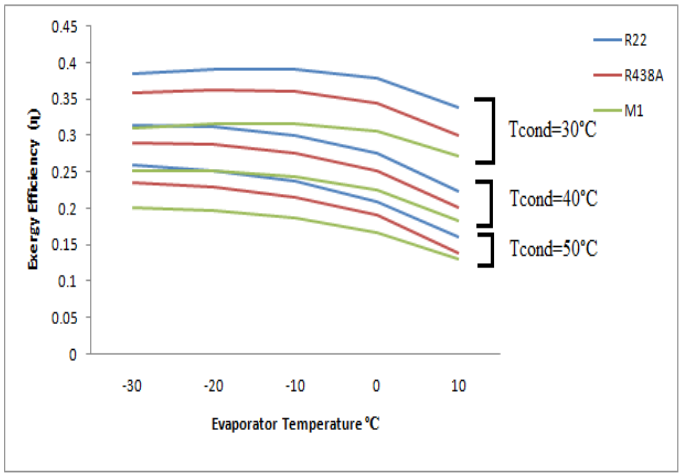


Fig.5. Variation of exergy efficiency with evaporator temperature and condenser temperature at heat exchanger effectiveness of 0.5.

V. CONCLUSION

The energy and exergy performance of two possible alternatives for R22, R438A and a new refrigerant mixture M1 (R32/R125/R600A) have been compared in a theoretical study. The results point out that the energy as well as exergy efficiency of both the refrigerants are lesser than that of R22. However, R438A is a better option since its COP as well as exergy efficiency works out to be higher than that of M1 throughout the evaporator and condenser temperature range. At 40°C condenser temperature and 10°C evaporator temperature, COP of R438A is higher by 10.8% as compared to M1 whereas the corresponding exergy efficiency is higher by 9.8%.

REFERENCES

[1] K.-J. Park, Y.-B. Shim and D. Jung, "Performance of R433A for replacing HCFC22 used in residential air-conditioners and heat pumps,"App. Energy, vol. 85, pp. 896–900, 2008.

[2] K.-J. Park, Y.-B. Shim and D. Jung, "Experimental performance of R432A to replace R22 in residential air-conditioners and heat pumps,"App. Therm. Eng.,vol. 29, pp. 597–600, 2009.

[3] D.J.Cleland,R.W.Keedwell and S.R.Adams, "Use of hydrocarbons as drop-in replacements for HCFC-22 in on-farm milk cooling equipment,"Int. J. Refrigeration vol. 32, pp. 1403–1411, 2009.

[4] C.C. Allgood and C.C.Lawson, "Performance of R-438A in R22 refrigeration and air conditioning systems," Int. Refrigeration and Air Conditioning Conference at Purdue, July 12-15,2010.

[5] Bock Compressors www.bock.de (accessed on 15.07.2015)

[6] D.L.G. Lopez, "The replacement of R-22,"Gas Technical Department of Gas Servei S.A., 2010.

[7] R. Cabello, E.Torrella,R.Llopis,D.Sánchez and J.A.Larumbe, " Energy influence of the IHX with R22 drop-in and long-termsubstitutes in refrigeration plants," App. Therm. Eng. Vol. 50, pp. 260-267, 2013.

[8] N.S.Ramu, P.S. Kumar and M.Mohanraj,"Energy Performance Assessment of R32/R125/R600a Mixtures as Possible Alternatives toR22 in Compression Refrigeration Systems," Int. J. Mech. Mechatronics Eng. Vol. 14, pp. 12-22., 2014.

[9] A.S.Dalkilic, O. Mahian, and S.Wongwises, "Selection of the most suitable refrigerant for a shell and tube condenser," Heat MassTransfer vol. 50, pp. 183-197, 2014.

[10] A.Arora, B.B. Arora, B.D. Pathak and H.L.Sachdev, "Exergy analysis of Vapour Compression Refrigeration system with R-22, R-407C and R-410A,"Int. J.Exergy, vol. 4, pp. 441–454, 2007.

PLOS ONE

RESEARCH ARTICLE

Computational Analysis and Predictive Cheminformatics Modeling of Small Molecule Inhibitors of Epigenetic Modifiers

Salma Jamal[1] ‡, **Sonam Arora**[2] ‡, **Vinod Scaria**[3]*

1 CSIR Open Source Drug Discovery Unit (CSIR-OSDD), Anusandhan Bhawan, Delhi, India, **2** Delhi Technological University, Delhi, India, **3** GN Ramachandran Knowledge Center for Genome Informatics, CSIR Institute of Genomics and Integrative Biology (CSIR-IGIB), Delhi, India

These authors contributed equally to this work.
‡ These authors are joint first authors on this work.
* vinods@igib.in

CrossMark
click for updates

OPEN ACCESS

Citation: Jamal S, Arora S, Scaria V (2016) Computational Analysis and Predictive Cheminformatics Modeling of Small Molecule Inhibitors of Epigenetic Modifiers. PLoS ONE 11(9): e0083032. doi:10.1371/journal.pone.0083032

Editor: Wei Yan, University of Nevada School of Medicine, UNITED STATES

Received: June 10, 2013

Accepted: October 30, 2013

Published: September 13, 2016

Copyright: © 2016 Jamal et al. This is an open access article distributed under the terms of the Creative Commons Attribution License, which permits unrestricted use, distribution, and reproduction in any medium, provided the original author and source are credited.

Funding: SJ acknowledges a Project Fellowship from CSIR-OSDD. This work was funded by the Council of Scientific and Industrial Research (CSIR), India through Grant BSC0122 (CARDIOMED). The funders had no role in study design, data collection and analysis, decision to publish, or preparation of the manuscript.

Competing Interests: The authors have declared that no competing interests exist.

Abstract

Background

The dynamic and differential regulation and expression of genes is majorly governed by the complex interactions of a subset of biomolecules in the cell operating at multiple levels starting from genome organisation to protein post-translational regulation. The regulatory layer contributed by the epigenetic layer has been one of the favourite areas of interest recently. This layer of regulation as we know today largely comprises of DNA modifications, histone modifications and noncoding RNA regulation and the interplay between each of these major components. Epigenetic regulation has been recently shown to be central to development of a number of disease processes. The availability of datasets of high-throughput screens for molecules for biological properties offer a new opportunity to develop computational methodologies which would enable in-silico screening of large molecular libraries.

Methods

In the present study, we have used data from high throughput screens for the inhibitors of epigenetic modifiers. Computational predictive models were constructed based on the molecular descriptors. Machine learning algorithms for supervised training, Naive Bayes and Random Forest, were used to generate predictive models for the small molecule inhibitors of histone methyl-transferases and demethylases. Random forest, with the accuracy of 80%, was identified as the most accurate classifier. Further we complemented the study with substructure search approach filtering out the probable pharmacophores from the active molecules leading to drug molecules.

Results

We show that effective use of appropriate computational algorithms could be used to learn molecular and structural correlates of biological activities of small molecules. The

computational models developed could be potentially used to screen and identify potential new biological activities of molecules from large molecular libraries and prioritise them for in-depth biological assays. To the best of our knowledge, this is the first and most comprehensive computational analysis towards understanding activities of small molecules inhibitors of epigenetic modifiers.

Introduction

Though all cells in an organism inherit the same genomic template, the dynamic expression of the genome provides for the cell-type and tissue specific organisation and functional organisation of multi-cellular organisms [1]. This dynamic regulation is largely dependent on the regulatory layer of interactions between multiple biomolecules, operating at the chromatin organisation, transcriptional and post-transcriptional levels [2]. The regulatory layer contributed by the Epigenetic layer has been one of the favourite areas of interest recently [3]. The epigenetic layer of regulation comprises largely of DNA modifications, histone modifications and noncoding RNA regulation and the interplay between each of these major components. The understanding of this epigenetic layer of gene regulation has largely been fuelled by large-scale genome-wide maps of both DNA modifications and histone modifications [4], thanks to the availability of high-throughput sequencing based assays to qualify epigenetic marks across the genome. Epigenetic modifications and their dysregulation has been implicated in the pathophysiology of a wide spectrum of diseases [3].Though present understanding of the role of epigenetic dysregulation contributing to the pathophysiology of diseases is rudimentary, a number of diseases including cancers [5] neuropsychiatric disorders [6], metabolic disorders [7] have been shown to have a strong association with epigenetic dysregulation.

Histone organization and post-transcriptional modification of histones contribute a major and well studied class of epigenetic marks. Histone proteins are integral components of the nucleosome and post-transcriptional modification of histones and their interplay with DNA base modifications largely regulate the transcription of genes. These post-transcriptional modifications of histones are modulated by proteins popularly known as histone modifiers, which dynamically regulate the pattern of modifications across the genome through a concerted, but poorly understood mechanism. Ample evidence in the recent years have shown that DNA methylation and histone modifications could modulate gene expression [8], mark gene boundaries [9] and potentially differentiate between protein-coding and noncoding gene promoters in the genome [10,11]. Histone modifiers or Epigenetic modifiers are largely categorised into three groups [12]. The first group of proteins largely post-translationally 'write' marks on the histone tail. Well studied examples of such proteins include histone Methyltransferases or acetyltransferases. The second group of proteins largely 'erase' existing marks on the histone, and include well characterized proteins like demethylases and deacetylases. The third and potentially poorly understood class of proteins recognise specific epigenetic marks and bind to the histone complex modulating their regulatory effect.

Epigenetic modifiers have been recently studied in detail as they could be attractive drug targets for diseases where epigenetic dysregulation play an important role, as in the case of some cancers [13]. This has been complemented by the availability of high throughput screening methodologies and assays for many of these proteins [14, 15]. The availability of these large-scale screening datasets in public domain also provide an immense opportunity to model the activities based on physicochemical and/or structural properties of molecules. These models

would be immensely useful in drug discovery applications to significantly reduce the time and effort by prioritising molecules with desirable activities for in-depth screening and biological validation. Such approaches have been extensively used by our group previously towards modelling activities [16–19].

In the present study, we employed four datasets of high-throughput screens for inhibitors of epigenetic modifiers. We used machine learning approaches using chemical descriptors to create accurate predictive models for the activities. We also use an independent substructure based approach to identify commonly enriched substructures associated with the activities. To the best of our knowledge, this is the first report of computational modelling of biological activities of small molecule inhibitors of epigenetic modifiers.

Methodology

Dataset source

The data for the potential inhibitors of Histone methyltransferases and demethylases was downloaded from PubChem repository of chemical compounds. The datasets were downloaded corresponding to AID 504332, AID 504339, AID 2147 and AID 540317.

Bioassay AID 504332. The qHTS was based on an assay developed for the inhibitors of G9a (Histone Lysine Methyltransferase) and included 30,875 active and 2, 67,000 inactive compounds. G9a is a histone methyltransferase which belongs to SET-domain containing family and specifically catalyzes methylation of Lys9 of histone H3 (H3K9) in mammalian euchromatic regions repressing the transcription [20, 21]. The knockdown of G9a results in transcriptional activation and inhibits cancer cells growth [22].

Bioassay AID 504339. The dataset contains inhibitors of JMJD2A-Tudor Domain JMJD2A, which is a jumonji-domain-containing histone demethylase (Lysine-specific demethylase 4A). JMJD2A binds to trimethylated H3K4 and H4K20 via the tudor domains and causes demethylation which may result in both, transcriptional repression and activation [23, 24]. Binding of JmjD2A to histone results in positioning of the enzymes for methylating adjacent regions causing rapid methylation over large area of chromatin [25, 26]. Targeting of the JMJD2A-tudor domain interaction with the methylation marks on lysine residues of histone, H3 and H4, tails may lead to selective demethylation of a given methyllysine locus based on the methylation state of adjacent histone marks. The demethylase activity follows radical attack mechanism using Fe (II) and α-ketoglutarate as co-factors. The substrate (mono, di or tri-methylated lysine) to be demethylated is determined by the association of enzymes with cofactors. The data contain 16,919 active compounds and 3, 38,945 inactive compounds.

Bioassay AID 2147. The dataset contains small molecule inhibitors of Human Jumonji Domain Containing 2E (JMJD2E). JMJD2E is a histone modifier enzyme and functions as a histone demethylase. Histone lysine demethylases catalyze the demethylation of methylated lysine side-chains on histones H3 and H4, thus acts to reverse the methylation reactions catalyzed by histone lysine methyltransferases. The high throughput data contained a total of 3,523 active and 1, 88,950 inactive compounds.

Bioassay AID 540317. The assay was developed to identify the first inhibitors of protein methyltransferases. The dataset contained 2,142 active and 3, 67,962 inactive compounds screened for potential inhibitors of HP1-beta chromodomain interactions with Methylated Histone Tails HP1 (Heterochromatin protein). The N- terminal chromodomain containing HP1 proteins bind to the methylated histones and further results in gene repression and heterochromatin formation. The interaction harbors an N- terminal chromodomain that binds to the tri-methylated lysine 9 of histone H3, H3K9me3, and a C-terminal chromoshadow domain. Compounds in PubChem are characterized based on Activity Score calculated using AC50.

AC50 is the concentration at which 50% of the activity is observed. Compounds having AC50 values less than or equal to 20 micromolar with corresponding activity score between 40–100 were considered as active compounds. Compounds having AC50 value greater than the highest concentration tested (for example 20 micromolar) and activity score 0 were considered as inactive compounds. The rest compounds with activity score between 1–39 were considered as inconclusive compounds.

All the datasets were obtained through the confirmatory bioassay screens conducted by NCGC, NIH Molecular Libraries Probe Production Network. The Amplified Luminescent Proximity Homogeneous Assay (AlphaScreen) from PerkinElmer was used for identification of these inhibitors. It is a homogeneous assay technology used for screening of different classes of targets and analytes. Donor and acceptor beads coated with a layer of hydrogel are utilized. The beads are conjugated with biological molecules. With excitation, ambient oxygen is converted to reactive singlet oxygen in the donor bead. The singlet oxygen species reacts with thioxene compounds in the acceptor bead to generate a chemiluminescent signal that emits at 370 nm. Streptavidin-coated and anti-IgG antibody-coated beads were employed for detecting the methylation state of biotinylated-histone peptide.

Pre-processing of data

The files obtained from PubChem in the Structure Data Format (SDF) were used to generate 2D molecular descriptors using PowerMV [27], a popular toolkit for computing chemical descriptors. PowerMV generated a total of 179 molecular descriptors describing the physicochemical properties of the molecule (like hydrogen bond donors, acceptors, number of rotatable bonds, charge, polarizability, aromaticity etc.). The descriptor file generated was saved in comma separated (CSV) format. The attributes having same bit string descriptor values throughout the dataset (all 0's or all 1's) were filtered out. The list of the descriptors generated and used is available as S1 Table.

Processing data and model building

The files saved in CSV format were then converted to ARFF (Attribute Relation File Format) compatible with Weka. The models were built using different classifications viz. Naive Bayes and Random Forest as described previously [16, 17, 18, 19]. For each base model we have used cost sensitive classifier in order to reduce the false negative rate. This was imperative as the datasets were highly imbalanced with a large inactive set compared to the active set. The misclassification cost is incremented on false negatives until the false positive rate reduces to 20%. Assignment of the cost is random irrespective of the base classifier used. Cost sensitive classification is based on cost-proportionate weighting of the training examples, which can be realized either by applying weights to the classification algorithm, or by resampling of instances according to costs. We used Weka 3.6 (Waikato Environment for Knowledge Analysis) [28] which is a toolbox for data mining and machine learning algorithms. Weka provides a simple GUI supporting data from various sources and in different file formats. It has multiple algorithms (including that of regression, association rule mining, clustering, classification etc.) and preprocessing tools that allow comparison of different methods. The workbench is used for both supervised as well as unsupervised algorithms. The data visualization facilities help in easy access and analysis of results. The dataset was then further randomly split into training and test sets. The training data comprising maximum part of complete data (80%) was used to train the model using different algorithms and the test set (20%) was to evaluate each of the models. All computation was performed on CDAC-Garuda supercomputing facility using the OSDD-Garuda web interface.

Cross validation

K-fold cross validation is one of the most popularly sued methods of cross-validation of the accuracy of a model. In k-fold cross validation, the entire data is divided into k subsets (folds) of equal sizes and training is done for (k-1) sets and testing is done on one set. The process is repeated k number of times so that each set is tested at least once. The average error rate is computed for all tests. We have used (k = 5) or a 5-fold cross validation here since the dataset was large.

Model performance evaluation

The 2X2 confusion matrix used by Weka contains the following values:

- True positives (TP): class members classified as class members.
- True negatives (TN): class non-members classified as non-members.
- False positives (FP): class non-members classified as class members.
- False negatives (FN): class members classified as class non-members.

We additionally used the following measures for the statistical evaluation of the models:

- **Sensitivity** is the proportion of actual positives which are predicted positive, i.e.TP / (TP + FN).
- **Specificity** is the proportion of actual negatives which are predicted negatives, i.e. TN / (TN + FP).
- **ROC** is receiver operating characteristic curve which is a 2D curve parameterized by one parameter of the classification algorithm, e.g. some threshold in the true positive rate /false positive rate.
- The **Matthews correlation coefficient** is a measure of correlation between the observed and predicted binary classifications and quality of the classifier. The values range between −1 and +1.
- **Balanced Classification Rate (BCR)** introduces a balance in the classification calculated as 1⁄2. (Sensitivity + Specificity).
- **Accuracy** is the efficiency of the classifier to predict true values, i.e. TP+TN) / (TP+TN+FP +FN) * 100).

Substructure search

Aligning structures on a key structural framework help chemists to interpret the influence of substituents on the template as initial point towards understanding structure-activity information. With the aim of finding molecules which have similar properties to act as a drug, similarity search of compounds was done. Library MCS, a tool from ChemAxon [29], based on hierarchical clustering algorithm was used to cluster the molecules and find the potential bioactive substructures. Hierarchical clustering only requires a measure of similarity between groups of data points. Maximal Common Substructure Search (MCS) is the process of finding the largest structure that is a substructure or part of all the molecules in a given set. Initial structures are found at the bottom of the hierarchy. The next level contains the maximum common structures of clusters of initial molecules; subsequent levels provide larger clusters of smaller common substructures.

Minimal MCS size refers to the smallest size of the maximum common substructure searched for by the algorithm. For different datasets different values were considered owing to

the number of top level clusters found and the level count. For AID 504332 and 540317, minimal MCS size was taken 9 and for AID 504339 and 2147 it was 10 and 11 respectively. After the clusters were formed using LibMCS, we got the molecular scaffolds in the form of sdf and SMILES file. The active and inactive 3D structure files were then used to search the similar substructures with the smiles generated. This was done using the jcsearch algorithm of ChemAxon [30]. The similarity is calculated on the basis of the molecular descriptor or fingerprint of the chemical structures to compare. The Substructures were evaluated for enrichment using chi-square test. The p-values were computed to evaluate the significance of enrichment. The substructures which had at least 1% matches among the active dataset entries, p-value less than 0.01 and enrichment factor more than 5 were considered significant.

Results

The datasets obtained from PubChem were processed to generate 2D molecular descriptors using PowerMV. The descriptors were finally culled to 155 from 179 descriptors after removing values which were either null or the same for the entire dataset and could not contribute to the classification (S1 Table). The complete data after splitting into train and test sets was loaded in Weka-3.6 to build different classifier models for the evaluation of compounds. Initially standard classification of the data was performed. However, since the datasets were skewed, cost sensitive classification was introduced. The misclassification cost was applied on false negatives and incremented until the rate of false positives reached 20%. The costs applied in different datasets for different models are shown in Table 1. Naive bayes used minimum cost for the classification of the objects.

Evaluation of models included various statistical parameters. The accuracy of Random forest was predicted to be the highest for all the datasets. A comparison between the sensitivity of both the classification models amongst different datasets was made depicting the sensitivity of Random forest more than the Naive Bayes in all cases. Recent studies on comparison of classifiers performance have reported that Random forest outperforms Naïve bayes in terms of accuracy of prediction [31]. Random forest uses multiple decision trees to place an instance into a particular class and the output is the average of the individual trees output whereas Naïve bayes is a probabilistic approach which calculates the probability of a compound being in a particular class on the basis of presence of certain independent features [32]. It has also been shown that the assembly of trees gives much accurate prediction than single one [33]. Our group has also previously shown that the Random forest has outperformed Naïve bayes in similar cheminformatics analyses [16–19] on bioassay datasets. Fig 1 shows the plot between sensitivity of Naive Bayes and Random Forest amongst AID 504332, 504339, 2147 and 540317. Similarly the specificity was compared where Naive Bayes outperforms in AID 504339 and 2147. In case of AID 540317 specificity of both was comparable and Random Forest showed higher specificity in AID 504332. Fig 2 is the comparative graph between the specificity of both classification models amongst all four datasets.

Table 1. Misclassification costs used for False Negatives (FN).

PubChem Assay ID	*Naive Bayes*	*Random Forest*
AID 504332	2	50
AID 504339	10	1000
AID 2147	45	3000
AID 540317	30	25000

doi:10.1371/journal.pone.0083032.t001

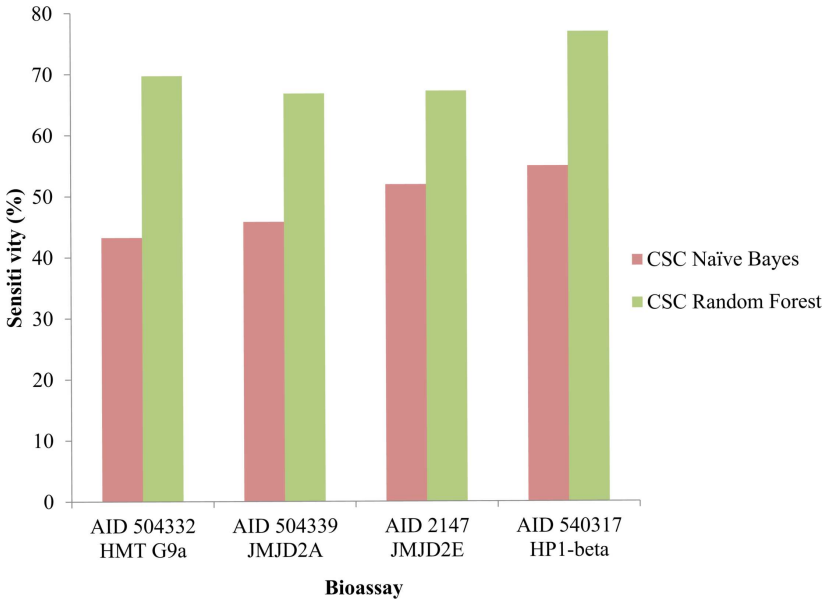


Fig 1. Graph between sensitivity of Naive Bayes and Random Forest amongst AID 504332, 504339, 2147 and 540317.

doi:10.1371/journal.pone.0083032.g001

The sensitivity and specificity were used to calculate the balanced classification rate for each model. Random forest showed the most balanced classification out of both. As a measure of quality, Matthews's correlation coefficient (MCC) was calculated. The Matthews correlation coefficient (MCC) also known as the phi coefficient is a measure of correlation between the actual and predicted classifications. Table 2 shows the classification results of all the datasets along with the statistical evaluation. The summary of the parameters are summarised in Table 3.

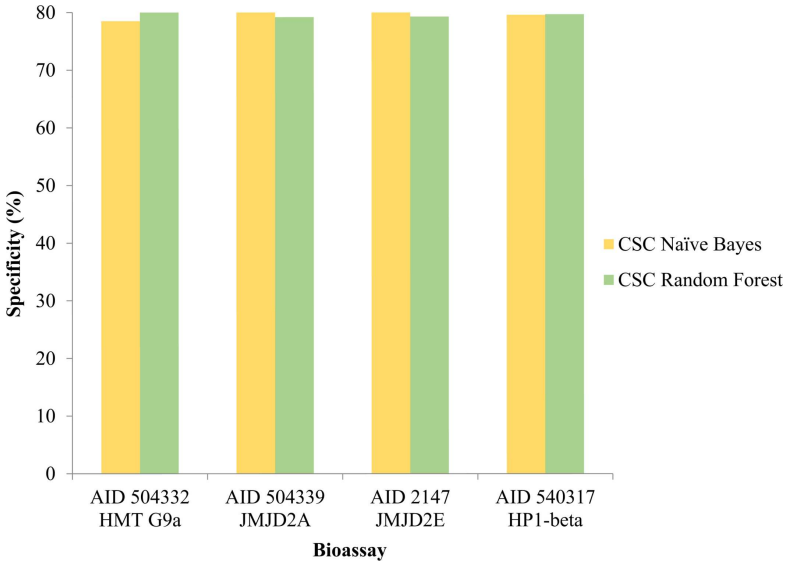


Fig 2. Comparative graph between the specificity of both classification models amongst all four datasets.

doi:10.1371/journal.pone.0083032.g002

Table 2. Overall summary of the performance of the models.

PubChem Assay ID	Classifer	TP Rate	FP Rate	ROC	Accuracy	MCC	BCR
AID 504332	CSCNB	43.2	21.5	66.5	74.84	0.15	60.89
	CSCRF	69.7	19.5	82.1	79.39	0.35	75.11
AID 504339	CSCNB	45.8	19.6	68.5	79.43	0.10	63.08
	CSCRF	66.8	20.8	79.4	78.88	0.17	72.99
AID 2147	CSCNB	51.9	20.0	72.4	79.58	0.09	65.97
	CSCRF	67.2	20.7	80.1	79.12	0.14	73.24
AID 540317	CSCNB	54.9	20.4	74.2	79.45	0.06	67.25
	CSCRF	76.9	20.3	85.8	79.67	0.10	78.28

doi:10.1371/journal.pone.0083032.t002

A perfect test would have 100% sensitivity and specificity, but in realistic scenarios, however this is seldom achieved and a balance between sensitivity and specificity is desirable. For that, a relation of sensitivity and specificity on a graph, called a "Receiver-Operator-Characteristic (ROC) curve" was plotted. Fig 3 summarises the ROC plot for Random Forest classification model for the four datasets. The Area under the curve for the ROC-plots was 0.82, 0.68, 0.80 and 0.67 for the AID 504332, AID 504339, AID 2147 and AID 540317 respectively.

Evaluation of significantly enriched scaffolds

In the process of drug discovery the local similarity between the structures proved to be useful in designing of new chemical compounds as potential drugs. We used JChem module, LibMCS and clustered the active compounds of all the datasets. In the present study, we have also evaluated enriched substructures, rather than substructures which are exclusive for the actives. Conceptually this would mean that the feature/substructure in consideration alone would not have necessary predictive ability to define activity, but rather has a larger probability to be found among the actives. It is believed that the compounds having similar structures often have similar properties and biological activities [34].Our analysis shows a subset of the substructures are significantly enriched in the actives compared to inactives by a few folds. The presence of the feature/substructure alone would not have necessary predictive ability to define activity, but rather has a larger probability to be found among the actives.

Clustering analysis of AID 504332

The 30875 active compounds clustered into a total of 5,150 clusters of which the 726 top level cluster compounds were considered. The compounds were clustered upto level 6 out of which 258 singletons were removed. The enrichment and its significance, was analyzed by chi-square test. Analysis revealed 19 significantly enriched scaffolds which had p-value less than 0.01 and an enrichment factor > 5.

Table 3. Shows the details of the LibMCS cluster report for different data sets studied.

LibMCS parameters	AID 504332	AID 504339	AID 2147	AID 540317
MCS size	9	10	11	9
Level Count	6	6	5	6
Top level cluster count	726	1026	702	216
Total Cluster Count	5150	7113	3791	1437
Singletons	258	416	365	93
Significant substructures	19	9	9	8

doi:10.1371/journal.pone.0083032.t003

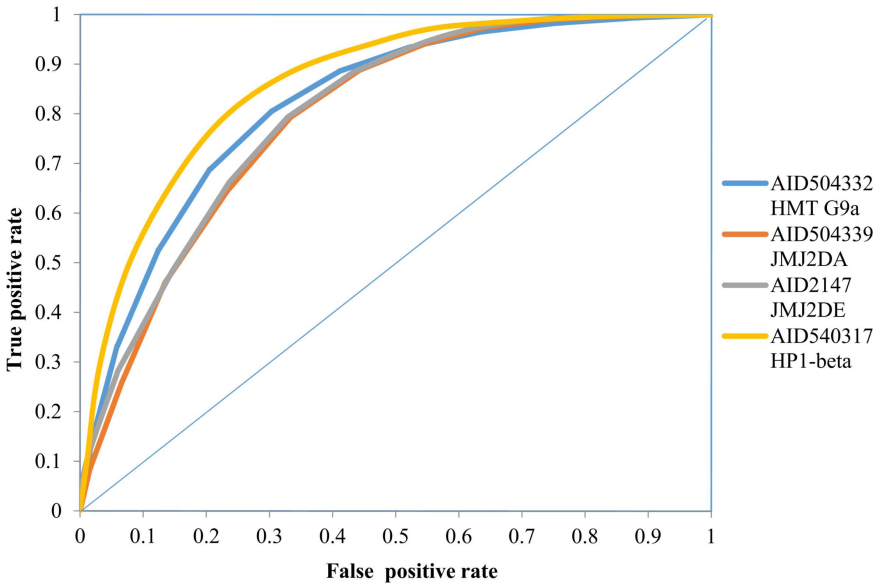


Fig 3. ROC plot for Random Forest classification model for the four datasets.

doi:10.1371/journal.pone.0083032.g003

Clustering analysis of AID 504339

A total of 16919 active compounds were clustered upto 6 levels at MCS size 10. 416 singletons were removed and 1026 compounds obtained at top level were taken for further analysis. We obtained 9 substructures prioritized by p-value (less than 0.01) and enrichment factor > 5.

Clustering analysis of AID 2147

The 3523 compounds were clustered keeping MCS size as 11, we obtained 3791 total clusters. A total of 702 compounds were obtained at level 5 out of which 365 singletons were removed. The final prioritization was done keeping p value less than 0.01 and enrichment factor > 5, the analysis resulted in 9 substructures.

Clustering analysis of AID 540317

The 2142 active compounds were clustered upto 6 levels keeping MCS size as 9. We obtained 216 compounds at top level after removing 93 singletons. Analysis revealed 8 significantly enriched scaffolds which had p-value less than 0.01 and an enrichment factor > 5.

The results for the clustering approach used and the enriched scaffold for each of the datasets considered have been summarised in tables (S2–S5 Tables).

Discussion

Understanding the function and regulation of epigenetic modifier proteins have been recently an actively pursued area of research [35]. This has been more so, with the increasingly understood mechanisms of epigenetic regulation in the pathophysiology of a number of diseases. The role of epigenetic modifiers has been extensively studied in a variety of neoplasms [36, 37, 38, 39, 40]. It has also been discussed that molecules that could target epigenetic modifiers could be a potential new avenue for drug development [41]. In fact, targeting epigenetic modifiers as potential drug targets have been extensively discussed and pursued [42, 43]. The cornerstone of any rational drug discovery process starts from systematic screening of molecular

libraries against target proteins, and assaying them for their biological outputs or phenotypes. Testing large libraries of molecules for specific biological activities are usually time consuming and extremely costly. Computational methods for pre-selecting molecules from large libraries would offer a plausible time and cost-effective alternative [41]. It has been suggested that accurate methodologies to pre-select molecules for in-depth biological assays would accelerate the process of drug discovery. A number of methodologies including molecular docking [44, 45] and other cheminformatics methods [46, 47, 48] have been extensively used to prioritise molecules in drug discovery process. Machine learning approaches have been used extensively now for building predictive models for pre-selecting molecules form large molecular databases [16–19]. The availability of datasets of high-throughput screens on large molecular libraries of small molecules which are quite diverse offers an enormous opportunity to learn molecular and structural properties of molecules and their association or correlation with phenotypic or biological outcomes.

The present manuscript discusses how computational methods could be used to mine potential actives based on chemical descriptors. We propose a computational pre-screening would improve the chance of finding an active from a given dataset, which could potentially imply savings in cost and resources. In real-life situations, chemists synthesize molecules based on scaffolds which are largely associated with activity. We have additionally used a substructure enrichment analysis to understand substructures which are largely associated with activity, nevertheless does not imply activity. This would allow chemists to suitably modify molecules or be able to synthesize molecules of a particular variety or based on a particular scaffold, so as to potentially improve the hit rate. We do find a significant large number, albeit a significant small number by proportion due to the very fact that there are a far higher number of molecules in the inactive set compared to that of actives.

We show that machine learning based approaches can provide computational models which are highly accurate which could be potentially used to screen large molecular libraries. The study is not without caveats, the first being the paucity of data sets in public domain encompassing inhibitors for a large number of epigenetic modifiers precludes us from creating a comprehensive suite of predictive models, which could be eventually possible with more data sets being available in public domain. In the future, many such computational models could be integrated to provide for desirable set of properties or biological activities and has the potential to be integrated into drug discovery pipelines, with significant gains in the cost and timespan associated with a conventional drug discovery process [49]. The present study also provides the first comprehensive overview and cheminformatics analysis of small molecule modulators of epigenetic modifiers.

Supporting Information

S1 Table. List of the molecular descriptors used from PowerMV.
(DOCX)

S2 Table. Depicts significantly enriched scaffolds found in AID 504332.
(DOCX)

S3 Table. Shows the significant substructures found in AID 504339 along with their p-value and chi-square statistics.
(DOCX)

S4 Table. Shows the enriched substructures in AID 2147 with a threshold of 5 for enrichment factor and p-value less than 0.01.
(DOCX)

S5 Table. Shows significantly enriched substructures in AID 540317.
(DOCX)

Acknowledgments

The authors thank Dr. Chetana Sachidanandan and Dr. Shantanu Sengupta for reviewing the manuscript. The authors are also thankful for discussions with members of the Open Source Drug Discovery (OSDD) Programme. SJ acknowledges a Project Fellowship from CSIR-OSDD. The authors acknowledge the support from National Knowledge Network (NKN) and CDAC-Garuda for computing. The authors acknowledge technical help and support from the CDAC-Garuda team, especially Ms. Janaki Chintalapati, Ms. Mangala N and Dr. Subrata Chattopadhyay.

Author Contributions

Conceived and designed the experiments: SJ VS.

Performed the experiments: SA SJ.

Analyzed the data: SA SJ.

Contributed reagents/materials/analysis tools: VS.

Wrote the paper: SA SJ VS.

References

1. Alberts B, Johnson A, Lewis J (2002) The Molecular Genetic Mechanisms That Create Specialized Cell Types. Molecular Biology of the Cell. 4th edition. New York: Garland Science.
2. Blake WJ (2003) Noise in eukaryotic gene expression. Nature 422: 633–637. PMID: 12687005
3. Miller-Jensen K (2011) Varying virulence: epigenetic control of expression noise and disease processes. Trends in Biotechnol. 29: 517–525.
4. Bird A (2007) Perceptions of epigenetics. Nature 447 (7143): 396–8. PMID: 17522671
5. Momparler RL (2003) Cancer epigenetics. Oncogene 22: 6479–6483. PMID: 14528271
6. Graff J, Kim D, Dobbin MM, Tsai LH (2011) Epigenetic Regulation of Gene Expression in Physiological and Pathological Brain Processes. Physiol Rev. 2011 91(2): 603–49. doi: 10.1152/physrev.00012.2010 PMID: 21527733
7. Volkmar M, Dedeurwaerder S, Cunha DA, Ndlovu MN, Defrance M, et al. (2012) DNA methylation profiling identifies epigenetic dysregulation in pancreatic islets from type 2 diabetic patients. EMBO J. 31 (6): 1405–26. doi: 10.1038/emboj.2011.503 PMID: 22293752
8. Handy DE, Castro R, Loscalzo J (2011) Epigenetic modifications: basic mechanisms and role in cardiovascular disease. Circulation. 123(19): 2145–56. doi: 10.1161/CIRCULATIONAHA.110.956839 PMID: 21576679
9. Bird A (2002) DNA methylation patterns and epigenetic memory. Genes and Dev. 16: 6–21. PMID: 11782440
10. Sati S, Ghosh S, Jain V, Scaria V, Sengupta S (2012) Genome-wide analysis reveals distinct patterns of epigenetic features in long non-coding RNA loci. Nucleic Acids Research 40(20): 10018–31. doi: 10.1093/nar/gks776 PMID: 22923516
11. Wang XQ, Crutchley JL, Dostie J (2011) Shaping the Genome with Non-Coding RNAs. Curr Genomics 12(5): 307–321. doi: 10.2174/138920211796429772 PMID: 21874119
12. Aiese CR, Sanseverino W, Cremona G, et al. (2013) Genome-wide analysis of histone modifiers in tomato: gaining an insight into their developmental roles. BMC Genomics 14:57. doi: 10.1186/1471-2164-14-57 PMID: 23356725
13. Arrowsmith CH, Bountra C, Fish PV, Lee K, Schapira M (2012) Epigenetic protein families: a new frontier for drug discovery. Nature Reviews Drug Discovery 11: 384–400. doi: 10.1038/nrd3674 PMID: 22498752

14. Quinn AM, Simeonov A (2011) Methods for Activity Analysis of the Proteins that Regulate Histone Methylation. Current Chemical Genomics 5: 95–105. doi: 10.2174/1875397301005010095 PMID: 21966349
15. Falk H, Connor T, Yang H, Loft KJ, Alcindor JL, et al. (2011) An efficient high-throughput screening method for MYST family acetyltransferases, a new class of epigenetic drug targets. J Biomol Screen. 16(10): 1196–205. doi: 10.1177/1087057111421631 PMID: 22086725
16. Periwal V, Rajappan JK, Jaleel AU, Scaria V (2011) Predictive models for antitubercular molecules using machine learning on high-throughput biological screening datasets. BMC Res Notes 4: 504. doi: 10.1186/1756-0500-4-504 PMID: 22099929
17. Periwal V, Kishtapuram S, Scaria V (2012) Computational models for in-vitro antitubercular activity of molecules based on high-throughput chemical biology screening datasets. *BMC Pharmacol*. 12:1. doi: 10.1186/1471-2210-12-1 PMID: 22463123
18. Jamal S, Periwal V, Consortium O, Scaria V (2012) Computational analysis and predictive modeling of small molecule modulators of microRNA. J Cheminform. 4:16. doi: 10.1186/1758-2946-4-16 PMID: 22889302
19. Jamal S, Periwal V, Open Source Drug Discovery Consortium, Scaria V (2013) Predictive modeling of antimalarial molecules inhibiting apicoplast formation. BMC Bioinformatics 14(1):55.
20. Shinkai Y, Tachibana M (2011) H3K9 methyltransferase G9a and the related molecule GLP. Genes & Dev. 25:781–788.
21. Tachibana M, Sugimoto K, Nozaki M, Ueda J, Ohta T, et al. (2002) G9a histone methyltransferase plays a dominant role in euchromatic histone H3 lysine 9 methylation and is essential for early embryogenesis. Genes & Dev. 16:1779–1791.
22. Kondo Y, Shen L, Ahmed S, Boumber Y, Sekido Y. Downregulation of Histone H3 Lysine 9 Methyltransferase G9a Induces Centrosome Disruption and Chromosome Instability in Cancer Cells. PLoS ONE. 3(4): e2037. doi: 10.1371/journal.pone.0002037 PMID: 18446223
23. Ozboyaci M, Gursoy A, Erman B, Keskin O (2011) Molecular Recognition of H3/H4 Histone Tails by the Tudor Domains of JMJD2A: A Comparative Molecular Dynamics Simulations Study. PLoS ONE 6(3): e14765. doi: 10.1371/journal.pone.0014765 PMID: 21464980
24. Cloos PA, Christensen J, Agger K, Helin K (2008) Erasing the methyl mark: histone demethylases at the center of cellular differentiation and disease. Genes Dev. 22:1115–1140. doi: 10.1101/gad.1652908 PMID: 18451103
25. Vermeulen M, Timmers HT (2010) Grasping trimethylation of histone H3 at lysine 4. Epigenomics 2 (3):395–406. doi: 10.2217/epi.10.11 PMID: 22121900
26. Musselman CA, Lalonde ME, Cote J, Kutateladze TG (2012) Perceiving the epigenetic landscape through histone readers. Nat Struct Mol Biol. 19(12):1218–27. doi: 10.1038/nsmb.2436 PMID: 23211769
27. Liu K, Feng J, Young SS (2005) PowerMV: a software environment for molecular viewing, descriptor generation, data analysis and hit evaluation. J Chem Inf Model 45:515–522. PMID: 15807517
28. Bouckaert RR, Frank E, Hall MA, Holmes G, Pfahringer B, et al. (2010) Weka -Experiences with a Java Open-Source Project. Journal of Machine Learning Research 2533–2541.
29. Budapest H. Chemaxon: Library MCS, version 0.7; 2008.
30. Budapest H. Chemaxon: Jcsearch, version 5.8.2.
31. Caruana R, Niculescu-Mizil A (2006) An empirical comparison of supervised learning algorithm. In Proceedings of the 23rd International Conference on Machine Learning, Pittsburg, PA. ACM: New York.
32. Bin C, Robert PS, Viktor H, Johannes HV (2012) Comparison of Random Forest and Pipeline Pilot Naive Bayes in Prospective QSAR Predictions. J. Chem. Inf. Model 52, 792–803. doi: 10.1021/ci200615h PMID: 22360769
33. Svetnick V, Wang T, Tong C, Liaw A, Sheridan RP (2005) Boosting: an ensemble learning tool for compound classification and QSAR modeling. J. Chem. Inf. Model 45, 786–799. PMID: 15921468
34. Johnson M, Maggiora G (1990) Concepts and Applications of Molecular Similarity. New York: Wiley.
35. Piekarz RL, Bates SE (2009) Epigenetic Modifiers: Basic Understanding and Clinical Development. Clin Cancer Res. 15:3918–26. doi: 10.1158/1078-0432.CCR-08-2788 PMID: 19509169
36. Shu XS, Geng H, Li L, Ying J, Ma C, et al. (2011) The epigenetic modifier PRDM5 functions as a tumor suppressor through modulating WNT/β-catenin signaling and is frequently silenced in multiple tumors. PLoS One. 6(11):e27346. doi: 10.1371/journal.pone.0027346 PMID: 22087297
37. Kaneda A, Feinberg AP (2005) Loss of imprinting of IGF2: a common epigenetic modifier of intestinal tumor risk. Cancer Res. 65(24):11236–40. PMID: 16357124

38. Mund C, Lyko F (2010) Epigenetic cancer therapy: Proof of concept and remaining challenges. Bioessays 32(11): 949–57. doi: 10.1002/bies.201000061 PMID: 21154865

39. Vlerken LE, Kiefer CM, Morehouse C, Li Y, Groves C (2013) EZH2 is required for breast and pancreatic cancer stem cell maintenance and can be used as a functional cancer stem cell reporter. Stem Cells Transl Med. 2(1):43–52. doi: 10.5966/sctm.2012-0036 PMID: 23283488

40. Leong HS, Chen K, Hu Y, Lee S, Blewitt ME (2013) Epigenetic regulator Smchd1 functions as a tumor suppressor. Cancer Res. 73(5):1591–9. doi: 10.1158/0008-5472.CAN-12-3019 PMID: 23269277

41. Unoki M (2011) Current and potential anticancer drugs targeting members of the UHRF1 complex including epigenetic modifiers. Recent Pat Anticancer Drug Discov. 6(1):116. PMID: 21110828

42. Xu J, Hagler A (2002) Chemoinformatics and Drug Discovery. Molecules 7:566–600.

43. Kumar N, Hendriks BS, Janes KA, de Graaf D, Lauffenburger DA (2006) Applying Computational modeling to drug discovery and development. Drug Discov Today. 11(17–18): 806–11. PMID: 16935748

44. Huang SY, Zou X (2010) Advances and challenges in protein-ligand docking. Int J Mol Sci. 11 (8):3016–34. doi: 10.3390/ijms11083016 PMID: 21152288

45. Diller DJ, Merz KM Jr (2001) High throughput docking for library design and library prioritization. Proteins 43(2):113–24. PMID: 11276081

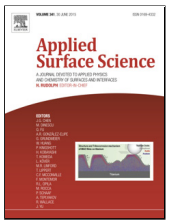
46. Lv S, Xu Y, Wang Q, Li X, Su B (2012) Prioritizing cancer therapeutic small molecules by integrating multiple OMICS datasets. OMICS. 16(10):552–9. doi: 10.1089/omi.2012.0005 PMID: 22917481

47. Rabinowitz JR, Goldsmith MR, Little SB, Pasquinelli MA (2008) Computational molecular modeling for evaluating the toxicity of environmental chemicals: prioritizing bioassay requirements. Environ Health Perspect. 116(5):573–7. doi: 10.1289/ehp.11077 PMID: 18470285

48. Sean E, Binghe W (2006) Computer Applications in Pharmaceutical Research and Development. Wiley Series in Drug Discovery and Development. 1st Edition.

49. Ekins S, Freundlich JS (2013) Computational Models for Tuberculosis Drug Discovery. Methods Mol Biol. 993: 245–62. doi: 10.1007/978-1-62703-342-8_16 PMID: 23568475

Accepted Manuscript



Title: Development of surface functionalized ZnO-doped $LiFePO_4$/C composites as alternative cathode material for lithium ion batteries

Author: Rakesh Saroha Amrish K. Panwar Yogesh Sharma Pawan K. Tyagi Sudipto Ghosh

PII: S0169-4332(16)31983-3
DOI: http://dx.doi.org/doi:10.1016/j.apsusc.2016.09.105
Reference: APSUSC 34034

To appear in: *APSUSC*

Received date: 27-5-2016
Revised date: 12-9-2016
Accepted date: 21-9-2016

Please cite this article as: Rakesh Saroha, Amrish K.Panwar, Yogesh Sharma, Pawan K.Tyagi, Sudipto Ghosh, Development of surface functionalized ZnO-doped LiFePO4/C composites as alternative cathode material for lithium ion batteries, Applied Surface Science http://dx.doi.org/10.1016/j.apsusc.2016.09.105

This is a PDF file of an unedited manuscript that has been accepted for publication. As a service to our customers we are providing this early version of the manuscript. The manuscript will undergo copyediting, typesetting, and review of the resulting proof before it is published in its final form. Please note that during the production process errors may be discovered which could affect the content, and all legal disclaimers that apply to the journal pertain.

ACCEPTED MANUSCRIPT

Development of surface functionalized ZnO-doped $LiFePO_4$/C composites as alternative cathode material for lithium ion batteries

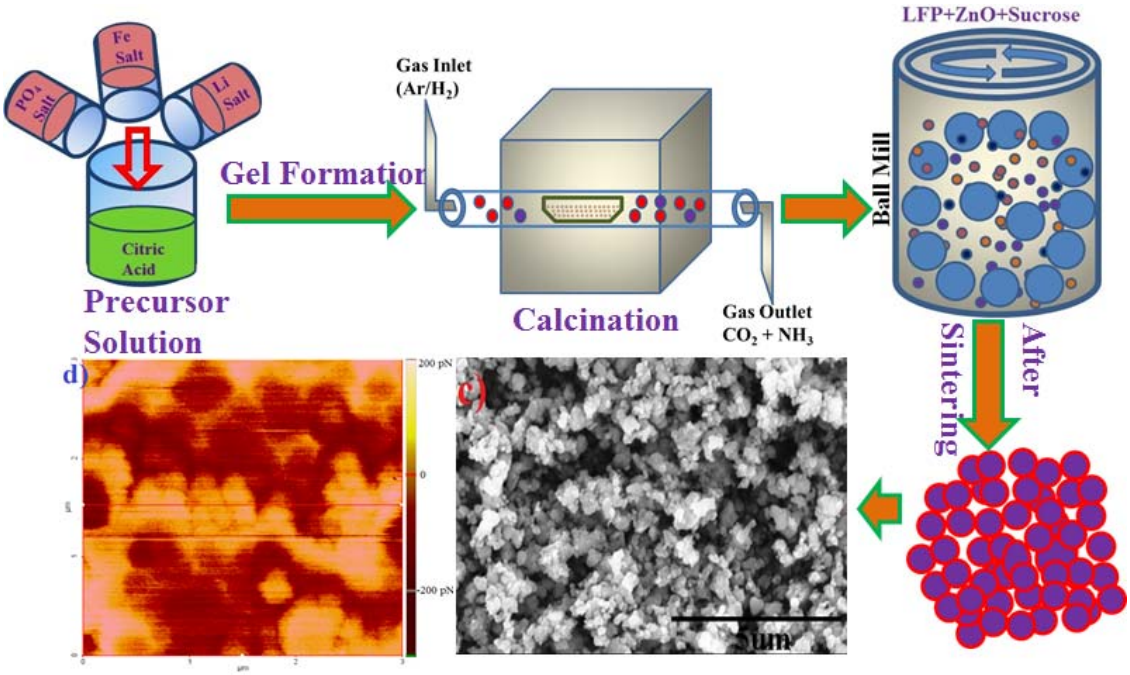
Rakesh Saroha[a], Amrish K. Panwar[a,*], Yogesh Sharma[b], Pawan K. Tyagi[a], and Sudipto Ghosh[c]

[a]*Department of Applied Physics, Delhi Technological University, Delhi-110042, India.*

[b]*Department of Physics, IIT Roorkee, Roorkee, Uttarakhand-247667, India.*

[c]*Department of Metallurgical & Materials Engineering, IIT Kharagpur, West Bengal-721302, India.*

Graphical Abstract:



Highlights

- Pristine $LiFePO_4$ and ZnO/C- hybrid coated $LiFePO_4$ samples has been synthesized using sol-gel assisted ball milling route.

ACCEPTED MANUSCRIPT

- Effect of ZnO/C-hybrid coating on the $LiFePO_4$ has been studied thoroughly.
- Electronic conductivity of pristine $LiFePO_4$ increases to 10^2-10^3 orders of magnitude for ZnO/C- coated samples.
- AFM results indicate the presence of more volumetric charge density at the surface for ZnO/C-coated $LiFePO_4$ sample.
- LFPZ2.5 shows best cycling and rate performances among all the prepared samples.
- Lithium ion diffusion coefficient increases significantly.

ABSTRACT

Surface modified olivine-type $LiFePO_4$/C-ZnO doped samples were synthesized using sol-gel assisted ball-milling route. In this work, the influence of ZnO-doping on the physiochemical, electrochemical and surface properties such as charge separation at solid-liquid interphase, surface force gradient, surface/ionic conductivity of pristine $LiFePO_4$/C (LFP) has been investigated thoroughly. Synthesized samples were characterized using X-ray diffraction, scanning electron microscopy, atomic force microscopy, and transmission electron microscopy. All the synthesized samples were indexed to the orthorhombic phase with *Pnma* space group. Pristine $LiFePO_4$ retain its structure for–higher ZnO concentrations (i.e. 2.5 and 5.0 wt.% of LFP). Surface topography and surface force gradient measurements by EFM revealed that the kinetics of charge carriers, e^-/Li^+ is more in ZnO-doped LFP samples, which may be attributed to diffusion or conduction process of the charges present at the surface. Among all the synthesized samples LFP/C with 2.5 wt.% of ZnO (LFPZ2.5) displays the highest discharge capacity at all C-rates and exhibit excellent rate performance. LFPZ2.5 delivers a specific discharge capacity of 164 (±3) $mAhg^{-1}$ at 0.1C rate. LFPZ2.5 shows best cycling performance as it provides a discharge capacity of 135 (±3) $mAhg^{-1}$ at 1C rate and shows almost 95 % capacity retention after 50 charge/discharge cycles. Energy density plot shows that LFPZ2.5 offers high energy and power density measured at high discharge rates (5C), proving its usability for hybrid vehicles application.

Keywords: Olivine-cathode; ZnO-doping; Charge separation; Surface force gradient; Ragone Plot.

ACCEPTED MANUSCRIPT

1. Introduction

Intense pressure on non-renewable sources of energy like coal, crude oil, etc. and problems associated with their use like air pollution, greenhouse gasses ejection, global warming has forced the research community to look for their substitute energy sources which prove to be environmental friendly and less health hazardous. At present, rechargeable lithium ion battery coupled with renewable energy sources like solar power are playing a vital role in the direction of developing such kind of energy storage devices which meet requirements of safety, non-toxic, low cost, high energy and power density to power electric vehicles (EV) and hybrid electric vehicles (HEV) [1, 2]. Olivine-type $LiFePO_4$ is one such kind of cathode material which proves to be most promising cathode material as far as structure stability, the flat charge/discharge voltage plateau and excellent rate performance have been concerned. It has undergone extensive research since it was first reported by Padhi et al. in 1997 [3]. It satisfies most of the requirements needed for a cathode material like high theoretical capacity (170 $mAhg^{-1}$), low cost, structural stability with excellent capacity retention and environmentally benign due to its non-toxicity [4-14]. It possesses a stable voltage plateau at around 3.45 V vs. Li^+/Li because of two-phase redox reaction corresponding to the transition metal $Fe^{2+/3+}$ couple. However, its low electronic conductivity ($10^{-9} – 10^{-11}$ S/cm) and sluggish lithium ion diffusion kinetics (~10^{-18} cm^2/s) have restricted its widespread use in automotive industry and hybrid vehicles [15-17]. Various ways have been adopted so far to increase the surface/electronic conductivity of pristine $LiFePO_4$ cathode material which includes carbon coating [18, 19] and cation doping at the lithium (M1) or iron (M2) site [20, 21]. Apart from this, enhancement in conductivity can be attained by coating/surface modification of $LiFePO_4$ material with electronically conductive materials like SnO_2 [1], CeO_2 [2], $LaPO_4$ [9], ZnO [10], CuO [11], FeP [14], Li_3PO_4 [17], NiO [22], NbC [23], TiO_2 [24], $CePO_4$ [25], LLTO [26], LTO [27], etc.

As far as coatings/surface modification aspect is concerned, carbon coating by using different carbon source has been widely applied to improve the conductivity and electrochemical performance of cathode active material. However, conducting carbon coatings attenuates tap density of $LiFePO_4$ cathode material and hence, degrades energy density [28]. Apart from conducting carbon coating, there are various reports on metal oxides coatings of $LiFePO_4$ material. Among such metal oxide

ACCEPTED MANUSCRIPT

conductive materials, Zinc oxide (ZnO) proves to be an excellent alternative due to its easiness of synthesis and widespread application in various areas. Being a large band gap semiconducting material, it provides good electrical contacts at the surface of the active electrode material particle and facilitates fast lithium ion/electron transfer. It has also been reported earlier that introduction of Zn into $LiFePO_4$ lattice introduce some kind of "pillar effect" which provides more space for lithium ion movement and consequently, the conductivity of $LiFePO_4$ has enhanced and so its lithium ion diffusion coefficient [29]. Hu et al. [30] studied ZnO-doped $LiFePO_4$ fabricated by hydrothermal method and found that ZnO-doped sample delivers discharge capacities of 132.3 $mAhg^{-1}$ and 80 $mAhg^{-1}$ at 0.1C and 1C, respectively. Till now there are no literature reports regarding how surface modification by ZnO-doping enhanced the electrochemical performance of the pristine $LiFePO_4$.

In this work, the effects of surface functionalization by ZnO-doping on the physicochemical, surface and electrochemical properties of the pristine $LiFePO_4$ have been systematically investigated. The effects of charge separation phenomenon at the interface of ZnO doped $LiFePO_4$/C has been discussed. Surface force imaging has been studied by observing the variation of surface electrostatic force/potential on the surface of pristine LFP and ZnO-doped LFP/C samples using atomic force microscopy. All the samples were synthesized using the sol-gel assisted wet-milling route with sucrose. All the synthesized samples were examined using XRD, SEM, AFM, TEM and FTIR. Rietveld refinement was performed to study the effect of ZnO-doping on the crystal lattice parameters of pristine LFP sample. Electrochemical characterization of as-prepared samples was carried out to study electrochemical properties and lithium ion kinetics.

2. Experimental

2.1. Material Synthesis

Stoichiometric amounts of $LiOH.H_2O$ (Sigma-Aldrich, ~99%), $Fe(NO_3)_3.9H_2O$ (CDH, 98%) and $H_9N_2O_4P$ (Sigma-Aldrich, ≥99%) were used as precursors for the synthesis of pristine $LiFePO_4$ and ZnO-doped $LiFePO_4$/C samples. Citric acid was used as a chelating agent. A separate solution of all the precursors in deionized water was prepared with continuous stirring and then added to citric acid solution one by one. The pH value of the resulting solution was maintained between 6 and 7. The ratio of metal ion to the citric acid was kept 1:1. The resulting solution of citric acid and precursors

ACCEPTED MANUSCRIPT

was heated at 70 °C at 400 rpm with continuous stirring until a transparent greenish gel was obtained. The gel thus obtained was decomposed at 350 °C for 5 h in a tubular furnace under reducing atmosphere. Decomposition causes removal of organic matter and volatile impurities in the form of gasses according to the following reaction;

$$LiOH.H_2O+Fe(NO_3)_3.9H_2O+H_9N_2O_4P = LiFePO_4+2NH_3+2CO_2+16H_2O \quad (1)$$

Thus yielded powder was reground together with ZnO and sucrose. Sucrose GR ($C_{12}H_{22}O_{11}$, MERCK) was used as an additive of carbon source and reducing agent as well. The quantity of sucrose was kept fixed at 10 wt.% of $LiFePO_4$ remains after decomposition while the amount of ZnO was varied as 1.0, 2.5 and 5.0 wt.% of $LiFePO_4$ for different compositions. The sucrose was added only to ZnO-treated LFP samples in order to have ZnO-doped $LiFePO_4$/C compositions. Finally, $LiFePO_4$, sucrose, and ZnO in different wt.% were ball milled for 2 h at 400 rpm in toluene media. The final product was obtained by heating the mixture at 750 °C for 12 h in slightly reducing atmosphere to assist the reduction of Fe^{3+} to Fe^{2+}. The tube furnace was evacuated for 20 min in advance before heating, and the heating rate was kept at 5 °C min^{-1}. The finally obtained powders were abbreviated as LFP, LFPZ1, LFPZ2.5, LFPZ5 corresponding to 0.0, 1.0, 2.5 and 5.0 wt.% of ZnO nanopowder. ZnO nanopowder was synthesized by a wet chemical method using Zinc acetate dihydrate ($(CH_3COO)_2$ $Zn.2H_2O$, Fischer scientific, 98.5%) as a precursor. Zinc acetate dihydrate was dissolved in triple distilled water with continuous stirring at 40 ^{0}C. After few hours of stirring a white powder was obtained which was subjected to decomposition at 450 ^{0}C for 24 hours in order to get ZnO nanopowder.

2.2. Material Characterization

Synthesized samples were characterized using RIGAKU make X-ray diffractometer coupled with $CuK_{\alpha 1}$ radiation (λ=1.540 Å) for quantitative analysis of crystal structure and phase composition of the synthesized samples. The XRD data was collected over an angular range of 10-70° with a step size of 0.02°. Rietveld refinement was done using 'X'pert high score plus' software. The morphological study was carried out using HITACHI make S-3700N scanning electron microscope with EDAX attachment working at 15 kV. Transmission electron microscopy analysis was done using FEI make model TWIN TF30 operated at 300 kV by employing carbon coated copper grids (CF200-Cu). The

ACCEPTED MANUSCRIPT

topography and surface force gradient of the synthesized samples were investigated in detail by atomic force microscopy and surface scanning probe microscopy techniques. Surface force measurements were performed in a non-contact mode at a scan rate of 2 Hz, and a bias voltage of 0.6V was applied between the sample and the ground tip. The Fourier transform infrared (FTIR) spectra were recorded with PERKIN ELMER make C91158 spectrometer in the range of 1400–400 cm^{-1} using KBr pellet method. The pristine LFP and ZnO-doped LFP/C samples were mixed with 2.5 wt.% of polyvinyl alcohol (PVA), pressed into circular discs with 10 mm diameter by applying pressure of 7 tons using a hydraulic press and then heated at 250 °C for 2 h in air to remove PVA. To make electrical contacts, silver (Ag) paste was applied on the both sides of pellets and consequently, dried up at 150 °C for 1 h in air to remove moisture. In order to measure electronic conductivity, a two-point probe setup (AGILENT 4284A) was used. Conductivity measurements were done at a bias voltage of 1.0 V, and the frequency range was kept from 20 Hz-1 MHz. The electronic conductivity (σ) is calculated by using following equation;

$$\sigma = \frac{1}{R}\left(\frac{L}{A}\right)$$

where, R is the resistance of the sample (Ω), L and A is thickness (cm) and cross-sectional area (cm^2) of the circular disc, respectively. Activation energy measurement was carried out at a source voltage of 1.0 V by using KEITHLEY 6517A high resistance electrometer. Activation energy (E_a) is calculated using Arrhenius equation;

$$\sigma = \sigma_0 \exp\left(\frac{-E_a}{K_B T}\right)$$

where, σ is electronic conductivity (S/cm), E_a is activation energy (eV), K_B is Boltzmann constant ($J.K^{-1}$), and T is temperature (K).

2.3. Electrode preparation and electrochemical characterization

For electrochemical studies, electrodes were prepared by dispersing active material (LFP or ZnO/C-coated LFP) conductive carbon (Super P) and binder (polyvinylidene difluoride, PVDF) in a weight percentage of 70:15:15 in N-methyl-2-pyrrolidinone (NM2P) as a solvent. The resulting mixture was then stirred for 10 h and coated on Al foil current collector using the "doctor blade" technique. The coatings were dried at 80 °C in a vacuum oven to evaporate the solvent and then circular electrodes of

ACCEPTED MANUSCRIPT

19 mm diameter were punched and weighed. Then electrodes were dried under vacuum at 60 ºC to remove moisture and finally brought inside the Mbraun make glove box workstation with O_2 and H_2O level ≤ 0.5 ppm. CR2032 coin cells were assembled for electrochemical testing of the synthesized samples. High purity Li chips were used as both counter and reference electrode. A microporous polypropylene sheet (Celgard 2400) was used as a separator while 1 M $LiPF_6$ in EC: DMC 1:1 v/v was used as the electrolyte. Cyclic voltammetry (CV) experiments were carried out over the potential range of 2.8-4.2 V vs. Li^+/Li. The galvanostatic charge/discharge (GCD) performance test, rate capability at different C-rates and Electrochemical Impedance Spectroscopy (EIS) using an AC voltage pulse of 5 mV in the frequency range of 10 kHz-10 mHz were performed. All the electrochemical tests were performed using EZstat-pro NuVant systems Inc. (U.S.A) cell test system at 298 K.

3. Results and discussion

3.1. Structural and Morphological analysis

The XRD patterns of the as-synthesized cathode material with different ZnO amount are shown in Fig. 1. It can be clearly seen from XRD patterns that all the diffraction peaks are well indexed to orthorhombic phase with *Pnma* space group of olivine-LFP. The sharp peaks for all the synthesized samples indicate that the samples are well crystalline in nature. No extra peak related to carbon was detected, indicating that the carbon present in the samples is amorphetic in nature. Likewise, no additional peaks related to ZnO were observed for the synthesized samples which suggest that Zn from ZnO might have gone inside the host lattice and therefore, ZnO act as a dopant. Rietveld refinement was performed for the synthesized samples to obtain quantitative structural information of ZnO-doping on the crystal lattice structure of LFP using 'X'pert high score plus' software. The observed, calculated and difference XRD patterns of pristine LFP and LFPZ2.5 sample are shown in Fig. 2. No background subtraction and data smoothening were done before refinement. The starting atomic position coordinates for pristine LFP were taken from Yanxuan et al. [31]. The structural refinement results are summarized in Table 1. The goodness of fitting factor, χ^2 of the refinement for pristine LFP and LFPZ2.5 is around 2.5% and 4%, respectively, which demonstrates that the results are reliable. It can be observed from the Table 1 that with increasing ZnO amount, the unit cell

ACCEPTED MANUSCRIPT

parameters, and unit cell volume increases. The increase in cell size from 289.736 to 290.776 $(Å)^3$ is mainly due to a slight increase in lattice parameter *b* and *c* whereas *a* decrease slightly (Fig. 3). The increase in unit cell size, thus provide more space for lithium ion movement and consequently better electrochemical properties.

Fig. 4(a)-(e) shows the effect of surface modification by ZnO-doping on the morphology of all synthesized samples. It can be seen from the SEM micrographs that the grains in pristine LFP sample are agglomerated (Fig. 4(a)), dense and possess a nearly spherical morphology with average micrometer size range (~1 μm). Fig. 4(b)-(d) shows micrographs of ZnO-doped LFP/C sample. Grains in ZnO-doped samples are found to be uniformly distributed and smaller in size (~500 nm). This variation in grain size of pristine LFP and ZnO-doped LFP/C samples can be explained on the basis of nucleation process. The addition of ZnO may enhance the nucleation process which could result in grain size refinement and hence, a decrease in grain size is noticed. Also, the small size of grains may be helpful in the enhancement of the electrochemical properties as grain size is related to the diffusion time of lithium ion given by the formula $\tau = L^2/D$, where L is characteristic diffusion length, D is the diffusion coefficient for Li-ion, and τ is particular time for lithium ion to diffuse through an electrode material. Thus, the decrease in particle size will significantly enhance electrochemical properties. Therefore, it may be concluded that the concentration of foreign dopant plays a key role in controlling the morphology and grain size distribution in synthesized samples. Fig. 4(e) shows the SEM micrograph of synthesized ZnO powder. SEM micrographs reveal that the size of particles in ZnO powder lies between 50-60 nm and are also uniformly distributed. Fig. S1(a) and (b) shows EDX pattern of the pristine LFP and LFPZ2.5 samples, respectively followed by the elemental mapping. Element mapping clearly indicates the homogeneous dispersion of Fe, Zn, P, and O.

Fig. 5(a) and (b) shows the TEM/HRTEM/SAED images of pristine LFP and LFPZ2.5 samples, respectively. In the TEM images, the LFP and LFPZ2.5 particles appear as dark and slightly grayish regions while carbon appeared as transparent. It can be observed from the TEM image of the pristine LFP and LFPZ2.5 samples that the morphology of the particles is nearly spherical. However, the particles in LFP sample are denser as compared to the particle in LFPZ2.5 as predicted by SEM analysis. Moreover, no carbon coating was observed over the surface of LFP particles as displayed in

ACCEPTED MANUSCRIPT

HRTEM image (inset of Fig. 5(a)). SAED patterns of the LFP sample (inset of Fig. 5(a)) reveals the crystalline nature of the sample as predicted by XRD results. However, the TEM micrographs of LFPZ2.5 clearly shows the presence of carbon network along with ZnO nanoparticles (indicated by circles) around the cathode active particle surface. The SAED pattern of the circled ZnO nanoparticle (shown in the inset of Fig. 5(b)) consist of prominent rings which are corresponding to (100), (102) and (201) planes of the wurtzite structure of synthesized ZnO nanopowder. Scattered dots seen in SAED pattern shows the presence of amorphous carbon. Therefore, the active cathode particle along with ZnO nanoparticles in the sample have been shielded by a network of amorphous carbon around them. Carbon network because of its electrical conducting nature not only provides easy diffusion path for electrons but also limits the growth of particles by reducing agglomeration. However, the absence of any peak related to ZnO in the observed XRD patterns indicates that the amount of ZnO in LFP samples is quite low and hence, diffraction peaks do not show any appreciable change.

3.2. FTIR study- Cation environment

The effect of ZnO-doping on the vibrational spectrum of the LFP is investigated by FTIR and results are shown in Fig. 6. The peaks of FTIR spectrum located from 463-1139 cm^{-1} may be attributed to the bending and stretching vibration of the tetrahedral (PO_4^{3-}) ion. The tetrahedral unit, PO_4^{3-} ion has its fundamental vibrational frequencies at 1082, 515, 980 and 363 cm^{-1} [16]. Small peak around 420 cm^{-1} corresponds to the stretching E2 (LO) mode of ZnO wurtzite structure which indicates that some traces of ZnO are also present in the synthesized samples [32].

3.3 Electronic and ionic conductivity measurements

The AC electrical resistance measurement results for all the synthesized samples in the frequency range of 20 Hz-1 MHz are shown in supporting information (Fig. S2(a)). The intercept at Z'-axis gives the AC resistance of the material. The AC conductivity of pristine LFP sample was calculated to be 10^{-9} S/cm which is in good agreement with the previous reports [15-17]. Table 2 shows the conductivity and activation energy results of as-synthesized samples. From Table 2, it can be perceived that ZnO-doped LFP/C samples show an increase of 10^3 in electronic conductivity as compared to pristine LFP. Among ZnO-doped samples, LFPZ2.5 has the highest conductivity due to its lowest AC resistance (~41 KΩ). The ionic conductivity measurement graphs of all the prepared

ACCEPTED MANUSCRIPT

compositions are shown in supporting information (Fig. S2(b)). The slope of the obtained curves gives a direct measurement of the activation energies, and consequently it determines the lithium ion kinetics. From Fig. S2(b), it can be seen that ZnO-doped LFP/C samples deliver nearly the similar range of activation energy. Here, it is observed that the activation energy for ZnO-doped samples reduces to ~36% to pristine LFP which clearly indicates that the ionic conductivity has improved for doped samples. AC resistance and ionic conductivity measurement collectively disclose that ZnO-doped samples are more conducting than pristine LFP as far as lithium ion and electron kinetics have been concerned. Therefore, ZnO-doped LFP/C samples can be considered as more ionic and electronic conductor as compared to pristine LFP, which behaves as an ionic and electronic insulator. These results clearly indicate that lithium ion kinetics has been enhanced, and this must be reflected in electrochemical performances.

3.4. Surface topography and surface force imaging

Prior to electrochemical measurements of the synthesized samples, surface topography, and surface force measurement for the LFP and ZnO-doped LFP/C samples has been performed using surface scanning probe microscopy. This technique measures local electric charge distribution on the surface of the specimen and hence, measures the surface force/potential of the material which can be correlated to the electrochemical performance of the synthesized samples. Fig. 7(a)-(d) shows the topographical image and surface force gradient imaging of the pristine LFP and optimized LFPZ2.5 samples. The corresponding topography and surface force images were taken at a bias voltage of 0.6 V, applied to the samples before scanning. Fig. 7(a) and (b) shows the topography and surface force gradient of the pristine LFP sample. Fig. 7(b) reveals less percentage of higher force gradient regions as compared to the low force gradient region. Higher force gradient regions are generally associated with accumulated charges present at the surface. It means there will be less density of charges and hence, conductivity will not be high. Moreover, the range of surface force gradient is not very large which means the volume of electrostatic charge present at the surface is not high. However, it can be seen clearly from the Fig. 7(d) that a non-uniformity of the surface force gradient is resulting due to regions of high and low surface force characterized by bright and dark areas respectively on the image. Surface force image for LFPZ2.5 sample has nearly equal volume of high as well as low force

ACCEPTED MANUSCRIPT

gradient regions which span from 200 pN to below -200 pN. It indicates the presence of more volumetric charge density at the surface which is due to the result of fast electrostatic charge transport mechanism across the interface of each grain. These results clearly indicate that ZnO-doping along with carbon coating provides an easy path for charge diffusion and hence, enhancement in surface/electrical conductivity will result in enhancing rate performance of the cathode material.

Fig. 8 schematically shows the possible charge transport phenomenon for a solid-liquid interface where ZnO-doped LFP/C surface interacts with the $LiPF_6$ electrolyte. Every solid surface possesses electrostatic charges and thus has surface force/potential. These electrostatic charges present on the solid surface attract the counter ions of the electrolyte ($LiPF_6$ in this case). This electrostatic interaction leads to rearrangement of charges on the solid surface and in the liquid. A layer of charges (e^- or Li^+) will form near to the solid surface of electrode material which attracted strongly towards the solid surface. This layer of charge generally contributes for surface/electrical conductivity. ZnO-doping coupled with carbon coating plays a major role in enhancing surface conductivity as ZnO act as a fast lithium ion conductor while carbon will facilitate the kinetics of electron. Therefore, the combined effect of ZnO-doping and carbon-coating favors not only fast lithium ion and electron kinetics over the surface of LFP particle but also prevents direct contact of active cathode surface to the electrolyte.

3.5. Electrochemical performance

Fig. 9 shows the cyclic voltammetry curves of pristine LFP and ZnO-doped LFP/C samples measured at a scan rate of 0.05 mVs^{-1} vs. Li^+/Li at room temperature. It can be seen from Fig. 9 that over the potential range of 2.8-4.2 V, the synthesized samples only exhibit the characteristic redox peaks of pristine LFP. CV curves possess peaks at around 3.5 and 3.4 V corresponding to the two-phase transition reaction between Fe^{3+} ($FePO_4$) and Fe^{2+} ($LiFePO_4$) as oxidation and reduction, respectively. As no additional peaks in CV profiles have been found, the dopant does not participate in the redox reaction. However, for ZnO-doped samples, it is found that the intensity of redox peaks increases monotonically up to LFPZ2.5 sample and then decrease for LFPZ5 sample. The LFPZ2.5 sample exhibits the highest redox intensity which indicates the fastest lithium ion diffusion and hence, enhanced electrode reaction reversibility inside the host lattice. Along with the intensities, redox

ACCEPTED MANUSCRIPT

peaks also becomes broader with an increase in ZnO content which indicates an increase in polarization potential of the electrode active material. These results confirmed that the ZnO amount is a dominant factor in the enhancement of the lithium-ion diffusion kinetics and electrochemical performance.

Fig. 10 shows the 1st galvanostatic charge/discharge voltage comparison curves of all cells at 0.1C rate (1C = 170 $mAhg^{-1}$) for the pristine LFP and ZnO-doped LFP/C samples in the potential range of 2.0-4.4 V vs. Li^+/Li at room temperature. It has been found that the discharge capacity of pristine LFP has greatly enhanced by ZnO-doping. Among all the synthesized samples LFPZ2.5 shows highest specific discharge capacity 164 (±3) $mAhg^{-1}$ (~96 % of theoretical capacity 170 $mAhg^{-1}$) because of its highest electronic conductivity. The discharge capacities of all samples for 0, 1.0, 2.5 and 5.0 wt.% of ZnO amount are found to be 87 (±3), 130 (±3), 164 (±3) and 123 (±3) $mAhg^{-1}$, respectively. It can also be noted from Fig. 10 that voltage plateau has been lengthened for the samples with ZnO content, which may be attributed to enhanced lithium ion kinetics and excellent electrochemical reactivity of ZnO-doped LFP/C. All the charge/discharge curves consisted of charge/discharge plateaus at around 3.5 V and 3.4 V. The potential difference between charge and discharge plateaus for all the samples is shown in the inset of Fig. 10 and summarized in Table 3. It can be observed that the potential difference (ΔV) improved effectively with ZnO-doping which consequently reduces the polarization potential and hence, lithium ion diffusion in doped LFP/C samples has been enhanced. These charge/discharge voltage plateau results are well synchronized with the CV profile and surface force imaging results indicating that the availability of the more volumetric charge density at the surface of the cathode active material not only provides fast electrostatic charge transport but also significantly enhance electrochemical performances.

Fig. 11(a)-(d) shows the initial charge/discharge curves of all synthesized samples measured at different C-rates of 0.1C-5C in the potential range of 2.0-4.4 V vs. Li^+/Li at room temperature. It can be seen from the graphs that among the entire synthesized samples, LFPZ2.5 delivers the highest discharge capacity at each rate. Among ZnO-doped samples, LFPZ5 delivers the lowest discharge capacity due to its high AC resistance and therefore, diminished lithium ion diffusion kinetics.

ACCEPTED MANUSCRIPT

Fig. 12(a) shows the stepwise electrochemical rate performance of the surface modified samples for different rates (0.1C to 5C) at room temperature. It can be seen from the Fig. 12(a) that LFPZ2.5 shows highest discharge capacity at each C-rate as compared to pristine LFP when the discharge current is increased from 0.1C to 5C. The discharge capacities of LFP, LFPZ1, LFPZ2.5, and LFPZ5, are found to 87 (±3), 130 (±3), 164 (±3) and 123 (±3) $mAhg^{-1}$, respectively at 0.1C. Among all synthesized samples, LFPZ2.5 shows highest capacity retention of nearly 56% i.e. 91 (±3) $mAhg^{-1}$ at 5C-rate.

Fig. 12(b) shows the cycling performance of pristine LFP and ZnO-doped LFP/C samples for 1C-rate at room temperature for 50 cycles. Table 4 displays the rate capacity retention ratios of all synthesized samples compared to 0.1C and 1C. The LFPZ2.5 reveals the best rate performance and excellent reversibility among all the samples. It shows an initial discharge capacity 135 (±3) $mAhg^{-1}$ (~79% of theoretical capacity) at 1C-rate and has 95% capacity retention even after 50 charge/discharge cycles at same C-rate. It is because of its lowest polarization potential which favors fast lithium ion mobility and electrochemical kinetics.

Fig. 13 shows the dependency of the rate capability on the ZnO wt.% amount of the synthesized samples. At the low C-rate, the doping effect on the electrochemical properties is mainly due to the differences in electrical conductivities and lithium ion diffusion coefficients. Under high C-rates, the difference in discharge capacities is primarily due to increase in polarization. These results reveal that the surface modification of LFP/C samples by ZnO-doping ensures better electron transfer and reduction in polarization potential.

EIS of fresh cells was performed to analyze the influence of ZnO-doping on the cell impedance. Fig. 14(a) shows the impedance spectra of LFP and ZnO-doped LFP/C samples measured with AC voltage amplitude of 5 mV. The scanning frequency range was kept at10 mHz-10 kHz. It is observed that all the curves contain a semicircle in the high-frequency region along with a straight line in the low-frequency region. Usually, an intercept at the Z' axis in the high-frequency region corresponds to the ohmic resistance (R_s) of the cell, which simply indicates the resistance due to electrolyte and electrode material. The semicircle in the middle-frequency range is mainly attributed to the electrochemical

ACCEPTED MANUSCRIPT

reactions occurring at the electrode/electrolyte interface, which indicates the charge transfer resistance (R_{ct}) [20, 33]. The inclined line in the low-frequency region represents the Warburg impedance (Z_w), which is associated with Li-ion diffusion in the electrode active material. The values of lithium ion diffusion coefficient in the bulk electrode materials can be calculated using the following equation [4, 5, 20]:

$$D=\frac{R^2T^2}{2A^2n^4F^4C^2\sigma_W^2} \quad (2)$$

where D is Li-ion diffusion coefficient (cm^2s^{-1}), R is gas constant (8.314 J mol^{-1} K^{-1}), T is absolute temperature (K), A is electrode area (cm^2), n is number of electrons involved in the redox process (assumed n=1 in this case), C is the lithium-ion concentration ($7.69x10^{-3}$ mol cm^{-3}), F is the faraday constant (96486 C mol^{-1}) and σ_W is the Warburg factor which is related to Z' by following equation [5]:

$$Z'=R_s+R_{ct}+\sigma_W\omega^{-0.5} \quad (3)$$

Based on the above equation (3), Warburg impedance coefficient was calculated and subsequently used in eq. (2) in order to calculate Li-ion diffusion coefficients of the synthesized samples. Fig. 14(b) shows the relationship plot between Z' and the reciprocal square root of angular frequency ($\omega^{-0.5}$) in the low-frequency region. The lithium-ion diffusion coefficients (D_{Li}) of the samples calculated by using equation (2) and (3) are listed in Table 5. From the Table, it is evident that LFPZ2.5 has least charge transfer resistance and highest D_{Li} ($5.04x10^{-14}$ cm^2/s) among all the prepared samples confirming the charge/discharge results. These results also indicate that the Li-ion diffusion coefficient of ZnO-doped LFP/C samples has enhanced.

In order to have practical applications, the relationship plot between power and energy density (so-called "Ragone plot") is superior in the evaluation of electrode materials. Fig. 15 shows the Ragone plot of pristine LFP and LFPZ2.5. It is known that lithium-ion battery electrode materials show an unwanted decrease in energy density with increasing power density, indicating less usefulness in real-life applications such as EVs and HEVs while working at high charge/discharge rates [34]. Fig. 15 clearly shows that LFPZ2.5 cathode material retains its energy storage capacity. Even at 6.3-minute charge/discharge rate (5C rate), LFPZ2.5 cathode gives the high energy density (~285 Wh/kg) and

ACCEPTED MANUSCRIPT

power density (~2105 W/kg) which are well above the standard requirements for the development of EVs [35], representing as alternative cathode material for commercial applications.

In order to examine the integrity of the electrode active material after 50 cycles at 1C rate, ex-situ SEM was performed for the LFPZ2.5 sample. The same cell has experienced various charging/discharging cycles at different C-rates (0.1-5C) before cycling test. The half-cell was dismantled inside the glove-box, and the active material electrode was washed with isopropyl alcohol and then dried at 50 °C for 20 minutes. Fig. 16 shows the obtained SEM micrographs of the active electrode before (Fig. 16(b)) and after cycling (Fig. 16(c)) along with the uncoated (without super P and binder) active electrode sample (Fig. 16(a)). On comparing Fig. 16(b) and (c), it can be seen that morphology of the active material dispersed in carbon and PVDF remains unaffected even after many charging/discharging cycles.

4. Conclusions

A series of ZnO-doped LFP/C samples were successfully synthesized using sol-gel assisted ball-milling route. XRD patterns reveal that all the synthesized samples are well crystalline without any impurity phase such as $LiZnPO_4$. Morphological analysis by SEM/TEM indicates that synthesized samples have nano-sized nearly spherical shaped particles. Surface properties like topography and surface force gradient reveals that mobility of charge carriers i.e. e^-/Li^+ is more in ZnO-doped LFP/C samples, which is mainly due to diffusion or conduction process at the surface. The availability of more local electric charge distribution on the surface of the ZnO-doped LFP/C as predicted by surface scanning probe microscopy results in enhanced electrochemical performance of the synthesized samples. Electrochemical results such as CV, galvanostatic charge/discharge and EIS reveals that LFPZ2.5 has the highest specific discharge capacity and superior electrochemical properties among all the synthesized samples. LFPZ2.5 shows great potential for application in EVs and HEVs because of its high energy and power density even at high discharging rates.

Acknowledgements

Authors are thankful to SERB, Department of Science and Technology (DST), New Delhi for financial support to carry out this work under the project FTP/PS/039/2011. Authors also give sincere

ACCEPTED MANUSCRIPT

thanks to Ms. Anshika Singh for helping in the EFM measurements with existing AFM facility at Advance Instrumentation Centre, DTU.

References

[1] D. Ziolkowska, K. Korona, B. Hamankiewicz, S.-H. Wu, M.-S. Chen, J. Jasinski, M. Kaminska, A. Czerwinski, The role of SnO_2 surface coating on the electrochemical performance of $LiFePO_4$ cathode materials, Electrochim. Acta 108 (2013) 532-539.

[2] J. Yao, F. Wu, X. Qiu, N. Li, Y. Su, Effect of CeO_2-coating on the electrochemical performances of $LiFePO_4$/C cathode material, Electrochim. Acta 56 (2011) 5587-5592.

[3] A.K. Padhi, K. Nanjundaswamy, J. Goodenough, Phospho-olivines as positive-electrode materials for rechargeable lithium batteries, J. Electrochem. Soc. 144 (1997) 1188-1194.

[4] Y.-J. Lv, J. Su, Y.-F. Long, X.-R. Cui, X.-Y. Lv, Y.-X. Wen, Effects of ball-to-powder weight ratio on the performance of $LiFePO_4$/C prepared by wet-milling assisted carbothermal reduction, Powder Technol. 253 (2014) 467-473.

[5] G. Qin, Q. Ma, C. Wang, A porous C/$LiFePO_4$/multiwalled carbon nanotubes cathode material for lithium ion batteries, Electrochim. Acta 115 (2014) 407-415.

[6] X. Lin, K. Wu, L. Shao, M. Shui, D. Wang, N. Long, Y. Ren, J. Shu, In situ growth of coiled carbon nanotubes on $LiFePO_4$ as high performance lithium storage material, J. Electroanal. Chem. 726 (2014) 71-76.

[7] J. Ma, B. Li, H. Du, C. Xu, F. Kang, Effects of tin doping on physicochemical and electrochemical performances of $LiFe_{1-x}Sn_xPO_4$/C ($0 \leq x \leq 0.07$) composite cathode materials, Electrochim. Acta 56 (2011) 7385-7391.

[8] F. Wang, J. Chen, Z. Tan, M. Wu, B. Yi, W. Su, Z. Wei, S. Liu, Low-temperature electrochemical performances of $LiFePO_4$ cathode materials for lithium ion batteries, J. Taiwan Inst. Chem. Eng. 45 (2014) 1321-1330.

[9] Z. Ma, Y. Peng, G. Wang, Y. Fan, J. Song, T. Liu, X. Qin, G. Shao, Enhancement of electrochemical performance for $LiFePO_4$ cathodes via hybrid coating with electron conductor carbon and lithium ion conductor $LaPO_4$, Electrochim. Acta 156 (2015) 77-85.

ACCEPTED MANUSCRIPT

[10] Y. Cui, X. Zhao, R. Guo, High rate electrochemical performances of nanosized ZnO and carbon co-coated $LiFePO_4$ cathode, Mater. Res. Bull. 45 (2010) 844-849.

[11] Y. Cui, X. Zhao, R. Guo, Enhanced electrochemical properties of $LiFePO_4$ cathode material by CuO and carbon co-coating, J. Alloys Compd. 490 (2010) 236-240.

[12] M. Minakshi, P. Singh, D. Appadoo, D.E. Martin, Synthesis and characterization of olivine $LiNiPO_4$ for aqueous rechargeable battery, Electrochim. Acta 56 (2011) 4356-4360.

[13] W. Zhang, Y. Hu, X. Tao, H. Huang, Y. Gan, C. Wang, Synthesis of spherical $LiFePO_4$/C via Ni doping, J. Phys. Chem. Solids 71 (2010) 1196-1200.

[14] Y. Lin, M. Gao, D. Zhu, Y. Liu, H. Pan, Effects of carbon coating and iron phosphides on the electrochemical properties of $LiFePO_4$/C, J. Power Sources 184 (2008) 444-448.

[15] J. Li, Q. Qu, L. Zhang, L. Zhang, H. Zheng, A monodispersed nano-hexahedral $LiFePO_4$ with improved power capability by carbon-coatings, J. Alloys Compd. 579 (2013) 377-383.

[16] Q. Liu, W. Liu, D. Li, H. Chen, Z. Wang, LiFe1-x$(Ni_{0.98}Co_{0.01}Mn_{0.01})_xPO_4$/C (x= 0.01, 0.03, 0.05, 0.07) as cathode materials for lithium-ion batteries, Electrochim. Acta 184 (2015) 143-150.

[17] S.-X. Zhao, H. Ding, Y.-C. Wang, B.-H. Li, C.-W. Nan, Improving rate performance of $LiFePO_4$ cathode materials by hybrid coating of nano-Li_3PO_4 and carbon, J. Alloys Compd. 566 (2013) 206-211.

[18] J. Chong, S. Xun, X. Song, P. Ridgway, G. Liu, V.S. Battaglia, Towards the understanding of coatings on rate performance of $LiFePO_4$, J. Power Sources 200 (2012) 67-76.

[19] Z. Tian, S. Liu, F. Ye, S. Yao, Z. Zhou, S. Wang, Synthesis and characterization of $LiFePO_4$ electrode materials coated by graphene, Appl. Surf. Sci. 305 (2014) 427-432.

[20] X. Yang, Z. Hu, J. Liang, Effects of sodium and vanadium co-doping on the structure and electrochemical performance of $LiFePO_4$/C cathode material for lithium-ion batteries, Ceram. Int. 41 (2015) 2863-2868.

[21] G. Wang, S. Bewlay, J. Yao, J.-H. Ahn, S. Dou, H.K. Liu, Characterization of $LiM_xFe_{1-x}PO_4$ (M= Mg, Zr, Ti) Cathode Materials Prepared by the Sol-Gel Method, Electrochem. Solid-State Lett. 7 (2004) A503-A506.

[22] M. Sivakumar, R. Muruganantham, R. Subadevi, Synthesis of surface modified $LiFePO_4$ cathode material via polyol technique for high rate lithium secondary battery, Appl. Surf. Sci. 337 (2015) 234-240.

ACCEPTED MANUSCRIPT

[23] J. Hu, Z. Tian, Synthesis and electrochemical performance of NbC-modified $LiFePO_4$/C as cathode material for lithium-ion batteries, Ceram. Int. 41 (2015) 3927-3931.

[24] H.-H. Chang, C.-C. Chang, C.-Y. Su, H.-C. Wu, M.-H. Yang, N.-L. Wu, Effects of TiO_2 coating on high-temperature cycle performance of $LiFePO_4$-based lithium-ion batteries, J. Power Sources 185 (2008) 466-472.

[25] Z. Ma, G. Shao, X. Qin, Y. Fan, G. Wang, J. Song, T. Liu, Ionic conductor cerous phosphate and carbon hybrid coating $LiFePO_4$ with improved electrochemical properties for lithium ion batteries, J. Power Sources 269 (2014) 194-202.

[26] H. Tang, J. Xu, Enhanced electrochemical performance of $LiFePO_4$ coated with $Li_{0.34}La_{0.51}TiO_{2.94}$ by rheological phase reaction method, Mater. Sci. Eng. B 178 (2013) 1503-1508.

[27] C.-C. Yang, J.-H. Jang, J.-R. Jiang, Study of electrochemical performances of lithium titanium oxide–coated $LiFePO_4$/C cathode composite at low and high temperatures, Appl. Energ. 162 (2016) 1419-1427.

[28] T. Hao, T. Long, X. Jun, Synthesis and characterization of $LiFePO_4$ coating with aluminum doped zinc oxide, Trans. Nonferrous Met. Soc. China 23 (2013) 451-455.

[29] A.Y. Shenouda, H.K. Liu, Studies on electrochemical behaviour of zinc-doped $LiFePO_4$ for lithium battery positive electrode, J. Alloys Compd. 477 (2009) 498-503.

[30] Y. Hu, J. Yao, Z. Zhao, M. Zhu, Y. Li, H. Jin, H. Zhao, J. Wang, ZnO-doped $LiFePO_4$ cathode material for lithium-ion battery fabricated by hydrothermal method, Mater. Chem. Phys. 141 (2013) 835-841.

[31] Y. Wen, L. Zeng, Z. Tong, L. Nong, W. Wei, Structure and properties of $LiFe_{0.9}V_{0.1}PO_4$, J. Alloys Compd. 416 (2006) 206-208.

[32] S. Husain, F. Rahman, N. Ali, P. Alvi, Nickel sub-lattice effects on the optical properties of ZnO nanocrystals, Journal of Optoelectronics Engineering 1 (2013) 28-32.

[33] H. Shu, X. Wang, Q. Wu, B. Hu, X. Yang, Q. Wei, Q. Liang, Y. Bai, M. Zhou, C. Wu, Improved electrochemical performance of $LiFePO_4$/C cathode via Ni and Mn co-doping for lithium-ion batteries, J. Power Sources 237 (2013) 149-155.

[34] C.-T. Hsieh, C.-T. Pai, Y.-F. Chen, I.-L. Chen, W.-Y. Chen, Preparation of lithium iron phosphate cathode materials with different carbon contents using glucose additive for Li-ion batteries, J. Taiwan Inst. Chem. Eng. 45 (2014) 1501-1508.

[35] K. Young, C. Wang, L. Wang, K. Strunz, Electric Vehicle Integration into Modern Power Networks, Power Electronics and Power Systems (2013).

ACCEPTED MANUSCRIPT

Figure Captions

Fig. 1. XRD patterns of as-synthesized LFP and ZnO-doped LFP/C samples.

Fig. 2. Rietveld refined XRD patterns (a) LFP; (b) LFPZ2.5.

Fig. 3. Unit cell parameters *a*, *b* and *c* for synthesized samples as a function of ZnO concentration.

Fig. 4. SEM micrographs of synthesized samples (a) LFP; (b) LFPZ1; (c) LFPZ2.5; (d) LFPZ5; (e) ZnO.

Fig. 5. TEM/HRTEM images of synthesized samples (a) LFP; (b) LFPZ2.5.

Fig. 6. FTIR spectrum of ZnO-doped LFP/C samples from 400-1400 cm^{-1}.

Fig. 7. Topography (left) and surface force gradient (right) images: (a, b) LFP; (c, d) LFPZ2.5.

Fig. 8. Schematic illustration of charge transport phenomenon for a solid-liquid interface of ZnO-doped electrode.

Fig. 9. Cyclic Voltammograms of the prepared samples at a scan rate of 0.05mVs^{-1}.

Fig. 10. 1st charge/discharge curves of LFP and ZnO-doped LFP/C samples at 0.1C-rate (i_{charge} = $i_{discharge}$).

Fig. 11. Charge/Discharge curves of synthesized samples at different C-rates (i_{charge} = $i_{discharge}$); (a) LFP; (b) LFPZ1; (c) LFPZ2.5; (d) LFPZ5.

Fig. 12. Performance of ZnO-doped LFP/C samples: (a) Rate performance at different current rates (i_{charge} = $i_{discharge}$); (b) Cycling performance of synthesized samples at 1 C for 50 cycles.

Fig. 13. Rate capability of the ZnO-doped LFP/C synthesized samples as a function of ZnO wt.%.

Fig. 14. (a) Impedance spectra of synthesized samples measured at AC amplitude of 5mV; (b) Relationship plot between Z' and $\omega^{-0.5}$ in low-frequency region.

Fig. 15. Ragone plot of energy density versus power density.

ACCEPTED MANUSCRIPT

Fig. 16. SEM micrograph of LFPZ2.5 (a) uncoated sample (b) electrode before cycling (c) electrode after 50 cycles.

ACCEPTED MANUSCRIPT

Figures

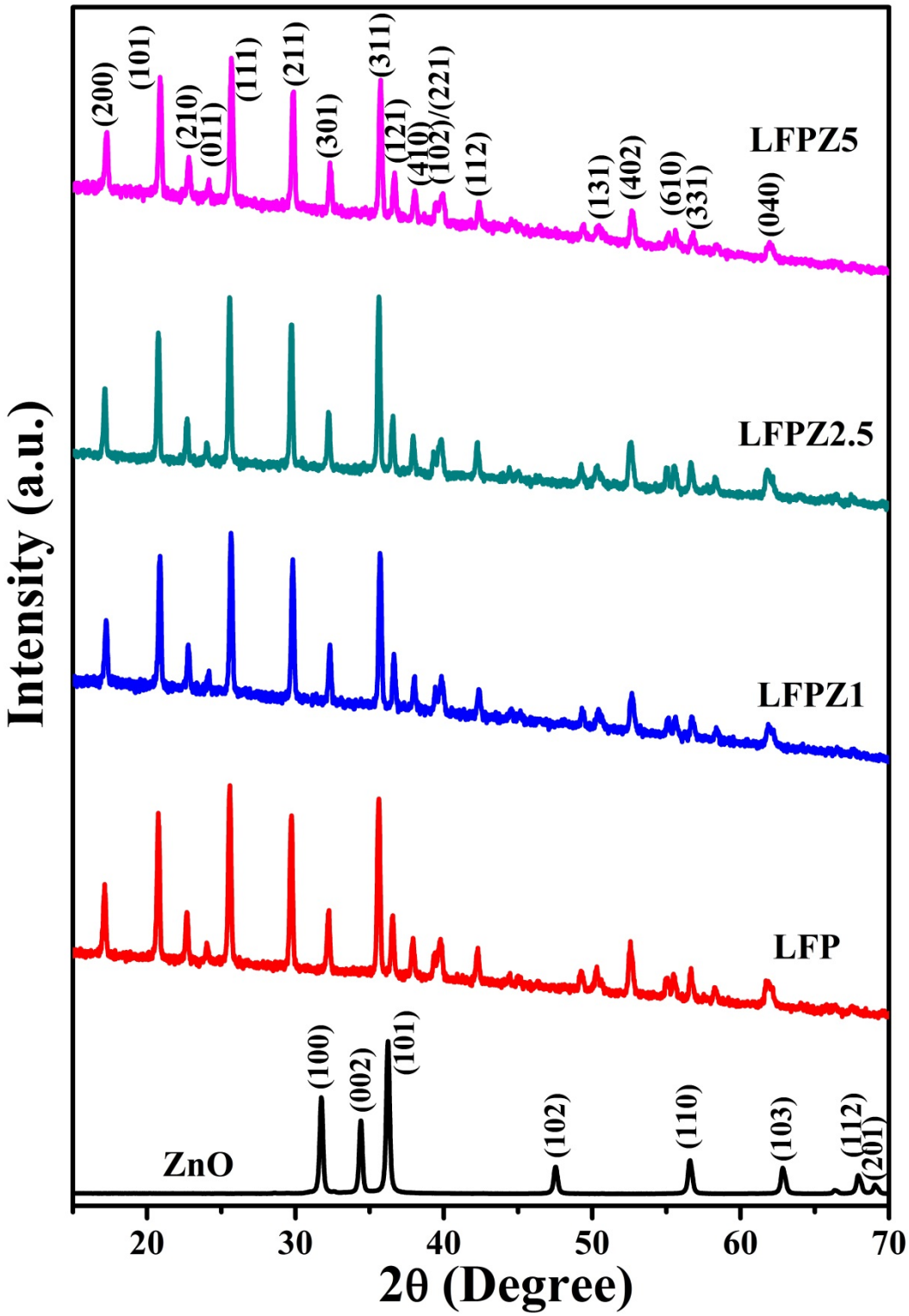


Fig. 1

ACCEPTED MANUSCRIPT

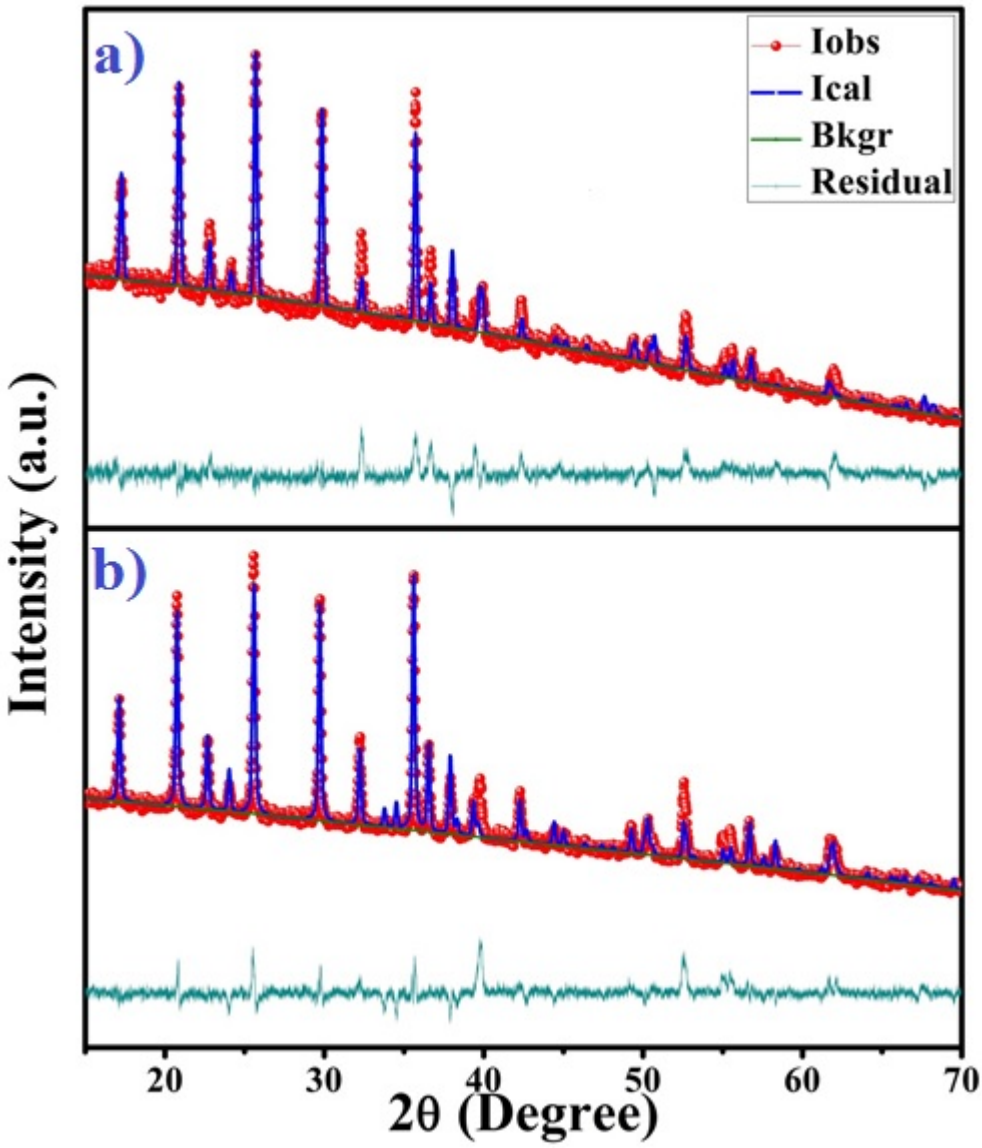


Fig. 2

ACCEPTED MANUSCRIPT

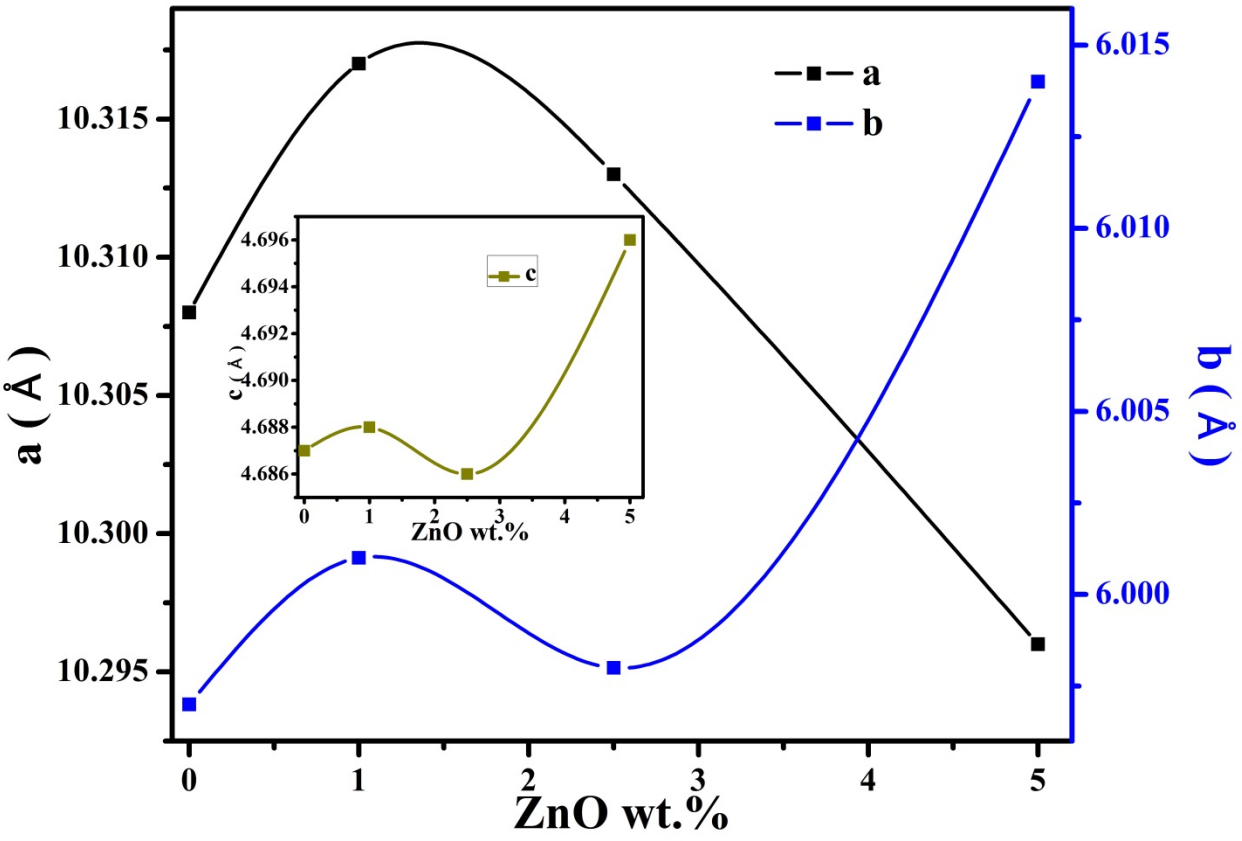


Fig. 3

ACCEPTED MANUSCRIPT

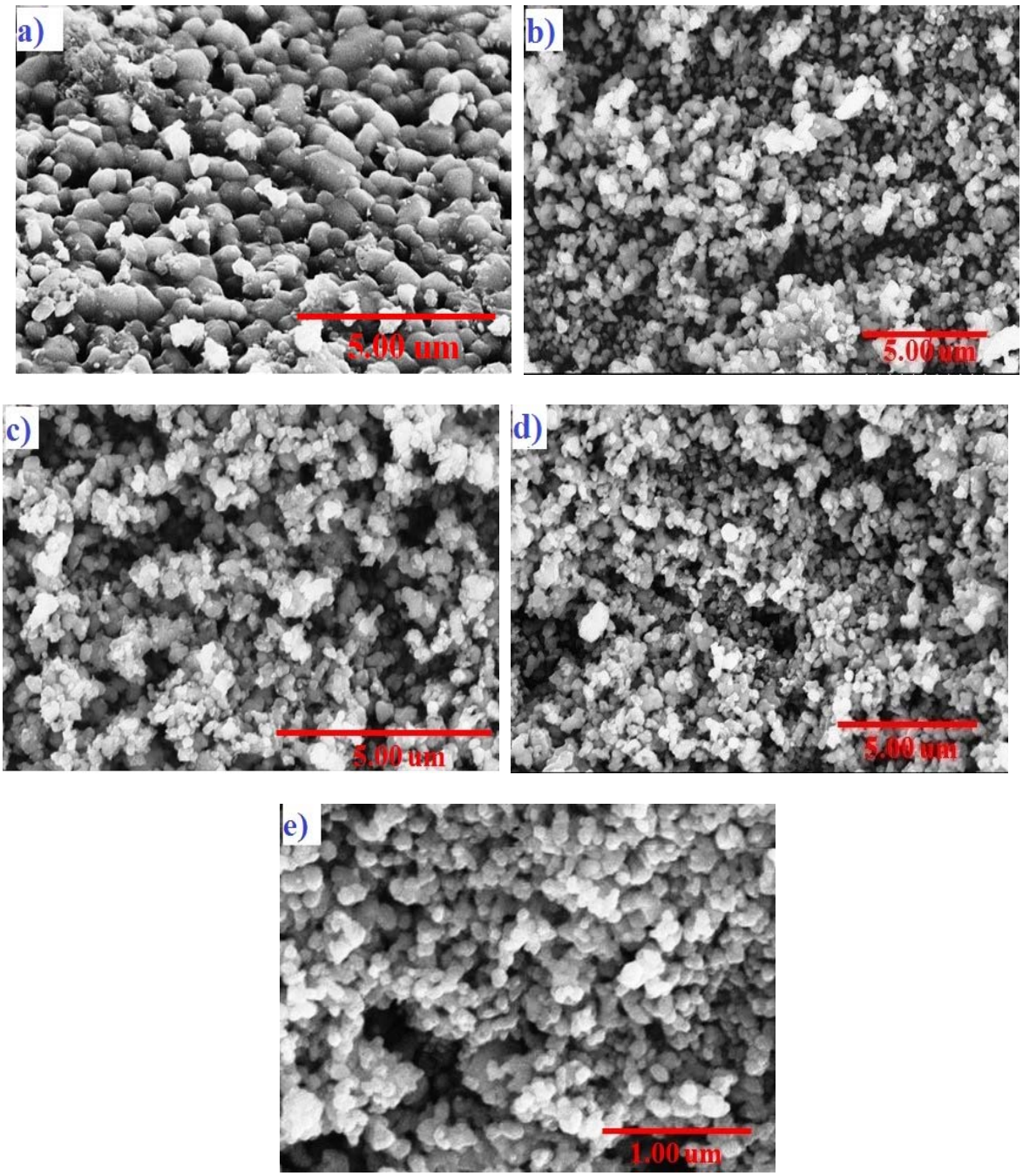


Fig. 4

ACCEPTED MANUSCRIPT

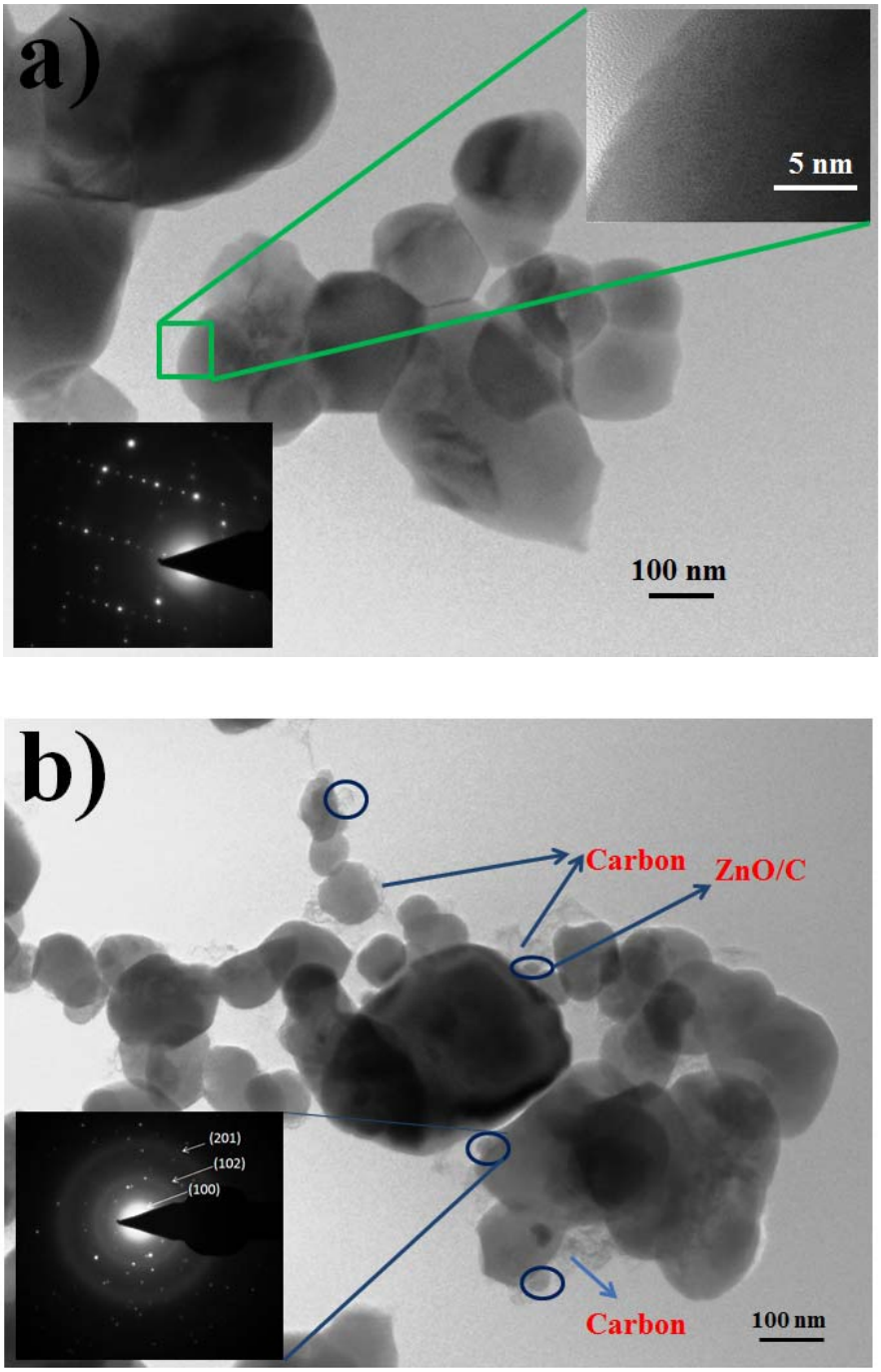


Fig. 5

ACCEPTED MANUSCRIPT

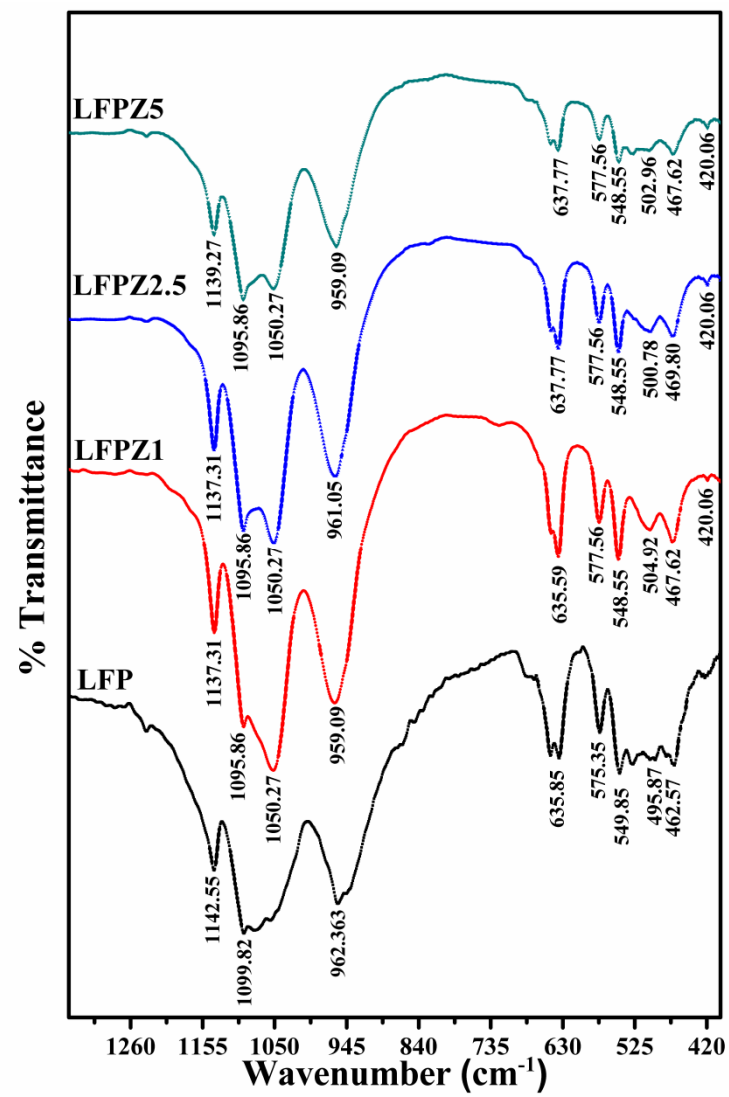


Fig. 6

ACCEPTED MANUSCRIPT

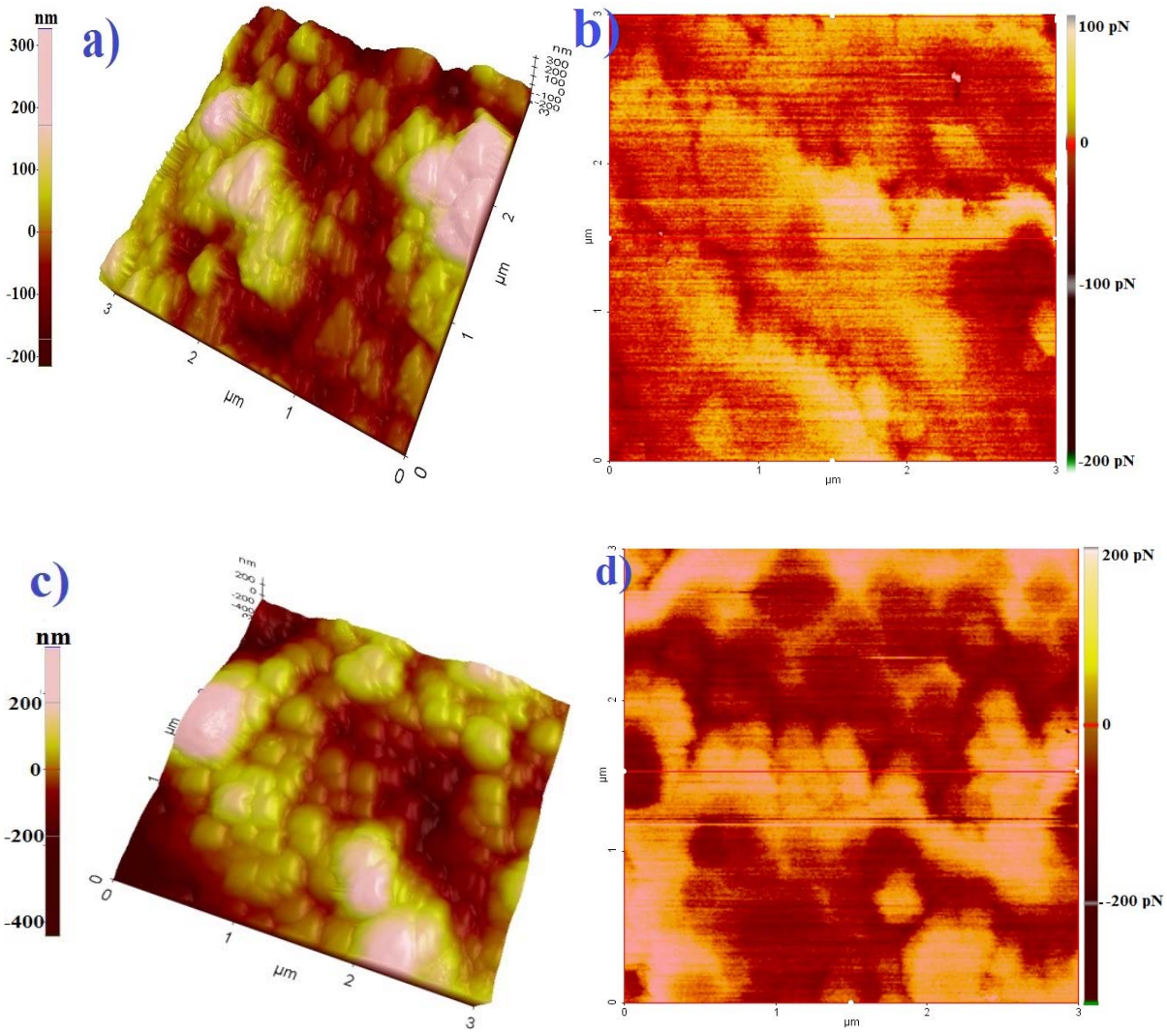


Fig. 7

ACCEPTED MANUSCRIPT

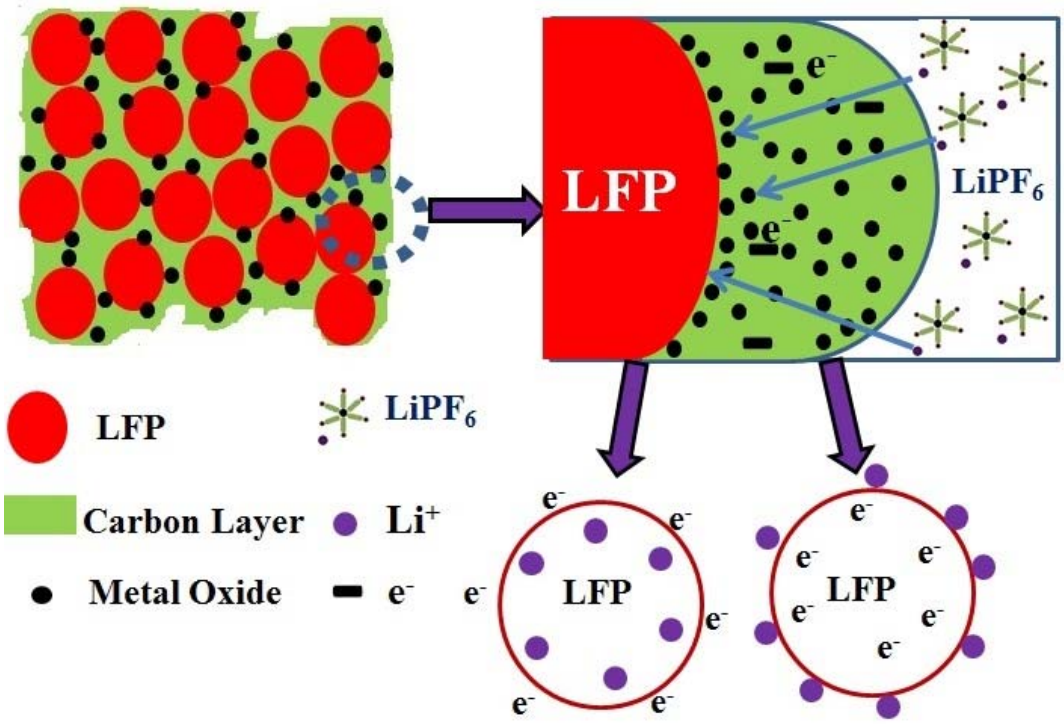


Fig. 8

ACCEPTED MANUSCRIPT

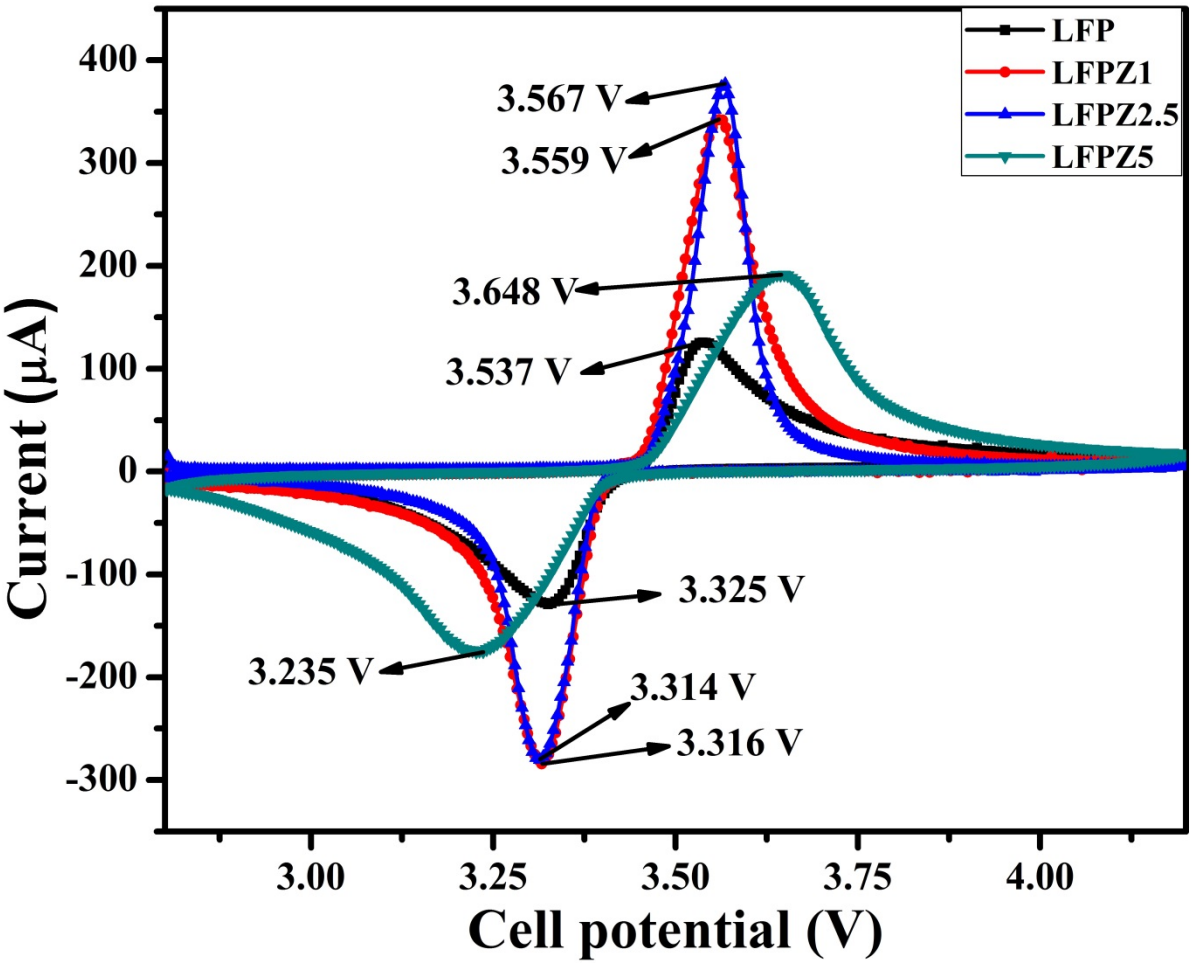


Fig. 9

ACCEPTED MANUSCRIPT

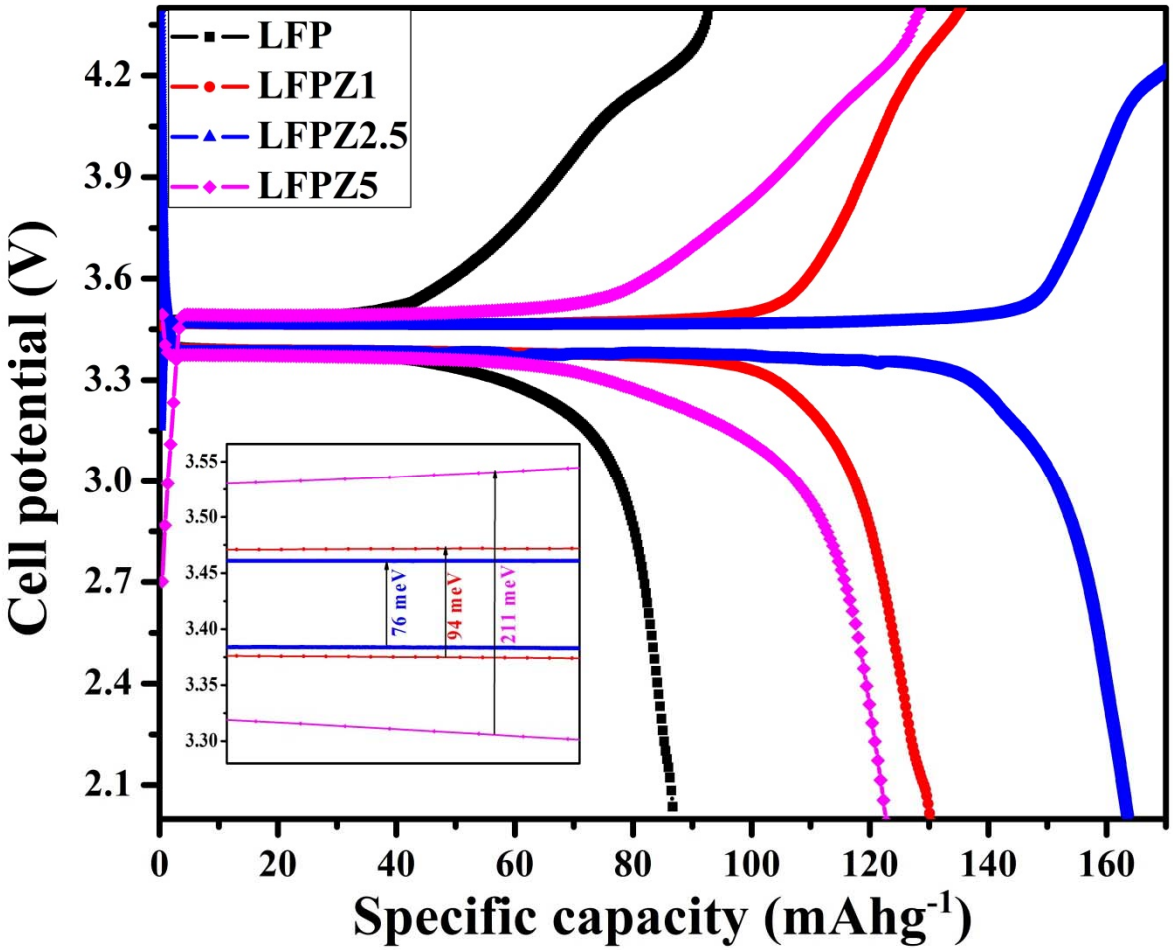


Fig. 10

ACCEPTED MANUSCRIPT

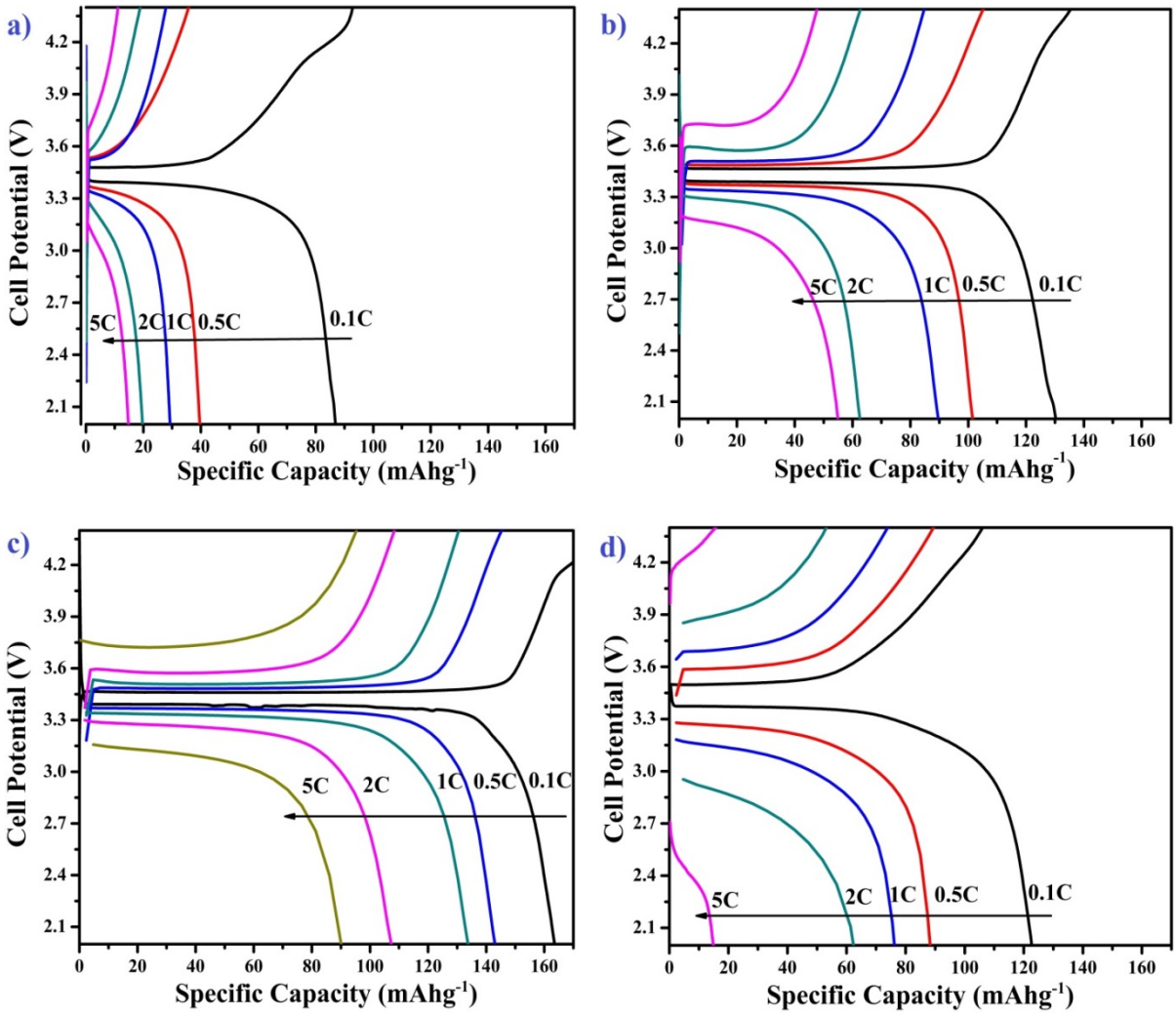


Fig. 11

ACCEPTED MANUSCRIPT

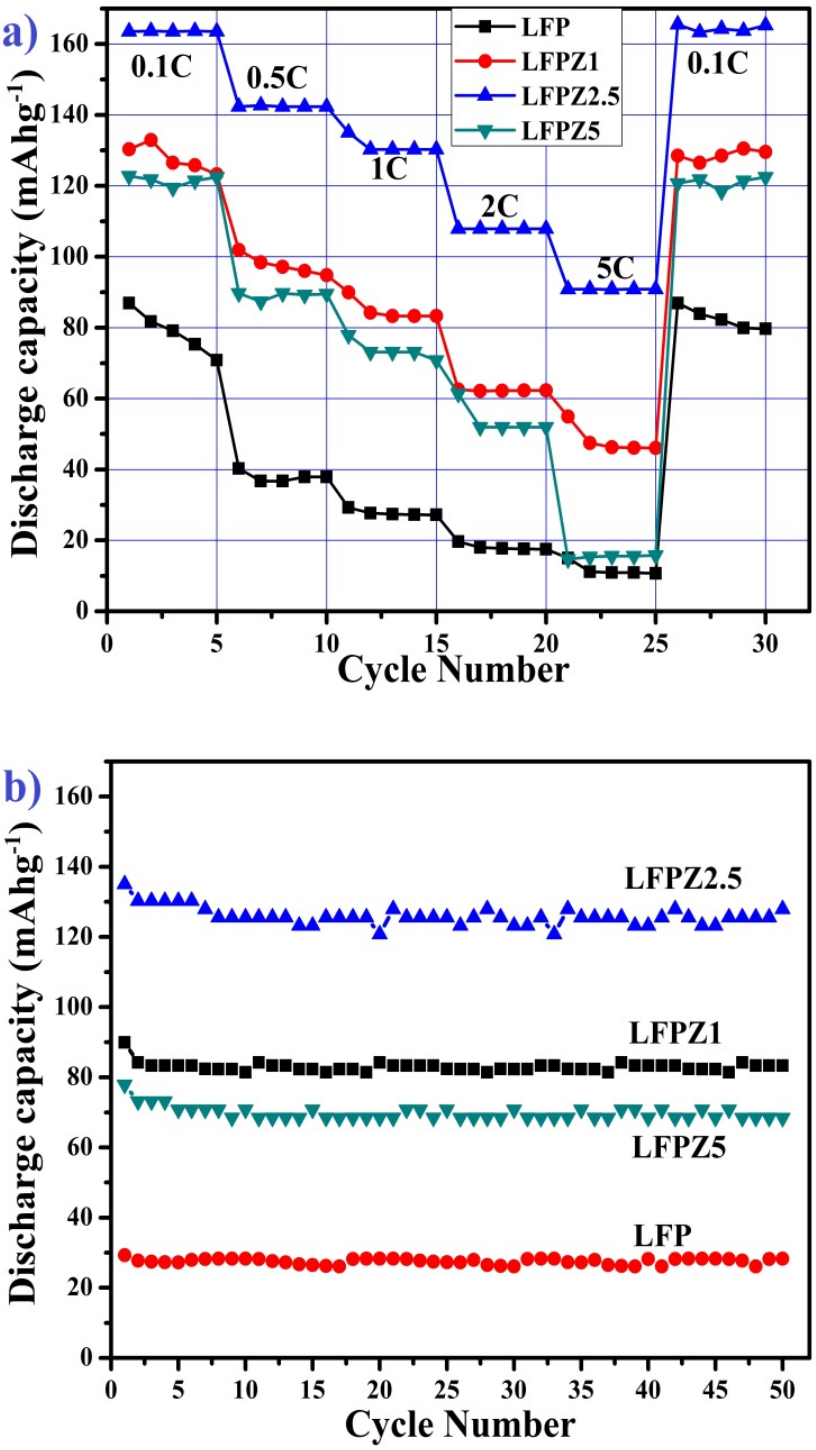


Fig. 12

ACCEPTED MANUSCRIPT

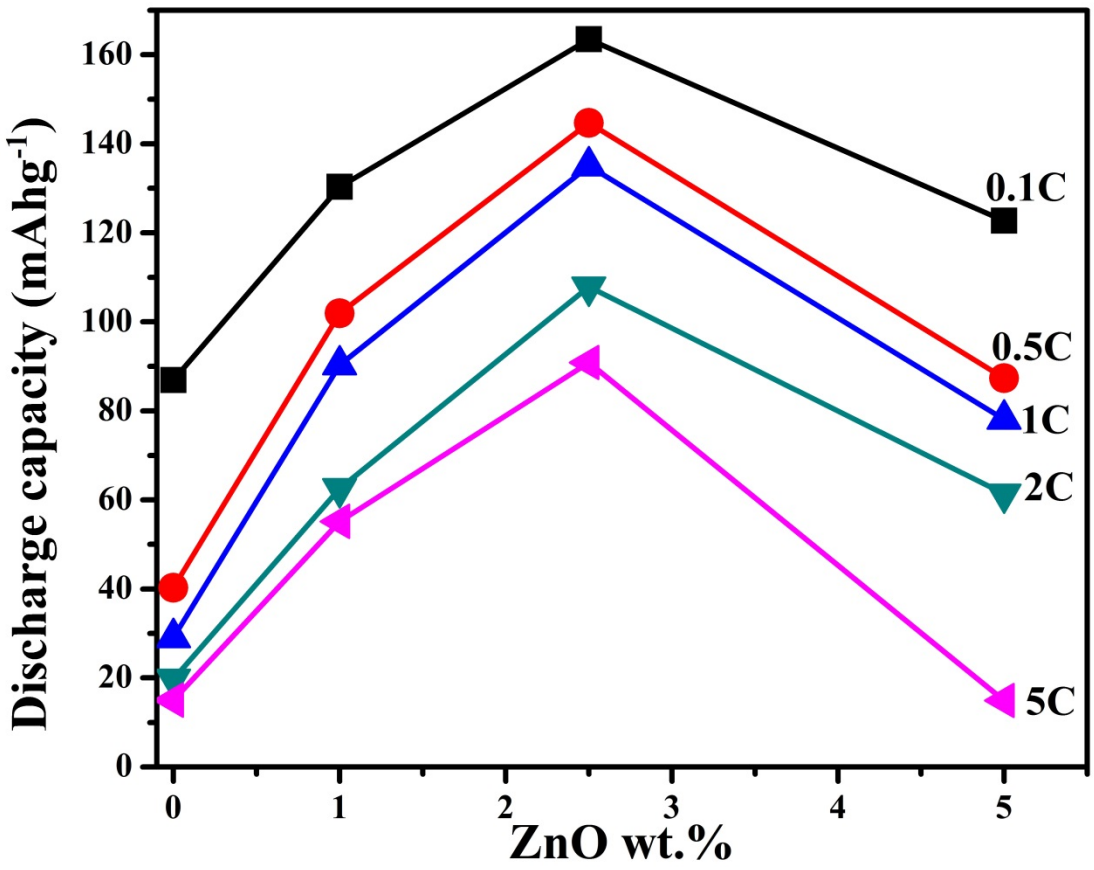


Fig. 13

ACCEPTED MANUSCRIPT

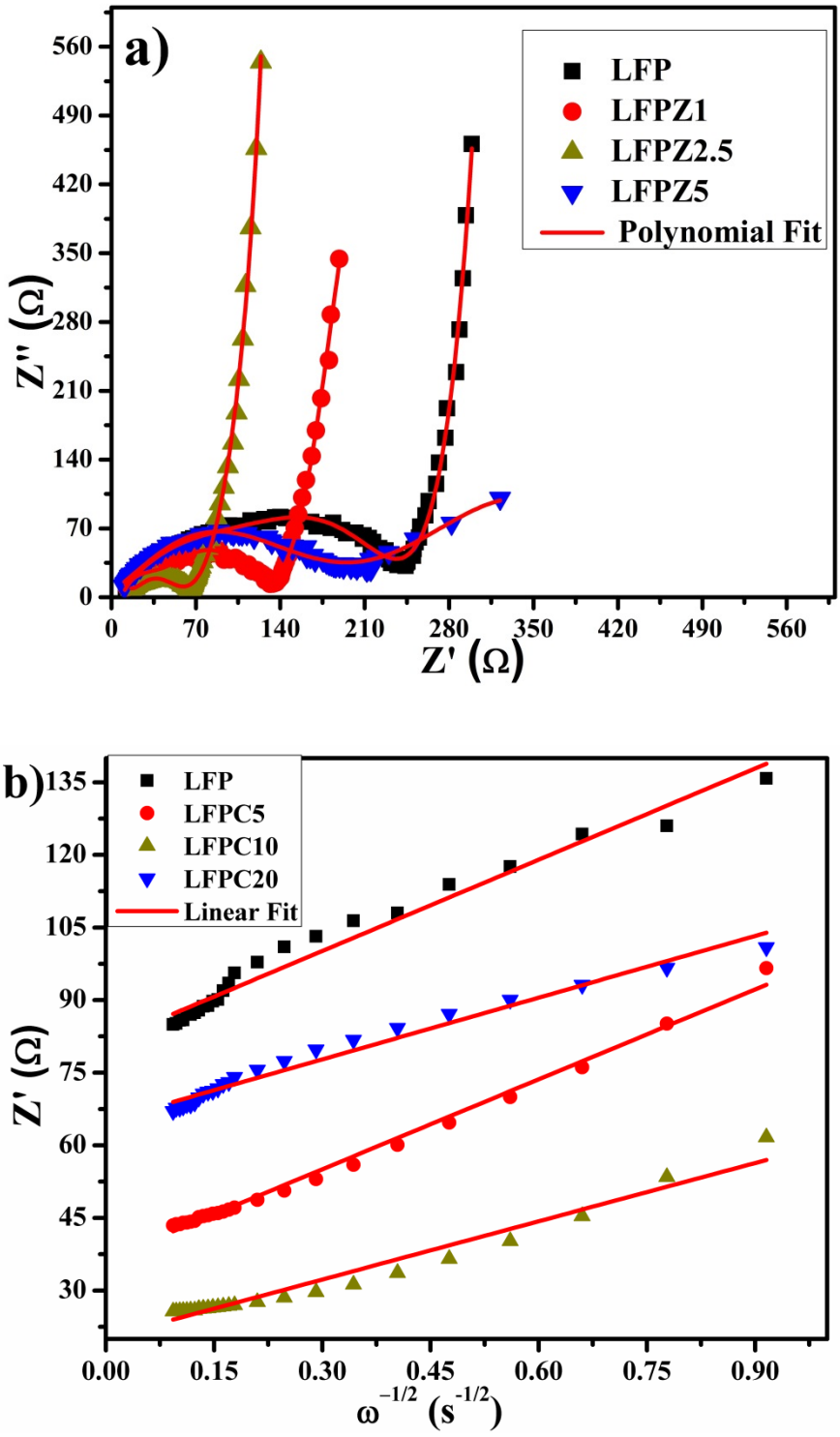


Fig. 14

ACCEPTED MANUSCRIPT

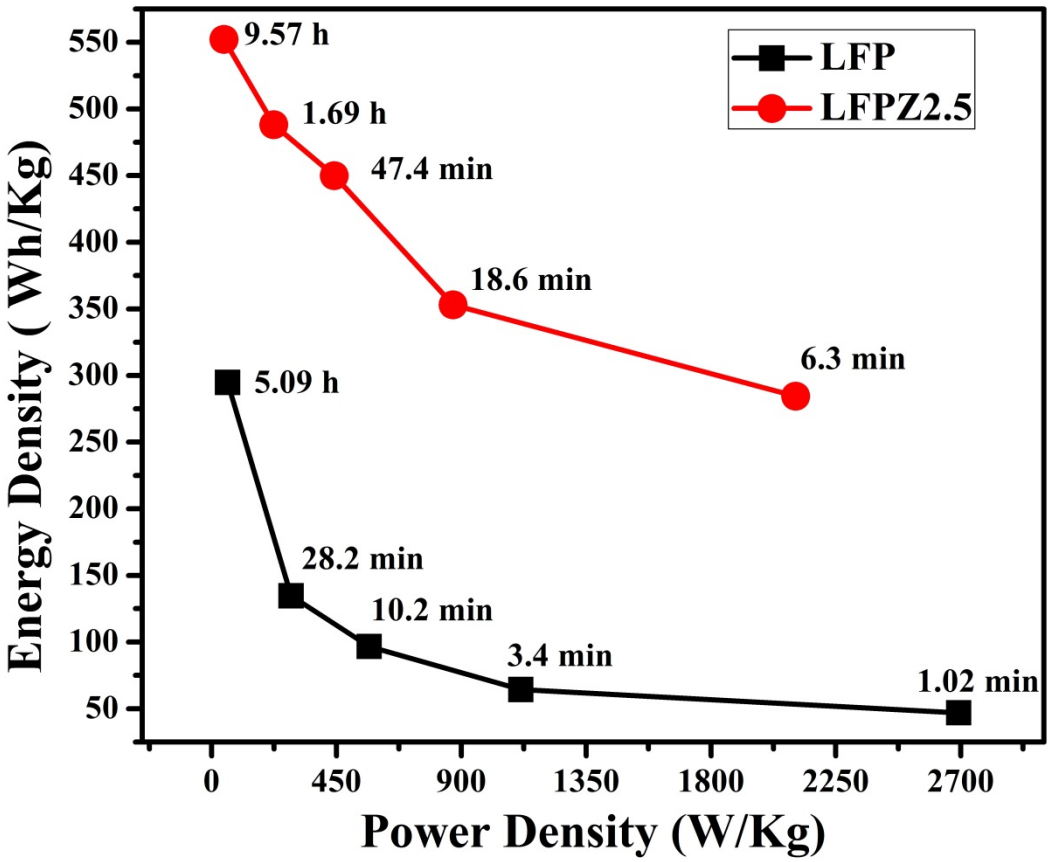


Fig. 15

ACCEPTED MANUSCRIPT

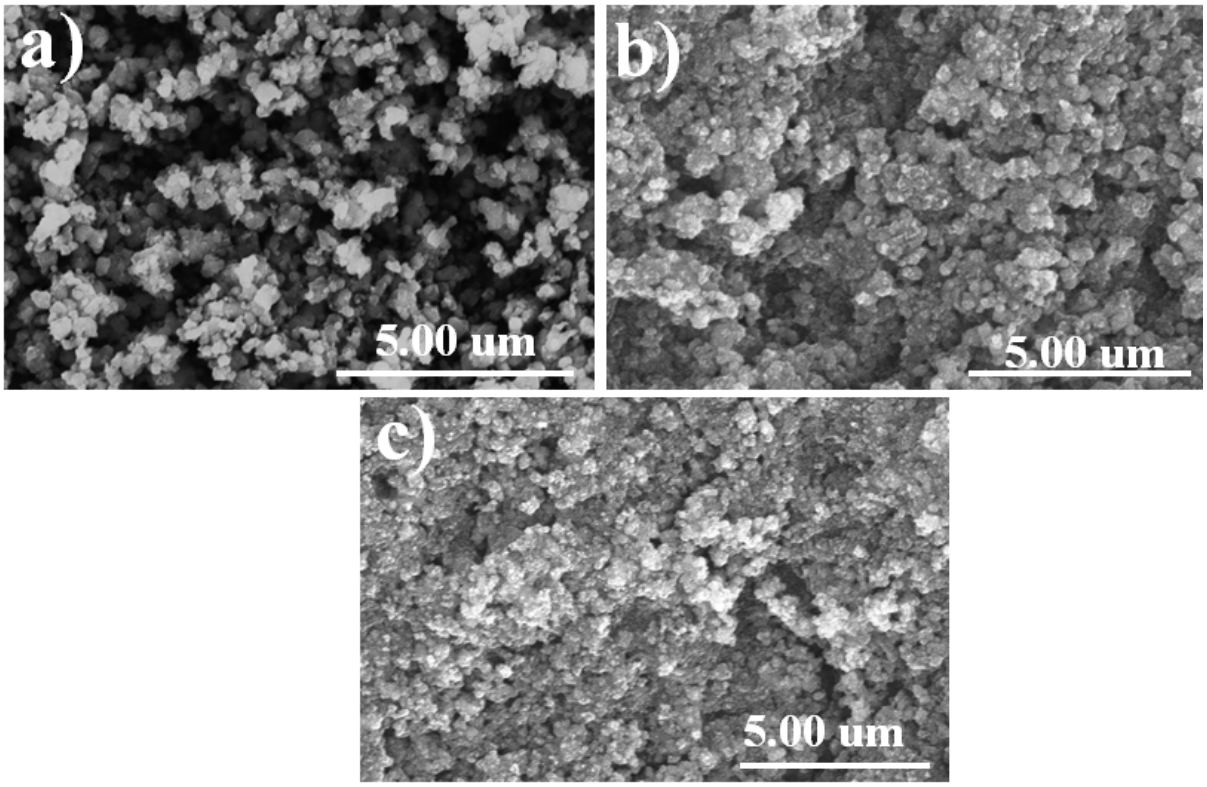


Fig. 16

Tables

Table 1. Rietveld refinement results for LFP and ZnO-doped LFP/C samples. All distance and lattice parameters units are in Å (10^{-10} m).

Samples	a (Å)	b (Å)	c (Å)	V $(Å)^3$	R_{exp}	R_p	χ^2
LFP	10.308	5.997	4.687	289.736	2.75	3.11	2.55
LFPZ1	10.317	6.001	4.688	290.244	2.41	2.88	2.98
LFPZ2.5	10.313	5.998	4.686	289.863	1.82	2.37	3.91
LFPZ5	10.296	6.014	4.696	290.776	1.88	2.84	4.98

ACCEPTED MANUSCRIPT

Table 2. Conductivity and activation energy results of LFP and ZnO-doped LFP/C samples.

Samples	$R_{A.C}$ (Ω)	$\sigma_{A.C}$ (S cm^{-1})	E_a (meV)
LFP	$39.0x10^{6}$	$4.35x10^{-9}$	694.7
LFPZ1	$158.7x10^{3}$	$5.11x10^{-7}$	248.0
LFPZ2.5	$40.5x10^{3}$	$1.765x10^{-6}$	227.0
LFPZ5	$503.5x10^{3}$	$1.74x10^{-7}$	223.9

Table 3. Galvanostatic Charge/Discharge performance of LFP and ZnO-doped LFP/C samples.

	Charge plateau	Discharge plateau	
Samples	**Voltage (V)**	**Voltage (V)**	**ΔV (V)**
LFP	3.490	3.388	0.102
LFPZ1	3.464	3.389	0.075
LFPZ2.5	3.462	3.391	0.071
LFPZ5	3.491	3.373	0.118

Table 4. Electrochemical performance of LFP and ZnO-doped LFP/C samples at different C-rates and cycling performance at 1C-rate.

Samples	**R^a (%)**						**1C (±3) ($mAhg^{-1}$)**		
	0.1C (±3) ($mAhg^{-1}$)	**0.1C**	**0.5C**	**1C**	**2C**	**5C**	**1^{st}**	**50^{th}**	**R^b (%)**
LFP	87	100.0	46.34	33.71	22.71	17.23	29	28	96.55
LFPZ1	130	100.0	78.21	68.99	47.98	42.31	90	83	92.22
LFPZ2.5	164	100.0	88.48	82.57	65.95	55.56	135	128	94.81
LFPZ5	123	100.0	73.09	63.44	49.97	12.13	78	68	87.17

[a] Capacity retention ratios of synthesized samples compared to the 0.1C at different C-rate

ACCEPTED MANUSCRIPT

[b] Capacity retention ratios of synthesized samples compared to the 1st cycle at 1C

Table 5. Electrode kinetic factors for LFP and ZnO-doped LFP/C samples.

Samples	**R_e (Ω)**	**R_{ct} (Ω)**	**σ_w** ($\Omega s^{-0.5}$)	**D** (cm^2s^{-1})
LFP	11.88	245.03	77.09	$3.80x10^{-14}$
LFPZ1	12.73	132.71	89.91	$2.79x10^{-14}$
LFPZ2.5	16.55	65.39	66.98	$5.04x10^{-14}$
LFPZ5	10.65	213.26	463.41	$1.05x10^{-15}$

Sensors and Actuators B 240 (2017) 1134–1140

Contents lists available at ScienceDirect

Sensors and Actuators B: Chemical

journal homepage: www.elsevier.com/locate/snb

Effect of single wall carbon nanotube networks on gas sensor response and detection limit

Deepak Kumar[a,b,*], Poornendu Chaturvedi[a], Praveen Saho[a], Pika Jha[a], Abhilasha Chouksey[a], Mohan Lal[a], J.S.B.S. Rawat[a], R.P. Tandon[b], P.K. Chaudhury[a]

[a] Solid State Physics Laboratory, Lucknow Road, Timarpur, Delhi 110054, India
[b] Department of Physics and Astrophysics, University of Delhi, Delhi 110007, India

ARTICLE INFO

Article history:
Received 27 February 2016
Received in revised form
15 September 2016
Accepted 16 September 2016
Available online 17 September 2016

Keywords:
Gas sensor
Response
Analyte
Network
Heterogeneity
Adsorption
Detection limit

ABSTRACT

In this work Single wall carbon nanotube (SWNT) based gas sensor is fabricated with mainly two type of surface-networks, (i) SWNT random network (CNT-TFR) and (ii) SWNT aligned network (CNT-μR). Investigations of sensor response and its signal-to-noise ratio have been carried out for both the networks. Sensing measurement is performed by exposing sensor to NO_2 concentration from 0.5 ppm to 20 ppm over CNT-TFR and CNT-μR. It has been found that the response of CNT-μR is higher than CNT-TFR. The variation of response with concentration for both sensors is investigated and it is observed that type of surface network affects the surface heterogeneity and hence adsorption capacity of sensor. The detection limit of these gas sensors is 125 ppt and 165 ppt for CNT-TFR and CNT-μR respectively. CNT-TFR has a better detection limit (DL) and signal-to-noise ratio as compared to CNT-μR due to better surface homogeneity of CNT-TFR. The detection limit for the aligned gas sensors decreases as network density decreases.

© 2016 Elsevier B.V. All rights reserved.

1. Introduction

SWNT based gas sensor has many advantage due to its fast response, large adsorption capacity, high sensitivity, room temperature operation and environmental stability [1–4]. SWNT based gas sensor can be used to detect various gas molecules and volatile organic compounds [5–7]. The large and fast response of SWNT gas sensor is attributed to interaction of analyte on gas sensor surface [8] and even in the presence of minute quantity of analyte, there is drastic change in conductance for these gas sensors [7]. In dispersed solution, SWNTs agglomerates to form bundles due to van der Waals' interaction and its high aspect ratio [9,10]. The network connectivity of prepared gas sensors from these dispersions depend on the density of SWNT in solution and also on their aspect ratio [11,12]. In a network, the effective **s**urface area of SWNT bundles plays an important role in gas sensing [13]. Different types of SWNT gas sensing networks have been prepared by various methods, and correspondingly the response of these networks towards analyte has been studied by various authors [1,14–21]. Lucci et al. fabricated aligned and disordered gas sensor with and without applied field respectively, and they observed that sensitivity is enhanced by two fold for NH_3 with the alignment of SWNT between electrodes [22]. Lim et al. have fabricated SWNT networks by drop-casting and dielectrophoresis, and they enhanced the response of align SWNT towards NH_3 [23]. Muangrat et al., analyzed the effect of structure and morphology of CNT for NO_2 sensing [24]. Other authors have prepared the sensing networks by using different methods and by controlling the surface network morphology, with aim to enhance response of these gas sensors. It has been reported that the surface network influences the signal-to-noise ratio of the gas sensor [25,26], which in turn affects the response, resolution and DL of the gas sensor [27–29]. However, the effect of SWNT networks on signal-to-noise ratio, detection limit and response has not been studied in detail.

To study the effect of random network (CNT-TFR) and aligned network (CNT-μR) on signal-to-noise ratio, the gas sensors are fabricated by two different methods: vacuum filtration and dielectrophoresis respectively. The vacuum filtration is regarded as the simplest process for the fabrication of random network of electrically conducting SWNT films [30], whereas the dielectrophoresis

* Corresponding author at: Solid State Physics Laboratory, Lucknow Road, Timarpur, Delhi 110054, India.
E-mail addresses: kum.k.deepak@gmail.com, deepakmanu1985@yahoo.com (D. Kumar).

http://dx.doi.org/10.1016/j.snb.2016.09.095
0925-4005/© 2016 Elsevier B.V. All rights reserved.

(DEP) is a controlled method used to align nanotubes between the microelectrode pads with high reliability and accessibility [14,15].

In this research paper, we have investigated the effect of random and aligned network of SWNT on sensor's response and signal-to-noise ratio. The response of these gas sensors is further analyzed to study the effect of these networks on the surface heterogeneity and adsorption capacity of sensor. The effect of network density on signal-to-noise ratio and detection limit is also investigated by controlling the density of aligned SWNT between electrodes.

2. Experimental technique

The random and aligned networks are fabricated on flexible polycarbonate membrane and silicon dioxide/silicon substrate using vacuum filtration and dielectrophoresis method, respectively. These films are prepared using P2-SWNT powder from Carbon Solution Inc. USA. The CNT-TFR is prepared by vacuum filtration method [31,32]. To prepare CNT-TFR, 0.5 mg of pristine SWNT is dispersed in 50% Dimethylformamide (DMF) solution and ultrasonicated for 2 h. Then, this solution is vacuum filtered over polycarbonate membrane. A small piece of prepared film is mounted on transistor outline header (TO-5 header) and contacts are made using gold wire for gas sensing study. In the second case, CNT-μR is prepared by aligning SWNT between pre-patterned electrode pads of Cr/Au over SiO_2/Si wafer using dielectrophoresis [33,34]. A small piece of die is mounted on TO-5 header having 3 microelectrodes of finger 1, 4 and 1 with gap of 4 μm each. To fabricate CNT-μR, SWNT suspension is made by dispersing 0.2 mg of SWNT in 100 ml of DMF and ultrasonicated for 2 h. SWNT suspension is, then dropped between electrode gaps using micropipette of 1 μl droplet and AC field of 1 MHz and peak-to-peak voltage 10 V_{pp} is applied for 5 s for alignment of SWNT. The resistance between these electrodes is 51, 6.4 and 8.1 kΩ. The gas sensor is annealed at 400 °C in the presence of N_2 for 10 min [35]. The contacts are made using gold wire bonding from electrode pads to TO-5 header legs. The gas sensor is placed inside a gas cell under constant environment of N_2 and all sensing measurement is done in closed gas cell. The gas sensing properties of these prepared films are studied by exposing different concentration of NO_2 to gas sensor. The gas flow is controlled by Bronkhorst mass flow controller and the different concentration of NO_2 is generated by using N_2 as diluting gas. We are able to generate minimum concentration of NO_2 upto 0.5 ppm due to the limitations of our exposure setup consisting of mass flow controller (MFC) and gas cylinder, etc. Gas sensing studies are carried out at room temperature at 23 °C and relative humidity is about 40–48%. The change in resistance of gas sensor is recorded by Fluke 289 multimeter. There are lots of variable, which affects the sensing performance of a gas sensor. This study focuses only on the effect of random and aligned network on sensor performance. The rest of parameters such as temperature, pressure, exposure duration and operating conditions remain constant during this study. Scanning electron microscope (SEM) studies are carried out using (FESEM) Ziess Supra 55. The UV lamp of 8 W is used for desorption of NO_2, which has UVC radiation of 2.4 W and exposed power to gas sensor is ~1.6 mW. The distance between UVC source and gas sensor remains constant in all experiments.

3. Result and discussion

3.1. Scanning electron microscope

The surface morphology of these gas sensors is studied by the SEM. The SEM images of the CNT-TFR and CNT-μR are shown in Fig. 1(a) and (b), respectively. The SEM image shows the over lapped and random network of SWNT bundles. It is observed that the average diameter of CNT-TFR sensor bundles is in the range of 20–32 nm. The SEM image shows a well aligned network of SWNT between 4-μm wide Au electrode pads for CNT-μR. The SWNT is bridged between electrode gaps in bundle form because the SWNT exists as bundle in dispersion due to their high aspect ratio and flexibility [11,12]. The average diameter of these bundles is in the range of 18–27 nm. The SWNT network is on CNT-μR surface and all sites are accessible to guest molecule, but in case of CNT-TFR gas has to diffuse through over layered network for gas sensor response.

3.2. Sensing

The gas sensing behavior is studied by exposing gas sensors to seventeen different concentrations 0.5–20 ppm of NO_2 gas for 1 min and the next cycle is applied after 1 min of the device recovery to baseline in the presence of UV and N_2. The change in the resistance with time is monitored for different exposed gas concentrations. Both devices show change in the resistance for NO_2 exposure and response of gas sensor increases with analyte concentration. These gas sensors have the ability to detect 0.5 ppm of NO_2 experimentally which is 40 times lower than immediately dangerous to life or health (IDLH) limit [9,18]. Furthermore, the response of these gas sensors is calculated by the given equation [36].

$$\frac{\Delta G}{G} = \left[\frac{(G_C - G_g)}{G_C}\right] \times 100, \text{for} t = t_r \quad (1)$$

where G_g is the film conductance in the presence of the test gas,G_c is conductance in the presence of carrier gas and t_r is exposure duration, i.e., 1 min.

Figs. 2 (a) and 3 (a) show the change in response of sample for a sequence of 1 min exposures to different concentration of NO_2. Thus large amount of analyte may be required to saturate TFRs. We have chosen to measure the response for fixed exposure duration for all the gas concentration, instead of waiting for the sensor to saturate. When these gas sensors are exposed to NO_2, resistance of

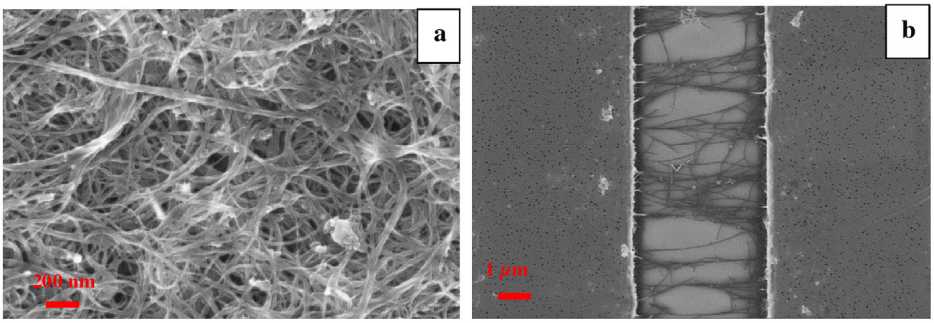


Fig. 1. SEM images of, a) CNT-TFR film and b) CNT-μR film.

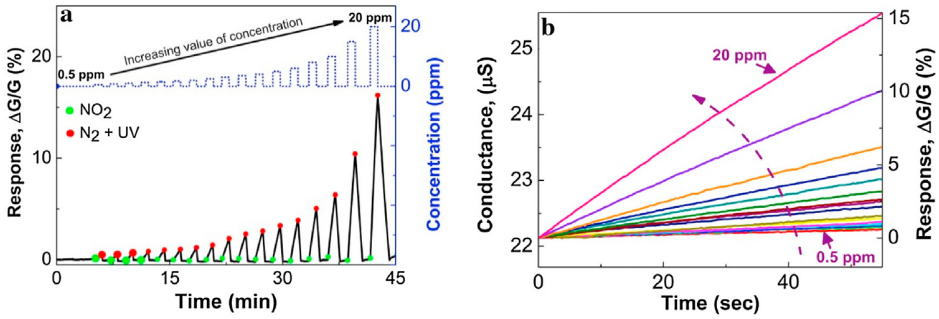


Fig. 2. a) Response of CNT-TFR to 1 min exposure of different NO_2 concentration and b) change in conductance and response curves are overlaid to show the different slope obtained for each concentration.

these devices changes. The change in resistance can be explained by charge transfer between SWNT and NO_2. SWNT is P-type in nature under ambient conditions due to adsorbed O_2 molecules [37,38]. NO_2 is oxidizing gas so it withdraws charge from SWNT surface [39,40]. This increases the majority charge concentration of SWNT and so resistance decreases [41,42]. As NO_2 is chemisorbed on the gas sensor surface [39,40,43] due to high binding energy, it does not recover to baseline even after long duration [8,41]. The UVC light is used as an external source for recovery of gas sensor [44,45]. The gas sensor is first exposed to NO_2, and then exposed to UVC during recovery time. The sensors completely recover to baseline after multiple exposure to different NO_2 concentration and the UV light consecutively, as shown in Figs. 2 (a) and 3 (a). The UV light is exposed to SWNT gas sensor in the presence of N_2 environment to protect SWNT from damage [44]. These gas sensors are exposed to UV during recovery time for short duration and this does not affect the gas sensor resistance. The baseline resistance of these gas sensors remain almost constant after multiple exposure of the analyte gas.

3.3. Effect of surface network on response

To understand the response of these gas sensors to an upcoming guest molecule, the response curves of these sensors are overlaid. The change in conducatnce of these sensors against the seventeen different exposed NO_2 concentration is ploted to illustrate that these gas sensors give different slope for different exposed concentration. These gas sensors give different slope for each concentration. The overlaid response curves for different NO_2 concentration are shown in Figs. 2 (b) and 3 (b) for CNT-TFR and CNT-μR. CNT-TFR response is found to vary linearly during period of observation. The response of CNT-μR is quite different from that of CNT-TFR. CNT-TFR shows linear behavior and CNT-μR shows a nonlinear behavior in the range of investigation. This may be due to the difference in surface coverage by the analyte gas for each gas sensor. CNT-μR shows saturation behaviour because small number of SWNTs are present on gas sensor surface. CNT-TFR shows unsaturated behaviour because the analyte molecule is required to diffuse through dense multiple layers of gas sensor network for saturation to occur. CNT-TFR gives response of 0.52% for one minute exposure to 0.5 ppm NO_2 concentration, while CNT-μR gives almost 7 times higher response of 4.4% for same concentration. The higher response of CNT-μR may be due to presence of SWNTs in small bundle form as observed from SEM image, and due to more surface area available for upcoming gas molecule which enhances the adsorption probability. There is a greater charge transfer effecienty per unit number for analyte in case of CNT-μR [2,46]. Moreover, CNT-TFR sensor response is impaired due to overlapping of SWNT and they remain inaccessible to analyte gas molecule, which limits the effective surface area and hence the adsorption probability.

CNT-TFR and CNT-μR film response vs concentration curve for 1 min exposure to NO_2 is shown in Fig. 4. The response of these gas sensors depends on the gas concentration of gas exposed. To study the variation of response with the gas concentration, we use Eq. (2) [2,5].

$$\frac{\Delta G}{G} = a[NO_2]^{\beta} \tag{2}$$

where a and β are coefficients which depend on operating temperature and testing material. The constant a is adsorption capacity, while β is the strength of adsorption [5,47]. β is a heterogeneity parameter, smaller the value greater the expected heterogeneity and value of β lies between 0 and 1, for normal adsorption. The value of a and β can be calculated by curve-fitting of the response curves. The value of a, β are (8.17, 0.675) and (0.8264, 1.00667) for CNT-μR and CNT-TFR respectively. Here the value of β is less than one, which indicates heterogeneous surface of CNT-μR and normal adsorption. In case of CNT-TFR β is approximately equal to one which indicates the linear adsorption on CNT-TFR. CNT-TFR

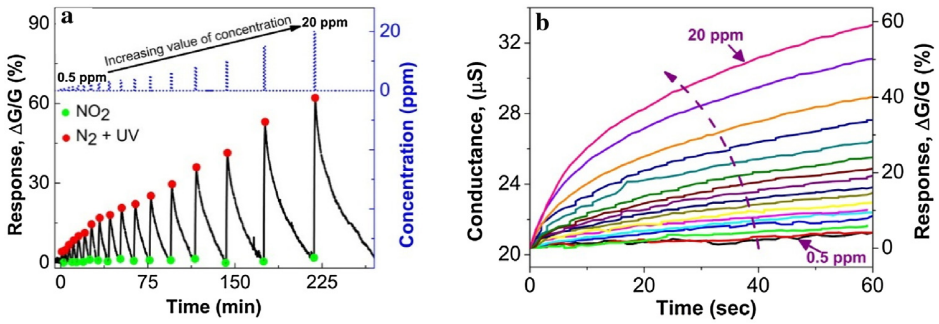


Fig. 3. a) Response of CNT-μR to 1 min exposure of different NO_2 concentration and b) change in conductance and response curves are overlaid, CNT-μR shows much higher response and saturation behaviour at higher concentration of NO_2.

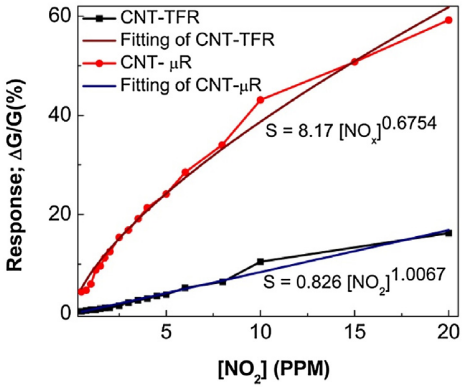


Fig. 4. Comparative response of CNT-TFR and CNT-μR.

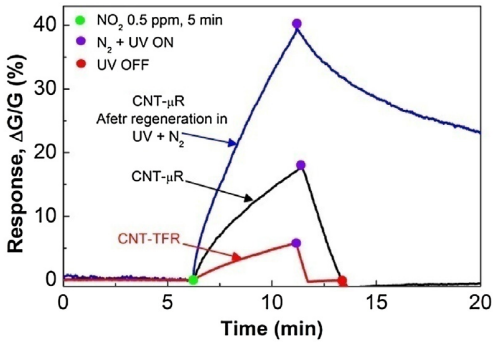


Fig. 5. Response of CNT-TFR, CNT- μR and after regeneration of CNT-μR gas sensor towards NO_2, 5 min exposure.

has more homogeneous surface network behaviour as compared to CNT-μR [23]. The value of adsorption capacity is higher for CNT-μR as compared to CNT-TFR. Thus, the response of CNT-μR is higher as compared to CNT-TFR (Fig. 5).

3.4. Effect of surface network on detection limit

The number of charge carriers plays an important role in gas sensor detection limit (DL). The noise depends on the number of channels (SWNT) present in the device. The device noise is proportional to its resistance [48,49]. To study the effect of these gas sensor networks on DL, these sensors are kept in N_2 environment for a long time until a stable baseline is formed. Thereafter, the sensors are exposed to 0.5 ppm of NO_2 for 6 min. For calculation of baseline noise, we observed baseline resistance for 6 min and fit the baseline data to third order polynomial and RMS noise is calculated using Eq. (4).

$$DL = \frac{3 \times Concentration}{S/N} \tag{3}$$

where RMS is residual sum of squares and is calculated using Eq. (4).

$$\text{RMS noise} = \frac{(Square\ root\ \ (sum\,[experimental\ data - data\ from\ curve\ fitting]^2)}{Number\ of\ \ data\ point} \tag{4}$$

The signal is given by Eq. (5),

$$\text{Signal} = R_{initial} - R_{final} \tag{5}$$

The DL is calculated using the equation given in paper [44] and is given in Eq. (3).

We observed that the noise in CNT-μR is higher due to the presence of small number of carriers. This is expected as there are less number of aligned nanotubes which creates higher surface heterogeneity. The signal-to-noise ratio of CNT-TFR gas sensor is 11956 for 5 min exposure, whereas signal-to-noise ratio of CNT-μR gas sensor is about 8856 for same exposure duration. The DL calculated using the above signal-to-noise ratio values for CNT-TFR and CNT-μR is less than 125 ppt and 169 ppt, respectively. CNT-TFR has less baseline noise and better signal-to-noise ratio as compared to CNT-μR which result in better detection limit in CNT-TFR. We now study the effect of regeneration of the sensor surface on the signal-to-noise ratio and DL for the CNT-μR. For this the gas sensor surface is regenerated by exposing it to UV in the presence of N_2 for long duration until a stable baseline is formed. After regeneration of CNT-μR sensor surface, gas sensor is exposed to 0.5 ppm of NO_2. CNT-μR gas sensor response is increased 1.5 times for CNT-μR as compared to pristine sensor but the signal-to-noise ratio decreases due to increase in baseline noise. The signal-to-noise ratio is 5770 as against 8856 before regeneration duration of exposure, i.e., 5 min and the calculated DL is less than 260 ppt. The increase in baseline noise with SWNT network can be explained as: the baseline stability in SWNT is determined by 1/f noise [25,48]. The 1/f noise is in terns related to the total number of free charge carriers, the fluctuation occurring at the contact and along the nanotube channel [25,50,51]. CNT-μR has less number of charge carriers which leads to large baseline noise. And SWNTs lie on the top of Au electrodes in case of CNT-μR which also cause noise due to contact resistance. The contact resistance of CNT-μR is improved by thermal annealing at 400 °C in the presence of N_2 for 10 min [35,52]. However in CNT-TFR, the contacts are placed on the top of the SWNT film, we expect this to reduce any fluctuation due to contact resistance. In case of CNT-μR, resistance of gas sensor increases after surface regeneration with desorption of adsorbed oxygen from sensor surface in the presence of UV and p-type nature of SWNT decreases [16,53,54]. The charge carrier decreases which leads to increase in baseline noise [50]. After regeneration, additional vacant sites become available on gas sensor surface which also causes baseline noise to increase due to turbulences around the sensor surface [2].

3.5. Effect of surface network density on detection limit

In the above study, it is observed that for gas sensor network the density, concentration of charge carrier, and contact resistance play an important role in signal-to-noise ratio. We now carry out these studies on a number of CNT-μR sensors by varying the density of aligned SWNT between electrodes of CNT-μR sensor. CNT-μR sensors are fabricated by bridging SWNT between micro electrodes of 1 μm gap and width of 7, 10, 12 μm using 0.15 mg SWNT in 100 ml DMF suspension. For alignment of SWNT, AC field of 1 MHz and peak-to-peak voltage 10 V_{pp} is applied field for 5 s. The gas sensor images are shown in Fig. 6. The SWNT network between electrodes decreases as CNT-μR-a > CNT-μR-b > CNT-μR-c and these networks have approximately 22, 14 and 7 aligned bundles between microelectrodes, respectively. All these gas sensors are exposed to NO_2 (0.5 ppm) for 5 min. The signal-to-noise ratio of CNT-μR-a, CNT-μR-b and CNT-μR-c is 116, 3.65 and 0.79, respectively and the DL of these gas sensors has been calculated to be 13 ppb, 411 ppb and 803 ppb, respectively. The DL decreases as the number of SWNTs decreases due to decrease in signal to noise ratio. It may be noted that detection limit of individual SWNT is reported to be 2 ppm for NO_2 [8].

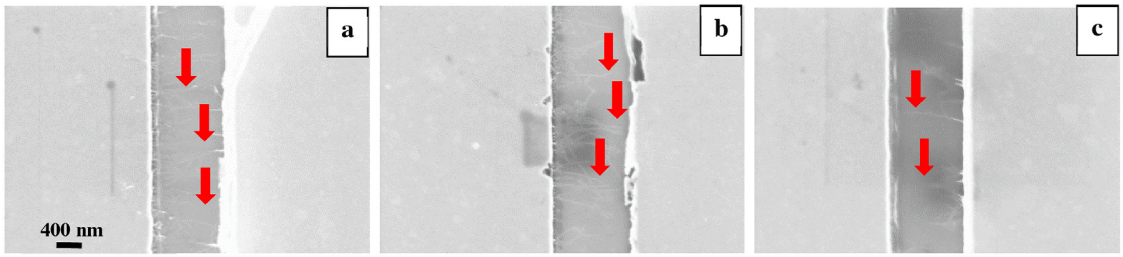


Fig. 6. SEM images of (a) CNT-μR-a, (b) CNT-μR-b and (c) CNT-μR-c sensor.

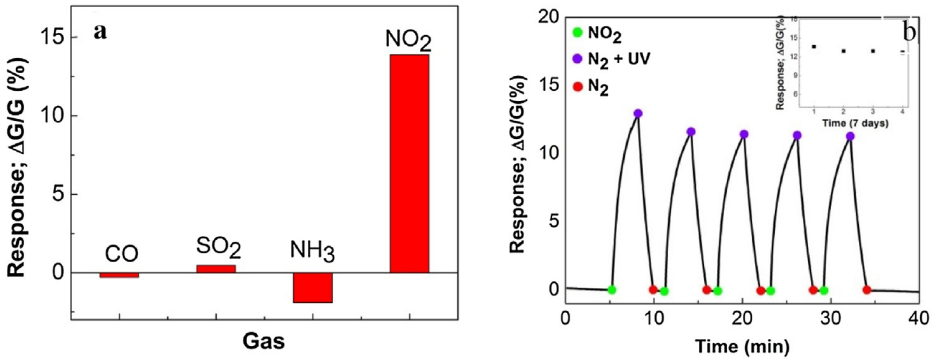


Fig. 7. a) Response of CNT-TFR towards different exposed gases of 5 ppm and b) Repeatability of gas sensor to multiple exposure and long-time stability (shown in inset graph).

3.6. Selectivity and durability

After having analyzed the various factors that contribute to the detection limit and signal-to-noise ratio, and hence the response of gas sensor, we now check our sensor for selectivity. For this, CNT-TFR is exposed to different gases of 5 ppm concentration, such as CO, SO_2, NH_3 and NO_2 for 5 min. Fig. 7a shows a bar graph of change in response when exposed to different gases. The gas sensor shows selective response towards NO_2 as compared to other gases. Next, gas sensor is exposed to 5 ppm of NO_2 for multiple times to check the repeatability of gas sensor. It is observed that the response of gas sensor is higher for the first exposure and the response remains almost constant for next exposures as shown in Fig. 7b. This could be due to the availability of more adsorption sites during the first exposer; it could be possible that on some of the above sites there is accumulation of analyte, which remains on the surface for the next few exposures. To check the long duration stability of gas sensor, it is exposed to the same concentration of NO_2 for a period of 1 month after an interval of 7 days. An initial dip is observed in the response on the 7th day compared to day 1, thereafter response remains constant for the period of observation (inset Fig. 7b).

To study the behavior of the CNT-TFR sensors in the presence of air and N_2. The numbers of gas sensors are exposed to NO_2 in the presence of air and N_2. The typical response of the sensor in the presence of air and N_2 is shown in Fig. 8a. The gas sensor gives approximately same response in the presence of air as in the presence of N_2. The gas sensor shows repeatable response in the presence of air and N_2.

To ascertain the contribution of atmospheric moisture to the response of the sensor, separate studies were carried out by exposing the gas sensor to the N_2 bubbled through water kept at room temperature (results not shown). The concentration of the water vapor is ~27,700 ppm, calculated by using equation given in reference [55]. The relative humidity was measured by a RH sensor installed at the output of the gas cell and was found to be ~56%. During multiple exposure to moisture laden N_2, the sensor showed a response of only ~0.35–0.41%, which is much less than its response to NO_2. The gas sensor does not give any additional response to

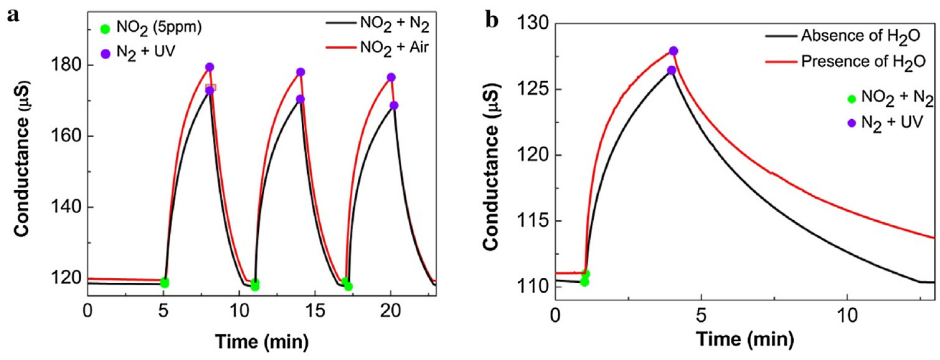


Fig. 8. a) The change in conductance w.r.t to time of the sensor in the presence of air and N_2 and b) The change in conductance w.r.t to time of the sensor in the presence and absence of water.

water vapor because SWNTs are hydrophobic in nature [56–58], showing a unique advantage of any CNT based gas sensor.

Additional studies were carried out to study the effect of water vapor on the NO_2 sensing characteristics of the gas sensor. This was done by studying the sensor response to NO_2 in the presence and absence of water vapor. There is approximately 4% change in response of gas sensor in the presence of water vapour as shown in Fig. 8b.

4. Conclusion

To study the effect of gas sensor networks, we prepared random film resistor (CNT-TFR) and aligned film resistor (CNT-μR) on flexible polycarbonate membrane and SiO_2/Si substrate respectively. CNT-TFR has a linear response curve but CNT-μR has saturated curve with increase in gas concentration. CNT-μR gives 7 times higher response as compared to CNT-TFR sensor for 500 ppb NO_2. CNT-μR has a better response for analyte as compared to the CNT-TFR due to more adsorption capacity. But CNT-μR has a small signal-to-noise ratio (S/N) ratio due to the presence of less number of charge carriers which creates surface heterogeneity and reduces the DL of gas sensor. The DL of CNT-TFR is 125 ppt and for CNT-μR is 169 ppt respectively. The regeneration of gas sensor surface and reduction of network density are found to have an adverse effect on the detection limit of gas sensor, possibly because of decrease in signal-to-noise ratio.

Acknowledgments

Authors gratefully acknowledge Dr. R. K. Sharma, Director, Solid State Physics Laboratory for the guidance and permission to publish the work. One of the authors (Deepak Kumar) is thankful to DRDO, for providing research fellowship.

References

[1] G.P. Evans, D.J. Buckley, N.T. Skipper, I.P. Parkin, Single-walled carbon nanotube composite inks for printed gas sensors: enhanced detection of NO_2, NH_3, EtOH and acetone, RSC Adv. 4 (2014) 51395–51403.
[2] F. Rigoni, S. Tognolini, P. Borghetti, G. Drera, S. Pagliara, A. Goldoni, L. Sangaletti, Enhancing the sensitivity of chemiresistor gas sensors based on pristine carbon nanotubes to detect low-ppb ammonia concentrations in the environment, Analyst 138 (2013) 7392–7399.
[3] J. Chaste, A. Eichler, J. Moser, G. Ceballos, R. Rurali, A. Bachtold, A nanomechanical mass sensor with yoctogram resolution, Nat. Nanotechnol. 7 (2012) 301–304.
[4] P. Vichchulada, Q. Zhang, M.D. Lay, Recent progress in chemical detection with single-walled carbon nanotube networks, Analyst 132 (2007) 719–723.
[5] I. Sayago, H. Santos, M.C. Horrillo, M. Aleixandre, M.J. Fernández, E. Terrado, I. Tacchini, R. Aroz, W.K. Maser, A.M. Benito, M.T. Martnez, J. Gutiérrez, E. Muñoz, Carbon nanotube networks as gas sensors for NO_2 detection, Talanta 77 (2008) 758–764.
[6] D.R. Kauffman, A. Star, Carbon nanotube gas and vapor sensors, Angew. Chem. Int. Ed. 47 (2008) 6550–6570.
[7] J. Li, Y. Lu, Q. Ye, M. Cinke, J. Han, M. Meyyappan, Carbon nanotube sensors for gas and organic vapor detection, Nano Lett. 3 (2003) 929–933.
[8] J. Kong, N.R. Franklin, C. Zhou, M.G. Chapline, S. Peng, K. Cho, H. Dai, Nanotube molecular wires as chemical sensors, Science 287 (2000) 622–625.
[9] M. Mittal, A. Kumar, Carbon nanotube (CNT) gas sensors for emissions from fossil fuel burning, Sens. Actuators B: Chem. 203 (2014) 349–362.
[10] Y.W. Wen, H.J. Liu, L. Pan, X.J. Tan, H.Y. Lv, J. Shi, X.F. Tang, A triplet form of (5,0) carbon nanotube with higher hydrogen storage capacity, J. Phys. Chem. C 115 (2011) 9227–9231.
[11] L.F.C. Pereira, M.S. Ferreira, Electronic transport on carbon nanotube networks: a multiscale computational approach, Nano Commun. Networks 2 (2011) 25–38.
[12] O. Kanoun, C. Muller, A. Benchirouf, A. Sanli, T. Dinh, A. Al-Hamry, L. Bu, C. Gerlach, A. Bouhamed, Flexible carbon nanotube films for high performance strain sensors, Sensors 14 (2014) 10042–10071.
[13] B. Bina, H. Pourzamani, A. Rashidi, M.M. Amin, Ethylbenzene removal by carbon nanotubes from aqueous solution, J. Environ. Public Health 2012 (2012) 8.
[14] J. Suehiro, G. Zhou, H. Imakiire, W. Ding, M. Hara, Controlled fabrication of carbon nanotube NO_2 gas sensor using dielectrophoretic impedance measurement, Sens. Actuators B: Chem. 108 (2005) 398–403.
[15] W.J. Shen, K.W. Sun, C.S. Lee, Electrical characterization and Raman spectroscopy of individual vanadium pentoxide nanowire, J. Nanopart. Res. 13 (2011) 4929–4936.
[16] T. Zhang, S. Mubeen, N.V. Myung, M.A. Deshusses, Recent progress in carbon nanotube-based gas sensors, Nanotechnology 19 (2008) 332001.
[17] S. Mao, G. Lu, J. Chen, Nanocarbon-based gas sensors: progress and challenges, J. Mater. Chem. A 2 (2014) 5573–5579.
[18] A.K. Naik, M.S. Hanay, W.K. Hiebert, X.L. Feng, M.L. Roukes, Towards single-molecule nanomechanical mass spectrometry, Nat. Nanotechnol. 4 (2009) 445–450.
[19] I. Sasaki, N. Minami, A. Karthigeyan, K. Iakoubovskii, Optimization and evaluation of networked single-wall carbon nanotubes as a NO_2 gas sensing material, Analyst 134 (2009) 325–330.
[20] D. Kumar, P. Chaturvedi, A. Chouksey, R.P. Tandon, P.K. Chaudhury, Investigation of single wall nanotube gas sensor recovery behavior in the presence of UV, Adv. Mater. Lett. 7 (2016) 262–266.
[21] D. Kumar, I. Kumar, P. Chaturvedi, A. Chouksey, R.P. Tandon, P.K. Chaudhury, Study of simultaneous reversible and irreversible adsorption on single-walled carbon nanotube gas sensor, Mater. Chem. Phys. 177 (2016) 276–282.
[22] M. Lucci, P. Regoliosi, A. Reale, A.D. Carlo, S. Orlanducci, E. Tamburri, M.L. Terranova, P. Lugli, C. Di Natale, A. D'Amico, R. Paolesse, Gas sensing using single wall carbon nanotubes ordered with dielectrophoresis, Sens. Actuators B: Chem. 111–112 (2005) 181–186.
[23] J.-H. Lim, N. Phiboolsirichit, S. Mubeen, Y. Rheem, M.A. Deshusses, A. Mulchandani, N.V. Myung, Electrical and sensing properties of single-walled carbon nanotubes network: effect of alignment and selective breakdown, Electroanalysis 22 (2010) 99–105.
[24] M. Worawut, G. Eakgapon, I. Chaisak, P. Wolfgang, Effect of structure and morphology of carbon nanotubes on NO_2 gas sensing, Songklanakarin J. Sci. Technol. 34 (6) (2012) 695–699.
[25] K. Chikkadi, M. Muoth, W. Liu, V. Maiwald, C. Hierold, Enhanced signal-to-noise ratio in pristine, suspended carbon nanotube gas sensors, Sens. Actuators B: Chem. 196 (2014) 682–690.
[26] M.E. Hasselmo, C. Linster, M. Patil, D. Ma, M. Cekic, Noradrenergic suppression of synaptic transmission may influence cortical signal-to-noise ratio, J. Neurophysiol. 77 (1997) 3326–3339.
[27] F. Schedin, A.K. Geim, S.V. Morozov, E.W. Hill, P. Blake, M.I. Katsnelson, K.S. Novoselov, Detection of individual gas molecules adsorbed on graphene, Nat. Mater. 6 (2007) 652–655.
[28] W. Moritz, V. Fillipov, L. Bartholomaus, A. Terentjev, T. Gabusjan, A. Vasiliev, S. Yakimov, High temperature semiconductor sensor for the detection of fluorine, Solid State Sensors and Actuators, 1997. TRANSDUCERS '97 Chicago., 1997 International Conference on, 1072 (1997) 1073–1076.
[29] Z. Zhu, Y. Xu, B. Jiang, A one ppm NDIR methane gas sensor with single frequency filter denoising algorithm, Sensors 12 (2012) 12729–12740.
[30] Z. Wu, Z. Chen, X. Du, J.M. Logan, J. Sippel, M. Nikolou, K. Kamaras, J.R. Reynolds, D.B. Tanner, A.F. Hebard, A.G. Rinzler, Transparent, conductive carbon nanotube films, Science 305 (2004) 1273–1276.
[31] L. Hu, D.S. Hecht, G. Grüner, Percolation in transparent and conducting carbon nanotube networks, Nano Lett. 4 (2004) 2513–2517.
[32] D. Zhang, K. Ryu, X. Liu, E. Polikarpov, J. Ly, M.E. Tompson, C. Zhou, Transparent, conductive, and flexible carbon nanotube films and their application in organic light-emitting diodes, Nano Lett. 6 (2006) 1880–1886.
[33] P. Li, W. Xue, Selective deposition and alignment of single-walled carbon nanotubes assisted by dielectrophoresis: from thin films to individual nanotubes, Nanoscale Res. Lett. 5 (2010) 1072–1078.
[34] S. Shekhar, P. Stokes, S.I. Khondaker, Ultrahigh density alignment of carbon nanotube arrays by dielectrophoresis, ACS Nano 5 (2011) 1739–1746.
[35] W.Q. Qin, W. Z.-Jun, R. L.-Ming, Z. H.-Bo, Ye T.-Yang, S. Z-.Jin, F. Y.-Yi, Z. Xing, H. Ru, Vertical assembly of carbon nanotubes for via interconnects, Chin. Phys. B 21 (2012).
[36] A.K. Debnath, S. Samanta, A. Singh, D.K. Aswal, S.K. Gupta, J.V. Yakhmi, Parts-per-billion level chlorine sensors with fast kinetics using ultrathin cobalt phthalocyanine films, Chem. Phys. Lett. 480 (2009) 185–188.
[37] A. Javey, M. Shim, H. Dai, Electrical properties and devices of large-diameter single-walled carbon nanotubes, Appl. Phys. Lett. 80 (2002) 1064–1066.
[38] D. Kang, N. park, J.-h. Ko, E. Bae, W. park, Oxygen-induced p-type doping of a long individual single-walled carbon nanotube, Nanotechnology 16 (2005) 1048.
[39] A. Ricca, C.W. Bauschlicher Jr., The adsorption of NO_2 on (9,0) and (10,0) carbon nanotubes, Chem. Phys. 323 (2006) 511–518.
[40] W.-L. Yim, X. Gong, Z.-F. Liu, Chemisorption of NO_2 on carbon nanotubes, J. Phys. Chem. B 107 (2003) 9363–9369.
[41] L.-C. Wang, K.-T. Tang, I.J. Teng, C.-T. Kuo, C.-L. Ho, H.-W. Kuo, T.-H. Su, S.-R. Yang, G.-N. Shi, C.-P. Chang, A single-walled carbon nanotube network gas sensing device, Sensors 11 (2011) 7763–7772.
[42] H. Chang, J.D. Lee, S.M. Lee, Y.H. Lee, Adsorption of NH_3 and NO_2 molecules on carbon nanotubes, Appl. Phys. Lett. 79 (2001) 3863–3865.
[43] K. Chikkadi, M. Muoth, C. Roman, M. Haluska, C. Hierold, Advances in NO_2 sensing with individual single-walled carbon nanotube transistors, Beilstein J. Nanotechnol. 5 (2014) 2179–2191.
[44] G. Chen, T.M. Paronyan, E.M. Pigos, A.R. Harutyunyan, Enhanced gas sensing in pristine carbon nanotubes under continuous ultraviolet light illumination, Sci. Rep. 2 (2012).
[45] Y. Wang, J.T.W. Yeow, A review of carbon nanotubes-based gas sensors, J. Sens. 2009 (2009) 24.

[46] W. Wongwiriyapan, S. Honda, H. Konishi, T. Mizuta, T. Ohmori, Y. Kishimoto, T. Ito, T. Maekawa, K. Suzuki, H. Ishikawa, T. Murakami, K. Kisoda, H. Harima, K. Oura, M. Katayama, Influence of the growth morphology of single-walled carbon nanotubes on gas sensing performance, Nanotechnology 17 (2006) 4424.
[47] A.O. Dada, A.P. Olalekan, A.M. Olatunya, O. DADA, Langmuir, Freundlich, Temkin and Dubinin–Radushkevich isotherms studies of equilibrium sorption of Zn^{2+} unto phosphoric acid modified rice husk, J. Appl. Chem. 3 (1) (2012) 38–45.
[48] P.G. Collins, M.S. Fuhrer, A. Zettl, 1/f noise in carbon nanotubes, Appl. Phys. Lett. 76 (2000) 894–896.
[49] E.S. Snow, J.P. Novak, M.D. Lay, F.K. Perkins, 1/f noise in single-walled carbon nanotube devices, Appl. Phys. Lett. 85 (2004) 4172–4174.
[50] Y.-M. Lin, J. Appenzeller, J. Knoch, Z. Chen, P. Avouris, Low-frequency current fluctuations in individual semiconducting single-wall carbon nanotubes, Nano Lett. 6 (2006) 930–936.
[51] J. Appenzeller, L. Yu-Ming, J. Knoch, C. Zhihong, P. Avouris, 1/f noise in carbon nanotube devices—on the impact of contacts and device geometry, IEEE Trans. Nanotechnol. 6 (2007) 368–373.
[52] A. Vijayaraghavan, S. Blatt, D. Weissenberger, M. Oron-Carl, F. Hennrich, D. Gerthsen, H. Hahn, R. Krupke, Ultra-large-scale directed assembly of single-walled carbon nanotube devices, Nano Lett. 7 (2007) 1556–1560.
[53] P. Gowda, A. Suri, S.K. Reddy, A. Misra, Chemical vapor detection using nonlinear electrical properties of carbon nanotube bundles, Nanotechnology 25 (2014) 025708.
[54] R.J. Chen, N.R. Franklin, J. Kong, J. Cao, T.W. Tombler, Y. Zhang, H. Dai, Molecular photodesorption from single-walled carbon nanotubes, Appl. Phys. Lett. 79 (2001) 2258–2260.
[55] Y. Wang, Z. Zhou, Z. Yang, X. Chen, D. Xu, Y. Zhang, Gas sensors based on deposited single-walled carbon nanotube networks for DMMP detection, Nanotechnology 20 (2009) 345502.
[56] S. Peng, K. Cho, Ab initio study of doped carbon nanotube sensors, Nano Lett. 3 (2003) 513–551.
[57] T. Ohba, S. Yamamoto, T. Kodaira, K. Hata, Changing water affinity from hydrophobic to hydrophilic in hydrophobic channels, Langmuir 31 (2015) 1058–1063.
[58] G. Hummer, J.C. Rasaiah, J.P. Noworyta, Water conduction through the hydrophobic channel of a carbon nanotube, Nature 414 (2001) 188–190.

Biographies

Deepak Kumar is a senior research fellow in Solid State Physics Laboratory (SSPL), Delhi. He did his M.Sc from Gurukul Kangri Vishwavidyalaya, Haridwar and pursuing Ph.D from University of Delhi, Delhi. His research is focused on the development of CNT based gas sensor.

Poornendu Chaturvedi is working as Scientist 'E' in Solid State Physics Laboratory (SSPL), Delhi. He did his B. Tech (Electronics) from Indian School of Mines Dhanbad in 2002 and is currently pursuing Ph.D from IIT Delhi. He has worked on growth and characterization of vertically aligned CNT, demonstration of CNT based field emission alphanumeric display. Currently he is working on the development of enabling technologies for carbon nanotube based sensors.

Praveen Saho is working as Scientist 'D' in Solid State Physics Laboratory, Delhi. He did his M.Sc in Physics from University of Lucknow (2000) and M.Tech in Polymer Science & Technology from IIT Delhi (2004). Currently he is working in the field of growth of graphene, growth of SWNT and CNT based FET sensor.

Dr. Pika Jha is a scientist 'E' in solid state physics laboratory. He received her Ph.D. Degree in Chemistry from IIT Delhi, India. She had earlier worked on the area of oxide dielectrics and on development of magnetoresistive and high thermal conductivity nanofluids. Her present research interests are in the field of carbon nanotubes and graphene. She is working on field emission behavior of carbon nanotubes with focus on obtaining high current density from large area cathodes, as well as in the field of carbon nanotubes and graphene based devices, with special focus on sensors.

Abhilasha Chouksey is working as Scientist 'C' in Solid State Physics Laboratory (SSPL), Delhi. She did her M.Sc Physics from Rani Durgavati Vishwavidyalaya, Jabalpur, India (2006). Currently she is working in the field of carbon nanotubes based gas sensors.

Mohan Lal has done B. E. in Electrical Engineering from Delhi College of Engineering (Delhi University) in 2008. Since than, he is working with the Solid State Physics Laboratory, DRDO as a Scientist. His research experience include fabrication of Carbon Nano tube, Graphene and High frequency devices based on Galliun Nitride.

J. S. B. S. Rawat is working as Scientist 'G' in Solid State Physics Laboratory (SSPL), Delhi. He did his BE and ME in E&C. He worked in circuit design and measurement of IR image. Currently he is working in the field of carbon nanotubes based field emission, CNT based gas sensors.

Prof. R. P. Tandon is working as professor in the Department of Physics and Astrophysics at the University of Delhi. He received his Ph.D. Degree in Physics in 1977 from University of Delhi, India. He worked at National Physical Laboratory during 1977–1998 and headed its Electroceramic Division for more than a decade. He worked as Research Associate at Massachusetts Institute of Technology (MIT, USA) during 1980–1982. His research interest includes ceramics, polymers, solar cells, graphene, magnetic nanoparticles for hyperthermia cancer treatment and glasses. Currently he is working in the field of solar cell, gas sensors and composite materials and its applications.

P. K. Chaudhury is working as Scientist 'G' and head of Nanotechlogy group in Solid State Physics Laboratory (SSPL), Delhi. He received his M.Phil degree (1980) and Ph.D. Degree in Physics in 1984 from University of Delhi, India. His research interest includes variety of semiconductor materials and devices including MCT, CdTe, II_VI compounds, Silicon. Currently he is working on growth of CNT, growth of graphene, CNT field emission and CNT based gas sensor etc.

ResearchGate

See discussions, stats, and author profiles for this publication at: https://www.researchgate.net/publication/307870257

Effect Of ZnO Coating On Physicochemical Properties Of LiFePO4 Cathode Material For Lithium Ion Batteries

Article · August 2016

DOI: 10.5185/amp.2016/118

CITATIONS
0

READS
6

3 authors, including:



Rakesh Saroha
Delhi Technological University
6 PUBLICATIONS **1** CITATION
SEE PROFILE



Aditya Jain
Delhi Technological University
7 PUBLICATIONS **2** CITATIONS
SEE PROFILE

Available from: Aditya Jain
Retrieved on: 28 September 2016

Research Article 1(1) 104-108 Advanced Materials Proceedings

Effect of ZnO coating on physicochemical properties of $LiFePO_4$ cathode material for lithium ion batteries

Rakesh Saroha, Aditya Jain, A. K. Panwar*

Department of Applied Physics, Delhi Technological University, Delhi, 110042, India

*Corresponding author, E-mail: panwaramar@gmail.com; Tel: +91-9891778307

Received: 31 March 2016, Revised: 27 July 2016 and Accepted: 03 August 2016

DOI: 10.5185/amp.2016/118
www.vbripress.com/amp

Abstract

The effects of ZnO nanoparticle coating on the physicochemical and electrochemical properties of $LiFePO_4$ (LFP) have been investigated in this work. ZnO-modified $LiFePO_4$ cathode materials were synthesized via sol-gel and modified by ZnO nanoparticle using ball mill method. The amount of ZnO additive is chosen as a controlling factor to tune ZnO content over the surface of LFP particles. Structure and morphology of the LFP material with and without ZnO-coating layer were studied using X-ray diffraction (XRD), scanning electron microscopy (SEM) and Fourier transform infrared (FTIR) spectra. The XRD patterns reveal that the proper phase of LFP is formed with the ordered olivine-type orthorhombic structure of *Pnma* space group, and no impurity phase like $LiZnPO_4$ has been noticed. AC conductivity measurements have shown that the ZnO-modified LFP samples significantly assists in lowering the resistance of cathode active material and enhancing the conductivity. It is found that the 2.5 wt% ZnO-doped LFP exhibits the highest conductivity than the 5 wt% ZnO and 1 wt% ZnO doped LFP or the un-doped sample**.** Among the synthesized samples, LFPZ2.5 displays highest discharge capacity 160 (±5) $mAhg^{-1}$ (~94% of the theoretical capacity of $LiFePO_4$) at 0.1C rate. These results indicate that 2.5 wt% ZnO coated pristine LFP sample proves to be alternative material for automotive industry and it may be possible alternate of cathode materials in hybrid electric vehicles. Copyright © 2016 VBRI Press

Keywords: Olivine, sol-gel, ZnO-modified LFP, conductivity, electrochemical performances.

Introduction

Olivine-type $LiFePO_4$ proves to be one of the most promising cathode material for lithium ion batteries. It has undergone extensive research since it was first reported by padhi et al. in 1997 [**1**]. It satisfies most of the requirements of high theoretical capacity (170 $mAhg^{-1}$), low cost and environmentally benign due to its non-toxicity [**2-5**]. The $(PO_4)^{3-}$ tetrahedral structure unit present in olivine structure modify the redox potential of the $Fe^{2+/3+}$ couple and thus producing steady voltage plateau at around 3.4 V vs. Li^+/Li [**3, 4**]. However, low electronic conductivity (10^{-9} – 10^{-11} S cm^{-1}) and poor electrochemical performances of pristine $LiFePO_4$ has restricted its commercial use in automotive industry for EVs and HEVs. Various ways have been adopted till date to increase the conductivity and electrochemical properties of pristine $LiFePO_4$ cathode material which mainly includes carbon coating [**6**] and cation doping at the M1/M2 site [**7,8**]. Apart from this, conductivity can also be enhanced by coating/ surface modification of pristine $LiFePO_4$ material with electronically conductive materials such as $LaPO_4$ [**9**], CuO [**10**], NbC [**11**], LTO [**12**] and much more.

Carbon coating has been widely applied to tune morphology of cathode active material. Apart from conducting carbon coating, there are various reports on metal oxides coatings of $LiFePO_4$ material [**10, 13**]. Zinc oxide (ZnO) one of the metal oxides, when coated over the surface of lithium iron phosphate particles assists lithium ion diffusion and increases electrochemical performances of pristine $LiFePO_4$. Incorporation of Zn into $LiFePO_4$ lattice induces some kind of "pillar effect" which provides more space for lithium ion movement and consequently, the conductivity of $LiFePO_4$ is enhanced [**13**]. Cui et al. [**14**] studied the effect of ZnO/C co-coated on the electrochemical properties of $LiFePO_4$ cathode material and revealed that ZnO-$LiFePO_4$ sample shows highest current exchange density and maximum discharge capacities of 147.7 $mAhg^{-1}$ and 138.5 $mAhg^{-1}$ at 1C and 2C rates, respectively. Hu et al. [**13**] studied ZnO-doped $LiFePO_4$ synthesized by hydrothermal method and found that ZnO-doped sample exhibits a discharge capacity of 132.3 $mAhg^{-1}$ and 80 $mAhg^{-1}$ at 0.1C and 1C, respectively. TANG et al. [**15**] investigate aluminum doped zinc oxide coated $LiFePO_4$ material and observed discharge

capacities of 165.8 $mAhg^{-1}$ and 158.1 $mAhg^{-1}$ at 0.1C and 1C, respectively in a charge/discharge voltage window of 4.0-2.0 V. However, there is no information available on the microstructure and electrochemical properties of the ZnO coating with different wt.% over the surface of pristine LFP, which prompted the authors to investigate the present composition.

The objective of this work is to investigate the effects of a surface coating of ZnO nanopowder on the surface of pristine $LiFePO_4$. The effect of a surface coating by ZnO over the surface of pristine $LiFePO_4$ has been systematically studied in terms of physicochemical and electrochemical properties. All the samples were synthesized using the sol-gel assisted ball-milling route with sucrose (10 wt %) as a carbon source. Physicochemical characteristics of the synthesized samples were examined by using XRD, SEM, and FTIR. Electrochemical characterization of as-prepared samples is carried out to investigate electrochemical properties.

Experimental

Materials

Pristine lithium iron phosphate ($LiFePO_4$) and ZnO-coated samples were synthesized by sol-gel route followed by ball-milling for ZnO coating. Stoichiometric amounts of $LiOH.H_2O$ (Sigma-Aldrich, U.S.A, ≥99%), $Fe(NO_3)_3.9H_2O$ (CDH, New Delhi, 98%) and $H_9N_2O_4P$ (Sigma-Aldrich, U.S.A, ≥99%) were used as precursors while sucrose GR (Mumbai, MERCK) was used as additive for carbon source and as a reducing agent. Citric acid (Sigma-Aldrich, U.S.A, ≥98%) was used as chelating agent.

Method

Separate solutions of all the precursors in deionized water were prepared and then added to the citric acid solution. The resulting solution of citric acid and precursors was heated at 70 ºC at 400 rpm with continuous stirring till a transparent gel was obtained. The gel thus obtained was decomposed at 350 ºC for 5 h in a tubular furnace under reducing atmosphere. The yielded powder after decomposition was reground together with ZnO and sucrose. Then it was ball milled for 2 h at 400 rpm in toluene media. The final product was obtained by calcination of the mixture at 750 ºC for 12 h in slightly reducing atmosphere of Ar/H_2. The pristine $LiFePO_4$ and coated with 1.0, 2.5, 5.0 wt % of ZnO nanoparticles were named as LFP, LFPZ1, LFPZ2.5and LFPZ5.

ZnO nanopowder was synthesized by a wet chemical method using Zinc acetate dihydrate ($(CH_3COO)_2$ $Zn.2H_2O$) as a precursor. Zinc acetate dehydrate was dissolved in deionized water with continuous stirring at 40 ^{0}C. After few hours of stirring a white powder was obtained which is subjected to calcination at 450 ^{0}C for 24 hours in order to get ZnO nanopowder.

Electrode preparation and electrochemical characterization

Synthesized samples were characterized using RIGAKU make X-ray diffractometer of CuK_α radiation (λ=1.54178 Å) for crystal structure and phase composition analysis. Rietveld refinement was done using X'pert high score plus software. The morphological study was carried out using HITACHI make scanning electron microscope of model S-3700 N. The Fourier transform infrared (FTIR) spectra were recorded with a PERKIN ELMER (C91158) make spectrometer in the wavenumber range of 1400–400 cm^{-1}. A two-point probe setup (AGILENT 4284A) was used to measure the electronic conductivity of the synthesized samples at a bias voltage of 1.0 V and in the frequency range of 20 Hz-1MHz. The electronic conductivity (σ) is calculated by using following equation

$$\sigma = \frac{1}{R}\left(\frac{L}{A}\right)$$

where, R is the resistance of the sample (**Ω)**, L and A is thickness (cm) and cross-sectional area (cm^2) of the pellets respectively. For electrochemical studies, electrodes were prepared by preparing slurries of the active material, conductive carbon and binder (PVDF) with a weight ratio of 70:15:15 in N-methyl-2-pyrrolidinone (NM2P) as a solvent. The resulting slurry was then coated on Al foil using "doctor blade" technique. The coating was dried in a vacuum oven for overnight to evaporate the solvent. The electrodes were then punched and dried under vacuum at 60 ºC and finally brought inside the glove box Mbraun make (O_2 and H_2O level below 0.5 ppm). The coin cells (CR2032) were assembled for electrochemical testing of the synthesized samples. A microporous polypropylene sheet (Celgard 2400) was used as a separator and the electrolyte used was 1 M $LiPF_6$ in EC: DMC 1:1 v/v. High purity Li chips were used as both counter and reference electrode. The galvanostatic charge/discharge (GCD) performance test was performed at 0.1C-rate. All the electrochemical tests were performed using EZstat-pro Nuvant systems Inc. (U.S.A) cell test system at 298 K (RT).

Results and discussion

Structural and Morphological Analysis

The XRD patterns of the as-synthesized samples with different ZnO amount are shown in **Fig. 1**. From XRD patterns, it is found that all the diffraction peaks can be well indexed to orthorhombic phase with *Pnma* space group of olivine-$LiFePO_4$. The sharp peaks for all the synthesized samples indicate that the samples are well crystalline in nature. No impurity phase like $LiZnPO_4$ has been detected in the synthesized samples. The unit cell parameters and unit cell volume of all the synthesized samples are listed in **Table 1**.

Copyright © 2016 VBRI Press

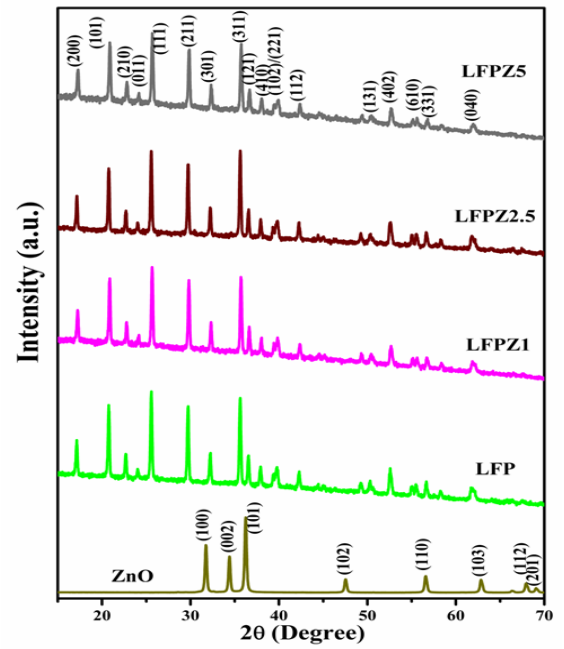


Fig. 1. XRD patterns of the LFP-ZnO synthesized samples.

From **Table 1**, it can be seen that for ZnO-coated samples, unit cell parameters, and unit cell volume increases as compared to the pristine LFP. The increase in cell size from 289.426 to 290.977 $(Å)^3$ is mainly due to a slight increase in lattice parameter *b* and *c* whereas *a* decrease slightly. It has been reported previously that introduction of Zn into $LiFePO_4$ lattice introduce some kind of "pillar effect" which provides more space for lithium ion movement and consequently, the conductivity of $LiFePO_4$ is enhanced and so its lithium ion diffusion coefficient [**13, 16**]. The increase in unit cell size, thus offer more space for lithium ion movement and consequently improved electrochemical properties.

Table 1. Results of the lattice parameters for LFP-ZnO synthesized samples. All distance and lattice parameters units are in Å (10-10 m).

Sample	a (Å)	b (Å)	c (Å)	V $(Å)^3$
LFP	10.307	5.995	4.684	289.426
LFPZ1	10.315	6.001	4.690	290.312
LFPZ2.5	10.312	5.999	4.689	290.069
LFPZ5	10.297	6.015	4.698	290.977

Fig. 2(a-e) shows the effect of a surface coating by ZnO on the morphology of the synthesized samples. It can be seen from **Fig. 2(a)** that the grains in the pristine $LiFePO_4$ sample are highly agglomerated possess nearly spherical morphology and are micrometer in size (~ 1 μm). **Fig. 2(b-d)** shows that ZnO coated samples are found to have grains with a smaller size (~500-700 nm) and are also uniformly distributed. Therefore, the concentration of alien dopant plays a crucial role in controlling the morphology of synthesized samples. **Fig. 2(e)** shows the SEM micrograph of ZnO nanoparticles. The size of ZnO nanoparticles lies between 50-100 nm and are homogeneously distributed.

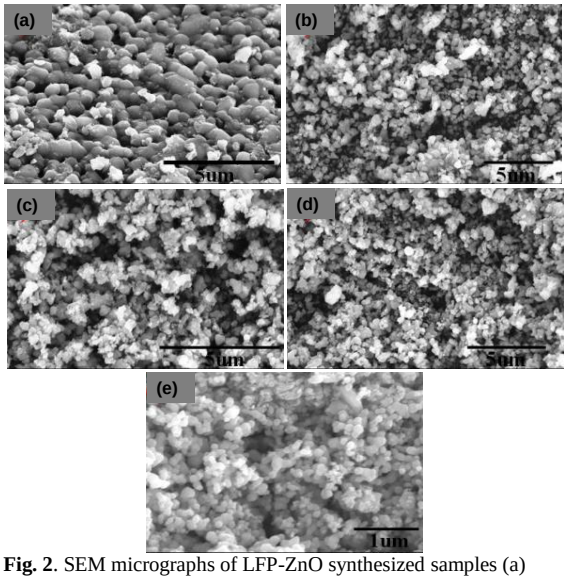


Fig. 2. SEM micrographs of LFP-ZnO synthesized samples (a) LFP; (b) LFPZ1; (c) LFPZ2.5; (d) LFPZ5; (e) ZnO.

FTIR study- Cation environment

The motion of cations with respect to the oxygen atom is generally assigned by vibrational modes which are much sensitive to the point group symmetry of the cations in the oxygen host matrix [**17**]. Therefore, the cations local environment in a crystal lattice of close-packed oxygen atoms can be analyzed using FTIR spectroscopy. It has been reported previously that alkali metal cations in their octahedral interstices (LiO_6) present in inorganic oxides have their resonant frequencies present in the frequency range of 200-400 cm^{-1}. The effect of ZnO coating on the vibrational spectrum of the LFP is investigated by FTIR and results are shown in **Fig. 3**.

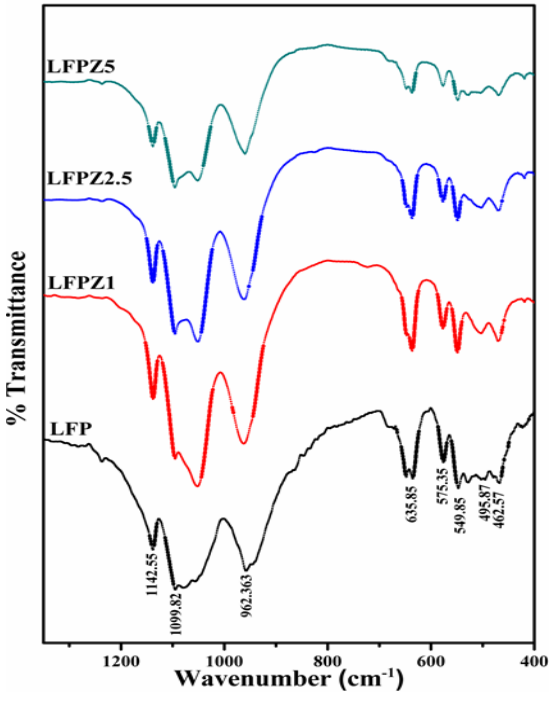


Fig. 3. FTIR spectrum of LFP-ZnO samples in a range of 400-1500 cm^{-1}.

Copyright © 2016 VBRI Press

The peaks of FTIR spectrum located from 463-1139 cm^{-1} may be attributed to the bending and stretching vibration of the tetrahedral (PO_4^{3-}) ion. The tetrahedral unit, (PO_4^{3-}) ion has its fundamental vibrational frequencies at 1082, 515, 980 and 363cm^{-1} [**17**]. Small peak around 420cm^{-1} corresponds to the stretching E2 (LO) mode of ZnO wurtzite structure as reported by Husain et al. [**18**]. Therefore, FTIR spectra reveal the presence of ZnO over LFP particles surface.

Electronic conductivity measurements

The conductivity (AC) of pristine LFP is found to be of the order 10^{-9} S cm^{-1}, which is in good agreement with the previous reports [**9**]. **Fig. 4** reveals the AC electrical resistance measurement for all the synthesized samples in the frequency range of 20 Hz-1MHz. The intercept at Z'-axis gives the AC resistance of the material.

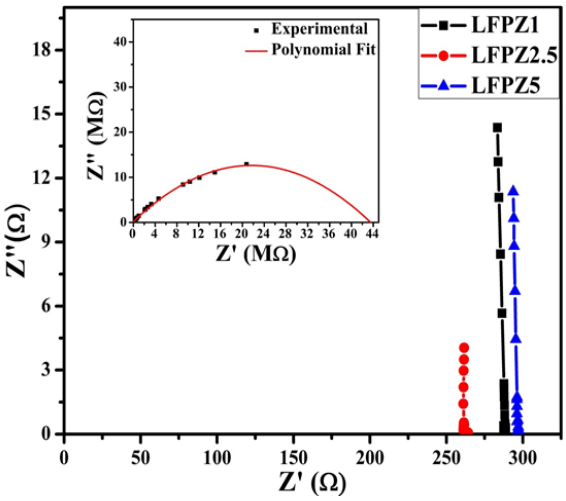


Fig. 4. AC Conductivity measurements of ZnO-coated synthesized samples in a frequency range of 20 Hz-1MHz.

From **Table 2**, it is evident that AC resistance measurement shows the pure conducting nature of ZnO-coated LFP samples. An increase of 10^5 in electronic conductivity has been obtained by coated samples. The tremendous increase in ZnO-coated LFP samples could be attributed to the presence of dangling bonds in ZnO, as zinc oxide quickly adsorb O^{2-} and O^- ions on its surface which consequently alter the surface energy and hence, the surface potential of active particle i.e. LFP [**19**].

Table 2. Parameters for the conductivity of LFP-ZnO synthesized samples.

Sample	$R_{A.C}$ (Ω)	$\sigma_{A.C}$ (S cm^{-1})
LFP	$43x10^6$	$4.95x10^{-9}$
LFPZ1	288	$7.98x10^{-4}$
LFPZ2.5	261	$8.22x10^{-4}$
LFPZ5	296	$7.17x10^{-4}$

Electrochemical performance of ZnO-coated LFP samples

Table 3 shows the initial galvanostatic charge/discharge curves of cells at 0.1C (1C = 170$mAhg^{-1}$) has been performed for the bare LFP and of all ZnO-LFP samples in the potential range of 2.0-4.4 V vs. Li^+/Li at room temperature. It is found that the discharge capacity of pristine $LiFePO_4$ is greatly enhanced by ZnO coating. Among all the synthesized samples LFPZ2.5 shows highest specific discharge capacity 160 (±5) $mAhg^{-1}$ (~94 % of theoretical capacity 170 $mAhg^{-1}$) because of its highest electronic conductivity. The discharge capacities of all samples for 0, 1.0, 2.5 and 5.0 wt % of ZnO amount are observed as 85 (±5), 128 (±5), 160 (±5) and 120 (±5) $mAhg^{-1}$, respectively. These results are fairly improved than previous studies [**13, 14, 20**]. The potential difference between charge and discharge plateaus for all the samples are shown in Table 3. It can be observed that the potential difference (ΔV) improved effectively with ZnO-coating. In other words, polarization potential reduces for ZnO-coated samples, indicating that reaction kinetics in $LiFePO_4$ have enhanced.

Hence, ZnO-coating over LFP surface effectively enhance the conductivity of pristine LFP and shows better electrochemical results as compared to pristine LFP.

Table 3. Galvanostatic Charge/Discharge parameters and Discharge capacity values of 1st charge/discharge cycle at 0.1C for LFP and ZnO-coated LFP samples.

Samples	Charge plateau Voltage (V)	Discharge plateau Voltage (V)	ΔV (V)	Discharge Capacity (mAh/g) (±5)
LFP	3.495	3.394	0.101	85
LFPZ1	3.469	3.395	0.074	128
LFPZ2.5	3.467	3.397	0.070	160
LFPZ5	3.496	3.379	0.117	120

Conclusion

The pristine $LiFePO_4$ and ZnO-coated $LiFePO_4$ samples were successfully synthesized using sol-gel assisted ball-milling method. XRD patterns reveal that all the synthesized samples are well crystalline and have orthorhombic lattice structure with *Pnma* space group. SEM images disclose the formation of nearly spherical shaped nano-sized particles. FTIR studies show the presence of vibrational modes corresponding to $(PO_4)^{3-}$ tetrahedral and stretching E2 (LO) mode of ZnO wurtzite structure. LFPZ2.5 shows the lowest resistance and, therefore, highest electrical conductivity which proves that it will possess best electrochemical kinetic properties among all the prepared samples. Galvanostatic charge/discharge curves confirm that LFPZ2.5 gives the highest discharge capacity at 0.1C rate.

Acknowledgements

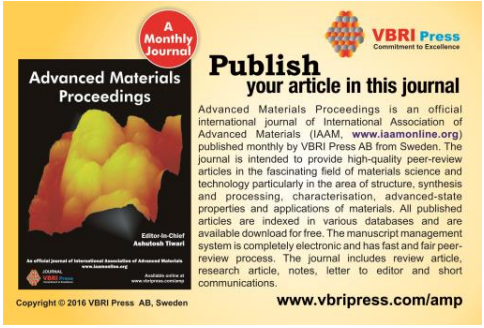
Authors are thankful to SERB and FIST, Department of Science and Technology (DST), New Delhi for financial support to carry

Copyright © 2016 VBRI Press

out this work under the project grants Nos.: SR/FTP/PS-039/2011 and SR/FST/PSI-164/2011(C), respectively.

References

1. A.K. Padhi, K.S. Nanjundaswamy, J.B. Goodenough; *J. Electrochem. Soc.* **1997**, *144*, 1188-1194.
2. Yi-Ju Lv, Jing Su, Yun-Fei Long, Xiao-Ru Cui, Xiao-Yan Lv, Yan-Xuan Wen; *Powder Technol.* **2014**, *253*, 467-473.
3. Guohui Qin, Qianqian Ma, Chengyang Wang; *Electrochim. Acta* **2014**, *115*, 407-415.
4. Xiaoting Lin, Kaiqiang Wu, Lianyi Shao, Miao Shui, Dongjie Wang, Nengbing Long, Yuanlong Ren, Jie Shu; *J. Electroanal. Chem.* **2014**, *726*, 71-76.
5. B. Scrosati, Low voltage lithium-ion cells (chapter 10), Advances in Lithium-Ion Batteries, Walter A. Van Schalkwijk and Bruno Scrosati, ebook.
6. Jin Chong, Shidi Xun, Xiangyun Song, Paul Ridgway, Gao Liu, Vincent S. Battaglia; *J. Power Sources* **2012,** *200*, 67-76.
7. Xujiao Yang, Zhendong Hu, Jun Liang; *Ceram. Int.* **2015**, *41*, 2863-2868.
8. G.X. Wang, S. Bewlay, J. Yao, J.H. Ahn, S.X. Dou, H.K. Liu; *Electrochem. Solid-State Lett.* **2004**, *7 (12)*, A503-A506.
9. Zhipeng Ma, Youshun Peng, Guiling Wang, Yuqian Fan, Jianjun Song, Tingting Liu, Xiujuan Qin; *Electrochim. Acta* **2015**, *156*, 77-85.
10. Yan Cui, Xiaoli Zhao, Ruisong Guo; *J. Alloys Compd*. **2010**, *490*, 236-240.
11. Jing Hu, Zaimin Tian; *Ceram. Int.* **2015**, *41*, 3927-3931.
12. Chun-Chen Yang, Jer Huan Jang, Jia-Rong Jiang; *Appl. Energy* **2016**, *162*, 1419-1427.
13. Yemin Hu, Jun Yao, Zhe Zhao, Mingyuan Zhu, Ying Li, Hongming Jin, Huijun Zhao, Jiazhao Wang; *Mater. Chem. Phys.* **2013**, *141*, 835-841.
14. Yan Cui, Xiaoli Zhao, Ruisong Guo; *Mater. Res. Bull.* **2010**, *45*, 844-849.
15. Hao TANG, Long TAN, Jun Xu; *Trans. Nonferrous Met. Soc. China* **2013**, *23*, 451-455.
16. Atef Y. Shenouda, Hua K. Liu; *J. Alloys Compd.* **2009**, *477*, 498-503.
17. N. Jayaprakash, N. Kalaiselvi; *Electrochem. Commun.* **2007**, *9*, 620-628.
18. Sajid Husain, F. Rahman, Nasir Ali, P. A. Alvi; *Journal of Optoelectronics Engineering* **2013**, Vol. 1, No. 1, 28-32.
19. Rakesh Saroha, A. K. Panwar; *Adv. Sci. Lett.* **2015**, *21*, 2750-2754.
20. Jungbae Lee, Purushottam Kumar, Jinhyung Lee, Brij M. Moudgil, Rajiv K. Singh; *J. Alloys Compd.* **2013**, *550*, 536-544.



Fibers and Polymers 2016, Vol.17, No.8, 1206-1216
DOI 10.1007/s12221-016-6345-7

ISSN 1229-9197 (print version)
ISSN 1875-0052 (electronic version)

Electrospun Sericin/PVA/Clay Nanofibrous Mats for Antimicrobial Air Filtration Mask

Roli Purwar*, K. Sai Goutham, and Chandra Mohan Srivastava

Department of Applied Chemistry and Polymer Technology, Delhi Technological University, Delhi 110042, India
(Received March 17, 2016; Revised June 19, 2016; Accepted June 23, 2016)

Abstract: In this study, Sericin/Poly Vinyl Alcohol (PVA)/Clay (Cloisite 30B) nanofibrous mats are prepared by electro-spinning technique for antimicrobial air filtration mask. The process parameters of electro-spinning machine such as acceleration voltage, nozzle flow rate and nozzle & collector distance are optimised on the basis of morphology of fibre observed through scanning electron microscopy (SEM). The optimum conditions for producing nanofibrous mat without bead are acceleration voltage 27.5 kV, nozzle collector distance 8 cm and flow rate 0.8 m*l*/hr using 10 % (w/v) solution of Sericin/PVA (1:1 wt/wt). The process parameters of electro-spinning machine for the processing of Sericin/PVA/Clay nanofibrous mats with varied clay concentrations ranging from 0.1-0.75 % are also optimized. The spun fibre diameter varied from 300-400 nm at different specified conditions. These nanofibrous mats are characterized for its structural, mechanical and antimicrobial properties. Respirable Suspended Particulate Matter (RSPM) test was conducted to check the particulate matter (PM 2.5) absorption capacity of nanofibrous mats. Results shows that sericin/PVA/clay nanofibrous mat would be a promising material for making protecting clothing based air filtration mask.

Keywords: Sericin, Poly vinyl alcohol, Clay, Nanofibers, Electrospinning

Introduction

Air borne particulate matter is one of India's most sever air pollution problem. Particulate matter is the term used to describe particles that are suspended in the air. Size of the particulate matter is the main determinant of the behaviour of atmospheric particles. Small particles less than 10 μm known as PM10 and fine particles with diameter not larger than 2.5 μm are inhable or breathable particles also known as Respirable Suspended Particulate Matter (RSPM). Studies indicate that particulate matter (coarse and fine) may induce sever effect on public health [1-3]. The major anthropogenic sources of particulate matter are re-suspension of industrial dust and soil, suspension of soil (farming, mining, unpaved roads), combustion of oil, coal wood and diesel exhaust particulates. In urban area of India about 50 % of the particulate matter is estimated to be from traffic generated emissions. The average concentration of particulate matter in various cities like Delhi, Patna, Gwalior and Raipur are 153, 149, 144, 134 mg/m^3, respectively which makes these cities figure in the top five list of most polluted cities of world [4]. These particulate matters are also carrier of microorganism such as bacteria, fungi and virus. It is found that microorganism along with particulate matter aggravate respiratory allergy and other pulmonary diseases [5].

Fibrous filters masks are simple and economical to remove sub micrometer particles efficiently from air stream. Nonwoven protective filter mask have been widely used to protect the human from inhaling the particulate matter [6-9]. Nonwoven filter media made through needle punched technique are composed of randomly fibers with sub micron to micron size diameter [9]. It is observed they are not able to remove particles lower than 0.5 μm such as virus, bacteria and smog, etc because the size of the pore formed with micron scale fibers is considerably large. Nanofibers with diameters in the sub micron range are known to provide filtration efficiency superior to non-woven filter media with larger, micron scale fibers. High efficient particulate air (HEPA) filters show an ability of extreme filtration efficiency, filtering out 99.97 % of particles greater than or equal to 0.3 μm in diameter. In comparison nylon 6 nanofibrous filter media made of 80-200 nm were found to be superior to that of commercial HEPA filters [15].

Electrospun nanofibrous mats have shown promising filter media for fine particles [10-12]. Controllable fiber diameter, remarkable specific surface area, highly open porosity and interconnected porous structure make them suitable for highly efficient filtration medium. Both physical and chemical properties of nanofibrous filter media are important to improving filtration performance. Various polymers blends and functionalized nanofibers such as polyacrylonitrile/polyacrylic acid, [15] chitosan/polycaprolactone [13], polyacrylonitrile/silica [12], polyamide 6/boehmite [16], cellulose coated with PAN nanofiber [17] have been prepared and shown high efficiency with respect to commercialize nonwoven textile filters. Nanofibrous membranes with pore size of 0.45 μm selectively remove bacteria. Recently, antimicrobial electrospun air filtration membranes from polylactic acid/polyhrdoxybutyrate functionalized with ammonium based ionic liquid [18], Polymer incorporated plant extract *Sophora flavesence* [19], Polylactic acid/titania [20] have shown high filtration efficiency along with good antimicrobial activity.

*Corresponding author: roli.purwar@dce.edu

There is intense research has been carried out in the area of polymer/layered silicate nanocomposite films and fibers [21,22]. The layered silicates filled polymer nanocomposites films and fibers exhibit enhanced mechanical, thermal, barrier and other physiochemical properties at low filler content [23,24]. Recent studies show that layered silicates modified with quaternary ammonium compound show excellent antimicrobial properties [25,26]. Such modified clay when incorporated into polymer matrix, the polymer/clay nanocomposites also show good antimicrobial property [26]. Commercial nanoclay Cloisite 30B, a quaternary ammonium modified montmorrilonite showed excellent antimicrobial activity against wide range of Gram positive and Gram negative bacteria [25-30]. Nanocomposite films of biodegradable polymers such as PLA/Cloisite 30B [27], Whey/Cloisite 30B [28,29] and Gelideum/Cloisite 30B [30], showed very good antimicrobial activity with barrier mechanism.

Sericin, a waste product of silk processing industries, is a promising biomaterial containing many hydrophilic amides, which gives it high hydrophilicity and sensitivity of chemical modification [31]. Polyvinyl alcohol (PVA) is synthetic, hot water soluble nontoxic, biodegradable polymer which can be easily blended with sericin [32-35]. Sericin/PVA blend films show application in the field of alcohol degradation by pervoration [32], wound dressing [33,34] and packaging [35]. In our previous study we have prepared Sericin/PVA blend film with 1:1 wt/wt ratio and its mechanical properties were enhanced by incorporating nanoclay [35]. Sericin/PVA nanofibers have been prepared by the several researchers [36-39]. Recently Sericin/β-cyclodextrin/PVA composite electrospun nanofibers are prepared as adsorbent for removal of methylnen blue dye [40]. Sericin/PVA nanofibers with wt./wt. ratio 1:3 has been prepared and used for tissue engineering applications [37].

So far, Sericin/PVA nanofibrous mats have not been exploited for making air filtration mask applications. The incorporation of nanoclay with antimicrobial properties in sericin/PVA blended nanofibers has also been not reported. For this study cloisite 30B, quaternary ammonium modified clay has been chosen. The addition of cloisite 30B will enhance the mechanical and antimicrobial properties of sericin/PVA nanofibers mats. Sericin/PVA/clay nanofobrous mat would be able to filter aerosols ($PM_{2.5}$ and PM_{10}) and bioaerosols (virus, fungi, bacteria). It also inhibits the growth of microorganism such as bacteria. In the present study an attempt has been made to develop sericin/PVA/clay nanofibrous mats for air filtration mask using electrospinning. The process parameters of electrospinning machine are optimized on the basis of morphology of the fibers. Amount of nanoclay is optimized on the basis of antimicrobial properties and dust accumulation efficiency. The sericin/PVA/clay nanofibrous mats are characterized.

Experimental

Materials

Bombyx mori silk cocoons were procured from Central Silk Research Board, Lucknow India. PVA (MW 14000) was purchased from Central Drug House Pvt Ltd. and Cloisite 30B was purchased from Southern Clay, USA. Distilled water was used for all the experiments.

Methods

Preparation of Sericin and Spinning Dope

The silk cocoons were cut into small piece and Sericin was extracted using high temperature high pressure degumming technique [35]. Briefly aqueous extraction of Sericin was carried out by boiling cut cocoons in autoclave at 120 ^{o}C for 1 hour keeping material to liquor ratio 1:15. The Sericin extracted aqueous solution then filtered with muslin cloth to remove fibroin and other suspended impurities. Solid Sericin (above MW 250 kDa) was obtained by heating Sericin solution at 40 ^{o}C. The dope solution was prepared in distilled water by dissolving equal weight (10 % wt/wt) of Sericin and PVA at 80 ^{o}C. The dope solution for Sericin/PVA/Clay was prepared by adding different clay concentrations ranging from 0.1-0.75 % (% of polymer) and subjected to ultrasonication.

The conductivity of the different dope solution was measured by Conductivity Meter (Decibel Scientific Industries). It was found that Cloisite 30B solution, Sericin/PVA solution and Sericin/PVA/Clay solution had the conductivity of 0.044, 1.010 and 1.056 m mho respectively.

Electrospinning

The nanofibrous mats were prepared using electrospinning machine Royal Electro spinner, India equipped with collector plate. The collector was covered with nylon net fabric to collect Sericin/PVA/clay nanofibrous mat. The process parameters for electro spinning machine were varied as acceleration voltage 18-28 kV, spinning distance 3-12 cm and flow rate 0.8-1.2 m*l*/hr.

Scanning Electron Microscopy

The morphology of Sericin/PVA nanofibrous mats and Sericin/PVA/Clay nanofibrous mats was examined using scanning electron microscope (Hitachi S-3700N SEM, Germany) at a voltage of 15 kV. Surface of the samples were coated with gold before analysis.

Energy Dispersive X-ray Spectroscopy

The elemental analysis of Sericin/PVA/Clay nanofibrous mats was carried out using energy dispersive X-ray spectroscopy (4486c-1UUS-SN, USA) at a voltage of 15 kV.

X-ray Diffraction

The exfoliation or intercalation of clay in Sericin/PVA/Clay nanofibers was examined using X-ray diffraction (D8 Advance, BRUKER) with 2θ varying from 0 to 10 degree.

Antimicrobial Test

The antimicrobial activity of Sericin/PVA/Clay nanofibrous

mats was investigated by agar diffusion assay (AATCC 30) against Gram positive *S.aureus* and Gram negative *E.coli* [41]. The nanofibrous mats were cut in the form of a circular disc of diameter 6 mm and sterilized under UV light in a laminar air flow for 24 h. The sterile samples were placed on agar plates which had been cultured with *S. aureus* and *E.coli* and pressed lightly to ensure close contact with the surface. Plates were incubated at 37 ^{o}C for 24 hours in an incubator. After incubation, the samples were placed in a 50 m*l* sterilized flask containing 10 m*l* sterilised distilled water. The flask was shaken for 1 h at 150 rpm to release the bacteria from the samples. Serial dilutions of inoculants (up to 10^{-5} time) was made in the sterilized water. The diluted inoculants were spread on an agar plate and the plates were incubated at 37 ^{o}C for 24 hours. After incubation, the bacterial colonies were counted. The antimicrobial activity was calculated using equation

$$\text{Anti bacterial activity (\%)} = (A - B)/A \times 100$$

where, A: the number of colonies in the control sample
B: number of colony in treated sample.

Burst Strength

The burst strength of Sericin/PVA/Clay nanofibrous mats was determined using burst strength tester (ENKAY DIGIMIX-109, Enkay Enterprise) in accordance with ASTM F 2054 with a circular sample of 44 mm diameter.

RSPM Test

The filtration efficiency of Sericin/PVA/Clay nanofibrous mats was carried out using Environmental Particle Air Monitor (EPAM-5000, HAZ-DUST, USA) at a flow rate of 4 *l*/min and a sample rate of 1 second for 6 hours. Sample rate is defined as the frequency of collection of a certain volume of air by the sample. In this test the particle size of 1 μm, 2.5 μm, 10 μm present in the volume ambient air were to be passed through the sample. The RSPM test would result in the determination of the filtration efficiency of the sample that is being subjected to test. This is expressed as the concentration of particulate matter collected in mg/m^3. The test was conducted at actual ambient condition of Delhi by placing the machine at road side of university campus.

Results and Discussion

Sericin solutions are electrospun in water may be because of complexion between water and amino group along the sericin chain, resulting in decreasing the rigid interaction among sericin molecules and enhancing the electrospinnability of sericin [36]. The preparation of PVA nanofibres from aqueous solution is well documented [42]. Eslah *et al.* [37] have reported that the electrospinning of aqueous solution of PVA/Sericin (80:20 wt/wt ration) is not possible due to fast gelation of polymer blend. Therefore, they have carried out electrospinning of PVA/Sericin solution prepared in DMSO/ Water/Urea.

In this study, we have successfully produced Sercin/PVA (50:50 wt/wt ratio) nanofibrous mat from aqueous solution. The process parameters were optimised in the term of nozzle flow rate, nozzle and collector plate distance, and acceleration voltage. Sericin/PVA/Clay nanofibrous mats of different clay concentrations were electrospun at optimized machine parameter, except nozzle collector plate distance. The morphology and structural properties of nanofibers were characterized through SEM and XRD, respectively. The effectiveness of these Sericin/PVA/Clay nanofibrous mats as air filters mask was evaluated by subjecting them to antimicrobial test, burst strength test and RSPM test. The studied observation and results are discussed below.

Preparation of Sericin/PVA and Sericin/PVA/clay Nanofibers Mats

In order to prepare Sericin/PVA electro spun nanofibers in optimum conditions, the effect of variable parameters including nozzle flow rate, voltage and nozzle and collector plate distance were varied and results are discussed as follows.

Effect of Nozzle Flow Rate

Very low and high flow rate are not preferable to produce very thin nanofibers. Too high flow rates did not produced fibers because the polymer solution was pushed out of the syringe so fast that it did not have time to evaporation. Since the long time needed to eject the solution, very low flow rate was also not choosen [39]. The effect of flow rate on the

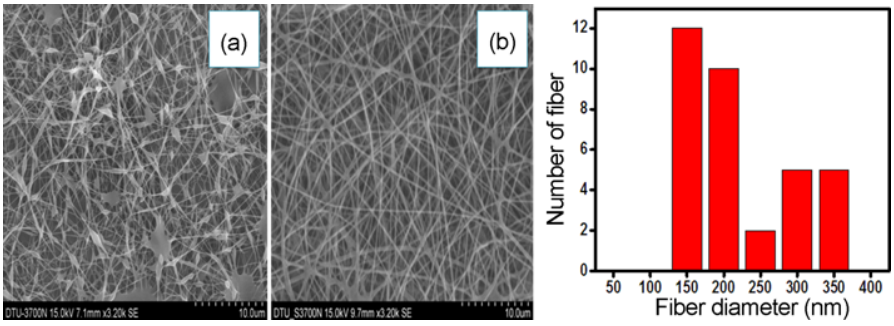


Figure 1. SEM images of sericin/PVA nanofibrous mats obtained at different flow rate; (a) 1.2 m*l*/h and (b) 0.8 m*l*/h.

morphology, the Sericin/PVA solution was electro spun at two different flow rates (0.8 m*l*/h and 1.2 m*l*/h). The SEM images of Sericin/PVA (1:1 wt/wt) at constant voltage 27.5 kV, nozzle and collector distance 8 cm and flow rate of 0.8 m*l*/h and 1.2 m*l*/h are shown in Figure 1. It was observed that the diameter of nano-fibres at flow rate 1.2 m*l*/h is finer than at 0.8 m*l*/h but the bead formation is higher. The average diameter of nanofibres obtained at 0.8 m*l*/h is 222 nm. The nanofibers formed at flow rate 0.8 m*l*/h had negligible bead formation compared to 1.2 m*l*/h because the fibre deposited on the aluminium foil would have time to settle down before the subsequent ejection of the next jet. As the flow rate increases the time gap to settle would reduce resulting in bead formation. However, Zhang *et al.* [39] have prepared sericin nanofibers from a silk hope cocoon and that continuous and fine sericin nanofibers can be produced even at low flow rate. The morphology of deposited sericin did not depend on the flow rate of sericin solution. It is also observed that the increase in flow rate increased the average diameter of electrospun fibers. For further studies, flow rate of 0.8 m*l*/h has been chosen as we obtained bead less fiber at this rate.

Effect of Nozzle and Collector Plate Distance

The working distance between the nozzle and collector plate varies the path length and solvent evaporation, so it greatly influences the mean diameter and uniformity of the fibers [39]. To study the effect of nozzle and collector plate

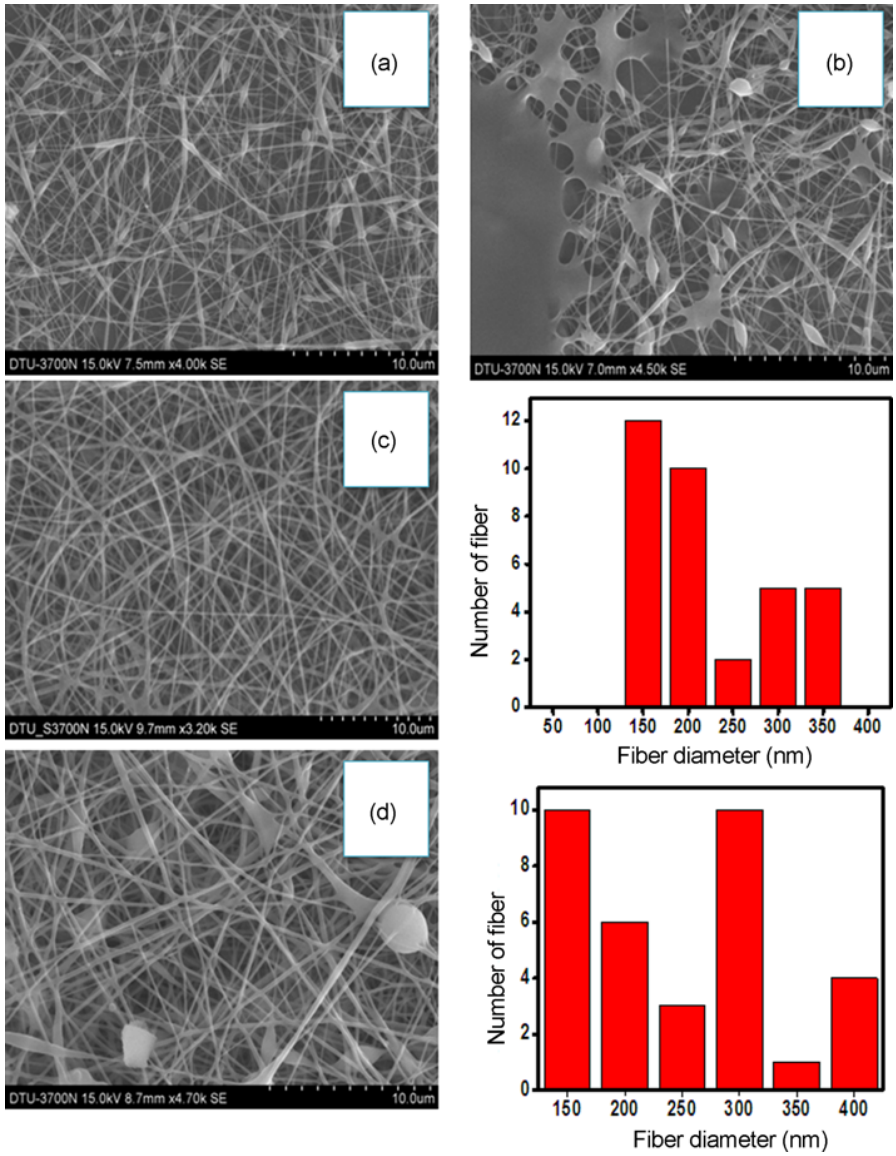


Figure 2. SEM images of sericin/PVA nanofibrous mats obtained at different collection distance; (a) 3 cm, (b) 6 cm, (c) 8 cm, and (d) 10 cm.

distance, the sericin/PVA solution was electrospun at different collection distance in the range of 3-10 cm under constant voltage 27.5 kV and flow rate 0.8 m*l*/h. The fiber morphology and diameter obtained at different collection distance are shown in Figure 2. At collection plate distance of 3 cm, large number of bead formed and there is no fibrous structure observed. With increase in plate distance from 3 cm to 6 cm, comparatively less number of are beads observed. However, smooth nanofibrous structure is not appeared. The fine and smooth surface with negligible bead is observed at collection distance of 8 cm (Figure 2(c)). Further increase in collection plate distance increases the fiber diameter and few beads appeared (Figure 2(d)). The presence of bead at collection distance of 3 cm and 6 cm, may be due to reduction in flight time which may cause incomplete drying of the jet prior to the deposition on the collection plate. At a short distance, the path trajectory of the jet is also short, which could lead to uneven stretching [39]. Further, increase in the collection distance of 8 cm resulted in the formation of smooth fibers of average diameter of 215 nm indicating that the jet is stretched enough prior to the deposition on the collector. Further, the diameter of nanofibers (248 nm) increased with increase in collection plate distance (Figure 2(d)). Similar results have been obtained for eletrospinning of silk sericin [39]. Increased collection distance caused the electrostatic field strength to decrease. The decreased electrostatic field strength causes both the electrostatic and the Coulombic repulsion forces to decreases. The decreased electrostatic force caused the onset for the bending instability to occur closer to the nozzle tip, resulting in an increase in the total path trajectory of a jet segment, thus the observed increase in the diameter of the as spun fiber mats and bead formation [42]. However, Eslah *et al.* [37] have found that the average nanofibrous diameter decreases with the increase the collection plate distance of 15 cm to 25 cm for PVA/sericin blend solution with 80:20 ratio. Further, increase in collector plate distance from 25 to 30 cm, the average diameter of nanofiber increases. In case of electrospinning of PVA nanofibers, the average fiber diameter decreases from 215 nm to 161 nm with increase in spinning distance from 5 to 15 cm. This may be due the increase in the total path trajectory of the jet that allows uniform stretching of the jet during its flight to the collector [42]. For further study, we have chosen spinning distance/collector distance 8 cm.

Effect of Acceleration Voltage

The SEM images of Sericin/PVA (1:1 wt/wt) nano-fibres prepared at 8 cm distance, 0.8 m*l*/h and varied voltages including 18 kV, 21 kV, 24 kV and 27.5 kV are shown in Figure 3. At 18 kV accelerating voltage nanofibers with large amount of bead are formed. With increase in voltage the nanofibres with few beads or without bead are formed (Figure 3(c), (e), (g)). The average diameter is also shown in Figure 3. The average diameter of nanofiber decreases from 242 nm to 215 nm with increase in voltages. Similar results have been obtained in electrospinning of sericin [36,39]. In case of electrospinning of PVA, the average diameter of nanofibers first decreases with increase in applied electric field and reaches at minimum value, and increase with further increase with applied electrical field [42]. However, in case of sericin/PVA (20:80) blend, average diameter increases with increase in applied voltage [37]. When higher voltages applied, more polymer solution eject from nozzle tip, therefore larger diameter nanofiber is formed. The increase in the applied electrical potential should cause the number of charges carried within a jet segment to increase, hence an increase in both the electrostatic and the Coulombic repulsion forces. The increased Coulombic repulsion force should cause the diameters of the as-spun fibers to decrease (due to increased stretching force exerting on the jet segment), while the increased electrostatic force should cause the diameters of the as-spun fibers to increase (due to both the increase in the speed of the jet segment and the increase in the mass flow rate, the phenomena that cause the onset for the bending instability to occur closer to the screen collector. It is observed that nanofibre at the voltages of 18 kV, had higher bead formation in comparison with other voltages but at the voltage of 27.5 kV the bead formation was negligible. Therefore, 27.5 kV was chosen to produce more suitable nanofibers.

In order to prepare the Sericin/PVA/Clay nanofibrous mats, the dope solutions containing varied amount of clay 0.1 to 0.75 % were electrospun at the optimised process parameters of Sericin/PVA dope solution i.e. acceleration voltage 27.5 kV, nozzle and collector distance 8 cm and flow rate of 0.8 m*l*/hr. The morphology of nanofibrous mat at these parameters showed nanofibers with large number of beads as shown in Figure 4(a)-(d). The bead formation takes place because of the presence of clay in sericin/PVA/clay solution. As clay would enhanced the size and the net weight of the fibres to be collected, resulting the decrease in time for the settlement of the preceding fibre and lead to bead formation. The addition of clay also enhanced the conductivity of the dope solution from 1.01 to 1.05 m mho. In order to obtain a beadless morphology in the presence of clay, the nozzle and collector plate distance was increase from 8 cm to 12 cm.

The results are shown in Figure 4(e)-(h). At the distance 12 cm it was observed that the nanofibers without bead were formed because of the longer distance leading to longer flight time before deposition on collector. Therefore at spinning distance of 12 cm was chosen to produce more suitable fibre. The effect of clay concentration on the fibre size was examined using the SEM images of the nanofibers as shown in Figure 4(e)-(h). The nanofibres that were produced from the solution with clay concentration of 0.1 % were found to be much finer than the fibre from the solution with higher clay concentration because of the greater

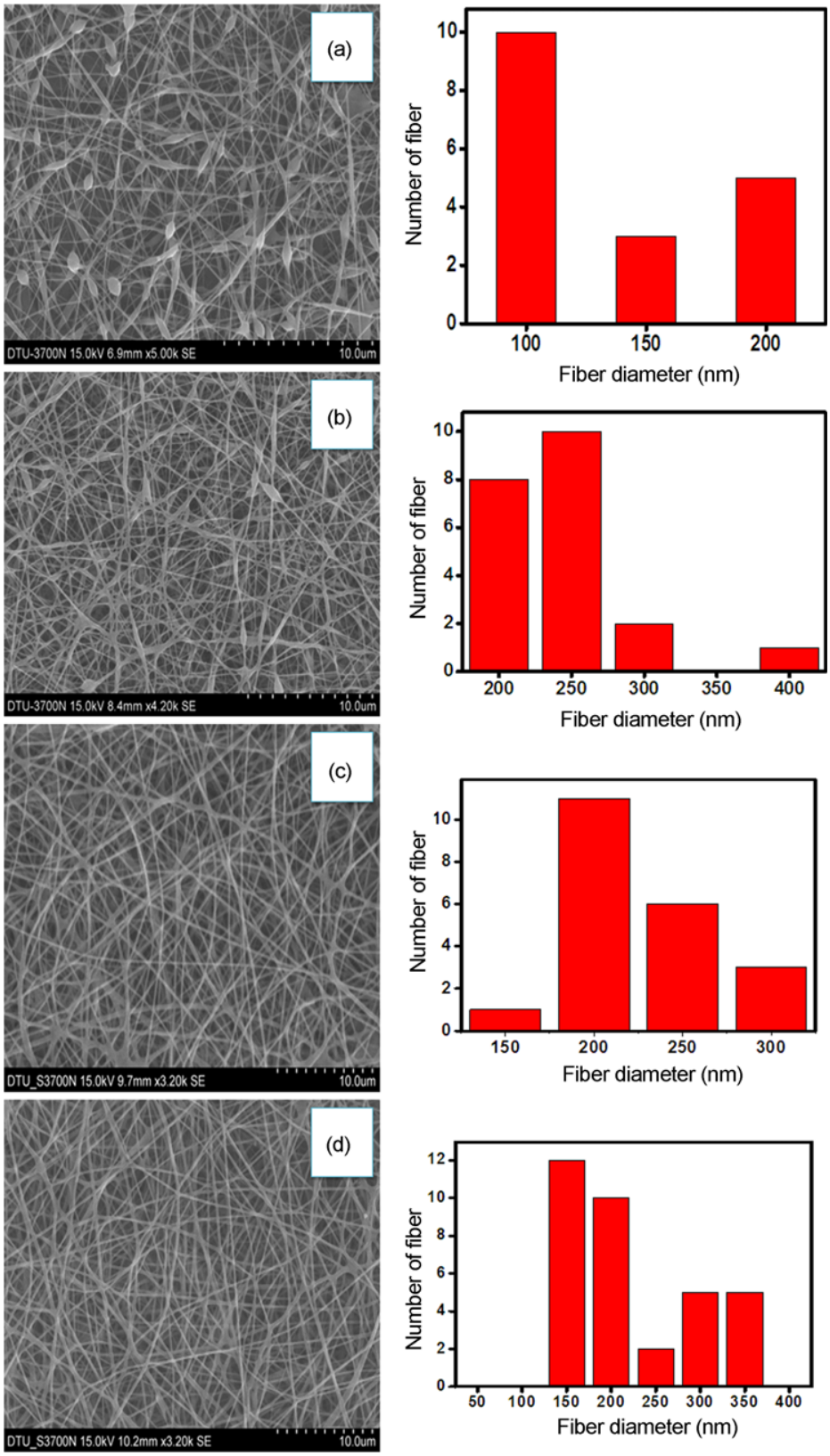


Figure 3. SEM images of sericin/PVA nanofibrous mats obtained at different voltage; (a) 18 kV, (b) 21 kV, (c) 24 kV, and (d) 27.5 kV.

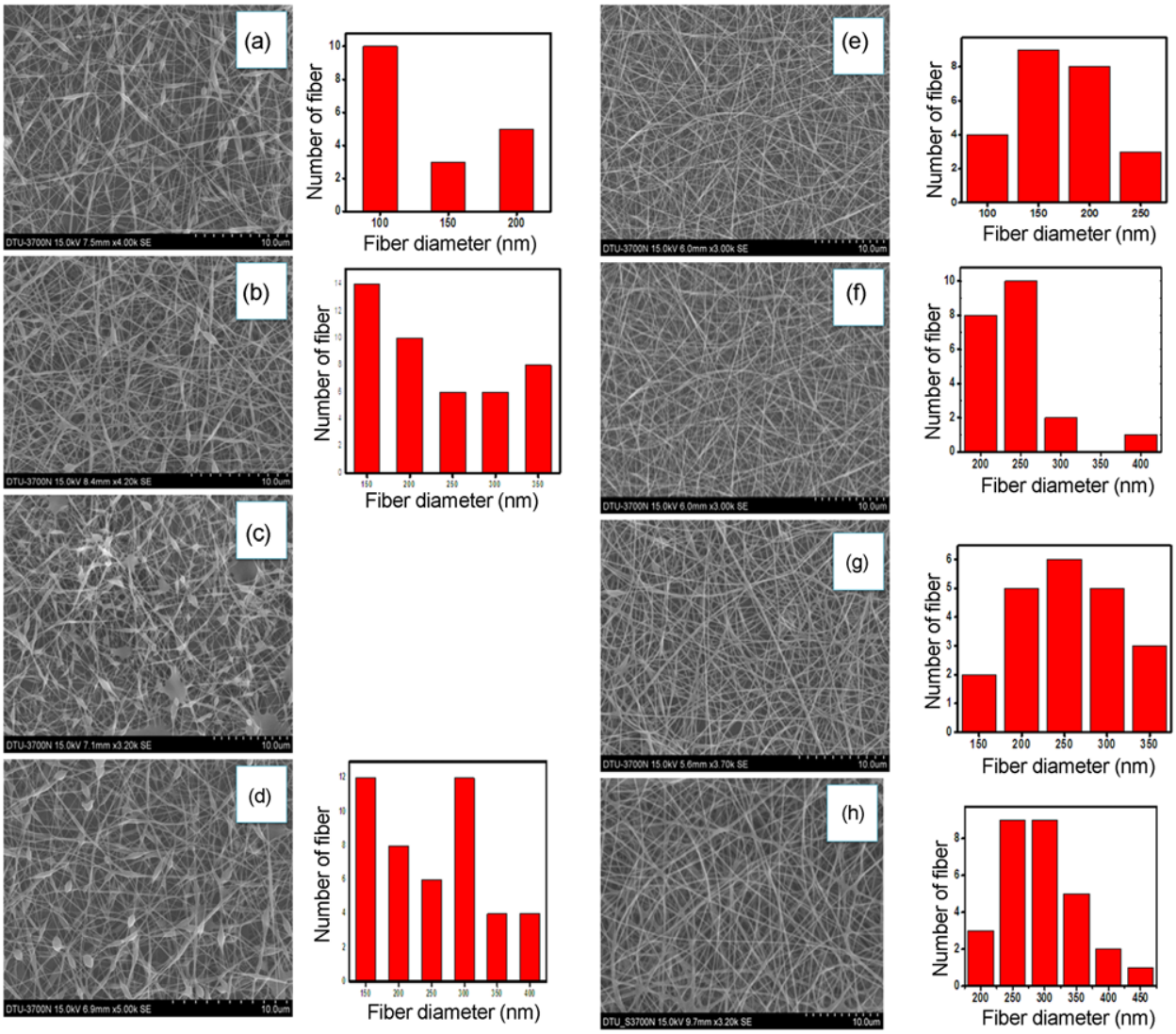


Figure 4. SEM images of sericin/PVA/clay nanofibrous mats at 8 cm; (a) 0.1 % wt/wt, (b) 0.25 % wt/wt, (c) 0.5 % wt/wt, (d) 0.75 % wt/wt and SEM images of sericin/PVA/clay nanofibrous mats at 12 cm; (e) 0.1 % wt/wt, (f) 0.25 % wt/wt, (g) 0.5 % wt/wt, and (h) 0.75 % wt/wt.

amount of clay being dispersed in later solution result in the thickening of the fibre. The average fibre diameter increases from 172 nm to 294 nm with increase in clay concentration from 0.1 % to 0.75 %. Upto 0.75 % clay concentration we were able to electrospun the beadless nanofibres. Further increase in clay concentrations, the nanofibrous mat with very large diameter with beads was formed. Similar results have been obtained for electrospinning of PVA/clay [43], PVA/chitosan/clay [44] solution with varying concentration of clay. The diameter of fibers and formation of beads are strongly influenced by the visco-elasticity of the solution. The addition of clay enhances the viscosity of the sericin/ PVA solution. As a consequence of the increased viscosity, the jet becomes more resistant to the stretching repulsion forces of charge during the electrospinning process. These factors contributed to the increase in diameter of electrospun fibers.

XRD

The spacing between clay platelets or gallery spacing is an indicator of the extent of intercalation/exfoliation of clay platelets within a polymer matrix and can be observed by using XRD (Figure 5). It is well known in a nanoclay-polymer composite unexfoliated or intercalated clay usually has a peak in the range 3-9 ^{o} (2θ). In exfoliated nanocomposites, where single silicate layer (1 nm thick) are homogenously dispersed in the polymer matrix, XRD pattern with no distinct diffraction peak in the range of 3-9 ^{o} (2θ) could be

observed [43,44].

The XRD micrographs of Cloisite 30B and the four samples of sericin/PVA containing varied clay concentrations are shown in Figure 5. The X-ray diffractogram of Cloisite 30B shows a diffraction peak at 2θ=5.2 ° corresponding to basal spacing 1.4 nm between the clay platelets. On comparison of diffractogram of pure Cloisite 30B with the other four samples, it was found that there is no crystalline peak at 2θ equal to 5-6 degrees for Sericin/PVA/Clay nanofibrous mats indicating the exfoliation of clay in the samples. Similar results have been observed by Lee *et al.* [43] in the preparation of PVA/clay nanocomposite nanofibers. In our previous study we have prepared sericin/PVA/clay nanocomposites films by casting methods and found that clay was only intercalated with the matrix [35].

A schematic diagram for proposed mechanism for exfoliation of clay under high electric field is shown in Figure 6. Cloisite 30B contains NH_4^+ ion in its interspace gallery. During electrospinning we have applied high positive charge at nozzle, which gives positive charge to the outer layer of dope solution. The high positive charge repels the cations present in the clay which may lead to breakdown of stacked structure of clay. The high electric field will align the clay platelets. The collector plate having negative charge will attract these clay platelets, which results in exfoliated Sericin/PVA/Clay nanocomposite structure.

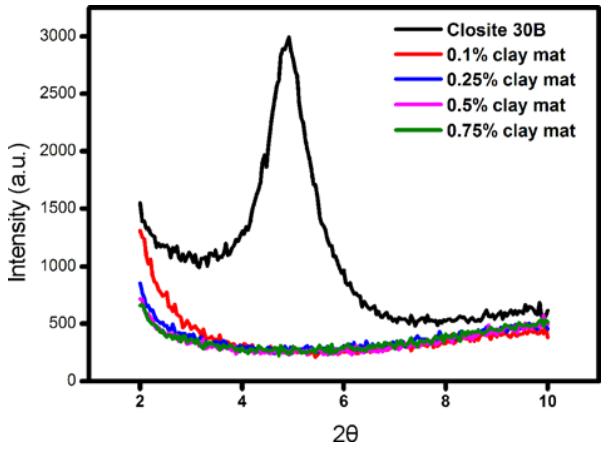


Figure 5. XRD pattern of sericin/PVA/clay nanofibrous mats.

Antimicrobial Activity

The organic clay containing benzyl or alkyl ammonium salt show antimicrobial activity [25]. Quaternary ammonium compounds containing C8-C12 carbon atom show antimicrobial activity against broad spectrum microorganism [43]. The molecular structure of cloisite 30B has single long tail of hydrogenated tallow with quaternary ammonium compound. The minimum inhibitory concentration for cloisite 30B is 0.5 mg/m*l* [44]. Biocides are exchangeable cation in an

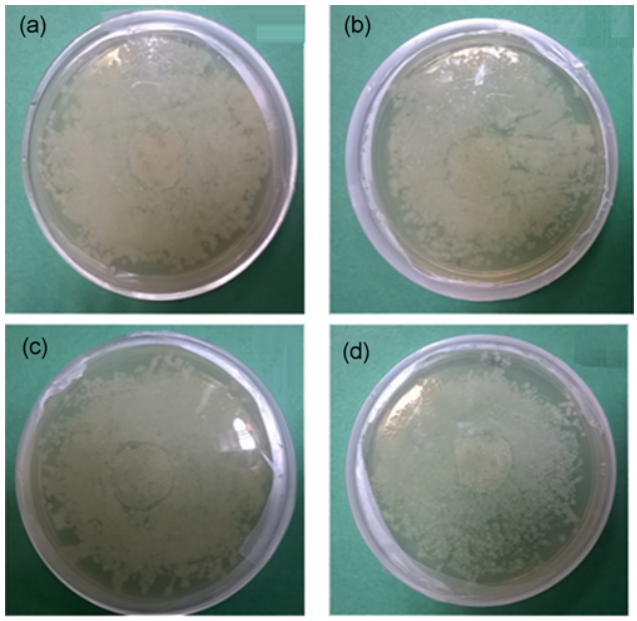


Figure 7. Disc diffusion test for (a) sericin/PVA against *S. aureus,* (b) sericin/PVA/clay (0.75 %) against *S. aureus,* (c) sericin/PVA against *E. coli,* and (d) sericin/PVA/clay (0.75 %) against *E. coli*.

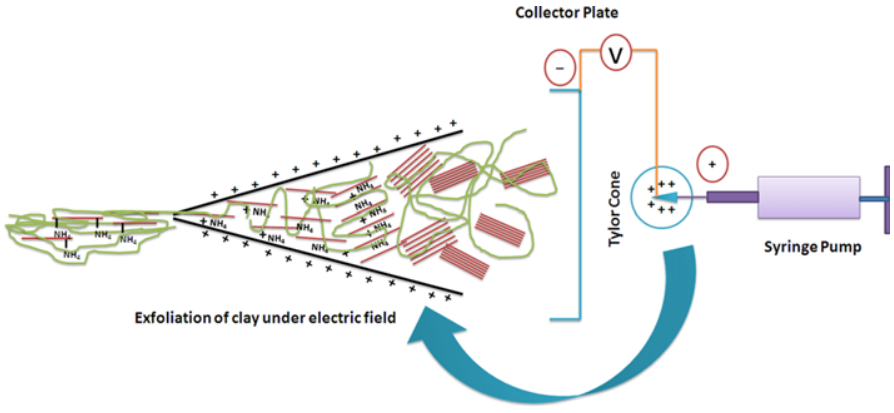


Figure 6. Schematic diagram for exfoliation of clay under high electric field.

Table 1. Antimicrobial activity of sericin/PVA/clay nanofibrous mat

S. no.	Clay concentration (%)	*E. coli*		*S. aureus*	
		CFU/ml $\times 10^5$	Antibacterial activity (%)	CFU/ml $\times 10^5$	Antibacterial activity
1	Control	175	-	200	-
2	0.1	8	95.4	50	75
3	0.25	6	96.6	42	79
4	0.5	4	97.7	9	95.5
5	0.75	3	98.3	6	97

organoclay structure; they can migrate from the clay and thereby affect bacteria as soluble antimicrobial agents.

The antimicrobial activity of the Sericin/PVA/Clay nanofibrous mats with different clay concentrations was examined using representative Gram positive (*S.aureus*) and Gram negative (*E.coli bacterial*) strain. It is observed that there was no zone of inhibition found around the samples (Figure 7). However there was no growth of bacteria observed underneath the samples. This shows that the nanofibrous mats have antmicrobial activity with barrier mechanism. The application of high positive charge on spinneret will give the electrospinning jet a positive charge and which further drive the positive charged clay to core of the fiber. The clay platlets entrapped between the polymer chains. Therefore, migration of clay from nanofibers would be negligible and the antimicrobial activity of sericin/PVA/clay nanofiber is dominating by barrier mechanism. It is observed that there was no zone of inhibition found around the samples (Figure 7). Similar results have been observed for Nylon/Cloisite 30B [45] and starch/Cloisite 30B [46] nanocomposite films. The antimicrobial action of composite films is due to solid by solid surface mode.

The amount of bacteria present on the surface of the nanofibrous mat was calculated using modified agar plate method as described in material and method section. The results are shown in Table 1. All the samples show very good antimicrobial activity against *E. coli*. Higher clay concentration (0.75 %) sample showed excellent antimicrobial activity with both the bacterial strains.

Burst Strength

The burst strength of nanofibrous mats plays a prominent role when they are used for the applications. The burst strength of the Sericin/PVA/Clay nanofibrous mats with different clay concentrations is shown in Figure 8. The burst strength of the mats increased as the clay concentration increased. The sample with the clay concentration of 0.75 % showed highest burst strength of 10 N/mm^2 and the sample with the clay concentration of 0.1 % showed the least burst strength of 4.3 N/mm^2. This variation in the burst strength is because of exfoliated clay acting as reinforcing filler for the

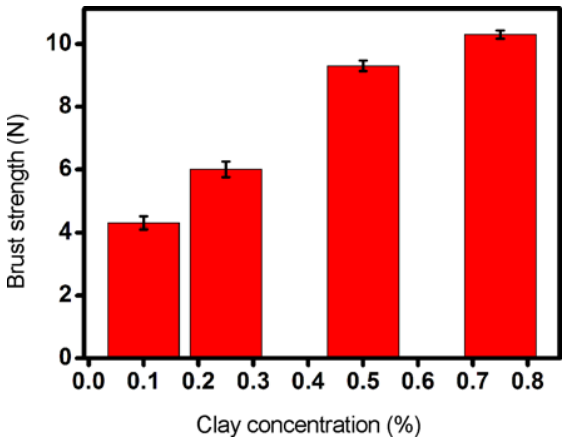


Figure 8. Burst strength of different sericin/PVA/clay nanofibrous mats.

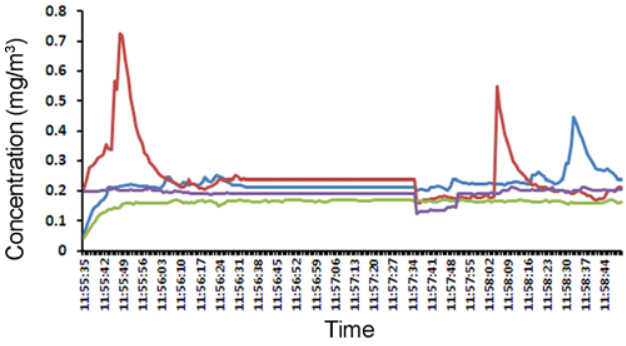


Figure 9. RSPM test of sericin/PVA/clay nanofibrous mats.

Table 2. Total concentration of particulate matter after RSPM

S. no.	Clay concentration (%)	Particle concentration (mg/m^3)
1	0.1	31.62
2	0.25	37.63
3	0.5	44.26
4	0.75	48.70

mats. Higher the concentration of clay, higher is the strength of the nanofibrous mats.

Filtration Efficiency

The filtration efficiency of the samples was checked by RSPM test. The concentration of particulate matter filtered per second by each of these nanofibrous mats is shown in Figure 9. Samples with varied clay concentrations showed variation in the concentration of the particulate matter filtered per second. The sample with clay concentration of 0.75 % filtered greater concentration i.e. 0.725 mg/m^3/s particulate matter of 1 μm size in comparison with the other samples with lesser clay concentrations i.e. 0.1 % clay

concentration sample filtered least concentration of particulate matter of 0.169 mg/m^3/s. The total concentration of particulate matter collected in 6 hours by the samples is shown in the Table 2. The sample with 0.75 % clay concentration showed greater particulate matter collection i.e. 48.702 mg/m^3 in comparison with the other samples where the sample with 0.1 % clay concentration collected least concentration of 31.62 mg/m^3. This is due to the variation in clay concentration, as the clay concentration increase the fibre diameter tends to increase in turn reducing the pore size and enhancing the filtration capability of the nanofibrous mats. The sample with the clay concentration of 0.75 % turned out to be efficient. As the sample with 0.75 % clay concentration was able to collect greater concentrations of particulate matter of 1 μm size, it was subjected to check the filtering capacity against 2.5 μm and 10 μm. This particular sample was able to collect particulate matter of size 2.5 μm in concentration of 1.407 mg/m^3/s and particulate matter of size 10 μm in concentration of 4.175 mg/m^3/s, respectively. The SEM micrographs of sample collected containing dust particle after RSPM tests are shown in Figure 10. The element analysis of the samples before and after RSPM test was carried out using EDX. The weight percentage distribution of elements present in the sample is given in Table 3. The nanofibrous mats before RSPM test show presence of small amount of silicon and aluminium, which is due to the presence of clay in the sample. It is observed that post RSPM test, sample contain sodium, higher amount of silicon aluminium, sulphur and iron. The results indicate that nanofibrous mat efficiently accumulate the dust particles.

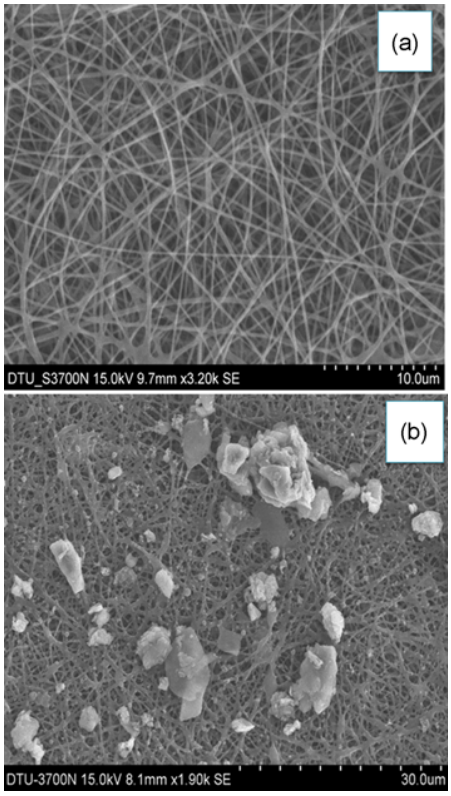


Figure 10. SEM micrographs of sericin/PVA/clay (0.75 %) nanofibrous mat; (a) before RSPM and (b) after RSPM.

Table 3. EDX analysis of sericin/PVA/clay nanofibrous mat

Elements	Pre-RSPM	Post-RSPM
	wt.%	wt.%
Oxygen	63.2	61.2
Sodium	-	1.6
Aluminum	0.17	1.7
Silicon	0.85	5.2
Sulphur	-	1.2
Iron	-	3.1

Conclusion

An efficient antimicrobial nanofibrous filter for particulate matter was successfully prepared using Sericin/PVA/Clay solution. Clay is acting as antimicrobial and reinforcing filler for Sericin/PVA/Clay nanofibrous mats. All the four samples of different clay concentrations were able to filter some concentrations of particulate matter. The sample with the clay concentration of 0.75 % showed greater efficiency of filtration by filtering particulate matter of concentration 0.725 gm/m^3/s in comparison with the other samples and have excellent antimicrobial activity against both the bacteria. From the above discussions it can be concluded that sample with the clay concentration of 0.75 % turned out to be efficient and effective nanofibrous mat for filtering particulate matter of the size of range 1 μm to 10 μm.

References

1. A. Franzetti, I. Gandolfi, E. Gaspari, R. Ambrosini, and G. Bestetti, *Appl. Microbiol. Biotechnol*., **90**, 745 (2011).
2. L. P. Singh, A. Bhardwaj, and K. K. Deepak, *ISRN Public Health*, **2013**, 8 (2013).
3. P. D. Charan and H. Sahel, *Appl. J. Hyg.*, **3**, 11 (2014).
4. WHO | Ambient (outdoor) Air Pollution in Cities Database 2014, (n.d.). http://www.who.int/phe/health_topics/outdoorair/databases/cities/en/ accessed March 13, 2016.
5. M. A. Alghamdi, M. Shamy, M. A. Redal, M. Khoder, A. H. Awad, and S. Elserougy, *Sci. Total Environ.*, **479-480**, 109 (2014).
6. K. Thangadurai, G. Thilagavathi, and A. Bhattacharyya, *J. Text. Inst*., **5000**, 1 (2014).
7. V. K. Kothari, A. Das, and A. Sarkar, *Ind. J. Fibre Text. Res.*, **32**, 196 (2007).
8. V. K. Kothari, A. Das, and S. Singh, *Ind. J. Fibre Text. Res*., **32**, 214 (2007).

9. S. S. Saleh, *J. Am. Sci.*, **8** 110 (2012).
10. D. Cho, A. Naydich, M. W. Frey, and Y. L. Joo, *Polymer*, **54**, 2364 (2013).
11. N. Wang, Y. Si, N. Wang, G. Sun, M. El-Newehy, S. S. Al-Deyab, and B. Ding, *Sep. Purif. Technol*., **126**, 44 (2014).
12. X. Mao, Y. Si, Y. Chen, L. Yang, F. Zhao, B. Ding, and J. Yu, *RSC Adv.*, **2**, 12216 (2012).
13. L. Van Der Schueren, I. Steyaert, B. De Schoenmaker, and K. De Clerck, *Carbohydr. Polym*., **88**, 1221 (2012).
14. A. Cooper, R. Oldinski, H. Ma, J. D. Bryers, and M. Zhang, *Carbohydr. Polym*., **92**, 254 (2013).
15. Y. Liu, M. Park, B. Ding, J. Kim, M. El-Newehy, S. S. Al-Deyab, and K. Hak-Yong, *Fiber. Polym*., **16**, 629 (2015).
16. B. Norder and S. J. Picken, *Thermochim. Acta*, **472**, 31 (2008).
17. Y. Wu, J. Bi, T. Lou, T. Song, and H. Yu, *Int. J. Min. Met. Mater*., **22**, 437 (2015).
18. A. Nicosia, W. Gieparda, J. Foksowicz-Flaczyk, J. Walentowska, D. Wesołek, B. Vazquez, F. Prodi, and F. Belosi, *Sep. Purif. Technol*., **154**, 154 (2015).
19. J. Choi, B. J. Yang, B. Gwi-Nam, and J. H. Jung, *ACS Appl. Mater. Interfaces*, **7**, 25313 (2015).
20. Z. Wang, Z. Pan, J. Wang, and R. Zhao, *J. Nanomater*., **2016**, 1 (2016).
21. S. Pavlidou and C. D. Papaspyrides, *Prog. Polym. Sci.,* **33**, 1119 (2008).
22. V. Mittal, *Materials*, **2**, 992 (2009).
23. M. Joshi, D. Biswas, A. Sarvanan, R. Purwar, and R. Mukhopadhaya, *J. Apply. Polym. Sci*., **125**, E224 (2011).
24. M. Joshi, K. Banerjee, and R. Prasanth, *Ind. J. Fibre Text. Res.*, **3**, 202 (2006).
25. S. I. Hong and J. W. Rhim, *J. Nanosci. Nanotechnol.*, **8**, 5818 (2008).
26. R. Nigmatullin and F. Gao, *J. Mater. Sci.*, **43**, 5728 (2008).
27. J.-W. Rhim, S.-I. Hong, and C.-S. Ha, *LWT-Food Sci. Technol*., **42**, 612 (2009).
28. R. Sothornvit, J.-W. Rhim, and S.-I. Hong, *J. Food Eng*., **91**, 468 (2009).
29. R. Sothornvit, S.-I. Hong, D. J. An, and J.-W. Rhim, *LWT-Food Sci. Technol*., **43**, 279 (2010).
30. G.-O. Lim, S.-A. Jang, and K. B. Song, *J. Food Eng*., **98**, 415 (2010).
31. M. L. Gulrajani, R. Purwar, R. K. Prasad, and M. Joshi, *J. Apply. Polym. Sci*., **113**, 2796 (2009).
32. B. B. Mandal, B. Ghosh, and S. C. Kundu, *Int. J. Biol. Macromol*., **49**, 125 (2011).
33. T. Siritientong, J. Ratanavaraporn, T. Srichana, and P. Aramwit, *BioMed. Res. Int.,* **1**, 2013 (2013).
34. P. Aramwit, T. Siritientong, S. Kanokpanont, and T. Srich, *Int. J. Biol. Macromol*., **47**, 668 (2010).
35. R. Purwar, S. Sharma, P. Sahoo, and C. M. Srivastava, *Fiber. Polym*., **16**, 761 (2015).
36. X. H. Zhang, M. Tsukada, Y. Satoh, and H. Morikawa, *Adv. Mater. Res*., **175-176**, 348 (2011).
37. S. Eslah, H. Tavanai, and M. Morshed, *J. Text. Inst*., **107**, 1 (2015).
38. X. Zhang, M. Tsukada, H. Morikawa, K. Aojima, G. Zhang, and M. Miura, *Nanoscale Res. Lett*., **6**, 510 (2011).
39. X. Zhang, M. M. R. Khan, T. Yamamoto, M. Tsukada, and H. Morikawa, *Int. J. Biol. Macromol*., **50**, 337 (2012).
40. R. Zhao, Y. Wang, X. Li, B. Sun, Z. Jiang, and C. Wang, *Colloid Surf. B-Biointerfaces*, **136**, 375 (2015).
41. R. Purwar, P. Mishra, and M. Joshi, *AATCC Rev.*, **8**, 36 (2008).
42. P. Supaphol and S. Chuangchote, *J. Appl. Polym. Sci.*, **108**, 969 (2008).
43. H. W. Lee, M. R. Karim, H. M. Ji, J. H. Choi, H. D. Ghim, S. M. Park, W. Oh, and J. H. Yeum, *J. Appl. Polym. Sci.*, **113**, 1860 (2009).
44. J. H. Park, H. W. Lee, D. K. Chae, W. Oh, J. D. Yun, Y. Deng, and J. H. Yeum, *Colloid. Polym. Sci*., **287**, 943 (2009).
45. C. P. McAdam, N. E. Hudson, J. J. Liggat, and R. A. Pethrick, *J. Appl. Polym. Sci.*, **108**, 2242 (2008).
46. M. Avella, J. J. De Vlieger, M. E. Errico, S. Fischer, P. Vacca, and M. G. Volpe, *Food Chem*., **93**, 467 (2005).

© *Apeejay Journal of Management and Technology*
January 2015, Vol. 10, No. 1, 62-69

EMPIRICAL ANALYSIS OF WORKFORCE DIVERSITY AND ITS MANAGEMENT IN TODAY'S IT ORGANIZATIONS

Shikha N. Khera
Karishma Gulati

The present research work emphasizes on the analysis of employee diversity in Information Technology (IT) industry and the importance of diversity management. It is empirical in nature, as 167 respondents are probed (using convenience sampling) from various IT companies of India. It is based on a primary survey conducted with the help of a well-structured questionnaire. The prime aim of the research is to understand the level of cross-cultural diversity in IT companies in India and to identify what procedures have been adopted to manage this diversity effectively, so as to remove any chances of conflict or issues based on cultural factors. The empirical findings reveal visible diversity at all levels of the organization. The recruitment is done from a diverse pool of candidates as well as there is reflection of diversity in company's literature, website etc. These form the most important hallmarks of a diverse organization. It further concludes that to manage diversity supervisors should show fair treatment towards their employees and employees should be aware of equal opportunity policies and provisions laid down by the organization. Hence, workforce diversity is found to be an important issue to be focused more in IT organizations.

Keywords: Cross Culture, Diversity Management, IT Organizations, Workforce Diversity

INTRODUCTION

"Diversity is differences amid individuals on any personal attributes that decide how people perceive one another" (Gonzales and Denisi, 2009). This is in line with Ongori and Agolla (2007), who acknowledged diversity as the co-existence of employees from various socio-cultural backgrounds within the company. Wentling and Palma-Rivas (2000) contended that diversity does not only include cultural factors like race, gender, age, color, physical ability etc but may include lifestyle, sexual orientation, values, religion, disability, education, language, beliefs, national origin, physical appearance, ethnic culture and economic status. Inhibition by the above stated factors may affect the diversity and employee's career aspirations (Bryan and Sohal, 1999).

Christian et al. (2006) argued that theoretical assumptions emphasized on both positive and negative effects of diversity in workgroups. In contrast, Carrel et al. (2006) believed that diversity can improve organizational effectiveness by budding experience and reputations for managing diversity as it will probably exert a pull on the best personnel. Ferlie et al. (2003) justified diversity as economically beneficial. This can be validated by the study that top management team diversity (Korn et al. 1992) and education and training of senior managers (Smith et al. 1994) added to positive financial returns. It is also established that heterogeneous groups make competitive and eminent decisions (Watson et al., 1993; Miller et al., 1998; Lawrence, 1997), engender more ingenious ideas (Bantel et al., 1989), slot in more ingenious problem solving (Nemeth and Wachter, 1983; Triandis et al., 1965) and have the prospective for improved productivity (Jackson, 1993).

Dr. Shikha N. Khera (author) is Assistant Professor, Delhi School of Management, Delhi Technological University (Formerly Delhi College of Engineering), Shahbad Daulatpur, Main Bhawan Road, Rohini, New Delhi. Email: shikhankhera@yahoo.co.in

Karishma Gulati (co-author) is Research scholar, Delhi School of Management, Delhi Technological University (Formerly Delhi College of Engineering), Shahbad Daulatpur, Main Bhawan Road, Rohini, New Delhi. Email: karishma.g86@gmail.com

In recent years, the outlook of diversity has radically changed to a proactive conception. The diversity in the workforce helps in gaining competitive advantage as diverse viewpoints can assist unique and creative approaches to problem-solving. This in turn leads to improved organizational performance (Allen et al., 2004). Diversity management can be defined as "The systematic and planned commitment by the organizations to recruit, retains, reward and promote a heterogeneous mix of employees" Ongori and Agolla (2007).

Managing diversity signifies creating an assorted workforce to perform at its best in an unbiased work environment that permits all individuals to utilize their full potential to accomplish organizational objectives (Jenner, 1994; Thomas, 1994) or where none of the members have an endeavour for efficiency, productivity and eventually competitive advantage (Brian and Sohal, 1999). Diversity management focuses on building specific skills, sketching particular policies and planning those practices that search out the best for each employee of diverse workforce. To manage the diversity an organization should incorporate diversity management principles with human resource practices like recruitment, training and development, performance appraisal etc. Although diversity has been clinched by many organizations, still it is deemed as merely a matter of compliance with legal requirements. The historically effective diversity management has been used to endow with a legally defensive position. This implies that an organization having assorted workforce could argue about their non-guilty of discrimination by presenting that their workforce demographics embodying the demographics of the local community (Ongori and Agolla, 2007).

Dong and Liu (2010) alleged that culture is peripheral source that influences employee's behaviors that in turn influences other employee's behavior within the organization, since each employee brings the external world into the workplace. Communally, the brunt of culture on individuals transforms the culture of the organization itself. Trice and Beyer (1993) argued that attitudes and strategies of organizational members under the influence of culture become the basis to manage uncertainties and ambiguities independently and communally. Managers from diverse nations show a discrepancy in their decision-making. Understanding culture is imperative for multinational companies and managers to be geared up to contend with firms of other countries. Understanding cultural differences is critical to the success of firms betrothed in international business (Hall, 1960). A society's culture affects the political, economic, social and ethical rules a firm must follow in its business dealings within that society. A society's culture can be effortlessly seen in its values, beliefs, behaviors, customs and attitudes as it is a learned behavior that is passed on by one individual of a society to another. The elements of culture are interconnected and strengthen each other. These elements are adaptive and changing as outside forces influence the society. Culture not only is shared by the society's members but also defines the society's membership.

REVIEW OF LITERATURE

Hofstede (1991) presented one of the most accepted frameworks for investigation of cross-cultural matter in human resource management. Later, Schwartz (1994), Maznevski & DiStefano (1995), Kossek and Lobel (1996), Trompenaar (1998), Richard and Johnson (1999, 2001), Benschop (2001), House, et al. (2004), and Richard et al. (2006) developed and tested other models of cross-cultural analysis and diversity of workforce.

Workforce diversity practices if implemented accurately in the area of human resources are alleged to augment employee and organizational performance (Adler, 1986; Fernandez and Barr, 1993; Hall and Parker, 1993; Deluca and McDowell, 1992; Grace, 1994). Managing diversity entailed in leveraging the cultural differences in people's skills, ideas and creativity to put in to a common goal so that the organization can achieve competitive edge (Deresky, 1994; Morrison, 1992). As per the literature by Hayles and Russel (1997), current studies have revealed that good diversity practices and profits have strong correlation. Diversity allows increased creativity and innovation, a wider range of perspectives for better decision making, better problem definition, greater success in marketing to foreign and domestic ethnic minority communities and a better distribution of economic opportunity (Adler, 1986; Cox, 1991; Cox and Blake, 1991). According to Watson et al., *(*1993), culturally diverse groups relative to homogeneous groups are more effective both in the interaction process and job performance. Some studies depict that greater diversity can create higher levels of dissatisfaction and turnover (Miliken and Martins, 1996). Hence to garner the benefits, diversity must be managed effectively as managing diversity can create a competitive advantage (Brian and Sohal, 1999).

Rynes and Rosen (1995) explored that in multiple organizations, diversity issues including organizational size, and the success of diversity training programs which were found to be positively correlated with top

management support, prioritization of diversity based objectives and staffing. Jehn (1999) through multi-method field study identified that information and social category diversity within the workgroup had positive outcomes (including increased efficiency and morale) but value diversity negatively affects intention to remain.

Richard and Kirby (1999) surveyed that use of organizational justice as a justification for diversity programs did improve hiring outcomes (where improvement was defined as a degree of success in hiring diverse candidates, but did not address skill levels of qualifications of candidates) but did not improve actual performance of these programs. Bunderson and Sutcliffe (2002) compared different concepts of functional diversity and concluded that performance and information sharing is much enhanced in dominant functional diversity, than in intrapersonal functional diversity. However, when considering intrapersonal functional diversity, information sharing and performance was negatively affected. Bunderson and Sutcliffe (2002), Simons and Kimberly (2011) also investigated the differences amid social and functional diversity and suggested that in order to manage diversity effectively, it is necessary for organizations to understand the difference between functional and social diversity, and to treat these forms of diversity differently in terms of creating functional and innovative teams. Zanoni and Janssens (2004) interviewed various HR managers (of different organizations) in order to determine diversity and its management. They found that power is a key component used by active HR professionals and leaders in the description of diversity. Pitts et al., (2010) conducted meta analysis to find out drivers in public administration for implementation of diversity management programs and observed that diversity management is obsessed by favorable environment, institutional isomorphism i.e. social similarity and environmental uncertainty, each having diverse effects.

OBJECTIVES OF THE STUDY

There can be many hallmarks that can define an organization as a diverse organization. The study elucidates the major features that enable an organization to be called as 'diverse' wherein people from various cross cultures come together to work for the organizational goal. In all the organizations which can be characteristically called "diverse", the study further looks into various procedures that have been inculcated into the organizational culture so as to manage this diversity in the most effective manner thereby managing various cross-cultural issues and conflicts which might crop up from time to time. It will focus on how various cross cultural dynamics are correlated to the workforce diversity. Correlation of various characteristics to the presence of diversity in an organization will be found. The study also puts an insight into whether the IT companies comply with statutory obligations as per diversity legislation in India and whether any findings of unlawful discrimination on these grounds have been seen in last three years. Hence, the objectives of the study stated categorically are:

- To determine the characteristics of a diverse organization
- To understand various procedures those have been put in place in IT organizations to manage workforce diversity.
- To identify correlation between cross cultural dimensions and workforce diversity.
- To find out whether statutory obligations are being met by the IT organizations in context of diversity in place.

RESEARCH METHODOLOGY

For conducting the research, a sample of 167 respondents was selected from 13 IT companies to examine whether they implement workforce diversity in their organizations. The data for study is obtained mainly from primary sources however secondary sources are also well thought-out. Primary sources include interaction with IT officials and filling up a well-structured questionnaire. The secondary data was collected from the internet, websites of various IT companies etc.

The structure of the questionnaire was divided into three primary parts:

1. Characteristics that define an organization as "Diverse".
2. According to the above mentioned hallmarks, can the recipient's organization be called a "Diverse/ Cross-cultural" organization.
3. If yes, then what procedures have been put in place by the organization to handle this diversity in an effective manner where no issues or conflicts happen due to cultural problems.

RESULTS AND DISCUSSIONS

Characteristics of a Diverse Organization

In order to identify the characteristics of a diverse organisation, the following statement has been administered to the respondents. The results for the same have been presented in the table 1.

Table 1. Mean, Standard Deviation and Variance of Various Characteristics of a Diverse Organization

Statement	Mean	Standard Deviation	Variance
There should be visible diversity at all the levels of the organization & employees should be recruited from a diverse pool of candidates.	1.63	.756	.571
Diversity should be reflected in company literature, website, and any photos or artwork on the walls.	1.67	.824	.678
People from different cultures and backgrounds should interact and share ideas and resources as opposed to clustering with only people who look and think like them.	1.72	.831	.691
Each person should have an equal chance to show what they can do, feel included in the organization and do their best for the company.	1.81	.973	.947
Top management should endorse and actively champion the company's diversity initiatives. It should not solely be an HR function.	2.06	.851	.724
Flexible working practices should be made available, as there is an appreciation that not everyone can and will work the same hours and in the same way. This will remove disadvantage and discrimination to participation in work.	2.12	.946	.895
There should be an existence of a widely accepted and practiced set of values that ensure the respect and dignity of all.	2.21	.913	.834
There should be processes in place to resolve conflicts and prevent miscommunication.	2.28	1.152	1.327

Source: Author's calculations based on primary data

The Table 1 underlines that lower the mean; the more significant the factor will be (since 1- Strongly Agree and 5- Strongly Disagree). Hence the following factors are found to be the most important:
(Enlisted in descending order of importance)

- There should be visible diversity at all levels of the organization & employees should be recruited from a diverse pool of candidates.
- Diversity should be reflected in company literature, website, and any photos or artwork on the walls.
- People from different cultures and backgrounds should interact and share ideas and resources as opposed to clustering with only people who look and think like them.
- Each person should have an equal chance to show what they can do, feel included in the organization and do their best for the company.

Procedures for Managing Workforce Diversity in Organisations.

Table 2 presents the results of procedures followed within IT organisations for managing workforce diversity. The descriptive statistics of the same have been shown in the table 2.

Table 2. Mean, Standard Deviation and Variance of Various Procedures to Manage Diversity

Statement	Mean	Standard Deviation	Variance
Supervisors seem fair in their treatment of most employees.	2.24	.923	.851
The organization makes employees aware of equal opportunity policies and provisions.	2.31	.941	.885
Employees demonstrate a commitment to meet the needs of underrepresented racial and ethnic employee populations as well as of employees with disabilities.	2.36	.883	.779
The recruitment procedures encourage diversity.	2.37	.885	.783
There are procedures in place for reporting discrimination.	2.37	.998	.995
The workplace guarantees promotions and pay rises based on merit only	2.39	1.154	1.332

The workplace provides equipment to make all areas accessible to people of all abilities (To curb language/ communication barrier, physical disabilities etc.)	2.54	1.185	1.404
There is widely known and adhered to "diversity policy" in your organization (eg. Regarding promotion, hiring, retention).	2.61	.969	.938
Presence of committees/support groups/ safe havens to resolve such conflicts in the organization.	2.70	.985	.970

Source: Author's calculations based on primary data

Results in Table 2 indicate that the lower the mean, more significant the factor will be (since 1- Strongly Agree and 5- Strongly Disagree). Hence accordingly, the five most important procedures to manage diversity in cross cultural environment are (in descending order of their importance):

- Fair treatment shown by supervisors towards their employees.
- Methods in place to create awareness among all the employees towards equal opportunity policies and provisions lay down by the organization.
- Creation of employee commitment to meet the needs of underrepresented racial and ethnic employee populations as well as of employees with disabilities.
- The recruitment procedures encourage diversity.
- Set procedures in place for reporting any kind of discrimination shown towards the culture or background of the employee.

Correlation Between Cross Cultural Dimensions and Workforce Diversity

Further, the correlation between cross cultural dimension and workforce diversity has been examined, where the cross cultural dimensions have been taken as independent variable and workforce diversity has been taken as the dependent variable.

Table 3. Correlation Matrix of Cross-Cultural Dimensions with Workforce Diversity

Independent Variables	Dependent Variable (Diverse Workforce) Correlation(r)	Significance Level
Flexible working practices should be made available, as there is an appreciation that not everyone can and will work the same hours and in the same way. This will remove disadvantage and discrimination to participation in work.	.617**	.000
There should be an existence of a widely accepted and practiced set of values that ensure the respect and dignity of all.	.553**	.000
Each person should have an equal chance to show what they can do, feel included in the organization and do their best for the company.	.551**	.000
Diversity should be reflected in company literature, website, and any photos or artwork on the walls.	.476**	.000
Top management should endorse and actively champion the company's diversity initiatives. It should not solely be an HR function.	.431**	.000
There should be visible diversity at all levels of the organization & employees should be recruited from a diverse pool of candidates.	.403**	.001
People from different cultures and backgrounds should interact and share ideas and resources as opposed to clustering with only people who look and think like them.	.380**	.002
There should be processes in place to resolve conflicts and prevent miscommunication.	-.040	.747

Source: Author's calculations based on primary data

** Shows significance at 1% level of significance

The Table 3 depicts the presence of flexible working practices, existence of a widely accepted and practiced set of values to ensure respect and dignity of all employees and equal chance to every employee in an

organization has a significantly strong positive correlation with workforce diversity. Although reflection of diversity in company's literature, website and on the walls along with the fact that, in a company the diversity initiatives should not solely be an HR function, and top management should endorse and actively champion it has a significantly moderate positive correlation with workforce diversity. A visible diversity at all levels of the organization and employee recruitment from a diverse pool of candidates also has a significantly moderate positive correlation with workforce diversity. A culture wherein people from different cultures and backgrounds should interact and share ideas as opposed to clustering with only people who look and think like them is a practice which has a significantly low positive correlation with workforce diversity.

Statutory Obligations Being Met by the Organization in Context of Diversity in Place

Lastly, table 4 presents the results whether statuary obligations have been met by the organisation or not. The discipline of the same has been mentioned below.

Table 4: Mean, Standard Deviation and Variance of Questions to Find Whether Statutory Obligations are Being Met by the Organization in Context of Diversity in Place

Statement	Mean	Standard Deviation	Variance
Organization complies with statutory obligations under all aspects of current equality and diversity legislation	2.24	.872	.760
In the last three years, there has been NO finding of unlawful discrimination on the grounds of age, race, sex, marital status, disability, religion or sexual orientation in the employment field been made against your organization	2.10	.819	.671

Source: Author's calculations based on primary data

It can be concluded from Table 4 that IT companies in India comply with statutory obligations as per diversity legislation and that no finding of unlawful discrimination on these grounds has been seen in last three years.

CONCLUSION

The empirical findings identified visible diversity at all levels of the organization, recruitment done from a diverse pool of candidates as well as reflection of diversity in company's literature, website etc. form the most important hallmarks of a diverse organization. Next it has been identified that proper management techniques of this diversity include fair treatment of employees by the supervisors and various methods lay down by the organization to create awareness among all the employees towards equal opportunity policies and provisions.

In addition, presence of flexible working practices in an organization along with the existence of a widely accepted and practiced set of values laid down to ensure respect and dignity of all employees have significantly strong positive correlation with workforce diversity. Also it can be seen that IT companies in India meet statutory obligations as per diversity legislation and that no finding of unlawful discrimination on these grounds has been seen in the last three years.

With the opening up of the Indian economy since 1991, cross cultural issues have attracted greater attention and assumed greater importance than ever before. However, cross cultural management has also come a long way, with a majority of the employees associated with the Indian IT industry expressing awareness of cross cultural challenges and the need for its management. The results indicate that Indian IT industries have a good legal framework in place, as confirmed by our research. No cases of unlawful discrimination in the workplace have been reported in the last three years. The need of the hour is to strengthen these regulations to increase the viability of the Indian workplace for professionals from around the globe. Companies and their zero-tolerance attitude to discrimination need greater visibility. Efforts should be made for greater employee integration, using their cultural backgrounds, not as a barrier but as a social fabric that will enable them to unite under the aegis of the company and work towards a greater good.

The research suffers from some limitations. Among IT professionals, job hopping is very prevalent and therefore employees may confuse the present company policies with their earlier organizations. At the same time, employees which are new to a company may not have complete information about company policies. There can

be probability that some employees might have grudges with the company for one reason or the other. Moreover some who intend to leave the organization would be disinterested in filling the questionnaire.

With all the limitations set aside, it can be concluded that in today's world it is imperative to realize that cultural diversity should be taken as a tool for better organizational progress rather than a managerial problem. Moreover if it is managed effectively, it can be a key to gain competitive edge and success.

REFERENCES

Abor, J. (2004). Technological innovations and banking in Ghana: An evaluation of customers' perceptions. *American Academy of Financial Management*, 1, 1-16.

Adler, N. J. (1986). Cultural synergy: Managing the impact of cultural diversity. *The 1986 annual: Developing Human Resources*, 229-38.

Allen R, Dawson G, Wheatley K, White,C. S. (2004). Diversity practices: Learning responses for modern organisation, *Development and Learning in Organisations: An International Journal,* 18 (6), 13-15.

Bantel, K. A., & Jackson, S. E. (1989). Top management and innovations in banking: does the composition of the top team make a difference?. *Strategic Management Journal*, 10(S1), 107-124.

Benschop, Y. (2001). Pride, prejudice and performance: relations between HRM, diversity and performance. *International Journal of Human Resource Management*, *12*(7), 1166-1181.

Bryan D., Sohal, A. S., (1999). Human resource practices and workforce diversity: an empirical assessment, *International Journal of Manpower*, 20(8), 530 – 547.

Bunderson, J. S., and Sutcliffe, K. M. (2002). Comparing alternative conceptualizations of functional diversity in management teams: Process and performance effects. *Academy of Management Journal*, *45*(5), 875-893.

Carrell, M. R., Mann, E. E., & Sigler, T. H. (2006). Defining workforce diversity programs and practices in organizations: A longitudinal study. *Labor Law Journal*, *57*(1), 5-12.

Christian, J., Porter, L. W., Moffitt, G. (2006). Workplace diversity and group relations: An overview. *Group Processes & Intergroup Relations*, 9(4), 459-466.

Cox, T. H., & Blake, S. (1991). Managing cultural diversity: Implications for organizational competitiveness. *The Executive*, 5(3), 45-56.

Cox, T. Jr (1991), The multicultural organization, *The Academy of Management Executive,* 34-47.

DeLuca, J. M., & McDowell, R. N. (1992). Managing diversity: A strategic 'grass roots' approach. *Diversity in the workplace: Human resources initiatives*, *1*, 227-247.

Deresky, H. (2000). *International Management: Managing Across Borders and Cultures*. Pearson Education India, New Delhi, Dorling Kindersley India Pvt. Ltd.

D'Netto, B., & Sohal, A. S. (1999). Human resource practices and workforce diversity: an empirical assessment. *International Journal of Manpower*, *20*(8), 530-547.

Dong, K., & Liu, Y. (2010). Cross-cultural management in China. *Cross Cultural Management: An International Journal*, *17*(3), 223-243.

Ferlie, E., Hartley, J., & Martin, S. (2003). Changing public service organizations: Current perspectives and future prospects. *British Journal of Management*, *14*(s1), S1-S14.

Fernandez, J. P., & Barr, M. (1993). *The diversity advantage: How American business can out-perform Japanese and European companies in the global marketplace*. New York: Lexington Books.

Gonzales, J. A., Denisi, A. S. (2009), Cross level effects of demography and diversity climate on organizational attachment and firm effectiveness, *Journal of Organizational Behavior*, 30(1), 21-40.

Grace, P. (1994). Danger-diversity training ahead: Addressing the myths of diversity training and offering alternatives. *The 1994 annual: Developing human resources*, 189-99.

Hall, D. T., & Parker, V. A. (1993). The role of workplace flexibility in managing diversity. *Organizational dynamics*, *22*(1), 5-18.

Hall, E. T. (1960). The silent language in overseas business. *Harvard Business Review*, *38*(3), 87-96.

Hayles, V. R., Hayles, R., & Russell, A. M. (1997). *The diversity directive: Why some initiatives fail & what to do about it*. McGraw-Hill.

Hofstede, G. H., (1991). Cultures and Organizations: Software of the Mind. London: McGraw-Hill, 1991.

House, R. J., Hanges, P. J., Javidan, M., Dorfman, P. W., & Gupta, V. (eds.) (2004) *Culture, Leadership, and Organizations: The GLOBE Study of 62 Societies*. Sage Publications: Thousand Oaks.

Jackson, S. E. (1993). *Diversity in the work place: Human resources initiatives*. Guilford Press: New York.

Jehn, K. A., Northcraft, G. B., & Neale, M. A. (1999). Why differences make a difference: A field study of diversity, conflict and performance in workgroups. *Administrative science quarterly*, *44*(4), 741-763.

Jenner, L. (1994), *Diversity Management: What Does it Mean*, Industrial Management, 36(1), 11.

Korn, H. J., Milliken, F. J., & Lant, T. K. (1992). Top management team change and organizational performance: The influence of succession, composition, and context. *Academy of Management Journal*, *33*, 129-150.

Kossek, E. E., & Lobel, S. A. (Eds.). (1996). *Managing diversity: Human resource strategies for transforming the workplace*. Cambridge, MA: Blackwell Business.

Lawrence, B. S. (1997). Perspective-The Black Box of Organizational Demography. *Organization Science*, *8*(1), 1-22.

Maznevski, M. L., & DiStefano, J. J. (1995). Measuring culture in international management: The cultural perspectives questionnaire. The University of Western Ontario Working Paper Series, 95-39.

McLeod, P. L., Lobel, S. A., & Cox, T. H. (1996). Ethnic diversity and creativity in small groups. *Small group research*, *27*(2), 248-264.

Miller, C. C., Burke, L. M., & Glick, W. H. (1998). Cognitive diversity among upper-echelon executives: Implications for strategic decision processes. *Strategic Management Journal*, *19*(1), 39-58.

Milliken, F. J., & Martins, L. L. (1996). Searching for common threads: Understanding the multiple effects of diversity in organizational groups. *Academy of Management Review*, *21*(2), 402-433.

Morrison, A. M. (1992). *The New Leaders: Guidelines on Leadership Diversity in America. Jossey-Bass Management Series*. Jossey-Bass, Inc., Publishers, 350 Sansome Street, San Francisco, CA 94104.

Nemeth, C. J., & Wachtler, J. (1983). Creative problem solving as a result of majority vs minority influence. *European Journal of Social Psychology*, *13*(1), 45-55.

Ongori, H., & Agolla, J. E. (2007). Critical review of literature on workforce diversity. *African Journal of Business Management*, 1(4), 72-76

Pitts, D. W., Hicklin, A. K., Hawes, D. P., & Melton, E. (2010). What drives the implementation of diversity management programs? Evidence from public organizations. *Journal of Public Administration Research and Theory*, *20*(4), 867-886.

Richard, O. C., & Johnson, N. B. (1999). Making the connection between formal human resource diversity practices and organizational effectiveness: Behind management fashion. *Performance Improvement Quarterly*, *12*(1), 77-96.

Richard, O. C., & Johnson, N. B. (2001). Understanding the impact of human resource diversity practices on firm performance. *Journal of Managerial Issues*, 13(1), 177-195.

Richard, O. C., & Kirby, S. L. (1999). Organizational justice and the justification of work force diversity programs. *Journal of Business and Psychology*, *14*(1), 109-118.

Richard, O. C., Ford, D., & Ismail, K. (2006). Exploring the performance effects of visible attribute diversity: the moderating role of span of control and organizational life cycle. *The International Journal of Human Resource Management*, *17*(12), 2091-2109.

Rynes, S., & Rosen, B. (1995). A field survey of factors affecting the adoption and perceived success of diversity training. *Personnel Psychology*, *48*(2), 247-270.

Schwartz, S. H. (1994). *Beyond individualism/collectivism: New cultural dimensions of values*. Sage Publications, Inc.

Simons, S. M., & Rowland, K. N. (2011). Diversity and its impact on organizational performance: The influence of diversity constructions on expectations and outcomes. *Journal of technology management & innovation*, *6*(3), 171-183.

Smith, K. G., Smith, K. A., Olian, J. D., Sims Jr, H. P., O'Bannon, D. P., & Scully, J. A. (1994). Top management team demography and process: The role of social integration and communication. *Administrative science quarterly*, 39(1), 412-438.

Thomas, R.R. (1994), *From Affirmative Action to Affirming diversity*", in Thomas, R.R. (Ed.), Differences that Work: Organisational Excellence through Diversity, A Harvard Business Review Book, HBS, Boston, MA.

Torres, C., & Bruxelles, M. (1992). Capitalizing on global diversity. *HR MAGAZINE*, *37*, 30-30.

Triandis, H. C., Hall, E. R., & Ewen, R. B. (1965). Member heterogeneity and dyadic creativity. *Human Relations*, 18, 33-35.

Trice, H. M., & Beyer, J. M. (1993). *The Cultures of Work Organizations*. Prentice-Hall, Inc.

Trompenaar, F., & Hampden-Turner, C. (1998). Riding the waves of culture: Understanding diversity in global business. *Nueva York: Mc Graw Hill.*

Watson, W. E., Kumar, K., & Michaelsen, L. K. (1993). Cultural diversity's impact on interaction process and performance: Comparing homogeneous and diverse task groups. *Academy of Management Journal*, *36*(3), 590-602.

Wentling, R. M., & Palma-Rivas, N. (2000). Current status of diversity initiatives in selected multinational corporations. *Human Resource Development Quarterly*, *11*(1), 35-60.

Zanoni, P., & Janssens, M. (2004). Deconstructing Difference: The rhetoric of human resource managers' diversity discourses. *Organization Studies*, *25*(1), 55-74.

Copyright of the Apeejay Institute of Management Technical Campus, all Rights Reserved.

Estimation of Electrical Energy Generation from Anaerobic Digestion Technology

Shubham Gupta*, Prof. R. S. Mishra#

**Post Graduate Student, Department of Mechanical Engineering Delhi Technological University, Delhi-110042, India*

#Department of Mechanical Engineering Delhi Technological University, Delhi-110042, India

***Abstract*: - The growth of Municipal Solid Waste (MSW) has been skyrocketing as a result of growing urban population and industrialization. Day to day increase in waste generation demands Renewable technology for solid waste management for an effective economic and social growth of the people. Anaerobic digestion is a biological method used to convert organic wastes into a stable product for different applications such as cooking, electricity generation, etc. with reduced environmental impacts. The biogas produced can be used as an alternative renewable energy source.Biogas productions is a great substitute for fossil fuels. This process can also utilize MSW for production of electricity. Electricity generation through biogas helps in solving environmental issues, electricity shortage and Solid waste management problem. This paper focuses on technical feasibility and electrical potential mappingof Haridwar City through Anaerobic Digestion Technology.**

***Key Words:* Waste to Energy, Anaerobic Digestion, Municipal Solid Waste, Solid Waste Management, Electricity Generation, Renewable Energy**

I. INTRODUCTION

The current trend of economic growth and standard of living of people increases municipal solid waste (MSW) generation and effects on current landfill scenario, unavailability of land, open burning landfill causes pollution and has greatly effects on public health. There is an urgency for an effective solid waste management due to all of these reasons. WTE incineration helps in reducing greenhouse gases (GHGs) by avoiding dumping to landfill, foils the methane emission from landfill and generating renewable energy in form of electricity which further helps in reducing dependency on fossil fuels. In Incineration Technology MSW is combusted in presence of oxygen. Heat produced then utilized to produce steam which turns the turbine and then alternator to produce electricity. Harmful flue gases are treated and then released in atmosphere. By product is utilized in cement factory. In Landfill gas recovery Anaerobic biodegradation results in methane production in landfill which is recovered to produce either electricity or heat. In Biomethanation technology. Organic matter of MSW is converted to biogas by means of anaerobic digestion in presence of methanogenic bacteria. This biogas can further be utilized for cooking or electricity production. In Refuse Derived Fuel technology fuses whole MSW irrespective of individual calorific value of organic and inorganic matter. It forms briquettes and pellets which can be used further as a fuel in many applications. Currently largest source of GHGs emissions in the world are landfills with an assessment of almost 21% of the total methane production. As a GHG Methane is 21 times stronger than carbon dioxide.

II. LITERATURE REVIEW

Mufeed Sharholy et.al (2007)[1]used ArcGIS technique which included MSW sample collection and questioner survey on randomly selected houses and concluded that 45.3% of organic matter and 40% miscellaneous material (glass, paper, plastics etc.) and mentioned the qualitative and quantitative characteristics of MSW for MSWM for developing GIS maps for city of Allahabad. He also explained MSWSM collection, storage and disposal methods. Tsai et.al (2014)[2]did content and chemical analysis of MSW from year 2008 to 2012 with the use of CHP technology and compared the efficiency of plants of Taiwan with different parts of Europe, Germany and Netherlands. He also classified plants on the basis of capacity of waste handling, power generation and efficiency was done and discussed use of district heating and cooling and its use and advantage. S Rathi et.al (2014)[3] used Dulong Formulae heat energy in incineration technology to calculate and analyse potential generation of electricity in Kanpur city of 33MW from MSW of 1200 tonnes/day by considering conversion efficiency, station allowance, unaccounted heat loss and net power generated and classified solid wastes on physical and chemical composition. NIE et.al (2008)[4]explained new technology of circulating fluidized bed and emission of reduction by using equipment such as house filtration, flue gas cleaning and activated carbon in incinerator, adopted by 30 plants for development of China. Biodegradable matter shares 31-36% of total MSW in big cities and 65% in small cities having calorific value of around 5000KJ/Kg. Dioxin emission was limited to 1.0ng TEQ/Nm^3. Ojha et.al (2011)[5] explained, classified and compared cities on the basis of population, MSW composition, total waste generated; very big city, big city, medium city, small city and calculated potential of 1700 MW electricity from WTE incineration with some solutions and suggestion to problems occurring in MSWM. Arena et.al (2015)[6]proposed the opinion to solve waste problem as using it as a resource. He explained WTE technology was successful and reliable because of thermal conversion, heat recovery and air pollution

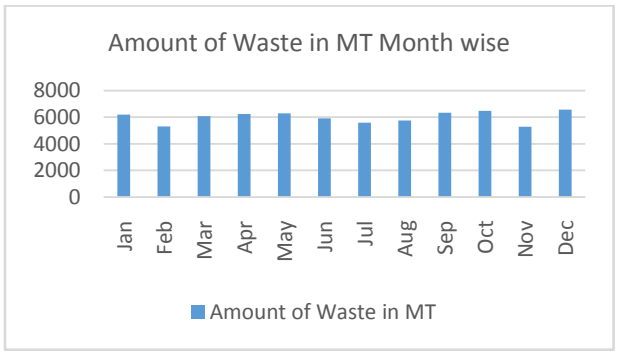
technique to reduce health and environmental risk, landfill substitute. Vikash Talyan et.al (2008)[8]discussed first incineration in Delhi, setup in 1989 at Timarpur to produce 3.7MW from 300 Tonnes of waste of calorific value higher 1000 Kcal/Kg but was closed in 21 days only due to falling of calorific value. First composting plant was setup in 1980 in Okhla and was shut down due to absence of market and high production cost. He explained three landfills in at Gazipur, Okhla and Bhalswa with LFG potential of energy generation $12.98*10^5$ Kwh/year. Ityona Amber et.al (2012)[7] calculated potential generation of 700KWh/tonne of electricity with calorific value of 17.23 MJ/Kg and conversion efficiency of 25% from incineration technology in Nigeria by considering methodology of analysing 5 samples of 10 Kg each of waste and evaluated that 43% of total MSW organic components are present while 8% are paper, cardboard, plastics. V G Sister (2006)[9] simulated plant model to improve the performance of waste incineration plant by considered gas turbine and steam cycle heat from outgoing fuel gases which resulted in efficiency of binary system gas incinerator of 42-45%. In addition, he said Pyrolysis in incineration increases its efficiency by providing high yield of components of CO, H_2, and CH_4.In addition, he compared conventional plant's energy content which was much higher than of Municipal Solid Waste (MSW) and also conventional power plants had higher efficiency than incineration plants. Dioxins emissions from incineration plants cause health issues.

III. CASE STUDY UNDERTAKEN

"Haridwar is a city in, Uttarakhand that is spread over a flat terrain with the grand spectacle of Himalayas ranges flanking it in the East and the North-east." It generates around 200 tonnes of waste daily

IV. AMOUNT OF WASTE GENERATED

The city generates, on an average, about 200MT of MSW per day. The major sources of MSW generation of the city are domestic, shops and commercial establishments, hotels, restaurants, dharamsalas and fruit and vegetable markets.



V. COMPUTATION OF ENERGY POTENTIAL

Only biodegradable fraction of total waste can be digested to produce gases so total amount of waste needs to be taken to generate 220 gm of CH_4 and 512.6 gm of CO_2 will be:

$$C_{25.41}H_{39.88}O_{14.25}N + 9.06\ H_2O = 13.75\ CH_4 + 11.65\ CO_2 + NH_3$$

Total amount of waste × .65 = 573.8 (mass of hydrocarbon)

Total Amount of Waste = 882.76 gm

Weight of CH_4 = (220/882.76)×22.39 = 5.57 Kg

Weight of CO_2 = (512.6/882.76)×22.39 = 13 Kg

Density of CH_4 and CO_2 are taken as 0.7167 g/l and 1.9768 g/l respectively.

Volume of CH_4= (5.57 / 0.7167) = 7.77 m^3

Volume of CO_2 = (13 / 1.9768) = 6.57 m^3

Total Volume of gas generated = 7.77+6.57=14.34 m^3

Percentage of CH_4 = (7.77/14.34) × 100 = 54.18 %

Percentage of CO_2 = (6.57/14.34) × 100 = 45.82 %

Amount of gas generated per kg = 14.34/100 = .1434 m^3/Kg.

Amount of waste generated in Haridwar City = 200000 Kg per day

Therefore, total biogas generated = 200000 × 0.1434 = 28680 m^3/day

Considering 60% digestion efficiency = 0.6×28680 = 17208 m^3/day

Net Calorific Value of Biogas = 5000 Kcal/m^3

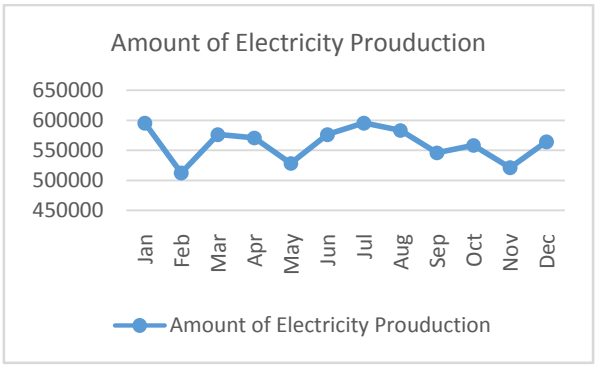
Energy Potential = 5000 × 17208 × 0.00116 = 99806.4 KWH

Power Generation = 99806.4/24 = 4158.6 KW

Conversion Efficiency (30 %)= 0.3 × 4158.6 = 1247.58 KW.

Considering Heat Loss (35 %) so net output =

0.65 × 1247.58 = **0.8 MW**



VI. RESULTS & DISCUSSION

The numerical computation has been carried out and following total energy potential is calculated which provides the feasibility of the Anaerobic Digestion in Haridwar City.

Total electricity production is 0.8 MW for 24hrs operation which can provides 6Lacunits monthly, which fulfil the 10% of total energy need of Haridwar city.

VII. CONCLUSION

It is a great step towards sustainable development as it saves coal resources which can be used by future generation while eliminating solid waste management problem which solves the land shortage problem and that extra land can be used to any fruitful work without Solid Waste Management that land is wasted as huge piles of solid waste just cover land making them useless and toxic. Also leachate problem is solved by waste management as open dump cause leachate to develop which even pollute the underground water. None of the single solution is capable of solving the entire solid waste management problem, although by favourable use of methodology of combined technologies- decrease at source, reutilizing, composting and incineration can be supportive. Decreasing the waste generation at source level only. Recycling & reprocessing new materials from used matter like paper, plastics, metals, glass, etc. By decomposing organic matter like kitchen waste, food waste in aerobic or anaerobic way compost can be prepared which further can be utilized as a fertilizer for soil. Combustion of waste in presence of air at high temperatures in Incinerator technology, it lowers the volume of waste up to 90%. Therefore, landfill can be avoided completely by above technologies. But from decades in India definition of energy means electricity and scarcity of electricity creates hindrance to growth and development so Anaerobic Digestion should be used for solid waste management as it provides all kind of process- reduce, recycle and regeneration.

REFERENCES

[1]. MufeedSharholy, k. A. (2007). Municipal solid waste characteristics and management in Allahabad, India. Waste Management, 490-496.

[2]. Tsai, W.-T. (2014). Analysis of Municipal solid waste incineration plants for promoting power generation efficiency in Taiwan. Master Cycles Waste Management.

[3]. S Rathi, D. P. (2014). Electrical Energy Recovery from Municipal Solid Waste of Kanpur City. International Journal of Scientific Research Engineering & technology (IJSRET), 923-929.

[4]. NIE, Y. (2008). Development and prospects of municipal solid waste (MSW) incineration in China. Environment Science Engineering China, 1-7.

[5]. Ojha, K. (2011). Status of MSW management system in northern India-an overview. Environmental Development Sustainable, 203-215.

[6]. Arena, U. (2015). From waste-to-energy to waste-to-resources: The new role of thermal treatments of solid waste in the Recycling Society Waste Management.

[7]. Ityona Amber, D. M. (2012). Generation, characteristics and energy potential of solid municipal waste in Nigeria. Journal of Energy in South Africa, 47-51.

[8]. VikashTalyan, R. P. (2008). Status of municipal solid waste management in Delhi, the capital of India. Waste Management, 1276-1287.

[9]. V G Sister, L. V. (2006). Ways of improving the performance of energy producing equipment at waste incineration plant. Chemical and Petroleum Engineering, 3-4.

Waste Biomass Valor
DOI 10.1007/s12649-016-9658-2

ORIGINAL PAPER

Experimental Investigations of Performance and Emissions Characteristics of Kusum (*Schleichera Oleosa*) Biodiesel in a Multi-Cylinder Transportation Diesel Engine

Ashok Kumar Yadav[1] · Mohd Emran Khan[2] · Amit Pal[3] · Alok Manas Dubey[1]

Received: 12 March 2016 / Accepted: 16 August 2016
© Springer Science+Business Media Dordrecht 2016

Abstract In the present work, an underutilized and promising feedstock, Kusum seed oil (KSO) is converted into biodiesel through transesterification process. The physico-chemical properties of Kusum biodiesel (Kusum oilmethyl ester; KOME), measured via standard methods, were well within the ASTM D6751/EN14214 standard limits. After that, experiments were conducted using various blends (B5, B10, B15, and B20) of methyl ester of KSO with diesel in a multi cylinder diesel engine at varying engine speeds, ranging from 1000 to 4000 rpm under full load conditions. Engine performance (brake power, brake specific fuel consumption, brake specific energy consumption and brake thermal efficiency) and emissions (CO, HC, NO_x and smoke opacity) were measured to analyse the behavior of the diesel engine running on biodiesel. The test results showed that with the increase of biodiesel in the blends CO, HC and smoke opacity reduces significantly while fuel consumption and NO_x emission of biodiesel increases slightly compared with diesel. Brake specific energy consumption decreases and thermal efficiency of engine slightly increases when operating on 10 % biodiesel than that operating on diesel. It may be concluded from the experimental investigations that Kusum biodiesel is a potential alternative to diesel fuel.

Keywords Multi cylinder diesel engine · Kusum oil biodiesel(KOME) · Performance and emissions

Abbreviations

KOME	Kusum oil methyl ester
B100	Neat biodiesel
B0	Neat diesel
B05	Blend of 05 % KOME and 95 % diesel
B10	Blend of 10 % KOME and 90 % diesel
B15	Blend of 15 % KOME and 85 % diesel
B20	Blend of 20 % KOME and 80 % diesel
CO	Carbon monoxide
UHC	Unburnt hydrocarbons
NO_x	Oxides of nitrogen
BTE	Brake thermal efficiency
BSFC	Brake specific fuel consumption
BSEC	Brake specific Energy consumption
Ppm	Parts per million
cSt	Centi-Stoke
kWh	Kilo-watt-hour
RPM	Rotations per minute

Introduction

The petroleum reserves are diminishing day by day. There has been an increase in effort to reduce the dependence on petroleum fuel for energy generation and transportation and attention is being focussed on alternate fuel. Biodiesel

✉ Ashok Kumar Yadav
ashokme014@gmail.com

Mohd Emran Khan
mikhan@jmi.ac.in

Amit Pal
amitpal@dce.ac.in

[1] Department of Mechanical Engineering, Raj Kumar Goel Institute of Technology, Ghaziabad 201003, India

[2] Department of Mechanical Engineering, Faculty of Engineering and Technology, Jamia Millia Islamia, New Delhi 110025, India

[3] Department of Mechanical Engineering, Delhi Technological University, Delhi 110042, India

Published online: 25 August 2016

is one of the best alternatives to petro–diesel [16]. Biodiesel is defined as mono-alkyl esters of vegetable oils or animal fats, obtained by transesterification of an oil or fat with an alcohol [24, 47]. Currently, more than 95 % of the world biodiesel is produced from edible vegetable oils such as rapeseed, soybean palm and sunflower oils. Since these edible vegetable oils are also used as food, their extensive use to produce biofuel can lead to food shortage. In order to avoid this conflict between energy and food demand, in recent years, the research has been shifted to produce biodiesel from non-edible resources such as Jatropha, Neem, Kusum, Yellow Oleander and Karanja oil [5].

Substantial research work related to the production and performance of biodiesel derived from variety of vegetable oils has been carried out. [11] investigated the production and performance of WCO biodiesel. Compared to diesel, the BSFC of B100 and its blends washigher with a noticeable increase when the blend ratio was raised from 50 to 100 %. [13] reported maximum torque for 10 and 20 % KOME blends which were higher than mineral diesel. Similarly, Raheman and Ghadge [36] compared the performance of Mahua bio diesel and its blends with petroleum based diesel. [25] have also reported a reduction in UHC and CO emissions but increased NO_x emission. [30] reported an optimum yield of C. inophyllum biodiesel at 9:1 methanol to oil ratio with 1 wt%. NaOH catalyst at 50 °C for 2 h. The performance and emission of 10 % C. inophyllum biodiesel blends (CIB10) gave a satisfactory result in diesel engines. Pali et al. [33] investigated the effect of Kusum biodiesel on an agricultural diesel engine and found that at full load, brake thermal efficiency dropped by 3.8 to 17 %, with increase of KB in the test fuel. Hydrocarbon and carbon monoxide emissions along with smoke opacity at full load were reduced by 7–42 %. However, emissions of oxides of nitrogen were found to increase marginally by 4–20 % as compared to D100. [18] optimized the production and performance of biodiesel from waste cooking oil, using RSM optimal input parameters and concluded that, CR = 17.99, IP = 250 bar and IT = 27 °C BTDC. [2] established that exergetic parameters were greatly influenced by engine speed and load and a significant reduction in emissions was obtained by adding soluble catalyst nanoparticles to diesel/biodiesel blends. It was concluded that the diesel/biodiesel blends containing amide-functionalized MWCNTs-CeO_2 catalyst might replace pure diesel fuel without any unfavorable change in the exergetic performance parameters of the DI engines. [4] prepared biodiesel from Palm kernel oil (PKO). The percentage yields of biodiesel obtained from PKO catalysed by CPA and KOH were 94 and 90 %, respectively. This investigation suggests that agricultural residues could be utilized in place of conventional catalysts. [26] used CaO/SiO_2, MgO/SiO_2 and BaO/SiO_2 as catalysts for biodiesel production from corn oil. A transesterification reaction was carried out after 8 h by mixing corn oil, methanol (methanol to oil molar ratio of 16:1) and 6 wt% catalyst at 60 °C and 600 rpm. Catalyst loading ranged from 40, 60 to 80 %. The yield of biodiesel for 60 % CaO/SiO_2 was higher than other catalysts. [28] produced biodiesel from waste cooking oil and the reaction was carried out for molar ratios of 24:1 and 22.5:1 in presence of 12 and 9.08 wt% of mussel shell-based, DM water treated precipitate-based catalysts. The effects of temperature (328, 333, 338, 343 and 348 K) and time (1, 3, 5, 7 and 8 h) at a stirrer speed of 350 rpm on the conversion of oil into biodiesel were investigated. The results obtained indicated a pseudo first order kinetics for the transesterification reactions. The activation energies in the presence of the DM water treated precipitate and mussel shell catalysts were 77.09 and 9.83 kJ mol^{-1} respectively. Accordingly, the DM water treated precipitate catalyst resulted in a faster reaction due to its lower activation energy. The catalysts were reused five times and the results showed that the methanol-driven extraction of CaO, contained in the DM water treated precipitate catalyst was lower than with waste mussel shell catalyst proving the higher stability of the new heterogeneous catalyst i.e. the calcinated DM water treated precipitates. [6] reported the production and characterization of Manketti methyl ester and its blends with diesel. The kinematic viscosity of biodiesel was found to be 8.34 mm^2/s, which was higher than the limit described by ASTM D6751 and EN 14214. This can be attributed to the high kinematic viscosity of the parent oil (132.75 mm^2/s). Nevertheless, blending with diesel improved this attribute. Moreover, it is observed that at all engine speeds, B5 produced lower brake power (1.18 %) and higher brake specific fuel consumption (2.26 %) compared to B0 (neat diesel). Compared to B0, B5 increased the CO and HC emissions by 32.27 and 37.5 %, respectively. However, B0 produced 5.26 % higher NO emissions than B5. [3] produced biodiesel from waste oil extracted from spend bleaching earth (SBE). The engine tests revealed that the exergetic parameters strongly depend on the engine speed and load. Generally, increasing engine speed remarkably decreased the exergy efficiency and sustainability index of the diesel engine. The maximum exergy efficiency and sustainability index of the diesel engine (i.e. 40.21 % and 1.67, respectively) were achieved by using B5 containing 50 g EPS/L biodiesel. Generally, the approach presented herein could be a promising strategy for energy recovery, emission reduction and performance improvement.

Apart from feedstock discussed in above literature, there may be many other feed stocks which are yet to be explored for biodiesel production and use as a fuel in diesel engine. If 10 % of diesel is to be substituted with fuel

derived from plant sources, then production of biodiesel from all potential sources is very essential. Existing sources such as Jatropha, Karanja etc. alone will not be sufficient to meet this huge biodiesel requirement.

Kusum (Schleichera oleosa) seeds could be a potential feedstock for biodiesel production in India which has an estimated annual production potential of 66 thousand tons per year in India [32]. *Schleichera oleosa* belonging to Sapindaceae family and also known as Kusum fruit. *S. oleosa* widely found in the sub-Himalayan region, throughout central and Southern India, Burma, Ceylon, Java and Timor. The flowers are yellowish green, fascicled in spike like axillary racemes 7.5–12.5 cm long. The fruits are berry shaped, globose or ovoid with a hard skin [15]. The seeds are brown, irregularly elliptic, slightly compressed, oily and enclosed in a succulent aril [8]. The oil content of the seed is around 59–72 % [40]. Figure 1 presents the plants of *S. Oleosa*, its seeds and oil.

In India, this plant has proved to be useful in several ways since ancient times. Its leaves, twigs and seed-cake are used as fodder to feed cattle. The wood is suitable for use as firewood and makes excellent charcoal. The oil extracted from the seed, called 'Kusum oil' is bitter in taste and not considered to be edible. In India this oil is generally used for soap making. The oil is also used for culinary, lighting purposes, lubrication, cure of itching, acne, burns, rheumatism (external massage), hair dressing and for promoting hair growth [15, 41]. The pinkish-brown heartwood is very hard, durable and excellent to make pestles, cartwheels, axles, ploughs, tool handles and rollers for sugar mills and oil presses. In India, it is used as host for the lac insect. In parts of southern India, it is a prominent bee plant for nectar [19]. It is used as a traditional medicine. The powdered seeds are applied to wounds and ulcers of cattle to remove maggots.

However no substantial work has been reported in literature on utilization of Kusum oil as a fuel for a CI engine. Significant work has been done on stationary diesel engines [1, 18, 22, 38, 39, 42, 45, 46] while limited work has been done on transportation engine [12, 13]. Therefore present study focuses on the experimental study of this fuel on a transportation engine. The objective of the present study is (1) To study the prospect of biodiesel production from Kusum seed oil (2) To evaluate the fatty acid composition of the Kusum seed oil (3) To determine the fuel properties of both the Kusum seed oil and it's biodiesel and (4) To carry out a performance test on a multi cylinder transportation diesel engine to investigate the behavior of Kusum biodiesel.

Materials and Methods

Kusum (Schleichera oleosa) oil used for biodiesel production in the present study was purchased from an oil industry in Delhi (India) and petro–diesel was purchased from a nearby petrol pump. Anhydrous methanol (99.8 % min.), Sulphuric acid (99 % min.) and Potassium hydroxide (85 % min.) was purchased from a chemical store.

Production and Characterization of KOME and Preparation of Blends

Biodiesel from Kusum oil was produced using transesterification process. Various steps of biodiesel production are shown in Figs. 2 and 3. In which, the triglycerides were reacted with methanol in presence of KOH as catalyst. The free fatty acid (FFA) content of the Kusum seed oil was more than 2 %, so a two stage transesterification process was used to produce Kusum oil methyl ester. The transesterification was conducted using 0.1 % (w/w) Potassium hydroxide as catalyst, at 60 °C reaction temperature and 60 min reaction time with constant stirring at 350 rpm. The same process parameters were used to produce large quantity of biodiesel. The physico-chemical properties were evaluated for all test fuels. A maximum blending percentage of 20 % was selected for the present work on the basis of literature as higher percentage of KOME



Fig. 1 *Schleichera Oleosa* plant, seeds and oil

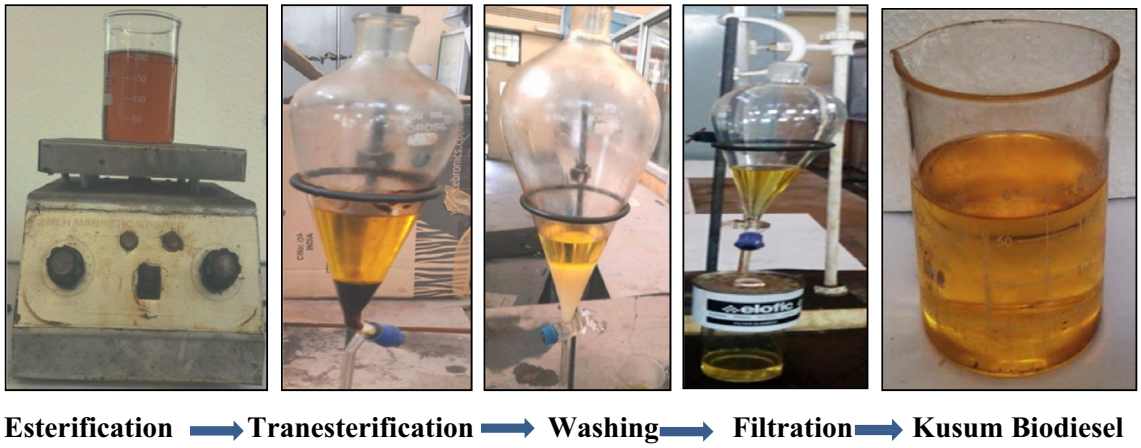


Fig. 2 Various steps of Kusum biodiesel production

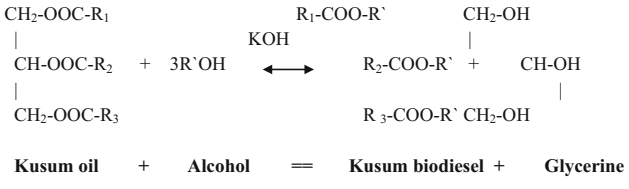


Fig. 3 Transesterification reaction

caused difficulties in engine operation. Four test fuel samples were prepared with 5, 10, 15 and 20 % of KOME with mineral diesel (v/v) and were designated as B5,B10, B15 and B20 respectively.

Experimental Engine Setup

The setup consists of a four cylinder, four stroke diesel engine connected to eddy current type dynamometer for load measurment. Rota meters are provided for cooling water and calorimeter water flow measurement. The line diagram of engine setup is shown in Fig. 4. The setup provides for the measurement of brake power, brake thermal efficiency, brake specific fuel consumption and brake specific energy consumption at different speeds, varying from 1000 to 4000 rpm at full load conditions. Windows based engine performance analysis software "Engine soft" is provided for on line performance evaluation. The technical specification of the test engine is presented in Table 1. The NO_x, HC, CO and smoke opacity were measured with AVL DIX (Emission Diagnostic System). The range and accuracy of measurements of AVL DIX emission diagnostic system is shown in Table 3.

Experimental Procedure

The engine was started by a battery with diesel as fuel and it was allowed to reach its steady state (for about 15 min).

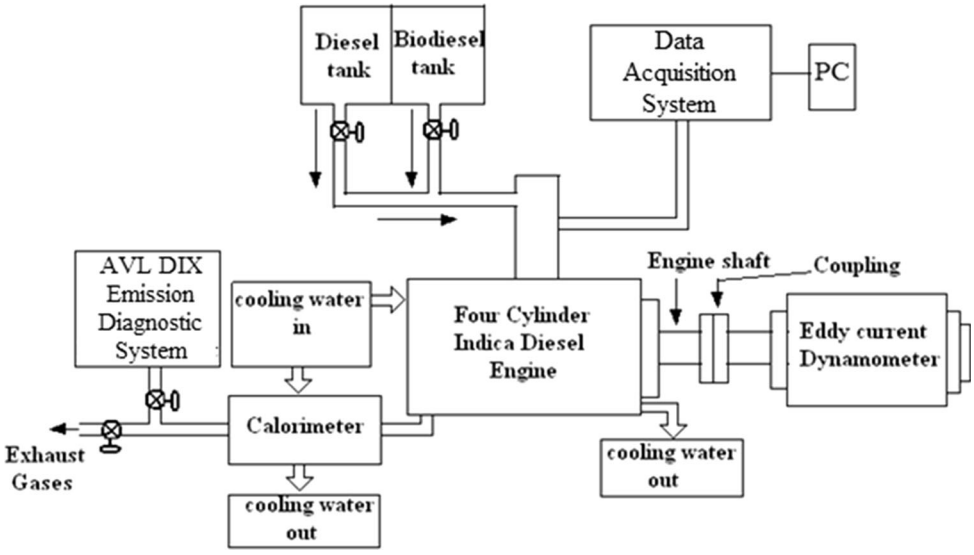


Fig. 4 Line diagram of experimental set up

Table 1 Technical specification of the test engine

Make	Telco, Model Tata Indica
Type	4 cylinder, 4 stroke, diesel water cooled
Rated Power	39 kW at 5000 rpm
Torque	85 Nm at 2500 rpm
Cylinder volume	1405 cc
Compression ratio	22:1
Dynamometer	Type eddy current, water cooled, with loading unit
Crank angle sensor	Resolution 1 deg., speed 5500 rpm
Load sensor	Load cell, type strain gauge, range 0–50 kg
Software	"Enginesoft" engine performance analysis software

Table 2 Range, accuracy and uncertainty of measurements

Measurements	Instrument	Range	Accuracy
Engine load	Strain gauge type load cell	0–25 kg	±0.1 kg
Speed	Speed sensor	0–10000 rpm	±20 rpm
Time	Stop watch	–	±0.5 %
Exhaust temperature	K-type thermocouple	0–1000 °C	±1 °C
Calculated results			Uncertainty
Engine power	–	0–50 kW	±1.0 %
Fuel consumption	Level sensor	–	±2.0 %
Air consumption	Turbine flow type	–	±1.0 %
BTE	–	–	±1.0 %
BSEC	–	–	±1.5 %

The engine was sufficiently warmed up and stabilized before taking all readings. The performance of the engine and emissions were studied at full throttle opening and variable speed (1000–4000 rpm) of the engine. After the engine stabilized, fuel consumption and brake power were measured and later brake specific fuel consumption, brake specific energy consumption and thermal efficiency were computed. The emissions parameter such as CO, HC, NO_x and smoke opacity were measured using an AVL DIX Emission analyzer. These performance and emission characteristics for different fuels are compared with that of baseline diesel. Each test was repeated thrice to obtaina reasonable value.

Statistical Analysis

The uncertainties and errors can arise from instrument selection, environmental conditions, calibration, testing and observations. Uncertainty, repeatability and random errors can be calculated analytically. An uncertainty analysis was performed using the technique described by J. P. Holman. The details of the instruments with their range, accuracy and uncertainty of measurements are given in Tables 2 and 3. The percentage of uncertainty in this experiment can be calculated as given below. The total percentage uncertainty = Square root of $[(\text{uncertainty of BP})^2+(\text{uncertainty of BSFC})^2+(\text{unc}(\text{ertainty of TFC})^2+(\text{uncertainty of BTE})^2+(\text{uncertai}(\text{nty of HC})^2+(\text{uncertainty of CO})^2+(\text{uncertainty of } NO_x)^2+(\text{Smoke opacity})^2+(\text{uncertainty of pressure pick up})^2+(\text{crank angle encoder})^2] = \pm 2.15\,\%$Due to uncertainties and errors associated with instrument, statistical analysis is required to prove the accuracy of the data. Statistical analysis was carried out by applying two-tailed Student's t test for independent variables to test for significant differences between samples set means using Microsoft Excel 2010. Differences between mean values for $p = 0.05$ (95 % confidence level) were considered statistically significant.

Results and Discussion

Fatty Acid Composition of Kusum Oil

Fatty acid compositions of Kusum seed oil were determined using GC-FID (Gas chromatography with flame ionization detector). For this analysis 0.2 µg of Kusum seed oil sample was injected into the GC chamber equipped with a split/split-less injection port. The split ratio was 50/1 and the injector and detector were maintained at 350 °C. Pure Nitrogen was used as a carrier gas for a flow rate of

Table 3 AVL DIX emission diagnostic system specifications

Exhaust emissions	Measurement range	Resolution	Accuracy
CO	0–10 vol. %	0.01 vol. %	<0.6 % vol.: ± 0.03 % vol
HC	0–20,000 ppm	<2000: 1 ppm vol.	<200 ppm vol.: ± 10 ppm
	>2000: 10 ppm		Vol. P200 ppm vol.: ± 5 % of ind. val
CO_2	0–20 vol. %	0.1 vol. % < 10 %	Vol.: ± 0.5 % vol
NO	0–5000 ppm	1 ppm vol.	<500 ppm vol.: ± 50 ppm vol
Opacity	0–100 %	0.001	±2 %

8 ml/min. The percentage compositions (wt%) of the individual acids were computed. The fatty acid profile of Kusum seed oil is reported in Table 4. The fatty acids composition indicate that the oil was rich in Oleic (48.51 %) and Arachidic acid (27.21 %).

Physico-Chemical Properties of Kusum Oil

Physico-chemical properties of Kusum oil and its biodiesel were determined according to standard methods. Table 5 presents the average values of physico-chemical properties of Kusum biodiesel, diesel and their blends. The obtained results show that all these properties are acceptable and conform to ASTM D6751 and EN 14214 standards.

Result of the Performance Testing

Figures 5, 6, 7, 8, 9, 10, 11, 12 shows the variation of performance and emission parameters with respect to speed/engine RPM. The fuels tested were diesel, B5, B10, B15, B20 blends of Kusum biodiesel and petro–diesel. The performance parameters include brake power, brake specific fuel consumption, brake specific energy consumption and brake thermal efficiency whereas the emission parameters include percentage of carbon monoxide, hydrocarbon, oxides of nitrogen and smoke opacity. All observations were taken for a speed range of 1000–4000 rpm at an increment of 500 rpm. The variation of engine performance parameters has been explained subsequently.

Table 4 Fatty acid composition of Kusum oil

Fatty acids	Chemical formula	Degree of unsaturation	Kusum oil
Palmitic	$C_{16}H_{32}O_2$	16:0	6.73
Palmitoleic	$C_{16}H_{30}O_2$	16:1	2.88
Stearic	$C_{18}H_{34}O_2$	18:1	5.81
Oleic	$C_{18}H_{32}O_2$	18:2	48.51
Linoleic	$C_{20}H_{40}O_2$	20:0	6.57
Arachidic	$C_{20}H_{38}O_2$	20:1	27.21
$\sum$ Saturated fatty acids			40.64
$\sum$ Unsaturated fatty acids			57.96

Brake Power Versus Engine RPM

The variation of brake power of Kusum biodiesel blends with engine speed is shown in Fig. 5. It is observed that for all speeds the power of diesel fuel is higher than biodiesel blends and the trend observed is similar. At all speed ranges the brake power is higher for B5 blend as compared to other biodiesel blends. This could be because the properties like viscosity, cetane number and calorific value of B5 is more or less compatible with the petro–diesel and are least affected as compared to other test fuel samples. It is observed that in comparison to petro–diesel there was a reduction in the brake power by 0.77, 1.62, 3.07 and 3.57 % for B5, B10, B15, and B20 respectively. These changes were significant for $0.01 < p < 0.03$. Hence it can be concluded that biodiesel has low heating value, (10 % lower than diesel) owing to presence of substantial amount of oxygen in the fuel but at the same time biodiesel has higher specific gravity (0.87) as compared to petro–diesel (0.82). Thus overall effect is approximately 5 % lower energy content per unit volume. Brake power for all blends increases in the range of 1000 to 3000 rpm. Beyond this, the BP decreased due to higher frictional force. Similar trend is reported by [12].

Brake Specific Fuel Consumption (BSFC) Versus Engine RPM

The BSFC can be defined as the ratio of mass of the fuel consumed to the brake power. Figure 6 shows the variation of BSFC for all test fuels as a function of engine speed under full load conditions. BSFC decreases with engine speed to a minimum value at 2000 rpm and then increases with an increase in engine speed due to the higher power output as confirmed by [30]. The decrease in BSFC is a result of better physical and chemical conditions for combustion at low engine speeds. The BSFC increased with the increase of biodiesel blends as reported by [14]. The increase of the specific fuel consumption for B5, B10, B15 and B20 relative to B0 is 5.59, 5.84, 6.94, and 7.33 %, respectively. From the percentage increase, it can be

Table 5 Physico-chemical properties of Kusum biodiesel and mineral diesel

Properties	Kusum oil	KOME	Diesel	Test method	ASTM D6751 limit of acceptance	EN 14214 limit of acceptance	Measurement apparatus
Density at 15 °C (g/cc)	0.88	0.87	0.82	ASTM D1298	0.88	860–900	Stabinger viscometer-SVM3000 (Anton Paar India Pvt. Ltd.)
Viscosity at 40 °C (cSt)	41.2	4.7	2.956	ASTM D445	1.9–6.0	3.5–5.0	Stabinger viscometer-SVM 3000
Flash point (°C)	223	152	61	ASTM D 92	Min. 130	Min. 120	Pensky–Martens closed cup apparatus
Fire point (°C)	229	156	63	ASTM D 92	–	–	Pensky–Martens closed cup apparatus
CFPP (°C)	–	−4.0	−8	ASTM D 6371	Max. 19	–	Automatic NTL 450 (Normalab, France)
Calorific value(MJ/kg)	37.8	39.45	43.32	ASTM D240	–	–	Parr 6100 calorimeter (IKA, UK)
Oxidation stability(h)	–	>6.5	–	EN 14112	–	Min. 3	873 Rancimat (Metrohm, Switzerland)

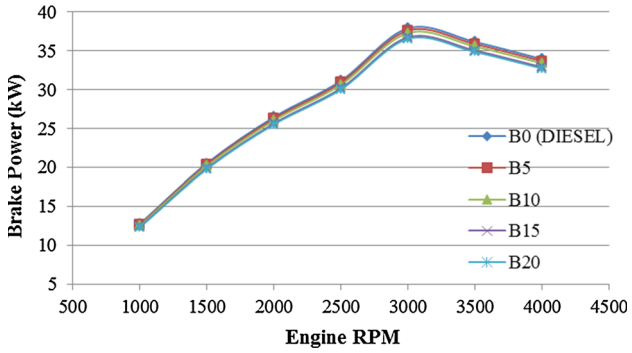


Fig. 5 Brake power versus engine RPM

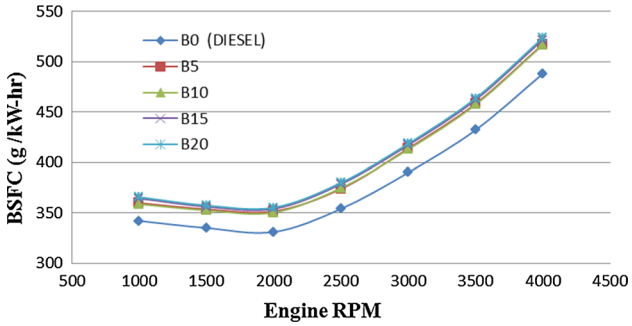


Fig. 6 Brake specific fuel consumption (BSFC) versus engine RPM

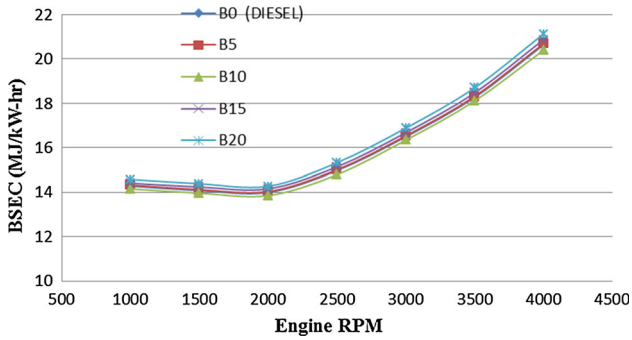


Fig. 7 Brake specific energy consumption (BSFC) versus engine RPM

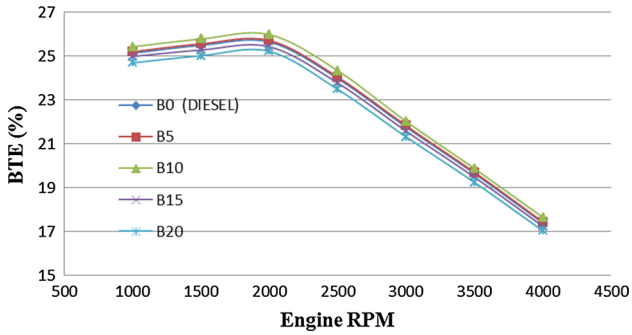


Fig. 8 Brake thermal efficiency versus engine RPM

marked that the B20 has the highest SFC and it consumes more fuel to produce 1 kW of power as compared to petro–diesel (B0). These changes compared with petro–diesel were significant for $0.01 < p < 0.02$. The higher SFC is due to the fact that biodiesel has a lower calorific value than the conventional petro–diesel. Moreover the density of Kusum oil is higher than the conventional diesel fuel, which gives the higher consumption. In addition, higher kinematic viscosity of biodiesel blends may cause poor atomization of the fuel and consequently poor mixing with air and result in higher BSFC as agreed well with [6]. [14] also found that the BSFC of biodiesel was higher compared

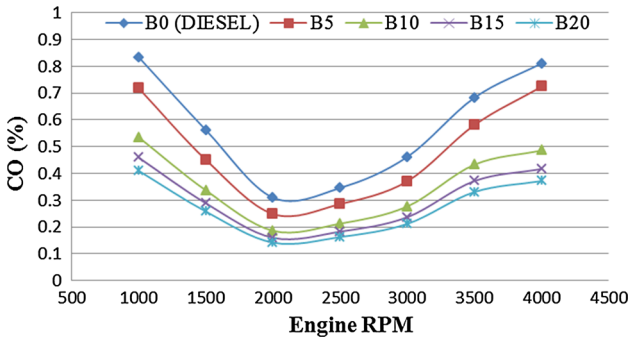


Fig. 9 Carbon monoxide versus engine RPM

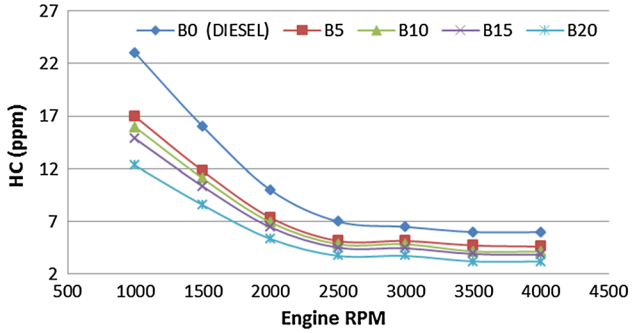


Fig. 10 Hydrocarbon versus engine RPM

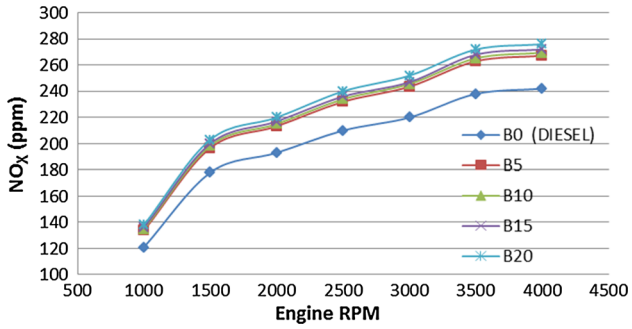


Fig. 11 Oxides of nitrogen versus engine RPM

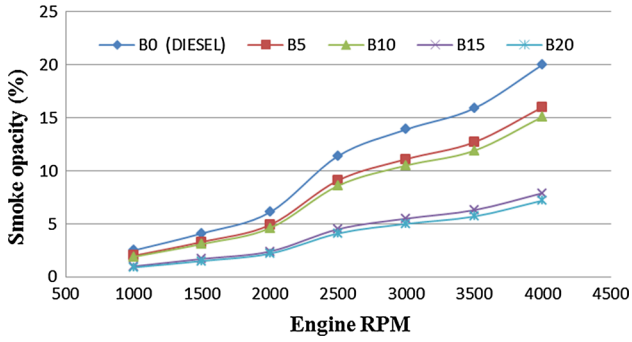


Fig. 12 Smoke opacity versus engine RPM

to diesel fuel due to the higher density, viscosity and lower calorific value. Previous researchers reported similar trends [29, 37, 39].

Brake Specific Energy Consumption (BSEC) Versus Engine RPM

BSFC and BSEC have the same significance when the fuel heating value is constant. However in the current work, as different blended fuels have different heating values, the use of BSEC would be more important to gain not only additional meaning about the fuel economy but also about the efficiency to convert its energy contents into useful power [1]. Figure 7 shows the variation of BSEC for different test fuels(B0, B5, B10, B15, and B20) with respect to engine speed at full load conditions. The variation of BSEC has a similar behavior as that of BSFC but the use of BSEC reflects the effect of changing the blended fuel heating value. Due to enhancement of combustion quality and the insignificant decrease in the heating value, the value of BSEC is lower for low blending ratio (B5 and B10) than that for neat diesel. BSEC for B10 is 13.85 MJ/kW h compared to 14.03 g/kW h for diesel fuel at 2000 rpm. These changes were significant for $0.01 < p < 0.02$. B5 and B10 show slightly lower BSEC than diesel fuel due to the presence of dissolved oxygen in the KOME that enables complete combustion and the negative effect of increased viscosity could not have be initiated. Besides, the BSEC of B15, and B20 was higher than B5, B10 and diesel fuel due to higher viscosity, density and lower volatility of these blends. This resulted in higher amount of fuel injected than the diesel fuel, which affects the formation of mixture and leads to more dominating diffusion combustion phase. The increased BSEC was also attributed to the higher density of Kusum biodiesel that led to higher discharge of fuel for the same displacement of the plunger in the fuel pump, thereby increasing the BSEC [14]. The other reason for low BSEC for lower blending ratios (B5 and B10) than diesel and higher for higher blending ratios (B15, and B20) could be the lower calorific value with increase in biodiesel percentage in the blends. At full load condition, the BSEC decreases with engine speed to a minimum value at 2000 rpm and then increases with an increase in engine speed. This is because the heat loss from the combustion chambers walls is proportionately greater at low speeds. The decrease in BSEC is a result of better physical and chemical conditions for combustion at low engine speeds. Similar trends of BSEC decrease with lower biodiesel blends ratio were also reported by other researchers [1, 42].

Brake Thermal Efficiency Versus Engine RPM

Brake thermal efficiency is the ratio between work output and the heat added through fuel injection. The percentage variation in the brake thermal efficiency of biodiesel blends at various speeds as compared to diesel is shown in Fig. 8. Almost similar behaviour of BTE with the diesel fuel for all biodiesel blends and neat diesel can be observed. The

maximum BTE values for all blends and diesel fuel were at 2000 rpm which decreased with further increase in engine speed up to 4000 rpm. B10 has lower viscosity and higher volatility compared to B15 and B20. This enhances the fuel atomization leading to improved air fuel mixing. Therefore, the thermal efficiency for B15 and B20 are lower than B5 and B10. This implies that fuel atomization characteristics are different in blends with higher ratios of biodiesel. It is clearly shown that BTE is inversely proportional to BSEC. This conforms with the observation of [42]. The maximum BTE values for biodiesel blends B5, B10, B15 and B20 were 25.71, 25.99,25.43 and 25.22 % respectively as compared to 25.651 % for diesel fuel at an engine speed of 2000 rpm, These changes were significant for $0.01 < p < 0.03$. B15 and B20, showed lower performance as compared to diesel due to the presence of oxygen and increase in fuel supply to the combustion chamber. This resulted in hindering the combustion phenomenon as explained by [48].

Result of the Emission Testing

Carbon Monoxide Versus Engine RPM

Carbon monoxide is formed during the combustion process with rich fuel–air mixture when there is insufficient oxygen to completely burn the carbon present in the fuel. The variations of CO produced by running the diesel engine using dieselfuel and biodiesel blends at various speeds are shown in Fig. 9. A similar trend was observed for CO in biodiesel blends and diesel fuel. From Fig. 9 it can be stated that the reduction in the percentage of CO is maximum in the case of B20 blend at 2000 rpm. The CO emission was 0.31, 0.249, 0.186, 0.16 and 0.142 % for diesel, B5, B10, B15 and B20 blends respectively. CO emission of all biodiesel blends (B5, B10, B15 and B20) was lower than diesel fuel. This was due to biodiesel blends containing more oxygen element, which gave better combustion phase [11]. High oxygen content resulted in higher combustion temperature, which facilitated more complete combustion and greater CO conversion into CO_2 as compared to diesel fuel as explained by [13]. It can be observed from Fig. 9 that the percentage of carbon monoxide initially decreased with speed up to 2000 rpm and then increased. This may be due to the increased fuel- air ratio at higher speeds when larger quantities of fuel are injected into the combustion chamber, a large amount of which goes unburnt into the exhaust. Similar findings were also reported by previous researchers [7, 9, 44] while testing different biodiesels.

Hydrocarbon Versus Engine RPM

A sample of diesel exhaust may be free from unburned hydrocarbons or can have heavy concentration depending on the engine type. Figure 10 shows the HC emissions for all the blended and petro–diesel fuel. The B20 produced the lowest HC emission (3 ppm) at 4000 rpm, followed by B15 (4 ppm) and B0 (6 ppm). Previous researchers have also reported that the engine fuelled with biodiesel could reduce the HC emission [20, 29, 35]. The reduction of the hydrocarbons in CI engines was due to a lower carbon to hydrogen ratio and presence of 11 % oxygen in its molecular structure. Hence, it could be stated that B20 fuel with the conventional petro–diesel could be an alternative fuel for diesel engines because it reduced the emission levels of HC.

Oxides of Nitrogen Versus Engine RPM

High peak temperature and availability of oxygen are two main reasons for the formation of NO_x. The variation of NO_x emissions against engine speed is shown in Fig. 11. From figure, it is apparent that NO_x emissions increased with the increase in engine speed. The NO_x emissions from biodiesel blends are found to be higher than those from diesel fuel. The average NO_x emission values for B0, B5, B10, B15 and B20 blends were 200, 221, 223, 225 and 228 ppm respectively. An ascending trend for NO_xemission was observed with increasing biodiesel blend ratio. This can be primarily due to an increase in volumetric efficiency and gas flow motion within the engine cylinder at higher engine speeds and higher loads, which led to a faster mixing between fuel and air and hence shorter ignition delay [23, 44]. Moreover, the problem of increased NO_x emission can be effectively tackled by retarding the fuel injection timing. Other researchers have also reported that NO_x emissions increased in a similar range [36] if biodiesel is used. The main reasons for higher NO_x emissions with an increase in biodiesel content could be due to the advance injection and advance combustion, as a result of its higher viscosity [21, 22, 45, 46]. Higher oxygen content enhances NO_x formation [45] and a higher cetane number shortens ignition delay and advances the combustion [27].

Smoke Opacity Versus Engine RPM

Smoke opacity is a direct measure of smoke and soot. The variation of smoke opacity with engine speed for Kusum biodiesel blends is shown in Fig. 12. It was observed that smoke opacity for, B5, B10, B15 and B20 was 7.2, 7.9, 15.1 and 16 % respectively at 4000 rpm. However, the highest smoke opacity was found 20 % for diesel fuel at the same speed. The Kusum biodiesel blended fuel has lower smoke opacity than diesel because of the oxygen content present in biodiesel blends. This is agreed with [36] which reported that smoke emissions for biodiesel diesel blends decreased due to the enrichment of oxygen content in the fuel. Besides, many researchers agreed that

the rich oxygen content in biodiesel will reduce smoke opacity [10, 34]. Another reason for smoke emissions reduction for biodiesel is because lower carbon to hydrogen ratio and absence of aromatic compounds as compared to diesel fuel. The lower carbon molecule and higher oxygen content can decrease the tendency of a fuel for soot production and reduce smoke opacity as observed by [31]. It was agreed by [17] that biodiesel contains rich in oxygen can decrease smoke formation. [48] observed that start of combustion for biodiesel blends is earlier than diesel. The result indicated that earlier start of combustion for biodiesel blends and advanced injection timing can reduce the smoke emission. High smoke opacity of diesel fuel was due to higher sulfur content compared to biodiesel [43]. It can also be interpreted that smoke level increased sharply with increase in speed beyond 2000 rpm for all tested fuels. It was mainly due to the decreased air–fuel ratio at higher loads when larger quantities of fuel are injected into the combustion chamber. Diesel has more smoke density in comparison to all tested fuels, which might be attributed to the relatively improved burning characteristics of biodiesel at elevated temperatures for higher loads.

Conclusions

In the present research work biodiesel is produced from Kusum oil and its physico-chemical characteristics were determined. The properties of KOME produced conform to both standards of EN 14214 and ASTM D 6751. Besides, it has been found that B10 blend of KOME gave good improvement in the engine performance with higher BTE from the engine performance test results. On the other hand, there is an improvement in fuel economy with lower BSEC by using B10 compared to diesel fuel. Furthermore, all biodiesel blends (B5, B10, B15 and B20) reduced the CO, HC and smoke opacity compared to diesel fuel but NO_x emission is slightly increased. The experimental results proved that Kusum biodiesel/diesel blends can be used effectively in diesel engine without modification. Finally, further studies on storage stability of biodiesel, tribology and fuel economy need to be carried out before the Kusum biodiesel/diesel blends can be used commercially in future.

References

1. Agarwal, D., Agarwal, A.K.: Performance and emissions characteristics of Jatropha oil (preheated and blends) in a direct injection compression ignition engine. Appl. Therm. Eng. **27**, 2314–2323 (2007)
2. Aghbashlo, M., Tabatabaei, M., Mohammadi, P., Mirzajanzadeh, M., Ardjmand, M., Rashidi, A.: Effect of an emission reducing soluble hybrid nanocatalyst in diesel/biodiesel blends on exergetic performance of a DI diesel engine. Renew. Energy **93**, 353–368 (2016)
3. Aghbashlo, M., Tabatabaei, M., Mohammadi, P., Pourvosoughi, N., Nikbakht, A.M., Goli, S.A.H.: Improving exergetic and sustainability parameters of a DI diesel engine using polymer waste dissolved in biodiesel as a novel diesel additive. Energy Convers. Manag. **105**, 328–337 (2015)
4. Aladetuyi, A., Olatunji, G.A., Ogunniyi, D.S., Odetoye, T.E.: Production and characterization of biodiesel using palm kernel oil, fresh and recovered from spent bleaching earth. Biofuel Res. J. **4**, 134–138 (2014)
5. Atabani, A.E., Silitonga, A.S.: Non-edible vegetable oils: a critical evaluation of oil extraction fatty acid compositions, biodiesel production, characteristics, engine performance and emissions production. Renew. Sustain. Energy Rev. **18**, 211–245 (2013)
6. Atabani, A.E., Mofijur, M., Masjuki, H.H., Badruddin, I.A., Chong, W.T., Cheng, S.F., Gouk, S.W.: A study of biodiesel production and characterization of Manketti (Ricinodendron rautonemii) methyl ester and its blends as a potential biodiesel. Biofuel Res. J. **4**, 139–146 (2014)
7. Bhale, P.V., Deshpande, N.V., Thombre, S.B.: Improving the low temperature properties of biodiesel fuel. Renew. Energy **34**, 794–800 (2009)
8. Bhatia, H., Kaur, J., Nandi, S., Gurnani, V., Chowdhury, A., Reddy, P.H., et al.: A review on *Schleichera oleosa*: pharmacological and environmental aspects. J. Pharm. Res. **6**(1), 224–229 (2013)
9. Carraretto, C., Macor, A., Mirandola, A., Stoppato, A., Tonon, S.: Biodiesel as alternative fuel: experimental analysis and energetic evaluations. Energy **29**, 2195–2211 (2004)
10. Chattopadhyay, S., Sen, R.: Fuel properties, engine performance and environmental benefits of biodiesel produced by a green process. Appl. Energy **105**, 319–326 (2013)
11. Cheikh, K., Sary, A., Khaled, L., Abdelkrim, L., Mohand, T.: Experimental assessment of performance and emissions maps for biodiesel fueled compression ignition engine. Appl. Energy **161**, 320–329 (2016)
12. Chuah, L.F., Rashid, A., Aziz, A., Yusu, S., Bokhari, A., Jarom, J., Abdullah, K.Z.: Performance and emission of diesel engine fuelled by waste cooking oil methyl ester derived from palm oil using hydrodynamic cavitation. Clean Technol. Environ. Policy **17**(8), 2229–2241 (2015)
13. Dhar, A., Agarwal, A.K.: Performance, emissions and combustion characteristics of Karanja biodiesel in a transportation engine. Fuel **119**, 70–80 (2014)
14. Dhar, A., Kevin, R., Agarwal, A.K.: Production of biodiesel from high-FFA neem oil and its performance, emission and combustion characterization in a single cylinder DICI engine. Fuel Process. Technol. **97**, 118–129 (2012)
15. Gandhi, M., Ramu, N., Raj, S.B.: Methyl ester production from Schlichera oleosa. Int. J. Pharm. Sci. Res. **2**(5), 1244–1250 (2011)
16. Giakoumis, E.G., Rakopoulos, C.D., Dimaratos, A.M., Rakopoulos, D.C.: Exhaust emissions of diesel engines operating under transient conditions with biodiesel fuel blends. Prog. Energy Combust. **38**, 691–715 (2012)
17. Gumus, M., Kasifoglu, S.: Performance and emission evaluation of a compression ignition engine using a biodiesel (apricot seed kernel oil methyl ester) and its blends with diesel fuel. Biomass Bioenergy **34**, 134–139 (2010)
18. Hirkude, J.B., Padalkar, A.S.: Performance optimization of CI engine fuelled with waste fried oil methyl ester-diesel blend using response surface methodology. Fuel **119**, 266–273 (2014)

19. Jhansi, P., Kalpana, T.P., Ramanujan, C.G.K.: Apidologie **25**, 289–296 (1994)
20. Karavalakis, G., Stournas, S., Bakeas, E.: Light vehicle regulated and unregulated emissions from different biodiesels. Sci. Total Environ. **407**, 3338–3346 (2009)
21. Labeckas, G., Slavinskas, S.: The effect of rapeseed oil methyl ester on direct injection diesel engine performance and exhaust emissions. Energy Convers. Manag. **47**, 1954–1967 (2006)
22. Lapuerta, M., Armas, O., Rodríguez-Fernández, J.: Effect of biodiesel fuels on diesel engine emissions. Prog. Energy Combust. Sci. **34**, 198–223 (2008)
23. Lin, C.Y., Lin, H.A.: Diesel engine performance and emission characteristics of biodieselproduced by the peroxidation process. Fuel **85**, 298–305 (2006)
24. Maleki, E., Aroua, M.K., Sulaiman, N.M.N.: Improved yield of solvent free enzymatic methanolysis of palm and jatropha oils blended with castor oil. Appl. Energy **104**, 905–909 (2013)
25. Mofijur, M., Masjuki, H.H., Kalam, M.A., Atabani, A.E.: Evaluation of biodiesel blending, engine performance and emissions characteristics of Jatropha curcas methyl ester: Malaysian perspective. Energy **55**, 879–887 (2013)
26. Mohadesi, M., Hojabri, Z., Moradi, G.: Biodiesel production using alkali earth metal oxides catalysts synthesized by sol-gel method. Biofuel Res. J. **1**, 30–33 (2014)
27. Monyem, A., Van Gerpen, J.H.: The effect of biodiesel oxidation on engine performance andemissions. Biomass Bioenergy **20**, 317–325 (2001)
28. Moradi, G.R., Mohadesi, M., Ghanbari, M., Moradi, M.J., Hosseini, Sh., Davoodbeygi, Y.: Kinetic comparison of two basic heterogenous catalysts obtained from sustainable resources for transesterification of waste cooking oil. Biofuel Res. J. **6**, 236–241 (2015)
29. Nabi, N., Mustafizur, R., Shamim, A.: Biodiesel from cotton seed oil and its effect on engine performance and exhaust emissions. Appl. Therm. Eng. **29**, 2265–2270 (2009)
30. Ong, H.C., Masjuki, H.H., Mahlia, T.M.I., Silitonga, A.S., Chong, W.T., Leong, K.Y.: Optimization of biodiesel production and engine performance from high free fatty acid Calophyllum inophyllum oil in CI diesel engine. Energy Convers. Manag. **81**, 30–40 (2014)
31. Pal, A., Verma, A., Kachhwaha, S.S., Maji, S.: Biodiesel production through hydrodynamic cavitation and performance testing. Renew. Energy **35**, 619–624 (2010)
32. Palanuvej, C., Vipunngeun, N.: Fatty acid constituents of *Schleichera oleosa* (Lour) Oken seed oil. J Health Res. **22**, 203–212 (2008)
33. Pali, H., Kumar, N., and Mishra, C. "Some experimental studies on combustion, emission and performance characteristics of an agricultural diesel engine fueled with blends of Kusum oil methyl ester and diesel," SAE Technical Paper 2014-01-1952, 2014, doi:10.4271/2014-01-1952
34. Panwar, N.L., Shrirame, H.Y., Rathore, N.S., Jindal, S., Kurchania, A.K.: Performance evaluation of a diesel engine fueled with methyl ester of castor seed oil. Appl. Therm. Eng. **30**, 245–249 (2010)
35. Puhan, S., Vedaraman, N., Sankaranarayanan, G., Ram, B.V.B.: Performance and emission study of Mahua oil (madhuca indica oil) ethyl ester in a 4-stroke natural aspirated direct injection diesel engine. Renew. Energy **30**, 1269–1278 (2005)
36. Raheman, H., Ghadge, S.V.: Performance of compression ignition engine with mahua (Madhuca indica) biodiesel. Fuel **86**, 2568–2573 (2007)
37. Rao, G.L.N., Prasad, B.D., Sampath, S., Rajagopal, K.: Combustion analysis of diesel engine fueled with jatropha oil methyl ester diesel blends. Int. J. Green Energy **4**(6), 645–658 (2009)
38. Sahoo, P.K., Das, L.M., Babu, M.K.G., Naik, S.N.: Biodiesel development from high acid value polanga seed oil and performance evaluation in a CI engine. Fuel **86**, 448–454 (2007)
39. Sharanappa, G., Murthy, C.H.S., Reddy, R.P.: 6BTA 5.9 G2-1 Cummins engine performance and emission tests using methyl ester mahua (Madhuca indica) oil/diesel blends. Renew. Energy **34**, 2172–2177 (2009)
40. Silitonga, A.S., Masjuki, H.H., Mahlia, T.M.I., Ong, H.C., Kusumo, F., Aditiya, H.B., Ghazali, N.N.N.: *Schleichera oleosa* L oil as feedstock for biodiesel production. Fuel **156**, 63–70 (2015)
41. Sudrajat, R., Pawoko, E., Hendra, D., Setiawan, D.: Biodiesel manufacturing from kesambi seed. J. For. Prod. Res. **28**(4), 332–3357 (2010)
42. Sureshkumar, K., Velraj, R., Ganesan, R.: Performance and exhaust emission characteristics of a CI engine fueled with Pongamia pinnata methyl ester (PPME) and its blends with diesel. Renew. Energy **33**, 2294–2302 (2008)
43. Usta, N.: An experimental study on performance and exhaust emissions of a diesel engine fuelled with tobacco seed oil methyl ester. Energy Convers. Manag. **46**, 2373–2386 (2005)
44. Utlu, Z., Kocak, M.S.: The effect of biodiesel fuel obtained from waste frying oil on direct injection diesel engine performance and exhaust emissions. Renew. Energy **33**, 1936–1941 (2008)
45. Xue, J., Grift, T.E., Hansen, A.C.: Effect of biodiesel on engine performances and emissions. Renew. Sustain. Energy Rev. **15**, 1098–1116 (2011)
46. Yamane, K., Ueta, A., Shimamoto, Y.: Influence of physical and chemical properties of biodiesel fuels on injection, combustin and exhaust emission characteristics in a direct injection compression ignition engine. Int. J. Engine Res. **2**, 249–261 (2001)
47. Yan, Y., Li, X., Wang, G., Gui, X., Li, G., Su, F.: Biotechnological preparation of biodiesel and its high-valued derivatives: a review. Appl. Energy **113**, 1614–1631 (2014)
48. Zhang, X., Gao, G., Li, L., Wu, Z., Hu, Z., Deng, J.: Characteristics of combustion and emissions in a DI engine fueled with biodiesel blends from soybean oil. SAE Technical Paper **1**, 1832–1835 (2008)

Available online at www.sciencedirect.com

ScienceDirect

Materials Today: Proceedings XX (2016) XXX–XXX

materialstoday: PROCEEDINGS

www.materialstoday.com/proceedings

PMME 2016

Failure investigations of a first stage Ni based super alloy gas turbine blade

Sushila Rani[a]*, Atul K Agrawal[b], Vikas Rastogi[c]

[a]*Assistant Professor-Department of Mechanical, Production and Automobile Engineering, Delhi Technological University, Delhi-110042, India*

[b]*Assistant Professor-Department of Mechanical, Production, and Automobile Engineering, Delhi Technological University, Delhi-110042, India*

[c]*Professor -Department of Mechanical, Production, Industrial and Automobile Engineering, Delhi Technological University, Delhi-110042, India*

Abstract

This paper deals with the failure investigations of the first stage gas turbine blade of 30MW gas turbine. This blade is manufacture with of nickel based super alloy IN738. The main focus of the paper is to found the causes of failure of the blade. The investigations included the visual inspection, SEM fractrography, chemical analysis, microstructure analysis, X-ray diffraction and stress evaluation by using Finite Element Software ANSYS. By these investigations, it is found that the blade failure takes place due to the combined effect of erosion, oxidation, overheating, and hot corrosion.
© 2016 Elsevier Ltd. All rights reserved.
Selection and Peer-review under responsibility of International Conference on Processing of Materials, Minerals and Energy (July 29th – 30th) 2016, Ongole, Andhra Pradesh, India.

Keywords: First stage gas turbine blade; Nickel based IN738LC alloy; SEM; overheating; hot corrosion.

1. Introduction

Turbine blade failure cause sudden stop of turbine which results in economic loss. In order to increase the reliability, efficiency of the turbine and to rectify the blade failure problems from the root it is necessary to perform the detailed failure analysis of turbine blade [1].The common failures found in gas turbine blade includes overheating [1], corrosion [2,3,4], oxidation [5,6], erosion [2], degradation of coating of turbine blade [3,5,7], creep [2,3] and fatigue [8, 9]. The failure of gas turbine blade is due to the combination of aforesaid failure mechanisms.

* Corresponding author. Tel.: 09873575460
E-mail address: sranidtu@gmail.com

2214-7853 © 2016 Elsevier Ltd. All rights reserved.
Selection and Peer-review under responsibility of International Conference on Processing of Materials, Minerals and Energy (July 29th – 30th) 2016, Ongole, Andhra Pradesh, India.

This paper presents failure investigations of a first stage gas turbine blade. Gas Turbine blade material composition analysis, visual inspection, SEM fractrography, chemical analysis, microstructure analysis, X-ray diffraction and stress evaluation by using Finite Element Software ANSYS were performed.

2. Background

A first stage gas turbine blade of 30 MW gas turbine with operating temperature 1100^0C having service exposure of 1,30,000 hrs was investigated (Fig. 1). The blade is manufactured with nickel-base super alloy Inconel 738LC by means of investment casting process, containing directional solidified grain structure. The blade has aluminide coating (Pt–Al_2) provided by means of diffusion process. Different views of gas turbine blade are shown in (Fig. 2).

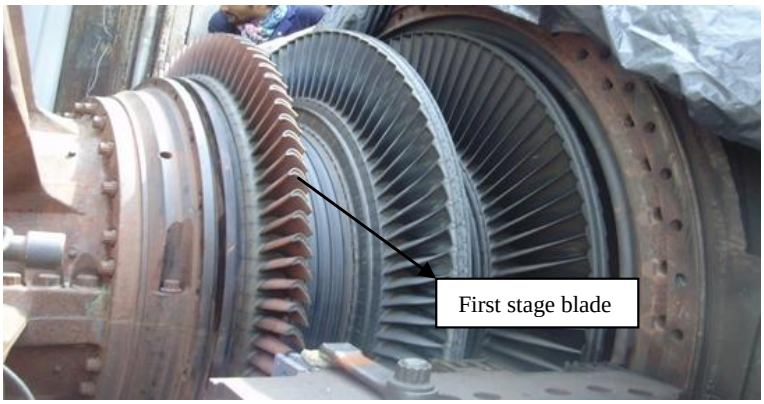


Fig. 1: General view of Gas turbine showing position of first stage blade



Fig. 2: Views of failed gas turbine blade (a) front view, (b) Rear view & (c) side view

3. Experimental details

The failed gas turbine blade is collected from Indraprastha Gas Power Plant, located in India. The blade has tip crack on both leading edge and trailing edge [4]. Two specimens about 15x10x5 mm^3 from the cracked tip of trailing edge and three specimens called as reference samples about 10x10x5 mm^3 from the bottom of trailing edge were cut by means of wire cutting process. Next, these specimens are polished using standard metallographic techniques and etched with acetone [5]. The scanning electronic microscope (SEM), Hitachi S-3700N equipped with an X-ray energy dispersive spectrometer (EDS) as shown in Fig. 3 were used to observe surface morphology, chemical compositions and microstructure of these specimens [4]. The stress analysis of a gas turbine blade was carried out using finite element software ANSYS [9].

4. Results and discussions

4.1. Visual examination

From the visual examination it is found that the failed gas turbine blade has crack on the tip of leading edge as well as on the tip of trailing edge. Both the leading edge and the trailing edge are found eroded along with the oxide scale formation in the airfoil region on both concave and convex sides.

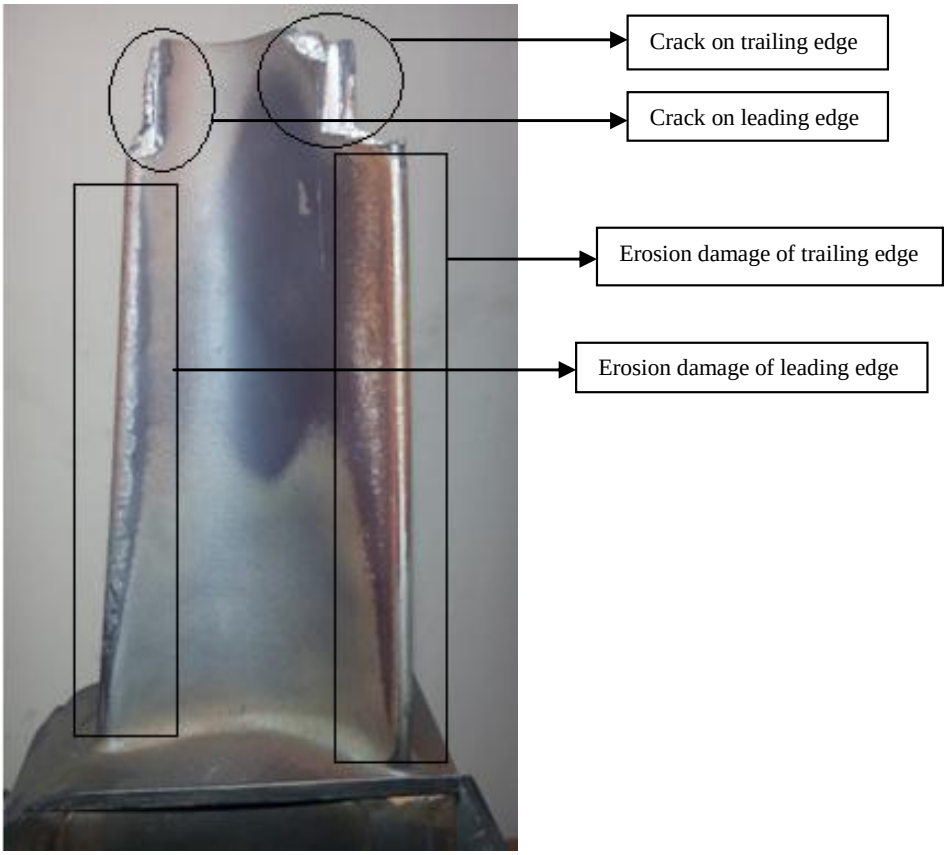


Fig. 3: Crack and Erosion damage found on leading and trailing edge of the first stage IN738 gas turbine blade

4.2 Chemical Analysis

From spectroscopy analysis, the composition (% wt) of blade material is given in Table 1 by using Optical Emission Analyzer spectrometer model- 49 DV4. The chemical analysis results shows that the blade material is in accordance with nickel based super alloy IN738 [12].

Table 1: *The Chemical composition of Inconel 738LC superalloy (wt%)*

Alloy	Cr	Co	Al	W	Ti	Ta	Mo	Ni
Std. IN738LC	16	8.3	3.4	2.6	3.38	1.75	1.7	Remaining
Failed turbine blade	14.63	10.49	2.83	3.54	4.65	0.31	1.11	62.28

4.3 Microstructure Evaluation

The microstructure investigation of the crack tip at the trailing edge was carried out. Two samples were cut by means of wire cutting operation over the trailing edge as shown in Fig. 4. For evaluating microstructure, a sample was prepared from the root region of the failed blade.

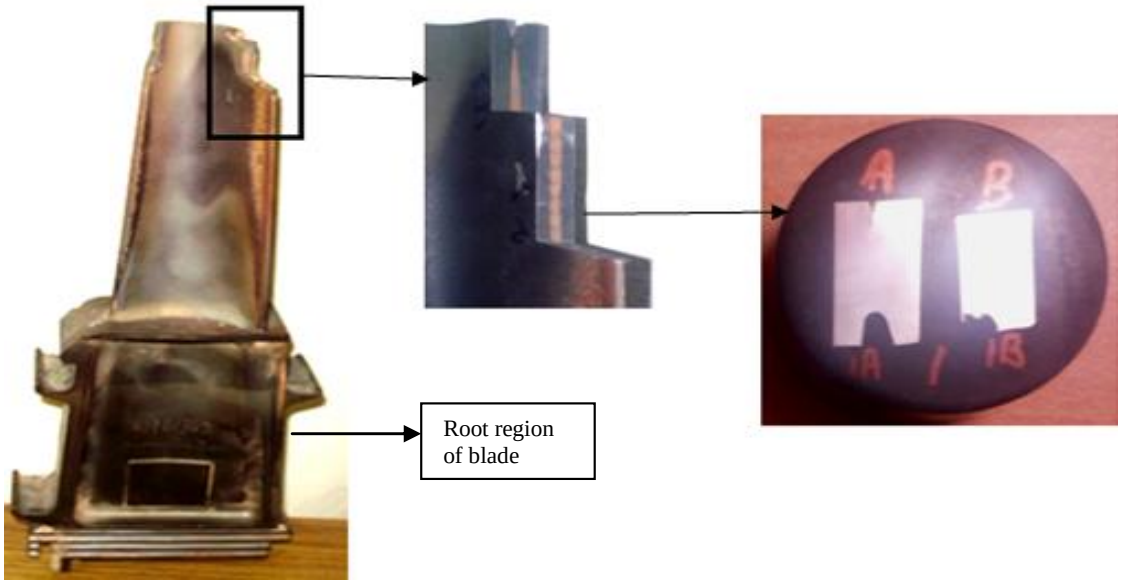


Fig. 4: Specimens cut from failed turbine blade

Fig. 5 shows the microstructure of the reference sample. It consists of carbides of MC precipitated on grain boundaries, grain interior and matrix. An EDS spectrum of turbine blade material is shown in Fig. 6.
Fig. 7 shows X-ray diffraction pattern of reference sample of turbine blade [13].

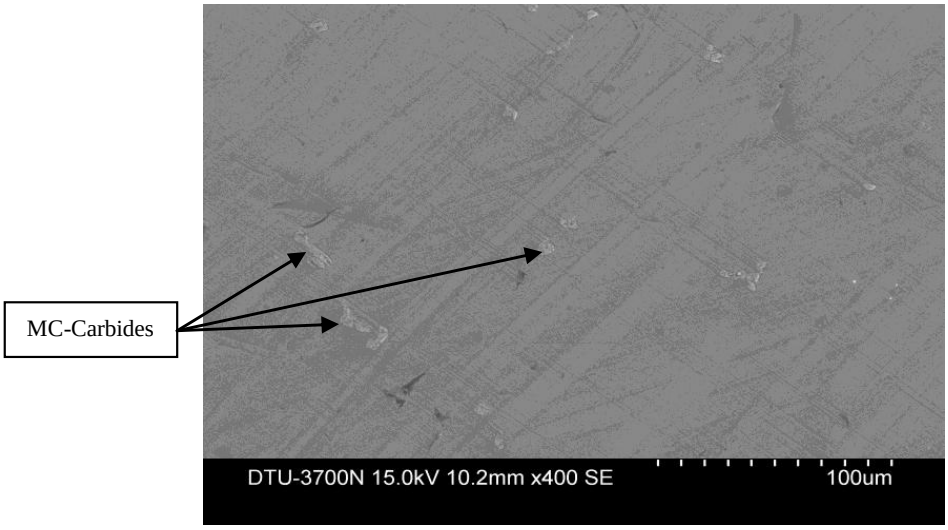


Fig. 5 : MC-carbides precipitated on grain boundaries and matrix

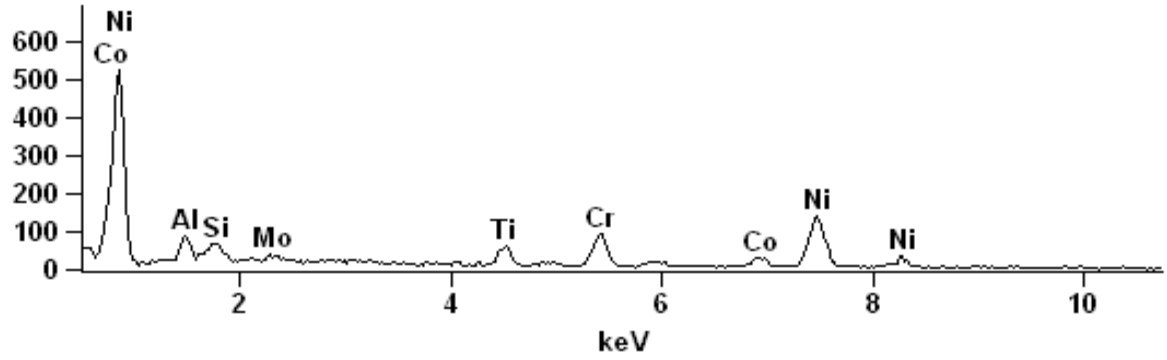


Fig. 6: An EDS spectrum of reference sample of turbine blade

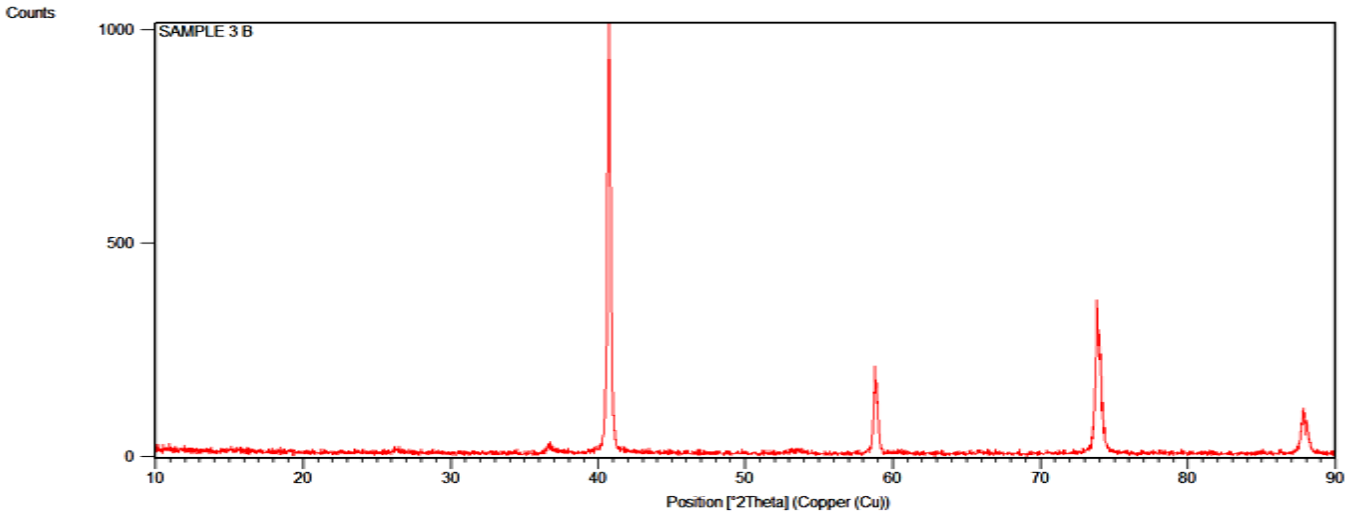


Fig. 7: X-ray diffraction pattern of reference sample of turbine blade

At high temperature working of turbine blade for long period results in the formation of topologically closed packed (TCP) phases as shown in Fig. 8. The mechanical properties of the blade material are degraded due to structure instability of the alloy which further results in decrease of turbine life.

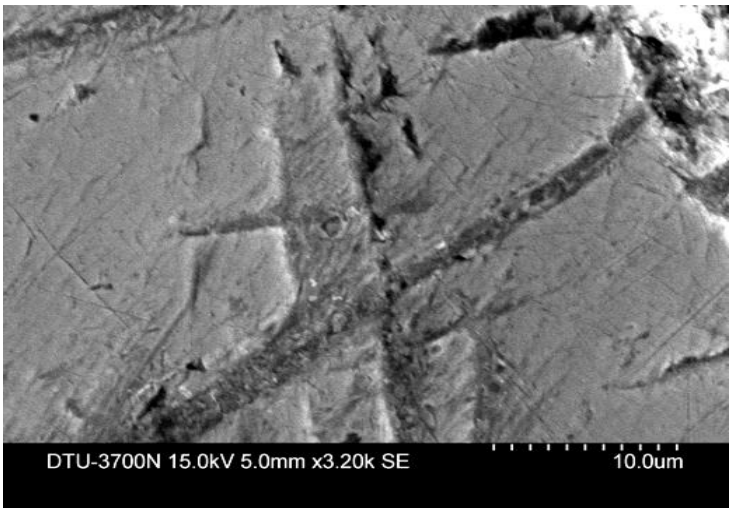


Fig. 8: Topologically Closed Packed (TCP) phase of the first stage IN738 gas turbine blade after service of 1,30,000 hrs

4.4 Crack evaluation

Fig. 9 shows rapid oxidation at high temperature in the presence of sodium sulfate which form by the combination of sulphur, oxygen and sodium. Sodium sulfate combine with chromium to form a mixture of salts and sulphur which is released due to the reduction of sodium sulphate. This released sulphur penetrates inward and react with chromium to form chromium sulfide in the substrate. Further, sulfides are converted to complex unstable metal oxides as corrosion proceeds and sulphur which is released penetrates deeply to form more sulfides into the substrate. An EDS spectrum confirmed the presence of corrosion products shown in Fig. 10. Fig. 11 shows X-ray diffraction pattern of sample collected from failed blade [13].

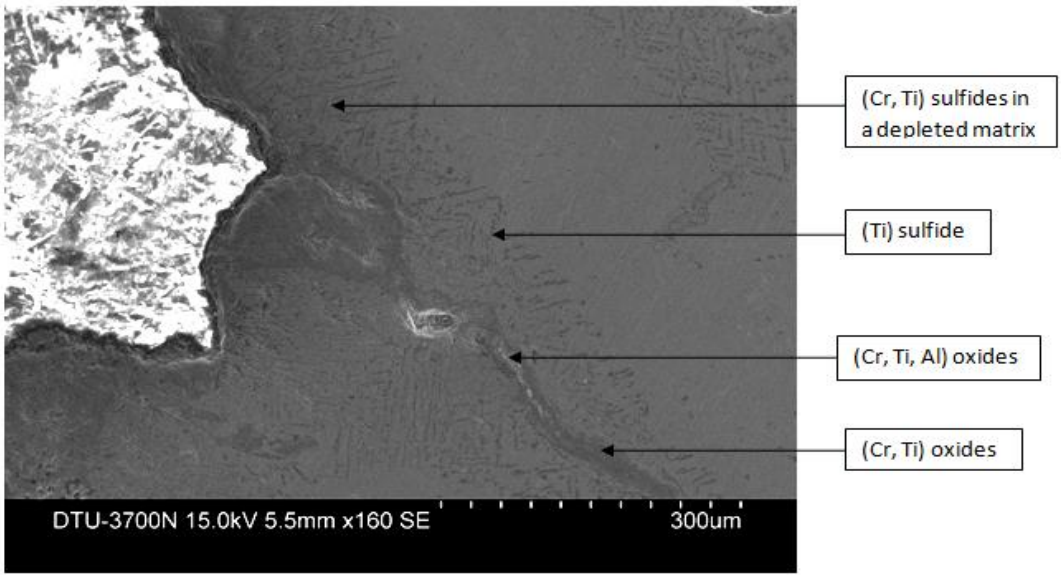


Fig. 9: Hot corrosion: subscale oxides and sulfides are visible in the substrate

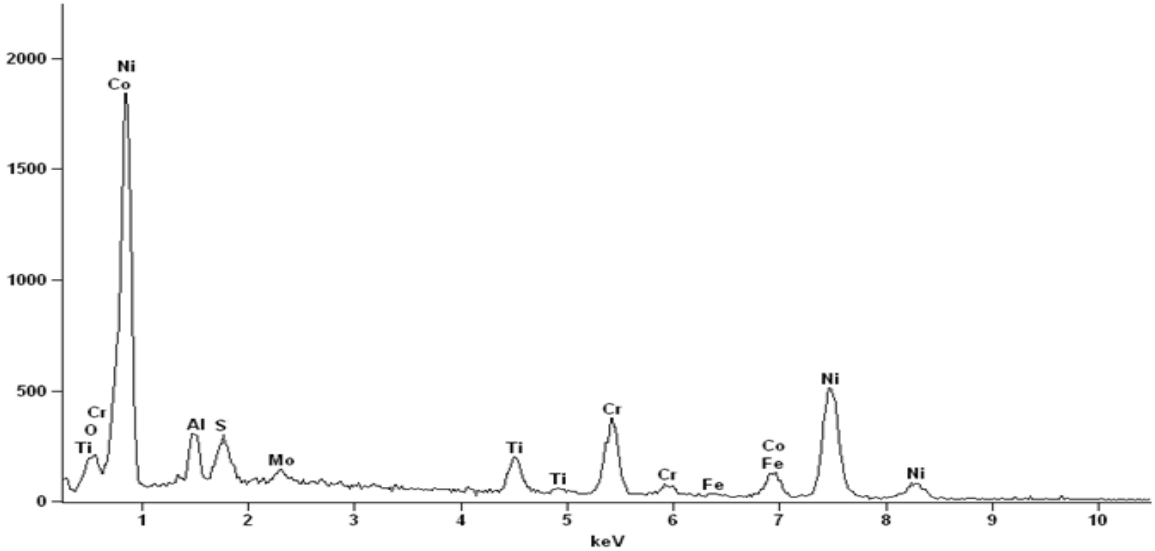


Fig. 10: The EDS spectrum of corrosion products confirm hot corrosion

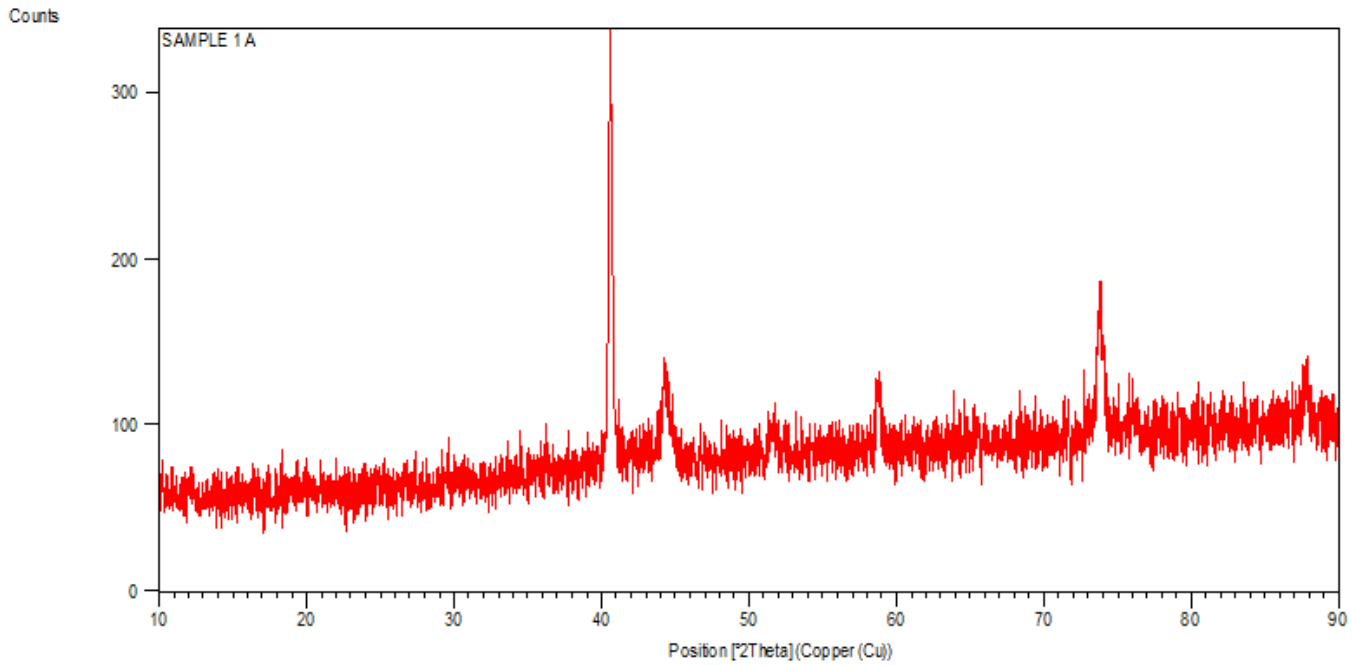


Fig. 11: X-ray diffraction pattern of failed blade

4.5 Stress Evaluation

The stress of first stage IN738 gas turbine blade is evaluated by performing static structural analysis of gas turbine blade on finite element software ANSYS [10]. The maximum tensile stress found approximately 393 MPa as shown in Fig. 12.

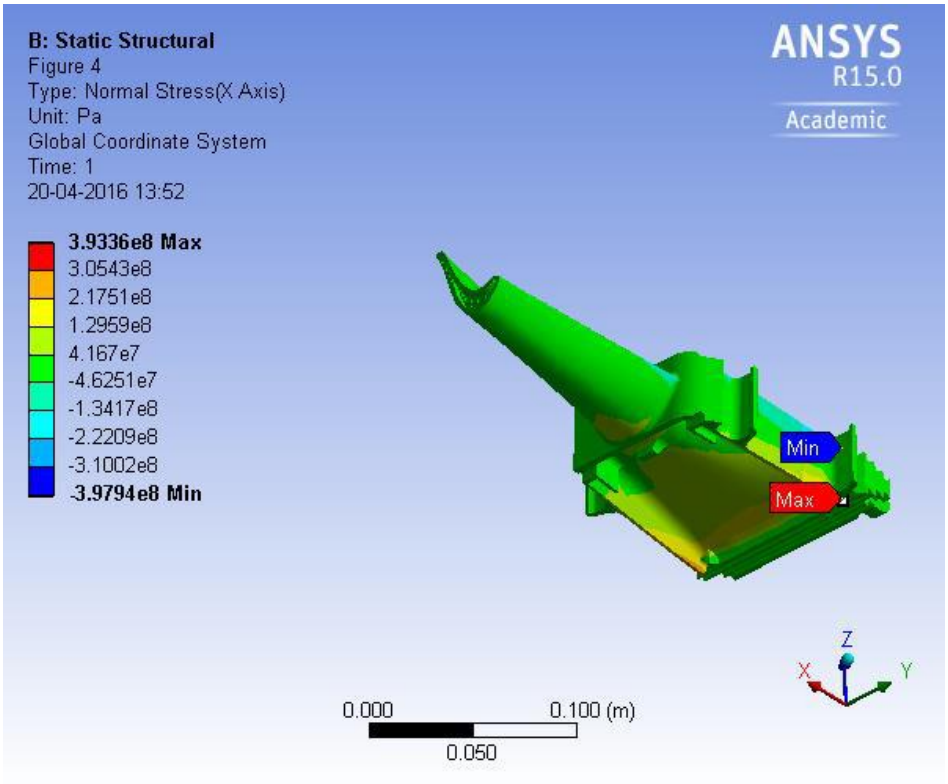


Fig. 12: Normal stress of the first stage gas turbine blade

Fig. 13(a) and 13(b) shows a very good agreement between crack location at the tip of trailing edge and leading edge of the failed first stage gas turbine blade and FEM results [10].



Fig. 13(a): Failed first stage gas turbine blade

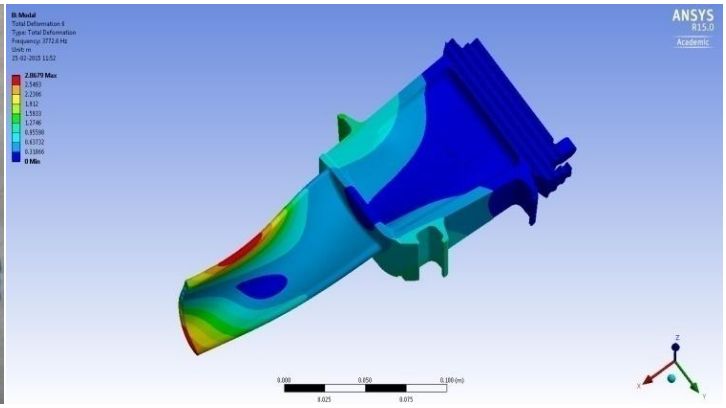


Fig. 13(b): Total deformation of the first stage gas turbine blade

5. Discussions:

The reddish color of blade surface is due to presence of aluminum oxide (Al_2O_3), which results due to oxidation of Al-Pt coating. The inclusions that flow in the hot gas stream are responsible for erosion of blade surface. These inclusions form oxides and impinge on the blade surface.

The alloy composition (% wt) of blade material obtained by using Optical Emission Analyzer spectrometer shows that the material of gas turbine blade has similar chemical composition as of the nickel based super alloy IN738. From the chemical composition, microstructure evolution and stress evaluation it is clear that blade was not failed due to material defects [11].

At high temperature operation of gas turbine blade carbides of MC type transforms to carbides of $M_{23}C_6$ type.

SEM images obtained by Hitachi S-3700N scanning electronic microscope shows the presence of sulfides and oxides in the substrate which are the by products of hot corrosion, and Topologically Closed Packed (TCP) phase of the first stage IN738 gas turbine blade which results due to overheating. The EDX spectrum confirms hot corrosion and overheating. X-ray diffraction patterns of samples collected from failed turbine blade are also shown. There x-ray patterns are similar to IN-738 nickel based alloy found in literature.

Therefore, the ultimate failure of gas turbine blade takes place due to the combined effect of erosion, oxidation, overheating and hot corrosion.

6. Conclusions:

1. Based upon the chemical composition, microstructure evolution and stress evaluation, it is clear that the blade was not failed due to material defect.
2. The surface metal of the blade degraded due to erosion and oxidation. The coating is heavily oxidized and offers no protection to base metal.
3. Formation of Topologically Closed Packed (TCP) phase results due to overheating.
4. Presence of sulfides and oxides in the substrate results due to hot corrosion.
5. The combination of erosion, oxidation, overheating and hot corrosion is responsible factors for ultimate failure of gas turbine blade.

Acknowledgements

The first stage failed gas turbine blade is collected from Indraprastha Gas Power Plant. The authors would be thankful to physics department of Delhi Technological University for help in conducting experiments in physics laboratory.

References:

1. Tawancy, H.M., Hadhrami, L.M., "Degradation of turbine blades and vanes by overheating in a power plant", Engineering Failure Analysis, vol. 16, 2009, pp-273-280.
2. Xie, Y., Wang, M., Zhang, G., "Analysis of super alloy turbine blade tip cracking during service", Engineering Failure Analysis, vol. 13, 2006, pp-1429-1436.
3. Khajavi, M.R., Shariat, M.H., "Failure of first stage turbine blades", Engineering Failure Analysis, vol. 11, 2004, pp-589-597.
4. Eliaz, N., Shemesh, G., Latanision, R.M., "Hot corrosion in gas turbine component", Engineering Failure Analysis, vol. 9, 2002, pp-31-43.
5. Mazur, Z., Ramirez, A., Amezcua, C.A., "Failure analysis of a gas turbine blade made of Inconel 738LC alloy", Engineering Failure Analysis, vol. 12, 2005, pp-474-486.
6. Vardar, N., Ekerim A., "Failure analysis of gas turbine blade in a thermal power plant", Engineering Failure Analysis vol. 14, 2007, pp-743-749.
7. Rybhinov,A.I., Gestov, L.B., Mozhaiskaya, N.V., " Operation experience with cast rotor blades made of Russian alloys in stationary gas turbines", Thermal Engineering, 2012, Vol. 59, No. 3, pp. 242–249. © Pleiades Publishing, Inc., 2012.
8. Kim, H., "Crack evaluation of the fourth stage blade in a low – pressure steam turbine", Engineering Failure Analysis, vol. 18, pp-907-913, 2011.Naeem, M.T., Jazayeri, S.A., Rezamahdi, N., "Failure analysis of gas turbine blades", Proceedings of The 2008 IAJC-IJME International Conference, paper 120,ENG 108.
9. Dowson,P., Dowson, D., " Selection of material and material related processes for FCC power recovery turbines" , Thirty eight turbo machinery symposium,2009, pp 187-212.
10. Naeem, M.T., Jazayeri, S.A., Rezamahdi, N., "Failure analysis of gas turbine blades", Proceedings of The 2008 IAJC-IJME International Conference, paper 120, ENG 108.
11. Bhagi, L., Rastogi, V., Gupta, P., "Fractographic investigations of the failure of L-1 low pressure steam turbine blade", case studies in Engineering Failure Analysis, vol. 1, 2013, pp-72-78.
12. Alloy IN738 technical data, Inco the international nickel company, Inc. One New York plaza, New York, N.Y. 10004.
13. Shishkovsky, I. V., Nazarov, A.P., "Comparison of Additive Technologies for Gradient Aerospace Part Fabrication from Nickel-Based Superalloys", Intech open science, chapter-10, 2015, pp-211-245.

OPSEARCH
DOI 10.1007/s12597-016-0282-5

THEORETICAL ARTICLE

Hierarchical clustering of interval-valued intuitionistic fuzzy relations and its application to elicit criteria weights in MCDM problems

Mamata Sahu[1] · **Anjana Gupta**[1] · **Aparna Mehra**[2]

Accepted: 17 August 2016
© Operational Research Society of India 2016

Abstract The paper aims to apply the $(\widetilde{\alpha}, \widetilde{\beta})$-cuts and the resolution form of the interval-valued intuitionistic fuzzy (IVIF) relations to develop a procedure for constructing a hierarchical clustering for IVIF max–min similarity relations. The advantage of the proposed scheme is illustrated in determining the criteria weights in multi-criteria decision making (MCDM) problems involving IVIF numbers. The problem of finding the criteria weights is of critical interest in the domain of MCDM problems. A complete procedure is drawn to generate criteria weights starting from the criteria-alternative matrix of the MCDM problem with entries provided by a decision maker as IVIF numbers.

Keywords Interval-valued intuitionistic fuzzy set · Interval-valued intuitionistic fuzzy similarity relation · Hierarchical clustering · Max–min composition · Multi-criteria decision making problem

1 Introduction

A *fuzzy set* (FS) is described by $A = \{\langle x, \mu_A(x)\rangle \mid x \in X\}$, where X is the universal set, and $\mu_A : X \to [0, 1]$ is the membership function with $\mu_A(x)$ depicting the

✉ Anjana Gupta
anjanagupta@dce.ac.in

Mamata Sahu
munmun.sahu@gmail.com

Aparna Mehra
apmehra@maths.iitd.ac.in

[1] Department of Applied Mathematics, Delhi Technological University, New Delhi, Delhi 110042, India

[2] Department of Mathematics, Indian Institute of Technology Delhi, Hauz Khas, Delhi 110016, India

Published online: 06 September 2016

membership value of an element x in the set $A \subset X$. The non-membership degree of x in A is taken as the standard negation of its membership degree, that is, $1 - \mu_A(x)$. This framework is not sufficient to model situations where one believes that $x \in A$ with some membership degree although not convinced on the value to be given to it and/or when some additional information is offered on the negation of the positive declaration.

Atanassov [1] generalized the conventional FS to *intuitionistic fuzzy set* (IFS) by ascribing the degree of non-membership of an element to a set along with its membership degree. More precisely, an IFS is described by $A = \{\langle x, \mu_A(x), \nu_A(x)\rangle \mid x \in X\}$, where the functions $\mu_A, \nu_A : X \to [0, 1]$ assign to each element x of the universe X, a membership degree $\mu_A(x) \in [0, 1]$, and a non-membership $\nu_A(x) \in [0, 1]$, such that $\mu_A(x) + \nu_A(x) \leq 1$. Thus, in IFS theory, the non-membership degree $\nu_A(x)$ is an independent degree with the only condition on it being less than or equal to $1 - \mu_A(x)$. An IFS can be seen as the first significant departure away from the FS.

Initially the very name intuitionistic fuzzy set was somewhat debatable (see, Dubois et al. [2]), but off late the same nomenclature has found acceptance with the range of research papers using it though sometime it is also referred by Atanassov's I-fuzzy set for more clarity. We shall be sticking to IFS in our present discussion.

Another prominent extension of FS is an *interval-valued fuzzy set* (IVFS) (see, Turksen [3]). The pivotal idea behind IVFS is that the membership degree can hardly be precise; the uncertainty in it can better be explained by an interval. Though later on the two notations, IVFS and IFS, turned out to be isomorphic (see, Deschrijver and Kerre [4]).

Taking further a step towards modeling more subjective vagueness, Atanassov and Gargov [5] introduced *interval-valued intuitionistic fuzzy set* (IVIFS). IVIFS is a natural extension of IVFS, where the membership as well as the non-membership degrees need not be specified with precision but rather allowed to lie in the interval [0, 1]. Xu and Cai [6] illustrated several real-life applications where the subjective granularity is enhanced by adding an additional layer of flexibility in expressing information using IVIFS. The rich structure supported by strong theory and several good aggregation operators, defined in literature over the years, makes an IVIF theory an intuitive and computationally efficient for handling uncertain and ambiguous information. The interval-valued membership and non-membership values offer more flexibility in terms of describing favoritism (or membership value) and rejection (non-membership).

On the application side of FS and its various variants, Bellmann et al. [7] and Ruspini [8] presented ideas of data clustering using FS theory. Fuzzy clustering is found to be useful in variety of areas (see, Bezdek [9], Yang [10], Hoppner et al. [11]). The fuzzy clustering methods can broadly be classified into two categories. One based on optimizing some distance-defined objective function. The fuzzy c-means (FCM) algorithm and its variations are the familiar approaches in this category (see, Baraldi and Blonda [12], Lee [13], Yu and Yang [14]). The FCM clustering allows one data to belong to two or more clusters simultaneously with corresponding membership degrees of belonging-ness. These methods require the

data to be present in form of feature vectors so to compute their distances from the prototypes.

The other category of fuzzy clustering is based on fuzzy relations. Zadeh [15] defined a *fuzzy relation R* between two sets X and Y as a fuzzy subset of $X \times Y$ by taking a membership function $\mu_R : X \times Y \to [0,1]$, with $\mu_R(x,y)$ equals a membership degree of $(x,y) \in R$. He [15] also defined a similarity relation which has been successfully applied to areas of data classification, matching and pattern recognition (see, Tamura et al. [16], Dunn [17], Yang and Shih [18]). Guh et al. [19] extended a fuzzy relation (FR) to *interval-valued fuzzy relation* (IVFR) and defined an interval-valued degree of similarity between any two elements $x \in X$ and $y \in Y$ as $[\underline{\mu}_R(x,y), \overline{\mu}_R(x,y)]$, with $0 \leq \underline{\mu}_R(x,y) \leq \overline{\mu}_R(x,y) \leq 1$. They developed some results for IVFR and applied them for performance evaluation by establishing a hierarchical clustering.

According to Guh [19], the $\tilde{\alpha}$-cut in the resolution form of the interval-valued similarity relation, is interval-valued with $\widetilde{\alpha} = (\underline{\alpha}, \overline{\alpha})$, $0 \leq \underline{\alpha} \leq \overline{\alpha} \leq 1$. In case of m number of $\widetilde{\alpha}$-cuts for interval-valued similarity relation, say $(\underline{\alpha}_1, \overline{\alpha}_1), \ldots, (\underline{\alpha}_m, \overline{\alpha}_m)$, the following conditions must be satisfied:

$$0 \leq \underline{\alpha}_1 \leq \ldots \leq \underline{\alpha}_m \leq 1, \quad 0 \leq \overline{\alpha}_1 \leq \ldots \leq \overline{\alpha}_m \leq 1.$$

But the same may fails to hold; for instance, if the $\tilde{\alpha}$-cuts are of the form $(0.4, 0.9)$, $(0.5, 0.6)$, $(1,1)$ then, although $0.4 < 0.5 < 1$ but $0.9 \not\leq 0.6 < 1$. On the other hand, Basnet [20] defined the (α, β)-cut for IFS A, for $0 \leq \alpha, \beta \leq 1$, $\alpha + \beta \leq 1$, by $A_{(\alpha,\beta)} = \{x \mid \mu_A(x) \geq \alpha \text{ and } \nu_A(x) \leq \beta\}$.

In this paper, we extend the work of Guh et al. [19] to IVIF scenario. We introduce the definition of $(\widetilde{\alpha}, \widetilde{\beta})$-cuts for an *interval-valued intuitionistic fuzzy relation* (IVIFR) and present decomposed resolution form of IVIFR. The same have been applied to create a hierarchical structure for IVIFR. An MCDM with IVIF numbers is considered, and an entropy measure [21] together with hierarchical clustering is applied to compute the global weights of the criteria involved in the problem. MATLAB codes are developed for all the proposed algorithms and methodologies. All codes are tested on a large number of matrices set-up in the domain backdrops of IVIF numbers, IF numbers, and IVIF numbers.

The now onwards flow of the paper is as follows. In Sect. 2, we modify the definition of $\widetilde{\alpha}$-cut for *interval-valued fuzzy relation* (IVFR) described in [19]. In Sect. 3, the hierarchical clustering procedure is developed to include *intuitionistic fuzzy relation* (IFR). Section 4 presents some operations on IVIFR along with its resolution form. Section 5 describes the hierarchical clustering procedure for IVIFR. Section 6 proposed a procedure to compute the global weights of the criteria in an MCDM problem set-up in IVIF environment. Section 7 summarizes the work.

2 $\widetilde{\alpha}$-cut for IVFR

Let X and Y be two non-empty sets, and $Int([0,1]) = \{(x_1, x_2) \mid x_1, x_2 \in [0,1], x_1 \leq x_2\}$.

Definition 1 [19] (*Interval valued fuzzy relation (IVFR)*) An IVFR $\widetilde{R}$ on X and Y is a mapping $\widetilde{R} : X \times Y \rightarrow Int([0, 1]$, defined as a fuzzy subset of $X \times Y$, with an interval-valued membership grade $\tilde{\mu}_{\widetilde{R}}(x, y) = [\underline{\mu}_{\widetilde{R}}(x, y),\ \overline{\mu}_{\widetilde{R}}(x, y)],\ \forall\ (x, y) \in X \times Y$.

Definition 2 [19] (*Interval-valued fuzzy proximity relation*) An IVFR $\widetilde{R}$ on X which is reflexive (that is, $\tilde{\mu}_{\widetilde{R}}(x, x) = [1, 1],\ \forall\ x \in X$) and symmetric (that is, $\tilde{\mu}_{\widetilde{R}}(x, y) = \tilde{\mu}_{\widetilde{R}}(y, x),\ \forall\ x, y \in X$) is called an interval-valued fuzzy proximity relation.

Definition 3 [19] (*Transitive IVFR*) An IVFR $\widetilde{R}$ on X is called (max–min) transitive if for all $x, y \in X$, the following hold:

$$\underline{\mu}_{\widetilde{R}}(x, y) \geq \max_{z \in X}\{\min\{\underline{\mu}_{\widetilde{R}}(x, z), \underline{\mu}_{\widetilde{R}}(z, y)\}\} \quad \text{and}$$
$$\overline{\mu}_{\widetilde{R}}(x, y) \geq \max_{z \in X}\{\min\{\overline{\mu}_{\widetilde{R}}(x, z), \overline{\mu}_{\widetilde{R}}(z, y)\}\}.$$

Definition 4 [19] (*Interval-valued fuzzy (max–min) similarity relation*) An interval-valued fuzzy proximity relation $\widetilde{R}$ on X with transitivity property (in the sense of Definition 3) is called an interval-valued fuzzy (max–min) similarity relation.

Guh et al. [19] showed that an interval-valued similarity relation $\widetilde{R}$ can be decomposed into its resolution form using $\widetilde{\alpha}$-cuts, as follows:

$$\begin{aligned}\widetilde{R} &= \bigcup_{\widetilde{\alpha}} (\underline{\mu}_{\alpha},\ \overline{\mu}_{\alpha})\ R_{\widetilde{\alpha}} \\ &= (\underline{\mu}_{\alpha_1},\ \overline{\mu}_{\alpha_1}) R_{\widetilde{\alpha}_1} + (\underline{\mu}_{\alpha_2}, \overline{\mu}_{\alpha_2})\ R_{\widetilde{\alpha}_2} + \cdots + (\underline{\mu}_{\alpha_m}, \overline{\mu}_{\alpha_m})\ R_{\widetilde{\alpha}_m},\end{aligned}$$

such that

$$0 \leq \underline{\mu}_{\alpha_1} \leq \underline{\mu}_{\alpha_2} \leq \ldots \leq \underline{\mu}_{\alpha_m} \leq 1, \quad 0 \leq \overline{\mu}_{\alpha_1} \leq \overline{\mu}_{\alpha_2} \leq \ldots \leq \overline{\mu}_{\alpha_m} \leq 1, \tag{1}$$

where $R_{\widetilde{\alpha}_i},\ i = 1, \ldots, m$, are the similarity relations, and $(\underline{\mu}_{\alpha_i}, \overline{\mu}_{\alpha_i}),\ i = 1, \ldots, m$, are the corresponding $\widetilde{\alpha}$-cut.

The same was noticed to be misleading in Sect. 1, Introduction. The following examples further justify our observation that (1) may not always hold.

Example 1 Consider the following interval-valued proximity relation matrix which is not (min–max) transitive.

$$\widetilde{R}^{(0)} = \begin{pmatrix} 1 & (0.1, 0.4) & (0.2, 0.3) & (0.6, 0.9) \\ (0.1, 0.4) & 1 & (0.7, 0.8) & (0.4, 0.7) \\ (0.2, 0.3) & (0.7, 0.8) & 1 & (0.3, 0.5) \\ (0.6, 0.9) & (0.4, 0.7) & (0.3, 0.5) & 1 \end{pmatrix}.$$

Using the conventional procedure, we first convert the above relation into a max–min transitive one. To accomplish this, we take $\tilde{R}^{(1)} = \tilde{R}^{(0)} \circ \tilde{R}^{(0)}$, where $\circ$ stands for the max–min composition, we get

$$\widetilde{R}^{(1)} = \begin{pmatrix} 1 & (0.4,0.7) & (0.3,0.5) & (0.6,0.9) \\ (0.4,0.7) & 1 & (0.7,0.8) & (0.4,0.7) \\ (0.3,0.5) & (0.7,0.8) & 1 & (0.4,0.7) \\ (0.6,0.9) & (0.4,0.7) & (0.4,0.7) & 1 \end{pmatrix}.$$

Note that $\tilde{R}^{(1)} \neq \tilde{R}^{(0)}$. Again obtain $\tilde{R}^{(2)} = \tilde{R}^{(1)} \circ \tilde{R}^{(1)}$. Then,

$$\widetilde{R}^{(2)} = \begin{pmatrix} 1 & (0.4,0.7) & (0.4,0.7) & (0.6,0.9) \\ (0.4,0.7) & 1 & (0.7,0.8) & (0.4,0.7) \\ (0.4,0.7) & (0.7,0.8) & 1 & (0.4,0.7) \\ (0.6,0.9) & (0.4,0.7) & (0.4,0.7) & 1 \end{pmatrix}.$$

Since $\widetilde{R}^{(2)} \neq \widetilde{R}^{(1)}$, we repeat the above procedure to get next relation from $\tilde{R}^{(2)}$ as follows:

$$\widetilde{R}^{(3)} = \begin{pmatrix} 1 & (0.4,0.7) & (0.4,0.7) & (0.6,0.9) \\ (0.4,0.7) & 1 & (0.7,0.8) & (0.4,0.7) \\ (0.4,0.7) & (0.7,0.8) & 1 & (0.4,0.7) \\ (0.6,0.9) & (0.4,0.7) & (0.4,0.7) & 1 \end{pmatrix}.$$

Now, $\widetilde{R}^{(3)} = \widetilde{R}^{(2)}$, hence $\widetilde{R}^{(2)}$ is an equivalence IVFR.

The $\widetilde{\alpha}$-cuts in $\tilde{R}^{(2)}$ are $(0.4,0.7)$, $(0.6,0.9)$, $(0.7,0.8)$, $(1,1)$ with $0.4<0.6<0.7<1$ but $0.7<0.9\not\leq 0.8<1$, i. e. condition (1) does not hold.

Example 2 Consider the interval-valued fuzzy max–min similarity relation $\widetilde{R}^{(0)}$

$$\widetilde{R}^{(0)} = \begin{pmatrix} 1 & (0.9,1) & (0.6,0.9) & (0.4,0.9) & (0.4,0.8) \\ (0.9,1) & 1 & (0.6,0.9) & (0.4,0.9) & (0.4,0.8) \\ (0.6,0.9) & (0.6,0.9) & 1 & (0.4,0.9) & (0.4,0.8) \\ (0.4,0.9) & (0.4,0.9) & (0.4,0.9) & 1 & (0.5,0.8) \\ (0.4,0.8) & (0.4,0.8) & (0.4,0.8) & (0.5,0.8) & 1 \end{pmatrix}.$$

It can easily be verified that $\tilde{R}^{(0)}$ is reflexive, symmetric and transitive IVFR. The $\widetilde{\alpha}$-cuts are $(0.4,0.8)$, $(0.4,0.9)$, $(0.5,0.8)$, $(0.6,0.9)$, $(0.9,1)$, $(1,1)$. Again the noteworthy point is that although the lower values of cuts satisfy the inequality in (1), the upper values of cut fail to meet (1) as $0.8 < 0.9 \not\leq 0.8 < 0.9 < 1$.

In this paper, we attempt to improve this shortcoming and develop a new definition of $\widetilde{\alpha}$-cut.

Definition 5 The $\widetilde{\alpha}$-cut of an IVFR $\tilde{R}$ is defined by $(\max(\underline{\mu}_i),\ \min(\overline{\mu}_i))$, among all $\tilde{\alpha}$-cut $(\underline{\mu}_\alpha, \overline{\mu}_\alpha)$ of the interval-valued similarity relation derived following the approach of Guh et al. [19].

For clarity of the above definition, we propose an algorithm for determining the $\widetilde{\alpha}$-cuts of IVFR.

Algorithm 1

1. First determine all $\widetilde{\alpha}$-cuts $(\underline{\mu}_i, \overline{\mu}_i)$ of IVFR by the conventional approach of Guh et al. [19]. Let this collection be denoted by S.
2. Among all the elements of S, choose the one with maximum value of the lower membership and fixed it. Then among all available pairs in S with this lower membership value, choose the one having minimum upper membership value. This way, we extract the first element in $\widetilde{\alpha}$-cut of IVFR. Note that the first $\widetilde{\alpha}$-cut is a member in S. Reduce the set S by deleting this element from it.
3. Continue the above procedure among all the remaining elements of the reduced S, till finally all elements are searched.

This way we are able to extract $\widetilde{\alpha}$-cut of IVFR from the set S.

Recall the $\widetilde{\alpha}$-cuts of Example 2. Then, by Definition 5, the extracted $\widetilde{\alpha}$-cuts of IVFR are given $(1,1), (0.9,1), (0.6,0.9), (0.5,0.8), (0.4,0.8)$. Moreover, the resolution form of the similarity relation is given by

$$\widetilde{R}^{(1)} = 1\begin{pmatrix} 1 & & & & \\ 0 & 1 & & & \\ 0 & 0 & 1 & & \\ 0 & 0 & 0 & 1 & \\ 0 & 0 & 0 & 0 & 1 \end{pmatrix} + (0.9,1)\begin{pmatrix} 1 & & & & \\ 1 & 1 & & & \\ 0 & 0 & 1 & & \\ 0 & 0 & 0 & 1 & \\ 0 & 0 & 0 & 0 & 1 \end{pmatrix}$$
$$+ (0.6,0.9)\begin{pmatrix} 1 & & & & \\ 1 & 1 & & & \\ 1 & 1 & 1 & & \\ 0 & 0 & 0 & 1 & \\ 0 & 0 & 0 & 0 & 1 \end{pmatrix} + (0.5,0.8)\begin{pmatrix} 1 & & & & \\ 1 & 1 & & & \\ 1 & 1 & 1 & & \\ 0 & 0 & 0 & 1 & \\ 0 & 0 & 0 & 1 & 1 \end{pmatrix}$$
$$+ (0.4,0.8)\begin{pmatrix} 1 & & & & \\ 1 & 1 & & & \\ 1 & 1 & 1 & & \\ 1 & 1 & 1 & 1 & \\ 1 & 1 & 1 & 1 & 1 \end{pmatrix}.$$

A MATLAB code is developed to construct the $\widetilde{\alpha}$-cuts of the IVFR of order m. The code is tested on randomly generated IVFR matrices. One of the illustration is shown below.

Example 3 Let $\widetilde{B}^{(0)}$ be a randomly generated interval-valued fuzzy proximity relation matrix of order 8.

$$\widetilde{B}^{(0)} = \begin{pmatrix} (1,1) & \begin{pmatrix}0.814724,\\0.936168\end{pmatrix} & \begin{pmatrix}0.905792,\\0.921919\end{pmatrix} & \begin{pmatrix}0.126987,\\0.743374\end{pmatrix} & \begin{pmatrix}0.913376,\\0.916133\end{pmatrix} & \begin{pmatrix}0.632359,\\0.734167\end{pmatrix} & \begin{pmatrix}0.09754,\\0.139208\end{pmatrix} & \begin{pmatrix}0.278498,\\0.348579\end{pmatrix} \\ \begin{pmatrix}0.814724,\\0.936168\end{pmatrix} & (1,1) & \begin{pmatrix}0.546882,\\0.920005\end{pmatrix} & \begin{pmatrix}0.957507,\\0.987032\end{pmatrix} & \begin{pmatrix}0.964889,\\0.976022\end{pmatrix} & \begin{pmatrix}0.157613,\\0.958068\end{pmatrix} & \begin{pmatrix}0.970593,\\0.971606\end{pmatrix} & \begin{pmatrix}0.957167,\\0.97596\end{pmatrix} \\ \begin{pmatrix}0.905792,\\0.921919\end{pmatrix} & \begin{pmatrix}0.546882,\\0.920005\end{pmatrix} & (1,1) & \begin{pmatrix}0.485376,\\0.681735\end{pmatrix} & \begin{pmatrix}0.80028,\\0.953169\end{pmatrix} & \begin{pmatrix}0.141886,\\0.824258\end{pmatrix} & \begin{pmatrix}0.421761,\\0.529818\end{pmatrix} & \begin{pmatrix}0.915736,\\0.957005\end{pmatrix} \\ \begin{pmatrix}0.126987,\\0.743374\end{pmatrix} & \begin{pmatrix}0.957507,\\0.987032\end{pmatrix} & \begin{pmatrix}0.485376,\\0.681735\end{pmatrix} & (1,1) & \begin{pmatrix}0.792207,\\0.884797\end{pmatrix} & \begin{pmatrix}0.959492,\\0.985673\end{pmatrix} & \begin{pmatrix}0.655741,\\0.899946\end{pmatrix} & \begin{pmatrix}0.035712,\\0.763447\end{pmatrix} \\ \begin{pmatrix}0.913376,\\0.916133\end{pmatrix} & \begin{pmatrix}0.964889,\\0.976022\end{pmatrix} & \begin{pmatrix}0.80028,\\0.953169\end{pmatrix} & \begin{pmatrix}0.792207,\\0.884797\end{pmatrix} & (1,1) & \begin{pmatrix}0.849129,\\0.890773\end{pmatrix} & \begin{pmatrix}0.933993,\\0.978858\end{pmatrix} & \begin{pmatrix}0.678735,\\0.889195\end{pmatrix} \\ \begin{pmatrix}0.632359,\\0.734167\end{pmatrix} & \begin{pmatrix}0.157613,\\0.958068\end{pmatrix} & \begin{pmatrix}0.141886,\\0.824258\end{pmatrix} & \begin{pmatrix}0.959492,\\0.985673\end{pmatrix} & \begin{pmatrix}0.849129,\\0.890773\end{pmatrix} & (1,1) & \begin{pmatrix}0.75774,\\0.797134\end{pmatrix} & \begin{pmatrix}0.743132,\\0.773699\end{pmatrix} \\ \begin{pmatrix}0.09754,\\0.139208\end{pmatrix} & \begin{pmatrix}0.970593,\\0.971606\end{pmatrix} & \begin{pmatrix}0.421761,\\0.529818\end{pmatrix} & \begin{pmatrix}0.655741,\\0.899946\end{pmatrix} & \begin{pmatrix}0.933993,\\0.978858\end{pmatrix} & \begin{pmatrix}0.75774,\\0.797134\end{pmatrix} & (1,1) & \begin{pmatrix}0.392227,\\0.695119\end{pmatrix} \\ \begin{pmatrix}0.278498,\\0.348579\end{pmatrix} & \begin{pmatrix}0.957167,\\0.97596\end{pmatrix} & \begin{pmatrix}0.915736,\\0.957005\end{pmatrix} & \begin{pmatrix}0.035712,\\0.763447\end{pmatrix} & \begin{pmatrix}0.678735,\\0.889195\end{pmatrix} & \begin{pmatrix}0.743132,\\0.773699\end{pmatrix} & \begin{pmatrix}0.392227,\\0.695119\end{pmatrix} & (1,1) \end{pmatrix}.$$

Using the max–min composition, an interval-valued max–min similarity relation is constructed and the same is given as follows:

$$\widetilde{B}^{(3)} = \begin{pmatrix} (1,1) & \begin{pmatrix}0.9134,\\0.9362\end{pmatrix} & \begin{pmatrix}0.9134,\\0.9362\end{pmatrix} & \begin{pmatrix}0.9134,\\0.9362\end{pmatrix} & \begin{pmatrix}0.9134,\\0.9362\end{pmatrix} & \begin{pmatrix}0.9134,\\0.9362\end{pmatrix} & \begin{pmatrix}0.9134,\\0.9362\end{pmatrix} & \begin{pmatrix}0.9134,\\0.9362\end{pmatrix} \\ \begin{pmatrix}0.9134,\\0.9362\end{pmatrix} & (1,1) & \begin{pmatrix}0.9157,\\0.9570\end{pmatrix} & \begin{pmatrix}0.9575,\\0.9870\end{pmatrix} & \begin{pmatrix}0.9649,\\0.9760\end{pmatrix} & \begin{pmatrix}0.9575,\\0.9857\end{pmatrix} & \begin{pmatrix}0.9706,\\0.9760\end{pmatrix} & \begin{pmatrix}0.9572,\\0.9760\end{pmatrix} \\ \begin{pmatrix}0.9134,\\0.9362\end{pmatrix} & \begin{pmatrix}0.9157,\\0.9570\end{pmatrix} & (1,1) & \begin{pmatrix}0.9157,\\0.9570\end{pmatrix} & \begin{pmatrix}0.9157,\\0.9570\end{pmatrix} & \begin{pmatrix}0.9157,\\0.9570\end{pmatrix} & \begin{pmatrix}0.9157,\\0.9570\end{pmatrix} & \begin{pmatrix}0.9157,\\0.9570\end{pmatrix} \\ \begin{pmatrix}0.9134,\\0.9362\end{pmatrix} & \begin{pmatrix}0.9575,\\0.9870\end{pmatrix} & \begin{pmatrix}0.9157,\\0.9570\end{pmatrix} & (1,1) & \begin{pmatrix}0.9575,\\0.9760\end{pmatrix} & \begin{pmatrix}0.9595,\\0.9857\end{pmatrix} & \begin{pmatrix}0.9575,\\0.9760\end{pmatrix} & \begin{pmatrix}0.9572,\\0.9760\end{pmatrix} \\ \begin{pmatrix}0.9134,\\0.9362\end{pmatrix} & \begin{pmatrix}0.9649,\\0.9760\end{pmatrix} & \begin{pmatrix}0.9157,\\0.9570\end{pmatrix} & \begin{pmatrix}0.9575,\\0.9760\end{pmatrix} & (1,1) & \begin{pmatrix}0.9575,\\0.9760\end{pmatrix} & \begin{pmatrix}0.9649,\\0.9789\end{pmatrix} & \begin{pmatrix}0.9572,\\0.9760\end{pmatrix} \\ \begin{pmatrix}0.9134,\\0.9362\end{pmatrix} & \begin{pmatrix}0.9575,\\0.9857\end{pmatrix} & \begin{pmatrix}0.9157,\\0.9570\end{pmatrix} & \begin{pmatrix}0.9595,\\0.9857\end{pmatrix} & \begin{pmatrix}0.9575,\\0.9760\end{pmatrix} & (1,1) & \begin{pmatrix}0.9575,\\0.9760\end{pmatrix} & \begin{pmatrix}0.9572,\\0.9760\end{pmatrix} \\ \begin{pmatrix}0.9134,\\0.9362\end{pmatrix} & \begin{pmatrix}0.9706,\\0.9760\end{pmatrix} & \begin{pmatrix}0.9157,\\0.9570\end{pmatrix} & \begin{pmatrix}0.9575,\\0.9760\end{pmatrix} & \begin{pmatrix}0.9649,\\0.9789\end{pmatrix} & \begin{pmatrix}0.9575,\\0.9760\end{pmatrix} & (1,1) & \begin{pmatrix}0.9572,\\0.9760\end{pmatrix} \\ \begin{pmatrix}0.9134,\\0.9362\end{pmatrix} & \begin{pmatrix}0.9572,\\0.9760\end{pmatrix} & \begin{pmatrix}0.9157,\\0.9570\end{pmatrix} & \begin{pmatrix}0.9572,\\0.9760\end{pmatrix} & \begin{pmatrix}0.9572,\\0.9760\end{pmatrix} & \begin{pmatrix}0.9572,\\0.9760\end{pmatrix} & \begin{pmatrix}0.9572,\\0.9760\end{pmatrix} & (1,1) \end{pmatrix}.$$

Using Definition 5, the $\widetilde{\alpha}$-cuts of $\widetilde{B}^{(3)}$ are

$$(0.9134, 0.9362),\ (0.9157, 0.9570),\ (0.9572, 0.9760),\ (0.9575, 0.9760),$$
$$(0.9595, 0.9857),\ (0.9649, 0.9760),\ (0.9706, 0.9760),\ (1, 1).$$

And it's resolution form is as follows:

$$\widetilde{B}^{(3)} = (0.9134, 0.9362)\begin{pmatrix}1\\1&1\\1&1&1\\1&1&1&1\\1&1&1&1&1\\1&1&1&1&1&1\\1&1&1&1&1&1&1\\1&1&1&1&1&1&1&1\end{pmatrix} + (0.9157, 0.9570)\begin{pmatrix}1\\0&1\\0&1&1\\0&1&1&1\\0&1&1&1&1\\0&1&1&1&1&1\\0&1&1&1&1&1&1\\0&1&1&1&1&1&1&1\end{pmatrix}$$

$$+ (0.9572, 0.9760)\begin{pmatrix}1\\0&1\\0&0&1\\0&1&0&1\\0&1&0&1&1\\0&1&0&1&1&1\\0&1&0&1&1&1&1\\0&1&0&1&1&1&1&1\end{pmatrix} + (0.9575, 0.9760)\begin{pmatrix}1\\0&1\\0&0&1\\0&1&0&1\\0&1&0&1&1\\0&1&0&1&1&1\\0&1&0&1&1&1&1\\0&0&0&0&0&0&0&1\end{pmatrix}$$

$$+ (0.9595, 0.9857)\begin{pmatrix}1\\0&1\\0&0&1\\0&0&0&1\\0&1&0&0&1\\0&0&0&1&0&1\\0&1&0&0&1&0&1\\0&0&0&0&0&0&0&1\end{pmatrix} + (0.9649, 0.9760)\begin{pmatrix}1\\0&1\\0&0&1\\0&0&0&1\\0&1&0&0&1\\0&0&0&0&0&1\\0&1&0&0&1&0&1\\0&0&0&0&0&0&0&1\end{pmatrix}$$

$$+ (0.9706, 0.9760)\begin{pmatrix}1\\0&1\\0&0&1\\0&0&0&1\\0&0&0&0&1\\0&0&0&0&0&1\\0&1&0&0&0&0&1\\0&0&0&0&0&0&0&1\end{pmatrix} + (1,1)\begin{pmatrix}1\\0&1\\0&0&1\\0&0&0&1\\0&0&0&0&1\\0&0&0&0&0&1\\0&0&0&0&0&0&1\\0&0&0&0&0&0&0&1\end{pmatrix}.$$

Consequently, the hierarchical structure of the IVFR is depicted in Fig. 1

3 (α, β)-cut for IFR

In this section we developed an algorithm to construct the (α, β)-cuts for an intuitionistic fuzzy relation (IFR). Taking motivation from IFS, Bustince and Burillo [22] defined IFR as follows.

Definition 6 (*Intuitionistic fuzzy relation (IFR)*) [22] An IFR R on the two sets X and Y is an intuitionistic fuzzy subset of $X \times Y$ defined by

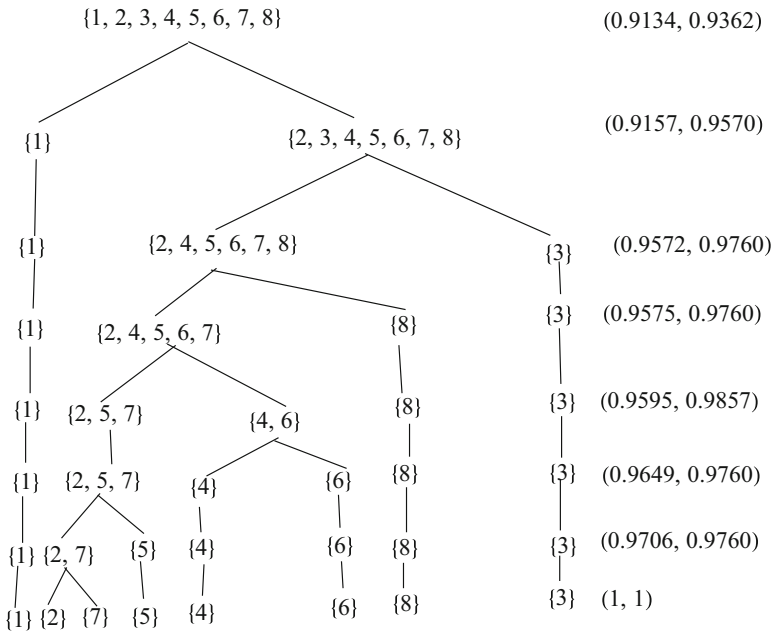


Fig. 1 Hierarchical clustering for IVFR in Example 3

$R = \{\langle (x, y), \mu_R(x, y), \nu_R(x, y)\rangle \mid x \in X,\ y \in Y\}$, where $\mu_R,\ \nu_R : X \times Y \to [0, 1]$ such that $0 \leq \mu_R(x, y) + \nu_R(x, y) \leq 1,\ \forall\, (x, y) \in X \times Y$.

Banerjee and Basnet [23] presented some properties of IFR.

Definition 7 (*Intuitionistic fuzzy proximity relation*) An IFR R on X is called intuitionistic fuzzy proximity relation if it satisfies the following properties:

1. Reflexive: $\mu_R(x, x) = 1,\ \nu_R(x, x) = 0, \forall\, x \in X$.
2. Symmetry: $\mu_R(x, y) = \mu_R(y, x),\ \nu_R(x, y) = \nu_R(y, x),\ \forall\, x, y \in X$.

Definition 8 (*Intuitionistic fuzzy (max–min) similarity relation*) An intuitionistic fuzzy proximity relation R on X is called an intuitionistic fuzzy (max–min) similarity relation if it satisfy the following transitive relation:

$$\mu_R(x, y) \geq \max_{z \in X}\{\min\{\mu_R(x, z), \mu_R(z, y)\}\},$$
$$\nu_R(x, y) \leq \min_{z \in X}\{\max\{\nu_R(x, z), \nu_R(z, y)\}\}.$$

Definition 9 The (α, β)-cut of an IFS A is defined in [20] as follows:

$$A_{(\alpha,\beta)} = \{x \in X \mid \mu_A(x) \geq \alpha,\ \nu_A(x) \leq \beta\}.$$

We propose an algorithm for determining the (α, β)-cut for intuitionistic fuzzy (max–min) similarity relation.

Algorithm 2

1. From all pair of (μ_i, v_i) in the matrix representation of IFR, first choose the maximum value of the membership μ_i, say μ_i^*.
2. Then among all possible tuples (μ_i^*, v_i), choose the one with maximum non-membership value. This gives the first (α, β)-cut of IFR.
3. Cross-off this selected cut value from matrix of IFR. And, continue this procedure to remaining elements (μ_i, v_i) of the matrix of IFR.

Remark 1 Instead of starting with membership function, one can also start with a non-membership function. For this, among all entries of the matrix representation of R, choose the one with minimum non-membership value, and then for this value choose the tuple with minimum membership value also. Continue this procedure with all elements of the IFR till each of them is searched out.

A MATLAB code is designed for finding (α, β)-cuts of IFR R of order m. We present below one instance of many examples generated through the code.

Example 4 Consider a randomly generated IFR proximity relation matrix of order 9 as follows:

$$\widetilde{B}^{(0)} = \begin{pmatrix} (1,0) & \binom{0.814724,}{0.128735} & \binom{0.905792,}{0.029873} & \binom{0.126987,}{0.829556} & \binom{0.913376,}{0.002984} & \binom{0.632359,}{0.1613} & \binom{0.09754,}{0.344341} & \binom{0.278498,}{0.552322} & \binom{0.546882,}{0.36032} \\ \binom{0.814724,}{0.128735} & (1,0) & \binom{0.957507,}{0.007941} & \binom{0.964889,}{0.017196} & \binom{0.157613,}{0.375356} & \binom{0.970593,}{0.019006} & \binom{0.957167,}{0.030384} & \binom{0.485376,}{0.38838} & \binom{0.80028,}{0.055128} \\ \binom{0.905792,}{0.029873} & \binom{0.957507,}{0.007941} & (1,0) & \binom{0.141886,}{0.583262} & \binom{0.421761,}{0.378803} & \binom{0.915736,}{0.013702} & \binom{0.792207,}{0.024727} & \binom{0.959492,}{0.020188} & \binom{0.655741,}{0.330401} \\ \binom{0.126987,}{0.829556} & \binom{0.964889,}{0.017196} & \binom{0.141886,}{0.583262} & (1,0) & \binom{0.035712,}{0.32823} & \binom{0.849129,}{0.0883} & \binom{0.933993,}{0.014773} & \binom{0.678735,}{0.241356} & \binom{0.75774,}{0.061799} \\ \binom{0.913376,}{0.002984} & \binom{,0.157613,}{0.375356} & \binom{0.421761,}{0.378803} & \binom{0.035712,}{0.32823} & (1,0) & \binom{0.743132,}{0.129964} & \binom{0.392227,}{0.42488} & \binom{0.655478,}{0.306936} & \binom{0.171187,}{0..795074} \\ \binom{0.632359,}{0.1613} & \binom{,0.970593,}{0.019006} & \binom{0.915736,}{0.013702} & \binom{0.849129,}{0.0883} & \binom{0.743132,}{0.129964} & (1,0) & \binom{0.706046,}{0.160856} & \binom{0.031833,}{0.134212} & \binom{0.276923,}{0.107951} \\ \binom{0.09754,}{0.344341} & \binom{0.957167,}{0.030384} & \binom{0.792207,}{0.024727} & \binom{0.933993,}{0.014773} & \binom{0.392227,}{0.42488} & \binom{0.706046,}{0.160856} & (1,0) & \binom{0.046171,}{0.245619} & \binom{0.097132,}{0.759057} \\ \binom{0.278498,}{0.552322} & \binom{0.485376,}{0.38838} & \binom{0.959492,}{0.020188} & \binom{0.678735,}{0.241356} & \binom{0.655478,}{0.306936} & \binom{0.031833,}{0.134212} & \binom{0.046171,}{0.245619} & (1,0) & \binom{0.823458,}{0.044892} \\ \binom{0.546882,}{0.36032} & \binom{0.80028,}{0.055128} & \binom{0.655741,}{0.330401} & \binom{0.75774,}{0.061799} & \binom{0.171187,}{0.795074} & \binom{0.276923,}{0.107951} & \binom{0.097132,}{0.759057} & \binom{0.823458,}{0.044892} & (1,0) \end{pmatrix}.$$

Applying the max–min composition the similarity relation matrix is generated.

$$\widetilde{B}^{(3)} = \begin{pmatrix} (1,0) & \begin{pmatrix}0.9058,\\0.0299\end{pmatrix} & \begin{pmatrix}0.9058,\\0.0299\end{pmatrix} & \begin{pmatrix}0.9058,\\0.0299\end{pmatrix} & \begin{pmatrix}0.9134,\\0.0030\end{pmatrix} & \begin{pmatrix}0.9058,\\0.0299\end{pmatrix} & \begin{pmatrix}0.9058,\\0.0299\end{pmatrix} & \begin{pmatrix}0.9058,\\0.0299\end{pmatrix} & \begin{pmatrix}0.8235,\\0.0449\end{pmatrix} \\ \begin{pmatrix}0.9058,\\0.0299\end{pmatrix} & (1,0) & \begin{pmatrix}0.9575,\\0.0079\end{pmatrix} & \begin{pmatrix}0.9649,\\0.0172\end{pmatrix} & \begin{pmatrix}0.9058,\\0.0299\end{pmatrix} & \begin{pmatrix}0.9706,\\0.0137\end{pmatrix} & \begin{pmatrix}0.9572,\\0.0172\end{pmatrix} & \begin{pmatrix}0.9575,\\0.0202\end{pmatrix} & \begin{pmatrix}0.8235,\\0.0449\end{pmatrix} \\ \begin{pmatrix}0.9058,\\0.0299\end{pmatrix} & \begin{pmatrix}0.9575,\\0.0079\end{pmatrix} & (1,0) & \begin{pmatrix}0.9575,\\0.0172\end{pmatrix} & \begin{pmatrix}0.9058,\\0.0299\end{pmatrix} & \begin{pmatrix}0.9575,\\0.0137\end{pmatrix} & \begin{pmatrix}0.9572,\\0.0172\end{pmatrix} & \begin{pmatrix}0.9595,\\0.0202\end{pmatrix} & \begin{pmatrix}0.8235,\\0.0449\end{pmatrix} \\ \begin{pmatrix}0.9058,\\0.0299\end{pmatrix} & \begin{pmatrix}0.9649,\\0.0172\end{pmatrix} & \begin{pmatrix}0.9575,\\0.0172\end{pmatrix} & (1,0) & \begin{pmatrix}0.9058,\\0.0299\end{pmatrix} & \begin{pmatrix}0.9649,\\0.0172\end{pmatrix} & \begin{pmatrix}0.9572,\\0.0148\end{pmatrix} & \begin{pmatrix}0.9575,\\0.0202\end{pmatrix} & \begin{pmatrix}0.8235,\\0.0449\end{pmatrix} \\ \begin{pmatrix}0.9134,\\0.0030\end{pmatrix} & \begin{pmatrix}0.9058,\\0.0299\end{pmatrix} & \begin{pmatrix}0.9058,\\0.0299\end{pmatrix} & \begin{pmatrix}0.9058,\\0.0299\end{pmatrix} & (1,0) & \begin{pmatrix}0.9058,\\0.0299\end{pmatrix} & \begin{pmatrix}0.9058,\\0.0299\end{pmatrix} & \begin{pmatrix}0.9058,\\0.0299\end{pmatrix} & \begin{pmatrix}0.8235,\\0.0449\end{pmatrix} \\ \begin{pmatrix}0.9058,\\0.0299\end{pmatrix} & \begin{pmatrix},0.9706,\\0.0137\end{pmatrix} & \begin{pmatrix}0.9575,\\0.0137\end{pmatrix} & \begin{pmatrix}0.9649,\\0.0172\end{pmatrix} & \begin{pmatrix}0.9058,\\0.0299\end{pmatrix} & (1,0) & \begin{pmatrix}0.9572,\\0.0172\end{pmatrix} & \begin{pmatrix}0.9575,\\0.0202\end{pmatrix} & \begin{pmatrix}0.8235,\\0.0449\end{pmatrix} \\ \begin{pmatrix}0.9058,\\0.0299\end{pmatrix} & \begin{pmatrix}0.9572,\\0.0172\end{pmatrix} & \begin{pmatrix}0.9572,\\0.0172\end{pmatrix} & \begin{pmatrix}0.9572,\\0.0148\end{pmatrix} & \begin{pmatrix}0.9058,\\0.0299\end{pmatrix} & \begin{pmatrix}0.9572,\\0.0172\end{pmatrix} & (1,0) & \begin{pmatrix}0.9572,\\0.0202\end{pmatrix} & \begin{pmatrix}0.8235,\\0.0449\end{pmatrix} \\ \begin{pmatrix}0.9058,\\0.0299\end{pmatrix} & \begin{pmatrix}0.9575,\\0.0202\end{pmatrix} & \begin{pmatrix}0.9595,\\0.0202\end{pmatrix} & \begin{pmatrix}0.9575,\\0.0202\end{pmatrix} & \begin{pmatrix}0.9058,\\0.0299\end{pmatrix} & \begin{pmatrix}0.9575,\\0.0202\end{pmatrix} & \begin{pmatrix}0.9572,\\0.0202\end{pmatrix} & (1,0) & \begin{pmatrix}0.8235,\\0.0449\end{pmatrix} \\ \begin{pmatrix}0.8235,\\0.0449\end{pmatrix} & \begin{pmatrix}0.8235,\\0.0449\end{pmatrix} & \begin{pmatrix}0.8235,\\0.0449\end{pmatrix} & \begin{pmatrix}0.8235,\\0.0449\end{pmatrix} & \begin{pmatrix}0.8235,\\0.0449\end{pmatrix} & \begin{pmatrix}0.8235,\\0.0449\end{pmatrix} & \begin{pmatrix}0.8235,\\0.0449\end{pmatrix} & \begin{pmatrix}0.8235,\\0.0449\end{pmatrix} & (1,0) \end{pmatrix}.$$

The (α, β)-cuts of $\widetilde{B}^{(3)}$ are

$(1,0),\ (0.9706, 0.0137),\ (0.9649, 0.0172),\ (0.9595, 0.0202),\ (0.9575, 0.0202),$
$(0.9572, 0.0202),\ (0.9134, 0.0030),\ (0.9058, 0.0299),\ (0.8235, 0.0449).$

The resolution form resulting in the hierarchy tree is explained in Fig 2.

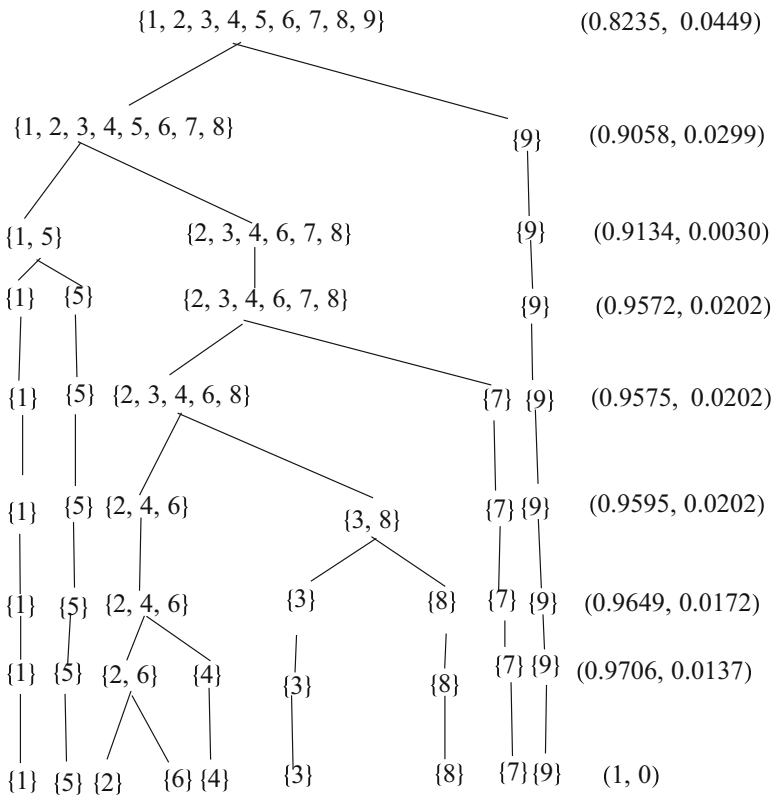


Fig. 2 Hierarchical clustering for IFR in Example 4

$$\widetilde{B}^{(3)} = (0.8235, 0.0449)\begin{pmatrix}1\\1&1\\1&1&1\\1&1&1&1\\1&1&1&1&1\\1&1&1&1&1&1\\1&1&1&1&1&1&1\\1&1&1&1&1&1&1&1\\1&1&1&1&1&1&1&1&1\end{pmatrix} + (0.9058, 0.0299)\begin{pmatrix}1\\1&1\\1&1&1\\1&1&1&1\\1&1&1&1&1\\1&1&1&1&1&1\\1&1&1&1&1&1&1\\1&1&1&1&1&1&1&1\\0&0&0&0&0&0&0&0&1\end{pmatrix}$$

$$+ (0.9134, 0.0030)\begin{pmatrix}1\\0&1\\0&1&1\\0&1&1&1\\1&0&0&0&1\\0&1&1&1&0&1\\0&1&1&1&0&1&1\\0&1&1&1&0&1&1&1\\0&0&0&0&0&0&0&0&1\end{pmatrix} + (0.9572, 0.0202)\begin{pmatrix}1\\0&1\\0&1&1\\0&1&1&1\\0&0&0&0&1\\0&1&1&1&0&1\\0&1&1&1&0&1&1\\0&1&1&1&0&1&1&1\\0&0&0&0&0&0&0&0&1\end{pmatrix}$$

$$+ (0.9649, 0.0172)\begin{pmatrix}1\\0&1\\0&0&1\\0&1&0&1\\0&0&0&0&1\\0&1&0&1&0&1\\0&0&0&0&0&0&1\\0&0&0&0&0&0&0&1\\0&0&0&0&0&0&0&0&1\end{pmatrix} + (0.9706, 0.0137)\begin{pmatrix}1\\0&1\\0&0&1\\0&0&0&1\\0&0&0&0&1\\0&1&0&0&0&1\\0&0&0&0&0&0&1\\0&0&0&0&0&0&0&1\\0&0&0&0&0&0&0&0&1\end{pmatrix}$$

$$+ (1, 0)\begin{pmatrix}1\\0&1\\0&0&1\\0&0&0&1\\0&0&0&0&1\\0&0&0&0&0&1\\0&0&0&0&0&0&1\\0&0&0&0&0&0&0&1\\0&0&0&0&0&0&0&0&1\end{pmatrix}.$$

4 Interval-valued Intuitionistic Fuzzy Relation (IVIFR) and Operations

In this section we focus on extending the methodologies detailed in previous sections on IVIFR.

Definition 10 [*Interval-valued intuitionistic fuzzy set (IVIFS)*] [5] An IVIFS A in X is described by

$$A = \{\langle x, \widetilde{\mu}_A(x), \widetilde{\nu}_A(x)\rangle \mid x \in X\},$$

where $\widetilde{\mu}_A(x) = [\underline{\mu}_A(x), \overline{\mu}_A(x)]$, and $\underline{\mu}_A(x)$ and $\overline{\mu}_A(x)$ are respectively the lower and the upper values of the membership degree, while $\widetilde{\nu}_A(x) = [\underline{\nu}_A(x), \overline{\nu}_A(x)]$, and $\underline{\nu}_A(x)$ and $\overline{\nu}_A(x)$ are respectively the lower and the upper values of the non-membership degree, such that the following hold.

$$0 \le \underline{\mu}_A(x) \le \overline{\mu}_A(x) \le 1, \quad 0 \le \underline{\nu}_A(x) \le \overline{\nu}_A(x) \le 1, \quad 0 \le \overline{\mu}_A(x) + \overline{\nu}_A(x) \le 1, \quad \forall\, x \in X.$$

For convenience, an interval-intuitionistic fuzzy value is abbreviated as $([\underline{\mu}(x),\ \overline{\mu}(x)],\ [\underline{\nu}(x),\ \overline{\nu}(x)])$.

The following is a natural extension of IFR.

Definition 11 (*Interval-valued intuitionistic fuzzy relation (IVIFR)*) [5] An IVIFR $\widetilde{R}$ between two sets X and Y is an interval-valued intuitionistic fuzzy subset of $X \times Y$ associated with an interval-valued membership $\widetilde{\mu}_{\widetilde{R}}(x,y) = [\underline{\mu}_{\widetilde{R}}(x,y),\ \overline{\mu}_{\widetilde{R}}(x,y)]$ and interval-valued non-membership $\widetilde{\nu}_{\widetilde{R}}(x,y) = [\underline{\nu}_{\widetilde{R}}(x,y),\ \overline{\nu}_{\widetilde{R}}(x,y)]$, for (x, y) in $X \times Y$. The values $\underline{\mu}_{\widetilde{R}}(x,y)$ and $\overline{\mu}_{\widetilde{R}}(x,y)$ denote the left and right endpoints of $\widetilde{\mu}_{\widetilde{R}}(x,y)$ with $0 \le \underline{\mu}_{\widetilde{R}}(x,y) \le \overline{\mu}_{\widetilde{R}}(x,y) \le 1$, and $\underline{\nu}_{\widetilde{R}}(x,y)$ and $\overline{\nu}_{\widetilde{R}}(x,y)$ denote the left and right end points of $\widetilde{\nu}_{\widetilde{R}}(x,y)$ with $0 \le \underline{\nu}_{\widetilde{R}}(x,y) \le \overline{\nu}_{\widetilde{R}}(x,y) \le 1$. An IVIFR $\widetilde{R}$ on $X = \{x_1, \ldots, x_m\}$ can be represented as follows:

$$\widetilde{R} = \begin{bmatrix} ([1,1],[0,0]) & (\tilde{\mu}_R(x_1,x_2), \tilde{\nu}_R(x_1,x_2)) & \cdots & (\tilde{\mu}_R(x_1,x_m), \tilde{\nu}_R(x_1,x_m)) \\ (\tilde{\mu}_R(x_2,x_1), \tilde{\nu}_R(x_2,x_1)) & ([1,1],[0,0]) & \cdots & (\tilde{\mu}_R(x_2,x_m), \tilde{\nu}_R(x_2,x_m)) \\ \vdots & \vdots & \cdots & \vdots \\ (\tilde{\mu}_R(x_m,x_1), \tilde{\nu}_R(x_m,x_1)) & (\tilde{\mu}_R(x_m,x_2), \tilde{\nu}_R(x_m,x_2)) & \cdots & ([1,1],[0,0]) \end{bmatrix}.$$

We define few operations and definitions on IVIFR.

Definition 12 (*Max and min operations for IVIFR*) Let $(\widetilde{\mu}_R(x_1,x_2), \widetilde{\nu}_R(x_1, x_2)) = ([\underline{\mu}_R(x_1,x_2),\ \overline{\mu}_R(x_1,x_2)],\ [\underline{\nu}_R(x_1,x_2),\ \overline{\nu}_R(x_1,x_2)])$, and $(\widetilde{\mu}_R(x_3,x_4), \widetilde{\nu}_R(x_3, x_4)) = ([\underline{\mu}_R(x_3,x_4),\ \overline{\mu}_R(x_3,x_4)],\ [\underline{\nu}_R(x_3,x_4), \overline{\nu}_R(x_3,x_4)])$ be two interval-valued intuitionistic fuzzy values of IVIFR $\widetilde{R}$ in X. Define

$$\min\{(\tilde{\mu}_R(x_1,x_2),\ \tilde{\nu}_R(x_1,x_2),\ (\tilde{\mu}_R(x_3,x_4), \tilde{\nu}_R(x_3,x_4))\} = ([\min\{\underline{\mu}_R(x_1,x_2), \underline{\mu}_R(x_3,x_4)\},$$
$$\min\{\overline{\mu}_R(x_1,x_2), \overline{\mu}_R(x_3,x_4)\}], [\max\{\underline{\nu}_R(x_1,x_2), \underline{\nu}_R(x_3,x_4)\}, \max\{\overline{\nu}_R(x_1,x_2), \overline{\nu}_R(x_3,x_4)\}]).$$
$$\max\{(\widetilde{\mu}_R(x_1,x_2),\ \widetilde{\nu}_R(x_1,x_2)),\ \ (\widetilde{\mu}_R(x_3,x_4), \widetilde{\nu}_R(x_3,x_4))\} = ([\max\{\underline{\mu}_R(x_1,x_2),\ \underline{\mu}_R(x_3,x_4)\},$$
$$\max\{\overline{\mu}_R(x_1,x_2),\ \overline{\mu}_R(x_3,x_4)\}], [\min\{\underline{\nu}_R(x_1,x_2),\ \underline{\nu}_R(x_3,x_4)\}, \min\{\overline{\nu}_R(x_1,x_2),\ \overline{\nu}_R(x_3,x_4)\}]).$$

Similar to the IVFR and IFR, we define the similarity relation for IVIFR.

Definition 13 (*Interval-valued intuitionistic fuzzy proximity relation*) An IVIFR $\widetilde{R}$ in X is called interval-valued intuitionistic fuzzy proximity relation if it satisfies the following two properties:

1. Reflexive: $\widetilde{\mu}_{\widetilde{R}}(x,x) = [1,1],\ \widetilde{\nu}_{\widetilde{R}}(x,x) = [0,0],\ \forall\, x \in X.$
2. Symmetry: $\widetilde{\mu}_{\widetilde{R}}(x,y) = \widetilde{\mu}_{\widetilde{R}}(y,x),\ \widetilde{\nu}_{\widetilde{R}}(x,y) = \widetilde{\nu}_{\widetilde{R}}(y,x),\ \forall\, x,y \in X.$

For example, the following $\widetilde{R}$ is an IVIF proximity relation on $X = \{x_1, x_2, x_3, x_4\}$.

$$\widetilde{R} = \begin{bmatrix} ([1,1],[0,0]) & ([0.2,0.4],[0.4,0.6]) & ([0.5,0.7],[0.1,0.3]) & ([0.3,0.6],[0.2,0.4]) \\ ([0.2,0.4],[0.4,0.6]) & ([1,1],[0,0]) & ([0.5,0.8],[0.1,0.2]) & ([0.7,0.8],[0.1,0.2]) \\ ([0.5,0.7],[0.1,0.3]) & ([0.5,0.8],[0.1,0.2]) & ([1,1],[0,0]) & ([0.2,0.3],[0.4,0.6]) \\ ([0.3,0.6],[0.2,0.4]) & ([0.7,0.8],[0.1,0.2]) & ([0.2,0.3],[0.4,0.6]) & ([1,1],[0,0]) \end{bmatrix}.$$

Definition 14 (*Interval-valued intuitionistic max–min similarity relation*) An IVIF proximity relation $\widetilde{R}$ on X is called an interval-valued intuitionistic (max–min) similarity relation if for any $x,y,z \in X$, and any two interval-valued intuitionistic fuzzy values,

$$(\widetilde{\mu}_{\widetilde{R}}(x,y),\ \widetilde{\nu}_{\widetilde{R}}(x,y)) = \left([\underline{\mu}_{\widetilde{R}}(x,y),\ \overline{\mu}_{\widetilde{R}}(x,y)],\ [\underline{\nu}_{\widetilde{R}}(x,y),\ \overline{\nu}_{\widetilde{R}}(x,y)]\right),$$

and

$$(\widetilde{\mu}_{\widetilde{R}}(y,z),\ \widetilde{\nu}_{\widetilde{R}}(y,z)) = \left([\underline{\mu}_{\widetilde{R}}(y,z),\ \overline{\mu}_{\widetilde{R}}(y,z)],\ [\underline{\nu}_{\widetilde{R}}(y,z),\ \overline{\nu}_{\widetilde{R}}(y,z)]\right),$$

the following transitivity property is satisfied.

$$\underline{\mu}_{\widetilde{R}}(x,z) \geq \max_{z\in X}\{\min\{\underline{\mu}_{\widetilde{R}}(x,y), \underline{\mu}_{R}(y,z)\}\},$$
$$\overline{\mu}_{\widetilde{R}}(x,z) \geq \max_{z\in X}\{\min\{\overline{\mu}_{\widetilde{R}}(x,y), \overline{\mu}_{\widetilde{R}}(y,z)\}\},$$

and

$$\underline{\nu}_{\widetilde{R}}(x,z) \leq \min_{z\in X}\{\max\{\underline{\nu}_{\widetilde{R}}(x,y), \underline{\nu}_{R}(y,z)\}\},$$
$$\overline{\nu}_{\widetilde{R}}(x,z) \leq \min_{z\in X}\{\max\{\overline{\nu}_{\widetilde{R}}(x,y), \overline{\nu}_{\widetilde{R}}(y,z)\}\}.$$

We now define the $(\tilde{\alpha},\tilde{\beta})$-cuts for IVIFS.

Definition 15 The $(\tilde{\alpha},\tilde{\beta})$-cut for an IVIFS is described by $A_{(\tilde{\alpha},\tilde{\beta})} = \{x \mid [\underline{\mu},\overline{\mu}] \geq \tilde{\alpha}\ \text{ and }\ [\underline{\nu},\overline{\nu}] \leq \tilde{\beta}\}$, where $\tilde{\alpha}$ and $\tilde{\beta}$ are also interval-valued type.

Note that $(\tilde{\alpha},\tilde{\beta})$-cut is an order pair of membership and non-membership values

with $(\tilde{\alpha},\tilde{\beta}) = (\tilde{\mu}_\alpha, \tilde{\nu}_\beta) = ([\underline{\mu}_\alpha, \overline{\mu}_\alpha],\ [\underline{\nu}_\beta, \overline{\nu}_\beta])$, where $0 \le \underline{\mu}_\alpha \le \overline{\mu}_\alpha \le 1$ and $0 \le \underline{\nu}_\beta \le \overline{\nu}_\beta \le 1,\ \ 0 \le \overline{\mu}_\alpha + \overline{\nu}_\beta \le 1$.

To explain Definition 15, we present an algorithm listing the procedure of constructing all $(\tilde{\alpha},\tilde{\beta})$-cuts in IVIFR $\widetilde{R}$.

Algorithm 3

1. Among all pairs of elements of the form $([\underline{\mu}_i, \overline{\mu}_i], [\underline{\nu}_i, \overline{\nu}_i])$ in the matrix representation of $\widetilde{R}$, choose the maximum value among the lower values of the membership, i. e. $\max_i\{\underline{\mu}_i\}$, and fixed it.
2. Thereafter, among all possible elements in $\widetilde{R}$ having this fixed lower membership value (as in preceding step), choose the one having minimum upper value of the membership.
3. Among all elements in $\widetilde{R}$ with the fixed interval membership degree (as obtained in the previous two steps), choose those having maximum lower value for the non-membership (fixed this one), and thereafter pick the corresponding maximum upper non-membership value. The respective pair of membership and non-membership degrees is the $(\tilde{\alpha},\tilde{\beta})$-cut.
4. Crossed-off this element from $\widetilde{R}$, and continue the above listed procedure with the remaining elements of $\widetilde{R}$, till all elements are searched through.

Definition 16 (*Resolution form for interval-valued intuitionistic similarity relation*) An IVIF (max–min) similarity relation $\widetilde{R}$ on X can be decomposed into a resolution form by using $(\widetilde{\alpha},\widetilde{\beta})$-cuts with corresponding $R_{(\widetilde{\alpha},\widetilde{\beta})}$ being reflexive, symmetric and transitive.

$$\widetilde{R} = \bigcup_{(\widetilde{\alpha},\widetilde{\beta})} (\widetilde{\alpha},\widetilde{\beta}) R_{(\widetilde{\alpha},\widetilde{\beta})} = \sum_{i=1}^{m} ([\underline{\mu}_{\alpha_i},\ \overline{\mu}_{\alpha_i}],\ [\underline{\nu}_{\beta_i},\ \overline{\nu}_{\beta_i}]) R_{(\widetilde{\alpha}_i,\widetilde{\beta}_i)},$$

$$\underline{\mu}_i \ge \underline{\mu}_{\alpha_i},\ \ \overline{\mu}_i \ge \overline{\mu}_{\alpha_i},\ \ \underline{\nu}_i \le \underline{\nu}_{\beta_i},\ \ \overline{\nu}_i \le \overline{\nu}_{\beta_i},\ \ \overline{\mu}_{\alpha_i} + \overline{\nu}_{\beta_i} \le 1.$$

with this background, we are ready to explain the clustering scheme for IVIFR.

5 Hierarchical Clustering for IVIFR

The subjective information is commonly represented by a matrix which in general is reflexive and symmetry but need not be transitive. However, transitivity is an essential property to build hierarchal clustering [19]. An *n*-step procedure is employed to get an interval-valued max–min similarity relation matrix using an interval-valued intuitionistic max–min composition, described as follows..

Definition 17 (*Interval-valued intuitionistic max–min composition*) Given an initial interval-valued intuitionistic relation matrix $\widetilde{R}^{(0)} = (\widetilde{\mu}_{r_{ij}^{(0)}}, \widetilde{\nu}_{r_{ij}^{(0)}})_{m\times m}$

$= ([\underline{\mu}_{r_{ij}^{(0)}}, \overline{\mu}_{r_{ij}^{(0)}}],\ [\underline{v}_{r_{ij}^{(0)}}, \overline{v}_{r_{ij}^{(0)}}])$. Then $\widetilde{R}^{(n)} = (\widetilde{\mu}_{r_{ij}^{(n)}}, \widetilde{v}_{r_{ij}^{(n)}})_{m\times m} = ([\underline{\mu}_{r_{ij}^{(n)}}, \overline{\mu}_{r_{ij}^{(n)}}],\ [\underline{v}_{r_{ij}^{(n)}}, \overline{v}_{r_{ij}^{(n)}}])$ with

$$\underline{\mu}_{r_{ij}^{(n)}} = \max_k\{\min\{\underline{\mu}_{r_{ik}^{(n-1)}},\ \underline{\mu}_{r_{kj}^{(n-1)}}\}\},\quad \overline{\mu}_{r_{ij}^{(n)}} = \max_k\{\min\{\overline{\mu}_{r_{ik}^{(n-1)}},\ \overline{\mu}_{r_{kj}^{(n-1)}}\}\},$$

and

$$\underline{v}_{r_{ij}^{(n)}} = \min_k\{\max\{\underline{v}_{r_{ik}^{(n-1)}},\ \underline{v}_{r_{kj}^{(n-1)}}\}\},\quad \overline{v}_{r_{ij}^{(n)}} = \min_k\{\max\{\overline{v}_{r_{ik}^{(n-1)}},\ \overline{v}_{r_{kj}^{(n-1)}}\}\},$$

$n = 1, 2, \ldots$, is called an interval-valued intuitionistic relation matrix through an n-step max–min composition.

Theorem 1 *Let* $R^{(0)} = (\mu_{r_{ij}^{(0)}}, v_{r_{ij}^{(0)}})_{m\times m}$ *and* $\widetilde{R}^{(0)} = (\widetilde{\mu}_{r_{ij}^{(0)}}, \widetilde{v}_{r_{ij}^{(0)}}) = ([\underline{\mu}_{r_{ij}^{(0)}}, \overline{\mu}_{r_{ij}^{(0)}}], [\underline{v}_{r_{ij}^{(0)}}, \overline{v}_{r_{ij}^{(0)}}])$ *be respectively IFR and IVIFR with* $\underline{\mu}_{r_{ij}^{(0)}} \le \mu_{r_{ij}^{(0)}} \le \overline{\mu}_{r_{ij}^{(0)}}$ *and* $\underline{v}_{r_{ij}^{(0)}} \le v_{r_{ij}^{(0)}} \le \overline{v}_{r_{ij}^{(0)}},\ \forall\ i,j$. *If* $R^{(n)} = (\mu_{r_{ij}^{(n)}}, v_{r_{ij}^{(n)}})$ *and* $\widetilde{R}^{(n)} = (\widetilde{\mu}_{r_{ij}^{(n)}}, \widetilde{v}_{r_{ij}^{(n)}}) = ([\underline{\mu}_{r_{ij}^{(n)}}, \overline{\mu}_{r_{ij}^{(n)}}],\ [\underline{v}_{r_{ij}^{(n)}}, \overline{v}_{r_{ij}^{(n)}}])_{m\times m}$ *are respectively IFR and IVIFR, through n-step max–min compositions, then we have* $\underline{\mu}_{r_{ij}^{(n)}} \le \mu_{r_{ij}^{(n)}} \le \overline{\mu}_{r_{ij}^{(n)}}$ *and* $\underline{v}_{r_{ij}^{(n)}} \le v_{r_{ij}^{(n)}} \le \overline{v}_{r_{ij}^{(n)}}$, for $n = 1, 2, \ldots$.

Proof Developing $\underline{\mu}_{r_{ij}^{(1)}}$, $\overline{\mu}_{r_{ij}^{(1)}}$, $\underline{v}_{r_{ij}^{(1)}}$, $\overline{v}_{r_{ij}^{(1)}}$, $\mu_{r_{ij}^{(1)}}$, and $v_{r_{ij}^{(1)}}$, we have,

$$\begin{aligned}
\underline{\mu}_{r_{ij}^{(1)}} &= \max_k\{\min(\underline{\mu}_{r_{ik}^{(0)}}, \underline{\mu}_{r_{kj}^{(0)}})\},\quad \overline{\mu}_{r_{ij}^{(1)}} = \max_k\{\min(\overline{\mu}_{r_{ik}^{(0)}}, \overline{\mu}_{r_{kj}^{(0)}})\}\\
\underline{v}_{r_{ij}^{(1)}} &= \min_k\{\max(\underline{v}_{r_{ik}^{(0)}}, \underline{v}_{r_{kj}^{(0)}})\},\quad \overline{v}_{r_{ij}^{(1)}} = \min_k\{\max(\overline{v}_{r_{ik}^{(0)}}, \overline{v}_{r_{kj}^{(0)}})\}\\
\mu_{r_{ij}^{(1)}} &= \max_k\{\min(\mu_{r_{ik}^{(0)}}, \mu_{r_{kj}^{(0)}})\},\quad v_{r_{ij}^{(1)}} = \min_k\{\max(v_{r_{ik}^{(0)}}, v_{r_{kj}^{(0)}})\}.
\end{aligned}$$

Since $\underline{\mu}_{r_{ij}^{(0)}} \le \mu_{r_{ij}^{(0)}} \le \overline{\mu}_{r_{ij}^{(0)}}$, and $\underline{v}_{r_{ij}^{(0)}} \le v_{r_{ij}^{(0)}} \le \overline{v}_{r_{ij}^{(0)}},\ \forall\ i,j$, it is easy to show that $\underline{\mu}_{r_{ij}^{(1)}} \le \mu_{r_{ij}^{(1)}} \le \overline{\mu}_{r_{ij}^{(1)}}$, and $\underline{v}_{r_{ij}^{(1)}} \le v_{r_{ij}^{(1)}} \le \overline{v}_{r_{ij}^{(1)}}$.

Following induction on n, we can easily obtain the requisite result; completeing the proof. □

Remark 2 Since $\underline{\mu}_{r_{ij}^{(n)}} \le \mu_{r_{ij}^{(n)}} \le \overline{\mu}_{r_{ij}^{(n)}}$, and $\underline{v}_{r_{ij}^{(n)}} \le v_{r_{ij}^{(n)}} \le \overline{v}_{r_{ij}^{(n)}}$, $n = 1, 2, 3, \ldots$, we have $\underline{\mu}_{R^{(n)}} \le \mu_{R^{(n)}} \le \overline{\mu}_{R^{(n)}}$ and $\underline{v}_{R^{(n)}} \le v_{R^{(n)}} \le \overline{v}_{R^{(n)}}$. It is implied that if a matrix representation of IFR $\widehat{R}^{(0)} = (\mu_{R^{(0)}},\ v_{R^{(0)}})$ is taken so as to satisfy $\underline{\mu}_{R^{(0)}} \le \mu_{R^{(0)}} \le \overline{\mu}_{R^{(0)}}$, $\underline{v}_{R^{(0)}} \le v_{R^{(0)}} \le \overline{v}_{R^{(0)}}$), then we always have $\underline{\mu}_{R^{(n)}} \le \mu_{R^{(n)}} \le \overline{\mu}_{R^{(n)}}$, and $\underline{v}_{R^{(n)}} \le v_{R^{(n)}} \le \overline{v}_{R^{(n)}},\ n = 1, 2, \ldots$.

The following algorithm provides the hierarchical clustering for IVIFR.

Algorithm 4 Let $\widetilde{R}^{(0)} = (\widetilde{\mu}_{R^{(0)}}, \widetilde{v}_{R^{(0)}}) = \left([\underline{\mu}_{R^{(0)}},\ \overline{\mu}_{R^{(0)}}],\ [\underline{v}_{R^{(0)}},\ \overline{v}_{R^{(0)}}]\right)$ be an IVIF proximity relation.

1. Initialize $k = 0$.
2. Set $\widetilde{R}^{(k+1)} = \widetilde{R}^{(k)} \circ \widetilde{R}^{(k)}$.
3. If $\widetilde{R}^{(k+1)} \neq \tilde{R}^{(k)}$, then set $k = k + 1$, and go to 2 above.
4. Else an IVIF (max–min) similarity relation $\widetilde{R}^{(k)}$ is obtained, and proceed to next step.
5. Decompose $\tilde{R}^{(k)}$ into resolution form using $(\widetilde{\alpha}, \widetilde{\beta})$-cuts with its corresponding $R_{(\widetilde{\alpha},\widetilde{\beta})}$ satisfying the reflexive, symmetric and transitivity properties.
6. Using resolution form, construct the hierarchical partition tree.

A MATLAB code is prepared to implement the above algorithm in which the matrix corresponding to an IVIFR is randomly generated matrix of order m. For illustration purpose, we present the following example.

Example 5 Consider the IVIF proximity relation:

$$\widetilde{R}^{(0)} = \begin{pmatrix} ([1,1],[0,0]) & & & & & & \\ \begin{pmatrix}[0.8147,0.8213],\\ [0.0956,0.1368]\end{pmatrix} & ([1,1],[0,0]) & & & & & \\ \begin{pmatrix}[0.9058,0.9857],\\ [0.0101,0.0113]\end{pmatrix} & \begin{pmatrix}[0.2785,0.5615],\\ [0.0801,0.3111]\end{pmatrix} & ([1,1],[0,0]) & & & & \\ \begin{pmatrix}[0.1269,0.9423],\\ [0.0103,0.0107]\end{pmatrix} & \begin{pmatrix}[0.5468,0.8438],\\ [0.0990,0.1178]\end{pmatrix} & \begin{pmatrix}[0.9706,0.9787],\\ [0.0032,0.0034]\end{pmatrix} & ([1,1],[0,0]) & & & \\ \begin{pmatrix}[0.9134,0.9722],\\ [0.0074,0.0136]\end{pmatrix} & \begin{pmatrix}[0.9575,0.9647],\\ [0.0024,0.0097]\end{pmatrix} & \begin{pmatrix}[0.9571,0.9591],\\ [0.0017,0.0048]\end{pmatrix} & \begin{pmatrix}[0.1418,0.7381],\\ [0.0549,0.0891]\end{pmatrix} & ([1,1],[0,0]) & & \\ \begin{pmatrix}[0.6323,0.9109],\\ [0.0055,0.0396]\end{pmatrix} & \begin{pmatrix}[0.9648,0.9896],\\ [0.0057,0.0070]\end{pmatrix} & \begin{pmatrix}[0.4854,0.5353],\\ [0.045523,0.231559]\end{pmatrix} & \begin{pmatrix}[0.4217,0.6051],\\ [0.1094,0.2311]\end{pmatrix} & \begin{pmatrix}[0.7922,0.7994],\\ [0.1252,0.1507]\end{pmatrix} & ([1,1],[0,0]) & \\ \begin{pmatrix}[0.0975,0.7682],\\ [0.0223,0.1498]\end{pmatrix} & \begin{pmatrix}[0.1576,0.1844],\\ [0.1301,0.5343]\end{pmatrix} & \begin{pmatrix}[0.8002,0.9647],\\ [0.0085,0.0338]\end{pmatrix} & \begin{pmatrix}[0.9157,0.9958],\\ [0.0003,0.0009]\end{pmatrix} & \begin{pmatrix}[0.9595,0.9772],\\ [0.0033,0.0058]\end{pmatrix} & \begin{pmatrix}[0.6557,0.7871],\\ [0.0592,0.1077]\end{pmatrix} & ([1,1],[0,0]) \end{pmatrix}.$$

Applying the n-step procedure described in Definition 17, an IVIF symmetric relation $\tilde{R}^{(3)}$ is obtained.

$$\widetilde{R}^{(3)} = \begin{pmatrix} ([1,1],[0,0]) & & & & & & \\ \begin{pmatrix}[0.9134,0.9648],\\ [0.0057,0.0108]\end{pmatrix} & ([1,1],[0,0]) & & & & & \\ \begin{pmatrix}[0.9134,0.9858],\\ [0.0057,0.0108]\end{pmatrix} & \begin{pmatrix}[0.9572,0.9648],\\ [0.0025,0.0097]\end{pmatrix} & ([1,1],[0,0]) & & & & \\ \begin{pmatrix}[0.9134,0.9787],\\ [0.0057,0.0108]\end{pmatrix} & \begin{pmatrix}[0.9572,0.9648],\\ [0.0032,0.0097]\end{pmatrix} & \begin{pmatrix}[0.9706,0.9787],\\ [0.0032,0.0035]\end{pmatrix} & ([1,1],[0,0]) & & & \\ \begin{pmatrix}[0.9134,0.9773],\\ [0.0057,0.0108]\end{pmatrix} & \begin{pmatrix}[0.9575,0.9648],\\ [0.0025,0.0097]\end{pmatrix} & \begin{pmatrix}[0.9572,0.9773],\\ [0.0017,0.0049]\end{pmatrix} & \begin{pmatrix}[0.9572,0.9773],\\ [0.0032,0.0049]\end{pmatrix} & ([1,1],[0,0]) & & \\ \begin{pmatrix}[0.9134,0.9648],\\ [0.0055,0.0108]\end{pmatrix} & \begin{pmatrix}[0.9649,0.9897],\\ [0.0057,0.0070]\end{pmatrix} & \begin{pmatrix}[0.9572,0.9648],\\ [0.0057,0.0097]\end{pmatrix} & \begin{pmatrix}[0.9572,0.9648],\\ [0.0057,0.0097]\end{pmatrix} & \begin{pmatrix}[0.9575,0.9648],\\ [0.0057,0.0097]\end{pmatrix} & ([1,1],[0,0]) & \\ \begin{pmatrix}[0.9134,0.9787],\\ [0.0057,0.0108]\end{pmatrix} & \begin{pmatrix}[0.9575,0.9648],\\ [0.0032,0.0097]\end{pmatrix} & \begin{pmatrix}[0.9572,0.9787],\\ [0.0032,0.0035]\end{pmatrix} & \begin{pmatrix}[0.9572,0.9958],\\ [0.0003,0.0009]\end{pmatrix} & \begin{pmatrix}[0.9595,0.9773],\\ [0.0032,0.0049]\end{pmatrix} & \begin{pmatrix}[0.9575,0.9648],\\ [0.0057,0.0097]\end{pmatrix} & ([1,1],[0,0]) \end{pmatrix}.$$

$\widetilde{R}^{(3)}$ is expressed in a resolution form as follows:

$$
\begin{aligned}
\tilde{R}^{(3)} \;=\; & ([0.9134, 0.9648], [0.0057, 0.0108]) \begin{pmatrix} 1 & & & & & & \\ 1 & 1 & & & & & \\ 1 & 1 & 1 & & & & \\ 1 & 1 & 1 & 1 & & & \\ 1 & 1 & 1 & 1 & 1 & & \\ 1 & 1 & 1 & 1 & 1 & 1 & \\ 1 & 1 & 1 & 1 & 1 & 1 & 1 \end{pmatrix} \\
& + ([0.9572, 0.9648], [0.0057, 0.0097]) \begin{pmatrix} 1 & & & & & & \\ 0 & 1 & & & & & \\ 0 & 1 & 1 & & & & \\ 0 & 1 & 1 & 1 & & & \\ 0 & 1 & 1 & 1 & 1 & & \\ 0 & 1 & 1 & 1 & 1 & 1 & \\ 0 & 1 & 1 & 1 & 1 & 1 & 1 \end{pmatrix} \\
& + ([0.9575, 0.9648], [0.0057, 0.0097]) \begin{pmatrix} 1 & & & & & & \\ 0 & 1 & & & & & \\ 0 & 0 & 1 & & & & \\ 0 & 0 & 1 & 1 & & & \\ 0 & 1 & 0 & 0 & 1 & & \\ 0 & 1 & 0 & 0 & 1 & 1 & \\ 0 & 1 & 0 & 0 & 1 & 1 & 1 \end{pmatrix} \\
& + ([0.9595, 0.9773], [0.0032, 0.0049]) \begin{pmatrix} 1 & & & & & & \\ 0 & 1 & & & & & \\ 0 & 0 & 1 & & & & \\ 0 & 0 & 1 & 1 & & & \\ 0 & 0 & 0 & 0 & 1 & & \\ 0 & 1 & 0 & 0 & 0 & 1 & \\ 0 & 0 & 0 & 0 & 1 & 0 & 1 \end{pmatrix}
\end{aligned}
$$

$$+([0.9649,0.9897],[0.0057,0.0070])\begin{pmatrix}1&&&&&&\\0&1&&&&&\\0&0&1&&&&\\0&0&1&1&&&\\0&0&0&0&1&&\\0&1&0&0&0&1&\\0&0&0&0&0&0&1\end{pmatrix}$$

$$+([0.9706,0.9787],[0.0032,0.0035])\begin{pmatrix}1&&&&&&\\0&1&&&&&\\0&0&1&&&&\\0&0&1&1&&&\\0&0&0&0&1&&\\0&0&0&0&0&1&\\0&0&0&0&0&0&1\end{pmatrix}$$

$$+([1,1],[0,0])\begin{pmatrix}1&&&&&&\\0&1&&&&&\\0&0&1&&&&\\0&0&0&1&&&\\0&0&0&0&1&&\\0&0&0&0&0&1&\\0&0&0&0&0&0&1\end{pmatrix}.$$

The same is summarized by a clustering tree in Fig 3.

We now present an application of the hierarchical structures created for IVIFR in multi-criteria decision making (MCDM) problems involving such relations.

6 Application to MCDM problem: determining the criteria weights

An MCDM problem involves comparing n available alternatives $A_1,\ldots,A_n$ of one type on m relevant criteria $C_1,\ldots,C_m$ resulting in an $m\times n$ criteria-alternative matrix. The entries of this matrix are provided by an expert/decision maker (DM). A DM has to quantify how he/she rates and alternative A_i on criterion C_j. These opinion entries together with the criteria weights are then used to aggregate the entire information so as to rank the alternatives on some preference scale. Various methods are available in literature to rank the alternatives in an MCDM problem, like TOPSIS, VIKOR, PROMETHEE, ELECTREE, to name a few. One can refer to several good texts, (see [20, 22–32]) and many more references cited therein, for detailed account of MCDM methodologies and their applications, especially when

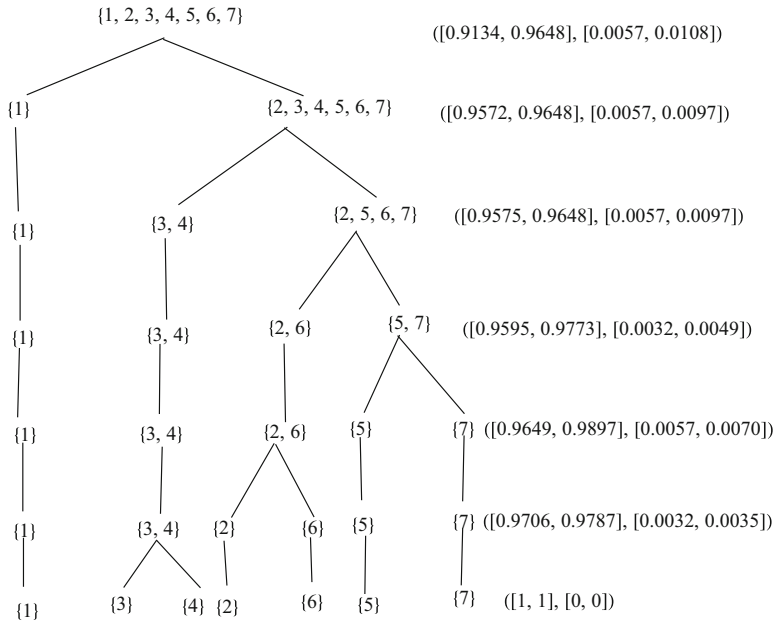


Fig. 3 Hierarchical clustering for IVIFR for Example 5

the MCDM problems are set in intuitionistic fuzzy framework. However, in this work, we only wish to exhibit an application of hierarchical clustering for IVIFR, developed in previous section, to one of the important sub-problem of determining the criteria weights within any MCDM problem.

In this section we propose a procedure to determine the global weights of the criteria in an MCDM problem represented by a criteria-alternative matrix of order $m \times n$ having entries as IVIF numbers.

Procedure (Algorithm 5):

Step 1: Seek criteria-alternatives matrix from DM with entries provided are IVIF numbers.

Step 2: Use the following concepts of covariance and correlation coefficient of IVIFS, introduced by Bustince and Burillo [33], to compute the correlation between criteria in the problem.

Definition 18 (*Correlation coefficient for IVIFN*) [33] Let $C_p = \{\langle x_j, \left[\underline{\mu}_{C_p}(x_j),\ \overline{\mu}_{C_p}(x_j)\right],\ [\underline{\nu}_{C_p}(x_j),\ \overline{\nu}_{C_p}(x_j)]\}$ and $C_q = \{\langle x_i, [\underline{\mu}_{C_q}(x_j),\ \overline{\mu}_{C_q}(x_j)],\ [\underline{\nu}_{C_q}(x_j),\ \overline{\nu}_{C_q}(x_j)]\}$ be two IVIF numbers. Define the covariance $\mathrm{COV}(C_p, C_q)$ and the correlation $R(C_p, C_q)$ between them, respectively, as follows:

$$\begin{aligned}\mathrm{COV}(C_p, C_q) = \frac{1}{2}\sum_{j=1}^{n}\Big[&\underline{\mu}_{C_p}(x_j)\,\underline{\mu}_{C_q}(x_j) + \overline{\mu}_{C_p}(x_j)\,\overline{\mu}_{C_q}(x_j)\Big] \\ &+ \underline{\nu}_{C_p}(x_j)\,\underline{\nu}_{C_q}(x_j) + \overline{\nu}_{C_p}(x_j)\,\overline{\nu}_{C_q}(x_j)].\end{aligned} \tag{2}$$

$$R(C_p, C_q) = \frac{\mathrm{COV}(C_p, C_q)}{\sqrt{\mathrm{COV}(C_p, C_p)\cdot \mathrm{COV}(C_q, C_q)}}$$

Note that $R(C_p, C_q)$ is an $m \times m$ reflexive and symmetric matrix with crisp entries.

Step 3: Convert the crisp correlation values into IVIFV resulting in a column vector of correlation IVIF values, denoted say by ϑ. We have briefly described a procedure by Yue and Jia [34] to achieve this step in the Appendix of this paper.

Step 4: Using the max–min composition for membership values and min–max composition for non-membership values, determine the product $\vartheta \times \vartheta$. Take a relation $\widetilde{R} \subset \vartheta \times \vartheta$ which is reflexive and symmetric.

Step 5: Construct the IVIF (max–min) similarity matrix from $\widetilde{R}$ by invoking Steps 1–4 of Algorithm 4.

Step 6: If the IVIF similarity matrix is order 7 or less, then compute the weights of the criteria using notion of entropy.

Definition 19 [21] For criterion C_i, the entropy is defined as follows:

$$E(C_i) = \frac{1}{m}\sum_{j=1}^{n} \frac{\begin{pmatrix} 2 - |\underline{\mu}_{ij} - \underline{\nu}_{ij}| \\ -|\overline{\mu}_{ij} - \overline{\nu}_{ij}| \\ +\underline{\pi}_{ij} + \overline{\pi}_{ij} \end{pmatrix}}{\begin{pmatrix} 2 + |\underline{\mu}_{ij} - \underline{\nu}_{ij}| \\ +|\overline{\mu}_{ij} - \overline{\nu}_{ij}| \\ +\underline{\pi}_{ij} + \overline{\pi}_{ij} \end{pmatrix}}. \tag{3}$$

The local weights are computed by

$$w_i = \frac{1 - E(C_i)}{m - \sum_{i=1}^{m} E(C_i)}. \tag{4}$$

However, for large IVIF similarity matrices, apply Algorithm 4 to construct the hierarchical clustering. Suppose we have k number of disjoint clusters, each having ≤ 7 criteria.

Step 7: Choose a pivot element (criterion) as the one having minimum score value defined by

$$\text{score}_{\ i} = \frac{\sum_{j=1}^{n} \overline{\mu}_{ij} - \sum_{j=1}^{n} \overline{\nu}_{ij} + \sum_{j=1}^{n} \underline{\mu}_{ij} - \sum_{j=1}^{n} \underline{\nu}_{ij}}{2}. \tag{5}$$

Assign this pivot element (criterion) to every cluster.

Step 8: Compute the local weights of the criteria within each cluster using (3) and (4).

Step 9: Compute the global weights of the criteria as described by Jalao et al. [35]. For each cluster l, $l = 1, \ldots, k$, divide the local weight of the criterion i in cluster l by the local weight of the pivot element to get $W(i, l)$. The global weight $W_G(i)$ of criterion i is calculated by

$$W_G(i) = \frac{W(i,l)}{\sum_{l=1}^{k} \sum_{i \in S_l} W(i,l) - k + 1}, \quad i = 1, \ldots, m. \tag{6}$$

The following flowchart summarizes the above procedure (Fig. 4).

Example 6 Suppose an Institute has to determine the most appropriate air conditioning system for installation in its library. A contractor offers 8 feasible alternatives A_j, $j = 1, \ldots, 8$. A decision is to be arrived at based on the following 10 criteria

C_1: size of room, C_2: correct location of air conditioning system, C_3: seasonal energy efficiency ratio (SEER), C_4: coefficient of performance (COP), C_5: installation and maintenance cost, C_6: refrigerants and global warming potential (GWP), C_7: specified cooling power (SCP), C_8: sound pressure level, C_9: tonnage of air conditioning system, C_{10}: miscellaneous. An Institute expert provides an IVIF criteria-alternatives matrix described in Table 1.

The correlation matrix between criteria is calculated using (2) in Table 2.

Following the method explained in "Appendix"), construct an IVIF numbers column vector ϑ of order 10 for criteria.

$$\vartheta = \begin{matrix} C_1 \\ C_2 \\ C_3 \\ C_4 \\ C_5 \\ C_6 \\ C_7 \\ C_8 \\ C_9 \\ C_{10} \end{matrix} \begin{bmatrix} ([0.0345, 0.7238], [0.0122, 0.2296]) \\ ([0.1481, 0.6187], [0.0371, 0.1962]) \\ ([0.0622, 0.7934], [0.0133, 0.1311]) \\ ([0.0101, 0.7929], [0.0985, 0.0985]) \\ ([0.0661, 0.834], [0.05, 0.04996]) \\ ([0.0032, 0.8068], [0.0566, 0.1333]) \\ ([0.0636, 0.9364], [0, 0]) \\ ([0.0096, 0.7532], [0.0303, 0.2069]) \\ ([0.0034, 0.8248], [0.0172, 01545]) \\ ([0.0183, 0.893], [0.0443, 0.0443]) \end{bmatrix}$$

Construct $\vartheta \times \vartheta$ using max–min (membership) and min–max (non-membership) operations. Take a relation $\widetilde{R} = \vartheta \times \vartheta$ with diagonal entries in $\widetilde{R}$ replaced by ([1, 1], [0, 0]) to make it reflexive.

Apply the hierarchical clustering (Algorithm 4), we obtain five clusters

$S_1 = \{C_1, C_2, C_3, C_5, C_7, C_{10}\}$, $S_2 = \{C_4\}$, $S_3 = \{C_8\}$, $S_4 = \{C_9\}$, $S_5 = \{C_6\}$.

The pivot element, from (5), turns out to be C_2; insert it in each S_l to get S_l', $l = 1, \ldots, 5$.

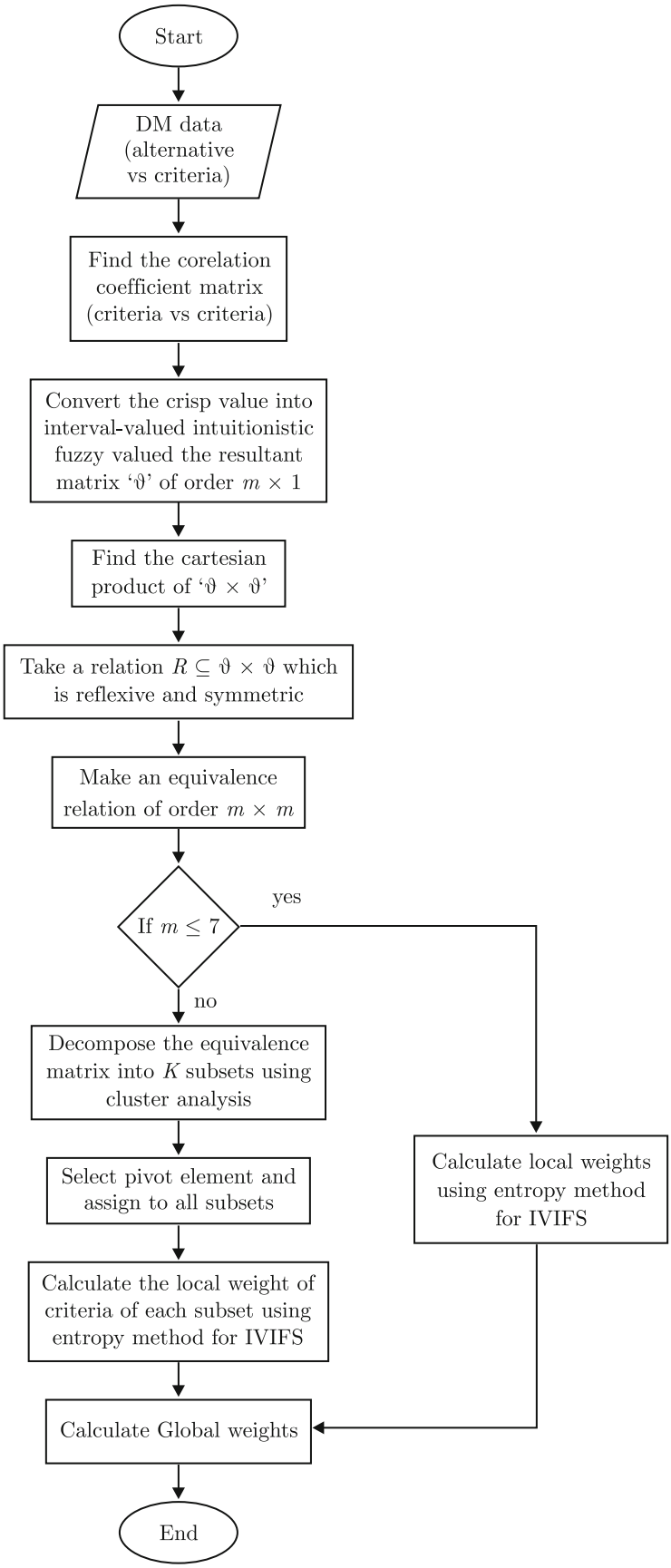


Fig. 4 Flow chart describing procedure (Algorithm 5) for eliciting criteria weights

$S_1' =$

	C_1	C_2	C_3	C_5	C_7	C_{10}
C_1	([1, 1], [0, 0])	([0.034, 0.62], [0.037, 0.23])	([0.034, 0.724], [0.013, 0.23])	([0.034, 0.724], [0.05, 0.23])	([0.034, 0.724], [0.012, 0.23])	([0.018, 0.724], [0.044, 0.23])
C_2	([0.034, 0.62], [0.037, 0.23])	([1, 1], [0, 0])	([0.0622, 0.62], [0.037, 0.196])	([0.066, 0.62], [0.05, 0.196])	([0.063, 0.62], [0.037, 0.196])	([0.018, 0.62], [0.05, 0.196])
C_3	([0.034, 0.724], [0.013, 0.23])	([0.0622, 0.62], [0.037, 0.196])	([1, 1], [0, 0])	([0.062, 0.793], [0.05, 0.131])	([0.062, 0.793], [0.13, 0.131])	([0.018, 0.793], [0.05, 0.131])
C_5	([0.034, 0.724], [0.05, 0.23])	([0.066, 0.62], [0.05, 0.196])	([0.062, 0.793], [0.05, 0.131])	([1, 1], [0, 0])	([0.063, 0.834], [0.05, 0.05])	([0.018, 0.534], [0.05, 0.05])
C_7	([0.034, 0.724], [0.012, 0.23])	([0.063, 0.62], [0.037, 0.196])	([0.062, 0.793], [0.013, 0.131])	([0.063, 0.834], [0.05, 0.05])	([1, 1], [0, 0])	([0.018, 0.893], [0.044, 0.044])
C_{10}	([0.018, 0.724], [0.044, 0.23])	([0.018, 0.627], [0.05, 0.196])	([0.018, 0.793], [0.05, 0.131])	([0.018, 0.834], [0.05, 0.05])	([0.018, 0.893], [0.044, 0.044])	([1, 1], [0, 0])

$S_2' =$

	C_2	C_4
C_2	$([1,1],[0,0])$	$([0.0101,0.62],[0.098,0.196])$
C_4	$([0.0101,0.6],[0.098,0.196])$	$([1,1],[0,0])$

$S_3' =$

	C_2	C_8
C_2	$([1,1],[0,0])$	$([0.0096,0.62],[0.037,0.196])$
C_8	$([0.0096,0.62],[0.037,0.196])$	$([1,1],[0,0])$

$S_4' =$

	C_2	C_9
C_2	$([1,1],[0,0])$	$([0.0034,0.62],[0.037,0.196])$
C_9	$([0.0034,0.62],[0.037,0.196])$	$([1,1],[0,0])$

$S_5' =$

	C_2	C_6
C_2	$([1,1],[0,0])$	$([0.0033,0.62],[0.06,0.196])$
C_6	$([0.0033,0.62],[0.06,0.196])$	$([1,1],[0,0])$

The local and global weights are given in Table 3.

Table 1 The criteria-alternative matrix

	A_1	A_2	A_3	A_4	A_5	A_6	A_7	A_8
C_1	$\begin{pmatrix}[0.5,0.6],\\ [02,0.3]\end{pmatrix}$	$\begin{pmatrix}[0.03,0.2],\\ [0,0.32]\end{pmatrix}$	$\begin{pmatrix}[0.7,0.75],\\ [0.10,0.5]\end{pmatrix}$	$\begin{pmatrix}[0,0.02],\\ [0.8,0.9]\end{pmatrix}$	$\begin{pmatrix}[0.15,0.2],\\ [0.6,0.65]\end{pmatrix}$	$\begin{pmatrix}[0,0.3],\\ [0.2,0.5]\end{pmatrix}$	$\begin{pmatrix}[0,0.1],\\ [0.08,0.1]\end{pmatrix}$	$\begin{pmatrix}[0.5,0.55],\\ [0.3,0.35]\end{pmatrix}$
C_2	$\begin{pmatrix}[0,0],\\ [1,1]\end{pmatrix}$	$\begin{pmatrix}[0.7,0.8],\\ [0.2,0.2]\end{pmatrix}$	$\begin{pmatrix}[0.10,0.15],\\ [0.05,0.06]\end{pmatrix}$	$\begin{pmatrix}[0.8,1],\\ [0,0]\end{pmatrix}$	$\begin{pmatrix}[0.05,0.07],\\ [0.1,0.2]\end{pmatrix}$	$\begin{pmatrix}[0.7,0.75],\\ [0.1,0.15]\end{pmatrix}$	$\begin{pmatrix}[0.1,0.2],\\ [0,0.3]\end{pmatrix}$	$\begin{pmatrix}[0.2,0.4],\\ [0.2,0.2]\end{pmatrix}$
C_3	$\begin{pmatrix}[0.3,0.4],\\ [0.4,0.6]\end{pmatrix}$	$\begin{pmatrix}[0.1,0.4],\\ [0.3,0.5]\end{pmatrix}$	$\begin{pmatrix}[0.2,0.3],\\ [0.2,0.3]\end{pmatrix}$	$\begin{pmatrix}[1,1],\\ [0,0]\end{pmatrix}$	$\begin{pmatrix}[0,0.07],\\ [0.2,0.2]\end{pmatrix}$	$\begin{pmatrix}[0.1,0.4],\\ [0.3,0.5]\end{pmatrix}$	$\begin{pmatrix}[0.15,0.3],\\ [0.2,0.3]\end{pmatrix}$	$\begin{pmatrix}[0,0],\\ [1,1]\end{pmatrix}$
C_4	$\begin{pmatrix}[0.01,0.3],\\ [0.25,0.30]\end{pmatrix}$	$\begin{pmatrix}[0.2,0.5],\\ [0.1,0.2]\end{pmatrix}$	$\begin{pmatrix}[0.4,0.5],\\ [0.2,0.3]\end{pmatrix}$	$\begin{pmatrix}[0.2,0.3],\\ [0.4,0.5]\end{pmatrix}$	$\begin{pmatrix}[0.3,0.5],\\ [0.4,0.5]\end{pmatrix}$	$\begin{pmatrix}[0.6,0.6],\\ [0.1,0.2]\end{pmatrix}$	$\begin{pmatrix}[0.1,0.4],\\ [0.3,0.5]\end{pmatrix}$	$\begin{pmatrix}[1,1],\\ [0,0]\end{pmatrix}$
C_5	$\begin{pmatrix}[0.3,0.6],\\ [0.1,0.2]\end{pmatrix}$	$\begin{pmatrix}[0.1,0.2],\\ [0.2,0.3]\end{pmatrix}$	$\begin{pmatrix}[0.4,0.6],\\ [0.02,0.03]\end{pmatrix}$	$\begin{pmatrix}[0.13,0.34],\\ [0,0.3]\end{pmatrix}$	$\begin{pmatrix}[0,0.9],\\ [0,0.01]\end{pmatrix}$	$\begin{pmatrix}[0.1,0.4],\\ [0.3,0.5]\end{pmatrix}$	$\begin{pmatrix}[0.05,0.5],\\ [0.3,0.4]\end{pmatrix}$	$\begin{pmatrix}[0.25,0.34],\\ [0.4,0.5]\end{pmatrix}$
C_6	$\begin{pmatrix}[0.1,0.2],\\ [0.2,0.7]\end{pmatrix}$	$\begin{pmatrix}[0.03,0.04],\\ [0.04,0.06]\end{pmatrix}$	$\begin{pmatrix}[0.2,0.3],\\ [0.4,0.6]\end{pmatrix}$	$\begin{pmatrix}[0,0],\\ [1,1]\end{pmatrix}$	$\begin{pmatrix}[0.4,0.5],\\ [0.3,0.2]\end{pmatrix}$	$\begin{pmatrix}[0.8,1],\\ [0,0]\end{pmatrix}$	$\begin{pmatrix}[0.1,0.2],\\ [0.6,0.7]\end{pmatrix}$	$\begin{pmatrix}[0.01,0.3],\\ [0.25,0.38]\end{pmatrix}$
C_7	$\begin{pmatrix}[0.1,0.5],\\ [0.4,0.4]\end{pmatrix}$	$\begin{pmatrix}[0.7,0.7],\\ [0.1,0.2]\end{pmatrix}$	$\begin{pmatrix}[0.2,0.3],\\ [0.2,0.3]\end{pmatrix}$	$\begin{pmatrix}[0.5,0.6],\\ [0.1,0.2]\end{pmatrix}$	$\begin{pmatrix}[0.2,0.2],\\ [0.2,0.2]\end{pmatrix}$	$\begin{pmatrix}[0.2,0.56],\\ [0.2,0.2]\end{pmatrix}$	$\begin{pmatrix}[0.1,0.4],\\ [0.3,0.5]\end{pmatrix}$	$\begin{pmatrix}[0.1,0.2],\\ [0.06,0.2]\end{pmatrix}$
C_8	$\begin{pmatrix}[0.9,1.0],\\ [0,0]\end{pmatrix}$	$\begin{pmatrix}[0.4,0.5],\\ [0.2,0.3]\end{pmatrix}$	$\begin{pmatrix}[0,0.08],\\ [0.1,0.2]\end{pmatrix}$	$\begin{pmatrix}[0.3,0.5],\\ [0.4,0.5]\end{pmatrix}$	$\begin{pmatrix}[0.9,1],\\ [0,0]\end{pmatrix}$	$\begin{pmatrix}[0.15,0.2],\\ [0.7,0.75]\end{pmatrix}$	$\begin{pmatrix}[0.2,0.3],\\ [0,0.3]\end{pmatrix}$	$\begin{pmatrix}[0.05,0.05],\\ [0.03,0.03]\end{pmatrix}$
C_9	$\begin{pmatrix}l[0.33,0.34],\\ [0.2,0.3]\end{pmatrix}$	$\begin{pmatrix}[0.5,0.6],\\ [0.05,0.09]\end{pmatrix}$	$\begin{pmatrix}[0,0],\\ [1,1]\end{pmatrix}$	$\begin{pmatrix}[0.1,0.2],\\ [0.06,0.5]\end{pmatrix}$	$\begin{pmatrix}[0.4,0.5],\\ [0.2,0.3]\end{pmatrix}$	$\begin{pmatrix}[0,0.1],\\ [0.75,0.8]\end{pmatrix}$	$\begin{pmatrix}[0.1,0.5],\\ [0.02,0.03]\end{pmatrix}$	$\begin{pmatrix}[0.05,0.07],\\ [0.1,0.2]\end{pmatrix}$
C_{10}	$\begin{pmatrix}[0,0.1],\\ [0.1,0.2]\end{pmatrix}$	$\begin{pmatrix}[0.3,0.5],\\ [0.1,0.4]\end{pmatrix}$	$\begin{pmatrix}[0.18,0.25],\\ [0,0.2]\end{pmatrix}$	$\begin{pmatrix}[0.04,0.44],\\ [0.23,0.3]\end{pmatrix}$	$\begin{pmatrix}[0.1,0.4],\\ [0.1,0.4]\end{pmatrix}$	$\begin{pmatrix}[0,1],\\ [0,0]\end{pmatrix}$	$\begin{pmatrix}[0.1,0.2],\\ [0.06,0.1]\end{pmatrix}$	$\begin{pmatrix}[0.1,0.3],\\ [0.03,0.2]\end{pmatrix}$

Table 2 Correlation matrix of criteria

	C_1	C_2	C_3	C_4	C_5	C_6	C_7	C_8	C_9	C_{10}
C_1	1	0.34143	0.4916	0.7519	0.6753	0.6545	0.5340	0.5456	0.5238	0.5916
C_2	0.34143	1	0.6818	0.6196	0.4701	0.4649	0.8425	0.3626	0.4063	0.7271
C_3	0.4916	0.6818	1	0.43789	0.7069	0.4174	0.7336	0.4799	0.4896	0.5392
C_4	0.7519	0.6196	0.43789	1	0.68274	0.7151	0.71781	0.50639	0.51029	0.7957
C_5	0.6753	0.4701	0.7069	0.6827	1	0.5608	0.6899	0.7058	0.5396	0.6407
C_6	0.6545	0.4649	0.4174	0.7151	0.5608	1	0.5822	0.4546	0.5021	0.712
C_7	0.5340	0.8425	0.7336	0.7178	0.6899	0.5822	1	0.6394	0.6318	0.7758
C_8	0.5456	0.3626	0.4799	0.5064	0.7058	0.4546	0.6394	1	0.7034	0.5102
C_9	0.5238	0.4063	0.4896	0.5103	0.5396	0.5021	0.6318	0.7034	1	0.4751
C_{10}	0.5916	0.7271	0.5392	0.7957	0.6407	0.712	0.7758	0.5102	0.4751	1

Table 3 Global weights of criteria

Clusters	Criteria	Local weight	Global weight
S_1'	C_1	0.1534	0.097
	C_2	0.1426	0.091
	C_3	0.1706	0.109
	C_5	0.1756	0.112
	C_7	0.1789	0.114
	C_{10}	0.1784	0.113
S_2'	C_2	0.5	0.091
	C_4	0.5	0.091
S_3'	C_2	0.5	0.091
	C_8	0.5	0.091
S_4'	C_2	0.5	0.091
	C_9	0.5	0.091
S_5'	C_2	0.5	0.091
	C_6	0.5	0.091

Once the global weight of the criteria are known, the entire information in the criteria-alternatives, with entries as IVIF numbers, along with the global weights can be aggregated to rank various alternatives in an MCDM problem. This can be achieved by variety of methods, like TOPSIS [36], VIKOR [37], ELECTRE [38], AHP with preference score [39], to name a few.

7 Conclusions

The paper extends the work of Guh et al. [19] to laid down the procedure for constructing hierarchical clustering for IVIFRs. MATLAB codes are developed for each algorithm presented in this work and the same are implemented on large number of matrices representation of IVIFRs. The paper includes instances of few such implementations for illustrative and explanatory purpose. To demonstarte the application of the proposed clustering scheme, an important problem of determining the criteria weights in an MCDM problem, with DM providing entries of criteria-alternative matrix as IVIF values, is addressed. A detailed procedure is presented with supportive illustration to compute the global weights of the criteria. It would be interesting to see if the hierarchy clustering approach can be extended to more than one IVIFR and hence can be applied to multi-criteria group decision making problems for computing weights of many decision makers along with the weights of the criteria.

Acknowledgments The authors wish to express their gratitude to the esteemed referees for their valuable observations and comments in improving the quality of this research work.

Appendix: Converting crisp value to an IVIF value (for detail reasoning, please refer to [34])

For each column i of the criteria correlation matrix, find the minimum and the maximum values among all values in (0.5, 1], yielding an interval $[\xi_i^l,\ \xi_i^u]$, called the satisfactory interval. Next, for the same i, find the minimum and the maximum values among all values in [0, 0.5) to generate the dissatisfactory interval $[\delta_i^l,\ \delta_i^u]$. If no entry in i-th column of the criteria correlation matrix lies in (0.5, 1] or [0, 0.5), then take the satisfactory interval or the dissatisfactory interval equals [0.5, 0.5].

For instance for the first column corresponding to criterion C_1 in Table 2, the satisfactory interval is [0.5238, 1] and the dissatisfactory interval is [0.3414, 0.4916].

Use the linear transformation $y = 2x - 1$ in the interval $[\xi_i^l,\ \xi_i^u]$ to transform it to interval $[\rho_i^l,\ \rho_i^u]$. Similarly the interval $[\delta_i^l, \delta_i^u]$ be transformed to $[\upsilon_i^l, \upsilon_i^u]$, using the linear transformation $y = 1 - 2x$.

Let $\tau_i = \rho_i^l + \rho_i^u + \upsilon_i^l + \upsilon_i^u$. Apply the transformation,

$$\underline{\mu}_i = \frac{\rho_i^l}{\tau_i}, \quad \overline{\mu}_i = \frac{\rho_i^u}{\tau_i}, \quad \underline{\nu}_i = \frac{\upsilon_i^l}{\tau_i}, \quad \overline{\nu}_i = \frac{\upsilon^u}{\tau_i},$$

to get an IVIF number $([\underline{\mu}_i,\ \overline{\nu}_i],\ [\underline{\nu}_i,\ \overline{\nu}_i]),\ \ i = 1, \ldots, m.$

For instance, from the first column in the criteria correlation matrix in Table 2, $\underline{\mu}_1 = 0.0345,\ \overline{\mu}_1 = 0.7238,\ \underline{\nu}_1 = 0.0121,\ \overline{\nu}_1 = 0.2295.$

References

1. Atanassov, K.: Intuitionistic fuzzy sets. Fuzzy Sets Syst. **20**, 87–96 (1986)
2. Dubois, D., Gottwald, S., Hajek, P., Kacprzyk, J., Prade, H.: Terminological difficulties in fuzzy set theory-the case of intuitionistic fuzzy sets. Fuzzy Sets Syst. **156**, 485–491 (2005)
3. Turksen, I.B.: Interval-valued strict preference with Zadeh triples. Fuzzy Sets Syst. **78**, 183–195 (1996)
4. Deschrijver, G., Kerre, E.E.: On the relationship between some extensions of fuzzy sets theory. Fuzzy Sets Syst. **133**, 227–235 (2003)
5. Atanassov, K., Gargov, G.: Interval-valued intuitionistic fuzzy sets. Fuzzy Sets Syst. **31**, 343–349 (1989)
6. Xu, Z., Cai, X.: Intuitionistic Fuzzy Information Aggregation: Theory and Applications. Science Press Beijing and Springer, Berlin (2012)
7. Bellman, R., Kalaba, R.L., Zadeh, L.A.: Abstraction and pattern classification. J. Math. Anal. Appl. **2**, 581–585 (1966)
8. Ruspini, E.H.: A new approach to clustering. Inf. Control. **15**, 22–32 (1969)
9. Bezdek, J.C.: Pattern Recognition with Fuzzy Objective Function Algorithms. Plenum Press, New York (1981)
10. Yang, M.S.: A survey of fuzzy clustering. Math. Comput. Modell. **18**, 1–16 (1993)
11. Hoppner, F., Klawonn, F., Kruse, R., Runkler, T.: Fuzzy Cluster Analysis: Methods for Classication data Analysis and Image Recognition. Wiley, New York (1999)
12. Baraldi, A., Blonda, P.: A survey of fuzzy clustering algorithms for pattern recognition: part I and II. IEEE Trans. Syst. Man Cybern. Part B **29**, 778–801 (1999)
13. Lee, H.S.: Automatic clustering of business process in business systems planning. Eur. J. Oper. Res. **114**, 354–362 (1999)

14. Yu, J., Yang, M.S.: Optimality test for generalized FCM and its application to parameter selection. IEEE Trans. Fuzzy Syst. **13**, 164–176 (2005)
15. Zadeh, L.A.: Similarity relations and fuzzy ordering. Inf. Sci. **3**, 177–200 (1971)
16. Tamura, E., Figuchi, S., Tanaka, K.: Pattern classification based on fuzzy relations. IEEE Trans. Syst. Man Cybern. **1**, 61–66 (1971)
17. Dunn, J.C.: A graph theoretic analysis of pattern classification via Tamura's fuzzy relation. IEEE Trans. Syst. Man Cybern. **4**, 310–313 (1974)
18. Yang, M.S., Shih, H.M.: Cluster analysis based on fuzzy relations. Fuzzy Sets Syst. **120**, 197–212 (2001)
19. Guh, Y.Y., Yang, M.S., Po, R.W., Lee, E.S.: Interval-valued fuzzy relation based clustering with its application to performance evaluation. Comput. Math. Appl. **57**, 841–849 (2009)
20. Basnet, D.K., Sarma, N.K.: A note on intuitionistic fuzzy equivalence relation. Int. Math. Forum. **5**(67), 3301–3307 (2010)
21. Wei, C.P., Pei, W., Yu, Z.Z.: Entropy, similarity measure of interval-valued intuitionistic fuzzy sets and their applications. Inf. Sci. **181**, 4273–4286 (2011)
22. Bustine, H., Burillo, P.: Structure on intuitionistic fuzzy relations. Fuzzy Sets Syst. **78**, 293–303 (1996)
23. Banerjee, B., Basnet, D.K.: Intuitionistic fuzzy subring and ideals. J. Fuzzy Math. **11**(1), 139–155 (2003)
24. Liu, P.D.: Some Hamacher aggregation operators based on the interval-valued intuitionistic fuzzy numbers and their application to Group Decision Making. IEEE Trans. Fuzzy Syst. **22**(1), 83–97 (2014)
25. Liu, P.D., Jin, F.: The trapezoid fuzzy linguistic Bonferroni mean operators and their application to multiple attribute decision making. Sci. Iran. Trans. E Ind. Eng. Sci. Iran. E **19**(6), 1947–1959 (2012)
26. Liu, P.D., Wang, Y.M.: Multiple attribute decision making method based on single valued neutrosophic normalized weighted bonferroni mean. Neural Comput. Appl. **25**(7–8), 2001–2010 (2014)
27. Liu, P.D., Liu, Z.M., Zhang, X.: Some intuitionistic uncertain linguistic Heronian mean operators and their application to group decision making. Appl. Math. Comput. **230**, 570–586 (2014)
28. Liu, P.D., Wang, Y.M.: Multiple attribute group decision making methods based on intuitionistic linguistic power generalized aggregation operators. Appl. Soft Comput. **17**, 90–104 (2014)
29. Liu, P.D., Chen, Y., Chu, Y.: Intuitionistic uncertain linguistic weighted Bonferroni OWA operator and its application to multiple attribute decision making. Cybern. Syst. **45**(5), 418–438 (2014)
30. Liu, P.D., Liu, Y.: An approach to multiple attribute group decision making based on intuitionistic trapezoidal fuzzy power generalized aggregation operator. Int. J. Comput. Intell. Syst. **7**(2), 291–304 (2014)
31. Liu, P.D., Yu, X.: 2-dimension uncertain linguistic power generalized weighted aggregation operator and its application for multiple attribute group decision making. Knowl. Based Syst. **57**(1), 69–80 (2014)
32. Tzeng, G.H., Huang, J.J.: Multiple Attribute Decision Making: Methods and Applications. CRC Press, Florida (2011)
33. Bustince, H., Burillo, P.: Correlation of interval-valued intuitionistic fuzzy sets. Fuzzy Sets Syst. **74**, 237–244 (1995)
34. Yue, Z., Jia, Y.: A method to agreegate crisp values into interval valued intuitionistic fuzzy information for group decision making. Appl. Soft Comput. **13**, 2304–2317 (2013)
35. Jalao, E.R., Wu, T., Shunk, D.: An intelligent decomposition of pairwise comparison matrices for large-scale decisions. Eur. J. Oper. Res. **238**, 270–280 (2014)
36. Chen, T-Yu.: The inclusion-based TOPSIS method with interval-valued intuitionistic fuzzy sets for multiple criteria group decision making. Appl. Soft Comput. **26**, 57–73 (2015)
37. Chaojie, L., Hongli, J.: Extension of VIKOR method with interval-valued intuitionistic fuzzy sets. Manag. Serv. Sci. (2011). http://ieeexplore.ieee.org/stamp/stamp.jsp?tp=&arnumber=5999210
38. Veeramachaneni, S., Kandikonda, H.: An ELECTRE approach for multicriteria interval-valued intuitionistic trapezoidal fuzzy group decision making problems. Adv. Fuzzy Syst. 2016 (2016) Article ID 1956303. http://dx.doi.org/10.1155/2016/1956303
39. Abdullah, L., Najib, L.: A new preference scale MCDM method based on interval-valued intuitionistic fuzzy sets and the analytic hierarchy process. Soft Comput. **20**, 511–523 (2016)

Holographic dark energy in Brans-Dicke theory with logarithmic form of scalar field

C. P. Singh* and Pankaj Kumar†
Department of Applied Mathematics,
Delhi Technological University, Delhi-110042, India
(Dated: September 7, 2016)

In this paper, an interacting holographic dark energy model with Hubble horizon as an infra-red cut-off is considered in the framework of Brans-Dicke theory. We propose a logarithmic form $\phi \propto ln(\alpha + \beta a)$ of the Brans-Dicke scalar field to alleviate the problems of interacting holographic dark energy models in Brans-Dicke theory. We find that the equation of state parameter w_h and deceleration parameter q are negative in the early time which shows the early time inflation. During the evolution the sign of parameter q changes from negative to positive which means that the Universe expands with decelerated rate whereas the sign of w_h may change or remain negative throughout the evolution depending on the values of parameters. It is also observed that w_h may cross the phantom divide line in the late time evolution. The sign of q changes from positive to negative during late time of evolution which explains the late time accelerated expansion of the Universe. Thus, we present a unified model of holographic dark energy which explains the early time acceleration (inflation), medieval time deceleration and late time acceleration. We also discuss the cosmic coincidence problem. We obtain a time-varying density ratio of holographic dark energy to dark matter which is a constant of order one ($r \sim \mathcal{O}(1)$) during early and late time evolution. Therefore, our model successfully resolves the cosmic coincidence problem.

arXiv:1609.01477v1 [gr-qc] 6 Sep 2016

I. INTRODUCTION

One of the present mysteries of modern cosmology is the recent accelerated expansion of the Universe predicted by the observations of supernovae Ia [1] and confirmed by the observations of Cosmic Microwave Background Radiation [2], Large-scale Structure [3], Baryon Acoustic Oscillation [4] and Planck data [5]. According to observations, the present epoch of evolution of the Universe is dominated by an exotic energy content dubbed as "dark energy" (DE), which has negative pressure required to explain the accelerated expansion. In the literature, a variety of DE candidates are available some of which are: cosmological constant [6], quintessence [7], phantom [8], chaplygin gas [9] etc. The standard Λ-cold dark matter (ΛCDM) model containing the cosmological constant Λ is the most natural and successful model of DE. However, it has some shortcomings in the form of fine-tuning and cosmic coincidence problems. The other DE candidates are also not free from problems. For a review on DE and DE candidates, see [10].

Recently, the holographic dark energy (HDE), which possesses some significant properties of the quantum theory, has been proposed as a candidate of DE to explain the recent phase transition of the Universe. The HDE is based on the holographic principle proposed by 't Hooft [11] and further discussed by Susskind [12] in the context of string theory. The origin of the HDE contains the more scientific approach in comparison of other DE candidates and presents a better way to deal with the accelerated expansion. Cohen et al. [13] have shown that the formation of black hole imposes an upper bound on the total energy of size L and should not exceed the mass of black hole of the same size. In the paper [14], the author assumed the largest infra-red (IR) cut-off to saturate the inequality imposed by black hole formation and obtained the density of HDE $\rho_h = 3c^2 M_p^2 L^{-2}$, where c^2 is a dimensionless constant, M_p stands for the reduced Planck mass and L denotes IR cut-off.

The Hubble horizon is a natural candidate for IR cut-off which is also free from causality but Hsu [15] found that it gives wrong equation of state (EoS) of DE. Later on, it was shown [16] that if there is an interaction between two dark components of the Universe the identification of L with Hubble horizon, $L = H^{-1}$, may give suitable EoS of DE. It also was shown that it necessarily implies a constant ratio of the energy densities of the two components regardless of the details of the interaction. Thus, the HDE models may also alleviate the cosmic coincidence problem which provides an advantage to HDE models over the other DE models.

The Brans-Dicke (BD) theory proposed by Brans and Dicke in 1961 [17] is a natural extension of general relativity (GR). In this theory, the gravitational constant G is replaced with a scalar field ϕ called BD scalar field which couples to gravity with coupling parameter ω. The inflationary epoch has been studied widely in this theory [18]. Recently, the BD theory has got interest to explain the accelerated expansion due to its association with the string theory and extra dimensional theories. This theory explains the recent accelerated expansion of the Universe and accommodates the observational data as well [19]. The BD theory provides a dynamical framework which is more suitable to study the HDE models as HDE belongs to the family of dynamical DE candidates. Therefore, it is quite natural to study the HDE models in the framework of BD theory. The HDE models have been studied in the framework of BD theory to

* cpsphd@radiffmail.com
† pankaj.11dtu@gmail.com

explain the recent accelerated expansion and to alleviate the problems associated with the DE models like cosmic coincidence problem [20–25].

In the literature, most of the models have been discussed in BD theory by assuming the power-law form of BD scalar field $\phi \propto a^n$, where a is the scale factor and n is a constant. It has been shown in the papers [26] that the assumption $\phi \propto a^n$ naturally leads to a constant deceleration parameter (DP) in BD theory irrespective of the matter content of the Universe. In the recent papers [22–25], authors have used the same power-law form of BD scalar field in HDE model and found a time-dependent DP. Thus, it has been observed that a constant as well as a time-dependent DP may be obtained with this power-law form of BD scalar field in HDE model. In our point of view there should not be two different values of DP with this form of BD scalar field. Therefore, it is natural to explore more options for the BD scalar field to over come from the shortcoming of this power-law form of BD scalar field. The very first purpose of this paper is to propose a suitable form of BD scalar field which gives only time-dependent DP to discuss the evolution of the Universe in the HDE models.

In this context, we propose a logarithmic form $\phi \propto ln(\alpha+\beta a)$ of BD scalar field, where a as usual denotes the scale factor, and α and β are positive constants such that $\alpha > 1$. Using this assumption, we explore the cosmological consequences of our model. This form of BD scalar field is free from the constant value of DP which naturally arises in the power-law form. We successfully obtain the equation of state (EoS) of DE and the time-dependent deceleration parameter which explain the recent phase transition of the Universe. Moreover, the unification of early time acceleration (inflation) and late time acceleration has been observed including matter dominated era. In the early and late time evolution we find that the density ratio of holographic dark energy to dark matter is a constant of order one ($r \sim \mathcal{O}(1)$) which successfully solve the cosmic coincidence problem. Therefore, we have successfully alleviated the problem associated with the power-law maintaining the good features of it. Further, the early time inflation has been explained in contrast to power-law form. The long lasting cosmic coincidence problem associated with DE models have been alleviated in a well manner in the present model in comparison to existing models.

The outline of our work is as follows. Section II presents the field equations of HDE model in BD theory by assuming the interaction between DM and HDE. In section III, we propose a logarithmic form of BD scalar field and discuss its cosmological consequences. Section IV is devoted to the cosmic coincidence problem. The summary of the results is discussed in section V.

II. HOLOGRAPHIC DARK ENERGY IN BRANS-DICKE THEORY

The modified Einstein-Hilbert action for the BD theory is given by [24]

$$S = \int d^4x\sqrt{-g}\left[\frac{1}{2}(-\phi R + \frac{\omega}{\phi}g^{\mu\nu}\partial_\mu\phi\,\partial_\nu\phi) + \mathcal{L}_m\right], \quad (1)$$

where R denotes the Ricci scalar curvature, $\phi = (8\pi G)^{-1}$ is a time-dependent scalar field called BD scalar field which couples with gravity, ω is a coupling parameter between scalar field and gravity called BD parameter and $\mathcal{L}_m$ represents the matter lagrangian density.

We consider a homogeneous and isotropic flat Friedmann-Robertson-Walker (FRW) Universe given by the line element

$$ds^2 = dt^2 - a^2(t)(dx^2 + dy^2 + dz^2), \quad (2)$$

where a denotes the cosmic scale factor of the Universe. We assume that the Universe is filled with perfect fluid containing pressureless dark matter (DM) excluding baryonic matter and HDE.

The variation of the action (1) with respect to the metric tensor, $g_{\mu\nu}$ for the line element (2) with the energy-momentum tensor of dust and HDE yield the following field equations.

$$H^2 + H\frac{\dot{\phi}}{\phi} - \frac{\omega}{6}\frac{\dot{\phi}^{\,2}}{\phi^{\,2}} = \frac{\rho_m + \rho_h}{3\phi}, \quad (3)$$

$$2\frac{\ddot{a}}{a} + H^2 + 2H\frac{\dot{\phi}}{\phi} + \frac{\omega}{2}\frac{\dot{\phi}^{\,2}}{\phi^{\,2}} + \frac{\ddot{\phi}}{\phi} = -\frac{p_h}{\phi}, \quad (4)$$

where ρ_m and ρ_h are, respectively the energy density of DM and HDE, and p_h denotes the pressure of HDE. Here, the over dot denotes the derivative with respect to the cosmic time t. Many cosmologists [27] have considered the interaction between DM and DE. The recent cosmological observations [28] also support this interaction. Considering the interaction factor Q between DM and HDE, the conservation equations of DM and HDE are respectively given by [22, 25]:

$$\dot{\rho}_m + 3H\rho_m = Q, \quad (5)$$

$$\dot{\rho}_h + 3H(\rho_h + p_h) = -Q, \quad (6)$$

where $Q = \Gamma\rho_h$, Γ stands for interaction rate. The sign of interaction rate Γ is crucial and defines the direction of the energy transfer, i.e., for $\Gamma > 0$, there is an energy transfer from HDE to DM, and for $\Gamma < 0$, there is an energy transfer from DM to HDE. In the literature [21, 25], Γ has been assumed to be proportional to the Hubble parameter, i.e., $\Gamma \propto H$ to maintain the interaction term Q as a function of a quantity with units of inverse of time multiplied with the energy density. Therefore, let

us consider $\Gamma = 3b^2H$ so that the interaction term becomes $Q = 3b^2H\rho_h$, where b^2 is a coupling constant. This assumption relies purely on dimension basis in the absence of a suitable theory.

The dynamical equation for the BD scalar field ϕ is given by

$$\ddot{\phi} + 3H\dot{\phi} = \frac{\rho_m + \rho_h - 3p_h}{2\omega + 3}. \tag{7}$$

Motivated by the holographic principle [11], Cohen et al. [13] obtained an upper bound on the total energy of size L imposed by black hole formation. Li [14] assumed the largest possible IR cut-off to saturate this inequality and obtained the density of HDE, $\rho_h = 3c^2M_p^2L^{-2}$. In the framework of BD theory, the HDE density has the form $\rho_h = 3c^2\phi L^{-2}$, where $\phi = M_p^2 = (8\pi G)^{-1}$ is a time dependent scalar field which couples to gravity with a coupling parameter ω. In the literature, there are various forms of HDE depending on the different choices of IR cut-off (L) like particle horizon, future event horizon, Hubble horizon, Granda-Oliveros cut-off etc. The Hubble horizon is the most natural and viable candidate of IR cut-off because it is free from causality problem. Here, in this paper we choose Hubble horizon as an IR cut-off which gives HDE density as:

$$\rho_h = 3\ c^2\phi H^2, \tag{8}$$

where c^2 is a dimensionless constant.

III. LOGARITHMIC FORM OF BD SCALAR FIELD AND COSMOLOGICAL CONSEQUENCES

Many authors [26] have assumed that the BD scalar field ϕ evolves as a power-law of the scale factor a, i.e., $\phi \propto a^n$. They have observed that this assumption leads to a constant value of DP. The constant value can be obtained irrespective of matter content of the Universe. However, some authors [22–25] have studied HDE model in BD theory with the same form of BD scalar field and have obtained a time-dependent DP. Now, the question is that why does the same form of BD scalar field lead to two different values of DP, constant and time-dependent in a same model?

In spite of several advantages of this form of BD scalar field, it seems from the above mentioned works that this may not be a suitable assumption to discuss the evolution of the Universe in HDE models. In other words, this form may not be suitable for those models where we want to study the phase transition of the Universe. Taking into consideration to this problem, we hereby propose that the BD scalar field evolves as a logarithmic function of the scale factor which is given by

$$\phi \propto ln(\alpha + \beta a), \tag{9}$$

where $\alpha > 1$ and $\beta > 0$ are constants.

In principle, the BD scalar field should evolve slowly to observe a slow variation of G. This logarithmic form of ϕ fulfills this requirement. In this process, the value of β also plays an important role. It is worth noting that GR can be recovered for $\beta = 0$. One can observe that this form does not give a constant value of deceleration parameter when we combine Eqs. (3) and (4) with (7). Thus, we have resolved the constant value problem of the power-law form. It provides an initial advantage to the logarithmic form over the power-law form of BD scalar field. Therefore, it will be interesting to investigate the role of this form in the evolution of the Universe in the framework of BD theory within the formalism of interacting HDE model.

From (6), we have

$$\dot{\rho}_h + 3H(1 + w_h)\rho_h = -3b^2H\rho_h, \tag{10}$$

where $w_h = p_h/\rho_h$ is the EoS parameter of the HDE. Using (8) and (9) into (10), we get

$$\frac{\beta a}{(\alpha + \beta a)ln(\alpha + \beta a)} + 2\frac{\dot{H}}{H^2} + 3(1 + w_h) = -3b^2. \tag{11}$$

From (3) and (4), we obtain

$$\frac{\dot{H}}{H^2} = \frac{1}{2 + \frac{\beta a}{(\alpha+\beta a)\ ln(\alpha+\beta a)}}\Big[-3 - \frac{\omega\beta^2a^2}{2(\alpha + \beta a)^2\ [ln(\alpha + \beta a)]^2} - \frac{3\beta a}{(\alpha + \beta a)\ ln(\alpha + \beta a)} + \frac{\beta^2a^2}{(\alpha + \beta a)^2\ ln(\alpha + \beta a)} - \frac{3w_h}{1 + r}\Big\{1 + \frac{\beta a}{(\alpha + \beta a)\ ln(\alpha + \beta a)} - \frac{\omega\beta^2a^2}{6(\alpha + \beta a)^2\ [ln(\alpha + \beta a)]^2}\Big\}\Big], \tag{12}$$

where $r = \rho_m/\rho_h$ represents the energy density ratio. Using (12) into (11), we get

$$w_h = \frac{(r+1)\left[-3b^2\left(2+\frac{\beta a}{(\alpha+\beta a)\,ln(\alpha+\beta a)}\right)-\frac{2\beta^2a^2}{(\alpha+\beta a)^2\,ln(\alpha+\beta a)}+\frac{\beta a}{(\alpha+\beta a)\,ln(\alpha+\beta a)}+\frac{(\omega-1)\beta^2a^2}{(\alpha+\beta a)^2\,[ln(\alpha+\beta a)]^2}\right]}{3\left[2r+\frac{(r-1)\beta a}{(\alpha+\beta a)\,ln(\alpha+\beta a)}+\frac{\omega\beta^2a^2}{3(\alpha+\beta a)^2\,[ln(\alpha+\beta a)]^2}\right]}. \quad (13)$$

To discuss the behavior of w_h, let us first discuss the terms present in (13) which have significant contribution in the behavior of w_h. We observe that the terms $\frac{\beta a}{(\alpha+\beta a)\,ln(\alpha+\beta a)}$ and $\frac{\beta^2a^2}{(\alpha+\beta a)^2\,ln(\alpha+\beta a)}$ are zero at $a=0$ and both the terms converse to zero as $a\to\infty$. We find that both the terms start from zero, achieve maximum value during the evolution and then converge to zero in the late time evolution. Further, we observe that both the terms attain the maximum value asymptotically for sufficiently small values of α and sufficiently large values of β. The maximum value of the term $\frac{\beta a}{(\alpha+\beta a)\,ln(\alpha+\beta a)}$ lies in the interval $]0,\,1[$ whereas the maximum value of the term $\frac{\beta^2a^2}{(\alpha+\beta a)^2\,ln(\alpha+\beta a)}$ lies in the interval $]0,\,0.41[$ depending on the value of α only. It is to be noted that the maximum value does not depend on the value of β in either term.

The values of ω and b^2 also play an important role in the value of w_h. The value of b^2 is expected to be a small positive constant. The value of BD parameter ω has been constrained by various astronomical and cosmological observations. The solar system experiment Cassini gave a very stringent high bound $\omega > 40000$ [29] for spherically symmetric solution in the parameterized post Newtonian formalism. The solar system constraints on ω may not be consistent at the cosmological scales, therefore, the cosmological constraints are required to study the large scale properties of the Universe. In this context, Acquaviva et al. [30] have found $\omega > 120$ at 95% confidence level, Wu and Chen [31] have found $\omega < -120$ or $\omega > 97.8$ at 95.5% confidence level whereas Li et al. [32] have obtained $\omega > 181.65$ at 95% confidence level. However, all these constraints on ω depend on the choice of a model. In the present paper, we will consider only the value $\omega > 0$.

Now, let us discuss the behavior of EoS parameter w_h of HDE as obtained in Eq. (13). The sign of w_h depends on the sign of numerator as the denominator has only positive values. In the beginning of the evolution ($a=0$), all the terms of the numerator are zero except the first term which has negative sign. Therefore, we observe a negative value of w_h as

$$w_h = -b^2\left(1+\frac{1}{r}\right). \quad (14)$$

Thus, HDE has EoS of DE in the beginning which is required to explain the inflation supposed to happen in very early time of the evolution. As the Universe evolves, the terms $\frac{\beta a}{(\alpha+\beta a)\,ln(\alpha+\beta a)}$ and $\frac{\beta^2a^2}{(\alpha+\beta a)^2\,ln(\alpha+\beta a)}$ attain their maximum value, therefore, the last term of numerator containing ω starts to dominate as a large value of ω has been expected from the observations. Thus, we may

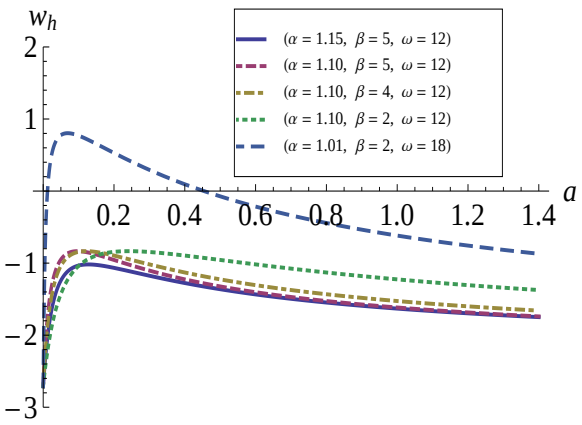


FIG. 1. The evolution of w_h verses a for different values of α, β and ω with $b = 1.05$ and $c = 0.77$.

observe a change in the sign of EoS parameter w_h from negative to positive and HDE may start behaving like radiation ($w_h > 0$). It is evident from (13) that the first term of the numerator has a constant part, and the terms $\frac{\beta a}{(\alpha+\beta a)\,ln(\alpha+\beta a)}$ and $\frac{\beta^2a^2}{(\alpha+\beta a)^2\,ln(\alpha+\beta a)}$ converse to zero in the late time evolution. Therefore, ultimately the sign of w_h changes from positive to negative. Thus, HDE achieves the EoS of DE again during the evolution which is required to explain the late time acceleration of the Universe. It is also obvious that HDE achieves dust like behavior ($w_h = 0$) whenever w_h changes sign from positive to negative or viceversa. Zimdahl and Pavón [33] for HDE, and Zlatev et al. [34] for tracker quintessence scalar field have also observed radiation and dust like behavior in the early time evolution.

We also emphasise that for a small value of ω or a large value of b^2 or a suitable combination of their values, the EoS parameter w_h is negative throughout the evolution. Thus, the HDE behaves like DE throughout the evolution. As it is mentioned that the maximum value of the terms $\frac{\beta a}{(\alpha+\beta a)\,ln(\alpha+\beta a)}$ and $\frac{\beta^2a^2}{(\alpha+\beta a)^2\,ln(\alpha+\beta a)}$ depend on the value of α, the change in sign of w_h also depends on the value of α. The possible behaviors of w_h are shown in Figs. 1 and 2 for different values of parameters which show the similar behaviors as discussed above. We have used value of r from (21) and have assumed the present value of scale factor $a_0 = 1$ here and thereafter for our convenience.

It is worthy to note that if we take constant value of Γ as taken in [16], the Eq. (13) in the late time evolution ($a\to\infty$) reduces to its respective expression in GR for

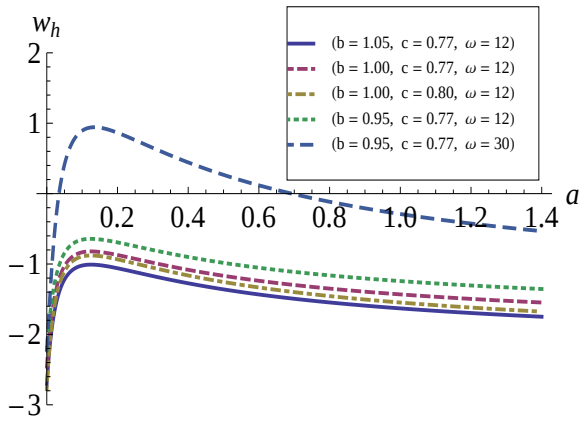


FIG. 2. The evolution of w_h verses a for different values of b, c and ω with $\alpha = 1.15$ and $\beta = 5$.

HDE model, that is,

$$w_h \approx -\left(1+\frac{1}{r}\right)\frac{\Gamma}{3H}. \tag{15}$$

Now, for time-dependent $\Gamma = 3b^2H$, we get the expression of w_h for late time evolution as

$$w_h \approx -b^2\left(1+\frac{1}{r}\right). \tag{16}$$

One can observe from (16) that the EoS parameter converses to a negative constant value in the late time evolution. It means that as the Universe enters in the late time accelerating phase, the HDE behave like DE forever. In the absence of interaction ($b^2 = 0$), we obtain a positive EoS parameter of HDE ($w_h > 0$) from (13) through out the evolution. It means accelerated expansion is not possible in this case as observed in the papers [16, 23]. It is also observed that w_h may cross the phantom divide ($w_h = -1$) for a suitable value of b^2 in the late time evolution.

In the present model, the dynamics of the Universe depends not only on DM and HDE, but also on the BD scalar field. It will be early to conclude about the evolution of the Universe only on the basis of EoS of HDE. Therefore, it is important to discuss the behavior of deceleration parameter, $q = -\frac{a\ddot{a}}{\dot{a}^2}$ to make a precise conclusion. We obtain the value of q after dividing Eq. (4) by H^2, and using (8) and (9) which is given as

$$q = \frac{3c^2w_h + 1 - \frac{\beta^2a^2}{(\alpha+\beta a)^2\,ln(\alpha+\beta a)} + \frac{2\beta a}{(\alpha+\beta a)\,ln(\alpha+\beta a)} + \frac{\omega\beta^2a^2}{2(\alpha+\beta a)^2\,[ln(\alpha+\beta a)]^2}}{2 + \frac{\beta a}{(\alpha+\beta a)\,ln(\alpha+\beta a)}} \tag{17}$$

Let us examine the sign of deceleration parameter to discuss the early and late time evolution. In the beginning of evolution at $a = 0$, we obtain $q = \frac{3c^2w_h+1}{2}$. Using the initial value of w_h given by Eq. (14), we get $q = \frac{1}{2}\left[1 - 3b^2c^2\left(1+\frac{1}{r}\right)\right]$, which produces accelerated expansion for $3b^2c^2\left(1+\frac{1}{r}\right) > 1$. Thus, we observe inflationary era which has been expected to happen in the beginning of the evolution to resolve the problems of Big-Bang cosmology. As w_h may show sign change from negative to positive during the evolution and the last term containing ω in numerator of Eq. (17) starts to dominate due to large value of ω, a change in the sign of deceleration parameter from negative to positive may also be observed. If w_h is negative throughout the evolution then also we observe sign change in q as shown in Figs. 3 and 4. Thus, we observe a decelerated expansion of the Universe after inflation. Since the terms $\frac{\beta a}{(\alpha+\beta a)\,ln(\alpha+\beta a)}$ and $\frac{\beta^2a^2}{(\alpha+\beta a)^2\,ln(\alpha+\beta a)}$ converse to zero in the late time evolution, the late time value of q is obtained as

$$q \approx \frac{3c^2w_h + 1}{2}, \tag{18}$$

Using the late time value of w_h given by (16) into (18), we get

$$q \approx \frac{1}{2}\left[1 - 3b^2c^2\left(1+\frac{1}{r}\right)\right]. \tag{19}$$

Here, q will be negative if $3b^2c^2\left(1+\frac{1}{r}\right) > 1$, the same as for early time. Therefore, a sign change of q from positive to negative may be observed which successfully explains the late time phase transition (deceleration to acceleration) of the Universe. Indeed, HDE shows almost same behavior in the early and late time evolution of the Universe. If there is no interaction ($b^2 = 0$), we observe $q > 0$ through out the evolution. Thus, using the value of q we reconfirm that the accelerated expansion is not possible in the case of no interaction. It can be seen that it is not only for $b^2 = 0$, but also for a small value of $b^2 << 1$, a decelerating Universe may be observed throughout the evolution. The other parameters of the model will not change this scenario. Further, we observe that a sufficiently large value of b^2 is able to accelerate the expansion through out the evolution. Therefore, the value of coupling parameter b^2 plays an important role to observe the evolution of the Universe which is consistent with the observations. It means that a suitable interaction between the dark components of the Universe, i.e., a

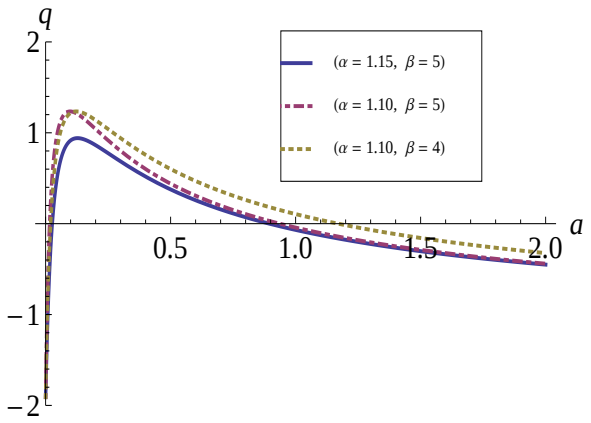


FIG. 3. The evolution of q verses a for different values of α and β with $b = 1.05$ and $c = 0.77$.

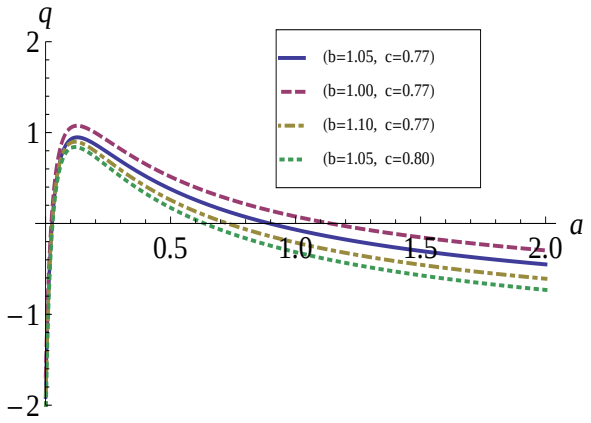


FIG. 4. The evolution of q verses a for different values of b and c with $\alpha = 1.15$ and $\beta = 5$.

suitable value of b^2 is required to be consistent with the observations.

After having a suitable interaction, the most important parameters are α and β, which are due to the logarithmic form of BD scalar field. The terms containing α and β in Eq. (17) start from zero, evolve up to maximum value and converse to zero in the late time which lead to observe two phase transitions of the Universe, i.e., the early time inflation and the late time acceleration. It is worthy to mention here that for the power-law form of BD scalar field, only a late time acceleration is possible. The values of α and β are important to decide the time when the phase transitions, inflation and late time acceleration, will happen which can be seen in Figs. 3 and 4. Thus, to accommodate the observed history of the Universe the value of α and β are significant. It is also evident from (17) that for a large value of ω the inflation ends early and the late time acceleration occurs late, and viceversa. So far we have observed that a number of combination of the parameters are possible to explain the whole history of the Universe but let observations to decide the best combination of the parameters.

We have shown that the present model of dark energy is able to explain the whole known history of the Universe starting from inflation to recent accelerated expansion of the Universe including the matter dominated era (radiation+dust). Thus, this model presents a unified model of interacting HDE in the framework of BD theory with logarithmic form of BD scalar field. We emphasise that the logarithmic form proposed in this paper has played an important role to explain the evolution of the Universe in more better way. In the next section, we will show that this form also plays a significant role to resolve the coincidence problem.

IV. COSMIC COINCIDENCE PROBLEM

Let us investigate the present model on the ground of cosmic coincidence problem [34, 35]. Using the conservation Eqs. (5) and (6), the evolution of energy density ratio r can be obtained as

$$\dot{r} = 3Hr\left[w_h + \left(\frac{1+r}{r}\right)b^2\right], \tag{20}$$

which is the same expression as obtained in [16, 22] except we have b^2 at the place of $\Gamma/3H$ because they have chosen Γ as a constant whereas we have taken $\Gamma = 3b^2H$. The nature of evolution of r in our model is different from the mentioned works as we have taken time-dependent Γ and it also depends on the value of w_h. Using the late time value of w_h given by (16) into (20) we obtain $\dot{r} = 0$, i.e., in the late time evolution r has a constant value which is a significant feature to solve the coincidence problem. Pavón and Zimdahl [16] have obtained a constant value of r in GR, however, r is expected to be a time-varying value. Therefore, the authors assumed a time-varying value of c to obtain a time-varying r. It has also been suggested to replace the Hubble horizon by the future event horizon to achieve a time-varying value of r [36]. Although Banerjee and Pavón [22] have obtained time-dependent value of r in Brans-Dicke theory but they achieved a soft coincidence only. They argued that r can vary more slowly in their model than in the conventional ΛCDM model. It have been demonstrated by Zhang et al. [37] that the interacting chaplygin gas model has a better chance to solve the coincidence problem in comparison of interacting quintessence and interacting phanton models. In the literature, many proposals have been made to solve the coincidence problem [38, 39] but the problem still exists.

Let us find the value of r for our model to analyse coincidence problem in more detail. From (3), the value of r is obtained as

$$r = -1 + \frac{1}{c^2} + \frac{\beta a}{c^2(\alpha+\beta a)\ ln(\alpha+\beta a)} - \frac{\omega\beta^2 a^2}{6c^2(\alpha+\beta a)^2\ [ln(\alpha+\beta a)]^2}. \tag{21}$$

Here, we obtain a time-dependent value of r which has a constant and finite value $r = -1 + \frac{1}{c^2}$ at the beginning of the evolution as the last two terms are zero at $a = 0$. In the late time evolution, we also obtain a constant and finite value $r \approx -1 + \frac{1}{c^2}$ as the last two terms converge to zero. The same constant value of r has been obtained through out the evolution in GR [16] but we have obtained a time-dependent value of r which has constant values in the early and late time evolution. Here, it will be interesting to quote a paper of Campo et al. [38] "Obviously, a mechanism that makes r tends to a constant today or decrease its rate to a lower value than the scale factor expansion rate ameliorates the coincidence problem significantly, but it does not solve it in full. To do so the said mechanism must also achieve $r_0 \sim \mathcal{O}(1)$". We have obtained $r_0 \sim -1 + \frac{1}{c^2}$ which excellently satisfies the requirement $r_0 \sim \mathcal{O}(1)$ as most of the observational constraints on c obtain $0.5 < c < 1$ [40–42]. In the other words, the cosmic coincidence problem has been resolve completely. In fact, we observe $r \sim \mathcal{O}(1)$ in the early time as well as in the late time evolution in our model. Therefore, the cosmic coincidence problem does not seem a problem because it is not a coincidence that we are living in a time where $r \sim \mathcal{O}(1)$, it have been observed in the early time also. Thus, in conclusion we can say that the cosmic coincidence problem has been resolved in a significantly well manner in the present model.

From (16) and (20), it is clear that whatever the value of b^2 be chosen, we obtain $\dot{r} = 0$ in the late time evolution. It means the coupling parameter b^2 between DM and HDE does not play a significant role in the alleviation of coincidence problem. This is also evident from the value of r given by (21) which has no b^2 term. Also, one may observe that the parameter c is not significant to resolve the coincidence problem. Although, it plays an important in the value of r at any given time. Actually, the last two terms in Eq. (21) which come due to the assumption of logarithmic form of BD scalar field, play an important role to decide the coincidence problem. These two terms converse to zero in the late time and may vary sufficiently slow at present due to which r converses to a constant value in the late time and vary sufficiently slow at present. The suitable values of the parameters α and β ensure the slow variation of r at present time. The variation of r is shown in the Fig. (5) which clearly verify our claim.

Let us find the value of c to match with the observational values using the observed value of r. According to recent observations, the present value of r is $\approx \frac{3}{7}$, where matter has $\approx 30\%$ and DE has $\approx 70\%$ of total energy content of the Universe. We obtain the value $c \approx 0.8367$ using the theoretical relation $r \approx -1 + \frac{1}{c^2}$ from (21) for late time evolution. Xu at al. [40] have obtained similar value $c = 0.807^{+0.165}_{-0.160}$ for the HDE model in the framework of Brans-Dicke theory. Using the observations from various probes like WMAP, BAO, Planck etc. Li et al. [41] have obtained values of c which also show similarity with the above values, however, all these models are different.

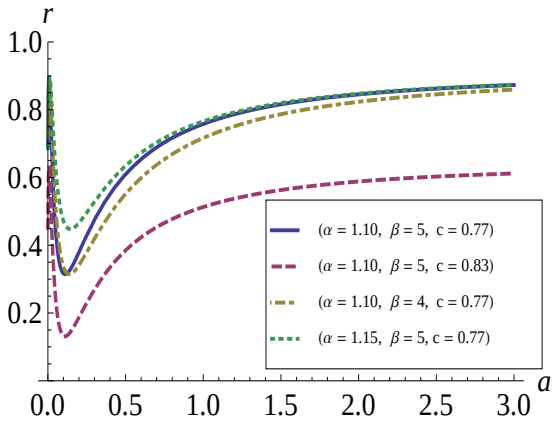


FIG. 5. The graph of r verses a for different values of α, β and c with $\omega = 12$.

V. CONCLUSION

In this paper, we have studied interacting HDE model with Hubble horizon as an IR cut-off in the framework of BD theory. We have pointed out a serious problem associated with the assumption of power-law form ($\phi \propto a^n$) of the BD scalar field. It has been observed that this form of BD scalar field gives constant and time-dependent deceleration parameter for same model. Therefore, taking into consideration of this problem, we have proposed a logarithmic form of BD scalar field which always gives a time-varying deceleration parameter. We have observed that this form of BD scalar field is consistent with the cosmic evolution of the Universe. We have obtained EoS parameter and deceleration parameter to discuss the early and late time evolution of the Universe. We have also discussed the cosmic coincident problem. A summary of the main findings is as follows.

In the early time evolution, we observe $w_h < 0$ and $q < 0$ which explains the inflationary era of the cosmic evolution supposed to happened in the very early Universe to resolve the problems of Big-Bang cosmology. Further, the sign change of q from negative to positive has been observed. Thus, we observe the matter dom-

inated era of the evolution. In the late time evolution, we have observed another sign change of q from positive to negative which explain the late time acceleration of the Universe. Thus, this model presents a unified model of interacting HDE in the framework of BD theory with logarithmic form of BD scalar field. If we consider Γ as a constant then the EoS parameter w_h reduces to the corresponding form of GR in the late time. The EoS parameter converges to a constant value and for a suitable value of b^2 it may cross the phantom-divide line $w_h = -1$ in the late time evolution. If there is no interaction between HDE and DM, i.e., $b^2 = 0$, it has been observed that the EoS parameter w_h and deceleration parameter q are always positive, therefore, the accelerated expansion is not possible in this case.

We have also discussed the cosmic coincidence problem, a long standing problem with DE models, which has been resolved effectively in this paper. We have observed a time-varying energy density ratio r which has a constant value in early and late time evolution of the Universe. The present value r_0 satisfies the condition $r_0 \sim \mathcal{O}(1)$ which is consistent with the observations. Using the present value of r obtained by observations, we get theoretical value $c = 0.8367$ which shows similarity with the observed values of c.

In conclusion, the advantage of our model is that we have alleviated the problem associated with the power-law containing the good features of it. In addition, our model presents a unification of early time inflation and late time acceleration including the matter dominated era which have not been obtained through power-law form. In the present model, the cosmic coincidence problem has been alleviated more effectively in comparison of existing models.

[1] A.G. Riess et al., Astron. J. **116**, 1009 (1998); S. Perlmutter et al., Astrophys. J. **517**, 565 (1999).
[2] C.L. Bennett et al., Astrophys. J. **148**, 1 (2003); E. Komatsu et al., Astrophys. J. Suppl. **192**, 18 (2011).
[3] K. Abazajian et al., Astron. J. **128**, 502 (2004); M. Tegmark et al., Phys. Rev. D **69**, 103501 (2004).
[4] W.J. Percival et al., Mon. Not. R. Astro. Soc. **401**, 2148 (2010).
[5] P.A.R. Ade et al., Astron. Astrophys. **571**, A16 (2014).
[6] S.M. Carroll, Living Rev. Relativity **4**, 1 (2001).
[7] R.R. Caldwell et al., Phys. Rev. Lett. **80**, 1582 (1998).
[8] R.R. Caldwell et al., Phys. Lett. B **545**, 23 (2002).
[9] A.Y. Kamenshchik et al., Phys. Lett. B **511**, 265 (2001); P.P. Avelino, K. Bolejko and G.F. Lewis, Phys. Rev. D **89**, 103004 (2014).
[10] E.J. Copeland, M. Sami and S. Tsujikawa, Int. J. Mod. Phys. D **15**, 1753 (2006).
[11] G. 't Hooft, arXiv:gr-qc/9310026 (1993).
[12] L. Susskind, J. Math. Phys. **36**, 6377 (1995).
[13] A.G. Cohen, D.B. Kaplan and A.E. Nelson, Phys. Rev. Lett. **82**, 4971 (1999).
[14] M. Li, Phys. Lett. B **603**, 1 (2004).
[15] S.D.H. Hsu, Phys. Lett. B **594**, 13 (2004).
[16] D. Pavón and W. Zimdahl, Phys. Lett. B **628**, 206 (2005).
[17] C. Brans and R.H. Dicke, Phys. Rev. **124**, 925 (1961).
[18] C. Mathiazhagen and V.B. Johri, Class. Quantum Grav. **1**, L29 (1984); D. La and P.J. Steinhardt, Phys. Rev. Lett. **62**, 376 (1989); A. Linde, Phys. Lett. B **238**, 160 (1990).
[19] O. Bertolami and P.J. Martins, Phys. Rev. D **61**, 064007 (2000); H. Kim, Mon. Not. R. Astron. Soc. Lett. **364**, 813 (2005); T. Clifton and J.D. Barrow, Phys. Rev. D **73**, 104022 (2006).
[20] M.R. Setare, Phys. Lett. B **644**, 99 (2007).
[21] A. Sheykhi and M. Jamil, Phys. Lett. B **694**, 284 (2011).
[22] N. Banerjee and D. Pavón, Phys. Lett. B **647**, 477 (2007).
[23] L. Xu, W. Li and J. Lu, Eur. Phys. J. C **60**, 135 (2009).
[24] A. Sheykhi, Phys. Lett. B **681**, 205 (2009).
[25] A. Sheykhi, Phys. Rev. D **81**, 023525 (2010).
[26] M.S. Berman and F.M. Gomide, Gen. Relativ. Gravit. **20**, 191 (1988); V.B. Johri and D. Kalyani, Gen. Relativ. Gravit. **26**, 1217 (1994); G.P. Singh and A. Beesham, Aust. J. Phys. **52**, 1039 (1999).
[27] L. Amendola and C. Quercellini, Phys. Rev. D **68**, 023514 (2003); W. Zimdahl and D. Pavón, Gen. Relativ. Gravit. **35**, 413 (2003); G. Farrar and P.J.E. Peebles, Astriohys. J. **604**, 1 (2004); B. Gumjudpai et al., J. cosmol. Astropart. Phys. **06**, 007 (2005); C. Skordis, A. Pourtsidou and E. J. Copeland, Phys. Rev. D **91**, 083537 (2015).
[28] G. Olivares, F. Atrio and D. Pavón, Phys. Rev. D **71**, 063523 (2005); C. Feng et al., J. Cosmol. Astropart. Phys. **09**, 005 (2007); S. Cao, N. Liang and Z-H Zhu, Mon. Not. R. Astron. Soc. **416**, 1099 (2011); A.A. Costa et al., Phys. Rev. D **89**, 103531 (2014).
[29] B. Bertotti, L. Iess and P. Tortora, Nature **426**, 374 (2003); C. Will, Living Rev. Relativity **9**, 3 (2006).
[30] V. Acquaviva et al., Phys. Rev. D **71**, 104025 (2005).
[31] F.-Q. Wu and X. Chen, Phys. Rev. D **82**, 083003 (2010).
[32] Y.-C. Li, F.-Q. Wu and X. Chen, Phys. Rev. D **88**, 084053 (2013).
[33] W. Zimdahl and D. Pavón, Class. Quantum Grav. **24**, 5461 (2007).
[34] I. Zlatev, L. Wang and P.J. Steinhardt, Phys. Rev Lett. **87**, 5 (1999).
[35] P. Steinhardt, in Critical Problems in Physics, edited by V.L. Fitch and D.R. Marlow (Princeton University Press, Princeton, NJ, 1997).
[36] B. Wang, Y Gong and E Abdalla, Phys. Lett. B **624**, 141 (2005).
[37] H. Zhang et al., Phys. Lett. B **678**, 331 (2009).
[38] S. del Campo, R. Herrera and D. Pavón, Phys. Rev. D **78**, 021302(R) (2008).
[39] H.E.S. Velten, R.F. vom Marttens and W. Zimdahl, Eur. Phys. J. C **74**, 3160 (2014); R. Bousso et al., Phys. Rev. Lett. **106**, 101303 (2011); A. Barreira and P.P. Avelino, Phys. Rev. D **83**, 103001 (2011); S.Z.W. Lip, Phys. Rev. D **83**, 023528 (2011); D.J. Shaw and J.D. Barrow, Phys. Rev. D **83**, 043518 (2011); J. Lee et al., Phys. Rev. D **90**, 123003 (2014).
[40] L. Xu et al., Mod. Phys. Lett. A **25**, 1441 (2010).

[41] M. Li et al., J. Cosmol. Astropart. Phys. **09**, 021 (2013).
[42] L. Xu , Phys. Rev. D **87**, 043525 (2013).

Ceramics International ∎ (∎∎∎∎) ∎∎∎–∎∎∎

Contents lists available at ScienceDirect

Ceramics International

journal homepage: www.elsevier.com/locate/ceramint

Influence of milling duration on microstructural, electrical, ferroelectric and piezoelectric properties of $Ba_{0.9}Sr_{0.1}Zr_{0.04}Ti_{0.96}O_3$ ceramic

Aditya Jain [a], Amrish K. Panwar [a,*], A.K. Jha [b]

[a] Department of Applied Physics, Delhi Technological University (Formerly Delhi College of Engineering), Bawana Road, Delhi 110042, India
[b] Department of Applied Science, A.I.A.C.T.R., Geeta Colony, Delhi 110031, India

ARTICLE INFO

Article history:
Received 25 July 2016
Received in revised form
27 August 2016
Accepted 2 September 2016

Keywords:
Dielectric
Ferroelectric
Perovskite
Ceramics
Microstructure

ABSTRACT

In an effort to explore lead-free ferroelectric ceramic material for capacitor applications, the Sr and Zr co-doped $BaTiO_3$ compound has been selected for investigation. A detailed study was carried out to study the effect of mechanical milling duration on structure, particle size, morphology, dielectric and piezoelectric properties. The $Ba_{0.9}Sr_{0.1}Zr_{0.04}Ti_{0.96}O_3$ ceramics were synthesized using mechanochemical activation technique for different milling duration of 25, 30, 35, 40 and 45 h. The Rietveld refinement analysis of X-ray diffraction pattern confirms the formation of tetragonal phase with *P4mm* space group for all the samples. When subjected to long duration mechanical milling, the samples have shown different grain size distribution. The average grain size reduces from 931 nm to 385 nm on increasing the milling duration from 25 h to 45 h. Ferroelectric studies reveal that the saturation and remnant polarization were found maximum for 35 h milled sample. Furthermore, piezoelectric constant, d_{33} were also found to be maximum for 35 h milled sample. The presence of Sr and Zr in barium titanate combined with optimized milling conditions may provide significant technological advances in the field of $BaTiO_3$ based ferroelectric devices.

© 2016 Elsevier Ltd and Techna Group S.r.l. All rights reserved.

1. Introduction

Barium titanate ($BaTiO_3$) based materials have superior dielectric properties and are broadly used in electronic components. Different dopants have been explored to improve properties of pure $BaTiO_3$. These dopants result in shift of transition temperature and change in microstructural and dielectric properties of $BaTiO_3$. It is to be noted that the shift of transition temperature and shape of transition curve cannot be simply explained by ionic size effects. Many of the dopants give rise to diffuse phase transition accompanied by a deviation from Curie–Weiss law, frequency dispersion and a spontaneous polarization over an extended temperature range [1–4]. $Ba_{1-x}Sr_xZr_yTi_{1-y}O_3$ ($0 < x, y < 1$) based ferroelectric materials are potential candidates for multilayered ceramic capacitors, varactors, filters, delay lines, etc. due to its high dielectric constant and low dielectric loss [5–7]. In recent years, a large number of complex oxides with perovskite structure (ABO_3) have been investigated in the quest for ferroelectric and multiferroic properties which have a wide range of applications [8–10]. $BaSr_xTi_{1-x}O_3$ (BST) and $BaZr_xTi_{1-x}O_3$ (BZT) are some of those materials which have found extensive applications in capacitors, optical devices, etc. Further, for microwave devices, low dielectric loss, good temperature stability and high tunability are required. Strontium and zirconium substitution can be used to reduce dielectric loss in lead-free $BaTiO_3$ system [11]. For BZT solid solutions, it has been observed that as the zirconium substitution is increased, there was a gradual decrease in the average grain size which results in subsequent decrease of maximum dielectric constant and dielectric loss. This decrease in dielectric constant and dielectric loss was attributed to grain scaling effect and not as an intrinsic effect due to the addition of zirconium [12]. Moreover, the addition of Sr and Zr on $BaTiO_3$ do not distort the perovskite crystal structure which is due to many factors including (1) comparable ionic radii, (2) charge neutrality and (3) solubility/miscibility [13]. Generally, Ba site is substituted by divalent atoms such as Ca, Sr and Pb while Ti site is substituted by tetravalent atoms such as Zr and Hf. Various rare earth and transition metal aliovalent ions have been replaced in $BaTiO_3$ lattice and have shown deviation from perovskite structure beyond a critical concentration of substituent atoms [14,15]. Both Sr and Zr substitution in barium titanate lowers the Curie temperature which leads to

* Corresponding author.
E-mail address: panwaramar@gmail.com (A.K. Panwar).

http://dx.doi.org/10.1016/j.ceramint.2016.09.018
0272-8842/© 2016 Elsevier Ltd and Techna Group S.r.l. All rights reserved.

Please cite this article as: A. Jain, et al., Influence of milling duration on microstructural, electrical, ferroelectric and piezoelectric properties of $Ba_{0.9}Sr_{0.1}Zr_{0.04}Ti_{0.96}O_3$ ceramic, Ceramics International (2016), http://dx.doi.org/10.1016/j.ceramint.2016.09.018

increase in dielectric constant of the material around room temperature [16]. Substitution of isovalent cation like Zr^{4+} which is chemically more stable compared to Ti^{4+} results in increase of dielectric constant and broaden the dielectric constant curve [17].

It is implied that proper selection of substituent and amount of substituent is a promising way to improve the dielectric properties of BT ceramics. In literature, the effect of Sr and Zr doping on barium titanate solid solution have been reported, However, there is no information available in the literature on the effect of milling duration in BSZT ceramic. In this study, a small amount of Sr and Zr are substituted in $BaTiO_3$ and an attempt have been made to obtain nano-sized particle of perovskite phase by using ball milling technique and their microstructural, electrical, ferroelectric and piezoelectric properties were investigated. Here, in the present work, ball milling technique has been employed, which could promote higher densification of the specimen at the lower sintering temperature.

2. Experimental

$Ba_{0.9}Sr_{0.1}Zr_{0.04}Ti_{0.96}O_3$ with different milling duration were prepared by mechanochemical activation technique. Reagent grade $BaCO_3$ (99.0%), $SrCO_3$ (99.9%), TiO_2 (99.8%) and ZrO_2 (99.0%) of Sigma-Aldrich make were taken as the starting materials. All precursor materials were taken in stoichiometric amount and milled in air at 450 rpm for effective 25, 30, 35, 40 and 45 h (abbreviated as BSZT25, BSZT30, BSZT35, BSZT40 and BSZT45, respectively). Ball milling was carried out using a *Retsch PM100* planetary ball mill. A Zirconia vial with a diameter of 45 mm and 30 Zirconia balls of diameter 10 mm were used as milling medium. The milled powders were calcined at 1100 °C for 4 h to form the desired phase. These solid solutions were mixed with 2.5 wt% of Poly Vinyl Alcohol (PVA) and pressed (at a force of 80 kN) into pellets with the dimension of 10 mm in diameter and approximately 1 mm in thickness. The pellets were then sintered at 1200 °C for 4 h.

The phase and crystallographic structure of BSZT specimens were examined by X-ray diffractometer (*Bruker D8 Advance*) using $CuK_{\alpha 1}$ radiation having the wavelength of 1.540 Å. The theoretical density and lattice parameters were calculated with the help of XRD data using *X'Pert Highscore Plus* software followed by Rietveld analysis. The microstructural features and surface morphology of sintered pellets were analyzed using scanning electron microscope (*Hitachi S-3700N*). *ImageJ* software has been used for grain size distribution analysis. TEM/HRTEM and SAED analysis of solid powder have been carried out using TEM (FEISTWIN PF30) at 300 kV by using copper grids (CF200-Cu). The sintered pellets of BSZT ceramics were polished to 1 mm thickness and silver paste was applied on both sides of pellets to form electrodes, the pellets were then cured at 180 °C for 20 min. Further, these pellets were used to perform dielectric measurement by an LCR meter (*Agilent 4284A*) at multiple frequencies. Temperature dependent dielectric measurement was carried out within the temperature range of 27–250 °C. The hysteresis loops of the BSZT samples were analyzed using a P-E loop tracer made by *M/s Marine Delhi, India*. Piezoelectric constant measurement was performed using *Piezotest Systems, UK*.

3. Results and discussion

3.1. X-ray diffraction (XRD)

The crystalline structure of different duration milled samples of $Ba_{0.9}Sr_{0.1}Zr_{0.04}Ti_{0.96}O_3$ (BSZT) was investigated. In order to understand the structural modification with milling duration in BSZT, structural refinement has been performed by Rietveld method using *X'Pert Highscore Plus* software. Fig. 1(a–e) shows the Rietveld refined X-ray diffraction pattern of $Ba_{0.9}Sr_{0.1}Zr_{0.04}Ti_{0.96}O_3$ for different milling duration of 25, 30, 35, 40 and 45 h. Barium titanate (JCPDS no. 01–074-1967) has been taken as a reference pattern and peaks were refined using the Pseudo-Voigt function. From Fig. 1(a–e) one can see that the samples possess a pure crystalline phase. All the profiles are almost identical, indicating that the crystalline phases of the samples with different milling duration are of similar crystallographic nature. A well-recognized tetragonal phase with *P4mm*(99) space group was observed for all the synthesized sample. Table 1 lists the detailed structural parameters obtained from the Rietveld refinement analysis. Rietveld refinement confirms that there is no change in crystal structure for all the five synthesized sample, although a slight change in lattice parameters was found with increasing milling duration. The unit cell volume of BSZT was observed to decrease as the milling duration increases from 25 h to 45 h. Using the Debye–Scherrer relation [18], the crystallite size has been calculated from the full

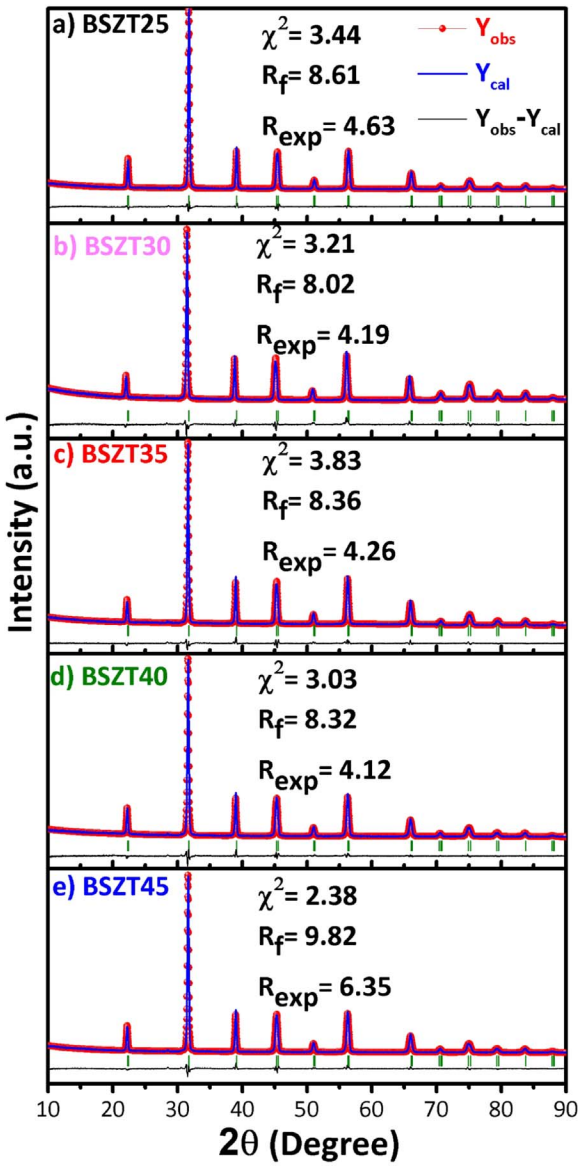


Fig. 1. Rietveld refined X-ray diffraction (XRD) patterns of BSZT samples milled for different duration: (a) 25 h, (b) 30 h, (c) 35 h, (d) 40 h and (e) 45 h.

Please cite this article as: A. Jain, et al., Influence of milling duration on microstructural, electrical, ferroelectric and piezoelectric properties of $Ba_{0.9}Sr_{0.1}Zr_{0.04}Ti_{0.96}O_3$ ceramic, Ceramics International (2016), http://dx.doi.org/10.1016/j.ceramint.2016.09.018

Table 1
Rietveld refined XRD parameters for BSZT25, BSZT30, BSZT35, BSZT40 and BSZT45.

Sample	Space group	Crystal structure	Lattice parameters (Å)	c/a	Cell volume (Å^3)	Density (gm/cm^3)	χ^2	R_{exp}	R_f	R_{Bragg}
BSZT25	*P4mm*	Tetragonal	a=3.9965 c=4.0143	1.0044	64.1164	5.81	3.44	4.63	8.61	1.72
BSZT30	*P4mm*	Tetragonal	a=3.9958 c=4.0137	1.0045	64.0844	5.79	3.67	4.49	8.61	3.19
BSZT35	*P4mm*	Tetragonal	a=3.9952 c=4.0134	1.0045	64.0603	5.78	3.83	4.26	8.36	2.56
BSZT40	*P4mm*	Tetragonal	a=3.9950 c=4.0133	1.0046	64.0523	5.76	3.60	4.67	8.87	2.91
BSZT45	*P4mm*	Tetragonal	a=3.9926 c=4.0113	1.0046	63.9441	5.73	2.38	6.35	9.82	2.65

width at half-maximum (FWHM) of the diffraction halo. For these specimens, the crystallite size was found to be in the range of 38–41 nm.

3.2. Microstructural studies

The effect of milling duration on $Ba_{0.9}Sr_{0.1}Zr_{0.04}Ti_{0.96}O_3$ is correlated with their microstructural development, densification and

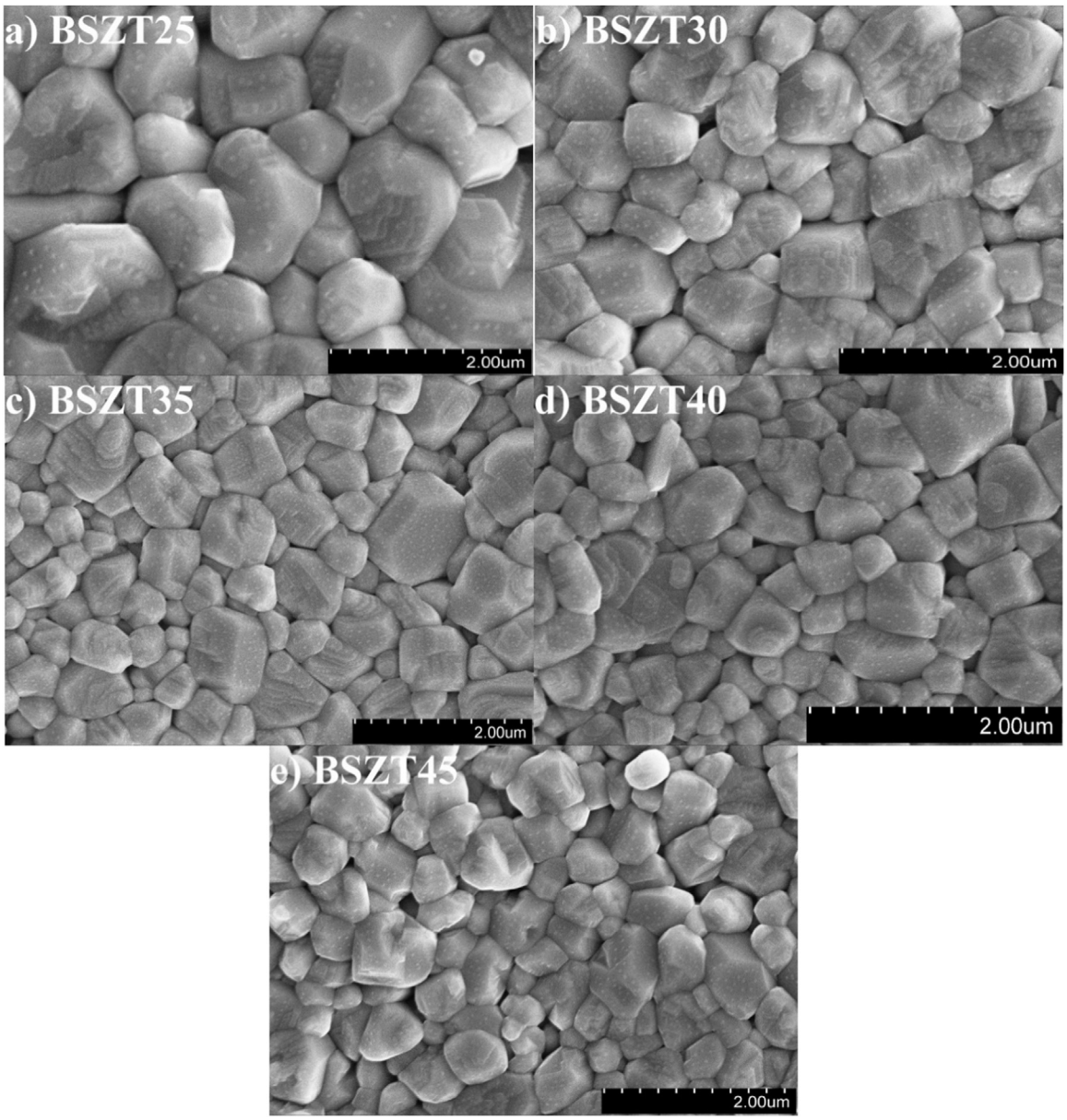


Fig. 2. SEM micrograph of sintered pellets of BSZT samples milled for different duration: (a) 25 h, (b) 30 h, (c) 35 h, (d) 40 h and (e) 45 h.

Please cite this article as: A. Jain, et al., Influence of milling duration on microstructural, electrical, ferroelectric and piezoelectric properties of $Ba_{0.9}Sr_{0.1}Zr_{0.04}Ti_{0.96}O_3$ ceramic, Ceramics International (2016), http://dx.doi.org/10.1016/j.ceramint.2016.09.018

grain growth behavior. Fig. 2(a–e) shows the SEM micrograph of BSZT samples milled for different duration. All of the samples show dense and relatively homogeneous microstructure with well faceted aggregate type grains and clearly distinguished grain boundaries. Milling duration has a significant effect on the grain size of BSZT ceramics. The average grain size of samples BSZT25, BSZT30, BSZT35, BSZT40 and BSZT45 are observed to be 931, 597, 517, 385 and 398 nm, respectively. All the samples have shown similar grain morphology with non-uniform grain size distribution. The grains are densely packed without many cracks and pores. It is observed that the average grain size of BSZT specimens decreases up to milling duration of 40 h. However, on further increasing the milling duration, no appreciable change in grain size is observed. Theoretical densities of BSZT specimens were measured to see the effect of milling duration. It is observed that as milling duration increases, the density of the samples decreases slightly. The decrease in density results in slight increase in porosity of the samples. In the present case, the density of material is a function of three variables namely milling duration, sintering temperature and sintering duration. These three parameters further affect the recrystallization and grain growth of the material [19]. Moreover, it is well-known fact that during milling acceleration between the balls is very large, even higher than the acceleration due to gravity at earth's surface [20]. Thus, a significant amount of energy is generated in ball milling and increasing the milling duration results in a continuous flow of high amount of energy which results in grain size reduction.

TEM and HRTEM studies of BSZT35 have been performed since it shows overall better properties among the five synthesized samples. The average particle size of BSZT35 powder estimated from TEM analysis (Fig. 3(a)) is measured to be ~110 nm. The lattice fringes do indicate the formation of crystallized BSZT ceramic. The high-resolution TEM image of BSZT35 particle (Fig. 3 (b)) shows lattice fringes corresponding to different planes with an inter-fringe distance of 0.238 nm and 0.121 nm, respectively. It can be seen in Fig. 3(b) that the continuous lattice fringes measurement with an inter-fringe distance of 0.238 nm and 0.121 nm could be assigned to the corresponding (101) and (113) planes with conventional d spacing of 0.242 nm and 0.120 for BSZT35 ceramic. The selected area electron diffraction (SAED) pattern shown in Fig. 3(c), also confirms the crystalline nature of BSZT35 powder. The typical SAED pattern depicts bright and dark spots that are assigned to different planes in the tetragonal crystal. The HRTEM image and the corresponding SAED pattern reveals that

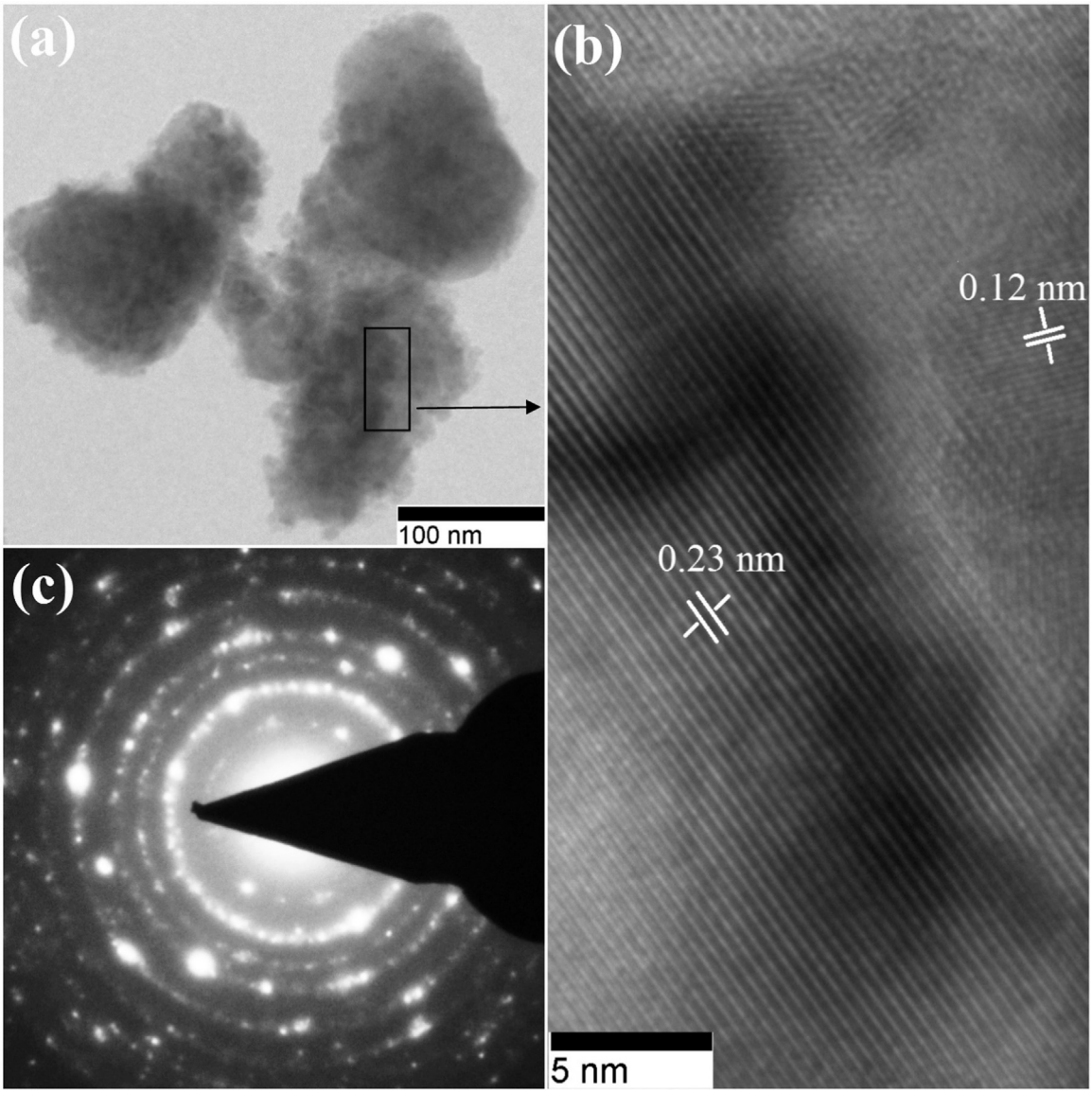


Fig. 3. TEM/HRTEM image of BSZT35: (a) TEM, (b) HRTEM, (c) SAED pattern.

Please cite this article as: A. Jain, et al., Influence of milling duration on microstructural, electrical, ferroelectric and piezoelectric properties of $Ba_{0.9}Sr_{0.1}Zr_{0.04}Ti_{0.96}O_3$ ceramic, Ceramics International (2016), http://dx.doi.org/10.1016/j.ceramint.2016.09.018

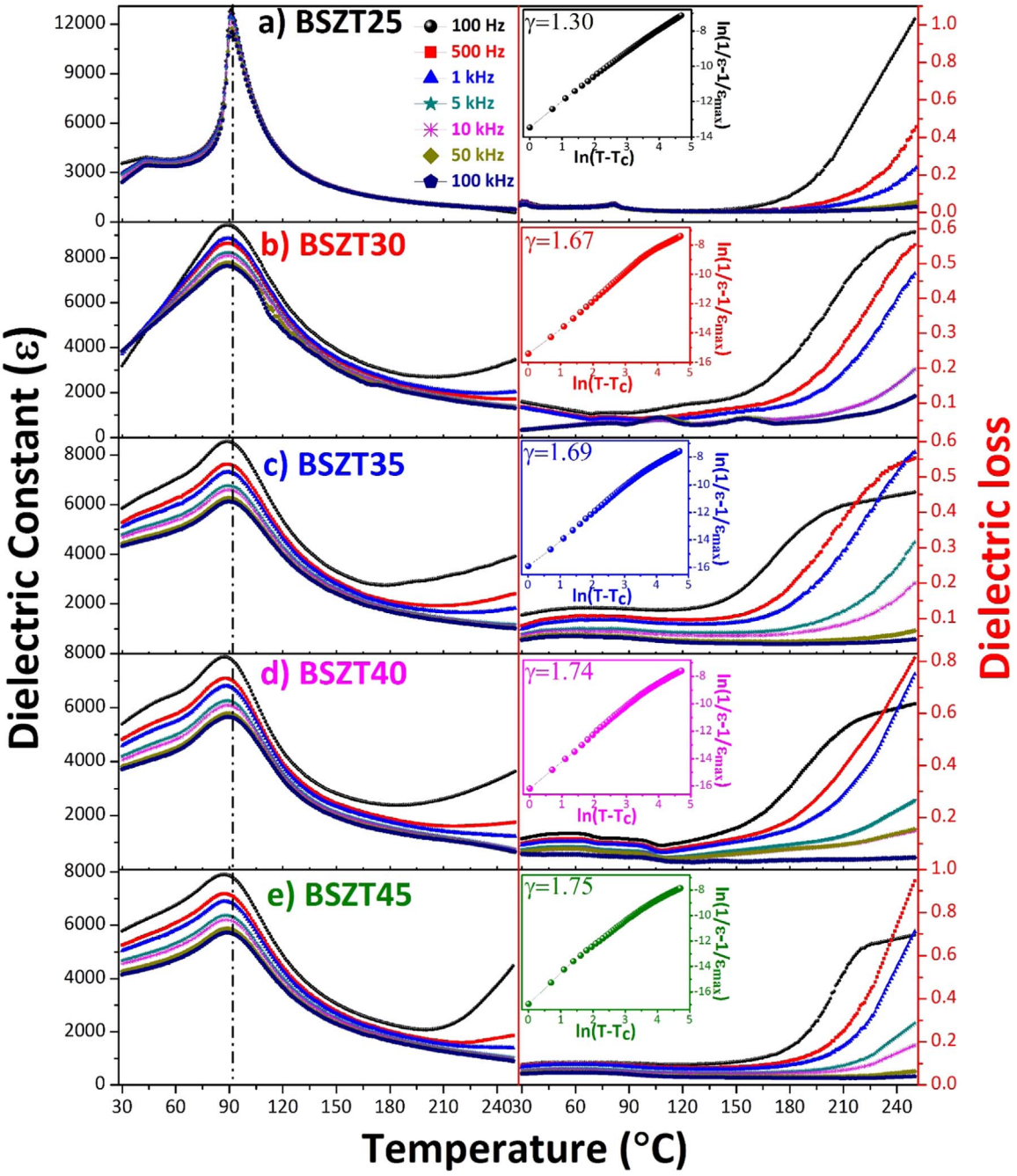


Fig. 4. Dielectric constant and dielectric loss as a function of temperature and inset shows the Plot of $\ln(1/\varepsilon - 1/\varepsilon_m)$ as a function of $\ln(T - T_c)$ for the BSZT samples: (a) BSZT25, (b) BSZT30, (c) BSZT35, (d) BSZT40 and (e) BSZT45.

the BSZT35 ceramic is polycrystalline in nature. Both of the HRTEM and SAED patterns recorded for the selected sample indicate that there are no significant structural defects in the observed BSZT35 polycrystalline sample.

3.3. *Dielectric studies*

Fig. 4 shows the temperature dependence of dielectric constant and dielectric loss measured in the frequency range of 100 Hz–100 kHz for the five synthesized samples. It is found that dielectric constant of BSZT samples decreases with increase in milling duration from 25 h to 45 h. The Curie temperature of samples BSZT25, BSZT30, BSZT35, BSZT40 and BSZT45 are observed to be at 91.5 °C, 89.5 °C, 88.0 °C, 87.5 °C and 87.0 °C, respectively. This small shift in Curie temperature towards low-temperature side may be caused by the occurrence of greater ion disorder and internal stress [21]. Ion disorders inside the material affect long-range interactions, resulting in decrease of transition temperature [22,23]. Another possibility of such decrease in Curie temperature may be attributed to increase in c/a ratio and decrease in grain size of the materials. This increase in c/a ratio indicates that the higher duration milled samples are becoming increasingly more tetragonal and thus resulting in decrease of Curie temperature [24]. The sharp transition in BSZT25 as compared to other samples may be attributed to more or less unidirectional distribution of dipoles inside the material. The dielectric constant value of BSZT ceramic samples increases with increase in temperature and around Curie temperature it shows a strong anomaly in the value of dielectric

Please cite this article as: A. Jain, et al., Influence of milling duration on microstructural, electrical, ferroelectric and piezoelectric properties of $Ba_{0.9}Sr_{0.1}Zr_{0.04}Ti_{0.96}O_3$ ceramic, Ceramics International (2016), http://dx.doi.org/10.1016/j.ceramint.2016.09.018

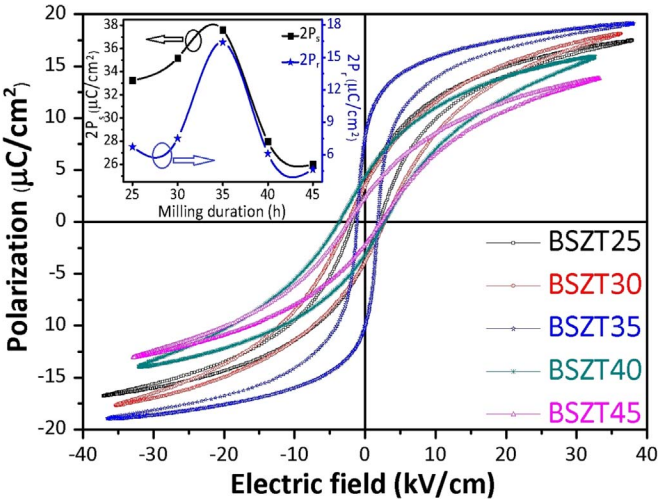


Fig. 5. Ferroelectric hysteresis loops of BSZT samples milled for the different duration at room temperature and inset shows the variation of remnant polarization ($2P_r$) and saturation polarization for different milling duration.

constant. This behavior can be described on the basis of increase in domain wall mobility with an increase in temperature.

The decrease in dielectric constant with the increase in milling duration can be attributed to decrease in grain size [25]. The decrease in grain size leads to an increase in the number of relatively more insulating grain boundary layer. The increase in number of grain boundary results in trapping of more and more space charge and as a result domain wall pinning is expected to be stronger which leads to decrease in dielectric constant value [8,26]. Moreover, the dielectric constant value of all the BSZT samples decreases with the increase in frequency. The decrease in dielectric constant value at higher frequency can be understood on the basis of decrease in polarization occurring between the grains and grain boundaries. Further, four types of polarization namely, dipolar, ionic, electronic and interfacial polarization contribute to the total polarization of a dielectric material [26]. At lower applied frequency of operation all four types of polarization contribute against the variation of time varying electric field but as the frequency increases, the contribution of different polarization mechanisms ceases to contribute, as a consequence, the total polarization of the material decreases which results in decrease of dielectric constant value. It can be seen from Fig. 4(a) that a sharp ferroelectric to paraelectric transition with no obvious frequency dispersion is observed around the dielectric constant maximum for the sample BSZT25. However, for higher duration milled samples a diffuse phase transition with broad dielectric constant maxima is observed. The dielectric broadening at the phase transition is attributed to micro-inhomogeneity and compositional fluctuation. Increase in dielectric broadening with an increase in milling duration suggests that the microscopic inhomogeneity is increasing in higher duration milled samples [27]. In all the samples except BSZT25, the diffused maximum is due to the difference in polarizations that correspond to each ion, which gives rise to different relaxation times [28].

It is observed that the dielectric loss of BSZT samples increases with the increase in temperature. This increase in dielectric loss at higher temperature may be attributed to the increased mobility of ions, imperfections in the material and shallow contribution of thermally activated charge carriers in the material which would hamper the dipolar polarization [29]. It is found that the dielectric loss of BSZT samples decreases with increasing milling duration, it becomes minimum for BSZT35 and then further increases on increasing the milling duration beyond 35 h. The decrease in dielectric loss for BSZT35 may be attributed to reduced leakage current that depends on the crystal structure impurities like dislocation, vacancies and ionic charge imbalance. It can also be seen that the dielectric constant and dielectric loss curves for all the five samples show no frequency dispersion.

Another feature of these BSZT solid solutions is the induction of diffuse phase transition with increasing milling duration. The extent of diffuseness of these samples can be analyzed by plotting ln (T–T_C) vs. ln($1/\varepsilon - 1/\varepsilon_{max}$). The inset (Fig. 4) of dielectric loss curve provides the diffuseness parameter. The diffuse nature of phase transition can be ascribed to polar structural distortions of octahedral and perturbed localized dynamics due to the substitution on A- and B-sites and higher milling duration [30]. Another reason for the diffused behavior in higher duration milled sample is due to arbitrary distributed strain field inside the microstructure, which may have aroused due to lattice distortion caused by the higher milling duration and decrease of the grain size [28]. A modified Curie-Weiss law is used to calculate the diffuseness parameter and is expressed as:

$$\frac{1}{\varepsilon} - \frac{1}{\varepsilon_m} = \frac{(T - T_c)^{\gamma}}{C'} \quad (1)$$

where γ represents diffuseness parameter, T_c is the Curie–Weiss temperature and C' denotes the Curie constant. The parameter γ provides information on phase transition characteristics of any material. The value of $\gamma = 1$ corresponds to normal ferroelectric behavior and $1 < \gamma < 2$ correspond to a diffuse phase transition [31]. The BSZT samples with diffuse phase transition and low dielectric loss around room temperature can be categorized under Class II dielectric materials and will be a potential candidate for fabrication of ceramic capacitors.

3.4. Ferroelectric studies

The electric field induced polarization of BSZT samples shown in Fig. 5 was examined by tracing the hysteresis loop. The measurement was carried out at room temperature up to an electric field of ~40 kV/cm and low operating frequency of 50 Hz. The saturated P–E hysteresis loops confirm the ferroelectric nature of BSZT ceramics. The remnant polarization ($2P_r$), saturation polarization ($2P_s$) and coercive field ($2E_c$) values for the studied samples are listed in Table 2. For all the five samples stronger ferroelectric character can be observed. This indicates that at room temperature the crystal structure is in ferroelectric phase which is in good agreement with the temperature dependence of relative permittivity (ε_r). The shapes of hysteresis *P–E* loop are related to the crystalline structure of the materials. The ferroelectricity in BSZT is due to off-centering of Ti^{4+}/Zr^{4+} ions in TiO_6/ZrO_6 octahedra [32]. It is observed that the highest value of remnant polarization ($2P_r$) and saturation polarization ($2P_s$) and lowest value of coercive field were observed for the BSZT35 sample. The higher value of remnant polarization for BSZT35 may be attributed to better crystallinity, uniform distribution of grains, absence of domain wall pinning centers, compositional homogeneity, etc. Another reason

Table 2
Saturation polarization (P_s), remnant polarization ($2P_r$), coercive field ($2E_c$), energy storage density (J) and piezoelectric constant (d_{33}) for BSZT25, BSZT30, BSZT35, BSZT40 and BSZT45.

Sample	$2P_s$ (μC/cm²)	$2P_r$ (μC/cm²)	$2E_c$ (kV/cm)	J (J/cm³)	d_{33} (pC/N)
BSZT25	33.24	6.74	3.77	0.151	386
BSZT30	35.20	7.52	5.30	0.169	364
BSZT35	37.60	16.4	2.93	0.096	392
BSZT40	27.98	6.12	6.38	0.118	340
BSZT45	26.02	4.64	4.66	0.128	332

Please cite this article as: A. Jain, et al., Influence of milling duration on microstructural, electrical, ferroelectric and piezoelectric properties of $Ba_{0.9}Sr_{0.1}Zr_{0.04}Ti_{0.96}O_3$ ceramic, Ceramics International (2016), http://dx.doi.org/10.1016/j.ceramint.2016.09.018

being that the BSZT35 exhibits a relatively lower density of defects with an optimum grain size so that it is inducing strong internal stress which is resulting in the increased degree of domain orientation [33]. The slim ferroelectric loop of BSZT indicates the presence of diffuse phase transition which agrees well with the observed dielectric results as described earlier [34].

Low coercive field ($2E_c$) of the samples suggests that the BSZT samples are ferroelectrically soft and very low electric field is sufficient to cause the switching of domains. It is a well-acclaimed fact that ferroelectric properties of materials are affected by their crystal phase, composition, microstructure, lattice defects and imperfections like oxygen vacancies [35]. Oxygen vacancies may disturb the domain wall motion by screening of the polarization charge. Also, the random field in the surrounding of dipolar defects can considerably reduce the activation barrier needed for the nucleation of ferroelectric domains, resulting in a lower value of E_c [36,37]. It can be observed that the coercive field increases gradually with decrease in grain size except for BSZT35 which shows higher remnant polarization and lower coercive field. In ferroelectric materials, for switching ferroelectric domains energy barrier must be broken and energy barrier increase as the grain size decreases. Therefore, the reversal polarization process of a ferroelectric domain is much easier inside a large grain compared to small grains [38].

The energy storage density of linear and non-linear dielectric materials can be measured by the discharged energy density under the application of an externally applied electric field which is represented by the integral function [39]:

$$J = \int EdP \tag{2}$$

where J represents the energy density, E is the applied electric field and P is the polarization or displacement charge. Eq. (2) have been used to evaluate the discharged energy density of the synthesized specimens and is listed in Table 2. It has been reported that the maximum energy storage density is not found in high dielectric constant materials instead, it is found in those materials which have intermediate dielectric constant and high breakdown voltage [40]. In the present study, discharge energy density of all the samples were obtained under ~40 kV/cm. A relatively slim ferroelectric loop with lower coercive field and remnant polarization is highly desired for high energy storage density [41,42]. It has been found that BSZT30 possesses the highest energy storage density which is due to high remnant polarization and coercive field compared to other samples.

3.5. Piezoelectric studies

The electromechanical response as a function of milling duration for the whole series of samples is measured. Fig. 6 shows the variation of piezoelectric constant (d_{33}), piezoelectric voltage coefficient (g_{33}) and electrostrictive coefficient (Q_{11}) as a function of milling duration. Electrical poling is a process in which on the application of an external electric field, materials with randomly distributed dipoles become polarized in the direction of the applied electric field [43]. Poling is crucial for any polycrystalline piezoelectric material for its enhanced piezoelectric properties. Also optimized poling conditions such as poling voltage, poling time and poling temperature plays a vital role in enhancing the piezoelectric properties of any material. Poling at appropriate temperature helps in charge carrier accumulation around the grain boundaries introducing an internal bias field which can increase the piezoelectric response of the poled materials [44,45]. In the present work, the samples were poled for 2 h at E~1 kV/mm at a poling temperature of T_P~85 °C, exhibited an optimum piezoelectric behavior. The magnitude of longitudinal piezoelectric

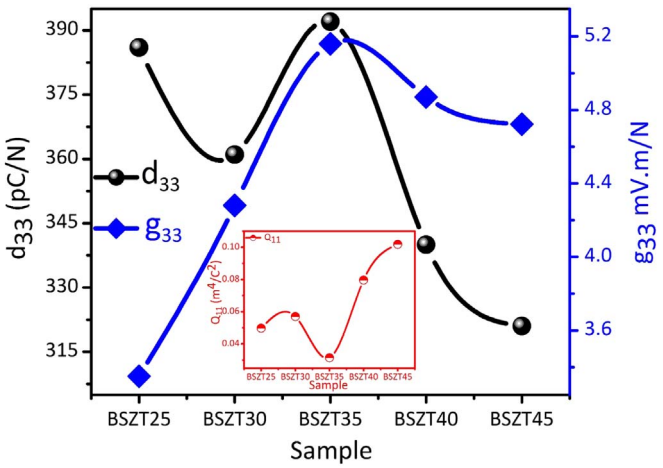


Fig. 6. Variation of piezoelectric constant (d_{33}), piezoelectric voltage coefficient (g_{33}) and electrostrictive coefficient (Q_{11}) (inset) as a function of milling duration.

constant (d_{33}) is observed to be maximum for BSZT35 and decreases on further increasing the milling duration. The d_{33} values of all the five samples are listed in Table 2. It is observed that BSZT25 have also shown a higher value of piezoelectric constant possibly because both density and grain size have an important effect on the piezoelectric properties of any ceramic material [46]. Moreover, according to thermodynamic theory of ferroelectricity, the piezoelectric constant is directly proportional to the dielectric permittivity and remnant polarization of the material and can be expressed by the relation [43]:

$$d_{33}=2Q_{11}P_r\varepsilon_{33} \tag{3}$$

where Q_{11} denotes the electrostrictive coefficient and ε_{33} is the dielectric permittivity of the system. Hence, it is obvious that for any piezoelectric material with high remnant polarization and dielectric permittivity will have high piezoelectric constant. Hence, considering the effect of grain size, density, dielectric constant and remnant polarization samples BSZT40 and BSZT45 were found to have the least value of piezoelectric constant. The g_{33} value can be calculated by dividing the piezoelectric constant (d_{33}) of the material by its permittivity, ε. In the present study, a maximum piezoelectric voltage constant, g_{33}~5.163 mV m/N is obtained for BSZT35 which is ascribed to higher piezoelectric constant (d_{33}) of the material. Finally, it can be concluded that BSZT35 possesses the optimum piezoelectric and ferroelectric properties among the five synthesized samples. Moreover, the piezoelectric coefficients, d_{33} and g_{33} are comparable to many lead-based ceramics reported in the literature [47,48].

4. Conclusion

In this investigation, a series of $Ba_{0.9}Sr_{0.1}Zr_{0.04}Ti_{0.96}O_3$ samples were synthesized using mechano-chemical activation technique with the aim of studying the effect of milling duration. The X-ray diffraction patterns and Rietveld refinement confirms a tetragonal phase with *P*4*mm* (99) space group for all the synthesized samples. There was no significant change in phase and crystal structure of the samples with increasing milling duration. The SEM images show that the grain size decreases with an increase in milling duration up to 40 h and then it shows no further remarkable change in grain size. The sample BSZT25 shows the highest dielectric constant, however, BSZT30 and BSZT35 exhibits optimal high dielectric constant combined with low dielectric loss compared to other three samples. The phase transition diffusivity

Please cite this article as: A. Jain, et al., Influence of milling duration on microstructural, electrical, ferroelectric and piezoelectric properties of $Ba_{0.9}Sr_{0.1}Zr_{0.04}Ti_{0.96}O_3$ ceramic, Ceramics International (2016), http://dx.doi.org/10.1016/j.ceramint.2016.09.018

increases with increasing milling duration. *P–E* hysteresis loops showed an increase in remnant polarization with an increase in milling duration up to 35 h and on further increasing the milling duration the remnant polarization decreases. The optimized polling conditions for BSZT ceramics yields high piezoelectric charge coefficient, d_{33}∼392 pC/N and an optimal value of piezoelectric voltage constant, g_{33}∼5.163 mV m/N for BSZT35. It can be concluded that BSZT35 possess the overall superior properties among the five synthesized samples and can proves to be a potential material for high power pulse capacitors.

Acknowledgements

Authors are thankful for the support of DST-SERB (Grant no. PS/039/2011), India to carry out this research work.

References

[1] D. Gulwade, P. Gopalan, Dielectric properties of A-and B-site doped $BaTiO_3$: effect of La and Ga, Phys. B Condens. Matter 404 (2009) 1799–1805.
[2] N.W. Thomas, A new framework for understanding relaxor ferroelectrics, J. Phys. Chem. Solids 51 (1990) 1419–1431.
[3] M. Aghayan, A. Khorsand Zak, M. Behdani, A. Manaf Hashim, Sol–gel combustion synthesis of Zr-doped $BaTiO_3$ nanopowders and ceramics: dielectric and ferroelectric studies, Ceram. Int. 40 (2014) 16141–16146.
[4] A. Jain, A.K. Panwar, A.K. Jha, Structural, dielectric and ferroelectric studies of $Ba_{1-x}Sr_xTiO_3$ ceramics prepared by mechanochemical activation technique, J. Mater. Sci. Mater. Electron. 27 (2016) 9911–9919.
[5] B. Stojanovic, C. Foschini, V. Pavlovic, V. Pavlovic, V. Pejovic, J.A. Varela, Barium titanate screen-printed thick films, Ceram. Int. 28 (2002) 293–298.
[6] Y. Li, R. Wang, X. Ma, Z. Li, R. Sang, Y. Qu, Dielectric behavior of samarium-doped $BaZr_{0.2}Ti_{0.8}O_3$ ceramics, Mater. Res. Bull. 49 (2014) 601–607.
[7] M. Ganguly, S. Rout, C. Ahn, I. Kim, M. Kar, Structural, electrical and optical properties of $Ba(Ti_{1-x}Yb_{4x/3})O_3$ ceramics, Ceram. Int. 39 (2013) 9511–9524.
[8] F. Zimmermann, M. Voigts, W. Menesklou, E. Ivers-Tiffée, $Ba_{0.6}Sr_{0.4}TiO_3$ and $BaZr_{0.3}Ti_{0.7}O_3$ thick films as tunable microwave dielectrics, J. Eur. Ceram. Soc. 24 (2004) 1729–1733.
[9] N. Sawangwan, J. Barrel, K. Mackenzie, T. Tunkasiri, The effect of Zr content on electrical properties of $Ba(Ti_{1-x}Zr_x)O_3$ ceramics, Appl. Phys. A 90 (2008) 723–727.
[10] N. Maikhuri, A.K. Panwar, A. Jha, Investigation of A-and B-site Fe substituted $BaTiO_3$ ceramics, J. Appl. Phys. 113 (2013) 17D915.
[11] H. Tian, D. Wang, J. Qi, Y. Wang, H. Chan, C. Choy, Synthesis of BaZr 0.75 Hf 0.25 O_3 by a solid-state reaction technique and characterizations of dielectric properties, J. Alloy. Compd. 402 (2005) 251–255.
[12] J.F. Ihlefeld, W.J. Borland, J.-P. Maria, Dielectric and microstructural properties of barium titanate hafnate thin films, Thin Solid Films 516 (2008) 3162–3166.
[13] S. Sen, R.N. Choudhary, Structural, dielectric and electrical properties of Ca modified $BaSn_{0.15}Ti_{0.85}$ O_3 ceramics, J. Mater. Sci. 40 (2005) 5457–5462.
[14] K. Watanabe, H. Ohsato, H. Kishi, Y. Okino, N. Kohzu, Y. Iguchi, T. Okuda, Solubility of La–Mg and La–Al in $BaTiO_3$, Solid State Ion. 108 (1998) 129–135.
[15] M. Kumar, A. Garg, R. Kumar, M.C. Bhatnagar, Structural, dielectric and ferroelectric study of $Ba_{0.9}Sr_{0.1}Zr_xTi_{1-x}O_3$ ceramics prepared by the sol–gel method, Phys. B Condens. Matter 403 (2008) 1819–1823.
[16] A. Jain, R. Saroha, M. Pastor, A.K. Jha, A.K. Panwar, Effect of sintering duration on structural and electrical properties of $Ba_{0.9}Sr_{0.1}Ti_{0.96}Zr_{0.04}O_3$ solid solution, Curr. Appl. Phys. 16 (2016) 859–866.
[17] R. Rani, S. Singh, J. Juneja, K. Raina, C. Prakash, Dielectric properties of Zr substituted BST ceramics, Ceram. Int. 37 (2011) 3755–3758.
[18] Y. Zhou, Y. Yang, F. Huang, J. Ren, S. Yuan, G. Chen, Characterization of new tellurite glasses and crystalline phases in the TeO_2–PbO–Bi_2O_3–B_2O_3 system, J. Non-Cryst. Solids 386 (2014) 90–94.
[19] P.A. Jha, A. Jha, Effect of sintering temperature on the grain growth and electrical properties of barium zirconate titanate ferroelectric ceramics, J. Mater. Sci. Mater. Electron. 24 (2013) 1511–1518.
[20] B. Antic, A. Kremenovic, N. Jovic, M. Pavlovic, C. Jovalekic, A. Nikolic, G. Goya, C. Weidenthaler, Magnetization enhancement and cation valences in non-stoichiometric $(Mn,Fe)_{3-\delta}O_4$ nanoparticles, J. Appl. Phys. 111 (2012) 074309.
[21] X. Chao, J. Wang, P. Liang, T. Zhang, L. Wei, Z. Yang, Phase transition and improved electrical performance of $Ba_{0.85}Ca_{0.15}Zr_{0.1}Ti_{0.9}O_3$–$Ca_{0.28}Ba_{0.72}Nb_2O_6$ ceramics with high Curie temperature, Mater. Des. 89 (2016) 465–469.
[22] Y. Wang, Y. Lu, M. Wu, D. Wang, Y. Li, Phase structure and enhanced piezoelectric properties of lead-free ceramics $(1-x)(K_{0.48}Na_{0.52})NbO_3$–$(x/5.15)K_{2.9}Li_{1.95}Nb_{5.15}O_{15.3}$ with high Curie temperature, Int. J. Appl. Ceram. Technol. 9 (2012) 221–227.
[23] N. Nanakorn, P. Jalupoom, N. Vaneesorn, A. Thanaboonsombut, Dielectric and ferroelectric properties of $Ba(Zr_xTi_{1-x})O_3$ ceramics, Ceram. Int. 34 (2008) 779–782.
[24] S. Rajan, P.M. Gazzali, G. Chandrasekaran, Electrical and magnetic phase transition studies of Fe and Mn co-doped $BaTiO_3$, J. Alloy. Compd. 656 (2016) 98–109.
[25] P. Mishra, P. Kumar, Effect of sintering temperature on dielectric, piezoelectric and ferroelectric properties of BZT–BCT 50/50 ceramics, J. Alloy. Compd. 545 (2012) 210–215.
[26] A.K. Singh, T. Goel, R. Mendiratta, O. Thakur, C. Prakash, Dielectric properties of Mn-substituted Ni-Zn ferrites, J. Appl. Phys. 91 (2002) 6626–6629.
[27] P. Mishra, P. Kumar, Enhanced dielectric and piezoelectric properties of BZT–BCT system near MPB, Ceram. Int. 40 (2014) 14149–14157.
[28] N. Adhlakha, K. Yadav, R. Singh, Effect of $BaTiO_3$ addition on structural, multiferroic and magneto-dielectric properties of $0.3CoFe_2O_4-0.7$ $BiFeO_3$ ceramics, Smart Mater. Struct. 23 (2014) 105024.
[29] C. Ang, Z. Yu, L. Cross, Oxygen-vacancy-related low-frequency dielectric relaxation and electrical conduction in Bi:$SrTiO_3$, Phys. Rev. B Condens. Matter 62 (2000) 228.
[30] D. Maurya, A. Kumar, V. Petkov, J.E. Mahaney, R.S. Katiyar, S. Priya, Local structure and piezoelectric instability in lead-free $(1-x)BaTiO_{3-x}A(Cu_{1/3}Nb_{2/3})O_3$ (A=Sr, Ca, Ba) solid solutions, RSC Adv. 4 (2014) 1283–1292.
[31] Z. Xiao-Li, C. Xiang-Ming, Ferroelectric transition and Curie—Weiss behavior in some filled tungsten bronze ceramics, Chin. Phys. Lett. 31 (2014) 015201.
[32] G. Laurita, K. Page, S. Suzuki, R. Seshadri, Average and local structure of the Pb-free ferroelectric perovskites (Sr,Sn)TiO_3 and (Ba, Ca, SN)TiO_3, Phys. Rev. B Condens. Matter 92 (2015) 214109.
[33] L. Jin, F. Li, S. Zhang, Decoding the fingerprint of ferroelectric loops: comprehension of the material properties and structures, J. Am. Ceram. Soc. 97 (2014) 1–27.
[34] X. Chen, X. Dong, G. Wang, F. Cao, Y. Wang, Doped Pb (Zr, Sn, Ti)O_3 slim-loop ferroelectric ceramics for high-power pulse capacitors application, Ferroelectrics 363 (2008) 56–63.
[35] T. Friessnegg, S. Aggarwal, R. Ramesh, B. Nielsen, E. Poindexter, D. Keeble, Vacancy formation in (Pb, La)(Zr, Ti)O_3 capacitors with oxygen deficiency and the effect on voltage offset, Appl. Phys. Lett. 77 (2000) 127–129.
[36] Z. Zhao, V. Buscaglia, M. Viviani, M.T. Buscaglia, L. Mitoseriu, A. Testino, M. Nygren, M. Johnsson, P. Nanni, Grain-size effects on the ferroelectric behavior of dense nanocrystalline $BaTiO_3$ ceramics, Phys. Rev. B Condens. Matter 70 (2004) 024107.
[37] D. Viehland, Y.-H. Chen, Random-field model for ferroelectric domain dynamics and polarization reversal, J. Appl. Phys. 88 (2000) 6696–6707.
[38] C.-C. Leu, C.-Y. Chen, C.-H. Chien, M.-N. Chang, F.-Y. Hsu, C.-T. Hu, Domain structure study of $SrBi_2Ta_2O_9$ ferroelectric thin films by scanning capacitance microscopy, Appl. Phys. Lett. 82 (2003) 3493.
[39] T. Wang, X. Wei, Q. Hu, L. Jin, Z. Xu, Y. Feng, Effects of $ZnNb_2O_6$ addition on $BaTiO_3$ ceramics for energy storage, Mater. Sci. Eng. B 178 (2013) 1081–1086.
[40] G.R. Love, Energy storage in ceramic dielectrics, J. Am. Ceram. Soc. 73 (1990) 323–328.
[41] T. Wang, L. Jin, Y. Tian, L. Shu, Q. Hu, X. Wei, Microstructure and ferroelectric properties of Nb_2O_5-modified $BiFeO_3$-$BaTiO_3$ lead-free ceramics for energy storage, Mater. Lett. 137 (2014) 79–81.
[42] P. Wawrzała, J. Korzekwa, Charge–discharge properties of PLZT x/90/10 ceramics, Ferroelectrics 446 (2013) 91–101.
[43] J.P. Praveen, T. Karthik, A. James, E. Chandrakala, S. Asthana, D. Das, Effect of poling process on piezoelectric properties of sol–gel derived BZT–BCT ceramics, J. Eur. Ceram. Soc. 35 (2015) 1785–1798.
[44] S. Su, R. Zuo, S. Lu, Z. Xu, X. Wang, L. Li, Poling dependence and stability of piezoelectric properties of $Ba(Zr_{0.2}Ti_{0.8})O_3$-$(Ba_{0.7}Ca_{0.3})TiO_3$ ceramics with huge piezoelectric coefficients, Curr. Appl. Phys. 11 (2011) S120–S123.
[45] J. Wu, D. Xiao, W. Wu, Q. Chen, J. Zhu, Z. Yang, J. Wang, Composition and poling condition-induced electrical behavior of $(Ba_{0.85}Ca_{0.15})(Ti_{1-x}Zr_x)O_3$ lead-free piezoelectric ceramics, J. Eur. Ceram. Soc. 32 (2012) 891–898.
[46] M. Zhu, L. Liu, Y. Hou, H. Wang, H. Yan, Microstructure and electrical properties of MnO-doped $(Na_{0.5}Bi_{0.5})_{0.92}Ba_{0.08}TiO_3$ lead-free piezoceramics, J. Am. Ceram. Soc. 90 (2007) 120–124.
[47] Z. Xing, H. Wang, B. Xu, G. Ma, Y. Huang, J. Kang, L. Zhu, Structural integrity and ferroelectric–piezoelectric properties of $PbTiO_3$ coating prepared via supersonic plasma spraying, Mater. Des. 62 (2014) 57–63.
[48] T. Li, X. Long, Piezo-/dielectric properties of perovskite-structure high-temperature relaxor ferroelectrics: The $Pb(Lu_{1/2}Nb_{1/2})O_3$–$Pb(Zn_{1/3}Nb_{2/3})O_3$–$PbTiO_3$ ternary ceramics, Mater. Res. Bull. 51 (2014) 251–257.

Please cite this article as: A. Jain, et al., Influence of milling duration on microstructural, electrical, ferroelectric and piezoelectric properties of $Ba_{0.9}Sr_{0.1}Zr_{0.04}Ti_{0.96}O_3$ ceramic, Ceramics International (2016), http://dx.doi.org/10.1016/j.ceramint.2016.09.018

ARTICLE IN PRESS
MR-12118; No of Pages 7
Microelectronics Reliability xxx (2016) xxx–xxx
Contents lists available at ScienceDirect
Microelectronics Reliability
journal homepage: www.elsevier.com/locate/mr

Investigation of temperature variations on analog/RF and linearity performance of stacked gate GEWE-SiNW MOSFET for improved device reliability

N. Gupta, R. Chaujar *

Microelectronics Research Lab, Department of Engineering Physics, Delhi Technological University, Delhi 110042, India

ARTICLE INFO

Article history:
Received 2 July 2016
Accepted 8 July 2016
Available online xxxx

Keywords:
Stacked gate
Silicon nanowire (SiNW)
Analog
RF
Linearity
GEWE
Ambient temperature
MOSFET

ABSTRACT

In this paper, reliability issues of Stacked Gate (SG)-Gate Electrode Workfunction Engineered (GEWE)-Silicon Nanowire (SiNW) MOSFET is examined over a wide range of ambient temperatures (200–600 K) and results so obtained are simultaneously compared with conventional SiNW and GEWE-SiNW MOSFET using 3D-technology computer aided design quantum simulation. The results indicate that two temperature compensation points (TCP) are obtained: one for drain current (I_{ds}) and other for cut-off frequency (f_T) where device Figure Of Merits (FOMs) become independent of temperature, and it is found at 0.65 V in SG-GEWE-SiNW in comparison to other devices, hence will open opportunities for wide range of temperature applications. Furthermore, significant improvement in Analog/RF performance of SG-GWEW-SiNW is observed in terms of I_{on}/I_{off}, Subthreshold Swing (SS), device efficiency, f_T, noise conductance and noise figure as temperature reduces. It is also observed that at low temperature SG-GEWE-SiNW unveils highly stable linearity performance owing to reduced distortions. These results explain the improved reliability of SG-GEWE-SiNW at low temperatures over GEWE-SiNW MOSFET.

© 2016 Elsevier Ltd. All rights reserved.

1. Introduction

CMOS devices are extensively used in the field of satellite communications, military, medical equipment, automobile, nuclear sectors, and wireless/mobile communications. For these applications and the demand of nanoscale transistor, it is important to investigate the device behavior at a wide range of temperatures [1]. Also, it has been demonstrated that the performance of MOS devices significantly improves when operating at low temperatures in terms of improved carrier mobilities, on-currents, gain, sub-threshold slope, cut-off frequency, short-channel effects and noise performance [2,3]. The unwanted flow of high leakage current through the junction and the presence of latch-up put a limit on the use of bulk MOS devices at high temperatures. Several technologies have been reported in the literature as an option for both low and high-temperature operations. Some of them are Silicon on Insulator (SOI) [4], Recessed Channel [5], III–V semiconductors [6], Nanowire transistors [7], etc. Among them, SiNW emerged as most favorable in electronic devices due to the fact that its concentration, dopant type can be changed during synthesis. Also, its mobility is higher than bulk silicon due to stronger 1D quantum confinement. The body thickness of the nanowire can readily be reduced to a few nm in size that is the major challenge to achieve using bulk silicon. Also, since hot carrier degradation is a major concern for short channel MOSFETs [8], several engineering schemes are reported in literature such as gate metal workfunction engineering [9], drain engineering and channel engineering to overcome this degradation. Moreover, the high-k gate dielectric is required for suppressing the leakage current with scaling of gate oxide. The high-k gate stack also improves Short Channel Effects (SCEs) and increases I_{on}/I_{off} ratio in sub-100 nm regime. Therefore, a novel device is proposed in which stacked gate architecture is implemented on Gate Electrode Workfunction Engineered (GEWE) Silicon Nanowire MOSFET. In this work, for the first time performance and reliability issues of SG-GEWE-SiNW MOSFET are examined in terms of Analog, RF/Noise and Linearity FOMs at different temperatures (200–600 K) with an aim to analyze the temperature at which the device is more reliable for analog and RF applications. The results so obtained are simultaneously compared with GEWE-SiNW and SiNW MOSFET. Section 2 explains the 2D cross-sectional view of three different device structures including all the necessary boundary conditions. In Section 3, all the default simulation models are described along with the calibration of simulation models with experimental results. Section 4 contains the results obtained by device variation at 200–600 K and conclusions are drawn in Section 5.

2. Device structure and its description

Fig. 1(a) shows the simulated 3-D device structure of SG-GEWE-SiNW MOSFET and its 2-D cross-sectional view along with GEWE-SiNW and SiNW MOSFET are shown in Fig. 1(b–c). The detailed

* Corresponding author.
E-mail addresses: nehagupta@dtu.ac.in (N. Gupta), rishu.phy@dce.edu (R. Chaujar).

http://dx.doi.org/10.1016/j.microrel.2016.07.095
0026-2714/© 2016 Elsevier Ltd. All rights reserved.

Please cite this article as: N. Gupta, R. Chaujar, Investigation of temperature variations on analog/RF and linearity performance of stacked gate GEWE-SiNW MOSFET for improved devic..., Microelectronics Reliability (2016), http://dx.doi.org/10.1016/j.microrel.2016.07.095

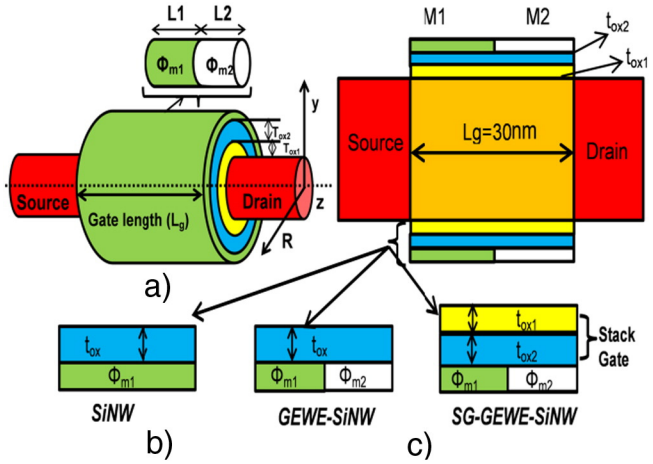


Fig. 1. (a) Simulated device structure of SG-GEWE-SiNW MOSFET, (b–c) 2-D schematic view of SiNW, GEWE-SiNW and SG-GEWE-SiNW MOSFET.

descriptions of all the three device structures are listed in Table 1. All simulations have been performed using ATLAS and DEVEDIT 3D device simulator.

With GEWE (workfunction transition) scheme, there is a significant reduction in the SCEs, current driving capability improves due to step potential which is due to two dissimilar metal gates, reduced electric field at the drain end thus providing hot-carrier reliability [10]. Further, we have already shown that integration of GEWE scheme onto GAA-SiNW MOSFET improves device efficiency, enhanced on-current, reduces short channel effects [11,12]. Moreover, Table 2 lists all the boundary conditions associated with the device structure.

3. Simulation methodology

All simulations have been performed using the ATLAS device simulator [13]. The physical models used during simulations are shown in Table 3. Moreover, the quantum confinement in the sub-nm scaled device may not be negligible [14] because the inversion layer thickness in the conducting silicon nanowire channel is comparable to the nanowire dimension. Thus, the quantization effect is also taken care of in the simulation. To incorporate all non-local effects, we have adopted the quantum mechanical models which are more accurate than drift-diffusion method. The Bohr Quantum Potential (BQP) Model [15] with alpha (α) = 0.5 and gamma (γ) = 1.2 was used to taking quantum mechanical effects into consideration. This model introduces a position dependent quantum potential, Q, which is added to the Potential Energy of a given carrier type. This quantum potential is derived using the Bohm interpretation of quantum mechanics [16] and is described below:

$$Q_{eff} = \frac{-\hbar^2}{2}\gamma\nabla\frac{\left[M^{-1}\nabla(n^{\alpha})\right]}{n^{\alpha}} \quad (1)$$

where M^{-1} is the inverse effective mass tensor, α and γ are two adjustable parameters, n is the electron (or hole) density and h is a Planck's constant. Additionally, numerical methods such as BICGST (bi-conjugate gradient stabilized) have been considered to obtain the solutions with improved convergence in 3D device structure [13]. Default simulator coefficients for all parameters have been employed. To fairly analyze the device performances, all the three devices are optimized to have the same threshold voltage, i.e. 0.4 V by changing channel doping. The calibration of model parameters used in simulation has been performed according to the experimental results [17] and closed proximity of simulated results with the experimental results as shown in Fig. 2 validates the choice of parameters invoked during simulation.

4. Results and discussion

4.1. Analog performance

In this sub-section, the analog performance of all three device structures is studied under different temperatures (200 K–600 K) with an aim to analyze the reliability issues in terms of analog FOMs such as on-current, device efficiency, switching ratio, Subthreshold swing (SS) and Threshold Voltage (V_{th}). Fig. 3(a) shows the transfer characteristics of SiNW, GEWE-SiNW and GS-GEWE-SiNW MOSFET for different temperatures. With the increase in temperature, the drain current rises but at a particular bias point, current starts decreasing with increase in temperature. This point is called Zero Crossing Point (ZCP) or Temperature Compensation Point (TCP). At this point, the effect of temperature is cancelled by two main controlling terms i.e. channel mobility (decreases I_D) and threshold voltage (increases I_D), since the temperature dependency of the drain current is influenced by V_{th} as given by $I_D \approx \mu_{eff}(T)\,[V_{gs} - V_{th}(T)]$. The TCP is desirable for wide temperature IC applications where the V—I characteristics show little or no variation with respect to temperature. With the increase in temperature, the on-current decreases due to degradation in mobility of carriers owing to more scattering of carriers. However, on-current of SG-GEWE-SiNW is comparatively high in comparison to GEWE-SiNW due to the incorporation of thin layer of HfO_2, which improves current driving capability of the device. The switching ratio is an important parameter for digital and analog applications and it is clearly evident from Fig. 3(b) that with an increase in temperature switching ratio degrades in an exponential manner for all three devices since phonon scattering is dominant at high temperature which degrades off-current. SG-GEWE-SiNW shows better switching performance in comparison to GEWE-SiNW due to lowering of tunneling carriers owing to gate stack engineering. Fig. 3(c) shows the device efficiency as a function of drain current for different temperatures. It is observed that device efficiency degrades in all three devices as temperature increases due to enhanced drain current in the linear region.

Fig. 4(a) indicates that the threshold voltage (V_{th}) degrades with an increase in temperature due to shift in Fermi level and band-gap energy. In general, MOSFET's I—V characteristics are proportional to the square of the overdrive voltage. Hence, a small change in V_{th} causes a significant

Table 1
Default design parameters used in the analysis.

Design parameters	SiNW	GEWE-SiNW	SG-GEWE-SiNW
Channel length (L_g)	30 nm	30 nm	30 nm
Substrate doping (N_A)	1×10^{16} cm^{-3}	1×10^{16} cm^{-3}	1×10^{16} cm^{-3}
Radius of nanowire (R)	5 nm	5 nm	5 nm
Source/drain doping (N_D^+)	5×10^{19} cm^{-3}	5×10^{19} cm^{-3}	5×10^{19} cm^{-3}
Effective oxide thickness (t_{ox})	$t_{ox} = 1.5$ nm	$t_{ox} = 1.5$ nm	$t_{ox} = 1.5$ nm $t_{ox1} = 1.2$ nm (SiO_2) $t_{ox2} = 1.85$ nm (HfO_2)
Dielectric constant	$k = 3.9$	$k = 3.9$	$k_1 = 3.9$, $k_2 = 24$
Gate metal work function	$\Phi_m = 4.8$ eV	$\Phi_{m1} = 4.8$ eV [Gold] $\Phi_{m2} = 4.4$ eV [Titanium]	$\Phi_{m1} = 4.8$ eV [Gold] $\Phi_{m2} = 4.4$ eV [Titanium]

Please cite this article as: N. Gupta, R. Chaujar, Investigation of temperature variations on analog/RF and linearity performance of stacked gate GEWE-SiNW MOSFET for improved devic..., Microelectronics Reliability (2016), http://dx.doi.org/10.1016/j.microrel.2016.07.095

Table 2
Boundary conditions.

Boundary conditions			
	SiNW	GEW-SiNW	SG-GEWE-SiNW
1. Surface potential			
a) At the interface of tow metals	φ_m	$\varphi_{m1} = \varphi_{m2}$	$\varphi_{m1} = \varphi_{m2}$
b) At source end ($z = 0$)	$\varphi = V_{bi}$	$\varphi = V_{bi}$	$\varphi = V_{bi}$
c) At drain end	$\varphi = V_{bi} + V_{ds}$	$\varphi_D = V_{bi} + V_{ds}$	$\varphi_D = V_{bi} + V_{ds}$
2. Electric field			
a) At the interface of two metals	$E = \frac{\partial \varphi_1(r,z)}{\partial z}$	$\frac{\partial \varphi_1(r,z)}{\partial z} = \frac{\partial \varphi_2(r,z)}{\partial z}$ at $z = L1$	$\frac{\partial \varphi_1(r,z)}{\partial z} = \frac{\partial \varphi_2(r,z)}{\partial z}$ at $z = L1$
b) At the center of cylindrical channel	$\frac{\partial \varphi_1(r,z)}{\partial r} = 0$	$\frac{\partial \varphi_1(r,z)}{\partial r} = 0$	$\frac{\partial \varphi_1(r,z)}{\partial r} = 0$
c) At Si/SiO_2 interface	$\frac{\partial \varphi_1(r,z)}{\partial r} = \frac{q.n_a}{\varepsilon_{si}} = C_{ox}(V_{gs} - V_{FB} - \varphi_s)$ $C_{ox} = \frac{\varepsilon_{SiO_2}}{R.\ln(1+\frac{t_{ox}}{R})}$	$\frac{\partial \varphi_1(r,z)}{\partial r} = \frac{q.n_a}{\varepsilon_{si}} = C_{ox}(V_{gs} - V_{FB1} - \varphi_s)$ $\frac{\partial \varphi_2(r,z)}{\partial r} = \frac{q.n_a}{\varepsilon_{si}} = C_{ox}(V_{gs} - V_{FB2} - \varphi_s)$ $C_{ox} = \frac{\varepsilon_{SiO_2}}{R.\ln(1+\frac{t_{ox}}{R})}$	$\frac{\partial \varphi_1(r,z)}{\partial r} = \frac{q.n_a}{\varepsilon_{si}} = C_{ox}(V_{gs} - V_{FB1} - \varphi_s)$ $\frac{\partial \varphi_2(r,z)}{\partial r} = \frac{q.n_a}{\varepsilon_{si}} = C_{ox}(V_{gs} - V_{FB2} - \varphi_s)$ $C_{ox} = \frac{\varepsilon_{SiO_2}}{R.\ln(1+\frac{t_{eff}}{R})}$ $t_{eff} = t_{SiO_2} + (\frac{\varepsilon_{SiO_2}}{\varepsilon_{high-k}})t_{high-k}$

Where V_{bi} = built in potential, φ_{m1} and φ_{m2} are surface potentials due to metal gates 1 and 2 respectively, V_{FB1} and V_{FB2} are flat band voltage due to metal gates 1 and 2 respectively, R is the radius of nanowire and t_{eff} is the effective oxide thickness of stack gate design.

shift in the output current. Therefore, it is essential to calculate the V_{th} accurately with temperature changes. This change is more prominent at high temperature (600 K) in SG-GEWE-SiNW MOSFET compared to its conventional counterparts. Further, the Subthreshold Swing (SS) is an important parameter for calculating the off-state current. At 200 K, a low sub-threshold swing results in high I_{on}/I_{off} ratio which indicates a faster transition between off and on states compared to 600 K. SS of SG-GEWE-SiNW is 53 mV/decade and 146 mV/decade for 200 K and 600 K respectively in comparison to GEWE-SiNW and SiNW MOSFET as shown in Fig. 4(b). These results show that SG-GEWE-SiNW is more reliable for analog and switching applications, at a lower temperature.

4.2. RF noise performance

In this sub-section, the impact of ambient temperature has been studied on the characteristics such as gate capacitance, cut-off frequency, intrinsic delay, energy delay product, noise conductance and minimum noise figure for SG-GEWE-SiNW MOSFET, GEWE-SiNW and SiNW MOSFET. If a MOSFET is operating in the linear region, both S/D regions are connected to the inversion layer, and C_g which is total gate capacitance is equally partitioned between source/drain i.e., $C_{gd} \approx C_{gs} \approx C_g/2$ where as in the saturation region, $C_{gs} \approx 2/3 \times C_g$ and $C_{gd} \approx 0$. Fig. 4(a) shows the bias dependent intrinsic parasitic gate capacitance (C_g) at different temperatures, and it is observed as temperature decreases, C_g also decreases resulting in device high speed which is desirable for switching and digital applications. Since, the gate capacitance is due to charges present in the inversion region including the depletion charges of source and drain regions. These charge carriers are temperature and bias dependent. C_g is sufficiently lower in the case of SG-GEWE-SiNW due to gate stacking engineering scheme and GEWE scheme which results in the improved screening of conducting channel from drain variations. For evaluating the RF performance of the device, cut-off frequency (f_T) is one of the utmost important parameter. It is a specification for high-speed digital applications and can be defined as follows:

$$f_T = \frac{g_m}{2\pi C_g} \tag{2}$$

where g_m is the transconductance. As is evident from Fig. 5(b), the peak value of f_T enhances in the case of GEWE-SiNW in comparison to SiNW and its value further enhances with the incorporation of GS technology. As the temperature reduces, peak value of f_T enhances. This is due to a reduction in parasitic capacitance as shown in Fig. 5(a) and improvement in current driving capability as shown in Fig. 3(a) at a lower temperature (200 K). Also, TCP in f_T is observed at 0.6 V in the case of GEWE-SiNW MOSFET, which is useful for RF applications operating at low or high temperatures. Intrinsic Delay (τ) is another significant parameter

Table 3
Physical Models.

S·No.	Physical models	Description
1.	*Mobility models*	Lombardi CVT and Constant Low Field Mobility Model
2.	*Recombination model*	Shockley Read Hall (SRH) Recombination is included to incorporate minority recombination effects with carrier lifetime = 1×10^{-7} s.
3.	*Statistics*	Boltzmann Transport Model The use of Boltzmann statistics is normally justified in semiconductor device theory, but Fermi-Dirac statistics are necessary to account for certain properties of very highly doped (degenerate) materials.
4.	*Energy transport model*	Hydrodynamic Model is used as it includes all nonlocal effects and is more accurate than the drift-diffusion method. Drift Diffusion Model shows shortcomings as channel length scales down to 50 nm.
5.	*Quantum mechanical model*	Quantum Mechanical Model plays an important role on determining the performance of surrounding gate MOSFET In this paper we take into account QMEs.

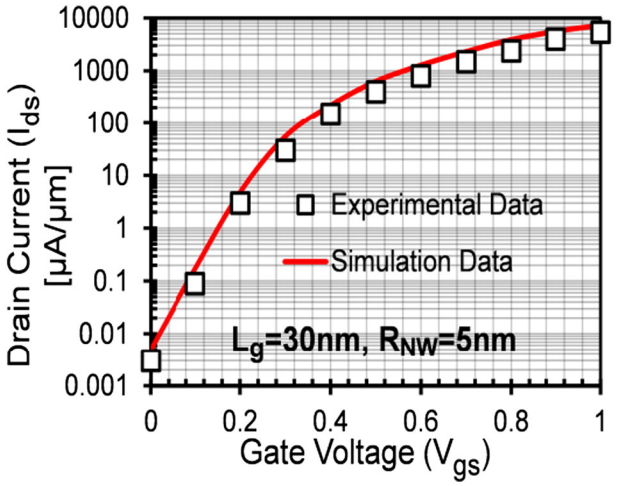


Fig. 2. Calibration of simulation model with experimental result to validate our simulation models [17].

Please cite this article as: N. Gupta, R. Chaujar, Investigation of temperature variations on analog/RF and linearity performance of stacked gate GEWE-SiNW MOSFET for improved devic..., Microelectronics Reliability (2016), http://dx.doi.org/10.1016/j.microrel.2016.07.095

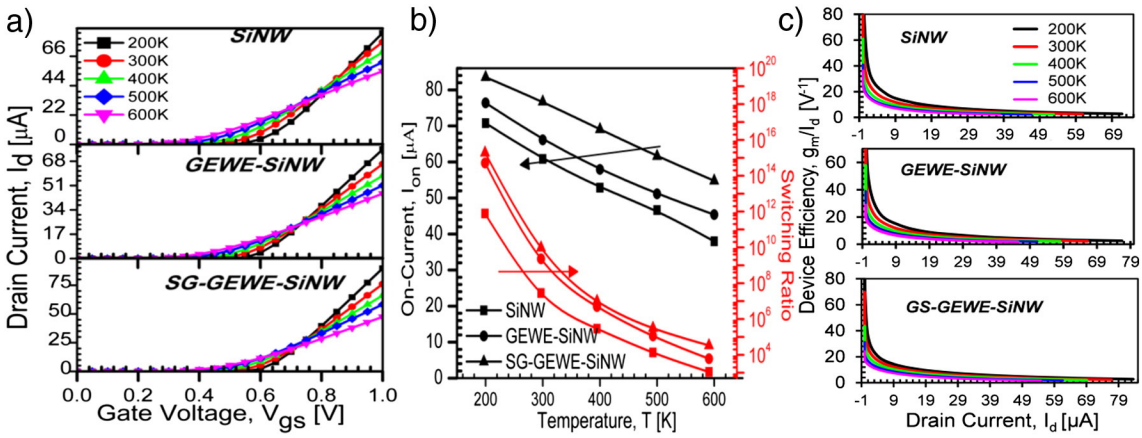


Fig. 3. (a) Transfer characteristics, (b) drain transconductance and (c) device efficiency of SiNW, GEWE-SiNW and GS-GEWE-SiNW MOSFET for different temperatures.

defined as a measure of switching performance of the device and is expressed as:

$$\tau = \frac{C_g . V_{ds}}{I_{ON}} \tag{3}$$

where V_{ds} is the bias voltage applied to drain and I_{on} is the on-current. Fig. 6(a) reveals as temperature increases; delay degrades due to degradation in parasitic capacitance with an increase in temperature as shown in Fig. 5(a). It is also observed that there is a noticeable reduction in intrinsic delay of SG-GEWE-SiNW MOSFET than its conventional counterpart due to the incorporation of HfO_2 as a gate stack which lowers the effective oxide thickness (EOT), reduces leakage current and thus enhances the on-current as is evident from Fig. 3(b), in addition reduction in parasitic capacitances also leads to a considerable reduction of intrinsic delay.

Apart from these FOMs, Energy Delay Product (EDP) is a valuable FOM as far as circuit applications are concerned. The EDP is a measure of energy and is defined by the product of the average energy (E_{ave}) and the gate delay (τ). It calculates the energy consumed per switching event (such as in logic families). EDP improves at lower values of temperature due to a reduction in intrinsic delay and parasitic gate

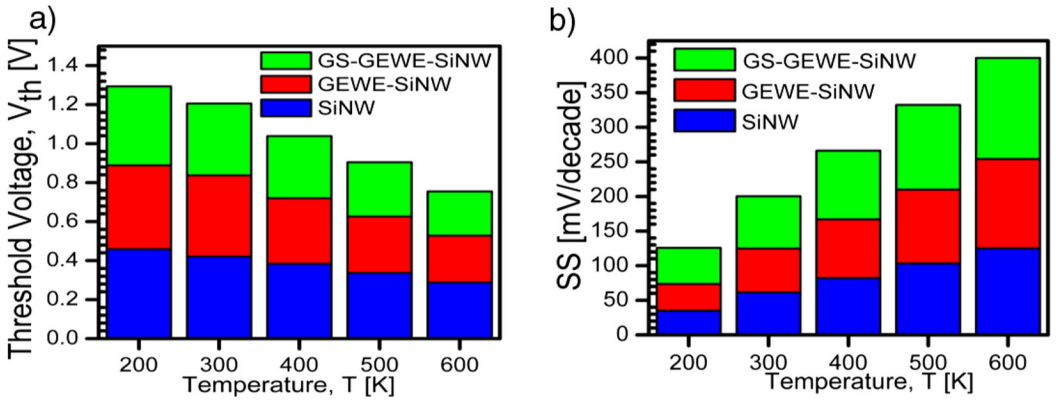


Fig. 4. (a) Threshold voltage, (b) subthreshold swing and of SiNW, GEWE-SiNW and GS-GEWE-SiNW MOSFET.

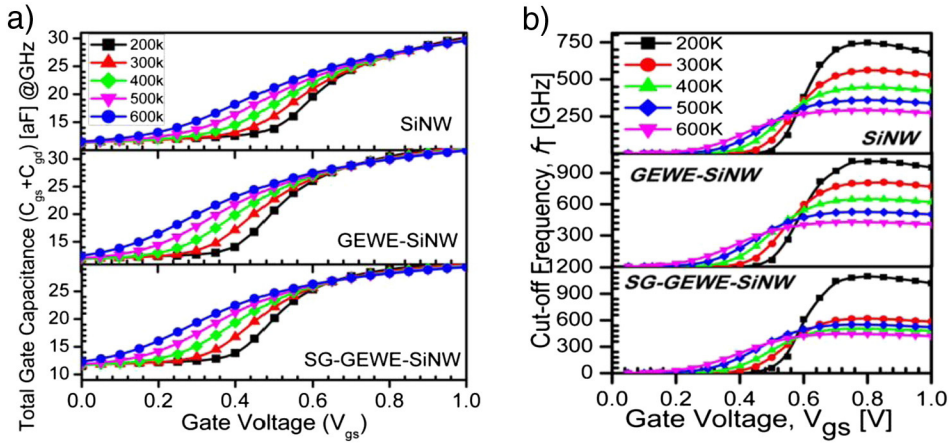


Fig. 5. (a) Total gate capacitance (C_g) and (b) cut-off frequency (f_T) of SiNW, GEWE-SiNW and GS-GEWE-SiNW MOSFET at $V_{ds} = 0.5$ V.

Please cite this article as: N. Gupta, R. Chaujar, Investigation of temperature variations on analog/RF and linearity performance of stacked gate GEWE-SiNW MOSFET for improved devic..., Microelectronics Reliability (2016), http://dx.doi.org/10.1016/j.microrel.2016.07.095

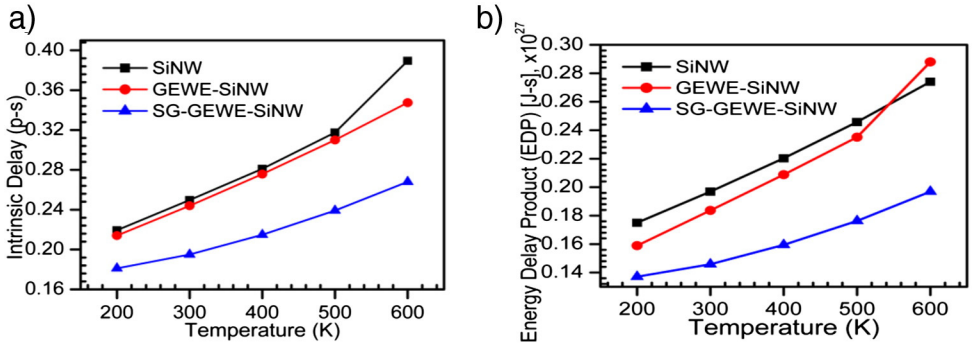


Fig. 6. (a) Intrinsic delay and (b) energy delay product (EDP) of SiNW, GEWE-SiNW and GS-GEWE-SiNW MOSFET at $V_{ds} = 0.5$ V.

capacitance (C_g) as evident from Fig. 6(b). Thus, SG-GEWE-SiNW MOSFET emerged as a promising device for RF applications such as in microwave/wireless working at low temperature in comparison to a higher temperature. Moreover, Noise FOMs such as Minimum noise figure (NF_{MIN}) and Noise Conductance (NC) are of utmost important for the designing of CMOS RF circuits at high frequency. Noise figure is an assessment of deterioration of signal to noise ratio caused by a component in RF signal chains. It is used to evaluate the performance of an amplifier or a radio receiver, with lower values specifying better performance. NC is used to estimate the power spectral density of noise current generators and low noise conductance is required in RF amplifiers and LNAs. As ambient temperature increases, both the NFmin and NC degrade for all three devices as shown in Fig. 7(a–b) due to high phonon scattering and the effect of temperature on noise FOMs is less observed in the case of SG-GEWE-SiNW, and its magnitude is comparatively low in comparison to other devices. Thus, the proposed design (SG-GEWE-SiNW) is more reliable and more thermally stable compared to SiNW at low temperature.

4.3. Linearity and harmonic distortions

Non-linearity of MOS amplifiers is generally from transconductance higher order harmonics term (g_{m3}) that may interfere with fundamental frequency (ω_0) and causes non-linearity. It is a major reliability concern at a device level. The lower the amplitude of g_{m3} the higher the linearity of the device. Fig. 8(a) shows that the amplitude of g_{m3} reduces as temperature increases, and SG-GEWE-SiNW is more linear in comparison to other conventional devices owing to reduced off (leakage) current due to the amalgamation of HfO_2 layer over SiO_2, which results in enhanced on-current and thus lowering of g_{m3}. VIP3 represents

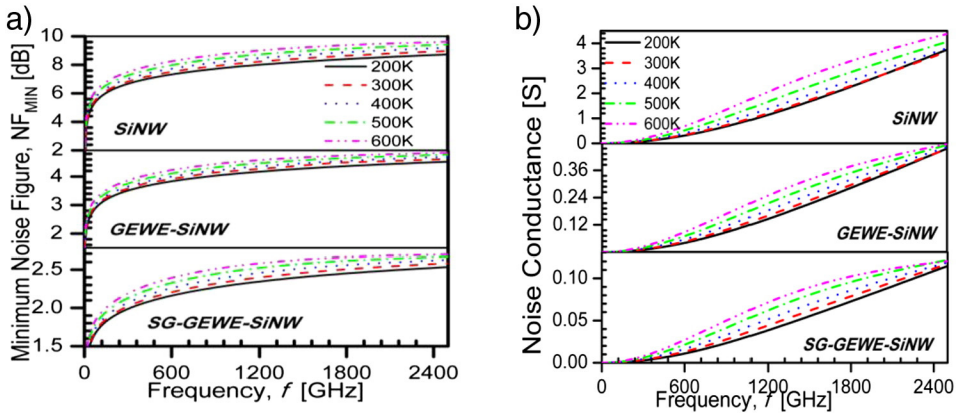


Fig. 7. (a) Minimum noise figure (NF_{MIN}) and (b) noise conductance as a function of frequency for SiNW, GEWE-SiNW and SG-GEWE-SiNW MOSFET at $V_{ds} = 0.5$ V and $V_{gs} = 1.0$ V.

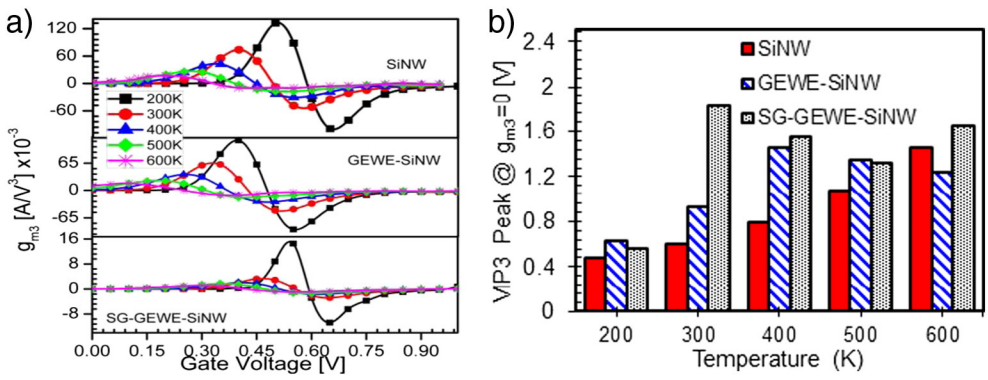


Fig. 8. (a) g_{m3} and (b) VIP3 of SiNW, GEWE-SiNW and GS-GEWE-SiNW MOSFET for different temperatures at $V_{gs} = 1.0$ V and $V_{ds} = 0.5$ V.

Please cite this article as: N. Gupta, R. Chaujar, Investigation of temperature variations on analog/RF and linearity performance of stacked gate GEWE-SiNW MOSFET for improved devic..., Microelectronics Reliability (2016), http://dx.doi.org/10.1016/j.microrel.2016.07.095

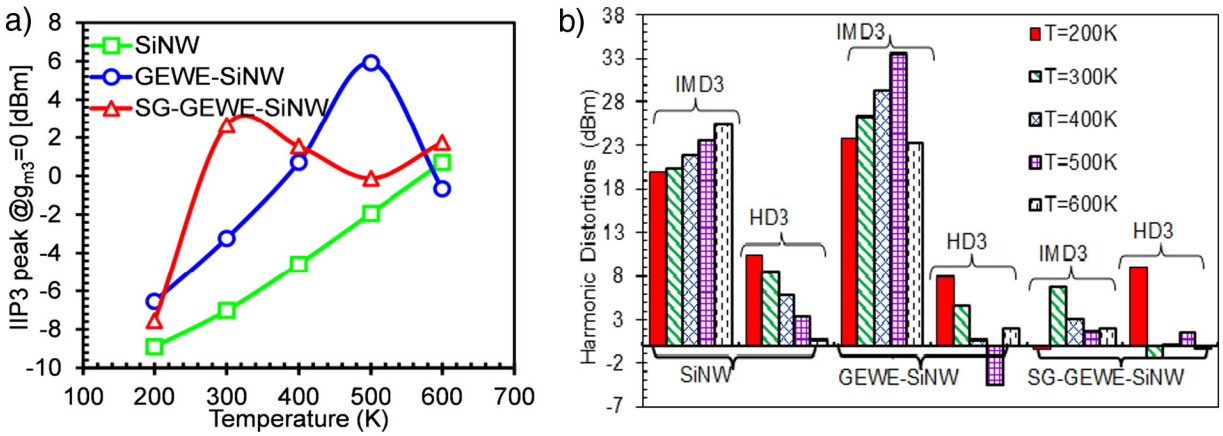


Fig. 9. (a) VIP3 and (b) IIP3 of SiNW, GEWE-SiNW and GS-GEWE-SiNW MOSFET for different temperatures at $V_{gs} = 1.0$ V and $V_{ds} = 0.5$ V.

extrapolated input voltage at which first and third order harmonics of drain current are equal. The peak of VIP3 reveals the cancellation of third-order nonlinearity coefficient by device internal feedback around second-order nonlinearity. Fig. 8(b) shows that peak value of VIP3 increases significantly in the case of gate-stack architecture at 300 K due to lowering of g_{m3} and enhancement in transconductance (g_m) owing to high on-current and improvement in carrier mobility.

Moreover, the main FOM which governs amplifier's efficiency and linearity is the third-order intercept point (IIP3). Third-order intercept is a theoretical point at which the third-order distortion signal amplitudes equal the input signals, and it is useful in determining the linearity condition of an amplifier. The peak value of IIP3 attains maximum value at 300 K in SG-GEWE-SiNW and as temperature increases its value deteriorates but in the case of GEWE-SiNW and SiNW peak value of IIP3 increases as temperature increases as is shown in Fig. 9(a). Thus to signify SG-GEWE-SiNW MOSFET is more linear and thus more reliable at a lower temperature. Harmonic distortion (HD) is another important reliability issue in analog and RF circuit applications that arises owing to the non-linear performance of devices. Nonlinearity may induce intermodulation (IM), which generates signals with frequencies different from the input ones. These unwanted signals may fall into the band of interest, interfering or even corrupting the desired components [18]. Therefore, Harmonic Distortions such as 2nd order HD (HD2), 3rd Order HD (HD3) and 3rd Order Intermodulation Distortion (IMD3) has also been studied.

$$\mathrm{HD3} = 0.25\, V_a^2 \frac{\left(\frac{d^2 g_{m1}}{dV^2{}_{GT}}\right)}{6 g_{m1}} \tag{4}$$

where V_a is the amplitude of AC signal and considered to be very small, of about 50 mV for the IFM analysis. Fig. 9(b) shows that HD3 significantly reduces as temperature increases due to higher transconductance owing to high on-current and is in accordance with Eq. (4) and reduction of HD3 is more prominent in SG-GEWE-SiNW MOSFET in comparison to its conventional counterparts. Furthermore, IMD3 plays a significant role in determining intermodulation distortion in CMOS RF amplifiers, since these applications make use of both phase and amplitude modulation. Therefore, reduction of IMD3 in the RF front-end transceiver parts is of great importance for maximizing overall system performance and minimizing distortions. It is clearly evident from Fig. 9(b) that IMD3 is reduced appreciably as temperature reduces due to a reduction in higher order harmonics and VIP3. Thus, linearity performance of SG-GEWE-SiNW MOSFET degrades at low temperature and performance improves as temperature rises.

5. Conclusion

The effect of temperature on the Analog/RF and Linearity performance has been studied with an aim to analyze the reliability issues of SG-GEWE-SiNW. Results reveal that with the incorporation of Stack Gate scheme, device performance enhances significantly due to reduction in leakage current. SG-GEWE-SiNW MOSFET exhibits 1.1 and 1.2 times improvement in I_{on} and thus 29% and 9.3% enhancement in f_T at low temperature (200 K) in comparison to GEWE-SiNW and SiNW MOSFET owing to decrement in off-current and gate capacitance. Moreover, Noise FOMs also improved at 200 K but linearity FOMs slightly degrade but show high linearity at 300 K in SG-GEWE-SiNW and will not hinder that much to the device performance. Therefore, SG-GEWE-SiNW can be very attractive for low temperature analog/digital circuits and in space technology. In addition, it is found that ZTC is observed at lower gate bias for SG-GEWE-SiNW, which leads to significant improvement in static and dynamic performance. Thus, the results so obtained can be serving as a worthy design tool for circuits operating at wide range of temperatures.

Acknowledgment

The authors would like to thank the Microelectronics Research Lab, Department of Engineering Physics, Delhi Technological University (formerly DCE) and one of the authors (Neha Gupta) is grateful to the University Grant Commission (UGC) (Ref.: 4003/NET-June 2013) for providing the necessary financial assistance to carry out this research work.

References

[1] H.–.S.P. Wong, et al., Nanoscale CMOS, Proc. IEEE 87 (4) (1990) 537–570.
[2] J. Sun, Y. Taur, R. Dennard, S. Klepner, Submicrometer-channel CMOS for low temperature operation, IEEE Trans. Electron Devices 34 (1) (1987) 19–27.
[3] S. Hong, et al., Low-temperature performance of nanoscale MOSFET for deep-space RF applications, IEEE Electron Device Lett. 29 (7) (2008) 775–777.
[4] J. Kim, et al., Thickness and temperature dependence of the leakage current in hafnium-based Si SOI MOSFETs, Microelectron. Reliab. 52 (12) (2012) 2907–2913.
[5] A. Kumar, N. Gupta, R. Chaujar, Power gain assessment of ITO-based transparent gate recessed channel (TGRC) MOSFET for RF/wireless applications, Superlattice. Microst. 91 (2016) 290–301.
[6] J.A. del Alamo, Nanometre-scale electronics with III–V compound semiconductors, Nature 479 (2011) 317–323.
[7] Y. Cui, et al., High performance silicon nanowire field effect transistors, Nano Lett. 3 (2003) 149–152.
[8] T. Grasser, Hot Carrier Degradation in Semiconductor Devices, Springer, 2014.
[9] W. Long, H. Ou, J.M. Kuo, K.K. Chin, Dual-material gate (DMG) field effect transistor, IEEE Trans. Electron Devices 46 (5) (May 1999) 865–870.
[10] C.Y. Zheng, The using of dual-material gate MOSFET in suppressing short-channel effects: a review, Presented at IEEE Int. Conference on Electronics, Communications and Control (ICECC) 2011, pp. 2979–2982.

Please cite this article as: N. Gupta, R. Chaujar, Investigation of temperature variations on analog/RF and linearity performance of stacked gate GEWE-SiNW MOSFET for improved devic..., Microelectronics Reliability (2016), http://dx.doi.org/10.1016/j.microrel.2016.07.095

ARTICLE IN PRESS

[11] N. Gupta, A. Kumar, R. Chaujar, Oxide bound impact on hot-carrier degradation for gate electrode workfunction engineered (GEWE) silicon nanowire MOSFET, Microsyst. Technol. (May 2015) 1–10.
[12] N. Gupta, A. Kumar, R. Chaujar, Impact of device parameter variation on RF performance of gate electrode workfunction engineered (GEWE)-silicon nanowire (SiNW) MOSFET, J. Comput. Electron. 14 (3) (Sep. 2015) 798–810.
[13] ATLAS, User's Manual, SILVACO Int., Santa Clara, CA, 2014.
[14] A. Chaudhry, J.N. Roy, MOSFET models, quantum mechanical effects and modeling approaches: a review, J. Semicond. Technol. Sci. 10 (2010) 20–27.
[15] V.S. Patnaik, A. Gheedia, M.J. Kumar, 3D simulation of nanowire FETs using quantum models, July, August, September, 2008.
[16] G. Iannaccone, G. Curatola, G. Fiori, Effective Bohm quantum potential for device simulators based on drift-diffusion and energy transport, Simulation of Semiconductor Processes and Devices (SISPAD) 2004, pp. 275–278.
[17] S.D. Suk, et al., High performance 5 nm radius twin silicon nanowire MOSFET (TSNWFET): fabrication on bulk Si wafer, characteristics, and reliability, IEEE IEDM Tech. Dig. (2005) 717–720.
[18] A. Dutta, K. Koley, C.K. Sarkar, Analysis of harmonic distortion in asymmetric underlap DG-MOSFET with a high-k spacer, Microelectron. Reliab. 54 (2014) 1125–1132.

Please cite this article as: N. Gupta, R. Chaujar, Investigation of temperature variations on analog/RF and linearity performance of stacked gate GEWE-SiNW MOSFET for improved devic..., Microelectronics Reliability (2016), http://dx.doi.org/10.1016/j.microrel.2016.07.095

Kirchhoff's laws from Tellegen's Theorem

V.C. Prasad

Faculty of Engineering, Dayalbagh Educational Institute, Dayalbagh, Agra 282005,India, prasadvishdelhi@gmail.com
(Retired from Indian Institute of Technology, Delhi)

***Summary*: It is well known that Kirchhoff's voltage (current) law and Tellegen's theorem ($\mathbf{v}^T\mathbf{i} = 0$) imply Kirchhoff's current (voltage) law where v and i refer to the same graph. Careful analysis shows that these statements are not applicable to practical networks unless v and i refer to different networks having the same graph. They are rewritten and proved to take care of this.**

Key words:
Kirchhoff's laws, Tellegen's theorem, circuit analysis, graphs and electrical networks, network theorems

1. INTRODUCTION

Let N_a and N_b be two networks with same incidence matrix. There is a one one correspondence between their vertices and elements. $\mathbf{v}_a$ ($\mathbf{v}_b$) be the vector of voltages of all elements of N_a (N_b). $\mathbf{i}_a$ and $\mathbf{i}_b$ be their current vectors. Let voltage and current directions be same in all elements. Then Tellegen's theorem [1,2,3] states that

$$\mathbf{v}^T_a\mathbf{i}_a = 0 \quad (1)$$

$$\mathbf{v}^T_b\mathbf{i}_b = 0 \quad (2)$$

$$\mathbf{v}^T_a\mathbf{i}_b = 0 \quad (3)$$

$$\mathbf{v}^T_b\mathbf{i}_a = 0 \quad (4)$$

They can be combined into a single equation $\mathbf{v}^T\mathbf{i} = 0$ where **v** and **i** refer to the same directed graph. But they may or may not belong to same network [1]. Penfield et al [2] studied this theorem extensively and suggested many applications in electrical networks. It is well known that any two of Kirchhoff's laws and Tellegen's theorem imply the other. More precisely the following statements are widely accepted [1,2,4]:

i. Tellegen's theorem is a consequence of Kirchhoff's laws.
ii. If, for **all v** satisfying KVL, $\mathbf{v}^T\mathbf{i} = 0$, then **i** satisfies KCL.
iii. If, for **all** i satisfying KCL, $\mathbf{v}^T\mathbf{i} = 0$, then **v** satisfies KVL.

Recently Willems [4] studied these statements for active and reactive components of currents and voltages of power networks. It is the purpose of this paper to clarify an important aspect of statements (ii) and (iii). v and i in these statements refer to the same graph. This is enough for statement (i). But this is not enough for statements (ii) and (iii). Following the experience of Tellegen's theorem one should not take **v** and **i** from same as well as different networks. Similarly one should not think that it is arbitrary or immaterial. **They must be taken from different networks** i.e. only equations (3) and (4) must be used. Equations (1) and (2) should not be used. Otherwise the conclusions of the statements will not be true except for pathological cases. This aspect is discussed in Section II. These statements and their proofs are rephrased to reflect this change. This is done in Section III.

2. ANALYSIS OF EXISTING RESULTS

First let us derive KCL from KVL and Tellegen's equation. Theorem 1 given below deals with this.

Theorem 1 [1]: Let **v** (**i**) be the vector of voltages (currents) of all edges of a directed graph G. Let $\mathbf{v}^T\mathbf{i} = 0$ for **all v** satisfying KVL. Then **i** satisfies KCL.

The statement of the theorem is silent on the networks from which **v** and **i** are taken. The proof refers to the graph only. It does not refer to any network and so one tends to think that it is immaterial. But this is not true from a practical point of view. It is important to understand that **v** and **i** must belong to different networks to make this theorem meaningful. The following example highlights this and other problems that arise if **v** and **i** belong to the same network.

Example 1: Consider the simple network shown in Fig. 1. We will assume that KVL and Tellegen's equation hold in this network and examine whether KCL is satisfied or not under different conditions.

i. $v_1 = 5$, $i_1 = -4$, $v_2 = 2$, $i_2 = 7$, $v_3 = 3$ and $i_3 = 2$ satisfy KVL ($v_1 = v_2 + v_3$), component equations ($v_1 = 5$, $v_2 = {}^2/_7\, i_2$, $v_3 = {}^3/_2\, i_3$) and the Tellegen's equation ($v_1i_1 + v_2i_2 + v_3i_3 = 0$). It is clear that the currents do not satisfy KCL. But Th. 1 is not violated because we considered only one set of values of voltages satisfying KVL whereas the theorem requires us to consider **all v**. Now consider a slightly different situation. Let $i_1 = -4$, $i_2 = 7$ and $i_3 = 2$. KCL is violated. Tellegen's equation gives $-4v_1 + 7v_2 + 2v_3 = 0$. Using KVL we get $3v_2 - 2v_3 = 0$. This is an additional constraint on voltages. It does not allow us to choose **all v** satisfying KVL. Hence Th. 1 is not applicable. On the other hand take $i_1 = -2$, $i_2 = 2$ and $i_3 = 2$. These currents satisfy KCL. Tellegen's equation gives $-2v_1 + 2v_2 + 2v_3 = 0$ which is same as KVL. Therefore there is no additional constraint on voltages and Th. 1 is applicable.
ii. Take $v_1 = E$ where E is any arbitrary value. Then $v_3 = E - {}^2/_7\, i_2 = {}^3/_2\, i_3$ from KVL and component equations. This gives

$$i_3 = {}^2/_{21}\,(7E - 2i_2) \quad (5)$$

From $\mathbf{v}^T\mathbf{i} = 0$, $Ei_1 + {}^2/_7\, i_2^2 + {}^3/_2\, i_3^2 = 0$. Substitute for i_3 from equation (5) and simplify. We get

$$Ei_1 + \frac{2}{7}i_2^2 + \frac{2}{49\times 3}(49E^2 + 4i_2^2 - 28Ei_2) = 0 \qquad (6)$$

Equations (5) and (6) do not imply the KCLs $i_2 = i_3$ and $i_1 + i_2 = 0$. As E is varied, v_1, v_2 and v_3 can take on different values satisfying KVL. In spite of that Th. 1 is not violated because the voltages have to satisfy component equations also in addition to KVL. $v_1 = 5$, $i_1 = -4$, $v_2 = 2$, $i_2 = 4$, $v_3 = 3$ and $i_3 = 4$ satisfy KVL and $\mathbf{v}^T\mathbf{i} = 0$ but not component equations, i.e. component equations do not allow voltages to take on all possible values satisfying KVL. But Th. 1 does not allow us to constrain voltages by component equations. Hence the theorem is not useful for practical circuits if **v** and **i** are taken from the same network intentionally or unintentionally. I.e., the theorem cannot be silent on this.

iii. Let all components in the network of Fig. 1 be ideal voltage sources. Let $v_1 = E_1$, $v_2 = E_2$, $v3 = E_3$ where E_1, E_2 and E_3 are arbitrary values. Then using KVL $\mathbf{v}^T\mathbf{i} = 0$ gives $E_2(i_1 + i_2) + E_3(i_1 + i_3) = 0$. Since E_2 and E_3 are arbitrary, $i_1 + i_2 = 0$ and $i_1 + i_3 = 0$. I.e., KCLs are true. In this case component equations do not constrain voltages and hence Th. 1 is true. Thus Th.1 is not true except for pathological networks if **v** and **i** are from the same network. Note that there is no way to compute these currents even though they satisfy KCL.

iv. Proof of Th.1 and later Th.3 select node voltages arbitrarily to prove KCL. Let us now look at this aspect. Choose node III as reference node. Let $v_{nI} = k$ and $v_{nII} = 0$ where k is any real number. Then $v_1 = k$, $v_2 = k$ and $v_3 = 0$. $i_2 = {}^7/_2\, k$ and $i_3 = 0$ from component equations. $\mathbf{v}^T\mathbf{i} = 0$ gives $i_1 = -{}^7/_2\, k$. Thus KCL is satisfied at node I for all k and the theorem is true. But this is only for specific set of values of currents whereas we want KCL for all values. Thus if we arbitrarily select node voltages, we get KCL. Further, note that KCL is not satisfied at node II.

Next consider the problem of deriving KVL from KCL and Tellegen's equation. Theorem 2 given below deals with this.

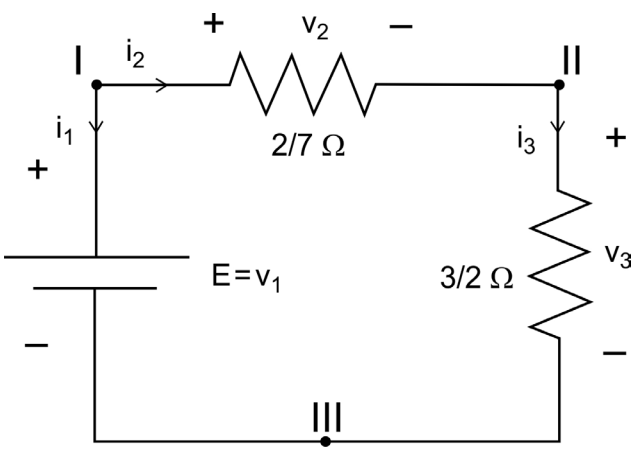


Fig. 1. An example network.

Theorem 2 [1]: Let **v**(**i**) be the vector of voltages (currents) of all edges of a directed graph G. Let $\mathbf{v}^T\mathbf{i} = 0$ for **all i** satisfying KCL. Then **v** satisfies KVL.

As in Th. 1 the statement of this theorem is also silent on the networks from which v and i are taken. The proof refers to the graph only. Consequently this theorem also has problems similar to those cited above. Here also **v** and **i** must belong to different networks to make this theorem meaningful. The following example illustrates the problems that arise if **v** and **i** belong to the same network.

Example 2: Consider the network shown in Fig. 2. We will assume that KCL and Tellegen's equation hold for this network and examine whether KVL is satisfied or not under different conditions.

i. $J = 4$, $v_1 = {}^5/_6$, $v_2 = 1$, $i_2 = 2$, $v_3 = {}^2/_3$, $i_3 = 2$ satisfy the KCL equation ($i_1 + i_2 + i_3 = 0$), component equations ($J = 4$, $i_2 = 2v_2$ and $i_3 = 3v_3$) and the Tellegen's equation ($v_1i_1 + v_2i_2 + v_3i_3 = 0$). But the voltages do not satisfy KVL. Th. 2 is not violated because we have not considered all possible values of currents satisfying KCL. Next consider $v_1 = {}^5/_6$, $v_2 = 1$, $v_3 = {}^2/_3$. Voltages do not satisfy KVL. Tellegen's equation gives ${}^5/_6\, i_1 + i_2 + {}^2/_3\, i_3 = 0$. This is an additional constraint on currents. This does not allow us to take **all i** satisfying KCL. Therefore Th. 2 is not applicable. On the other hand take $v_1 = 1$, $v_2 = 1$, $v_3 = 1$. These voltages satisfy KVL and the Tellegen's equation is same as KCL. Therefore there is no additional constraint on currents and Th. 2 is applicable.

ii. Take $i_1 = -J$ where J is any arbitrary value. Using KCL $i_3 = J - i_2$ and $i_3 = 3v_3$ we get

$$v_3 = \frac{1}{3}(J - 2v_2) \qquad (7)$$

$$\mathbf{v}^T\mathbf{i} = -Jv_1 + 2v\frac{2}{2} + 3v\frac{2}{3} \qquad \text{gives}$$

$$-Jv_1 + 2v\frac{2}{2} + \frac{1}{3}(J - 2v_2)^2 = 0 \qquad (8)$$

Equations (7) and (8) do not imply the KVL equations $v_1 = v_2 = v_3$. Since J is arbitrary the currents can take on many values satisfying KCL. But Th. 2 is not violated because currents cannot take on all possible values because of component equations. Thus Th. 2 does not allow the component equations to constrain currents. Hence this theorem cannot be applied to practical networks if **v** and **i** are taken from the same network intentionally or unintentionally. I.e., the theorem cannot be silent on this.

iii. Let all components in the network of Fig. 2 be ideal current sources. Let $i_1 = J_1$, $i_2 = J_2$, $i_3 = J_3$ where J_1, J_2 and J_3 are arbitrary values. Then using KCL $\mathbf{v}^T\mathbf{i} = 0$ gives $J_2(-v_1 + v_2) + J_3(-v_1 + v_3) = 0$. Since J_2 and J_3 are arbitrary, $v_1 = v_2$ and $v_1 = v_3$. I.e., KVLs are true. In this case component equations do not constrain currents and hence Th. 2 is true. Thus Th. 2 is true if all elements are ideal cur-

rent sources if v and i are from the same network. But these networks have no practical value. Note that there is no way to compute these voltages although they satisfy KVL.

iv. Proof of Th. 2 and later Th. 5 select currents arbitrarily to prove KVL. Let us now look at this aspect. Choose $i_1 = -k$ and $i_3 = 0$ where k is any real number. Then $i_2 = k$ from KCL. $v_2 = k/2$ and $v_3 = 0$ from component equations. $\mathbf{v}^T\mathbf{i} = 0$ gives $v_1 = k/2$. Therefore v_1 and v_2 satisfy KVL for all k. I.e., Th. 2 is satisfied for v_1 and v_2. But this is only for specific set of values whereas we want KVL for all values. Thus if we arbitrarily choose currents we get KVL. But it is limited to specific values only. Further, note that KVL is not satisfied for v_2 and v_3.

3. MODIFIED THEOREMS

In this section Theorems 1 and 2 are stated and proved more clearly so that they are realistic. Let G be the directed graph of the given network N. Let G_a and G_b be two identical copies of G. They may be derived from two identical copies of N. We will rewrite these theorems and their proofs using G_a and G_b. $\mathbf{v}_a$ ($\mathbf{v}_b$) are the vectors of voltages of all edges of G_a (G_b). $\mathbf{i}_a$ and $\mathbf{i}_b$ are their current vectors. Since each network has one graph only, it is clear that G_a and G_b refer to two physically different networks.

Theorem 3: Let $\mathbf{v}^T_b\mathbf{i}_a = 0$ for **all** $\mathbf{v_b}$ satisfying KVL. Then $\mathbf{i}_a$ satisfies KCL.

Proof: Consider the node transformation $\mathbf{v}_b = \mathbf{A}^T\mathbf{v}_{nb}$. It follows from this that taking all $\mathbf{v}_b$ satisfying KVL in G_b, implies taking **all** values of $\mathbf{v}_{nb}$ without any constraints. From Tellegen's equation we have

$$\mathbf{v}^T_b\mathbf{i}_a = \mathbf{v}^T_{nb}\,\mathbf{A}\mathbf{i}_a = 0 \qquad (9)$$

Since $\mathbf{v}_{nb}$ and $\mathbf{i}_a$ belong to different graphs (networks), choosing $\mathbf{v}_{nb}$ has no effect on $\mathbf{i}_a$.
Taking $v_{nb1} = 1$, $v_{nb2} = v_{nb3} = \ldots = 0$ we get KCL at node I for **all** $\mathbf{i}_a$ from equation (9). Similarly we get KCLs at other nodes also. This proves the theorem.

Corollary 4: Let KVL and Tellegen's equations be universally true (i.e., KVL is true for **all** networks and Tellegen's equations hold for **all** pairs of networks having same graph) then KCL is also universally true.

Proof: Let N be any network to which we want to prove KCL. Let G be its graph. Let G_a and G_b be two copies of G. Applying Th. 3 KCL is true for N. But N is arbitrary. Hence KCL is true for all networks. b

Example 3: Let us now look at the observations of Example 1 using this knowledge. N_a is the network given in Fig.1. Take another copy of this network and call it N_b.

i. Let $i_{a1} = -4$, $i_{a2} = 7$ and $i_{a3} = 2$. KCL is violated in N_a. Tellegen's equation gives $-4v_{b1} + 7v_{b2} + 2v_{b3} = 0$. Using KVL we get $3v_{b2} - 2v_{b3} = 0$. This is an additional constraint on voltages. It does not allow us to choose **all v** satisfying KVL in N_b. Hence Th. 3 is not applicable. If we take $i_{a1} = -4$, $i_{a2} = 2$ and $i_{a3} = 2$ KCL is satisfied. Tellegen's equation gives $-4v_{b1} + 2v_{b2} + 2v_{b3} = 0$. This satisfies KVL and hence this is not an additional constraint. Hence Th. 3 is applicable.

ii. Since choosing voltages in N_b (G_b) does not affect currents in N_a (G_a) the problem in observation (ii) of Example 1 does not arise now.

iii. Even if all the elements are ideal voltage sources, Th. 3 is satisfied. This can be easily verified. I.e., Th.1 can afford to be silent on the networks of **v** and **i** for such networks.

iv. Take node III as the reference node in N_b. Take $vn_{bI} = 1$ and $vn_{bII} = 0$. Then $v_{b1} = v_{b2} = 1$ and $v_{b3} = 0$. $\mathbf{v}^T_b\mathbf{i}a = (1)i_{a1} + (1)i_{a2} + (0)i_{a3} = 0$. This gives KCL at node I of Na for all possible currents. This does not constrain KCL at node II. That has to be determined separately. We get KCL at node II by taking $v_{nbI} = 0$ and $v_{nbII} = 1$ whereas KCL is not satisfied at node II in observation (iv) of Example 1.

Thus the problems of Example 1 do not exist anymore.

Theorem 5: Let $\mathbf{v}^T_a\mathbf{i}_b = 0$ for **all** $\mathbf{i}_b$ satisfying KCL. Then $\mathbf{v}_a$ satisfies KVL.

Proof: Consider the mesh transformation $\mathbf{i}_b = \mathbf{B}^T\mathbf{i}_{mb}$ where $\mathbf{i}_{mb}$ is the vector of all independent mesh currents in G_b (In general $\mathbf{i}_{mb}$ is the vector of all link currents). It follows from this equation that choosing **all** $\mathbf{i}_b$ in G_b satisfying KCL implies choosing **all** values of $\mathbf{i}_{mb}$ without any constraints. From Tellegen's equation we have

$$\mathbf{v}^T_a\mathbf{i}_b = (\mathbf{B}\mathbf{v}_a)^T\mathbf{i}_{mb} = 0 \qquad (10)$$

Since $\mathbf{i}_m$ and $\mathbf{v}_a$ belong to different graphs (networks), choosing $\mathbf{i}_{mb}$ has no effect on $\mathbf{v}_a$. Taking $i_{mb1} = 1$, $i_{mb2} = i_{mb3} = \ldots = 0$ we get KVL for the first loop from equation (10) for **all** $\mathbf{v}_a$. Similarly we get KVLs for other loops also. This proves the theorem.

Corollary 6: Let KCL and Tellegen's equations be universally true (i.e., KCL is true for **all** networks and Tellegen's equations hold for **all** pairs of networks having same graph) then KVL is also universally true.

Proof: Let N be any network to which we want to prove KVL. Let G be its graph. Let G_a and G_b be two copies of G. Applying Th. 5 KVL is true for N. But N is arbitrary. Hence KVL is true for all networks.

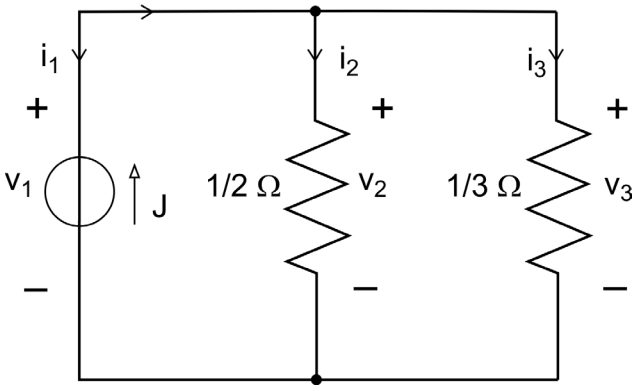


Fig. 2. An example network.

Example 4: Let us now look at the observations of Example 2 using this knowledge. Na is the network given in Fig. 2. Take another copy of this network and call it N_b.

i. Consider $v_{a1} = {}^5/_6$, $v_{a2} = 1$, $v_{a3} = {}^2/_3$. Voltages do not satisfy KVL in Na. Tellegen's equation gives ${}^5/_6\, i_{b1} + i_{b2} + {}^2/_3\, i_{b3} = 0$. This is an additional constraint on currents. This does not allow us to take **all** $\mathbf{i}_b$ satisfying KCL in N_b. Therefore Th. 5 is not applicable. Now take $v_{a1} = 1$, $v_{a2} = 1$, $v_{a3} = 1$. Voltages satisfy KVL in N_a. Tellegen's equation is same as KCL. Thus there is no additional constraint on currents. Hence Th. 5 is applicable.

ii. Since choosing currents in N_b does not affect voltages in N_a the problem in observation (ii) of Example 2 does not arise now.

iii. Even if all the elements are ideal current sources, Th. 5 is satisfied. This can be easily verified. I.e., Th. 2 can afford to be silent on the networks of **v** and **i** for such networks.

iv. Choose $i_{b1} = 1$ and $i_{b3} = 0$. Then $i_{b2} = -1$ from KCL. $\mathbf{v}^T_a\mathbf{i}_b =$ gives $v_{a1} = v_{a2}$. I.e., KVL holds for loop 1 in N_a. We get KVL $v_{a2} = v_{a3}$ by taking $i_{b1} = 0$ and $i_{b3} = 1$ whereas KVL is not satisfied for this loop in observation (iv) of Example 2.

Thus the problems of Example 2 do not exist anymore.

Remarks:

1. It is clear from the proofs of Theorems 3 and 5 that (i) the networks to which **v** and **i** belong cannot be arbitrarily decided and (ii) **v** and **i** don't have to be chosen from the same network in addition to choosing them from different networks.
2. Tellgen's theorem refers to one graph only whereas Ths. 3 and 5 refer to two graphs. It is interesting to note that Tellegen's theorem can also be stated using two different graphs. We can state Tellegen's equation as $\mathbf{v}^T\mathbf{i} = 0$ where **v** and **i** refer to two separate but identical graphs. Equations (3) and (4) follow from this. When N_b is a copy of N_a both of them have same voltages and currents. So equations (3) and (4) give equations (1) and (2). Thus all four Tellegen's equations can be put as a single equation using two graphs also. Further this allows us to put all three statements mentioned in the Introduction in a common frame work by choosing **v** and **i** from different graphs always.

4. CONCLUSIONS

It is well known that KVL (KCL) together with Tellegen's equation implies KCL (KVL). It is shown here that voltages and currents must be taken from different networks to achieve this. More precisely they need two separate but identical graphs. We can do this even for Tellegen's theorem.

REFERENCES

1. Chua L.O., Desoer C.A., Kuh E.S.: Linear and Nonlinear Circuits. Mc Graw – Hill, New York 1987.
2. Penfield P., Spence R., Duinker S.: Tellegen's Theorem and Electrical Networks. MIT Press, Cambridge MA, 1970.
3. Tellegen B.D.H.: A general network theorem with applications. Philips Research Report 1952, Vol. 7, pp. 259-269.
4. Willems J.L.: Active Current, Reactive Current, Kirchhoff 's Laws and Tellegen's Theorem. Electrical Power Quality and Utilisation Journal 2007, No. 1, pp. 5-8.



Vishnuvajjula Charan PRASAD Bachelor's degree from Indian Institute of Science, Bangalore, Master's and Ph.D from Indian Institute of Technology, Delhi. Asst. Research Engineer during 1978-1979 at University of California, Berkeley; 1974 -1978: lecturer Delhi college of Engineering. During 1978-1983: Reader Dayalbagh Educational Institute, Dayalbagh, Agra. Since 1983 he was with Indian Institute of Technology Delhi in various capacities till he voluntarily retired in 2006 as a Professor of Electrical Engineering. He worked as a Professor in a Malaysian University till 2012. Since then he is with Dayalbagh Educational Institute as an honorary Professor. His research interests are in nonlinear networks, analog fault diagnosis, network reliability, graph algorithms and binary decision diagrams and their applications.

DISCUSSION

(Both the Author and the Reviewer authorized publication of their discussion)

Reviewer's comments 1:

There are no novel ideas in the paper. Tellegen's theorem depicts only the interconnection properties of the circuit. It does not contain a clear physical meaning. Components of different vectors of voltages and currents those are sufficient to the Tellegen's theorem but not always sufficient to physical equations.

Consider a directed graph G and a vector of voltages $\mathbf{v} = [V_1, V_2, \ldots, V_n]$, which is sufficient to the KVL for G. The equation of $X_1{*}V_1 + X_2{*}V_2 + \ldots + X_n{*}V_n = 0$ has innumerous solutions. If one of these solutions is the vector $\mathbf{x} = [X_1, X_2, \ldots, X_3]$ and if it would be implemented to Tellegen's theorem, then it would be adequate to the theorem, but it would be adequate to the KCL only for special case. Willems noted this feature for the case of active currents in the mentioned paper. Hence Tellegen's theorem is correct and does not need any remarks.

Author's answers:

1. Tellegen's theorem does not contain a clear physical meaning and it is only about interconnection. I don't agree with this view. Tellegen's theorem emphasizes interconnections. But it uses voltages and currents which have to come from somewhere. Wherefrom will they come if there is no associated

network. There is no Tellegen's equation if there are no voltages and currents. Interconnection information is contained in the graph of the network. A directed graph G has edges and vertices. It has no voltages and currents unless the graph is derived from some physical network. So we cannot ignore the underlying network completely. Tellegen's theorem is not about graphs. Tellegen's theorem is about networks. This itself shows that interconnection (graph) alone is not enough. Emphasizing interconnection is merely to highlight its generality. I.e, it applies to any network. This does not mean that there is no network at all. We cannot delink the theorem from networks. Emphasizing interconnection is only to say that any set of quantities satisfying KVL (call them voltages) and any set of quantities satisfying KCL (call them currents) satisfy Tellegen's equation . We may be able to state some Tellegen's equations using fictitious voltages and fictitious currents. But this does not mean that they are always fictitious quantities only. They have to be associated with some network if Tellegen's theorem has to be meaningful. Thus Tellegen's theorem emphasizes interconnection. But it is not about interconnection only. I.e., we cannot keep interconnection only in our minds when we talk of Tellegen's theorem for real life situations.

2. "Consider a directed graph G and a vector of voltages $\mathbf{v} = [V_1,V_2,\ldots,V_n]$, which is sufficient to the KVL for G.
The equation of $X_1*V_1 + X_2*V_2 +\ldots+ X_n*V_n = 0$ has innumerous solutions. If one of these solutions is the vector $\mathbf{x} = [X_1,X_2,\ldots,X_3]$ and if it would be implemented to Tellegen's theorem, then it would be adequate to the theorem, but it would be adequate to the KCL only for special case. Willems noted this feature for the case of active currents in the mentioned paper."
My arguments are not inconsistent with what Willems said in his paper. As the reviewer pointed out, Willems noted the feature of active currents of power networks and made some interesting observations in his paper. But that is a physical network. It is not just interconnections only. Thus when it comes to reality we cannot ignore networks and harp only graphs.
3. "Hence Tellegen's theorem is correct and does not need any remarks."
First let me clarify that my paper does not say that Tellegen's theorem is wrong. My paper is not on Tellegen's theorem at all. Nor it is about remarks on Tellegen's theorem. It is about KVL (KCL) as a consequence of Tellegen's theorem and KCL (KVL). So I accept Tellegen's theorem and I have no remarks on Tellegen's theorem itself. I did not even say that the existing statements on Kirchhoff's laws from Tellegen's theorem are inherently wrong. I only tried to sharpen the statements. My modified theorems are sharpened versions of existing theorems. This is necessary if we have to use and understand these statements correctly on real life networks. My paper makes this point amply clear. I believe that this paper is important even if it has no novel ideas because it polishes fundamentals. Since KVL and KCL are fundamental to all electrical engineers, I think that this paper should be of interest to many electrical engineers and not specialists only.
My paper is about KVL (KCL) from Tellegen's theorem and KCL (KVL) and not Tellegen's theorem. In the first place the voltages and currents must come from physical networks if these statements have to be meaningful. Secondly these statements are not true even for fictitious voltages and fictitious currents unless we assume that they are unrelated. The existing proofs don't say this. But they assume this unknowingly. Tellegen's theorem does not require this whereas KVL / KCL from Tellegen's theorem requires this extra constraint. Component equations in networks do not allow voltages and currents to be unrelated. The whole paper is about this. This constraint is satisfied by taking them from two different networks/graphs. If you insist on interconnection only, I will also state in terms of interconnection only. I will say two different graphs instead of networks. In fact I did this in the paper. But in reality they have to come from two different networks even if they are identical. If you try to prove these statements yourself or read my proofs carefully, you will realize the importance of what I am saying. I am only trying to make the fundamentals more precise.

Reviewer's comments 2:

On the first remark: the citation from the book "Linear and nonlinear circuits" you refer to is "Clearly, Tellegen's theorem depict only the interconnection properties of the circuit or the topology of digraph". I am fully agreed with that statement as there is no point in limiting the theorem with particular physical phenomenon. I agree with you that in order to use Tellegen's theorem the correspondence of voltages and currents to component equations must be examined.

I do not contradistinguish your paper to professor's Williams paper. The example given in the previous review shows that for known set of voltages the given equation has infinite number of solutions. Some of them match with Kirchhoff law for particular directed graph and only one of them has physical meaning. It is a well-known fact and it is considered by characteristics of the Tellegen's theorem related to Kirchhoff law. Professor's Williams paper was mentioned only as an example.

Your paper incorporates an important idea that two voltage and current vectors which meet Kirchhoff's law requirements for the circuit with particular directed graph and therefore Tellegen's theorem may not match to component equations.

In your paper you proposed the way of specifying the definitions of Tellegen's theorem`s conclusions related to Kirchhoff law in order to eliminate inaccuracy. However nor theorem itself neither conclusions from it do confirm that voltage and current vectors should match

with component equations. Only the matching of Kirchhoff law with directed graph of particular circuit is stated. Therefore there is no need to additionally logically limit conclusions of the theorem. This is the idea that I tried to explain in my previous review. Purely the conclusions of the theorem were meant. I apologize for my incorrect wording.

I see no reason to include any additional limits to the definitions of the Tellegen's theorem conclusions which refer to Kirchhoff's law. However I agree with you that although the main idea of a paper about two vectors of voltage and current corresponding to Kirchhoff's law for particular directed graph is not new, it could be interesting for readers. Moreover I think that some of the readers may not be familiar enough with that topic. Your paper would be useful for the readers and I recommend it for publication in discussion section of the journal.

Author's answers 2:

1. At graph level we have KVL, KCL and Tellegen's equation. At network level we have KVL, KCL, Tellegen's equation and component equations. I.e., the network has more constraints than the graph. Therefore, a proof given at graph level need not hold at network level. Chua et al proved KVL/KCL at graph level only. They did not examine KVL/KCL at network level. That is why their proofs did not require component equations. But in reality we want KVL and KCL at network level and networks have components. Therefore, we cannot ignore components. We must consider the effect of component equations on the **proofs** of the statements. However, my theorems are also on graphs only. I got rid of the influence of component equations by using two graphs.
2. Chua et al. proved KVL and KCL at graph level. We cannot say that their statements are applicable to networks unless we understand the implications. For example, we need to know whether graph level statements and proofs are true at network level also or not. That is exactly what I did. My paper should be seen as an adaptation/extension/study of graph level statements to understand KVL and KCL at network level given Tellegen's equation. This is important because we have interest in KVL and KCL at network level and not graph level.
3. It is clear from the above explanation that the various ideas present in the paper like discussion concerning component equations and taking two graphs instead of one are necessary. There are no unnecessary "additional limitations" in the paper.

ISFT 2016

V[th] International Symposium on "Fusion of Science & Technology",
New Delhi, India, January 18-22, 2016

ID: 2016-ISFT-313

Micro Structural and Mechanical Behaviours of Nano-TiC-Reinforced AA6082 FSW Joints

Mohd Rashid[1], N. Yuvraj[2], Shailesh Kumar Singh[3]

[1]*Production Engineering, Delhi Technological University, New Delhi, 110042, India*
[2]*Department of Mechanical Engineering, Delhi Technological University, New Delhi, 110042, India*
[3]*Production Engineering, Delhi Technological University, New Delhi, 110042, India*
[1]*rashid.khan04@gmail.com*

Abstract: *Friction Stir Welding (FSW) is a solid state welding process for joining materials. In this process a high speed tool is introduced into the weld seam and due to localized frictional heat, plastic deformation and transverse movement along the weld seam, joining is accomplished. This welding technique is energy efficient, environment friendly, and versatile. In particular, it can be used to join high-strength aluminium alloys and other metallic alloys that are hard to weld by conventional fusion welding. The present work focuses on FSW of 6082 AA-T651 aluminium (Al) alloy which have gained wide acceptance in the fabrication of light weight structures requiring higher strength, and excellent corrosion resistance.FSW of AA6082 was done with and without reinforcement of nano sized titanium carbide (TiC) particles of size 10-30nm. The effect of processing parameters and reinforcement on the mechanical and microstructural properties of 6082 AA-T651 joints was analysed in this study. Welded specimens were produced by employing different combinations of welding speeds and tool rotational speeds. Tensile test, microstructure, micro hardness and EDX (Energy dispersive X-ray spectroscopy) analysis has been performed to evaluate the weld zone molecular characteristics and strength of friction stir welded alloy. Result shows that welding process reduces the strength and hardness of material which can be partially regain by reinforcement of TiCnanoparticles during welding process. Scanning electron microscope (SEM) equipped with (EDX) was used to analyse the chemical compositions of the alloy and titanium carbide particles of the weld nugget zone (NZ), it indicates that TiC is uniformly distributed in NZ.*

Keywords: *FSW, SEM, EDX*

1. INTRODUCTION

Aluminium matrix composites (AMCs) have enhanced properties as compared to their base material. However, their use are limited because they encountered difficulties during machining, forming, and when joined by traditional fusion welding processes [1].Recently particulate reinforced aluminium matrix composites have become a major focus of attention in aerospace, motor sport and automotive industries due to their several attractive advantages over conventional base alloys, such as high specific stiffness and strength to weight ratio at room or elevated temperatures, excellent fatigue properties, high formability and improved wear resistance [2, 3]. However, one of the main limitations for the particulate reinforced aluminium matrix composites is the difficulty in using conventional fusion welding methods because of the porosity, hot cracking, segregation and deleterious reactions between the reinforcement particles and liquid aluminium in the fusion zone [4, 5]. Friction stir welding is a promising candidate for joining particulate reinforced aluminium matrix composites since this method is a solid state process, therefore, the formation of brittle solidification products are not easily produced, the energy input and distortion are significantly lower than fusion welding techniques, thus improving the welding properties. Most of the previous studies on the joining of particulate reinforced aluminium matrix composites have dealt with gas shielded metal arc welding [6], laser welding, gas tungsten arc welding [4], electron beam welding [4] and friction welding but now friction stir welding is widely used for making joint of aluminium matrix composites [7-10].

Friction stir welding (FSW) is a relatively new solid-state joining technique which eliminated most of the problems that are encountered during conventional fusion arc welding. Low distortion, low energy consumption, high quality joints, better fatigue property, lower residual stresses, fewer weld defects, no harmful emission, high level of dimensional stability, repeatability and low production cost makes FSW an important solid-state joining process. It has expanded rapidly since it was invented at, The Welding Institute (TWI) of UK in 1991 [11].The basic concept of FSW is very simple**.** A non-consumable rotating tool with a specially designed pin and shoulder is inserted into the abutting edges of sheets or plates to be joined and traversed along the line of joint. The two primary functions of tools are heating of work piece and Stirring/ intermixing of material to produce the joint.

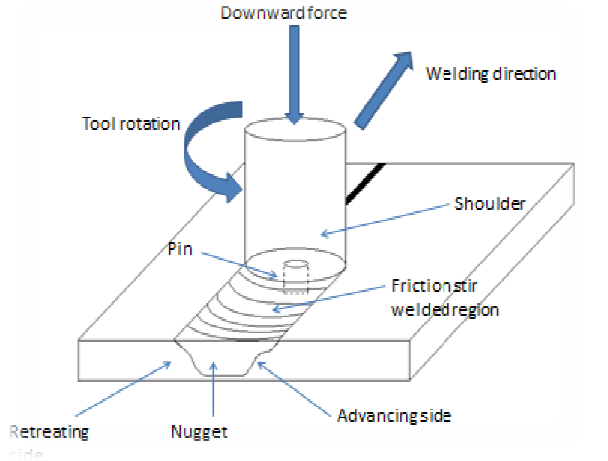


Fig. 1. Schematic diagram of FSW

The heating is accomplished by friction between the tool and the work piece. During FSW process, the material undergoes intense plastic deformation at elevated temperature, resulting in the generation of fine and equiaxed recrystallized grains [12]. Since the amount of heat supplied is smaller than fusion welding, heat distortions and residual stresses are reduced [13].

The 6xxx-group of Aluminum Alloys (AA) contains magnesium and silicon as the major alloying elements. Al–Mg–Si alloys have recently been used for automotive body sheet panel for weight saving [12]. In spite of the importance of 6xxx series AA to various industries a limited number of research work have been devoted to FSW of this series. Koumoulosa et al. [14] studied the FSW of AA6082-T6 and find that welding process softens the material, since the weld nugget is the region where the most deformations are recorded. Scialpi et al. [15] suggested that Tool with cavity and fillet can be considered the best tool for FSW of 6082-T6. Cavaliere et al. [16] find that AA6082 friction stir welded with the advancing speed of 115mm/min exhibited the best fatigue properties and the higher fatigue limit. H.J.liu et al. [17] reported that the tensile strength of FS Welded 6061-T6 aluminum alloy defect free joint increases with the welding speed and maximum tensile strength is equivalent to the 69% of that of base material. Many studies that have focused on the FSW of 6xxx AA series alloys were devoted for the 6061 and 6063 alloys, but limited attention was given to particularly the 6082 alloy. AA6082 has very good weldability but strength is lowered in the weld zone. Applications of AA6082 are typically used in highly stressed applications, Trusses, Bridges, Cranes, Transport applications, Beer barrels etc.

The present work focuses on the application of different welding parameters (rotational speed; rpm, feed rate; mm/min) on friction stir welding of AA 6082 plates in T651 condition and evaluating the mechanical properties and microstructural characteristics of the welded condition as well as after reinforcing with Titanium carbide (TiC) nano-particles

2. EXPERIMENTAL PROCEDURE

A commercial 6082-T651 AA plate which is solution heat treated, stress relieved by stretching then artificially aged is used as specimen for FSW.

The chemical composition of AA6082-T651.

TABLE 1.

Element	Si	Mg	Mn	Fe	Cr	Zn	Ti	Cu	Other	Al
Wt.%	1.2	.75	.79	.40	.15	.10	.07	.06	.10	Balance

Plate of 6 mm thickness, 80 mm width and 200 mm length was prepared by machining through milling. Subsequently, a 0.6 mm wide, 5 mm deep and adequately long profile was created on the faying surface of each plate. When two plates were fixed under a purpose-built fixture, asymmetrical bottom-closed groove was made lengthwise as shown in figure 2. Next, the TiC nano particles were added into the groove and pressed tightly. Using square shape pin as shown in figure 3, FSW was carried out with and without TiC nano particles.

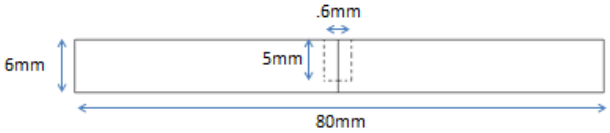


Fig. 2. Cross section of plate to be welded

Tool was fabricated from H13 hot working steel and heat treated to 58HRC (Hardness, Rockwell C-scale). This tool had a 5.7 mm long pin. The diagonal of square pin was 6 mm, Shoulder diameter of tool is18 mm.



Fig. 3. Square shape pin tool

All the joints were produced with the following optimized welding speed and tool rotational speed.

TABLE 2.

	Specimen with reinforcement				Specimen without reinforcement	
	R_1	R_2	R_3	R_4	B_1	B_2
Tool rotational speed (rpm)	1200	1200	1000	1000	1200	1000
Welding speed (mm/min)	90	60	90	60	90	60

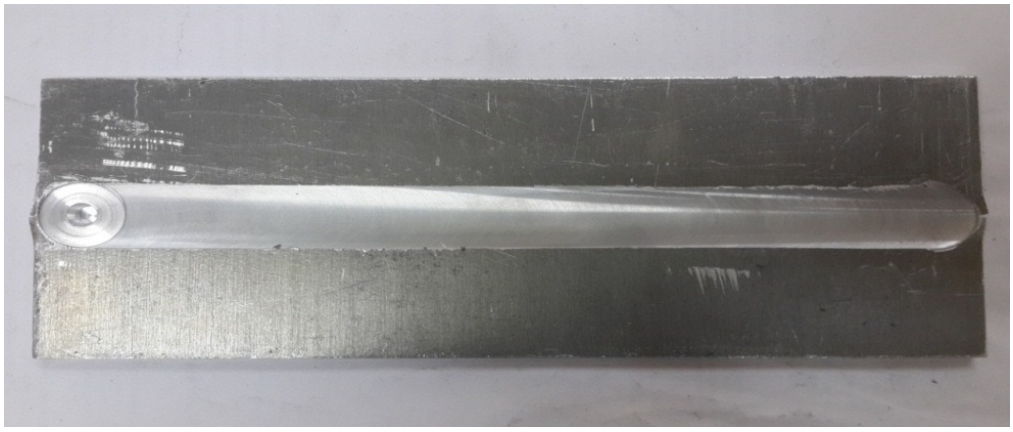


Fig. 4. Friction Stir welded AA6082 plate

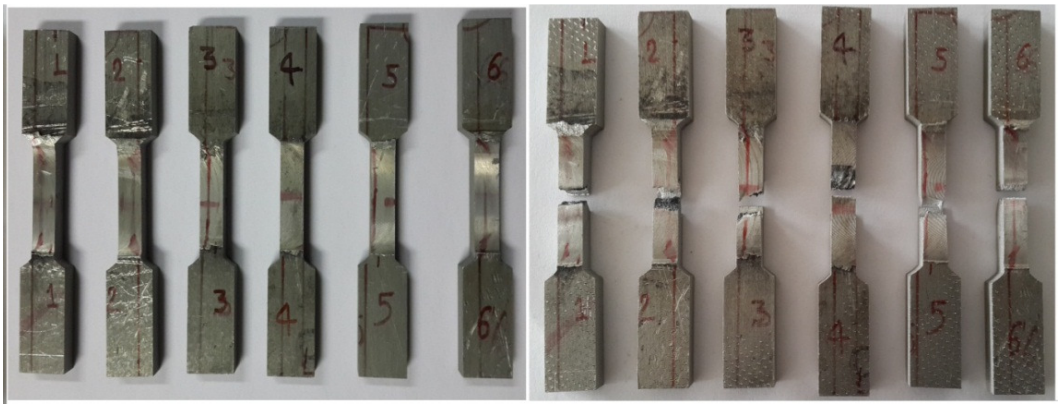


Fig. 5. Tensile test specimen before and after the test

Uniaxial tensile tests at room temperature were performed in order to evaluate the mechanical properties of the joints. To determine the tensile strength of the stir zone, small tensile test specimens were sectioned in transverse direction of the weld line with an electrical discharge machine (EDM). Specimen is cut as per ASTM:B557-06 standard. Tensile test is performed at a speed of 1mm/min.

Vickers hardness of friction stir welded AA6082 samples were measured using Vickers hardness tester. The test load applied was 200 gf and the dwell time was 5 seconds. All samples were taken from the transverse section of the welded area at the middle of the sheet thickness.Optical microscope was used to investigate the microstructure of a material.The sample preparation for the microscopic investigation includes grinding, dry and wet polishing with Al_2O_3 nano powder. After polishing Keller's etchant is applied on surface to reveal the grain boundary and micro structure of welded zone. It gives the clear view of different microstructural zone like stir zone (SZ), heat affected zone (HAZ), thermo mechanical affected zone (TMAZ). It also revealed the distribution of TiCnanoparticle in stir zone.Scanning electron microscopy (SEM) is used to investigate the microstructural modifications induced by the FSW process on the aluminium alloy matrix and reinforcement particles.The chemical compositions of the aluminium alloy matrix and titanium carbide particles of the weld nugget were analysed by a scanning electron microscope equipped with an energy dispersive X-ray

spectroscopy (EDX) analysis system. The specimens were polished using conventional polishing methods and etched before analysis.

3. RESULTS AND DISCUSSION

Study on FSW of 6082-T6 with processing parameters ranging from 1000 to1200 rpm and 60 and 90 mm/min is conducted. Tensile test result shows that, tensile strength of Friction stir joint decreases with respect to the base material strength (302 MPa). Ehab A. El-Danaf et al [12] also reported this phenomenon of, softening in the stir zone(SZ) and thermo mechanical affected zone (TMAZ) in Friction stir welding of AA 6082 - T651. To avoid the softening of stir zone or reduction of tensile strength TiCnanoparticles is added during Friction stir welding. Tensile test results clearly shows that inclusition of TiCpartical partially amended the strength loss that occurred with FSW.Tensile strength of different F S Welded specimen is given in figure 6.

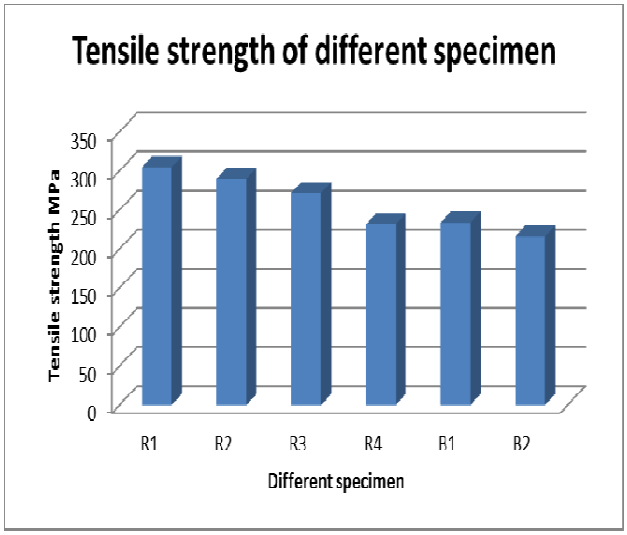


Fig. 6. Tensile strength of different specimen

Micro-hardness values of friction stir welded AA 6082 alloy and FS welded AA6082 with Tic nano particles at 1200 rpm, 90 mm/min is shown in figure 7. Joint obtained at optimized parameters shows that softening occurs in the stir zone (SZ) and thermo mechanical affected zone (TMAZ) compared to the unaffected base. The softening with respect to the base metal is due to the decomposition of needle-shaped β" precipitates which is the main source of hardening and strengthening, the coarsening of precipitates into semi- and non-coherent rod-shaped β' precipitates (over-aged precipitate structure) and the low dislocation density associated with the dynamically recrystallized structure [18]. TiCnano particles are induced during welding to increase the strength and hardness of joint. The microstructural changes induced by the reinforcement of TiC particles are responsible forthe improvement in mechanical properties.

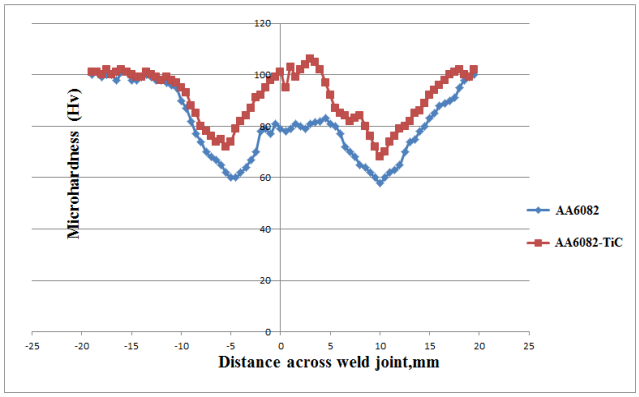


Fig.7. Micro hardness value of different specimen

Optical micrographs in Figure 8 show the typical zones of the weld nugget or stirred zone (SZ), the transitional zone (TZ) and the base material (BM). The transitional zones in FSW unreinforced aluminium alloys generally consisted of the thermo-mechanical affected zone (TMAZ) and heat-affected zone (HAZ), but probably due to the well-known lower sensitivity to thermal variations of ceramic reinforced composites, it was difficult to identify the HAZ, as also reported by Amirizad et al. [19]. The welded zone was mainly identified by a different size of the reinforcement particles and the aluminium alloy matrix with respect to the base material.

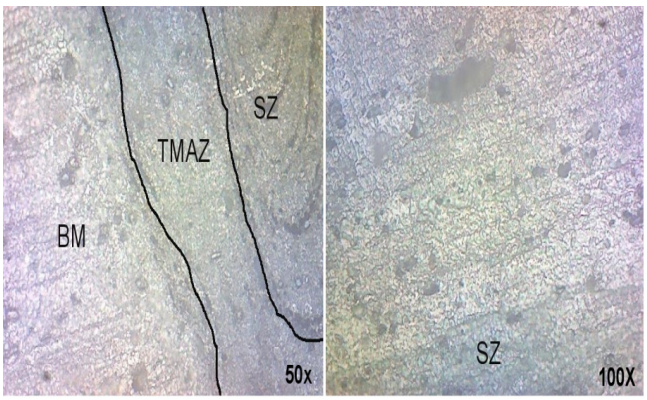


Fig. 8. Micro structure of FSW AA 6082 -TiC alloy

The SEM micrographs of the friction stir welded specimen are shown in Figure 9. The distribution of TiC particles is fairly homogeneous in the stir zone. The light regions in the macrostructure (Figure 9) exhibit bands of TiC particles. The grains are not clearly visible in Figure 9 because they are ultrafine in nature.The grain modification can be attributed to the presence of TiC particles in the joint because TiC particle acted as an effective grain refiner. The stirring action of the tool and the intense plastic strain were known to break the ceramic particles.TiC particles retained the original size and morphology which can be attributed to their initial smaller size. This result agrees with the findings of Chen et al. [20] who did not observe fragmentation of

B_4C particles in FSWof AA6063/ B4C AMC due to its smaller size.

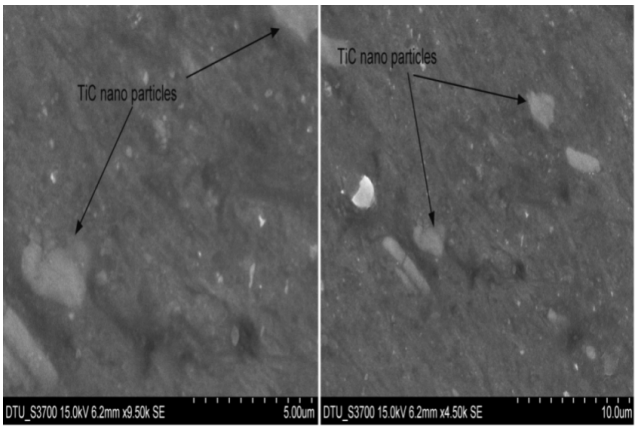


Fig. 9. SEM micro graph of FSW AA66082-TiC joint

The chemical compositions of the matrix and titanium carbide particles of the weld nugget were analysed by a scanning electron microscope equipped with an energy dispersive X-ray spectroscopy (EDX) analysis system. This analysis indicates that distribution of TiC particles is uniform in weld nugget zone.

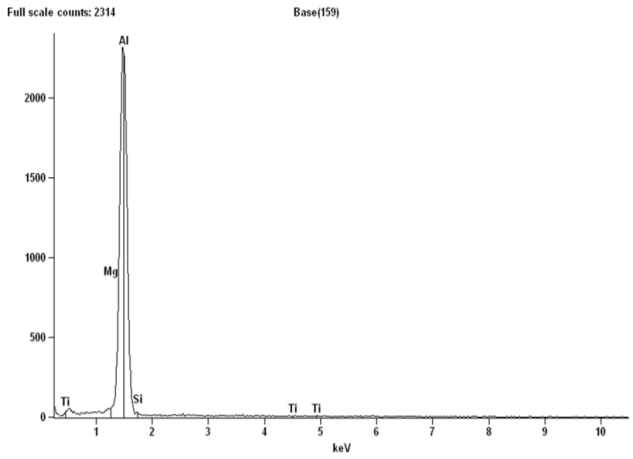


Fig. 10. EDX analysis graph

4. CONCLUSIONS

An AA6082–T651 alloy was friction stir welded, using different welding parameters, and the effects of this process on microstructure, tensile and micro-hardness were investigated.

1. Rotational speed is the factor that has greater influence on tensile strength, followed by welding speed and Shoulder diameter to pin diameter ratio.
2. Tensile strength at optimum condition were lower in small quantity as compare to the parent material due to presence of reinforcement particles which make the metal matrix brittle.
3. Micro hardness at optimum condition was higher in small quantity as compare to the parent material due to grain refinement.
4. Welding of AA6082 results in softening in the SZ and TMAZ being more significant. This negative effect on the welded joints strength and hardness can be partially recovered by inclusion of TiCnano particles during welding.
5. Microstructural and SEM analysis clearly indicate that distribution of TiCnano particles is homogenous in Stir zone (SZ).

REFERENCES

[1] Root J.M.; Field D.P.; Nelson T.W.; Crystallographic texture in the friction-stir welded metal matrix composite Al6061 with 10 Vol % Al_2O_3.Metallurgical and Materials Transactions A, 2009, 40 2109–2114.

[2] Chidambaram A.; Bhole S.D.; Metallographic preparation of aluminum–alumina metal matrix composites. Materials characterization, 1997, 38, 187–91.

[3] Key property data for AMC's products. Available from: www.amcmmc.co.uk.

[4] Storjohann D.; Babu S.S.; David S.A.; Sklad P. Report on U.S. Department of Energy, Office of Heavy Vehicle Technology and Office of Transportation under contract number DE-ACO5-000R22725 with UT-Battelle LLC, 2002, 1–4.

[5] Clyne T.W.; Withers P.J.; An introduction to metal matrix composites. Cambridge University Press, 1993.

[6] Lean P.P.; Gil L.; Urefia A.; Dissimilar welds between unreinforced AA6082 and AA6092/SiC/25p composite by pulsed-MIG arc welding using unreinforced filler alloys (Al–5Mg and Al–5Si). Journal of Materials Processing Technology, 2003, 143–144.

[7] Spowart J.E.; Zong-Yi, M.; Mishra R.S.; The effect of friction stir processing (FSP) on the spatial heterogeneity of discontinuously reinforced aluminum (DRA) microstructures, Friction stir welding and processing II. TMS Publication, 243–52.

[8] Wert J.A. Microstructures of friction stir weld joints between an aluminium base metal matrix composite and a monolithic aluminium alloy, ScriptaMaterialia, 2003, 49, 607–12.

[9] Femandez G.J.; Murr L.E. Characterization of tool wear and weld optimization in the friction-stir welding of cast aluminium 359 + 20% SiC metal–matrix composite. Materials Characterization, 2004, 52, 65–75.

[10] Nakata K.; Inoki S.; Nagano Y.; Ushio M. Friction stir welding of Al_2O_3 particulate 6061 Al alloy composite. Material Sciemce Forum, 2003, 426-432.

[11] Gibsona B.T.; Lammlein D.H.; Prater T.J. et al. Friction stir welding: Process, automation, and control. Journal of Manufacturing Processes, 2014, 16, 56–73.

[12] El-Danaf E.A.; El-Rayes M. M.; Microstructure and mechanical properties of friction stir welded 6082 AA in as welded and post weld heat treated conditions. Materials and Design, 2013, 46, 561–572.

[13] Ericsson M.; Sandstrom R.; Influence of welding speed on the fatigue of friction stir welds, and comparison with MIG and TIG. International Journal of Fatigue, 2003, 25, 1379–87.

[14] Koumoulos E.P.; Charitidis C.A.; Daniolos N.M.; Pantelis D.I.Nanomechanical properties of friction stir welded AA6082-T6 aluminum alloy. Materials Science and Engineering B, 2011, 176, 1585– 1589.

[15] Scialpi A.; Filippis L.A.C.; Cavaliere P. Influence of shoulder geometry on microstructure and mechanical properties of friction stir welded 6082 aluminium alloy, Materials and Design, 2007, 28, 1124–29.

[16] Cavaliere P.; De Santis A.; Panella F.; Squillace A. Effect of welding parameters on mechanical and microstructural properties of dissimilar AA6082–AA2024 joints produced by friction stir welding. Materials and Design, 2009, 30, 609–16.

[17] Liu H.J.; Hou J.C.; Guo H. Effect of welding speed on microstructure and mechanical properties of self-reacting friction stir welded 6061-T6 aluminum alloy. Materials and Design, 2013, 50, 872–78.

[18] El-Rayes M.M.; El-Danaf E.A.; The influence of multi-pass friction stir processingon the microstructural and mechanical properties of Aluminum Alloy 6082, Journal of Materials Processing Technology, 2012, 212, 1157–68.

[19] Amirizad M.; Kokabi A.H.; AbbasiGharacheh M.; Sarrafi R.; Shalchi B.;Azizieh M. Evaluation of microstructure and mechanical properties in friction stir welded A356 + 15% SiCp cast composite. Materials Letters, 2006, 60, 565–8.

[20] Chen X.G.; Silva M. Da, Gougeon P.; St-Georges L. Materials Science and Engineering A. 2009, 518, 174–184.

Research Article Adv. Mater. Lett. 2016, **7**(10), 806-812 Advanced Materials *Letters*

www.vbripress.com/aml, DOI: 10.5185/amlett.2016.6204 Published online by the VBRI Press in 2016

Morphology control in the bulk heterojunction blend of inverted organic solar cell via co- solvent addition

Sarita S Nair, D Kumar*

Department of Applied Chemistry & Polymer Technology, Delhi Technological University, (Formerly Delhi College of Engineering), Shahbad Daulatpur, Bawana Road, Delhi 110042, India

*Corresponding author. Tel: (+91) 9811425817; E-mail: dkumar@dce.ac.in; drdkumar@yahoo.co.uk

Received: 07 October 2015, Revised: 08 February 2016 and Accepted: 25 May 2016

ABSTRACT

This work is supposed to expand the concept of solvent induced crystallisation of donor poly(3-hexylthiophene) (P3HT) polymer, to the photoactive blend of inverted organic solar cells. With the optimised concentration of cyclohexanone (CHN) co-solvent and ageing period of 2 h for the active layer precursor solution, the power conversion efficiency of a typical device increased to 3.09% compared with 2.77% efficiency achieved in a similar kind of inverted device without CHN modification. This improvement of 10% in the efficiency of inverted device with CHN addition was related to the increased current density and fill factor of the device. Increased P3HT crystallinity for efficient photo-absorption and commensurate vertical concentration gradient observed in the P3HT fractions of the blend for efficient hole transport is possibly responsible for the betterment of the photovoltaic parameters in the modified device. Copyright © 2016 VBRI Press.

Keywords: Crystallisation; morphology; inverted organic solar cell; non-solvent.

Introduction

The advent of bulk heterojunction (BHJ) concept in the photoactive layer composed of conjugated polymer donor and soluble fullerene acceptor extends the advantage of thicker photoactive layer implementation in organic solar cells (OSCs). And, unlike their inorganic counterparts, organic materials with strongly bounded electron-hole pair (excitons) require external driving force for excitons separation and charge generation. So, such a model with intermixed domains also presents extended interfacial area between the blended photoactive nanophases for bulk separation of photo generated excitons [**1**]. The photoactive blend of poly(3-hexylthiophene) (P3HT) donor and [6, 6]-phenyl C_{61}-butyric acid methyl ester (PCBM) acceptor has been one of the most interesting systems proposed for photocurrent generation. In the recent past, there has been a great boost in the efficiency of OSC utilizing this donor-acceptor mixture in the photoactive layer [**2**]. One of the key parameters that is under continuous investigation is the morphology transformation in this donor-acceptor pair with the changes in processing parameters for further possible improvements in the performance of devices prepared thereof. Optimum morphology pertaining to the donor-acceptor pair is the one where there is steady equilibrium between the crystallinity (molecular ordering) within each phase and nanoscale phase separation between intermixed domains [**3, 4**]. Definite order in the donor and acceptor moieties is responsible for photo absorption and carrier mobility. And, bi-continuous interphases in between the nanoscale donor-acceptor interpenetrating domains provide successful exciton dissociation and bi-directional pathways for carriers transport to their analogous electrodes [**5**].

Solution processing practice for active layer preparation in OSC allows manipulation over several parameters including blending ratios of the two components, solvent system employed, post treatments such as thermal and solvent annealing etc., for modifying the photoactive layer morphology [**6**]. Though, post treatment methods such as solvent vapour annealing and thermal annealing have been doing well to improve the morphology and hence, the efficiency in OSCs. However, such methods may not prove to be effective for large scale manufacturing practice. On the other hand, solvent system employed for preparing active layer spin coating solution has an immense effect on the morphology of the thin film casted thereof. Earlier practice was to have a single solvent dissolving both the components of the blend. Such a system though may seem simple in practice however, is associated with the complications of interference from one component in the crystallisation process of the other component in the blend. And since, different materials have different solubility in a particular solvent, so single solvent may not be sufficient to serve the desired purpose.

Recently, solvent-co-solvent mixture approach has been successfully adopted to get the desired morphology. In such an approach, apart from the main solvent dissolving both the components equally, second solvent is introduced which offers limited solubility to one of the component (predominantly P3HT component) [**7**]. Accordingly, this solvent-non-solvent system can keep the PCBM well dissolved in the solution mixture so, that undissolved P3HT chains start to crystallise first in the solution itself without being interfered by the completely dissolved component (PCBM). So far, this approach of solvent-non-solvent mixture has been put to practice for modifying the morphology of the active layer in normal OSCs [**8**]. However, declining future of the normal architecture in OSCs due to its instability and degradation from oxygen

 Copyright © 2016 VBRI Press

and moisture of the atmosphere shifted the interest towards its inverted configuration. This instability is caused by the presence of low work function reactive metal like aluminium at the top interfacing with the air in the normal architecture. Replacement of low work function metal by a high work function metal like silver (Ag) or gold (Au) can act to stabilize the system as a whole from the detrimental effect of moisture or air [**9**]. **Fig. 1** represents layer sequence in inverted configuration of OSC.

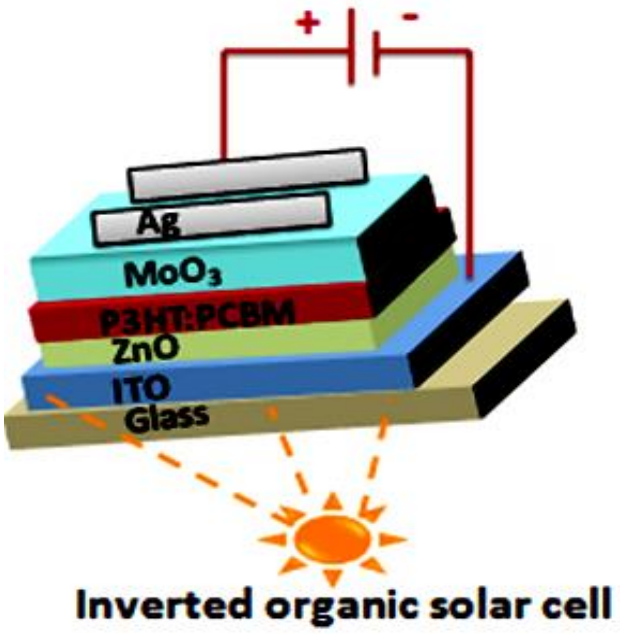


Fig. 1. Schematic illustration of the layer sequence in inverted configuration of organic solar cell.

We considered studying in detail the co-solvent addition during the preparation of active layer in inverted OSCs. The effect of co-solvent addition on the parameters crucial to device performance was studied. Solvent-cosolvent mixture method works by dissolving one component (mostly PCBM) of the blended mixture, avoiding interference of this component in the crystallisation process of the other component (i.e., P3HT donor polymer). As, there have been very limited studies on morphological modification of the active layer in inverted OSC via solvent mixture approach so, we considered carrying out a comprehensive study on the effect of ortho-dichlorobenzene (o-DCB)-cyclohexanone (CHN) solvent mixture on P3HT-PCBM layer in inverted OSC. This effect is worth studying, as the underlying and overlying layers positioned with the active layer in inverted configuration will cause the P3HT-PCBM mixture to behave differently from that of the normal OSCs to the solvent mixture modification.

Experimental

Materials

Poly(3-hexylthiophene) (P3HT) polymer and [6, 6]-phenyl C_{61}-butyric acid methyl ester (PCBM) were acquired of Sigma Aldrich. Solvents ortho-dichlorobenzene (o-DCB) and cyclohexanone (CHN) used in this study were of analytical research grade and were also obtained from Sigma Aldrich. Indium tin oxide (ITO) coated glass substrates (5 × 5 cm sizes) with sheet resistance of less than 20 Ω/sq were obtained from Moserbaer India Ltd. Zinc acetate dihydrate, ethanolamine and 2-methoxyethanol for zinc oxide (ZnO) preparation also from Sigma Aldrich were used as received. Molybdenum oxide (MoO_3) and silver (Ag) wire were purchased from Central Drug House (CDH).

Methods

Constituent layer structure in inverted polymer solar cells comprises of ITO/ ZnO/ P3HT: PCBM/MoO_3/Ag. ITO coated glass substrates were first patterned using a diode-pumped Q-switch neodymium-doped yttrium aluminium garnet (Nd:$Y_3Al_5O_{12}$, Nd:YAG) laser scriber at its fundamental wavelength (λ=1047nm) and laser power of 1.0 W and cleaned thereafter via ultrasonication for 20 min each in a soap solution at 50 °C, demineralised water, acetone and isopropanol in succession. The cleaned substrates were then dried using nitrogen and treated further for 26 min in an UV-ozone chamber. Firstly, a ZnO (30 nm) layer was deposited on ITO using a 0.50M ZnO solution prepared by mixing (0.46 g) zinc acetate dihydrate with ethanolamine (stabilizer) and 2-methoxyethanol (solvent). Subsequent curing of the deposited ZnO layer was carried out at 250 °C for 10 min in air. Active layer spin coating solution was prepared by dissolving 18.7 mg of P3HT polymer and 11.3 mg of PCBM in 1 ml of good solvent i.e., o-DCB by means of stirring overnight at 50 °C on a hot plate. For active layer modification, cyclohexanone (CHN) co-solvent (5 volume %) was added to the above prepared active layer spin coating solution and stirred further for 2 h. Active layer (140 ± 10 nm thick) was then spin coated at 600 rpm for 2 min using this solution and deposited layer was cured at 85 °C for 30 min. Thereafter, 7 nm thick molybdenum oxide (MoO_3) and 150 nm thick silver (Ag) layers were thermally deposited at a deposition rate of 0.5Å s^{-1} and 1.0 Å s^{-1} respectively, in a vacuum chamber maintained at a base pressure of 5×10^{-6} mbar. Final photovoltaic devices with an active area of 0.09 cm^2 were prepared with and without co-solvent modification in the active layer. And, a comparison of the performance of these devices with and without co-solvent modification was made.

Measurements

Device preparation was carried out in the nitrogen environment within a glove box from Jacomex with ΔP = 3.0 mbar & oxygen level of 0.3 ppm. The current density (J)–voltage (V) characteristics of the photovoltaic devices were measured using a Keithley Model 2420 source meter under a solar simulator (Model SS150AAA Photo Emission Technology Inc.) equipped with AM 1.5 G filter and with an illumination intensity of 100 mW cm^{-2}. The UV–visible absorption measurements were carried out using a Perkin Elmer lambda 35 UV–visible spectrophotometer. Surface morphology studies were done using atomic force microscope (AFM), VEECO DI-3100, with Nanoscope (III) in tapping mode. Grazing incidence X-ray diffraction (GI-XRD) measurements were done using Rigaku ultima IV X-ray diffractometer (λ=1.54 Å) with

Copyright © 2016 VBRI Press

Cu-Kα radiation source at grazing incidence angles of 0.11^0 and 0.3^0.

Results and discussion

Effect of ageing of precursor solution

P3HT:PCBM blend solution in solvent-non solvent mixture was known to undergo P3HT aggregation in a way similar to pure P3HT bulk solution in a non-solvent or marginal solvent. The aggregation of P3HT is known to take place by transition of P3HT from coil to extended rod owing to its solvophobic interaction with a marginal solvent followed by π-π stacking of the extended chains [**10**]. Aggregation can be stated in terms of disordered to ordered transformation of crystallising P3HT chains in a marginal solvent. Co-solvent used in our case is cyclohexanone solvent (CHN). CHN solvent is a marginal solvent for P3HT offering limited or lesser solubility to P3HT chains and more solubility to PCBM aggregates. Aggregation kinetics of P3HT in P3HT-PCBM blend solution in o-DCB-CHN solvent will be different from the aggregation of P3HT chains in pure P3HT bulk solution due to interference from the dissolved PCBM portions in the former [**11**]. Such an aggregation in P3HT-PCBM solution on marginal solvent addition is marked by increased absorption and enhanced P3HT crystallinity with subsequent changes in the colour of the solution from orange to purple. This process of aggregation is more recognizable with ageing i.e., storing the solution for a sufficient time at room temperature, manifested by increased viscosity and darkening of solution colour due to increasing amount of non-dissolved P3HT portions in the solution [**12**]. However, longer ageing and higher percentage of co-solvent can bring about gelling of the solution thus, making the solution incompatible for the spin coating operation [**13**]. So, an optimisation of the ageing phase and co-solvent amount is prerequisite for successful preparation of the active layer.

The absorption spectra of P3HT-PCBM films casted from o-DCB-CHN solvent mixture aged for various time was observed **(Fig. 2a)** for evaluating the dependence of ageing time on aggregation and subsequent absorption improvements. The absorption spectra of the films were characterized by a main peak around 512 nm, with two "shoulders" towards the higher wavelength region. The main peak is the characteristic of intrachain transitions in P3HT chains promoting decreased chain entanglement. Absorption shoulders towards higher wavelength are related to extended chain length absorption and interchain lamella stacking [**14**]. With ageing, these spectral features were found to be more pronounced. From the absorption spectra, it's been clear that there is considerable improvement in absorption with ageing for 1 h to 4 h at room temperature indicating evolution of ordered P3HT structures with ageing. However, a decrease in the absorption was noticed in the solution aged for 5 h possibly due to larger aggregate formation with no more advancement towards P3HT ordered arrangement [**15**]. Again, the difference in absorption intensity between 2, 3 and 4 h aged solution was modest. So, for our study we optimised the ageing period to 2 h, as longer treatment time may not be a feasible idea for large scale production practice.

To gain better insight on the effect of ageing and crystallinity improvement upon ageing, grazing incidence X-ray diffraction (GI-XRD) measurements were carried out for P3HT-PCBM films at a grazing incidence angle of 0.3^0 **(Fig. 2b).** GI-XRD can provide valuable information about the crystallinity of P3HT in the blend film. A relative indication of crystallinity in P3HT: PCBM films casted from precursor solution aged for different times (1-5 h) was analysed by comparing the (100) reflection peak intensities observed at 2θ value of 5.426^0. 2 h aged precursor solution with highest (100) peak intensity signifies most ordered P3HT arrangements [**16**]. Also, equally intense higher order diffractions in films prepared from 2h aged solution suggest higher crystallinity and self organisation ability in the blend film. So, aging time could be used as a management control towards attaining highly oriented crystals of P3HT in P3HT-PCBM blend films via solvent mixture approach. Such a molecularly ordered film of P3HT-PCBM can be taken advantage of, as an active layer of OSCs.

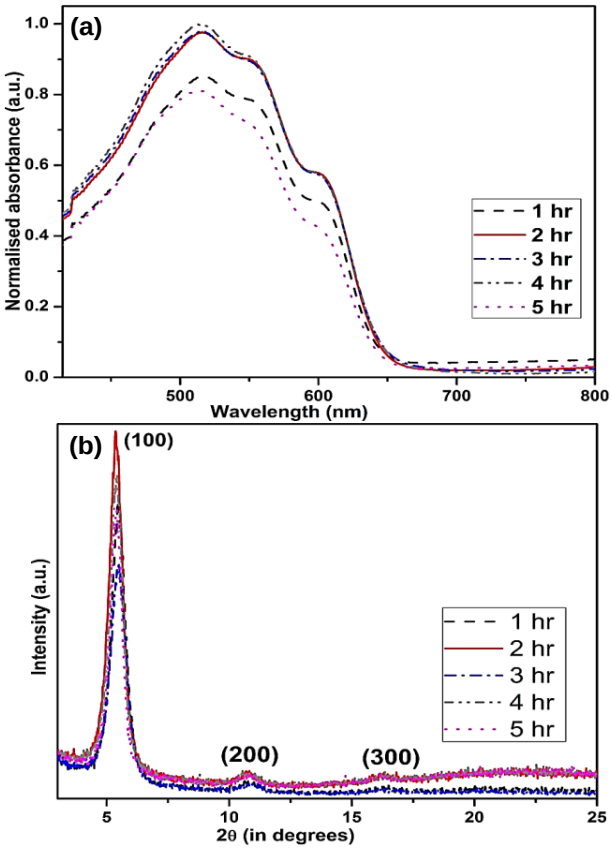


Fig. 2. (a) Absorption spectra of P3HT-PCBM films casted of precursor solutions aged for different times in o-DCB-CHN mixture (b) Out of plane GI-XRD patterns for P3HT-PCBM films casted of precursor solutions aged for different times in o-DCB-CHN mixture.

Again, the amount of marginal solvent was also optimised to be 5 volume %. As, lesser amount than this could not bring about significant crystallisation in the blend film. And also, larger amount of the CHN co-solvent would result in greater non-dissolved P3HT crystallites in the

Copyright © 2016 VBRI Press

precursor solution and subsequent gelling of the solution on keeping the same for few hours. So, using the optimised ageing time (2 h) and co-solvent amount (5 volume %), the effect of introducing this modified P3HT-PCBM layer as active layer in inverted OSC was further considered.

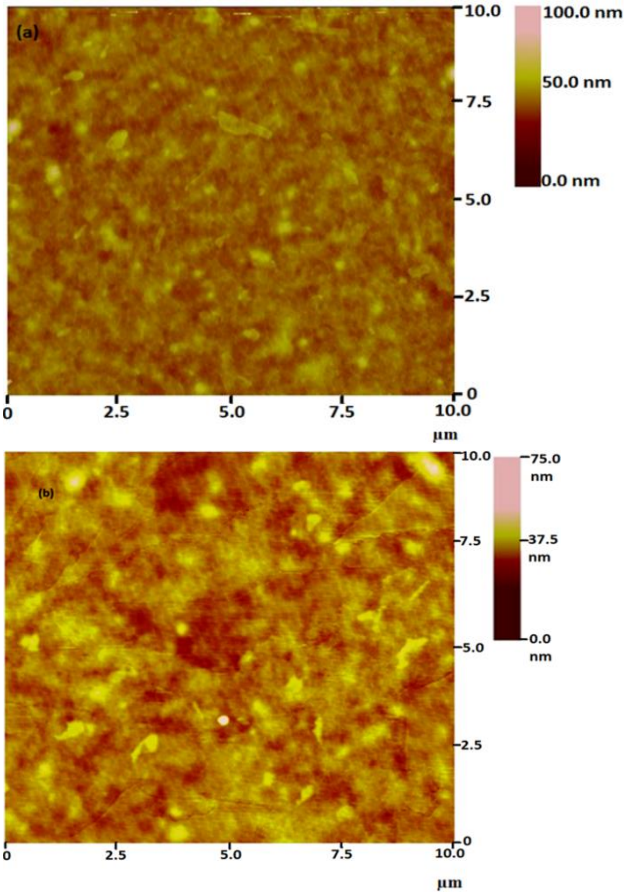


Fig. 3. Tapping mode AFM image scans (10 ×10 µm) of P3HT: PCBM films (a) Without any modification (b) with CHN modification.

Morphological characterization

Morphological studies of P3HT-PCBM layer casted with and without CHN addition was carried out using tapping mode atomic force microscopy (AFM). **Fig. 3 a, b** shows the topographical AFM image of P3HT-PCBM film without any modification and with CHN modification, respectively. Surface images show significant dependence of film morphology on the solvent mixture used to dissolve the blend materials. In a conventional film with single good solvent (o-DCB) dissolving both the components of the mixture, no clear separation between P3HT (brighter region) and PCBM (darker regions) phases was noticeable. Such a homogenous feature all through the conventional film could possibly be resulting from co-precipitation of both components from the mixture at the same time. However, with CHN addition, the extent of phase separation between two components seems to be improved. Such a phase separation could be a result of preferential crystallisation and aggregation of P3HT component directing further demixing of the phases on spin casting and subsequent annealing [**17**]. Such a lateral phase separation between the components of the blend at all depths of the film is required for efficient dissociation of the photoinduced exciton for charge generation. So, CHN addition seems to be beneficial in giving the blend film the desired morphology.

UV-visible absorption measurements

The analysis of absorption spectra of P3HT-PCBM films in the visible range was carried out to see the effect of CHN addition on the relative light absorption properties and crystal structure arrangement of P3HT chains in the active layer. **Fig. 4** shows the comparative UV-visible absorption spectrum of P3HT-PCBM layer spin coated from a solution with and without CHN modification. As discussed previously, absorption spectra show one main peak around 512 nm and two absorption shoulders in the lower energy region corresponding to absorption by the highly organized solid P3HT aggregates. Upon CHN addition, a slight shift in the peak to higher wavelength side and an equivalent increase in intensities of main absorption peak and low energy vibronic bands were observed. Absorption spectrum of the modified film reveals growth of more well ordered P3HT crystals. This well controlled growth in P3HT crystals is supported by coil to extended rod spontaneous transition induced by decreased polymer-poor solvent interaction. This transformation follows on to aggregation in polymer domains by stronger π-π interaction set among these extended P3HT chains [**18**]. However, in a conventional P3HT-PCBM film casted of a single good solvent (o-DCB), such a transformation is not very feasible due to well dissolved P3HT chains in o-DCB.

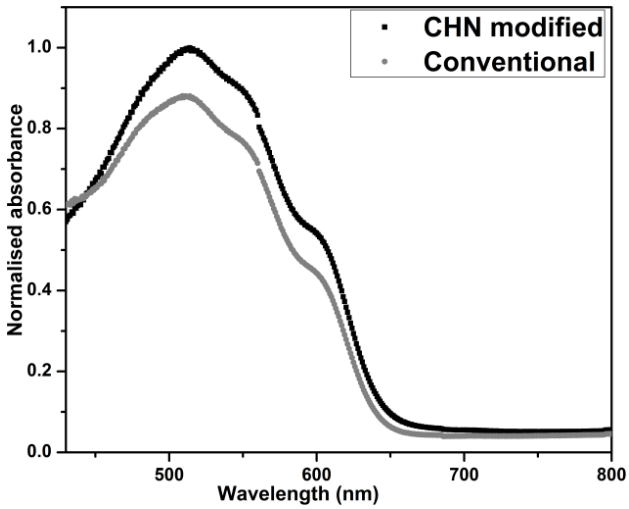


Fig. 4. Absorption spectra of P3HT-PCBM films with and without co-solvent modification.

Grazing incidence x-ray diffraction (GI-XRD) measurements

To substantiate the effect of CHN addition on the crystalline structure and molecular ordering in the active layer of inverted OSC, GI-XRD measurements were carried out on spin coated films of P3HT-PCBM. For outlining the structural characteristics through the depth profiling of the P3HT-PCBM thin film, GI-XRD measurements were carried out at two grazing incidence angles. Considering some recent papers reporting GIXRD measurements using

 Copyright © 2016 VBRI Press

lab instruments for stronger scattering films, we determined on carrying out depth profiling of the P3HT-PCBM thin film with our laboratory source GI-XRD instrument [19]. At grazing incidence angle less than the critical angle for P3HT-PCBM film (i.e., at 0.11^0), total exterior reflection takes place with X-ray penetrating to merely ~10-12 nm underneath the surface of the film. So, diffraction patterns at 0.11^0 grazing incidence angle consist of reflections mainly occurring from the interlayer spacing between P3HT crystallites present at the surface of the film [20]. While, keeping incidence angle greater than the critical angle for P3HT-PCBM film and less than the critical angle of the substrate (i.e., at 0.3^0), X-ray can be made to penetrate the entire thin film. So, at 0.3^0 grazing incidence angle, reflections from the whole bulk of the film can be obtained.

Fig. 5(a, b) depicts the X-ray diffractograms of the P3HT-PCBM film at two grazing incidence angles 0.11^0 and 0.3^0, respectively. Interlayer distances (d) and crystallite sizes of P3HT domains calculated of the (100) diffraction peaks are given in **Table 1**. Crystallite sizes are calculated using the Scherrer's formula via taking in to account the peak broadening in the corresponding diffraction patterns.

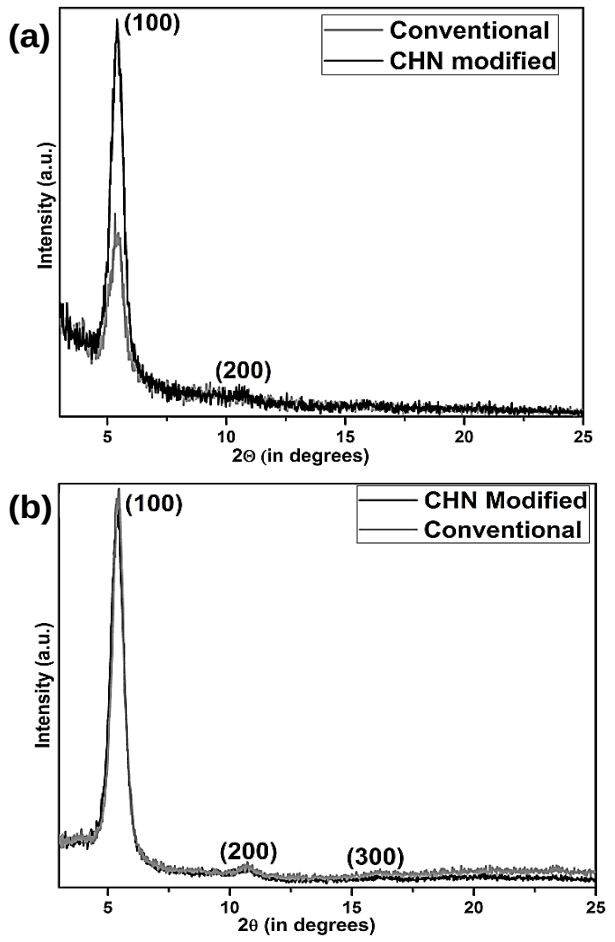


Fig. 5. (a) Grazing incidence X-ray diffraction (GI-XRD) profiles of P3HT: PCBM composite films with and without CHN modification at grazing incidence of 0.11^0 (b) GI-XRD profiles of films at grazing incidence of 0.3^0.

$T = K\lambda/\beta \cos\theta$ where, β = full width half maximum (FWHM), λ = wavelength of X-ray (1.54 Å) and T = crystallite size. Both the diffractograms mainly show three peaks corresponding to reflections from (100), (200) and (300) axis orientation of lamellar P3HT chains [**21**].

Table 1. Summary of interlayer distances (d) and the size of P3HT crystallites determined of the (100) diffraction peak at two grazing incidences 0.11^0 and 0.3^0 in the XRD pattern.

S.No.	Device	Grazing incidence angle(degree)	2θ value (degree)	Interlayer distance d_{100}(Å)	FWHM	Grain size (nm)
1.	Cyclohexanone modified	0.11°	5.4	16.27	0.608	13.0
2.	Cyclohexanone modified	0.3°	5.3	16.48	0.654	12.02
3.	Conventional	0.11°	5.4	16.29	0.654	12.03
4.	Conventional	0.3°	5.4	16.37	0.585	13.44

A comparison of the (100) reflection peak intensities at 0.11^0 grazing incidence angle from unmodified and CHN modified P3HT-PCBM films were done to analyse the crystalline characteristic of P3HT phase at the film surface. An increase in the intensity of (100) reflection peak observed at $2\theta = 5.426^0$ in the CHN modified film as compared to unmodified film signifies higher level of ordering and orientation of P3HT chains at the surface of the film upon CHN addition. However, much difference was not noted in the higher order diffraction peaks of the two films or these peaks were very less pronounced as only a transient beam of X-ray was made to fall on a smaller depth of P3HT-PCBM film at 0.11^0 incidence. A comparison of the crystallite sizes and interlayer spacing between P3HT chains reveals larger well developed closely spaced P3HT crystallites in CHN modified sample as compared to limitedly crystallised smaller crystallites at the surface of unmodified sample. The reason for such a distinctive feature observed with mixed solvent approach is associated with the CHN (poor solvent for P3HT) induced preferential self assembly of P3HT in the good solvent-poor solvent mixture [**22**].

Again, a comparison of (100) diffraction peak intensity at grazing incidence angle of 0.3^0 revealed slightly more number of better crystallised P3HT domains in the bulk of conventional unmodified film as compared to CHN modified P3HT-PCBM film. Higher order diffraction peaks (200) and (300) were also more pronounced in the bulk of the conventional unmodified sample than the CHN modified sample. As, the blend films with the identical thickness and concentration have same number of P3HT chains so, it can be stated that solvent-non solvent mixture method not only brings about the preferential crystallisation of P3HT domains but also, stimulates upward distribution of P3HT fractions. Although, it is known that in a solution processing technique such as spin coating the P3HT fractions with the lower surface energy factor have a tendency to occupy surface of the film [**23**]. Such a probability is however, found to be more enhanced with the practice of solvent-non solvent mixture for spin coating. This vertical concentration gradient in the blend film with CHN modification must benefit the inverted device prepared thereof with the modified P3HT-PCBM layer being employed as active layer for photoabsorption. As more crystallised P3HT domains occupy the surface of the active layer in contact with the MoO_3 (hole transporting

Copyright © 2016 VBRI Press

layer, HTL) layer with CHN modification, hole transport to the silver anode would be enhanced. In addition, leakage current due to wrong carrier ion transport to anode would be minimised. GI-XRD measurement thus confirms favourable vertical concentration gradient of P3HT fractions with CHN addition.

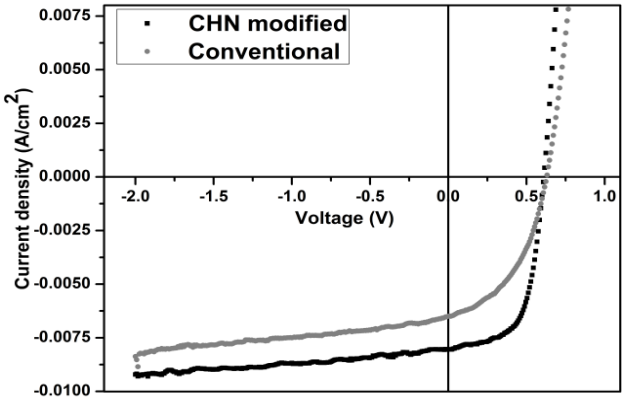


Fig. 6. Current density-voltage (J-V) characteristic of devices fabricated with and without co-solvent modification in the active layer under AM 1.5 G white light illumination.

Photovoltaic characteristics

We then fabricated an inverted device with layer sequence of Glass/ITO/ZnO/P3HT-PCBM/MoO_3/ Ag, to consider the effect of CHN addition to the active layer spin coating solution on the photovoltaic characteristic of the prepared device. Each photovoltaic device consists of four cells each with an active area of 0.09 cm^2 and device properties were measured under an illumination intensity of 100 mW cm^{-2}, AM 1.5 G condition. **Fig. 6** compares the current density-voltage (J-V) characteristics of the devices prepared with and without CHN modification to the active layer spin coating solution. Photovoltaic parameters of the as prepared inverted devices are summarised in **Table 2**.

Table 2. Summary of photovoltaic device parameters for ITO/ZnO/ P3HT: PCBM/MoO_3/Ag polymer solar cell under AM 1.5 G white light illumination, with and without CHN modification in the active layer preparation.

[b]Substrate	Cell No.	Device	V_{oc} (V)	J_{sc} (Acm^{-2})	FF	%E	R_{sh} (Ωcm^2)	R_s (Ωcm^2)
1	1	[a]cyclohexanone modified	0.61	8.04E-03	0.61	3.01	700	12
1	2	cyclohexanone modified	0.61	8.14E-03	0.62	3.09	600	12
1	3	cyclohexanone modified	0.62	7.94E-03	0.61	3.00	1167	12
1	4	cyclohexanone modified	0.62	7.62E-03	0.64	3.01	1391	12
2	1	[a]Conventional	0.61	7.41E-03	0.61	2.77	1123	14
2	2	Conventional	0.61	7.66E-03	0.58	2.72	634	15
2	3	Conventional	0.61	7.45E-03	0.60	2.74	489	13
2	4	Conventional	0.62	7.28E-03	0.60	2.69	654	14

[a]Conventional device = Device prepared with active layer casted from a good solvent (O-DCB).
Cyclohexanone modified= Device prepared with active layer modified by cyclohexanone addition
[b]Substrate is a 5cm × 5cm ITO glass substrate with inverted cell layer sequence comprising 4 cells each of area 0.09 cm^2.

It can be observed that conventional photovoltaic device fabricated with active layer casted from a single good solvent showed a power conversion efficiency (PCE) of 2.77% resulting from the short circuit current density (J_{sc}) of 7.41E-03 A cm^{-2}, open circuit voltage (V_{oc}) of 0.61 V and fill factor (FF) of 0.61. However, o-DCB-CHN mixed solvent casted active layer in a typical inverted device could result in a PCE of 3.09% with a J_{sc} value of 8.14E-03 A cm^{-2}, V_{oc} of 0.61V and FF of 0.62. The resulting increase in efficiency from 2.77% to 3.09% with the addition of poor solvent (CHN) to the main solvent (o-DCB) during the preparation of active layer precursor solution could possibly be due to the increase in the photocurrent generation and increasing fill factor of the device. Improved crystallisation in the polymer donor domains evident of the UV-vis and GI-XRD measurements could be the reason for realising increased current density in the modified devices [**24**].

Favourable upright concentration gradient must have brought about the observed increase in the FF of the device. As the fractions of P3HT close to the HTL layer increases, series resistance in the device decreases and smoother efficient pathway for hole transport must be set in. So, CHN addition in the active layer preparation of inverted OSC benefits the device prepared thereof in two ways. Firstly, by improved crystallisation of the donor polymer for enhanced photo absorption and hole transport and secondly, by setting up a favourable upright concentration gradient in the active layer with better crystallised P3HT at the top in close contact with HTL for efficient hole transport to anode.

Conclusion

This work described the optimisation of amount of non-solvent added and ageing period of the precursor solution for obtaining the best possible crystallisation in the donor phase. Increasing the ordering in the precursor solution by addition of poor solvent (cyclohexanone) enhances appreciably the crystallinity and order in the P3HT-PCBM films compared with films prepared from disordered precursor solution. Practice of the CHN modified P3HT-PCBM film as active layer of inverted OSC improves the PCE to a value of 3.09% as compared to 2.77% in the unmodified device. This improvement was related to the increased current density and fill factor of the device with CHN addition. Characteristics of well ordered donor phase in the active layer and favourable concentration gradient with encouraging distribution of donor domains closer to hole transport layer are introduced to the inverted OSC via CHN addition.

Acknowledgements

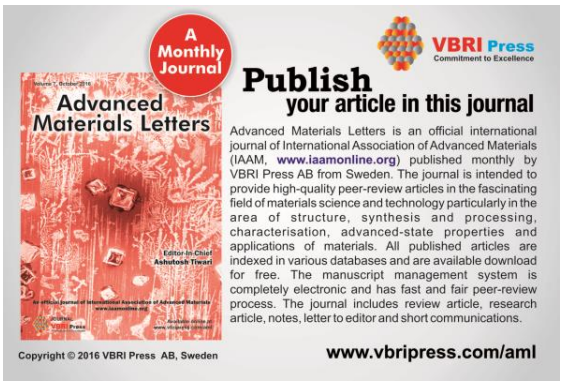
Authors are thankful to Prof. Pradeep kumar, Vice-Chancellor, Delhi Technological University, Delhi for encouragement and support. A financial support to one of the author, Sarita is also acknowledged gratefully. The authors are also grateful to Moserbaer India Ltd. for their assistance in performing the experiment and characterization.

References

1. Halls, J.J.M.; Walsh, C.A.; Marseglia, E.A.; Friend, R.H.; Moratti, S.C. and Holmes, A.B., *Nature*, **1995**, *376*, 498. **DOI:** *10.1038/376498a0*
2. Thompson, B.C. and Frechet, J.M.J., *Angew Chem. Int. Ed.*, **2008**, *47*, 58. **DOI:** 10.1002/anie.200702506
3. Chen, L.-M.; Hong, Z.; Li, G. and Yang, Y., *Adv. Mater*., **2009**, *21*, 1434. **DOI:** 10.1002/adma.200802854
4. Wang, Y.; Wei, W.; Liu, X. and Gu, Y., *Sol. Energy Mater. Sol. Cells*, **2012**, *98*, 129. **DOI:** 10.1016/j.solmat.2011.10.003

 Copyright © 2016 VBRI Press

5. Hoppe, H.; Niggemann, M.; Winder, C.; Kraut, J.; Hiesgen, R.; Hinsch, A.; Meissner, D. and Sariciftci, N.S., *Adv. Funct. Mater.*, **2004**, *14*, 1005.
DOI: 10.1002/adfm.200305026
6. Li, G.; Shrotriya, V.; Yao, Y.; Huang, J. and Yang, Y., *J. Mater. Chem.*, **2007**, *17*, 3126.
DOI: 10.1039/B703075B
7. Reisdorffer, F.; Haas, O.; Le Rendu, P. and Nguyen, T.P., *Synth. Met.*, **2012**, *161*, 2544.
DOI: 10.1016/j.synthmet.2011.08.005
8. Yusli, M.N.; Yun, T.W. and Sulaiman, K., *Mater. Lett.*, **2009**, *63*, 2691.
DOI: 10.1016/j.matlet.2009.09.044
9. Zhang, F.; Xu, X.; Tang, W.; Zhang, J.; Zhuo, Z.; Wang, J.; Wang, J.; Xu, Z. and Wang, Y., *Sol. Energy Mater. Sol. Cells*, **2011**, *95*, 1785.
DOI: 10.1016/j.solmat.2011.02.002
10. Xu, W.; Li, L.; Tang, H.; Li, H.; Zhao, X. and Yang, X., J. Phys. Chem. B, **2011**, *115*, 6412.
DOI: 10.1021/jp201044b
11. Liu, J.; Shao, S.; Wang, H.; Zhao, K.; Xue, L.; Gao, X.; Xie, Z. and Han, Y., *Org. Electron.*, **2010**, *11*, 775.
DOI:10.1016/j.orgel.2010.01.017
12. Bielecka, U.; Lutsyk, P.; Janus, K.; Sworakowski, J. and Bartkowiak, W., *Org. Electron.*, **2011**, *12*, 1768..
DOI: 10.1016/j.orgel.2011.06.027
13. Huang, W.Y.; Huang, P.T.; Han, Y.K.; Lee, C.C.; Hsieh, T.L. and Chang, M.Y., *Macromolecules*, **2008**, *41*, 7485.
DOI: 10.1021/ma801368z
14. Kim, J.S.; Lee, J.H.; Park, J.H.; Shim, C.; Sim, M. and Cho, K., *Adv. Funct. Mater.*, **2011**, *21*, 480.
DOI: 10.1002/adfm.201000971
15. Park, Y.D.; Lee, S.G.; Lee, H.S.; Kwak, D.; Lee, D.H. and Cho, K., *J. Mater. Chem.*, **2011**, *21*, 2338.
DOI: 10.1039/C0JM03114C
16. Jeon, J.H.; Lee, H.K.; Wang, D.H.; Park, J.H. and Park, O.O., *Sol. Energy Mater. Sol. Cells*, **2012**, *102*, 196.
DOI: 10.1016/j.solmat.2012.03.002
17. Li, L.; Tang, H.; Wu, H.; Lu, G. and Yang, X., *Org Electron*, **2009**, *10*, 1334.
DOI: 10.1016/j.orgel.2009.07.016
18. Moulé, A.J. and Meerholz, K., *Adv. Mater.*, **2008**, *20*, 240.
DOI: 10.1002/adma.200701519
19. Gundlach, D.J.; Royer, J.E.; Park, S.K.; Subramanian, S.; Jurchescu, O.D.; Hamadani, B.H.; Moad, A.J.; Kline, R.J.; et al., *Nat. Mater.*, **2008**, *7*, 216.
DOI:10.1038/nmat2122
20. Treat, N.D.; Brady, M.A.; Smith, G.; Toney, M.F.; Kramer, E.J.; Hawker, C.J. and Chabinyc, M.L., *Adv. Energy Mater.*, **2011**, *1*, 82.
DOI: 10.1002/aenm.201000023
21. Chen, F.-C.; Ko, C.-J.; Wu, J.-L. and Chen, W.-C., *Sol. Energy Mater. Sol. Cells*, **2010**, *94*, 2426.
DOI: 10.1016/j.solmat.2010.09.004
22. Park, Y.D.; Lee, H.S.; Choi, Y.J.; Kwak, D.; Cho, J.H.; Lee, S. and Cho, K., *Adv. Funct. Mater.*, **2009**, *19*, 1200.
DOI: 10.1002/adfm.200801763
23. Karagiannidis, P.G.; Georgiou, D.; Pitsalidis, C.; Laskarakis, A. and Logothetidis, S., *Mater. Chem. Phys.*, **2011**, 129, 1207.
DOI: 10.1016/j.matchemphys.2011.06.007
24. Zhao, Y.; Shao, S.; Xie, Z.; Geng, Y. and Wang, L., *J. Phys. Chem. C*, **2009**, *113*, 17235.
DOI: 10.1021/jp9038286



 Copyright © 2016 VBRI Press

Microelectronics Journal 57 (2016) 13–20

Contents lists available at ScienceDirect

Microelectronics Journal

journal homepage: www.elsevier.com/locate/mejo

MOS current mode logic exclusive-OR gate using multi-threshold triple-tail cells

Neeta Pandey*, Kirti Gupta, Garima Bhatia, Bharat Choudhary

Delhi Technological University (Formerly Delhi College of Engineering), Delhi, India

ARTICLE INFO

Article history:
Received 13 August 2015
Received in revised form
18 May 2016
Accepted 25 August 2016

Keywords:
MOS current mode logic
Exclusive-OR gate
Multi-threshold
Triple-tail cells

ABSTRACT

This paper presents a modified low-voltage MOS current mode logic (MCML) exclusive-OR (XOR) gate. The proposed topology introduces multiple threshold voltage transistors in the triple-tail cell of a MCML XOR gate. This scheme allows reduction in the implementation area of a triple-tail cell and the logic gate employing it. The impact of employing multiple threshold voltage transistors on the operation of the XOR gate is investigated; and mathematical formulations for the static and delay parameters are derived. A design procedure based on the static model is put forward. The accuracy of the models is verified by designing and simulating the proposed XOR gate for wide operating conditions. The model parameters of TSMC 0.18 μm CMOS technology are used. An assessment in terms of implementation area and the process variations is conducted for the proposed and the available XOR gates. Finally, the performance of all the XOR topologies is compared for different design cases and the favorable cases are identified.

© 2016 Elsevier Ltd. All rights reserved.

1. Introduction

MOS current mode logic (MCML) style is widely used as an alternative to CMOS logic style in mixed-signal applications. MCML circuits in contrast to the CMOS circuits provide an analog friendly environment to the sensitive analog circuits fabricated on same silicon chip. Other advantages of MCML style includes improved signal integrity, reduced power consumption, better power-delay product at high frequencies, stability with technology generations and improved security in cryptography applications [1–5]. Thus, MCML circuits are becoming the integral parts of the high performance systems. An exclusive-OR (XOR) gate serves as a building block of complex circuits such as comparators, adders, multipliers, test pattern generators etc. [6–10]. The realization of the traditional XOR gate consists of two levels of source-coupled transistor pairs [11–14]. To reduce the transistor pair levels, an attractive low-voltage XOR gate topology is presented in [15] which employ transistors with different aspect ratios in triple-tail cells for proper operation.

In this paper, an alternate topology for XOR gate is proposed. The new topology introduces multiple threshold voltage transistors in the triple-tail cell [16] and avoids the use of different sized transistors. The paper briefly describes the operation of the traditional and the existing low-voltage XOR gate [15] in Section 2. Thereafter, the new XOR gate topology is presented and investigated in Section 3. Its behavior is modeled in terms of static and delay parameters and an approach to design the gate is described. Extensive SPICE simulations are carried out to verify the mathematical formulations. Further, an investigation on the implementation area and the impact of parameter variations is conducted for the proposed, the traditional and the low-voltage [15] XOR topologies in Section 4. Also, the performance of the proposed XOR gate is compared with available counterparts for the three design cases namely high-speed, power-efficient, and low-power. Section 5 concludes the paper.

2. Existing MCML XOR gate topologies

2.1. Traditional XOR gate

The realization of the traditional XOR gate with differential inputs A and B is shown in Fig. 1. The transistors M_{TR1}, $M_{TR2\text{-}7}$ and $M_{TR8\text{-}9}$ implements the current source (bias current I_{SS}), pull down network (PDN) and the load respectively. The PDN consists of two levels of source-coupled transistor pairs arranged in accordance with the series gating approach. The upper level and lower level transistor pairs are driven by differential inputs A and B respectively. When differential input B is low, M_{TR2} is off, the bias current I_{SS} flows through M_{TR3} and is steered either to M_{TR6} or M_{TR7} according to the differential input A. The bias current I_{SS} is converted to the differential output voltage ($V_Q - \bar{V}_Q$) through the load transistors M_{TR8} and M_{TR9} [16]. The load capacitance C_L includes the effect of fan-out, and the interconnect capacitances.

* Corresponding author.
E-mail address: n66pandey@rediffmail.com (N. Pandey).

http://dx.doi.org/10.1016/j.mejo.2016.08.016
0026-2692/© 2016 Elsevier Ltd. All rights reserved.

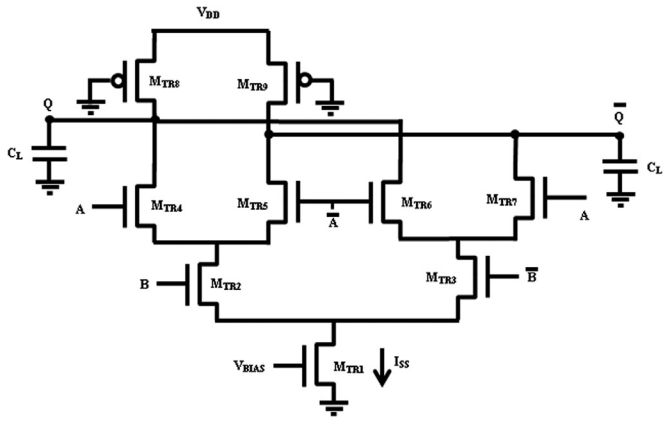


Fig. 1. Traditional MCML XOR gate.

2.2. Low-voltage XOR gate using triple-tail cell [15]

The schematic of the low-voltage XOR gate [15] is shown in Fig. 2. It employs two triple-tail cells (M_{LV3},M_{LV4}, M_{LV7}) and (M_{LV5},M_{LV6}, M_{LV8}) to lower the value of minimum power supply required by the XOR gate in comparison to the traditional one. The differential input A drives the transistor pairs M_{LV3} – M_{LV4} and M_{LV5} – M_{LV6} while the transistors M_{LV7} and M_{LV8} are controlled by input B. For a low value of the differential input B the transistor M_{LV8} is turned on, such that the transistor pair M_{LV5} – M_{LV6} is deactivated. At the same time, the transistor M_{LV7} turns off and the bias current flows through the transistor pair M_{LV3} – M_{LV4} which produces the output according to the differential input A. Similarly, a high value of differential input B, activates the transistor pair M_{LV5} – M_{LV6} and generates the corresponding output. To achieve proper activation/deactivation of the triple-tail cell, this topology makes the aspect ratio of transistors M_{LV7} and M_{LV8} larger than (N times) the other transistors (M_{LV3-6}) [15,16].

In this paper, an alternate approach to activate/deactivate the triple-tail cell is suggested. The basic structure of the triple-tail cell is modified by employing multiple threshold voltage transistors. The merits and demerits of the modified XOR topology over the traditional and the available low-voltage are explored.

3. Proposed MCML XOR gate topology

The circuit of the proposed XOR gate with differential inputs A and B is shown in Fig. 3. It consists of two triple-tail cells (M_{SA3}, M_{SA4}, M_{SA7}) and (M_{SA5}, M_{SA6}, M_{SA8}) biased by two separate current sources of $I_{SS}/2$ value. The operation and the value of the minimum power supply of the proposed XOR gate are similar to the available low-voltage XOR gate [15]. The proposed topology differs from the available one as it employs equal aspect ratios of all transistors in triple-tail cells. The threshold voltage ($V_{T,7}$; $V_{T,8}$) of the transistors (M_{SA7} and M_{SA8}) is lowered by a factor of δ than that of

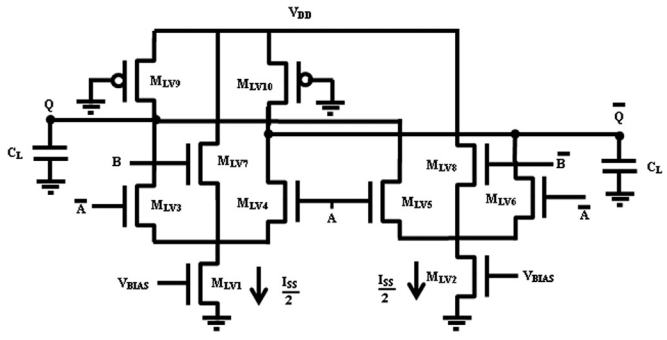


Fig. 2. Low voltage MCML XOR gate [15].

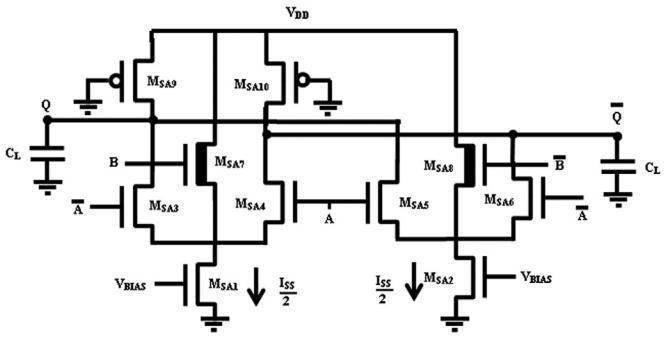


Fig. 3. Proposed MCML XOR gate.

transistors M_{SA3-6} ($V_{T,n}$) and is differentiated by bold lines in the Fig. 3. For high values of the differential inputs A and B, since the gate-source voltages of transistors M_{SA4} and M_{SA7} are same, the currents flowing through these ($i_{D,SA4}$ and $i_{D,SA7}$) [6] can be written as

$$i_{D,SA4} = \frac{\mu_{eff,n} C_{ox}}{2} \frac{W_N}{L_N} (V_{GS} - V_{T,n})^2 \tag{1a}$$

$$i_{D,SA7} = \frac{\mu_{eff,n} C_{ox}}{2} \frac{W_N}{L_N} \left(V_{GS} - \frac{V_{T,n}}{\delta}\right)^2 \tag{1b}$$

where $\mu_{eff,n}$,C_{OX},W_n, L_n, $V_{T,n}$ are effective electron mobility, oxide capacitance per unit area, the effective channel width, effective channel length respectively.

From Fig. 3, the sum of the drain currents of M_{SA4} ($i_{D,SA4}$)and M_{SA7} ($i_{D,SA7}$)should be equal to $\frac{I_{SS}}{2}$. Using this, the above equations can be solved as.

From Fig. 3, the sum of the drain currents $i_{D,SA4}$and$i_{D,SA7}$should be equal to $\frac{I_{SS}}{2}$. Using this, Eqs. (1a)-(1b) can be solved as

$$i_{D,SA4} = \frac{I_{SS}}{4} - \frac{\sqrt{\frac{\mu_{eff,n} C_{ox}}{2} \frac{W_N}{L_N} V_{T,n}{}^2 (\frac{\delta - 1}{\delta})^2}}{2} \sqrt{I_{SS} - \frac{\mu_{eff,n} C_{ox}}{2} \frac{W_N}{L_N} V_{T,n}{}^2 (\frac{\delta - 1}{\delta})^2} \tag{2a}$$

$$i_{D,SA7} = \frac{I_{SS}}{4} + \frac{\sqrt{\frac{\mu_{eff,n} C_{ox}}{2} \frac{W_N}{L_N} V_{T,n}{}^2 (\frac{\delta - 1}{\delta})^2}}{2} \sqrt{I_{SS} - \frac{\mu_{eff,n} C_{ox}}{2} \frac{W_N}{L_N} V_{T,n}{}^2 (\frac{\delta - 1}{\delta})^2} \tag{2b}$$

By substituting $x = (\frac{\mu_{eff,n} C_{ox}}{2} \frac{W_n}{L_n} V_{T,n}{}^2 \left(\frac{\delta - 1}{\delta}\right)^2)$ the Eqs. (2a) and (2b) can be simplified as

$$i_{D,SA4} = \frac{I_{SS}}{4} - \frac{\sqrt{x}}{2} \sqrt{I_{SS} - x} \tag{2c}$$

$$i_{D,SA7} = \frac{I_{SS}}{4} + \frac{\sqrt{x}}{2} \sqrt{I_{SS} - x} \tag{2d}$$

3.1. Analysis of the proposed XOR gate

The behavior of the proposed XOR gate is analyzed in terms of the static and delay parameters. The models are derived by substituting the load transistors M_{SA9-10} by an equivalent linear resistance, R_P [13] whose value is computed as

Table 1
Output in the form of differential voltage for various input combination when applied to proposed XOR gate.

Differential Inputs		Current through the transistors						Differential output
A	B	M_{SA3}	M_{SA4}	M_{SA5}	M_{SA6}	M_{SA7}	M_{SA8}	$V_Q - \bar{V}_Q$
L	L	I_1	0	0	I_3	0	I_2	$V_{OL}=\frac{R_P}{2}(\frac{I_{SS}}{2}-\sqrt{x}\sqrt{I_{SS}-x})$
L	H	I_3	0	0	I_1	I_2	0	$V_{OH}=\frac{R_P}{2}(\frac{I_{SS}}{2}+\sqrt{x}\sqrt{I_{SS}-x})$
H	L	0	I_1	I_3	0	0	I_2	$V_{OH}=\frac{R_P}{2}(\frac{I_{SS}}{2}-\sqrt{x}\sqrt{I_{SS}-x})$
H	H	0	I_3	I_1	0	I_2	0	$V_{OL}=\frac{R_P}{2}(\frac{I_{SS}}{2}+\sqrt{x}\sqrt{I_{SS}-x})$

Here $I_1=\frac{I_{SS}}{2}$, $I_2=\frac{I_{SS}}{4}+\frac{\sqrt{x}}{2}\sqrt{I_{SS}-x}$ and $I_3=\frac{I_{SS}}{4}-\frac{\sqrt{x}}{2}\sqrt{I_{SS}-x}$, where $x=\frac{\mu_{eff,n}C_{ox}}{2}\frac{W}{L}V_{T1}^2(\frac{\delta-1}{\delta})^2$.

$$R_P=\frac{R_{int}}{1-\frac{(R_{DSW}*10^{-6})/W_P}{R_{int}}} \tag{3}$$

where R_{DSW} is the empirical model parameter, W_P is the effective width of the transistor M_{SA9-10} and the parameter R_{int} is the intrinsic resistance of the PMOS transistor in the linear region and is given as

$$R_{int}=[\mu_{eff,p}C_{ox}\frac{W_P}{L_P}(V_{DD}-|V_{T,P}|)]^{-1} \tag{4}$$

where $\mu_{eff,p}$ is effective hole mobility, $V_{T,P}$ is the threshold voltage, W_P and L_P represent the effective channel width and effective channel length of the transistors M_{SA9-10}.

3.1.1. Static model

The behavior of the proposed XOR gate is modeled in terms of the static parameters namely, voltage swing, small signal voltage gain and the noise margin.

The voltage swing (V_{SWING}) is defined as the difference of the high and the low output differential voltages. To formulate the expression for the voltage swing, the values of the high (V_{OH}) and the low output differential voltage (V_{OL}) should be determined. Let the differential voltages on the inputs A and B be low and high respectively. This input condition produces a high differential output which can be computed as

$$V_{OH}=V_Q-\bar{V}_Q=R_P[(i_{D,SA4}+i_{D,SA6})-(i_{D,SA3}+i_{D,SA5})]$$
$$=\frac{R_P}{2}(\frac{I_{SS}}{2}+\sqrt{x}\sqrt{I_{SS}-x}) \tag{5}$$

where $i_{D,\,SAj}$ is drain current flowing through transistor M_{SAj} (j =3,4,5,6). Similarly, the expressions of the differential output voltage for different input combinations are listed in Table 1. On closer examination of the results, the voltage swing of the circuit can be expressed as

$$V_{SWING}=V_{OH}-V_{OL}=R_P(\frac{I_{SS}}{2}+\sqrt{x}\sqrt{I_{SS}-x}) \tag{6}$$

The small-signal voltage gain (A_v) and noise margin (NM) for the proposed XOR gate are computed by the method outlined in [12–14] as

$$A_v=g_{m,n}R_P=\frac{V_{SWING}}{2}\left(\frac{1}{\frac{1}{2}+\frac{\sqrt{x}}{I_{SS}}\sqrt{I_{SS}-x}}\right)\sqrt{2\mu_{eff,n}C_{OX}\frac{W_N}{L_N}.\frac{1}{I_{SS}}} \tag{7}$$

$$NM=\frac{V_{SWING}}{2}[1-\frac{\sqrt{2}}{A_v}] \tag{8}$$

where $g_{m,n}$ is the transconductance of transistors M_{SA3-6}.

3.1.2. Delay model

The delay of the proposed XOR gate is derived by considering the effects of the parasitic capacitances associated with the transistors as well as output load capacitance. For a high-to-low transition on differential input B the output switches by activating (deactivating) the transistor pair $M_{SA3}-M_{SA4}$ ($M_{SA5}-M_{SA6}$), the circuit reduces to a simple MCML inverter. The equivalent linear half circuit is shown in Fig. 4. In general, the capacitances C_{gdj} and C_{dbj} represents the gate–drain capacitance and the drain–bulk junction capacitance of the j^{th} transistor. The gate–drain capacitance for an NMOS transistor operating in saturation region is computed as the overlap capacitance $C_{gdo}W_n$ between the gate and the drain [12] while for the PMOS transistor operating in linear region, it is determined as the sum of the overlap capacitance and the intrinsic contribution associated with its channel charge [12]. The drain–bulk junction capacitance for a transistor is evaluated by as suggested in [13].

The delay of the proposed XOR gate can be expressed as

$$t_{PD}=0.69R_P(C_{db3}+C_{gd3}+C_{gd9}+C_{db9}+C_{db5}+C_{gd5}+C_L) \tag{9}$$

By assuming $C_{db3}=C_{db5}$, $C_{gd3}=C_{gd5}$ and substituting $R_P=\frac{V_{SWING}}{\left(\frac{I_{SS}}{2}+\sqrt{x}\sqrt{I_{SS}-x}\right)}$, Eq. (9) can be rewritten as

$$t_{PD}=0.69\frac{V_{SWING}}{\left(\frac{I_{SS}}{2}+\sqrt{x}\sqrt{I_{SS}-x}\right)}(2C_{db3}+2C_{gd3}+C_{gd9}+C_{db9}+C_L) \tag{10}$$

3.2. Design of the proposed XOR gate

In this section, the design procedure based on the static model is derived. For a given value of noise margin, and the small-signal voltage gain (≥ 1.4 for MCML [2,12,14]), the voltage swing of the proposed XOR gate using Eq. (8) is calculated as

$$V_{SWING}=\frac{2NM}{1-\frac{\sqrt{2}}{A_v}} \tag{11}$$

It may be noted that V_{SWING} should be lower than the maximum value of $2V_{T,n}$ so as to ensure that transistors M_{SA3-6} operates in saturation region. Using Eq. (6), for a specified value of the bias current I_{SS}, the resistance of the load transistor R_P is given as

$$R_P=\frac{V_{SWING}}{\left(\frac{I_{SS}}{2}+\sqrt{x}\sqrt{I_{SS}-x}\right)} \tag{12}$$

To determine the aspect ratio of the load transistors M_{SA9-10}, equivalent resistance of the minimum sized PMOS, R_{P_MIN}, is determined first. Then, for the required voltage swing, the bias current I_{HIGH} is determined as

$$I_{HIGH}=\frac{V_{SWING}}{R_{P_MIN}} \tag{13}$$

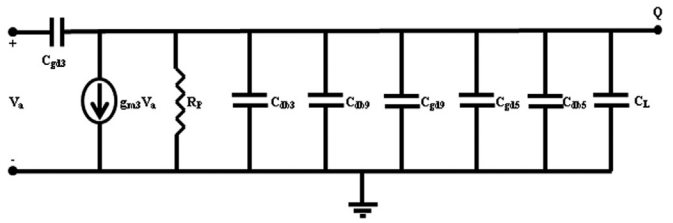


Fig. 4. Linear half circuit (with low value of differential input A).

If the bias current is higher than I_{HIGH}, then R_P should be less than R_{P_MIN} and to achieve this $L_P$is set to its minimum value i.e. L_{MIN} and W_P which is calculated by solving Eqs. (3)–(4) as

$$W_P = \frac{\left(\frac{I_{SS}}{2} + \sqrt{x}\sqrt{I_{SS}-x}\right)}{V_{SWING}} * \frac{L_{MIN}}{\left[\mu_{eff,p}C_{ox}\frac{W_P}{L_P}(V_{DD}-|V_{T,P}|)\right]\left[1-\frac{(R_{DSW}*10^{-6})}{L_{MIN}}\mu_{eff,p}C_{ox}\frac{W_P}{L_P}(V_{DD}-|V_{T,P}|)\right]} \quad (14)$$

Similarly, for the bias current values lower thanI_{HIGH}, R_P is made be greater than R_{P_MIN}. This requires W_P to be minimum i.e. W_{MIN} and L_P to be calculated as

$$L_P = \mu_{eff,p}C_{ox}W_{MIN}(V_{DD}-|V_{T,P}|)\left(\frac{V_{SWING}}{\left(\frac{I_{SS}}{2} + \sqrt{x}\sqrt{I_{SS}-x}\right)} - \frac{R_{DSW}*10^{-6}}{W_{MIN}}\right) \quad (15)$$

For sizing the transistors M_{SA3-6}, the small-signal voltage gain A_v (Eq. (7)) is used. The width of the transistors by assuming minimum channel length, can be computed as

$$W_N = 2\left(\frac{A_v}{V_{SWING}}\right)^2\left(\frac{1}{2} + \frac{\sqrt{x}}{I_{SS}}\sqrt{I_{SS}-x}\right)^2\frac{L_{MIN}I_{SS}}{\mu_{eff,n}C_{ox}} \quad (16a)$$

It is found in some cases that for bias current values lower than the current of the minimum sized NMOS transistor (I_{LOW}), the above equation (Eq. (16a)) results in W_N value lower than the minimum channel width. Therefore in such situations, the W_N is made equal to W_{MIN} [13]. The I_{LOW} can be evaluated by using Eq. (7) as

$$I_{LOW} = \frac{1}{2}\left(\frac{V_{SWING}}{A_v}\right)^2\frac{W_{MIN}}{L_{MIN}}\frac{1}{\left(\frac{1}{2} + \frac{\sqrt{x}}{I_{SS}}\sqrt{I_{SS}-x}\right)^2}\mu_{eff,n}C_{ox} \quad (16b)$$

It may be noted that the above design expressions (Eqs. (14)–(16)) relate the dimensions of the transistor to the bias current and the voltage swing. Hence, these can be further used to express the capacitances used in the delay equation (Eq. (10)) in order to establish the dependency of the delay on the bias current and voltage swing.

For the bias current I_{SS} ranging from I_{LOW} to I_{HIGH} and using Eqs. (14)–(16), various capacitances in Eq. (10) may be expressed as

$$C_{gd3} = C_{gd0}W_3 = 2A^2{}_vC_{gd0}\left(\frac{1}{2} + \frac{\sqrt{x}}{Iss}\sqrt{I_{ss}-x}\right)^2\frac{L_{MIN}}{\mu_{eff,n}C_{ox}}\frac{I_{SS}}{(V_{SWING})^2} \quad (17)$$

whereC_{gd0} is the drain–gate overlap capacitance per unit transistor width.

$$C_{db3} = W_3\left(K_{jn}C_{in}L_{dn} + 2K_{jswn}C_{jswn}\right) + 2K_{jswn}C_{jswn}L_{dn} \quad (18)$$

Table 2
Coefficients of the capacitances for the proposed XOR gate.

NMOS coefficients	
a_{db3}	$\frac{2A^2{}_vL_{MIN}}{\mu_{eff,n}C_{ox}}\left(K_{jn}C_{jn}L_{dn} + 2K_{jswn}C_{jswn}\right)$
a_{gd3}	$2A^2{}_vC_{gd0}\frac{L_{MIN}}{\mu_{eff,n}C_{ox}}$
c_{db3}	$2K_{jswn}C_{jswn}L_{dn}$
b_{db3}, b_{gd3} and c_{gd3}	0
PMOS coefficients	
b_{gd9}	$\frac{3}{4}A_{bulk,max}\mu_{eff,p}C^2{}_{ox}W^2{}_{MIN}\left(V_{DD}-\lvert V_{T,p}\rvert\right)$
c_{gd9}	$C_{gd0}W_{MIN} - \frac{3}{4}A_{bulk,max}\mu_{eff,p}C^2{}_{ox}W_{MIN}\left(V_{DD}-\lvert V_{T,p}\rvert\right)R_{DSW}*10^{-6}$
c_{db9}	$K_{jp}C_{jp}L_{dp}W_{MIN} + 2K_{jswp}C_{jswp}\left(L_{dp} + W_{MIN}\right)$
a_{gd9}, a_{db9} and b_{db9}	0

Where the symbols have their usual meaning.

$$= 2A^2{}_v\frac{L_{MIN}}{\mu_{eff,n}C_{ox}}\left(\frac{1}{2} + \frac{\sqrt{x}}{Iss}\sqrt{I_{ss}-x}\right)^2\left(K_{jn}C_{in}L_{dn} + 2K_{jswn}C_{jswn}\right)\frac{I_{SS}}{(V_{swing})^2} + 2K_{jswn}C_{jswn} \quad (19)$$

where C_{jn}, and C_{jswn} are the zero-bias junction capacitance per unit area and zero-bias sidewall capacitance per unit parameter respectively. The coefficients K_{jn}, and K_{jswn} are the voltage equivalence factor for the junction and the sidewall capacitances [13].

$$C_{gd9} = C_{gd0}W_{MIN} + \frac{3}{4}A_{bulk,max}W_{MIN}L_PC_{ox} \quad (20)$$

$$= C_{gd0}W_{MIN} + \frac{3}{4}A_{bulk,max}W_{MIN}C_{ox}\left\{\mu_{eff,p}C_{ox}W_{MIN}(V_{DD}-|V_{TP}|)\left(\frac{V_{SWING}}{\left(\frac{I_{SS}}{2} + \sqrt{x}\sqrt{I_{SS}-x}\right)} - \frac{R_{DSW}*10^{-6}}{W_{MIN}}\right)\right\} \quad (21)$$

where $A_{bulk,max}$ is a parameter defined in the BSIM3V3 model [13].

$$C_{db9} = W_{MIN}\left(K_{jp}C_{jp}L_{dp} + 2K_{jswp}C_{jswp}\right) + 2K_{jswp}C_{jswp}L_{dp} \quad (22)$$

Therefore, the capacitances may be expressed in terms of the bias current and the voltage swing as

$$C_{xy} = \frac{a_{xy}}{(V_{swing})^2}p^2I_{ss} + \frac{b_{xy}V_{swing}}{pI_{ss}{}^2} + c_{xy} \quad (23)$$

where $p = \frac{1}{2} + \frac{\sqrt{x}}{Iss}\sqrt{I_{ss}-x}$ has been substituted. The expressions of the coefficients a_{xy}, b_{xy} and c_{xy} in all the capacitances in Eq. (23) are summarized in Table 2.

Using Eqs. (17)–(23), Eq. (10) can be written as

$$t_{PD} = 0.69V_{swing}\left(\frac{ap}{V^2{}_{swing}} + b\frac{V_{swing}}{p^2{\bullet}I^2{}_{SS}} + \frac{c+C_L}{p{\bullet}I_{ss}}\right) \quad (24)$$

Where

$$a = 2a_{db3} + 2a_{gd3} \quad (24a)$$

$$b = b_{gd9} \quad (24b)$$

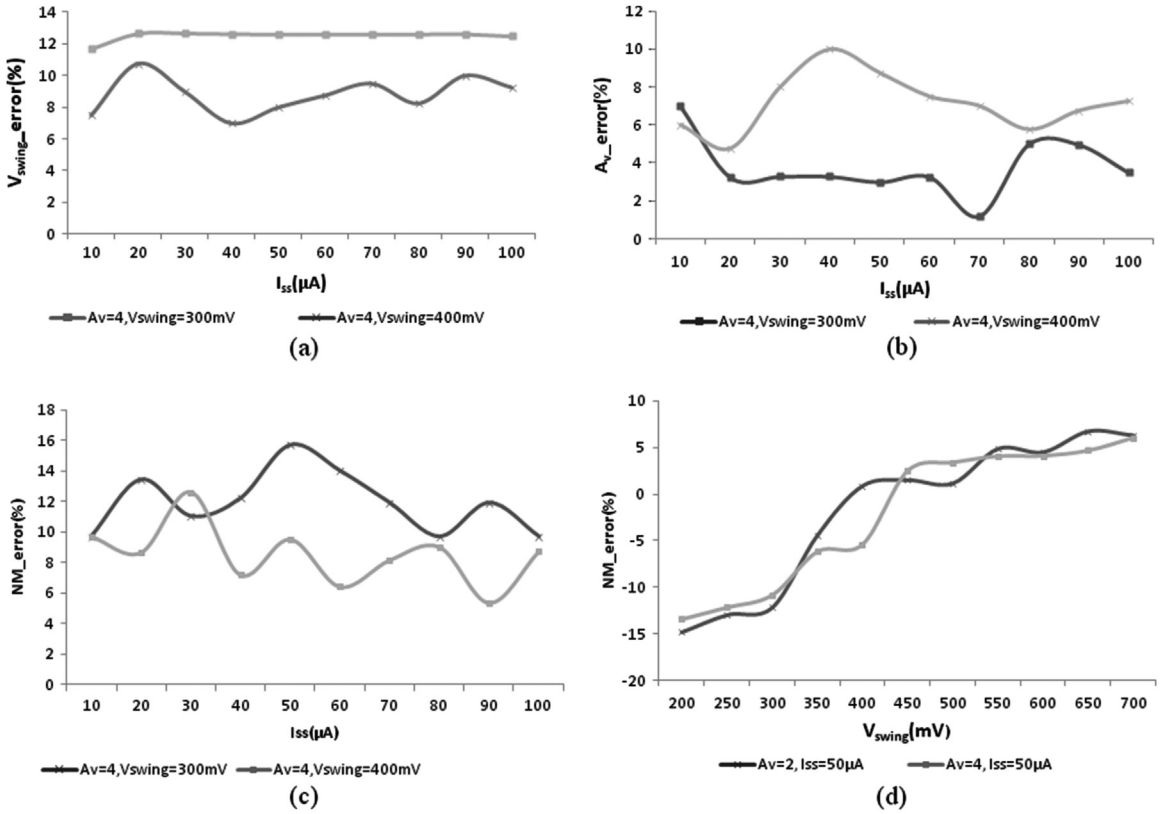


Fig. 5. Error in the static parameters.

$$c = 2c_{db3} + c_{gd9} + c_{db9} \quad (24c)$$

For the completeness of the delay model it is necessary to discuss its validity for I_{ss} values lying outside the range $I_{LOW}$to I_{HIGH}. For $I_{SS} > I_{HIGH}$, it can be observed that the capacitance coefficients of PMOS transistor in Eq. (24) differ as explained in Section 3.1.2. But it may be noted that for such values ofI_{SS}, the capacitive contribution of PMOS transistor is negligible therefore Eq. (24) can predict the delay. Similarly, for $I_{SS} < I_{LOW}$, the delay majorly depends on the capacitances of PMOS transistor therefore the capacitance coefficients of NMOS transistor do not affect the delay. So, the delay expression represented in (Eq. (24)) can estimate the delay.

3.3. Validation of the static and the delay models

In this section, the accuracy of the static and the delay models are validated through SPICE simulations by using TSMC 0.18 μm CMOS technology parameters and with a power supply of 1.1 V. The proposed XOR gate was designed and simulated for wide range of operating conditions: voltage swing of 300 mV and 400 mV, small-signal voltage gain of 2 and 4, δ = 1.5, and the bias current ranging from 10 μA to 100 μA. The plots displaying the errors in the simulated and the predicted values of the static parameters for small-signal voltage gain of 4 and voltage swing of 300 mV and 400 mV are shown in Fig. 5a–c. A close inspection of the plots reveals that for the simulation condition with V_{swing}=300mV, A_v=4, the maximum, minimum errors in V_{SWING}, NM and Av are respectively (13%, 16%, 7%), (11%, 6%, 1%) with average errors of (12%, 4%, 11%) showing maximum variation of ± 5% around the average values. Similarly, for V_{swing}=400mV, A_v=4, the maximum, minimum and average error in V_{SWING}, NM and Av are respectively (11%, 13%, 11%), (7%, 5%, 5%) and (9%, 9% , 8%) with a maximum variation of ± 4% around the average values. Therefore it can be stated that the proposed models will show a maximum variation of ± 5% around the average values in static parameters. The dependence of the noise margin on the voltage swing is evaluated and an error plot of noise margin by varying the voltage swing from 0.2 V to 0.7 V is shown in Fig. 5d. It may be observed that the maximum error in noise margin is 14.8%. The delay is also noted for the above conditions; and the simulated and the predicted delay values in particular for V_{swing}=400mV, A_v=4 and the load capacitances of 0 fF, 10 fF, 100 fF and 1 pF are plotted in Fig. 6. The error of Eq. (24) with respect to simulations under the same load conditions is shown in Fig. 7. The maximum, minimum and average errors in gate delay having load capacitance of 0 fF, 10 fF, 100 fF and 1 pF are (22%, −3%, 9.5%), (10%, −10%, 0%), (16%, 5%, 10.5%) and (4%, −3%, 0.5%) respectively. It is worth noting that the error is maximum for the zero load capacitance which is strongly an unrealistic case. Finally, the inspection of Fig. 7 indicates that the error tends to settle to a constant value for high values of the bias current.

After the verification of the models, it is necessary to determine the optimum value of the scaling factor. To find out the value, the proposed XOR gate is designed for A_v=4, NM=130mV, I_{SS}=50μA and the propagation delay and the implementation area are plotted in Fig. 8 as a function of δ. It is observed that the delay increases with the increase in δ whereas an opposite trend is noted in implementation area. The area reduction may be attributed to the fact that a high value of δ, lowers the threshold voltage of$M_{SA7,8}$ and results in small-sized M_{SA3-8} thereby lowering the overall area. Therefore an increase in area can be viewed as a trade-off for delay reduction as demonstrated by the plot. On closer examination, the value of δ = 1.3 is the optimum choice in terms of both delay and area.

4. Performance comparison

In this section the implementation area of the proposed and the available XOR gates is estimated and compared. Thereafter, the impact of the process variations on the gates is also investigated.

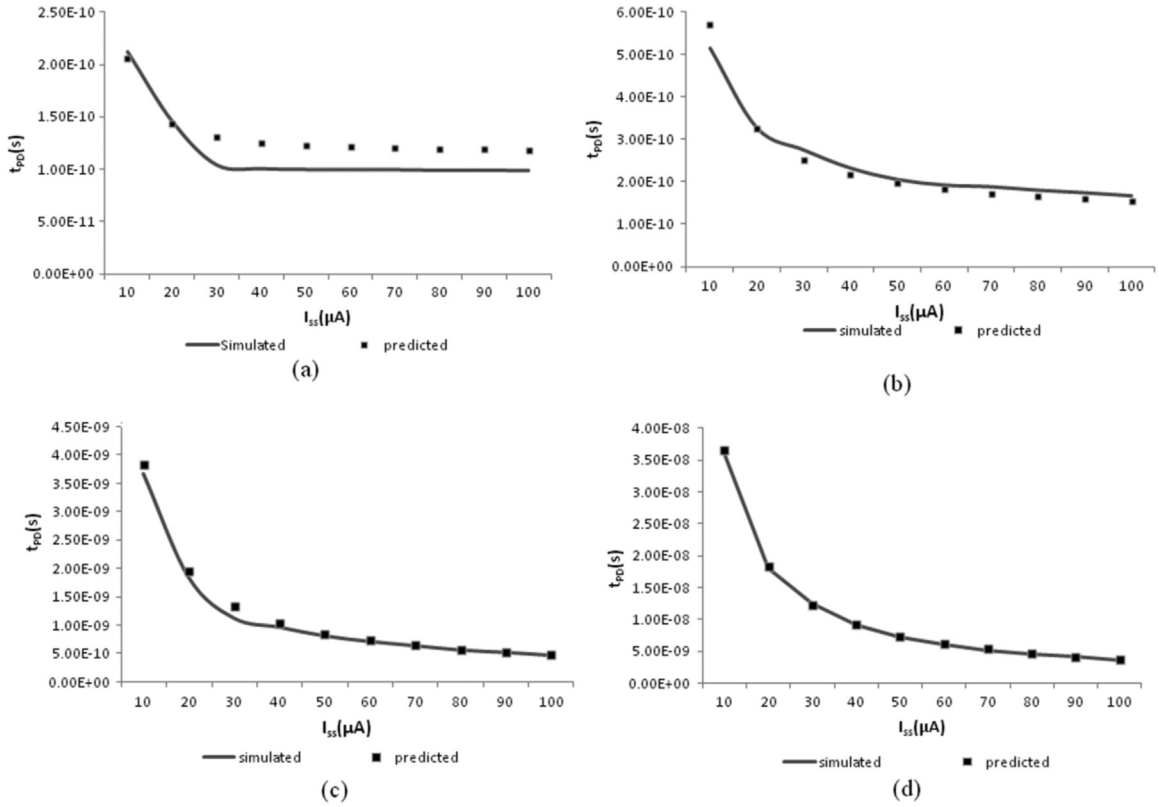


Fig. 6. Simulated and predicted delay of the proposed XOR gate vs. Iss with NM = 130 mV, Av = 4 for different C_L values (a) 0fF, (b) 10fF, (c) 100fF and (d) 1 pF.

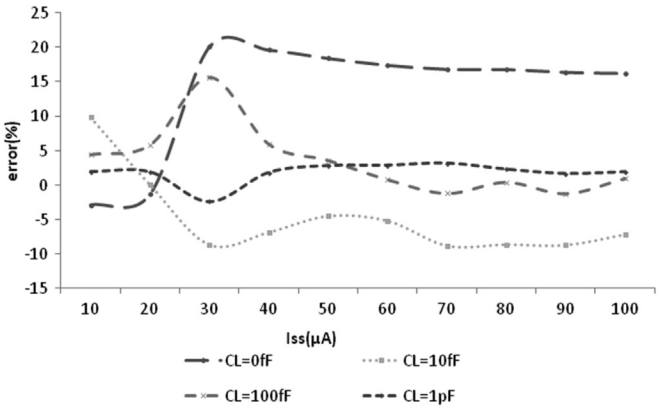


Fig. 7. Error of the EXOR gate predicted delay with respect to simulated delay.

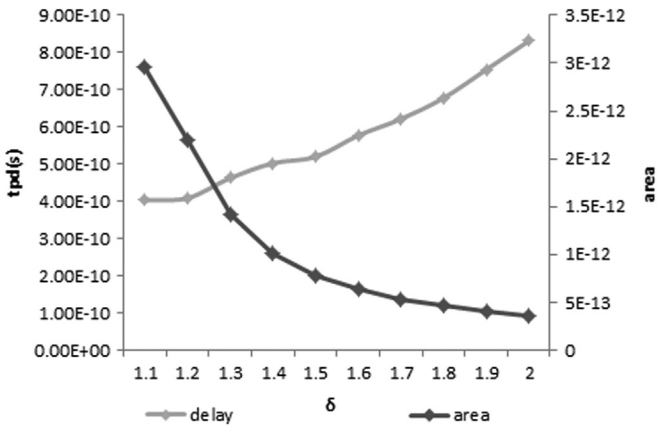


Fig. 8. Propagation Delay and area vs. δ.

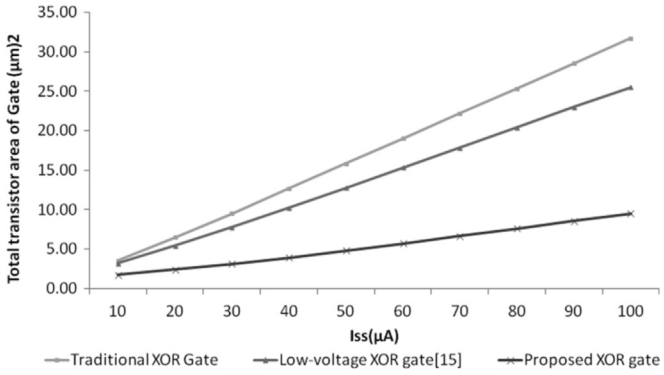


Fig. 9. Total transistor area required to design the proposed MCML, traditional and low voltage XOR gate [15].

Finally, the performance of the proposed and the available XOR gates is compared by designing the gates for different design cases. In all the simulations, the XOR gates are designed with minimum power supply, noise margin of 130 mV, small signal gain of 4, and load capacitance of 50 fF.

4.1. Area comparison

The proposed XOR gate is evaluated on the basis of the area. It is difficult to find out exact area without layout; therefore preliminary area estimation is done on the basis of multiplying length and width of individual transistor employed in the circuit [17]. The area is computed for the traditional, low-voltage [15] and the proposed XOR gates for bias current ranging from 10 μA and 100 μA while keeping the simulation conditions described in the beginning of the current section. The findings are reported in Fig. 9 which identifies the proposed topology as the smallest one. Further, at lower bias currents the area is almost half of the both low-voltage [15] and the

Table 3
Effect of process variation on static parameters of the proposed and the available XOR gates.

Parameter	NMOS PMOS	T T	F F	S S	F S	S F
Simulation conditions: A_v=4, V_{swing}=. 4V, C_L=50 fF, I_{SS}=100μA δ=1.5						
V_{swing}(mV)	Proposed	352.03	377.165	306.725	362.318	348.452
	Low-voltage [15]	348	373	272	370	350
	Traditional	381	387	330	378	379
A_v	Proposed	3.59	3.13	4.28	3.57	3.57
	Low-voltage [15]	3.1	2.1	4.9	3.1	3.1
	Traditional	2.1	2.12	2.12	2.1	2.1
NM(mV)	Proposed	126.175	102.13	142.282	155.705	104.698
	Low-voltage [15]	125.3	122.8	120.5	118	127
	Traditional	139.6	139.5	139.6	141.2	140.7
t_{PD}(ps)	Proposed	329.338	309.19	366.903	315.687	324.485
	Low-voltage [15]	340.404	322.62	370.386	328.8	330.578
	Traditional	542.3	513.4	672.5	527	538.6
Simulation conditions: A_v=4, V_{swing}=. 4V, C_L=50 fF, I_{SS}=10μAδ=1.5						
V_{swing}(mV)	Proposed	380.5	339.635	278.541	306.8	310.763
	Low-voltage [15]	374	472	278	426	415
	Traditional	384	381	342	380	377
A_v	Proposed	3.29	3.03	1.9	3.15	3.15
	Low-voltage [15]	3.8	2.9	4.3	3.5	3.7
	Traditional	2.09	2.12	2.13	2.1	2.1
NM(mV)	Proposed	123.49	126.175	112.752	115.436	144.96
	Low-voltage [15]	139	144	146	134	148
	Traditional	139.57	142.28	140.1	135.4	137.8
t_{PD}(ns)	Proposed	2.19	2.08	2.28	2.05	2.08.
	Low-voltage [15]	2.45	1.68	3.11	2.12	2.3
	Traditional	3.4	3.32	4.5	3.54	3.6

traditional XOR gate topologies while at higher bias currents it is around one third. Thus the observations corroborates with the objective. Theoretically also, larger sizes of individual transistors are needed in PDN to support the design constraints at higher bias current in existing topologies. Therefore, there is sharp increase in PDN transistor sizes in existing topologies whereas the sizes of activating/ deactivating transistors in proposed topology remain small due to the use of multiple threshold transistors.

4.2. The impact of parameter variation

The impact of parameter variation at different design corners and effect of mismatch are examined for the proposed and the available XOR gates. The findings for various operating conditions are comprehended in Table 3. The maximum variation in the voltage swing, small-signal voltage gain, noise margin and the delay of the proposed XOR gate between the best and the worst cases is observed to be by a factor of 1.73. The corresponding maximum variation in low-voltage and traditional XOR gate is by a factor of 2.3 and 1.3. Thus, the proposed XOR gate show slightly higher variations than the traditional XOR gate which can be attributed to the smaller aspect ratio of transistors in the proposed XOR [2]. The widths of the transistors are varied by 10% corresponding to which the variations in voltage swing, small-signal voltage gain, noise margin are within 4% and delay for the gates.

4.3. Design cases

The performance of the proposed XOR gate is compared with the available ones for the different design cases. In literature, three design cases namely high speed, power efficient and the low power have been considered. Therefore, for the sake of fair comparison, the proposed XOR gate is designed for different performance. The analysis suggested in [13] and [15] is used for the conventional and the available low-voltage ones for the comparison. The value of N (=5) and δ (=1.3) are taken for designing the low-voltage and proposed XOR gate respectively. To compute bias current for high speed, power efficient and low power design cases, analysis similar to the one presented in [13] and [15] is carried out using the design equations for proposed method and corresponding bias currents are computed as 121.5 μA, 7.683 μA and 2 μA respectively.

In high speed design case, the basic aim is to design the XOR gate topologies with minimum delay. The traditional, low-voltage and the proposed XOR gates designed for this purpose results in a delay of 492.426 ps, 269.714 ps and 242.375 ps respectively. This indicates that the proposed XOR gate can achieve higher speed than the traditional and low-voltage XOR gate [15].

For power efficient design, the minimization of the power-delay product (PDP) is considered. The XOR gates designed under this design case result in PDP values of 21.58 fJ, 19.53 fJ and 23.38 fJ for the proposed gate, low-voltage [15] and traditional XOR gates respectively. The result indicates that the proposed XOR gate results in higher PDP values than the traditional one.

In low power designs, the motive is to achieve a low value of bias current for reducing the power consumption of the gate. The low power XOR gates having a load capacitance of 5fF gives a power consumption of 2.8 μW, 2.2 μW and 2.2 μW for the traditional, low-voltage [15] and proposed topologies. The comparison for different design cases is summarized in Table 4.

5. Conclusion

An alternate topology to implement low-voltage MCML XOR gate is presented. It uses multiple threshold voltage transistors in

Table 4
Comparison of XOR gate topologies in relation to traditional topology.

Design cases	Performance parameter		Proposed XOR gate	Traditional XOR gate	Low-voltage XOR gate [15]
High-speed	Delay	Value	242.375 ps	492.426 ps	269.714 ps
		Improvement	50.7%	–	45.22%
		Analysis	Fastest	–	faster
Power-efficient	PDP	Value	21.58 fJ	23.38 fJ	19.53 fJ
		Improvement	7.6%	–	16.4%
		Analysis	Lesser	–	least
Low power	Power	Value	2.2 μW	2.8 μW	2.2 μW
		Improvement	21.4%	–	21.4%
		Analysis	Low	–	low

the triple-tail cell of a MCML XOR gate to allow reduction in the implementation area. Analytical formulation for static and delay parameters are put forward to show the effect of multiple threshold voltage transistors and is followed by the design procedure. The theoretical formulations are validated by designing and simulating the proposed gate by using TSMC CMOS technology parameters. A performance comparison with the existing MCML XOR topologies indicates that the proposed one is beneficial in terms of area, speed and power.

References

[1] M. Yamashina, H. Yamada, An MOS current mode logic (MCML) circuit for low-power sub-GHz processors, IEICE Trans. Electron. E75-C (1992) 1181–1187.

[2] H. Hassan, M. Anis, M. Elmasry, MOS current mode circuits: analysis, design, and variability, IEEE Trans. Very Large Scale Integr. (VLSI) Syst. 13 (2005) 885–898.

[3] S. Bruma, Impact of on-chip process variations on MCML performance, in: Proceedings of the IEEE Conference on Systems-on-Chip, 2003, pp.135–140.

[4] M. Anis, M. Allam, M. Elmasry, Impact of technology scaling on CMOS logic styles, IEEE Trans. Circuits Syst. II 49 (2002) 577–588.

[5] Z. Toprak, Y. Leblebici, Low-power current mode logic for improved DPA-resistance in embedded systems, in: Proceedings of the IEEE International Symposium on Circuits System, May 2005.

[6] J. Rabaey, Digital Integrated Circuits (A Design Perspective), Prentice-Hall, Englewood Cliffs, NJ, 1996.

[7] M. Alioto, R. Mita, G. Palumbo, Design of high-speed power efficient MOS current mode logic frequency dividers, IEEE Trans. Circuits Syst. – II: Express Briefs 53 (2006) 1165–1169.

[8] V. Srinivasan, S.H. Dong, J.B. Sulistyo, Gigahertz-range MCML multiplier architectures, in: Proceedings of the International Symposium on Circuits System, 2004, pp.785–788.

[9] Y. Delcan, A. Morgul, High performance 16-bit MCML multiplier, in: Proceedings of the IEEE European Conference on Circuit Theory and Design, 2009, pp.157–160.

[10] J.M. Musicer, J. Rabaey, MOS current mode logic for low power, low noise, CORDIC computation in mixed-signal environments, in: Proceedings of the International Symposium of Low Power Electronics and Design, 2000, pp. 102–107.

[11] M. Alioto, G. Palumbo, Power-delay optimization of D-latch/MUX source coupled logic gates, Int. J. Circuit Theory Appl. 33 (2005) 65–85.

[12] M. Alioto, G. Palumbo, S. Pennisi, Modelling of source-coupled logic gates, Int. J. Circuit Theory Appl. 30 (2002) 459–477.

[13] M. Alioto, G. Palumbo, Model and Design of Bipolar and MOS Current-Mode Logic (CML, ECL and SCL Digital Circuits), Springer, Netherlands, 2005.

[14] M. Alioto, G. Palumbo, Design strategies for source-coupled logic gates, IEEE Trans. Circuits Syst. – I 50 (2003) 640–654.

[15] K. Gupta, N. Pandey, M. Gupta, Analysis and design of MOS current mode logic exclusive-OR gate using triple-tail cells, Microelectron. J. 44 (2013) 561–567.

[16] H. Hassan, M. Anis, M. Elmasry, Analysis and design of low-power multi-threshold MCML, in: Proceedings of the IEEE International Conference on System-on-Chip, 2004, pp. 25-29.

[17] M. Alioto, L. Pancioni, S. Rocchi, V. Vignoli, Power-delay-area-noise margin trade-offs in positive-feedback MOS current-mode logic, IEEE Trans. Circuits Syst. – I Regul. Pap. 54 (2007) 1916–1928.

ResearchGate

See discussions, stats, and author profiles for this publication at: https://www.researchgate.net/publication/308200143

Nash Commitment for Energy Trading in Liberalized Power Market: a State of Art Review

Article · August 2016

DOI: 10.15866/iree.v11i4.9049

CITATIONS
0

READS
13

5 authors, including:



Madanmohan Tripathi
Delhi Technological University
35 PUBLICATIONS **65** CITATIONS

SEE PROFILE

All in-text references underlined in blue are linked to publications on ResearchGate, letting you access and read them immediately.

Available from: Madanmohan Tripathi
Retrieved on: 27 September 2016

Praise Worthy Prize

International Review of Electrical Engineering (I.R.E.E.), Vol. 11, N. 4
ISSN 1827- 6660 *July – August 2016*

Nash Commitment for Energy Trading in Liberalized Power Market: a State of Art Review

M. M. Tripathi[1], Anil Pandey[2], Amit Verma[3], K. G. Upadhyay[4], D. Chandra[5]

Abstract – *With the leading reforms in power sector from regulation to liberalization, monopoly has been transformed to challenging market places of competitive electrical power participants. The manifesto reforms include highly governed power transmission utility, effective price prediction with efficient cost of production and mitigation of long term monopoly of industrial relationship.*

Liberalized power market includes Independent Power Producer (IPP), aiming at maximizing the market profit and Independent System Operator (ISO), ensuring common welfare with guaranteed system stability, market operator (MO) providing platform for physical and financial power trading to participants and many new entities such as franchise, retailer etc.

With the notion that power generating players play "Power Game" by knowing the strategies of other competitors for refining the bid strategy, the theory of Nash Commitment is applied to the electricity market for proper energy trading both at suppliers end and consumers end. This paper investigates and represents the work done so far in the field of electrical power trading using Nash game theory. ***Copyright © 2016 Praise Worthy Prize S.r.l. - All rights reserved.***

Keywords*: Nash Equilibrium, Game Theory, Electricity Market, Strategic Bidding*

I. Introduction

Under the deregulated liberalized power industry, different players namely generating companies and distribution companies which supply electricity to consumer need a proper market place for trading the electricity. In the present scenario of competitive electricity market, research wings of power industries are engaged in developing tools and algorithms for designing better bidding strategies.

The typical wholesale electricity market is shown in Fig. 1. In such a market, ISO plays a crucial role of coordination between supplier and retailer by allocating and supplying power from generating unit to consumer via retailers. Suppliers submit the bid showing amount of energy for sale subject to trade-off between available revenue collected and the energy stored. Similarly buyers follow sellers and independently submit unit wise price bid to the ISO [1].

Due to lack of number of IPPs and heavy capital investment in power generation and transmission, bigger power market player shows characteristics of imperfect competition. This imperfect nature of market makes them to bid at much higher prices than their marginal cost of production. This defines a strategic bidding problem [2].

In such a market there is a chance that market players would play "Power Game" by knowing the bidding strategies of other competitors for refining their own bid strategy. The theory of Nash commitment is applied to the electricity market for proper energy trading both at suppliers end and consumers end. In the imperfect market, IPPs act as non-cooperative market players and choose strategies of power as an output rather than pricing tag, making Nash–Carnout equilibrium more efficient than Nash-Bertrand model of equilibrium [3]. In this paper, a detailed review of Nash commitment for energy trading in the Liberalized power market is presented.

The paper discusses the various formulations of bidding, methodologies adopted and tools applied for strategic bidding in the electricity market. In the next sections, the related literature is arranged in following manner. Section II discusses the formulation of bidding strategy in energy trading in wholesale electricity market. Section III refers to the methodologies used in Nash equilibrium game theory in electricity market. Section IV presents the conclusion.

II. Formulation of Bidding Strategy in Energy Trading

According to the available literature on recent trends of market participant's behavior, energy trading modeling can be categorized in the following types [2]:

- *Optimization Model*

It is applicable for single participant for maximizing the profit in whole sale market.

- *Equilibrium Model*

It is related to Nashian commitment involving multiplayers in overall competition.

Copyright © 2016 Praise Worthy Prize S.r.l. - All rights reserved DOI: 10.15866/iree.v11i4.9049

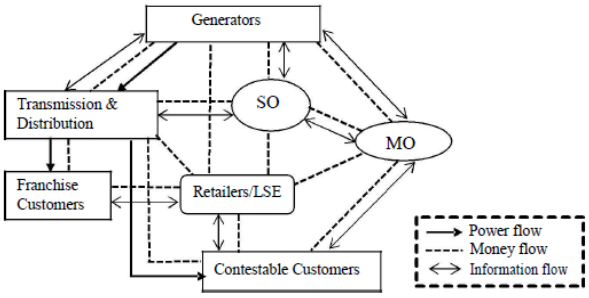


Fig. 1. The Generalised Electricity Market

- *Simulation Model*

This model works as per some rule based concepts of agents interacting with other participants dynamically.

III. Methodologies Used in Nash Equilibrium Game Theory for Bidding in Electricity Market

Researchers have proposed and adopted various equilibrium models with different competition rules in electricity market such as Nash Bertrand rule, Nash Cournot rule, Stackleberg game of multi-leader and multi-follower rule, Supply function equilibrium.

In the early 90s, S. M. Shahidehpour [4] gave the very first work in the field of estimating bid using Nash theory. According to him, an Independent System Operator (ISO) gets offers from Pool members and characterizes exchanges among members by searching for the base value that fulfils the interest in the Pool.

The opposition among Pool members is displayed as a non-helpful amusement with fragmented data and every Pool member knows its own particular operation costs but does not know his adversaries' operation costs.

The diversion with fragmented data is changed into a diversion with complete, yet defective data and explained utilizing the Nash harmony thoughts. The acquired methodologies for the Nash balance of the diversion, augments the normal restrictive pay-off to members.

In this method members get maximum profit which makes the acquired Nash balance methodologies significantly, more appropriate for participants.

Fig. 2 shows that how offers by generators and also loads make a spot market for power. The spot price is compiled by considering the last generator dispatched by the ISO to adjust the Pool supply and demand.

Transmission limitations may force markets from being completely focused; permitting firms to practice market power and raise costs above marginal cost.

A vital gaming model for examining such markets is presented in [5]. It speaks of an oligopolistic business sector economy comprising of a few overwhelming firms in an electric power system. Each producing firm submits offers to an ISO, picking its offers to augment benefits subject to expected responses by adversary firms.

The single-firm model is detailed as a numerical system with harmony requirements with a parameter-subordinate spatial value harmony issue as the internal issue. The harmony is a supply work harmony, in which all matched generators streamline their offer bids under the supposition that other firms won't change theirs. A diversion hypothesis application for dissecting power exchanges in a deregulated energy market where Pool members, particularly producing power firms expand their net benefits through ideal offering procedures (i.e., offering costs and offering eras) is presented in [6]. The power market for energy exchanges is demonstrated as a non-co-operative amusement with complete data, where the arrangement is resolved in a methodology having plan of action to the Nash harmony thought. A two-sided market in which producing organizations submit offers to stacks and determined essential and adequate states of Nash equilibrium (NE) offering system in a respective power market is analysed. With the essential what's more, adequate conditions, system advancement method is connected to develop NE offering methodologies [7].

Specifically, it is demonstrated that under the presumption that every one of the loads request and clear the offers all the while, productive distribution is accomplished in any NE and all NE are income proportional for the generators. A first value fixed offer auction mechanism is embraced to accomplish an exchange. Generators submit offers to a load.

The least offer is the triumphant offer if this offer cost is lower than the load's ability to pay. Another offering system for day-ahead power markets has been displayed [8]. A basic element model of patterned request and supply is in which there is a time slack between the reactions of makers to an adjustment in cost. The bidding model proposed takes into account the idea of Cournot iterative equilibrium, as a consequence of an organization augmenting its advantage, considering that the contender's conduct is settled. A Cournot like iterative system just considers amounts as variables, not costs.

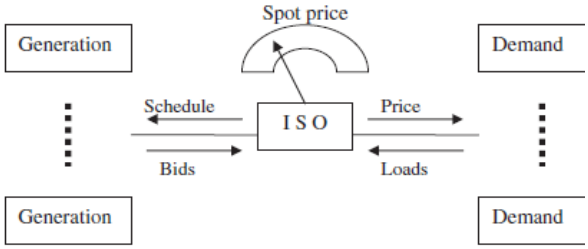


Fig. 2. The Pool Model

III.1. Price Takers

Their offer is not expected to coordinate the interest. Slight varieties in their offer result in slight changes in the market cost. They are likewise called "competitive fringe.

III.2. Cournot Competitors

Total interest can't be met without them. They have a

Copyright © 2016 Praise Worthy Prize S.r.l. - All rights reserved

major effect over the cost due to their market power.

In a genuine power sector both sorts of operators would contend with one another and their separate bidding strategies would be very distinctive. That distinction originates from the idea of residual demand curve as it can be found in Figs. 3 and 4, individually.

The cobweb procedure starts with the operators' estimation of the last market cost. After that, the specialists computes its ideal generation in light of the evaluated cost, and afterward watches the impact. When the cost is watched, the operators re-figure the ideal creation with the new cost. The procedure continues until merging in costs is come to, a two-period value cycle or undammed oscillations start.

The union case is demonstrated in Fig. 5 for direct supply and interest curve. An algorithm that permits a market participant to boost its individual welfare in power spot markets is displayed and utilization of the algorithm in deciding market balance focuses, called Nash equilibrium, is illustrated [9]. Start of the algorithm is a spot market display that uses the open power flow (OPF) with a full representation of the transmission framework and incorporation of buyer offering.

The algorithm uses value and dispatch sensitivities, accessible from the Hessian network and inclination of the OPF to help focus an ideal change in a singular's offered. The algorithm is demonstrated to be fruitful in deciding nearby welfare maxima, and the prospects for scaling the algorithm up to reasonably estimated frameworks are great. Nash equilibrium is explored expecting all participants endeavour to amplify their individual welfare. This is finished by iteratively fathoming the individual welfare expansion algorithm until all people quit adjusting their offers. A game-theoretic structure for the maintenance scheduling of generating units (MSU) issue is proposed which is pertinent to competitive power markets. The structure empowers to consider the associations of contending generating companies which are the critical concerns in the aggressive power market environment. In this structure, the MSU issue is considered into a multistage dynamic non cooperative amusement with complete data [10]. The market harmony arrangement is described by the Nash balance and can be acquired by the regressive impelling plan in view of the sub-game impeccable balance idea. The numerical representation for two-player diversion is given to exhibit the essential thoughts of the proposed plan, and substantial scale IEEE dependability test frameworks are additionally considered to demonstrate the pertinence of the proposed structure. Beyond idealized situation where transmission framework is not a constraint but Congestion in the transmission framework may permit a few members to appreciate compelling profit, bringing about higher costs.

This component is investigated in the system of amusement game hypothesis and it demonstrates that the deviation from glorified price taker conduct is more genuine when some market players experience the ill effects of the congestion issue [11].

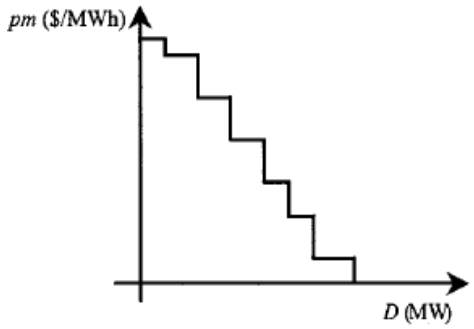


Fig. 3. Residual demand for Price Taker

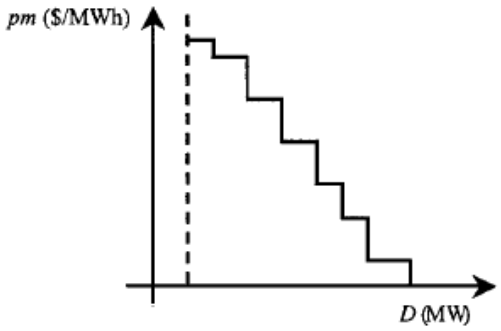


Fig. 4. Residual demand for Cornout Competitor

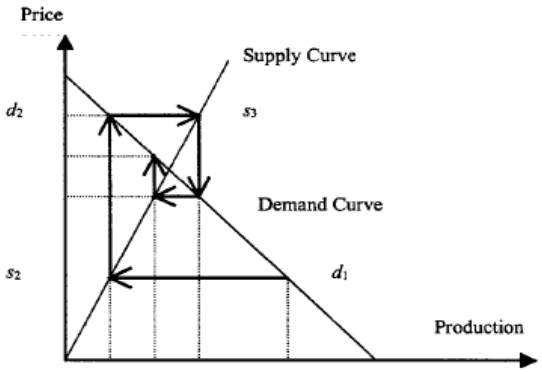


Fig. 5. Union case for direct supply and interest curve

The issue of discovering numerous market equilibria for multi-machine frameworks that possibly yield an unmanageable number of pursuit search regions (districts) is addressed in [12]. The technique proposed dispenses with the dominant part of those districts through progressive sifting flow solutions to feasible optimal power flow solutions. The methodologies for discovering the NE have had two noteworthy bottlenecks known as calculation of blended methodology harmony and treatment of multiplayer diversions. A payoff network is proposed with an approach that determines these bottlenecks [13]. The proposed technique can proficiently locate a blended method harmony in a multiplayer diversion. The plan of the NE condition for a three-player amusement is presented and an essential reckoning plan of unravelling nonlinear uniformities and checking disparities is proposed.

Another way to deal with discovered Nash equilibria

Copyright © 2016 Praise Worthy Prize S.r.l. - All rights reserved

in power markets is presented in [14]. It is taking into account the Nikaido–Isoda capacity and a relaxation algorithm (NIRA). The Nikaido–Isoda capacity demonstrates when the Nash balance has been reached (i.e., the players can't enhance their benefits).

The relaxation algorithm is the best approach to join to the Nash harmony by emphasizing with a weighted normal of the players' profit. Ref. [15] presents a three-stage procedure to discover equilibria.

Initial, a point by point model of an electricity market is introduced, considering multi-period bidding, value versatility, and system displaying. Second, an iterative reproduction procedure is raced to distinguish members' bidding methods understood in the improved generation coming about because of the recreation. At last, yield information from the test system are dissected to get Nash equilibria. Iterated cancellation is utilized as a part of the last stride to uproot methodologies that are ruled by others that produce higher benefits.

A bilateral electricity market model is reanalysed with suppliers possessing numerous generators. It illuminated some verifiable suppositions in the model and demonstrated that, under one point by point determination of the suppositions, the beforehand proposed Nash equilibria for the model are conflicting with the meaning of Nash harmony [17]. It Proposed a Nash harmony model taking into record transmission imperatives for an offer based-pool market is detailed as a bid based non-linear complementarities issue.

The bid based non-linear complementarily issue is acquired by social affair the KKT states of the improvement issue of each key producing firm.

All together to explain it, the non-linear complementarily strategy is utilized with a unique non-linear complementarily capacity function. The outcomes demonstrate that the generating firms could practice their market control by over-creation under congestion, or by limit withholding if there should arise an occurrence of power shortage. The methodology gives an effective path to the arrangement of substantial scale, entangled harmony models for power markets.

It is demonstrated that the aggregate expected income for the NEs under uniform evaluating and pay-as-offer estimating is generally not identical [18].

Ref. [19] Provided the representation of inadequate and lopsided data in key recreations together with a percentage of the transmission framework imperatives by addressing the issue of discovering Bayesian Nash equilibria in a concentrated (Pool) market where the generator's sorts are displayed as deficient data utilizing two-stage, data saving Monte Carlo approach for discovering the Bayesian Nash equilibria. It concentrates on a particular vital amusement model alluded to as the IWM. Numerical samples, utilizing the IEEE 57-BUS framework, that arrangement with the power flow equality constraints are exhibited as representation of the ideas driving the proposed Bayesian amusements.

Ref. [20] proposed a technique for investigating the opposition among transmission-compelled Generating Companies (GENCOs) with inadequate information.

The rivalry is displayed as a bi-level problem with the upper sub-problem speaking to individual GENCOs and the lower sub-problem speaking to the Independent System Operator (ISO). The upper sub-problem augments the individual GENCO's settlements and the lower sub-problem takes care of the ISO's market clearing problem for minimizing buyers' instalments. In this paper, the opposition among GENCOs is displayed as a bi-level problem, and sensitivities of GENCO's result regarding bidding strategies are produced for tackling the bi-level problem. An 8-bus system is utilized to show the proposed system.

The test outcomes demonstrate that the exchange ability has a noteworthy effect on GENCOs' bidding strategies and their normal settlements. Be that as it may, by applying the proposed technique, GENCOs can procure more than the situation when they offer at their peripheral expenses. The system can be stretched out to consider the vital bidding of GENCOs in multi-periods.

The proposed system can likewise be utilized by the ISO to screen conceivable market power opportunities.

The flowchart for an incomplete game is shown in Fig. 6 [20]. Ref. [21] formulated optimal generator bidding when there is a solitary demand is considered.

The improvements to the MPEC managed by the notion of deterministic MPEC. The problem is considered with and without supply limit imperatives. By considering each of these cases as a game hypothesis problem, the presence and uniqueness of Nash focuses are analysed. These properties of the Nash point are then deduced onto the stochastic problem.

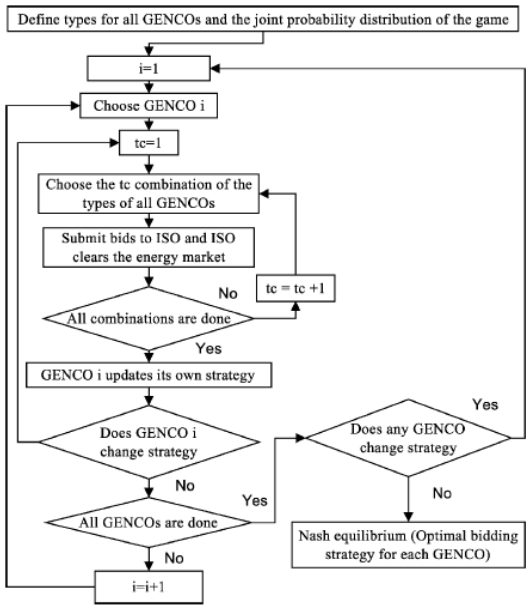


Fig. 6. Solution for incomplete game

Ref. [22] proposed the effects of power suppliers learning conduct on power spot-market harmony under rehashed direct linear supply-capacity function bidding. In such markets, every individual supplier will lead

Copyright © 2016 Praise Worthy Prize S.r.l. - All rights reserved

"learning" to enhance its key offering with a specific end goal to gain more benefit. first settled up the numerical model for a supplier's optimal bidding, which is utilized to illuminate for the Nash harmony and demonstrated that supply-function equilibrium is a Nash balance; and that, in specific conditions, the general learning conduct will reduce the market clearing price, which then expands customers' surplus and reductions suppliers' benefits; while in some different conditions the outcomes are the polar opposite. In either case, the MCP at balance prompted by the general learning conduct mirrors the genuine relationship of supply and demand of interest. Numerical results bolster the systematic conclusions extremely well.

Ref. [23] addressed the unit-responsibility problem confronted by players as they have to self-submit their units in a market structure. This key problem is figured through a probabilistic-element programming model, where the likelihood of a specific generator being web amid a particular market period is situated by its proprietor. The arrangements embraced for that problem are Nash equilibria in mixed blended techniques. a general probabilistic-dynamic programming structure for the problem of self-submitting committed units when there are numerous non-cooperative market agents with clashing interest. Equilibria in mixed integer linear problem (MILP) for the limited time horizon proposed as proper response for strategic Unit Commitment problem.

Ref. [24] presented mixed integer linear programming solution approach for the harmony equilibrium problem with balanced imperatives problem of discovering the Nash balance (NE) in key offering in transient power markets. A binary expansion (BE) plan is utilized to change the nonlinear, nonconvex, NE problem into a blended mixed integer linear problem (MILP), which can be comprehended by industrially accessible computational frameworks. The BE plan is utilized to change the nonlinear, nonconvex, NE problem into a blended whole number straight problem, which can be comprehended by economically accessible computational systems. The BE plan is material to Cournot, Bertrand, or joint value/amount bidding models, including multi-plant operation costs, unit duty, and the count of different Nash equilibria. The methodology is considered with an example as case study of configurations from the Brazilian system.

Ref. [25] proposed the vicinity of transmission limitations confine rivalry among suppliers and give more chances to suppliers to practice market power. An expository approach through discovering a Nash balance is exhibited for mulling over the impacts of long haul contracts on market balance in an offer based pool with transmission requirements. The investigation demonstrates that the vicinity of long haul contracts may bring about diminished expected social welfare.

A co-evolutionary way to deal with supply function equilibrium (SFE) models of an oligopolistic power market is presented in [26]. Simulation results demonstrates that the co-evolutionary approach quickly merges to SFE in the relative supply function model re-enactment and powerfully meets to SFE in all instances of the piece-wise relative supply function model simulation. Two distinctive oligopolistic power market models are utilized as a part of examination. In the Cournot diversion the organizations settle on their amount choices in the meantime to expand their own benefits, while in the surly function equilibrium (SFE) demonstrate every firm picks as its system a "supply capacity" relating its amount to its cost. Diverse parameterization instances of the supply capacity model are investigated. Simulation results demonstrated that the co- evolutionary methodology unites to the Nash equilibria quickly in all cases and is profoundly proficient in market re-enactment. Since the co-evolutionary methodology utilizes the general purposed hereditary genetic algorithm or other transformative evolutionary algorithm for firms' versatile vital taking in, the complex sensible conditions in power market can be displayed.

An altered fortification learning methodology in light of Q-balanced strengthening has been connected to focus the ideal procedure for a power supplier in a power market with numerous sources is presented in [27]. A changed IEEE 30-bus framework has been considered and the simulation results are indicated to be the same as with standard amusement hypothesis. The fundamental point of preference of the proposed strategy is that no data about different members is needed.

Examination demonstrates that if all members utilize this strategy they will stay in Nash harmony. Ref. [28] investigated oligopolistic rivalry in an electric power market portrayed by a multi-pioneer single-devotee game, and detailed as a nonlinear programming (NLP) issue. An AC system is utilized to speak to the transmission framework, and is demonstrated utilizing rectangular coordinates. The adherent is made out of a situated of aggressive suppliers, requests and the framework administrator, while the pioneers are the prevailing suppliers. The AC approach permits one to catch the strategic behaviour of suppliers with respect to dynamic as well as reactive power.

Ref. [29] proposed a systematic examination for over effects of system imperatives available harmony equilibrium in oligopolistic power markets.

The ISO dispatches generation and decides nodal costs by means of taking care of an OPF issue; and the individual generator enhances its supply work with Nash-Cournot system, subsequent to making into note of the ISO's choice making process on dispatched power and nodal costs. The conditions for the presence of balance are given, and it is demonstrated that there may be numerous equilibria; and the balance, if exists, will be at a point where generators pay no clogging or congestion charge.

Systematic models and methods in view of generation framework and load information for probabilistically speaking to two distinctive market rivalry models—one is in view of flawless rivalry and the other taking into

Copyright © 2016 Praise Worthy Prize S.r.l. - All rights reserved

account lopsided oligopoly (cournot) are presented [30]. An inside point calculation in view of a.c. system model for deciding the Nash supply work harmony (SFE) of offer based power markets [31]. The SFE issue is considered as a bi-level amusement. At the first level, the issue starts with the detailing of an optimal power flow (OPF) inside point-based calculation to handle the ISO issue for augmenting social welfare. This calculation is in light of the OPF with a.c. system transmission model considering all the working perspectives, for example, the generation capacity limit, bus voltage limits, transmission line limitations, system misfortunes and particularly the impact of the responsive reactive power influence.

The subsequent Karush-Kuhn-Tucker (KKT) states of the issue at the first level are then reformulated utilizing nonlinear complementarily limitations and fused as correspondence imperatives in the second-level detailing for expanding the individual benefit for each key generating firm. By utilizing an extraordinary nonlinear complementarily work, the complementarily limitations are then changed into nonlinear logarithmic expressions, in this way the KKT states of the subsequent joined issue can be inferred. The last issue is then illuminated iteratively taking into account the arrangement methods of the inside point algorithm. The arrangement strategy of the nonlinear interior point calculation for deciding the power market balance proposed in Fig. 7.

Ref. [32] demonstrated that the limited discerning subjects with awry maker expense capacities can reach hypothetical static Cournot-Nash harmony in rehashed games. The outcomes demonstrate that the market competition rivalry will merge to the outcomes between impeccable rivalry balance and Nash harmony in oligopolistic power markets with awry creation expense capacities and rehashed play among the Gencos.

The choice support tool of Gencos have critical impacts on exploratory results. The market concentrates to static Cournot-Nash balance when the limited bounded-rational subject over and again play, furnished with the tools that can give best reaction response systems. The exploratory technique gives a supplement to the hypothetical examination and simulation re-enactment and has numerous benefits in displaying sensible power markets.

The vital conditions for power market results bolstered by immaculate system Nash equilibria (NE) to exist when generating companies (Gencos) amusement through their incremental expense offers or supply works, then, built up a mixed-integer linear programming (MILP) plan to discover the NE without close estimations or cycles/ iterations [33]-[34]. It also demonstrated how to utilize these NE to infer an overwhelming offer methodology regarding gaming or not gaming that best meet the danger/advantage desires of the taking an interest GENCOs.

Ref. [35] proposed a power market model taking into account a guess value reaction balance to speak to specialists' vital conduct, and makes utilization of plausibility disseminations to display the operators RDC vulnerability taking into record the risk-averse attitudes.

The exhibited contextual analysis affirms, from one perspective, that the proposed determination technique can settle, with worthy execution times, genuine size genuine issues with very nearly 200 generating units and more than 100 000 constraints and variables. Then again, it affirms that the arrangement acquired is sensible, and more vigorous under vulnerability than the deterministic one, since, for instance, benefit scatterings have a tendency to be lower. At last, harmony conduct under vulnerability has a tendency to move specialists towards their expected conditions, which is cognizant with operators' hazard avoidance presumptions. Ref. [36] demonstrated that if the IC block offers can change, the market results upheld by Nash equilibria (NE) are less than or equivalent to the quantity of GENCOs and can all be registered through a mixed-integer linear programming (MILP) plan.

It introduced more productive numerical plan to discover the NE that does not require the utilization of parallel variables and MILP. Tests demonstrate that Lambda - iterative methodology is of the request of 1000 times quicker.

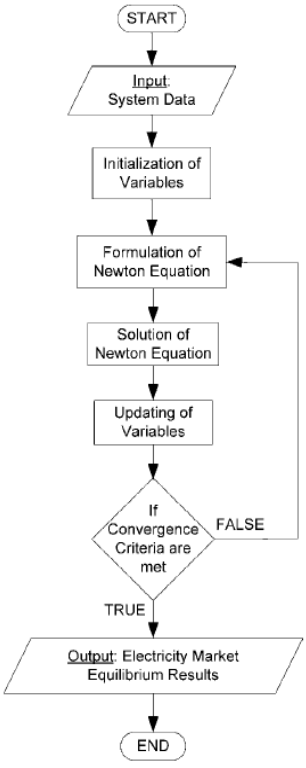


Fig. 7. Solution procedure of the electricity market equilibrium algorithm

A general multi-leader-one-supporter nonlinear bi-level (MLNB) is proposed with improved idea and related definitions in view of the summed up Nash balance, then applied particle swarm-optimisation based calculation to take care of the issue characterized in the MLNB choice model [37].

Copyright © 2016 Praise Worthy Prize S.r.l. - All rights reserved

The examination results demonstrate that the proposed PSO-based MLNB calculation can accomplish a GNE for a MLNB issue in a power advertise by furnishing the producing organizations with aggressive vital offering inside of the system security limitations. Outline of PSO based MLNB algorithm in shown in Fig. 8.

Ref. [38] provided the key issue in pool-based power markets considering mutually cost and amount vital offers in a multi-specialists, multi-period, and multi-piece amusement game to develop stochastic EPEC as MILP. [39] proposed a method, based on the payoff matrix methodology, to conquer the transmission constraints.

The proposed strategy basically lies in the disintegration of the diversion by method for the accompanying backings: in the first place, the NE condition is changed over to a polynomial arrangement of mathematical statements with disparity imperatives for every conceivable support; second, the homotopic continuation calculation is utilized to get every one of the arrangements of the polynomial framework; third, every arrangement of the framework is checked to confirm whether it fulfils the inequality requirements.

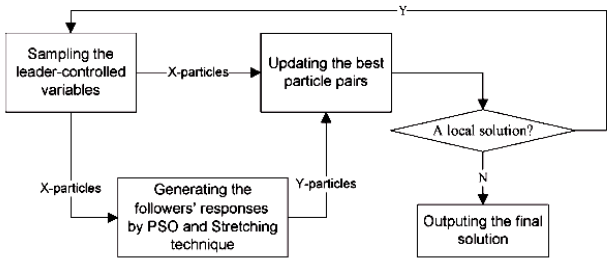


Fig. 8. Outline of PSO based MLNB algorithm

An optimal game theoretic time-of-use (TOU) power estimating methodology (GT-TOU) is proposed which is composed of utility capacities for both service companies and clients, and unravelled for a Nash harmony, which gives ideal costs and client reactions [40].

The arrangement structure for figuring multi-member Nash equilibria in a transmission-obliged power market is revealed in [41]. The proposed structure, which is for the most part pertinent to different gaming conditions in power markets, is utilized here for non-agreeable complete data amusement between market players with discrete offering techniques is shown in Fig. 9.

Ref. [42] proposed a distributed demand-side management (DSM) technique planned for grid network clients with load forecast abilities, who potentially utilize dispatch able vitality era and capacity gadgets. Ref. [43] delivered an investigative solution for bidding strategy problem of transmission-constrained generating companies (GENCOs) in half an hour-ahead power market. Here, for demonstrating a bidding strategy under supply function equilibrium, a bi-level programming (BLP) strategy is utilized.

Ref. [44] Provides deterministic and stochastic circumstances of a deregulated electric power market have been displayed and considered through simulation re-enactments utilizing agent based co-evolutionary approach and investigated two choice making systems, specifically model-based and learning-based offering procedures, are proposed and analyzed, for rehashed Cournot rivalry of the generators in a day-ahead power market.

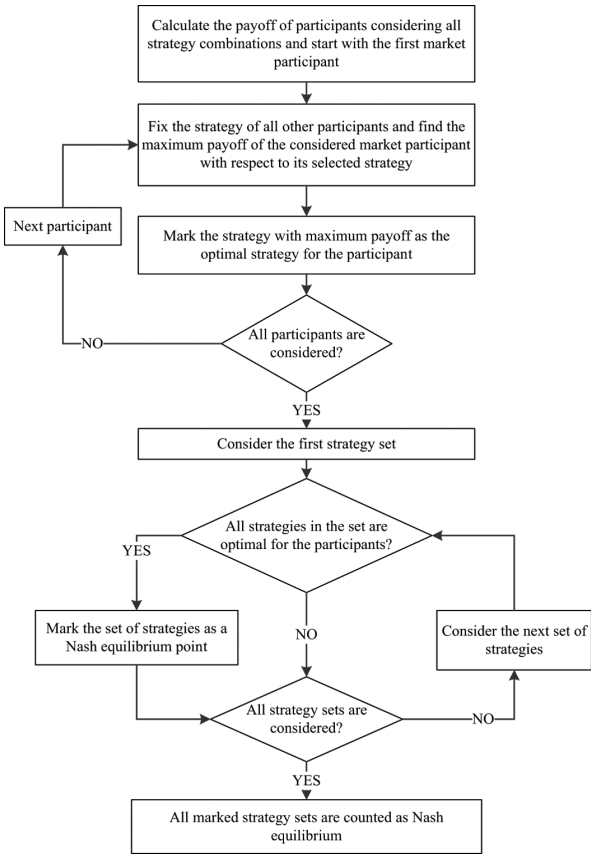


Fig. 9. Finding Nash Equilibrium points for n- participants

The entirety of the rivals' offered amounts is considered as the condition of the operators and its esteem is assessed utilizing a versatile desire technique.

Ref. [45] considered a dynamic market model for demand response where ac power is connected to match power supply deficiency or excess and described the subsequent equilibria in aggressive and oligopolistic markets and proposed dispersed distributed demand response algorithm to accomplish the equilibria.

Also have demonstrated that the harmony in focused market augments social welfare, and the balance in oligopolistic market has limited effectiveness misfortune under certain gentle suspicions**.**

A day-ahead grid optimization is formulated using generalized Nash equilibrium problem, which allows formal adjustment of generation and storage strategies to reduce the real time deviation in respect of energy negotiated in DA market. A bi-level optimization problem which includes strategic bid stands good for market having incomplete information and solves the clearing prices of the market. Since bi-level optimization approach is non-convex and unable to handle the

Copyright © 2016 Praise Worthy Prize S.r.l. - All rights reserved

problem under global optima, a novel prey predator optimization approach is applied at the very first level of bi-level optimization [46].

Ref. [47] proposed a theoretic way to deal with configuration a disseminated ongoing real time power evaluating system. Proposed methodology is novel in that it promises single rationality, implying that it gives suppliers and customers an ensured motivator to take an interest in the continuous evaluating market price. Such a motivating incentive is concocted by offering a period changing, circumstance subordinate sponsorship that ensures that a supplier/customer benefits by changing from a settled value contract to the constant evaluating contract. Suppliers and buyers choose supply and interest amounts in a completely circulated way to amplify their own particular benefit, the proposed system ensures under moderate conditions that the business meets through an iterative procedure to a Nash balance that boosts social welfare. Moreover, with a specific end goal to ensure safe operation of an electrical network, by estimating component expands soundness of load frequency control, and in the meantime, accomplishes supply-demand harmony by expressly considering a balance limitation through dual decomposition method.

A simulation model is presented in light of the Nash balance thought for the sale based day ahead power generation market [48]. The exhibited model upgrades a past formalism proposed in the related writing by utilizing observational information dispersions of the power market clearing cost as enrolled by power market authority (e.g. the Independent System Operator).

The model is successful when power suppliers with diverse power limits are considered, uniquely in contrast to the beginning model that unreasonably expect rise to limits. The proposed methodology goes for assessing the power market aggressiveness as to the bidder systems with a specific end goal to keep their anticompetitive activities. The structure is connected to genuine information set with respect to the Italian power market to edify its viability in distinctive situations, shifting the number and limit of interested participating bidders.

With the changing environment of smart grid, the introduction of micro grids (MGs) into the utility grid postures new difficulties in the vitality administration outline because of the discontinuous attributes of renewable vitality sources and constrained storage limit. Ref. [49] tended to an issue in which a few micro-grids connect by trading vitality to minimize the worldwide operation expense while as yet fulfilling their local demands. In this connection, creators proposed an iterative conveyed calculation that is versatile in the quantity of micro-grids and keeps local cost distributed algorithm. More in particular, every algorithm cycle comprises of a neighborhood local minimization step took after by a market clearing procedure.

Ref. [51] proposed a distributed energy management algorithm by mulling over the associations and interconnections among service organizations, MGs, and clients, and displayed the energy management issue as a two-stage Stackelberg diversion, in which service organizations and MGs are amusement pioneers, and clients are diversion supporters. Service organizations and MGs decide about what cost to offer their power to clients. Clients confirm their power acquisition sums taking into account the costs offered by service organizations and MGs. Paper also demonstrated that a Nash harmony exists in the proposed two-stage Stackelberg amusement, and the ideal arrangements got by the distributed energy management algorithm is precisely the Nash balance [50]. Addressed and build up a diagnostic model of a multileader and multi-follower Stackelberg diversion approach and propose a bi-level multi-objective evolution developmental algorithm to discover optimal procedures that augment the benefit of utilities, and minimize carbon outflows in an open energy market among interconnected micro sources.

Supply function models have been widely used in optimal energy trading, since individual generating trader submit the bid in the form of supply function for representing the authentication of generating the required supply at various electricity price [52]-[55].

Ref. [52] dealt with the Supply Function Equilibrium (SFE) as a model of rivalry in power markets. It presents hypothetical progression through unwinding customary suspicions of coherence of supply capacities and gives an establishment to effective computational algorithms. Extraordinary accentuation is put on investigating the presence of equilibria and on the players' capacity to learn subject to data accessible to them. The hypothesis is connected to demonstrating simulation models of power showcases in the United States.

IV. Conclusion

This paper has exhibited a brief writing overview of the most important contributions analyzing the bidding strategies in competitive electricity market.

The distinctive market structure, closeout mechanism and bidding practices in the restructured electricity markets are investigated. Nash Harmony models speak about the general market conduct taking into account their own strategy and the rivalry among all members.

The methodology expects that every player in the market tries to boost its benefit. Consequently execution of bid by a market member is influenced by other member’s practices. All players are thought to be judicious which does not hold well for the most part as a general rule. These models are created with point of improving the effectiveness of the bids.

Artificial intelligence tools and optimization tools have been extensively used in modeling the bidding strategy in the electricity market and have shown good results. These tools become more relevant while bidding in an electricity market with additions of micro grids.

References

[1] Joohyung Lee; Jun Guo; Jun Kyun Choi; Zukerman, M.,

Copyright © 2016 Praise Worthy Prize S.r.l. - All rights reserved

"Distributed Energy Trading in Microgrids: A Game-Theoretic Model and Its Equilibrium Analysis," *Industrial Electronics, IEEE Transactions,* vol.62, no.6, pp.3524-3533, June 2015.

[2] M Prabhavati; R Gnadass., "Enegy biiding stretegies for restructured electricity market," *International Journal of Eelctrical Power & Energy Systems,* vol. 64, pp. 956-966, January 2015.

[3] Magdelena Klemun; "Application of Nash Equilibria in Electricity Market," *Term Paper on Electrical Power Networks* 2012.

[4] Ferrero, R.W.; Rivera, J.F.; Shahidehpour, S.M., "Application of games with incomplete information for pricing electricity in deregulated power pools," *Power Systems, IEEE Transactions on*, vol.13, no.1, pp.184,189, Feb 1998.

[5] Hobbs, B.F.; Metzler, C.B.; Pang, J.-S., "Strategic gaming analysis for electric power systems: an MPEC approach," *Power Systems, IEEE Transactions on*, vol.15, no.2, pp.638,645, May 2000.

[6] Jong-Bae Park; Jin-Ho Kim; Jin-Ho Kim; Man-Ho Jung; Jong-Keun Park, "A continuous strategy game for power transactions analysis in competitive electricity markets," *Power Systems, IEEE Transactions on*, vol.16, no.4, pp.847,855, Nov 2001.

[7] Song, H.; Chen-Ching Liu; Lawarree, J., "Nash equilibrium bidding strategies in a bilateral electricity market," *Power Systems, IEEE Transactions on*, vol.17, no.1, pp.73,79, Feb 2002.

[8] Contreras, J.; Candiles, O.; de la Fuente, J.I.; Gómez, T., "A cobweb bidding model for competitive electricity markets," *Power Systems, IEEE Transactions on*, vol.17, no.1, pp.148,153, Feb 2002.

[9] Weber, J.D.; Overbye, T.J., "An individual welfare maximization algorithm for electricity markets," *Power Systems, IEEE Transactions on*, vol.17, no.3, pp.590,596, Aug 2002.

[10] in-Ho Kim; Jong-Bae Park; Jong-Keun Park; Jin-Ho Kim, "A new game-theoretic framework for maintenance strategy analysis," *Power Systems, IEEE Transactions on*, vol.18, no.2, pp.698,706, May 2003.

[11] Tengshun Peng; Tomsovic, K., "Congestion influence on bidding strategies in an electricity market," *Power Systems, IEEE Transactions on*, vol.18, no.3, pp.1054,1061, Aug. 2003.

[12] Correia, Pedro F.; Overbye, T.J.; Hiskens, I.A., "Searching for noncooperative equilibria in centralized electricity markets," *Power Systems, IEEE Transactions on*, vol.18, no.4, pp.1417,1424, Nov. 2003.

[13] Kwang-Ho Lee; Baldick, R., "Solving three-player games by the matrix approach with application to an electric power market," *Power Systems, IEEE Transactions on*, vol.18, no.4, pp.1573,1580, Nov. 2003.

[14] Contreras, J.; Klusch, M.; Krawczyk, J.B., "Numerical solutions to Nash-Cournot equilibria in coupled constraint electricity markets," *Power Systems, IEEE Transactions on*, vol.19, no.1, pp.195,206, Feb. 2004.

[15] de la Torre, S.; Contreras, J.; Conejo, A.J., "Finding multiperiod Nash equilibria in pool-based electricity markets," *Power Systems, IEEE Transactions on*, vol.19, no.1, pp.643,651, Feb. 2004.

[16] Son, Y.S.; Baldick, R.; Shams Siddiqi, "Reanalysis of "Nash equilibrium bidding strategies in a bilateral electricity market"," *Power Systems, IEEE Transactions on*, vol.19, no.2, pp.1243,1244, May 2004.

[17] Wang Xian; Li Yuzeng; Zhang Shaohua, "Oligopolistic equilibrium analysis for electricity markets: a nonlinear complementarity approach," *Power Systems, IEEE Transactions on*, vol.19, no.3, pp.1348,1355, Aug. 2004.

[18] You Seok Son; Baldick, R.; Kwang-Ho Lee; Shams Siddiqi, "Short-term electricity market auction game analysis: uniform and pay-as-bid pricing," *Power Systems, IEEE Transactions on*, vol.19, no.4, pp.1990,1998, Nov. 2004.

[19] Correia, Pedro F., "Games with incomplete and asymmetric information in poolco markets," *Power Systems, IEEE Transactions on*, vol.20, no.1, pp.83,89, Feb. 2005.

[20] Tao Li; Shahidehpour, M., "Strategic bidding of transmission-constrained GENCOs with incomplete information," *Power Systems, IEEE Transactions on*, vol.20, no.1, pp.437,447, Feb. 2005.

[21] Couchman, P.; Kouvaritakis, B.; Cannon, M.; Prashad, F., "Gaming Strategy for Electric Power With Random Demand," *Power Systems, IEEE Transactions on*, vol.20, no.3, pp.1283,1292, Aug. 2005.

[22] Liu, Y.F.; Ni, Y.X.; Wu, F.F., "Impacts of suppliers' learning behaviour on market equilibrium under repeated linear supply-function bidding," *Generation, Transmission and Distribution, IEE Proceedings-*, vol.153, no.1, pp.44,50, 12 Jan. 2006.

[23] Correia, P.F., "Decentralised unit commitment in a market structure: problem formulation and solution advancement," *Generation, Transmission and Distribution, IEE Proceedings-*, vol.153, no.1, pp.121,126, 12 Jan. 2006.

[24] Barroso, L.A.; Carneiro, R.D.; Granville, S.; Pereira, M.V.; Fampa, M.H.C., "Nash equilibrium in strategic bidding: a binary expansion approach," *Power Systems, IEEE Transactions on*, vol.21, no.2, pp.629,638, May 2006.

[25] Nam, Y.W.; Park, J.K.; Yoon, Y.T.; Kim, S.-S., "Analysis of long-term contract effects on market equilibrium in the electricity market with transmission constraints," *Generation, Transmission and Distribution, IEE Proceedings-*, vol.153, no.4, pp.383,390, 13 July 2006.

[26] Chen, H.; Wong, K.P.; Wang, X.; Chung, C.Y., "A coevolutionary approach to modeling oligopolistic electricity markets," *Power Engineering Society General Meeting, 2005. IEEE*, vol., no., pp.230,236 Vol. 1, 12-16 June 2005.

[27] Naghibi-Sistani, M.B.; Akbarzadeh-T, M.-R.; B, M.H.J.-D.; Rajabi-Mashhadi, H., "Q-adjusted annealing for Q-learning of bid selection in market-based multisource power systems," *Generation, Transmission and Distribution, IEE Proceedings-*, vol.153, no.6, pp.653,660, November 2006.

[28] Bautista, G.; Anjos, M.; Vannelli, A., "Formulation of Oligopolistic Competition in AC Power Networks: An NLP Approach," *Power Engineering Society General Meeting, 2007. IEEE*, vol., no., pp.1,1, 24-28 June 2007.

[29] Youfei Liu; Wu, F.F., "Impacts of network constraints on electricity market equilibrium," *Power Engineering Society General Meeting, 2006.*

[30] Valenzuela, J.; Mazumdar, M., "Cournot Prices Considering Generator Availability and Demand Uncertainty," *Power Systems, IEEE Transactions on*, vol.22, no.1, pp.116,125, Feb. 2007.

[31] Petoussis, S.G.; Zhang, X.-P.; Godfrey, K.R., "Electricity market equilibrium analysis based on nonlinear interior point algorithm with complementarity constraints," *Generation, Transmission & Distribution, IET*, vol.1, no.4, pp.603,612, July 2007.

[32] Haoyong Chen; Xifan Wang, "Strategic Behavior and Equilibrium in Experimental Oligopolistic Electricity Markets," *Power Systems, IEEE Transactions on*, vol.22, no.4, pp.1707,1716, Nov. 2007.

[33] Hasan, E.; Galiana, F.D.; Conejo, A.J., "Electricity Markets Cleared by Merit Order—Part I: Finding the Market Outcomes Supported by Pure Strategy Nash Equilibria," *Power Systems, IEEE Transactions on*, vol.23, no.2, pp.361,371, May 2008.

[34] Hasan, E.; Galiana, F.D., "Electricity Markets Cleared by Merit Order—Part II: Strategic Offers and Market Power," *Power Systems, IEEE Transactions on*, vol.23, no.2, pp.372,379, May 2008.

[35] Campos, F.A.; Villar, J.; Barquin, J.; Reneses, J., "Variational inequalities for solving possibilistic risk-averse electricity market quilibrium," *Generation, Transmission & Distribution, IET*, vol.2, no.5, pp.632,645, September 2008.

[36] Hasan, E.; Galiana, F.D., "Fast Computation of Pure Strategy Nash Equilibria in Electricity Markets Cleared by Merit Order," *Power Systems, IEEE Transactions on*, vol.25, no.2, pp.722,728, May 2010.

[37] Guangquan Zhang; Guoli Zhang; Ya Gao; Jie Lu, "Competitive Strategic Bidding Optimization in Electricity Markets Using Bilevel Programming and Swarm Technique," *Industrial Electronics, IEEE Transactions on*, vol.58, no.6, pp.2138,2146, June 2011.

[38] Pozo, D.; Contreras, J., "Finding Multiple Nash Equilibria in Pool-Based Markets: A Stochastic EPEC Approach," *Power Systems, IEEE Transactions on*, vol.26, no.3, pp.1744,1752, Aug. 2011.

[39] Yan Yang; Yao Zhang; Fangxing Li; Haoyong Chen, "Computing

Copyright © 2016 Praise Worthy Prize S.r.l. - All rights reserved

All Nash Equilibria of Multiplayer Games in Electricity Markets by Solving Polynomial Equations," *Power Systems, IEEE Transactions on*, vol.27, no.1, pp.81,91, Feb. 2012.

[40] Peng Yang; Gongguo Tang; Nehorai, A., "A game-theoretic approach for optimal time-of-use electricity pricing," *Power Systems, IEEE Transactions on*, vol.28, no.2, pp.884,892, May 2013.

[41] Khodayar, M.E.; Shahidehpour, M., "Optimal Strategies for Multiple Participants in Electricity Markets," *Power Systems, IEEE Transactions on*, vol.29, no.2, pp.986,987, March 2014.

[42] Atzeni, I.; Ordonez, L.G.; Scutari, G.; Palomar, D.P.; Fonollosa, J.R., "Noncooperative Day-Ahead Bidding Strategies for Demand-Side Expected Cost Minimization With Real-Time Adjustments: A GNEP Approach," *Signal Processing, IEEE Transactions on*, vol.62, no.9, pp.2397,2412, May1, 2014.

[43] Taheri, I.; Rashidinejad, M.; Badri, A.; Rahimi-Kian, A., "Analytical Approach in Computing Nash Equilibrium for Oligopolistic Competition of Transmission-Constrained GENCOs," *Systems Journal, IEEE*, vol.PP, no.99, pp.1, Early Access.

[44] Kebriaei, H.; Rahimi-Kian, A.; Ahmadabadi, M.N., "Model-Based and Learning-Based Decision Making in Incomplete Information Cournot Games: A State Estimation Approach," *Systems, Man, and Cybernetics: Systems, IEEE Transactions on*, vol.45, no.4, pp.713,718, April 2015.

[45] Na Li; Lijun Chen; Dahleh, M.A., "Demand Response Using Linear Supply Function Bidding," *Smart Grid, IEEE Transactions on*, vol.6, no.4, pp.1827,1838, July 2015.

[46] Bahmani-Firouzi, B.; Sharifinia, S.; Azizipanah-Abarghooee, R.; Niknam, T., "Scenario-Based Optimal Bidding Strategies of GENCOs in the Incomplete Information Electricity Market Using a New Improved Prey—Predator Optimization Algorithm," *Systems Journal, IEEE*, vol.PP, no.99, Early Access.

[47] Namerikawa, T.; Okubo, N.; Sato, R.; Okawa, Y.; Ono, M., "Real-Time Pricing Mechanism for Electricity Market With Built-In Incentive for Participation," *Smart Grid, IEEE Transactions on*, vol.PP, no.99,Early Access.

[48] Mariagrazia Dotoli; Nicola Epicoco; marco Falagario; Fabio Sciancalepore., "A Nash equilibrium simulation model for the competitiveness evaluation of the auction based day ahead electricity market," *Elsvier Journal of Computer in Industries*, vol. 65, pp. 774-785, March 2014.

[49] Gregoratti, D.; Matamoros, J., "Distributed Energy Trading: The Multiple-Microgrid Case," *Industrial Electronics, IEEE Transactions on*, vol.62, no.4, pp.2551,2559, April 2015.

[50] Belgana, A.; Rimal, B.P.; Maier, M., "Open Energy Market Strategies in Microgrids: A Stackelberg Game Approach Based on a Hybrid Multiobjective Evolutionary Algorithm," *Smart Grid, IEEE Transactions on*, vol.6, no.3, pp.1243,1252, May 2015.

[51] Zhenyu Zhou; Jinfang Bai; Sheng Zho, "A Stackelberg Game Approach for Energy Management in Smart Distribution Systems with Multiple Microgrids," *Autonomous Decentralized Systems (ISADS), 2015 IEEE Twelfth International Symposium on*, vol., no., pp.248,253, 25-27 March 2015.

[52] Rudkevich A., "Supply function equilibrium: theory and applications," *Proceeding of the 36th Hawaii international conference on system sciences,;* pp. 1–5, 2003.

[53] Baldick R.; Grant R.; Kahn E.. "Linear supply function equilibrium: generalizations, applications, and limitations." *Power working paper (PWP-078),* University of California Energy Institute; 2000.

[54] Baldick R.; Hogan W., "Capacity constrained supply function equilibrium models of electricity markets: stability, nondecreasing constraints, and function space iterations*," Power working paper (PWP-089)*, University of California Energy Institute, 2002.

[55] C.J. Day; B.F. Hobbs; J.S. Pang, "Oligopolistic competition in power networks: a conjectured supply function approach," IEEE Trans Power Syst, vol. 17, pp. 597–607, 2002.

Authors' information

[1]Delhi Technological University, Delhi, India.

[2]Uttar Pradesh Power Corporation Limited, Lucknow, India.

[3]Utarrakhand Technical University, Dehradun, India.

[4]Madan Mohan Malaviya University of Technology, Gorakhpur, India.

[5]Motilal Nehru National Institute of Technology, Allahabad, India.



Madan Mohan Tripathi received his B. Tech. from Madan Mohan Malaviya Engineering College, Gorakhpur, India, and his Ph.D. from G. B. Technical University, Lucknow, India, in 1994 and 2010, respectively. He has worked as an Engineer-SC with the Institute for Plasma Research, Gandhinagar, India, and the National Institute of Electronics & Information Technology, New Delhi. Presently he is Associate Professor at Delhi Technological University, New Delhi. His research interests include sustainable energy, power system restructuring, ANN application to power system problems and the application of IT in power system control and monitoring. He is the member of IEEE and PSSI.



Anil Kumar Pandey received his B. E. from M. M. M. Engineering College, Gorakhpur, India, and his M. Tech. from Allahabad University, Allahabad, India, in 1985 and 1988, respectively. Presently he is working with Uttar Pradesh Power Corporation Limited, Lucknow, India. His research interests include power system restructuring and ANN application to power system problems.



Amit Verma received his B. E. from M. M. M. Engineering College, Gorakhpur, India, and his M. Tech. degree from M. M. M. Engineering College, Gorakhpur, India, in 2003. Presently he is Assistant Professor at Uttarakhand Technical University, Dehradun, India. His research interests include Power system restructuring, Price forecasting and renewable energy.



K. G. Upadhyay is a faculty member in the Department of Electrical Engineering of M.M.M. Engineering College in Gorakhpur. His research interests include power systems operation and control, FACTS, and deregulation. He received his M.Tech. and Ph.D. degrees from IIT Delhi, and U.P. Technical University in Lucknow in 1989 and 2002, respectively.



Dinesh Chandra received his B. E. from M. M. M. Engineering College, Gorakhpur, India, and his M.E. and Ph.D. degrees from Motilal Nehru National Institute of Technology (MNNIT), Allahabad, India, in 1973, 1979, and 2000, respectively. Presently Dr. Chandra is Professor at MNNIT. His research interests include control systems, model reduction techniques, optimization theory and fuzzy systems.

Copyright © 2016 Praise Worthy Prize S.r.l. - All rights reserved

New agegraphic dark energy in Brans-Dicke theory with logarithmic form of scalar field

Pankaj Kumar [2], **C. P. Singh** [1]

[1,2]Department of Applied Mathematics,
Delhi Technological University
Bawana Road, Delhi-110 042, India.
[1]cpsphd@rediffmail.com
[2]pankaj.11dtu@gmail.com

arXiv:1609.02751v1 [gr-qc] 9 Sep 2016

Abstract Recently, the current authors (arXiv:gr-qc/1609.01477) have proposed and analyzed in detail the logarithmic form of Brans-Dicke scalar field ϕ as $\phi \propto ln(\alpha+\beta a)$, where α and β are positive constants, to alleviate the problems of interacting holographic dark energy models in Brans-Dicke theory. In this paper, the cosmological evolution of a new agegraphic dark energy (NADE) model within the framework of Friedmann-Robertson-Walker Universe is analyzed with the same form of scalar field in Brans-Dicke theory. We derive the equation of state parameter w_D and deceleration parameter q of NADE model. It is observed that $w_D \to -1$ when $a \to \infty$, i.e., the NADE mimics cosmological constant in the late time evolution. Indeed, due to the assumption of logarithmic form of Brans-Dicke scalar field the NADE in Brans-Dicke theory behaves like NADE in general relativity in the late time evolution. The NADE model shows a phase transition from matter dominated phase in early time to accelerated phase in late time. We further extend NADE model by including the interaction between dark matter and NADE. In this case, w_D definitely crosses the phantom divide line ($w_D = -1$) in the late time evolution. The phase transition from matter dominated to NADE dominated phase may be achieved at early stage in interacting model. Further, we show that the interacting NADE model resolves the cosmic coincidence problem as the energy density ratio may evolve sufficiently slow at present.

Keywords- New agegraphic dark energy, Brans-Dicke theory, Coincidence problem.

[1]Corresponding author

1 Introduction

The cosmological observations like type Ia supernovae [1, 2] have provided the convincing evidence that our Universe is dominated by two dark components containing dark matter (DM) and dark energy (DE). The nature of DM and DE is one of the most important issues today in modern cosmology. The dark matter plays a role in explaining galactic curves and large scale structure where as dark energy explains the present cosmic accelerated expansion of the Universe. In the literature, the accelerating cosmologies have been described by two ways : dark energy content and modified gravity. In DE models, the accelerated expansion has been explained by modifying the right-hand side of the Einstein equations, i.e., by modifying the energy-momentum tensor. The modified gravity theory corresponds to modifying the left-hand side of Einstein equations, i.e., by modifying the geometric part. We refer [3, 4] for detail study of DE models and modified gravity.

However, we are still far from a compelling theory which could explain not only the recent accelerated expansion but also the primordial cosmology, structure formation, dark matter problem etc. without facing any problem. Whatever the way we choose to explain these problems, the quantum effects should be incorporated to come up with an accurate theory of gravity. The gravity theory which incorporates the principles of quantum mechanics, known as quantum theory of gravity. Although, the quantum gravity is not a well established theory, there are some concepts which have been proposed based on the principles of quantum gravity. In this context, the holographic dark energy (HDE) and agegraphic dark energy (ADE), which contain some significant properties of the quantum gravity, have been proposed as a candidate of DE to explain the recent accelerated expansion of the Universe. These DE models are able to present a unified model of the Universe and explain some other problems of the modern cosmology like coincidence problem [5].

The HDE models are based on the holographic principle [6] and have been studied extensively in the literature [7, 8, 9, 10, 11, 12, 13, 14] . On the other hand, the ADE models are based on the quantum fluctuations of the space-time. Using the concept of quantum fluctuations of space-time, Károlyházy and his collaborators [15, 16, 17] have observed that the distance t in Minkowaski space-time can not be known to a better accuracy than

$$\delta t = \gamma\, t_p^{2/3}\, t^{1/3}, \tag{1}$$

where t_p denotes reduced Planck time and γ is a dimensionless constant of order unity. We assume $\hbar = k_b = c = 1$ throughout in this paper. Maziashvili [18, 19] has argued that the quantum energy density of the metric fluctuations of Minkowaski space-time can be estimated using the relation (1) with the time-energy uncertainty relation. Maziashvili [18, 19] and Sasakura [20] have independently obtained the energy density of metric fluctuations of Minkowaski space-time which is given by

$$\rho_D \sim \frac{1}{t_p^2 t^2} \sim \frac{M_p^2}{t^2}, \tag{2}$$

where $M_p^2 = (8\pi G)^{-1}$ represents the reduced Planck mass. This energy density can be viewed as the density of DE, i.e., the ADE. Following the line of the relations (1) and (2), Cai [21] proposed the original ADE model in which the energy density of the ADE has the form

$$\rho_D = \frac{3n^2 {M_p}^2}{T^2}, \tag{3}$$

where T is age of the Universe. The numerical factor $3n^2$ has been introduced to parameterize some uncertainties like the species of quantum fields in the Universe, the effects of curved space-time, etc. A number of papers on ADE models are available which deal with various aspects of the evolution of the Universe [22, 23, 24, 25, 26]. Wei and Cai [27] have proposed

a new version of this model referred as "new agegraphic dark energy" model, abbreviated as NADE by replacing the cosmic age T with the cosmic conformal age η for the time scale in (3). Thus, in this model, the dark energy density is of the form

$$\rho_D = 3n^2 M_p^2 \, \eta^{-2}, \tag{4}$$

where the conformal time η is defined as

$$\eta = \int_0^t \frac{dt}{a} = \int_0^a \frac{da}{Ha^2}, \tag{5}$$

where a is the scale factor of the Universe and $H = \dot{a}/a$ is the Hubble parameter. Here, an overdot denotes derivative with respect to the cosmic time t. The most attractive merit of the NADE is that it has been proven to fit the data well. The cosmological constraints and other aspects of NADE models have been studied in the literature [28, 29, 30, 31].

The Brans-Dicke (BD) theory [32], which is a natural alternative and simple generalization of general relativity, provides a suitable framework for dynamical DE models. In this theory, the gravitational constant G is replaced with the inverse of a time-dependent BD scalar field ϕ, namely, $\phi = (8\pi G)^{-1}$ which couples to gravity with a coupling parameter w. One important property of BD theory is that it gives simple expanding solutions for scalar field and scale factor which are compatible with the solar system observations. The BD theory explains the recent accelerated expansion of the Universe and accommodates the observational data as well [33, 34, 35].

In the BD theory, the NADE models have been studied to discuss the recent accelerated expansion of the Universe [36, 37, 38, 39]. To the best of our knowledge in all the papers available in the literature on HDE, ADE and NADE models in the framework of BD theory, it has been assumed that the BD scalar field evolves as a power law of scale factor, $\phi \propto a^m$, m is a constant. In our previous paper [40], we have discussed the drawback of this relation of BD scalar field in BD theory. One can observe that this relation would always give the constant deceleration parameter (DP) irrespective of the matter content. This means that the phase transition of the Universe can not be obtained with the power-law form of BD scalar field. Therefore, to over come from this problem we have proposed a new relation between BD scalar field and scale factor, namely, a logarithmic form $\phi \propto ln(\alpha + \beta a)$ which is free from this problem. In the paper we have demonstrated that the logarithmic form of BD scalar field is not only suitable to explain the phase transition of the Universe but also it resolves the cosmic coincidence problem in an effective way.

As the logarithmic form of BD scalar field presents some interesting results in HDE model, therefore, it is worthwhile to discuss the evolution of the NADE model with this form. In this paper, we extend our previous work to analyze the evolution of the Universe in the NADE model in BD theory with the logarithmic form of BD scalar field. We derive the equation of state (EoS) parameter w_D and DP q of NADE model to discuss the evolution of the Universe. We further extend NADE model by including the interaction between dark matter and NADE in BD theory. We show that the interacting NADE model resolves the cosmic coincidence problem as the energy density ratio may evolve sufficiently slow at present.

The paper is organized as follows: In section 2, we present the equations of motion of NADE model in the framework of BD theory. Further, section 2 is divided into two subsections 2.1 and 2.2. In subsection 2.1, we discuss the non-interacting NADE model. Subsection 2.2 is devoted to interacting NADE model. The summary of our findings is presented in section 3.

2 NADE in BD theory with logarithmic scalar field

The action for the BD theory in the Jordan frame is given by

$$S = \int d^4x\sqrt{-g}\left[\frac{1}{2}(-\phi R + \frac{\omega}{\phi} g^{\mu\nu}\partial_\mu\phi \, \partial_\nu\phi) + \mathcal{L}_m\right], \tag{6}$$

where R, g and $\mathcal{L}_m$ represent the Ricci scalar curvature, determinant of the metric tensor $g_{\mu\nu}$ and the matter Lagrangian density, respectively. Here, ϕ and ω denote BD scalar field and BD coupling parameter, respectively. In this theory, the Newtonian constant G is replaced with a time dependent scalar field ϕ such that $\phi = (8\pi G)^{-1}$. The dimensionless parameter ω is introduced to represent a coupling between scalar field and gravity. In Jordan frame, the scalar field and matter field do not interact and matter minimally couples to the metric.

We assume a homogeneous and isotropic FRW space-time to discuss the evolution of the Universe. The FRW line element is given by

$$ds^2 = dt^2 - a^2(t)\left[\frac{dr^2}{1-kr^2} + r^2(d\theta^2 + \sin^2\theta\, d\phi^2)\right], \tag{7}$$

where a is the cosmic scale factor and k is curvature parameter. The curvature parameter has three possible values $k = -1, 0, 1$ which represent to open, flat and closed geometry of the Universe, respectively. We assume that the Universe is filled with pressureless dark matter (DM) and NADE. We exclude baryonic matter and radiation due to their negligible contribution to total energy budget in the late time evolution.

The variation of the action (6) with respect to the metric tensor, $g_{\mu\nu}$ for the line element (7) yield the following field equations.

$$H^2 + \frac{k}{a^2} + H\frac{\dot{\phi}}{\phi} - \frac{\omega}{6}\frac{\dot{\phi}^{\,2}}{\phi^{\,2}} = \frac{\rho_m + \rho_D}{3\phi}, \tag{8}$$

$$2\frac{\ddot{a}}{a} + H^2 + \frac{k}{a^2} + 2H\frac{\dot{\phi}}{\phi} + \frac{\omega}{2}\frac{\dot{\phi}^{\,2}}{\phi^{\,2}} + \frac{\ddot{\phi}}{\phi} = -\frac{p_D}{\phi}, \tag{9}$$

$$\ddot{\phi} + 3H\dot{\phi} = \frac{\rho_m + \rho_D - 3p_D}{2\omega + 3}, \tag{10}$$

where ρ_m and ρ_D denote the energy density of DM and NADE respectively, and p_D is the pressure of NADE. The Eq. (10) is known as the wave equation of the BD scalar field.

Let us assume the relation between BD scalar field and scale factor as [40]

$$\phi = \phi_0\, ln(\alpha + \beta a), \tag{11}$$

where ϕ_0, $\alpha > 1$ and $\beta > 0$ are constants. Substituting (11) into (8) we find

$$H^2\left(1 + \frac{k}{a^2} + \frac{\beta a}{(\alpha+\beta a)\, ln(\alpha+\beta a)} - \frac{w}{6}\frac{\beta^2 a^2}{(\alpha+\beta a)^2\, \{ln(\alpha+\beta a)\}^2}\right) = \frac{\rho_m + \rho_D}{3\phi}. \tag{12}$$

It is easy to observe from the Friedmann equation (12) in BD theory that the standard cosmology of GR will be recovered in the limit of $\beta \to 0$.

In BD theory, the BD scalar field is taken as $\phi = (8\pi G)^{-1}$ which implies $\phi = M_p^2$. Therefore, in this theory the energy density of NADE in (4) is now becomes

$$\rho_D = 3n^2\phi\, \eta^{-2}. \tag{13}$$

The critical energy density ρ_{cr} and energy density of the curvature ρ_k can be defined as follows

$$\rho_{cr} = 3\phi H^2, \qquad \rho_k = 3k\phi a^{-2}. \tag{14}$$

It has been observed that the representation of quantities and equations in the terms of fractional energy densities are useful from the point of view of calculation as well as from the point of view of physical interpretation of the results. The fractional energy densities can be defined in their usual forms as

$$\Omega_m = \frac{\rho_m}{\rho_{cr}} = \frac{\rho_m}{3\phi H^2}, \tag{15}$$

$$\Omega_D = \frac{\rho_D}{\rho_{cr}} = \frac{n^2}{\eta^2 H^2}, \tag{16}$$

$$\Omega_k = \frac{\rho_k}{\rho_{cr}} = \frac{k}{a^2 H^2}. \tag{17}$$

In what follows, we consider the non-interacting and interacting NADE models, and discuss their physical behaviors.

2.1 Non-interacting NADE model

Let us assume that DM and NADE do not interact and their energy densities follow the conservation equations

$$\dot{\rho}_m + 3H\rho_m = 0, \tag{18}$$

$$\dot{\rho}_D + 3H(1 + w_D)\rho_D = 0, \tag{19}$$

where $w_D = p_D/\rho_D$ denotes the equation of state (EoS) parameter of NADE. Using (11), (13) and (16) in the conservation equation (19), one can find the value of w_D as

$$w_D = -1 - \frac{\beta a}{3(\alpha + \beta a)\, ln(\alpha + \beta a)} + \frac{2}{3na}\sqrt{\Omega_D}. \tag{20}$$

It is to be noted that the EoS parameter w_D of NADE given by (20) reduces to its respective form in GR [22] for $\beta = 0$, that is,

$$w_D = -1 + \frac{2}{3na}\sqrt{\Omega_D}. \tag{21}$$

From (21) we observe that the w_D does not cross the phantom divide line $w_D = -1$ in the framework of GR.

Let us examine the behavior of the term $\frac{\beta a}{(\alpha+\beta a)\, ln(\alpha+\beta a)}$ present in (20) to discuss the behavior of w_D. We observe that the term $\frac{\beta a}{(\alpha+\beta a)\, ln(\alpha+\beta a)}$ is zero at $a = 0$, achieves its maximum value during the evolution, and converges to zero as $a \to \infty$ in the late time evolution . The maximum value of the term $\frac{\beta a}{(\alpha+\beta a)\, ln(\alpha+\beta a)}$ lies in the interval]0, 1[depending on the value of α. We observe that $\max\{\frac{\beta a}{(\alpha+\beta a) ln(\alpha+\beta a)}\} \to 1$ as $\alpha \to 1$ and for large value of α we get a small maximum value of the term. It is to be noted that the maximum value does not depend on the value of β. The time when the term will attain its maximum value depends on the values of α and β. For a large value of α, it occurs in the late time and for a large value of β, it will occur in the early time, and vice-versa.

Now, from (20) we observe that $w_D \to -1$ in the late time as the last two terms converge to zero, i.e., the NADE mimics the cosmological constant in the late time evolution. Wei and Cai [22] have also observed in GR that NADE mimics cosmological constant in the late time evolution. Indeed, the NADE with logarithmic form of BD scalar field in the BD theory behaves like NADE in GR in the late time evolution due to the term $\frac{\beta a}{(\alpha+\beta a) ln(\alpha+\beta a)}$ which converses to zero as $a \to \infty$. However, in the power law form of BD scalar field the NADE crosses the phantom divide line in the late time evolution because the second term is a constant $\frac{2m}{3}$ for power-law form $\phi \propto a^m$ [36]. It is also interesting to note that w_D may cross the phantom divide line if $\sqrt{\Omega_D} < [\frac{\beta n a^2}{2(\alpha+\beta a)\, ln(\alpha+\beta a)}]$ during the evolution but ultimately it will mimic the cosmological constant in the late time evolution. However, for a sufficiently large value of α and a sufficiently small value of n the phantom divide line crossing is not possible. If α has a small value ($\alpha \to 1$) and n a large value then the value of β is crucial to observe the phantom divide crossing and therefore for sufficiently small value of β the possibility of $w_D < -1$ may be observed.

Let us discuss the evolution of the Universe using the deceleration parameter which is

defined by $q = -\frac{a\ddot{a}}{\dot{a}^2}$. Using (11), (13), (16) and (17) in (9), the deceleration parameter q can be obtained as

$$q = \frac{1 + 3w_D\Omega_D + \Omega_k - \frac{\beta^2 a^2}{(\alpha+\beta a)^2\, ln(\alpha+\beta a)} + \frac{2\beta a}{(\alpha+\beta a)\, ln(\alpha+\beta a)} + \frac{\omega\beta^2 a^2}{2(\alpha+\beta a)^2\, \{ln(\alpha+\beta a)\}^2}}{2 + \frac{\beta a}{(\alpha+\beta a)\, ln(\alpha+\beta a)}}. \tag{22}$$

The value of BD parameter ω plays an important role in the value of q. The solar system experiment Cassini gave a very stringent high bound result on w as $|\omega| > 40000$ [41, 42]. However, the cosmological observations put relatively lower bounds on ω [43, 44, 45]. The term $\frac{\beta^2 a^2}{(\alpha+\beta a)^2\, ln(\alpha+\beta a)}$ present in (22) is zero at $a = 0$ which achieves its maximum value during the evolution and converges to zero in the late time evolution like the term $\frac{\beta a}{(\alpha+\beta a)\, ln(\alpha+\beta a)}$. The maximum value of this term lies in the interval $]0,\ 0.41[$ depending on the value of α. Due to a large value of ω suggested by the observations, the last term of the numerator in (22) containing ω will dominate in the early phase of the evolution of the Universe. Thus, we observe a positive value of q, i.e., the Universe evolves under the decelerated rate of the expansion. It means that the matter dominates the early phase of the expansion of the Universe. Thus, the NADE model with logarithmic form $\phi \propto ln(\alpha + \beta a)$ explains the matter dominated phase of the Universe. Since, in the late time evolution $w_D \to -1$, and last three terms of numerator and last term of denominator of (22) converge to zero, therefore, we obtain the late time value of q as

$$q \approx \frac{1 - 3\Omega_D + \Omega_k}{2}. \tag{23}$$

It is expected that $\Omega_D \to 1$ in the late time evolution. There are three possibilities for Ω_k: (i) $\Omega_k > 0$ for close Universe ($k > 0$), (ii) $\Omega_k = 0$ for flat Universe ($k = 0$), and (iii) $\Omega_k < 0$ for open Universe ($k < 0$). However, the observations suggest that our Universe is almost flat ($k \approx 0$) at present time. Therefore, if we take $k = 0$, i.e., $\Omega_k = 0$ for late time evolution then we have $q \approx \frac{1-3\Omega_D}{2}$. Thus, we may obtain an accelerated expansion for $\Omega_D > 1/3$. If we take present value $\Omega_D = 0.70$ obtained by resent observations then we get $q = -0.55$ which shows the accelerated expansion. One can observe that the accelerated expansion occurs more easily if we consider the open geometry of the Universe ($\Omega_k < 0$). In the case of close Universe ($\Omega_k > 0$), the accelerated expansion is possible but a relatively large value of Ω_D is required, i.e, a large value of n^2 is required to achieve it.

So far, we have obtained decelerated expansion in the early phase of the evolution which explains the matter dominated phase and accelerated expansion in the late time evolution which explains the NADE dominated phase. Thus, the present model successfully explains the recent phase transition of the Universe from decelerated expansion to accelerated expansion. The time of phase transition depends on the values of the parameters of the model α, β, n^2 and ω. It may be observed from (22) that if phase transition occurs at time t_1 for value ω_1 then it will happen at time t_2 for ω_2 where $t_1 < t_2$ and $\omega_1 < \omega_2$. For a large value of n^2 it occurs at earlier stage. In the similar way, one can see the effects of α and β depending on their effects on the terms $\frac{\beta a}{(\alpha+\beta a)\, ln(\alpha+\beta a)}$ and $\frac{\beta^2 a^2}{(\alpha+\beta a)^2\, ln(\alpha+\beta a)}$ as discussed above.

The logarithmic form in NADE model is free from the constant deceleration parameter problem of the power-law form and explains the phase transition of the Universe in the framework of the BD theory. Thus, this form serves our propose well.

Let us discuss the cosmic coincidence problem which has not been addressed for NADE models in the framework of BD theory. Steinhardt [46] addressed first time the coincidence problem- why are the matter and DE densities comparable at present time? In the conventional ΛCDM model very specific conditions of very early Universe are required to observe the matter and DE densities of the same order today. There are two ways to resolve the coincidence problem. In one of the ways, we should observe the energy density ratio $r_0 \sim \mathcal{O}(1)$ for a wide range of the initial conditions. In the other way, either r should converse to a constant value or evolve very slowly in the late time evolution(including present time) such that $r_0 \sim \mathcal{O}(1)$.

In the ΛCDM model, the energy density ratio r evolves as $|\frac{\dot{r}}{r}|_0 = 3H_0$. Here and throughout the paper, the zero subscript denotes the present value of the quantity. Using (18) and (19) one can obtain the evolution of r as

$$\dot{r} = 3rHw_D. \tag{24}$$

As we have observed that NADE mimics cosmological constant in the late time when $a \to \infty$. Therefore, if we take $w_{D0} = -1$, we get $|\frac{\dot{r}}{r}|_0 = 3H_0$ which is same as in the ΛCDM model. Thus, there is no reduction in the acuteness of coincidence problem. However, we have a time-dependent w_D, therefore, it is possible to have a less acute coincidence problem if we have $w_{D0} > -1$. The quintessence like EoS ($w_D > -1$) may be achieved for $\sqrt{\Omega_D} > \frac{\beta n a^2}{2(\alpha+\beta a)\ ln(\alpha+\beta a)}$ as can be observed from (20). It is to be noted that Eq. (20) has a time-dependent second term which converses to zero in the late time whereas the second term is a constant in case of power-law form. Therefore, the quintessence like EoS may be achieved more easily with logarithmic form in comparison to the power-law form of BD scalar field in the present time. Thus, the logarithmic form is more suitable to achieve a less acute coincidence problem. The observations also suggest quintessence like EoS of NADE [28]. Let us assume $w_{D0} = -2/3$, we obtain $|\frac{\dot{r}}{r}|_0 = 2H_0$ which is less acute coincidence problem in comparison to the ΛCDM model. On the other hand, the problem is more acute if w_D has phantom like EoS ($w_D < -1$). In this case, the coincidence problem becomes more worse than the ΛCDM model.

In conclusion, the coincidence problem may not be resolved significantly for non-interacting NADE model in the framework of BD theory, however, there are possibilities to achieve a less acute problem. The logarithmic form of BD scalar field is more suitable to have a less acute coincidence problem than power-law form.

2.2 Interacting NADE model

A number of authors [47, 48, 49, 50, 51] have studied the interaction between DM and DE and recent cosmological observations [52, 53, 54, 55] also support it. The interacting DE models have also been studied as a possible candidate to resolve the coincidence problem [56, 57, 58]. Therefore, in this subsection we extend the NADE model by considering the interaction between DM and NADE.

Assuming that the DM and NADE exchange energy through the interaction Q, the continuity equations become

$$\dot{\rho}_m + 3H\rho_m = Q, \tag{25}$$

$$\dot{\rho}_D + 3(1 + w_D)H\rho_D = -Q. \tag{26}$$

The sign of interaction term Q is crucial and defines the direction of the energy transfer, i.e., for $Q > 0$, there is an energy transfer from NADE to DM, and for $Q < 0$, there is an energy transfer from DM to NADE. The interaction between DM and NADE is a quantum scale phenomenon, therefore, the interaction term Q should be defined by the theory of quantum gravity. We do not have a satisfactory theory of quantum gravity, therefore, the dimension of the conservation equation has been used to choose a suitable form of Q in the literature. The conservation equations of DM and NADE imply that the interaction term should has the units of energy density $\times$ $(time)^{-1}$. Therefore, we may have the interaction term of the following forms: (i) $Q \propto H\rho_D$, (ii) $Q \propto H\rho_m$ or (iii) $Q \propto H(\rho_m + \rho_D)$. In this paper, we use the last assumption which is more general than first two. This form can be rewritten as

$$Q = 3b^2H(\rho_m + \rho_D), \tag{27}$$

where b^2 is a coupling constant. Using (11), (13), (16) and (27) in (26), we get

$$w_D = -1 - b^2(1 + r) - \frac{\beta a}{3(\alpha + \beta a)\ ln(\alpha + \beta a)} + \frac{2}{3na}\sqrt{\Omega_D}. \tag{28}$$

It is easy to observe that the EoS parameter of NADE achieves its respective form in GR for $\beta = 0$. We observe that w_D contains the third term as time-dependent whereas it is constant term in this place in power-law form of BD scalar field. Therefore, the evolution of w_D in our model will be different from that of power-law form. As discussed in section 2.1, analyzing the terms in w_D in (28), one can observe that w_D will definitely cross the phantom divide in the late time evolution, where $w_D \to -1 - b^2(1+r)$ as $a \to \infty$. The interaction between DM and NADE is the deriving force behind the phantom crossing in the late time. The late time value of w_D depends on the values of coupling constant b^2 and density ratio r. It means that it depends on how DM and NADE interact and what is the ratio of their densities. In the interacting NADE model, we observe that w_D may cross the phantom divide line more easily and earlier in the framework of BD theory than GR.

The expression of q remains same as in the case of non-interacting NADE which is given by (22). However, the evolution of q is different due to different value of w_D for interacting NADE given by (28). From (20) and (28), we observe that the EoS parameter of interacting NADE has an extra term $b^2(1+r)$ with negative sign than non-interacting NADE. Therefore, it is easy to observe from (22) that the recent phase transition of the Universe from matter dominated phase to NADE dominated phase is more easily achieved and we may achieve it at earlier stage in the interacting case. Thus, the interacting NADE model explains the recent phase transition of evolution of the Universe in the framework BD theory with logarithmic form of BD scalar field.

Let us study the evolution of r to check whether the interaction between DM and NADE is able to alleviate the coincidence problem or not. Using (25), (26) and (27), the evolution of r can be obtained as

$$\dot{r} = 3rH\left[w_D + b^2\frac{(1+r)^2}{r}\right]. \tag{29}$$

Here, we have the sum of the terms w_D and $b^2\frac{(1+r)^2}{r}$ which have negative and positive value respectively. Thus, the resultant value of terms within bracket will be less than $|w_D|$. Moreover, for a suitable value of b^2, we may achieve $|w_D + b^2\frac{(1+r)^2}{r}| << |w_D|$. Now, it is evident from (24) and (29) that the energy density ratio r may evolve more slowly in interacting NADE model than the ΛCDM model and non-interacting NADE model. Therefore, the interaction between dark components of the Universe may play an important role in the explanation of the coincidence problem. To achieve a soft coincidence we should observe $|\frac{\dot{r}}{r}|_0 \leq H_0$ [59]. The condition of soft coincidence may be easily achieved in our model if b^2 satisfies the condition, $b^2 \leq \frac{(1-3w_{D0})r_0}{3(1+r_0)^2}$. If we use the present observational values $r_0 \simeq 3/7$ and $w_{D0} \simeq -1$, we obtain the constraint $b^2 \leq 7/25$ to achieve soft coincidence problem. Even for a suitably small values of b^2, r may evolve more slowly at present which may resolve the coincidence problem more effectively. For example, if we take $b^2 = \frac{1}{5}$ and $w_{D0} = -1$ then we obtain $|\frac{\dot{r}}{r}|_0 \leq \frac{H_0}{7}$ which shows significantly slow variation of r compare to conventional ΛCDM model and condition mentioned above for soft coincidence.

Feng et al. [60] found that a small coupling constant b^2 is compatible with observation and also required to alleviate the coincidence problem. It also required to satisfy the second law of thermodynamics (also, see references within [60]). We also observe that the coupling constant b^2 should be a small quantity to avoid the coincidence problem which shows the compatibility with the observations. Thus, the interaction between DM and NADE in the framework of BD theory with logarithmic BD scalar field may resolve the coincidence problem effectively.

3 Conclusion

In this paper, we have investigated how the NADE model evolves in BD theory by assuming the logarithmic form of BD scalar field. The motive is that the existing power-law form of BD scalar field, $\phi = \phi_0\, a^m$ gives a constant value of DP whatever may be the energy content.

Therefore, it can not describe the phase transition of the Universe. However, many authors have found time-dependent DP by using the same power-law form which shows a contradiction. To overcome from this problem we have recently proposed and analyzed the logarithmic form of BD scalar field, $\phi = \phi_0\, ln(\alpha+\beta a)$ in HDE model (see, Ref.[40]). This form of BD scalar field is free from the above described problem and plays an important role in explaining the evolution of the Universe. It also resolves the cosmic coincidence problem. Therefore, analyzing the importance of this form, we have extended our work to NADE model within the framework of FRW line element in BD theory. We have discussed the dynamics of non-interacting and interacting NADE models by EoS parameter w_D and DP q. We have also discussed the cosmic coincidence problem. The results of these two models are summarized as follows:

In non-interacting NADE model, we have observed that the NADE model successfully explains the recent phase transition from matter dominated to NADE dominated phase. In this model the NADE mimics cosmological constant in the late time whereas it achieves phantom like behavior for power-law form [36]. It has also been observed that w_D may cross the phantom divide line under certain constraint but ultimately it will mimic the cosmological constant in late time evolution. Further, we have shown that a less acute coincidence problem than conventional ΛCDM model may be achieved, however, it is not able to alleviate the problem effectively. The logarithmic form of BD scalar field is more suitable to achieve a less acute coincidence problem than power-law form.

In interacting NADE model, the recent phase transition from decelerated phase to accelerated phase has also been achieved. However, the accelerated expansion may be achieved earlier in this model than non-interacting model. In the late time evolution, it has been analyzed that w_D definitely crosses the phantom divide line. We have shown that the energy density ratio r may evolve sufficiently slow in the present time which resolves the coincidence problem. Thus, the interacting NADE model may be able to alleviate the coincidence problem effectively.

In conclusion, we can say that the logarithmic form of BD scalar field is suitable to explain the recent accelerated expansion of the Universe in NADE model. This model shows the phase transition of the evolution of the Universe as we get the time dependent DP. It also resolves the cosmic coincidence problem effectively. Also, in the limit $\beta \to 0$, the NADE model in general relativity is recovered.

References

[1] A.G. Riess et al., Astron. J. **116**, 1009 (1998)

[2] S. Perlmutter et al., Astrophys. J. **517**, 565 (1999)

[3] E.J. Copeland, M. Sami, S. Tsujikawa, Int. J. Mod. Phys. D **15**, 1753 (2006)

[4] K. Bamba et al., Astrophys. Space Sci., 342, 155 (2012), arXiv:gr-qc/1205.3421

[5] S. Nojiri, S.D. Odintsov, Gen. Rel. Grav. **38**, 1285 (2006), arXiv:hep-th/0506212

[6] G. 't Hooft, arXiv:gr-qc/9310026 (1993)

[7] M. Li, Phys. Lett. B **603**, 1 (2004)

[8] D. Pavón, W. Zimdahl, Phys. Lett. B **628**, 206 (2005)

[9] M.R. Setare, Phys. Lett. B **644**, 99 (2007)

[10] N. Banerjee, D. Pavón, Phys. Lett. B **647**, 477 (2007)

[11] L. Xu, W. Li, J. Lu, Eur. Phys. J. C **60**, 135 (2009)

[12] A. Sheykhi, Phys. Lett. B **681**, 205 (2009)

[13] M. Li et al., J. Cosmol. Astropart. Phys. **09**, 021 (2013)

[14] S. Ghaffari, M.H. Dehghani, A. Sheykhi, Phys. Rev. D **89**, 123009 (2014)

[15] F. Károlyházy, Nuovo. Cim. A**42**, 390 (1966)

[16] F. Károlyházy, A. Frenkel, B. Lukács, In Physics as Natural Philosophy (Eds. A. Shimony, H. Feschbach, MIT Press, Cambridge, MA, 1982)

[17] F. Károlyházy, A. Frenkel, B. Lukács, In Quantum Concepts in Space and Time (Eds. R. Penrose, C.J. Isham, Clarendon Press, Oxford, 1986)

[18] M. Maziashvili, Phys. Lett. B **652**, 165 (2007)

[19] M. Maziashvili, Int. J. Mod. Phys. D **75**, 1531 (2007)

[20] N. Sasakura, Prog. Theor. Phys. **102**, 169 (1999)

[21] R.G. Cai, Phys. Lett. B **657**, 228 (2007)

[22] H. Wei, R.G. Cai, Phys. Lett. B **665**, 1 (2007)

[23] K.Y. Kim, H. W. Lee, Y.S. Myung, Phys. Lett. B **660**, 118 (2008)

[24] I.P. Neupane, Phys. Lett. B **673**, 111 (2009)

[25] H. Wei, R.G. Cai, Eur. Phys. J. C **59**, 99 (2009)

[26] O.A. Lemets, D.A. Yerokhin, L.G. Zazunov, J. Cosmol. Astropart. Phys. **01**, 007 (2011)

[27] H. Wei, R.G. Cai, Phys. Lett. B **660**, 113 (2008)

[28] H. Wei, R.G. Cai, Phys. Lett. B **663**, 1 (2008)

[29] M.R. Setare, Astrophys. Space Sci. **326**, 27 (2010)

[30] K. Saaidi, H. Sheikhahmadi, A.H. Mohammadi, Astrophys. Space Sci. **338**, 355 (2012)

[31] J.F. Zhang, Y.H. Lee, X. Zhang, Eur. Phys. J. C **73**, 2280 (2013)

[32] C. Brans, R.H. Dicke, Phys. Rev. **124**, 925 (1961)

[33] O. Bertolami, P.J. Martins, Phys. Rev. D **61**, 064007 (2000)

[34] H. Kim, Mon. Not. R. Astron. Soc. Lett. **364**, 813 (2005)

[35] T. Clifton, J.D. Barrow, Phys. Rev. D **73**, 104022 (2006)

[36] A. Sheykhi, Phys. Rev. D **81**, 023525 (2010)

[37] A. Sheykhi, M. Jamil, Phys. Lett. B **694**, 284 (2011)

[38] A. Pasqua, S. Chattopadhyay, Astrophys. Space Sci. **348**, 284 (2013)

[39] V. Fayaz, Astrophys. Space Sci. **361**, 86 (2016)

[40] C.P.Singh, Pankaj Kumar, arXiv:1609.01477[gr-qc]

[41] B. Bertotti, L. Iess, P. Tortora, Nature **426**, 374 (2003)

[42] C. Will, Living Rev. Relativity **9**, 3 (2006)

[43] V. Acquaviva et al., Phys. Rev. D **71**, 104025 (2005)

[44] F.Q. Wu, X. Chen, Phys. Rev. D **82**, 083003 (2010)

[45] Y.C. Li, F.Q. Wu, X. Chen, Phys. Rev. D **88**, 084053 (2013)

[46] P. Steinhardt, in Critical Problems in Physics, edited by V.L. Fitch, D.R. Marlow (Princeton University Press, Princeton, NJ, 1997)

[47] L. Amendola, C. Quercellini, Phys. Rev. D **68**, 023514 (2003)

[48] W. Zimdahl, D. Pavón, Gen. Relativ. Gravit. **35**, 413 (2003)

[49] G. Farrar, P.J.E. Peebles, Astriohys. J. **604**, 1 (2004)

[50] B. Gumjudpai et al., J. cosmol. Astropart. Phys. **06**, 007 (2005)

[51] C. Skordis, A. Pourtsidou, E.J. Copeland, Phys. Rev. D **91**, 083537 (2015)

[52] G. Olivares, F. Atrio, D. Pavón, Phys. Rev. D **71**, 063523 (2005)

[53] C. Feng et al., J. Cosmol. Astropart. Phys. **09**, 005 (2007)

[54] S. Cao, N. Liang, Z.H. Zhu, Mon. Not. R. Astron. Soc. **416**, 1099 (2011)

[55] A.A. Costa et al., Phys. Rev. D **89**, 103531 (2014)

[56] M.S. Berger, H. Shojaei, Phys. Rev. D **73**, 083528 (2006)

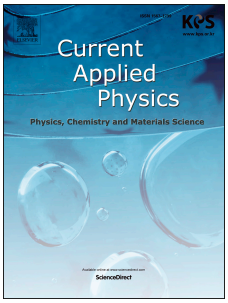
[57] S. del Campo et al., Phys. Rev. D **74**, 023501 (2006)

[58] S. del Campo, R. Herrera, D. Pavón, J. Cosmol. Astropart. Phys. **01**, 020 (2009)

[59] S. del Campo, R. Herrera, D. Pavón, Phys. Rev. D **78**, 021302 (2008)

[60] C. Feng et al., Phys. Lett B **665**, 111 (2008)

Accepted Manuscript



Numerical simulation of rear contact silicon solar cell with a novel front surface design for the suppression of interface recombination and improved absorption

Rahul Pandey, Rishu Chaujar

PII: S1567-1739(16)30239-5

DOI: 10.1016/j.cap.2016.09.002

Reference: CAP 4318

To appear in: *Current Applied Physics*

Received Date: 29 June 2016

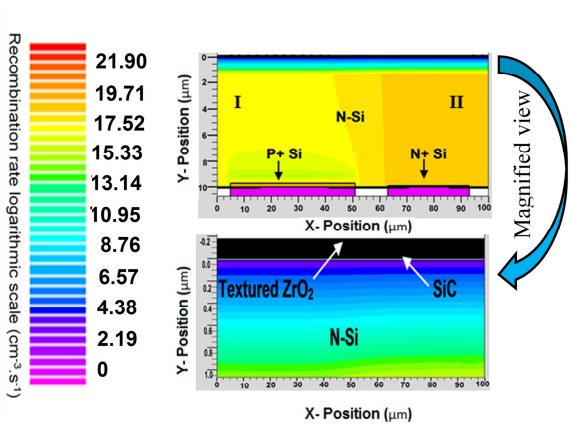
Revised Date: 19 August 2016

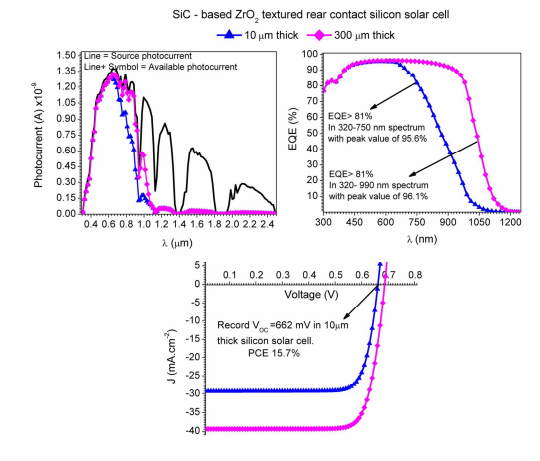
Accepted Date: 2 September 2016

Please cite this article as: R. Pandey, R. Chaujar, Numerical simulation of rear contact silicon solar cell with a novel front surface design for the suppression of interface recombination and improved absorption, *Current Applied Physics* (2016), doi: 10.1016/j.cap.2016.09.002.

This is a PDF file of an unedited manuscript that has been accepted for publication. As a service to our customers we are providing this early version of the manuscript. The manuscript will undergo copyediting, typesetting, and review of the resulting proof before it is published in its final form. Please note that during the production process errors may be discovered which could affect the content, and all legal disclaimers that apply to the journal pertain.

ACCEPTED MANUSCRIPT





ACCEPTED MANUSCRIPT

ACCEPTED MANUSCRIPT

Numerical simulation of rear contact silicon solar cell with a novel front surface design for the suppression of interface recombination and improved absorption

Rahul Pandey and Rishu Chaujar*

Microelectronics Research Laboratory, Department of Engineering physics, Delhi Technological University, New Delhi 110042, India

ABSTRACT

Nanostructuring has been projected as an appropriate technique to make thin silicon an efficient absorber. Although nano-textured surfaces have shown an anti-reflective effect, their surface passivation properties are found to be generally worse compared to standard micro-textured surfaces. Here, a novel front surface design has been proposed and simulated to balance the photonic and electronic effects together. ZrO_2 based texturing has been used along with SiC-based front surface passivation for the suppression of interface recombination and improvement of open-circuit voltage (V_{OC}). The device under investigation shows record V_{OC} of 662 mV in the sub-10µm-thick rear contact silicon solar cell. The presence of ZrO_2 and SiC significantly improves the optical as well as the electrical behavior of the device. The device exhibits external quantum efficiency (EQE) > 81% in the spectrum range of 320-720 nm wavelength spectrum with a maximum of 95.6% at wavelength 560 nm. These improvements lead to 15.7% efficient rear contact silicon solar cell, in the sub-10µm-thick regime. In second approach power conversion efficiency (PCE) of 21.6% has been achieved, by introducing the same front surface design to a 300 µm thick device. All the simulations have been done using calibrated software program in ATLAS device simulation.

Keywords

Absorption; recombination; solar cell; silicon carbide (SiC); ZrO_2

Correspondence

***E-mail:** Rishu.phy@dce.edu

1. INTRODUCTION

Photovoltaic (PV) is a simple and elegant method of coupling the sun's energy. Solar cells are exceptional in that they directly convert the incident solar radiation into electricity, with no pollution and noise, making them robust, reliable and long lasting. Solar cells are attractive candidates for clean and renewable power [1]. Silicon (Si) is the most extensively used material for solar cell production due to its abundance, reliability, nontoxicity, and mature fabrication techniques. Further, solar cell technology is a function of efficiency, cost, and a lifetime of the cell. Hence, large-scale implementation is not economically feasible. To absorb the solar spectrum, the thickness of the planar cell is typically more than 100µm [2]. This requirement results in higher cost. Also, in order to increase the collection of the generated carriers, the dimension of the device should be comparable to the carrier diffusion length. Thinner silicon solar cells with high efficiency are fruitful for cost-effective energy solution [3, 4]. Further, to maximize solar cell efficiency, it is necessary to optimize both, the

device electrical characteristics and the optical absorption of thin devices [5, 6]. Nanostructuring has been projected as an appropriate method to make thin silicon an efficient absorber. However, these cells are not efficient due to Auger and surface recombination as the surface to volume ratio of the cells is large. However, recently, a method to minimize the surface recombination for nanostructured based ~ 300µm thick devices has been presented which results in 20% and 22% efficient cells. The PCE of nanostructured Si solar cell remains below 22.2 % for thick devices [7, 8] and below 11% for thin devices [9], except 13.7% and 15.7 % reported in [9, 10] for the 10 µm thick devices. In previous work, a 14.3% efficient ZrO_2 textured rear contact solar cell has been proposed. The work shows efficient photon absorption in the sub-10-µm-thick device [11]. ZrO_2 is a material of great technology due to its outstanding mechanical and electrical properties and high dielectric constant. Large band gap (E_g ~ 6eV) and dielectric properties (ε ~ 25) suggested its potential to replace SiO_2 in the advance semiconductor device and optical applications [12]. Also, it has an excellent thermal stability. This work further extends the study of ZrO_2 textured front surface based rear contact silicon solar cell having thin defect free SiC layer at the ZrO_2/Si interface. The presence of thin SiC layer minimizes the reflectivity [13-14]. Previous work shows, embedding 3C-SiC nanoparticles significantly reduces the photo reflectivity in UV/visible spectrum region [15]. The SiC is an indirect (Eg = 2.2 eV) semiconductor with wide energy band gap, high thermal conductivity, large breakdown field, and high saturation velocity make this material an ideal choice for high temperature, high power, high voltage electron devices. Its high melting point, chemical inertness, high wear resistance, and extreme hardness, make it possible to fabricate sensors and actuators capable of performing in harsh environments [16]. The SiC film formation has been done for Si solar cell passivation. The film was deposited on silicon (100) and glass substrates by an RF magnetron co-sputtering system [17]. Recently, SiC passivated SiGe wafer based rear contact solar cells have been proposed for ultra-high efficiency in sub 10 micron thick devices; work shows improved optical absorption without the need of complex texturing [18, 19].

Moreover, this work shows that the presence of SiC improves the photovoltaic parameters of ZrO_2 based rear contact solar cell. The discussed device shows J_{SC} and V_{OC} of 29.3 mA.cm^{-2}, 662 mV respectively. This results, in 15.7% PCE in sub 10-micron thick solar cell, which is equivalent to the experimentally achieved record PCE of 15.7% using periodic nanostructure [10]. However, present work shows superior V_{OC}, which shows that the surface recombination issue has truly been solved and SiC passivation based nanostructured silicon solar cell have real potential for industrial production. The rear contact silicon solar cell has been selected because it is a promising high-efficiency solar cell having both, junction and the electrodes at the back side of the device. Now, since the junction and contacts are on the back side, front surface can be designed for optimum optical performance [20].

2. DEVICE STRUCTURE AND SIMULATION

In this section, the calibrated software program is written in Silvaco ATLAS device simulator as per the results reported by (*sangmoo jeong et al., 2013*) for 10 µm thick rear contact solar cell with antireflection (AR) coating [9]. The dimensions and the doping density of the planar device were identical to the referenced cell and named as Device A as shown in Fig. 1. The device geometry in the simulation was (50-µm-wide pitch, 46µm-wide *P+*, and 30-µm-wide *N+*). The substrate was *N-type*, with doping density (3 x 10^{15} cm^{-3}). *P+* region was doped with boron (4 x 10^{20} cm^{-3}, depth of 300

nm). *N*+ region was doped with phosphorous (1 x 10^{20} cm^{-3}, depth of 100 nm).

Further, in the presence of heavy doping, (>10^{18} cm^{-3}), experimental work has shown that the *PN* product in silicon turns out to be doping dependent [21]. As the doping level rises, a decrease in the bandgap occurs, where the valence band raises by the approximately same amount as the conduction band is lowered. Discussed structure has heavily doped *P* and *N* regions, and so bandgap narrowing effects are enabled. These effects can be described by an analytic expression relating the variation in the bandgap, ΔEg to the doping concentration, N [22]. Furthermore, the solar cells are the carrier recombination affected devices. Therefore, Auger and Shockley- Read- Hall (SRH) recombination models are selected during the simulation. Phonon transitions occur in the presence of a trap or defect within the forbidden gap of the semiconductor [23, 24]. Basic for the SRH model are the assumptions of one trap level in the forbidden band and drift-diffusion assumption for the transport of electrons and holes, and the assumption that the dynamics of the trapped carrier is quasi-stationary [25]. Auger recombination occurs through a three particle transition whereby a mobile carrier is either captured or emitted. The underlying physics of such processes is unclear, and normally a more qualitative understanding is sufficient [26]. The auger coefficients, C_p=9.9x10^{-32} $cm^6.s^{-1}$ and C_n=2.8x10^{-31} $cm^6.s^{-1}$ have been used for *P*-type and *N*-type silicon, respectively, at 300K temperature [27].The concentration dependent mobility and field dependent mobility models have also been selected during simulation. The consistent set of models and parameters for the simulation of Si solar cell have been used as suggested in already published article [28]

To obtain the current density (J)- voltage (V) curve under illumination, the standard AM1.5 solar spectrum has been used. Also, as the contact interface between metal and semiconductor is highly doped both for the *P*+ and *N*+ region i.e. ~ 10^{20} cm^{-3}, therefore, the ohmic contacts are used in this work. This has been done to avoid Schottky barriers, and thus unnecessarily higher computation time. Result reveals, the software program, is well calibrated within the acceptable range shown in Table 1.

3. RESULTS

The result section is divided into two parts, first, designing a ZrO_2 textured and thin SiC-based ZrO_2 textured 10x10µm thick *N-type* silicon wafer for optimal spectrum response and second, the designed ZrO_2 pattern with and without SiC has been introduced to Device A, by removing anti-reflective coating (ARC) layer. ZrO_2 textured 10µm thick rear contact silicon solar cell is called as Device B, and ZrO_2 textured device with SiC layer at the ZrO_2/*N*-Si interface is termed as Device C.

3.1 Spectrum response of ZrO_2 textured SiC-based silicon wafer

In this section, a 10x10µm thick *N*-type Si wafer without ARC, with ARC, textured ZrO_2 and textured ZrO_2 having SiC (20nm) layer at ZrO_2/ *N*-Si interface have been designed and simulated to obtain the spectrum response. The entire front surface is covered with repeated ZrO_2 facet structures and optimized height, 175 nm, and width, 250 nm is used for texturing. The smaller and larger width size than 250 nm will show lower optical coupling and lower conversion efficiency, as suggested in [29]. In the real cell, the nanopatterns can be fabricated via inexpensive and scalable imprinting technique. The complex refractive index of various materials has been obtained from Sopra database [30] and presented in Fig. 2 (a-b). Fig. 2a shows, as wavelength changes from 300 to 1200 nm, the reflective index, n of ZrO_2 changes from 2.45-2.17. the n values of ZrO_2 are close to the n values of nitride, which is usually used as AR coating for silicon solar cell [31-33].

Further, the spectral response of Si wafers is presented in Fig. 3(a-b). Result shows, planar silicon wafer without coating is highly reflective i.e. absorption is small in the range of 300-1000 nm wavelength spectrum. Also, ARC coating based Si wafer shows > 96% absorption in the spectrum range of 500-625 nm wavelength. Lower and higher wavelength response is however not remarkable. The ZrO_2 textured wafer shows improved optical behavior compared to ARC coating based wafer due to anti-reflection and light scattering. This concludes that higher absorption is achieved in the ZrO_2 textured wafer, which further results in higher available photocurrent shown in Fig. 3b. Results also indicate that throughout the spectrum range (300-1000 nm), ZrO_2 textured wafer shows enhanced absorption as compared to ARC coated wafer. At a wavelength equivalent to 300 nm, 77% absorption is achieved in the silicon wafer. Also, photon absorption > 82% has been achieved in the spectrum range of 325-850 nm wavelength with a maximum of 98.2%. This shows spectrum response has been improved due to ZrO_2 textured front surface. Further, optical behavior of SiC-based ZrO_2 textured wafer has also been obtained. The efficiency of a solar cell is directly related to the amount of light entering the cell. Antireflection coating is used to reduce the reflection of the useful light while not absorbing it. Our previous work shows that the photon coupling in underlying substrate is higher for 20 nm thick SiC-based device. Whereas, increasing the SiC thickness results in parasitic absorbance in SiC, and lower photon coupling in underlying substrate. Since, absorbance directly depends on the thickness of the material. This further results in lower short circuit current density and power conversion efficiency [18]. Therefore, the thickness of SiC used in the simulation is only 20 nm whose absorption is negligible hence, optical coupling in underlying silicon is higher. Also, the optical properties i.e. refractive index (n) and extinction coefficient (k) required for an AR coating depends on the refractive index of the underlying substrate, encapsulated cover, and the operating wavelengths. The material having low absorption of useful light is needed, to reduce the absorption of useful light in ARC. Therefore, low k values are required, k value of 0.01 corresponds to less than 1% absorption, since $\alpha=4\pi k/\lambda$. Fig. 2a and Fig. 2b shows that SiC has n between 2.9 and 2.5 in the spectrum range of 300 -1200 nm and k of less than 0.01 for the wavelengths greater than 430 nm. Also, according to the patented work of *Allen et al.* [34] SiC film having n between 2.7 and 2.3 and k of less than 0.01 at a wavelength of 630 nm is a good candidate for antireflective coating for solar cells. This confirms that presence of SiC will not degrade the optical behaviors of ZrO_2 based wafer. Furthermore, a contour plot of photons absorption rate in the wafers is also shown in Fig. 4(a-d). Higher photon coupling has been observed in both ZrO_2 based and SiC- based ZrO_2 textured wafer. This results in higher absorption rate as well as higher absorption depth compared to ARC based device, as shown in Fig. 4c&d and Fig. 4g&h.

3.2 Rear-contact solar cell with ZrO_2 textured front surface

Spectral results as discussed shows that the optical performance of Si wafer is significantly improved in the case of ZrO_2 textured front surface. Therefore, ARC coating of Device A is replaced with ZrO_2 textured front surface with rest of the device parameters being the same. In this section, the performance of two ZrO_2 textured solar cells has been obtained, one with 20nm thick SiC layer at the interface (Device B) and another without SiC layer at the interface (Device C). Also, the results of the devices are compared with planar rear contact device as shown in Fig. 1.

Here, Device B and Device C have been simulated with the help of calibrated program

written for device A. Results of previous section shows, an amalgamation of thin SiC layer does not degrade the optical behavior of the wafer. Hence, both the devices i.e. device B and device C shows significant improvement in device photovoltaic parameters: in terms of short circuit current density (J_{SC}), V_{OC}, fill factor (FF), and PCE compared to device A. Fig. 5(a-f), shows the contour plot of recombination rate in Device A, Device B, and Device C, respectively. The device architecture is such that the holes generated at point 1, in Fig. 1 need to travel shorter to arrive at $N — P+$ interface, whereas the holes generated at point 2, needs to travel a greater lateral distance. Under short-circuit condition, a space charge region is formed around the junction having an associated electric field that collects the generated electron-hole pairs, and the collection is complete near $P+$ region. However, outside the $P+$ region, the substrate is neutral, and the collection will be by diffusion of electrons and holes towards the field region where they will be collected and separated. The electrons and holes generated in a region greater than the diffusion length will never reach the junction, and the recombination process will balance out. This results in higher recombination rate in region II compared to the region I, shown in Fig. 5. Further, Fig. 5c&f shows that significant improvement in surface recombination has been obtained in Device C compared to Device A and Device B. The analysis reveals that recombination rate near the SiC/N-Si interface is small compared to the bulk region (N-Si) of the device. The presence of SiC creates an electric field at the interface and is directed from SiC to Si, rendering it energetically unfavorable for holes transport to SiC/N-Si interface, resulting in a low concentration of holes at the passivating interface [17, 35]. Thus, sinking the holes concentration at the interface will produce higher concentration difference between electrons and holes, and results in lower surface recombination rate [36].

Results conclude that presence of ZrO_2 textured front surface increases the optical response and presence of SiC at the ZrO_2/N-Si interface minimizes the surface recombination. Therefore, the dual advantage has been obtained with the help of SiC and ZrO_2. Further, the J-V curve is presented in Fig. 6, for Device A, Device B, and Device C, respectively. Also, the photovoltaic parameters are concluded in Table 1. The J-V curve of Device A is identical to the J-V curve of the planar 10-µm-thick solar cell with anti-reflection (AR) layer, presented by (*sangmoo jeong et al., 2013*) [9]. This also validates the calibration of the software program. Moreover, lower recombination and higher Photogeneration lead to improved J_{SC} and V_{OC} in Device B and Device C compared to Device A. The J_{SC}, V_{OC} of 28.6 mA.cm^{-2}, 623 mV, and 29.3 mA.cm^{-2}, 662 mV have been obtained in Device B and Device C, respectively, as shown in Fig. 6. Hence, 32% higher J_{SC} and 7 % higher V_{OC} has been obtained in Device C compared to Device A. Also, the V_{OC} of the Device C is 6 % higher compared to Device B which shows that the presence of SiC in ZrO_2 textured rear contact device significantly boost the photovoltaic performance of the device by suppressing the surface recombination. The overall PCE of the Device C is 42% and 11% higher compared to Device A and Device B respectively.

Moreover, the impact of minority carrier lifetime has been studied to obtain the effect of material quality on photovoltaic parameters, and the results are presented in Fig. 7(a-d). The discussed device is thin compared to conventional silicon solar cells and hence, the device can be fabricated with inexpensive, less pure material. Also, the charge carriers in discussed device need to diffuse shorter length whereas, in conventional rear contact device, a long carrier lifetime is required to collect the

carrier because the thickness is usually >150µm. This results in, increased module cost since high- purity material is required. Results show that the impact of minority carrier lifetime is negligible on all the three devices. However, the overall photovoltaic parameters of the Device C are superior compared to Device A and Device B. At τ equivalent to 10^{-2} s, the PCE of 11.3%, 14.7%, and 16.5% have been obtained in Device A, Device B, and Device C respectively, whereas, for τ equivalent to 10^{-5} s, the values are 11.0%, 14.4%, and 15.7%, respectively. This shows only 4% change in PCE is observed for Device C, as carrier lifetime changes from 10^{-2} s to 10^{-5} s. All the photovoltaic parameters of Device C are good compared to Device A and Device B as shown in Fig. 7 (a-d).

3.3 SiC- based ZrO_2 textured 300µm thick rear contact solar cell

The results of the previous section show that the performance of silicon solar cell is improved with the help of SiC- based ZrO_2 texturing, however, optical absorption falls to lower values in the wavelength range of 900-100 nm, whereas simulated spectrum goes up to 1200 nm. The absorption coefficient of silicon is small at higher wavelength [37, 38] and hence to increase the absorption up to 1200 nm, thicker silicon is required. Therefore, a 300µm thick SiC-based ZrO_2 textured rear contact solar cell has also been designed and its optical, as well as electrical parameters, are compared with 10 µm thick device as discussed in previous sections. Fig. 8 show the optical behavior of the devices i.e. 10 microns and 300 micron thick devices, respectively. The available photocurrent is shown in Fig. 8a along with source photocurrent of the spectrum. Improved available photocurrent has also been obtained in 300 µm thick device in higher wavelength regime. The EQEs of the two devices have also been obtained and presented in Fig. 8b. Results show, significant improvement in the higher wavelength region. The EQE fall to lower values at higher wavelength compared to 10-micron thick device, as shown in Fig. 8b. Further, J-V curve of the devices is shown in Fig. 9. Results indicate that improved optical response of 300µm thick device leads to significant improvement in J_{SC}. The minority carrier lifetime of 1ms has been selected for the thicker device to prevent the bulk recombination of generated carriers. The J_{SC} (39.40 mA.cm^{-2}), V_{OC} (687mV), FF (80%), and PCE (21.6%) have been obtained. In experimental work, modulated surface textured (MST) based rear contact device shows J_{SC}, V_{OC}, FF, and PCE values of 40.5 mA.cm^{-2}, 635 mV, 77%, and 19.8%, respectively [7]. This shows that simulated results are in good agreement with experimental results. The V_{OC} value of the experimental device is lower compared to the device under investigation. This concludes that the optimum surface passivation has been achieved in this work compared to experimental results due to the presence of SiC. This shows that the amalgamation of SiC in experimental devices can significantly suppress the carrier recombination at the interface and lead to higher open circuit voltage. The photovoltaic parameters of the devices are shown in Table 2 along with already available experimental results.

4. CONCLUSIONS

This work presents an efficient optical absorption and improved surface passivation in sub-10µm-thick Si solar cell device. ZrO_2 and SiC based front surface are designed for the silicon wafer, and spectrum response is obtained. The wafer shows absorption (87%) at short wavelengths (300 nm). Results show that throughout the wavelength spectrum 300-1000 nm i.e. (UV-Visible-Infrared), ZrO_2 textured wafer having thin SiC at the interface (ZrO_2/N-Si) shows significant improvement in optical absorption. Hence, ZrO_2 textured SiC-based rear contact solar cell has been designed

and simulated to achieve lower interface recombination and improved open-circuit voltage (V_{OC}). This results in enhanced photovoltaic parameters compared to the conventional rear contact solar cell with AR coating. The J_{SC} and V_{OC} of 29.3 mA.cm^{-2}, 661 mV have been obtained. This results in 15.7% PCE in the sub-10µm-thick rear contact silicon solar cell. Further, a 21.6% efficient 300µm thick device has also been designed and simulated. Results show that if fabricated experimentally it can prove to be a cost-effective solution for energy efficient applications.

ACKNOWLEDGMENT

The authors would like to thank Microelectronics Research Lab, Department of Engineering Physics, Delhi Technological University to carry out this work. Rahul Pandey (JRF) acknowledge UGC, Govt. of India for providing fellowship.

REFERENCES

1. B. Tian, X. Zheng, T. J. Kempa, Y. Fang, N. Yu, G. Yu, J. Huang and C. M. Lieber, "Coaxial silicon nanowires as solar cells and nanoelectronic power sources," *Nature*, vol. 449, pp. 885-889, 2007.
2. A. Deinega, S. Eyderman, and S. John, "Coupled optical and electrical modeling of solar cell based on conical pore silicon photonic crystals "*J. Appl. Phys.*, vol. 113, pp. 1-9, 2013.
3. R. Pandey and R.Chaujar, "TCAD Analysis of Silicon-Germanium (SiGe) based Back-Contact Back-Junction (BC-BJ) solar cell as an alternative for silicon based cells" *TechConnectWorld Innovation Conference and Expo*, pp. 199-202, June 14-17, 2015 Washington DC, USA.DOI: 10.13140/RG.2.1.1008.6246
4. C.V. Lare, F. Lenzmann, M. Verschuuren and A. Polman, "Dielectric scattering patterns for efficient light trapping in thin-film solar cells", *Nano Letters*, 24 June 2015, DOI: 10.1021/nl5045583.
5. N. Dwivedi, S. Kumar, A. Bisht, K. Patel and S Sudhakar, "Simulation approach for optimization of device structure and thickness of HIT solar cells to achieve∼ 27% efficiency," *Solar energy*, vol. 88, pp. 31-41, 2013.
6. E. Garnett and P. Yang, "Light Trapping in Silicon Nanowire Solar Cells," *Nano Letters*, vol. 10, pp. 1082-1087, 2010.
7. A. Ingenito, O. Isabella, and M. Zeman, "Nano-cones on micro-pyramids: modulated surface textures for maximal spectral response and high-efficiency solar cells," *Prog. Photovoltaics Res. Appl.*, vol. 20, no. 1, p. 6, 2015.
8. H. Savin, P. Repo, G. von Gastrow, P. Ortega, E. Calle, M. Garín, and R. Alcubilla, "Black silicon solar cells with interdigitated back-contacts achieve 22.1% efficiency.," *Nat. Nanotechnol.*, vol. 10, no. May, pp. 1–6, 2015
9. S. Jeong, M. D. McGehee, and Y. Cui, "All-back-contact ultra-thin silicon nanocone solar cells with 13.7% power conversion efficiency" *Nature Communications*, vol. 4, 2950 pp 1-7, 2013.
10. M.S. Branham, W.-C. Hsu, S. Yerci, J. Loomis, S. V Boriskina, B.R. Hoard, et al., 15.7% Efficient 10-µm-Thick Crystalline Silicon Solar Cells Using Periodic Nanostructures., Adv. Mater. (2015) 2182–2188. doi:10.1002/adma.201405511.
11. R. Pandey and R. Chaujar, "Rear contact solar cell with ZrO_2 Nano structured front surface for efficient light trapping and enhanced surface passivation" *IEEE PVSC 42nd*, Jun 14-19, 2015, New Orleans, USA.
12. J. C. Garcia and L. M. R. Scolfaro, "Structural, electronics, and optical properties of ZrO_2 from ab initio calculation", *J. Appl. Phys*., vol. 100, pp 1-9, 2006
13. R. Pandey and R. Chaujar, "Novel back-contact back-junction SiGe (BC-BJ SiGe) solar cell for improved power conversion efficiency", *Microsystem Technologies*, DOI: 10.1007/s00542-015-2552-1. Available: http://link.springer.com/article/10.1007%2Fs00542-015-2552-1#page-1.
14. R. Pandey and R. Chaujar, "Novel SiC Encapsulated Coaxial Silicon Nanowire Solar Cell for Optimal Photovoltaic Performance"

ACCEPTED MANUSCRIPT

IEEE PVSC 42nd, June 14-19, New Orleans, USA.
15. B. Parida, J. Choi, G. Lim, K. Kim, Enhanced Visible Light Absorption by 3C-SiC Nanoparticles Embedded in Si Solar Cells by Plasma-Enhanced Chemical Vapor Deposition, J. Nanomater. 2013 (2013) 1–10. doi:10.1155/2013/953790.
16. G. S. Chung, K. S. Kim, and F. Yakuphanoglu, "Electrical characterization of Au/3C-SiC/n-Si/Al Schottky junction," *J. Alloys Compd.*, vol. 507, no. 2, pp. 508–512, 2010.
17. Y.-H. Joung, H. Kang, J. Kim, H.-S. Lee, J. Lee, and W. Choi, "SiC formation for a solar cell passivation layer using an RF magnetron co-sputtering system," *Nanoscale Res. Lett.*, vol. 7, no. 1, p. 22, 2012.
18. R. Pandey, R. Chaujar, "Rear contact SiGe solar cell with SiC passivated front surface for > 90-percent external quantum efficiency and improved power conversion efficiency ", Sol. Energy. 135 (2016) 242–252. doi:10.1016/j.solener.2016.05.056.
19. R. Pandey, A. Jain, A. Kumar, R. Chaujar, Impact of Minority Carrier Lifetime and Temperature on SiC Based Rear Contact SiGe Solar Cell for Concentrator Photovoltaic (CPV) Applications, in: 32nd Eur. Photovolt. Sol. Energy Conf. Exhib., 2016: pp. 270–273. doi:10.4229/EUPVSEC20162016-1BV.6.45.
20. E. V. Kerschaver and G. Beaucarne, "Back-contact solar cells: a review", *Prog. Photovolt: Res. Appl.*, vol. 14, pp 107-123, 2006.
21. J. W. Slotboom, "The pn-product in silicon," *Solid. State. Electron.*, vol. 20, no. 4, pp. 279–283, Apr. 1977.
22. J.W. Slotboom and H.C. De Graaf, "Measurements of Bandgap Narrowing in Silicon Bipolar Transistors", *Solid State Electronics*, Vol. 19, pp. 857-862, 1976
23. W. Shockley and W.T. Read, "Statistics of the Recombinations of Holes and Electrons", *Phys. Rev.*, vol. 87, pp. 835-842, 1952
24. R.N. Hall, "Electron Hole Recombination in Germanium", *Phys. Rev.*, vol. 87, pp. 835-842, 1952
25. T. Goudon, V. Miljanović, and C. Schmeiser, "On the Shockley–Read–Hall Model: Generation-Recombination in Semiconductors," *SIAM J. Appl. Math.*, vol. 67, no. 4, pp. 1183–1201, 2007.
26. S. Selberherr, "Analysis and Simulation of Semiconductor Devices". Wien, New York: Springer-Verlag, 1984.
27. J. Dziewior and W. Schmid, "Auger Coefficient for Highly Doped and Highly Excited Silicon", *Appl. Phys. Lett.*, vol. 31 pp. 346-348, 1977
28. P.P. Altermatt, "Models for numerical device simulations of crystalline silicon solar cells—a review, " J. Comput. Electron. 10 (2011) 314–330. doi:10.1007/s10825-011-0367-6.
29. S. Yoshinaga, Y. Ishikawa, S. Araki, Y. Uraoka, Light trapping effect of nanoimprinted-textured crystalline silicon solar cells, in: 2013 IEEE 39th Photovolt. Spec. Conf., IEEE, 2013: pp. 1310–1313. doi:10.1109/PVSC.2013.6744383.
30. Atlas user manual, *Silvaco, Inc.* Santa Clara, pp. 1565-1574. 2014
31. H. R. Philipp, "Optical Properties of Silicon Nitride," *J. Electrochem. Soc.*, vol. 120, no. 2, p. 295, Feb. 1973.
32. T. Bååk, "Silicon oxynitride; a material for GRIN optics.," *Appl. Opt.*, vol. 21, no. 6, pp. 1069–72, Mar. 1982.
33. http://refractiveindex.info/?shelf=main&book=Si3N4
34. Allen, S., Awad, Y., Gaumond, A. and Davies, M., 2009. *Silicon carbide-based antireflective coating*. U.S. Patent Application 12/994,973.
35. R. Pandey and R. Chaujar, "Front Surface Passivation Scheme for Back-Contact Back-Junction (BC-BJ) Silicon Solar Cell," *Adv. Sci. Lett.* 22, 815-820 (2016)
36. A.G. Aberle, "Surface passivation of crystalline silicon solar cells: a review," Prog. Photovoltaics Res. Appl. 8 (2000) 473–487. doi:10.1002/1099-159X(200009/10)8:5<473::AID-PIP337>3.0.CO;2-D.
37. M. A. Green and M. J. Keevers, "Optical properties of intrinsic silicon at 300 K," *Prog. Photovoltaics Res. Appl.*, vol. 3, no. 3, pp. 189–192, 1995.
38. M. A. Green, "Self-consistent optical parameters of intrinsic silicon at 300K including temperature coefficients," *Sol. Energy Mater. Sol. Cells*, vol. 92, no. 11, pp. 1305–1310, Nov. 2008.

ACCEPTED MANUSCRIPT

ACCEPTED MANUSCRIPT

Table 1. Photovoltaic parameters of 10µm thick devices: Device A, Device B, and Device C corresponds to Si_3N_4 coated, ZrO_2 textured, and SiC-based ZrO_2 textured devices, respectively.

Device	**J_{SC} (mA.cm^{-2})**	**V_{OC} (mV)**	**FF (%)**	**PCE (%)**
Reference cell [9]	22.2	615	80.2	10.9
Device A	22.2	616	80.8	11.0
Device B	28.6	623	80.9	14.4
Device C	29.3	662	80.9	15.7
Periodic nanostructure based silicon solar cell [10]	33.9	589	78.5	15.7

Table 2. Photovoltaic parameters of 300 µm thick SiC-based rear contact silicon solar cell along with already published experimental results.

Device	**Thickness (µm)**	**J_{SC} (mA.cm^{-2})**	**V_{OC} (mV)**	**FF (%)**	**PCE (%)**
SiC based ZrO_2 textured	**300**	39.4	687	80.0	21.6
MST based device [7]	**285±25**	40.5	635	77.0	19.8

Figure 1. The simulated device structure i.e. 10µm thick rear-contact silicon solar cell with the anti-reflective (AR) coating.

Figure 2. Wavelength-dependent optical properties of the materials used in simulation: (a) Real index, and (b) Absorption coefficient of silicon. Inset shows the extinction coefficient of SiC

Figure 3. Spectral response of (10 µm x10 µm) thick Si wafer with the different type of front surface. (a) Absorption, and (b) Source and available photocurrent. Si_3N_4 was used with the thickness of 80nm for anti-reflection (AR) layer

Figure 4. Photon absorption rate (cm^{-3}.s^{-1}) in the silicon wafer with the different type of front surface: (a) Without ARC, (b) with ARC, (c) ZrO_2 textured, and (d) SiC-based ZrO_2 textured. Fig.4 (e-h) shows the magnified view near the interface for uncoated, ARC based, ZrO_2 textured, and SiC based ZrO_2 textured wafers, respectively

Figure 5. Contour representation of Recombination rate (cm^{-3}.s^{-1}): (a) Si_3N_4 coated device, (b) ZrO_2 textured device, and (c) SiC-based ZrO_2 textured device. Fig. 5 (d-f) shows the magnified view of Si_3N_4/N-Si, ZrO_2/N-Si, and ZrO_2/SiC/N-Si interfaces, respectively.

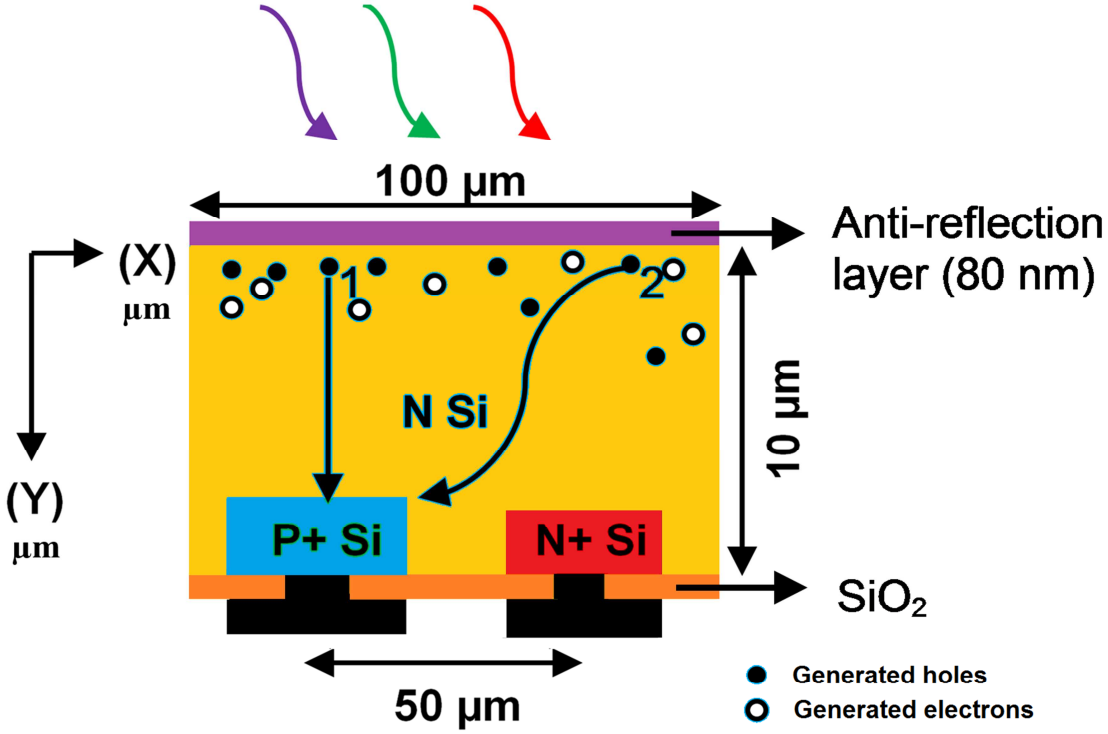
Figure 6. Current density – voltage (J-V) curve under illumination for different devices: (a) Si_3N_4 coated device, (b) ZrO_2 textured device, and (c) SiC-based ZrO_2 textured device.

Figure 7. Impact of minority carrier lifetime on photovoltaic parameters of Si_3N_4 coated, ZrO_2 textured, and SiC-based ZrO_2 textured devices: (a) V_{OC}, (b) J_{SC}, (c) PCE and (d) FF

Figure 8. (a) Available photocurrent in the 10µm and 300µm thick SiC-based ZrO_2 textured devices, respectively under AM1.5 illumination, and (b) EQE of the 10µm and 300µm thick SiC-based ZrO_2 textured devices, respectively.

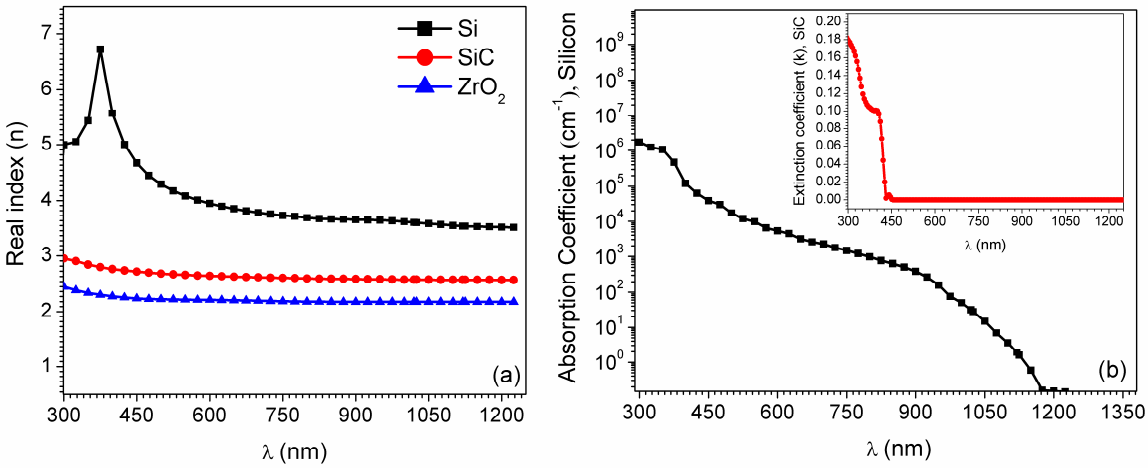
Figure 9. The J-V curve of the 10 µm and 300µm thick SiC-based ZrO_2 textured devices, respectively.

ACCEPTED MANUSCRIPT



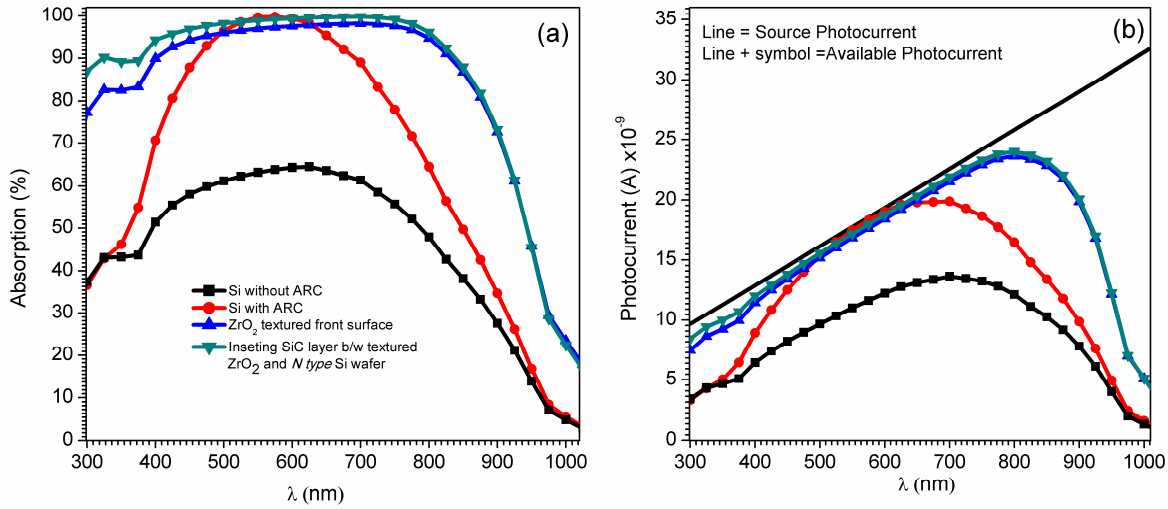
ACCEPTED MANUSCRIPT

ACCEPTED MANUSCRIPT



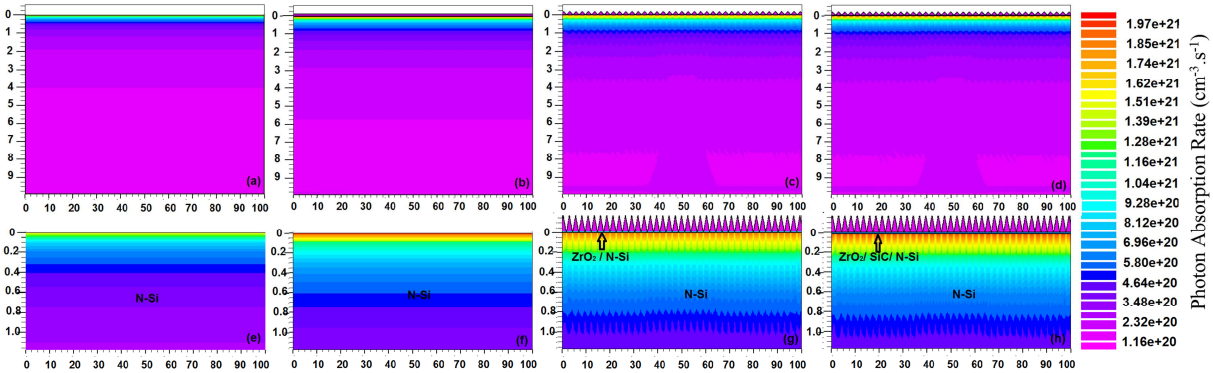
ACCEPTED

ACCEPTED MANUSCRIPT



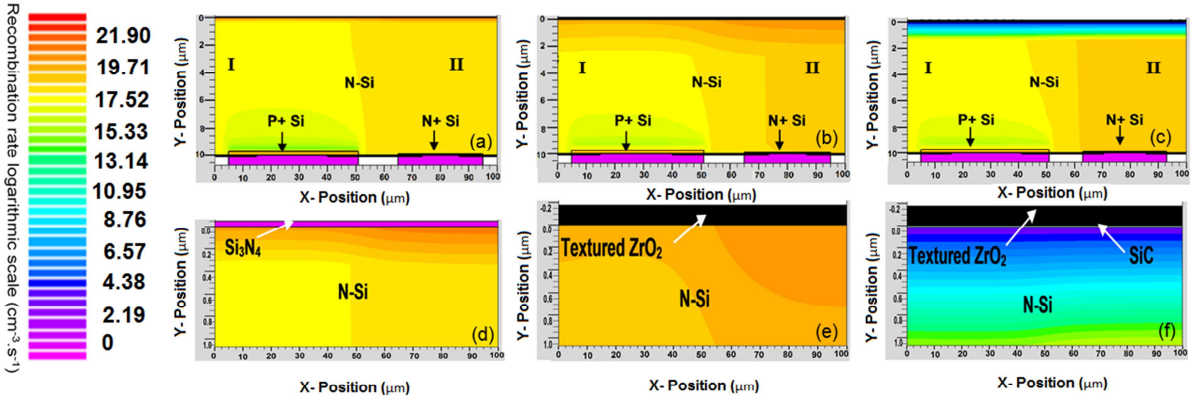
ACCEPTED

ACCEPTED MANUSCRIPT

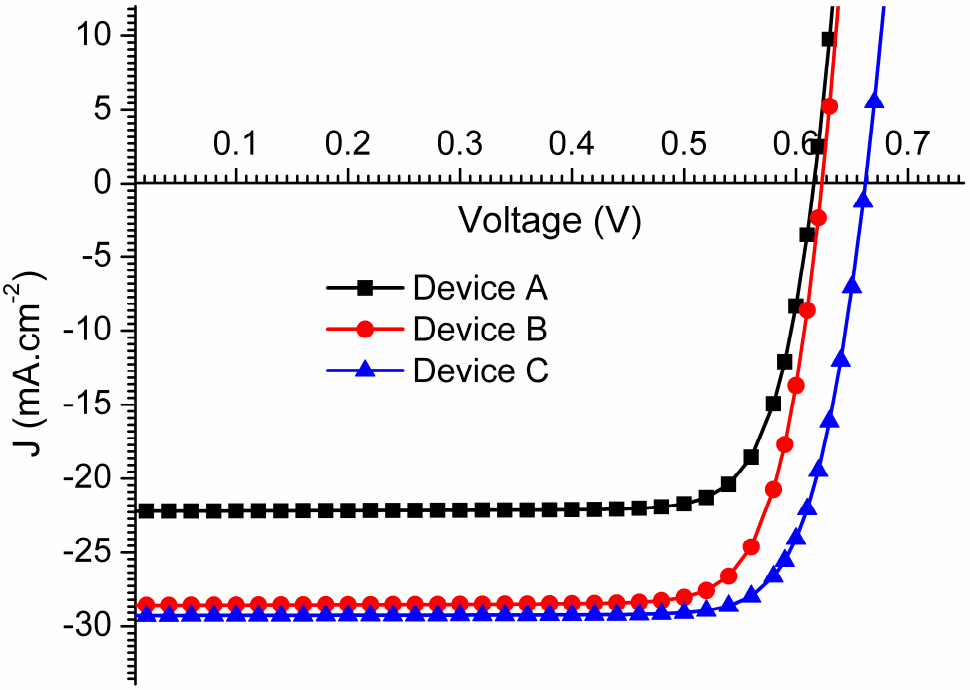


ACCEPTED MANUSCRIPT

ACCEPTED MANUSCRIPT

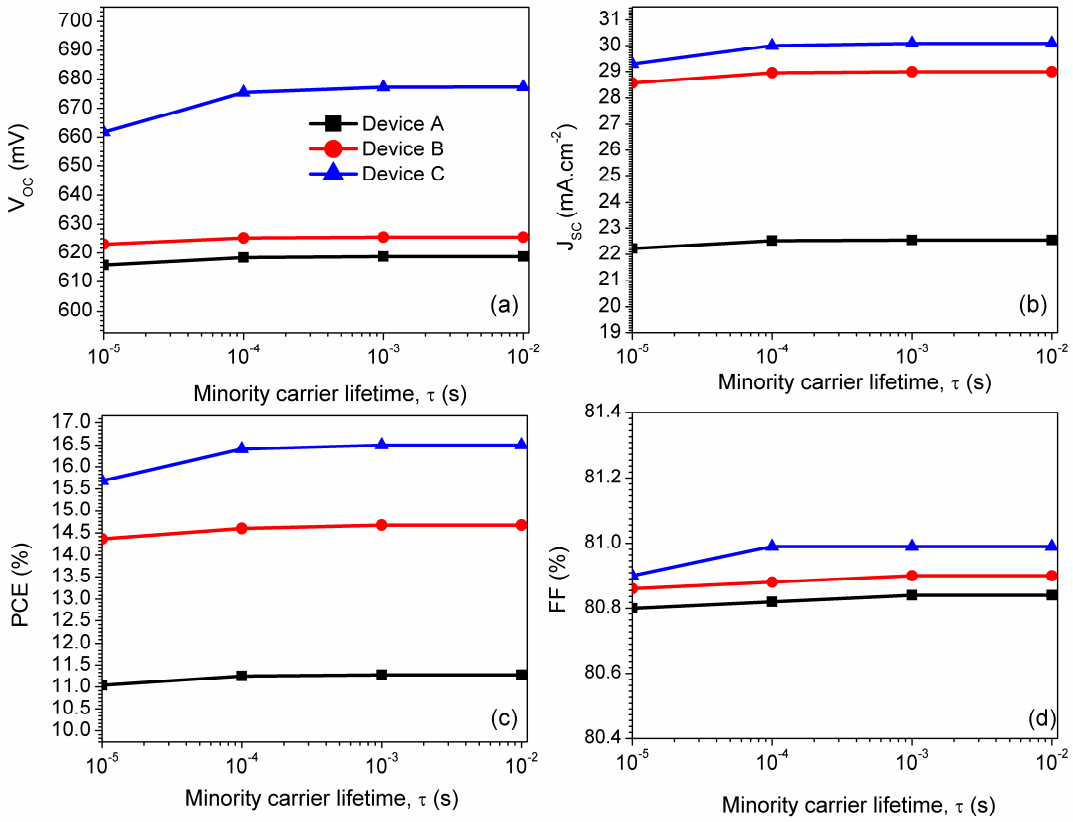


ACCEPTED MANUSCRIPT


10
5
0
-5
-10
-15
-20
-25
-30
0.1
0.2
0.3
0.4
0.5
0.6
0.7
Voltage (V)
J (mA.cm-2)
Device A
Device B
Device C

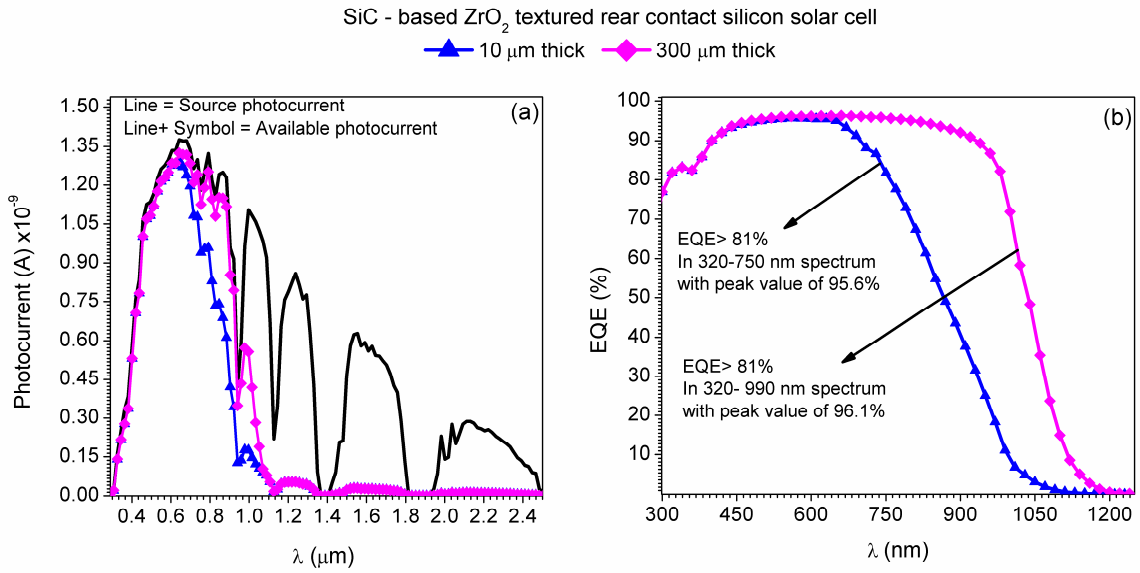
ACCEPTED

ACCEPTED MANUSCRIPT



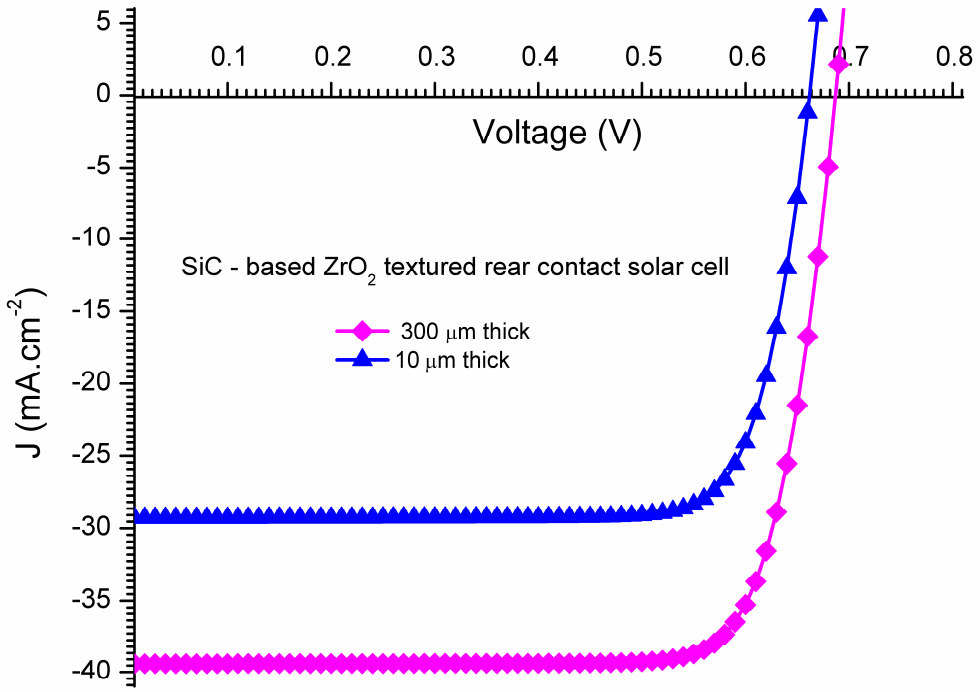
ACCEPTED

ACCEPTED MANUSCRIPT



ACCEPTED

ACCEPTED MANUSCRIPT



ACCEPTED

ACCEPTED MANUSCRIPT

Highlights

- The innovative front surface design has been proposed for silicon solar cell.
- ZrO_2 based texturing has been used along with SiC-based front surface passivation.
- The PCE of 15.7 % has been achieved in sub 10-micron thick device.
- Record V_{OC} of 662 mV has been achieved in sub 10-micron thick device.
- Further, a 21.6% efficient 300µm thick device has also been designed

ACCEPTED MANUSCRIPT

International Journal of Research & Development in Technology and Management Science –Kailash
Volume - 22| Issue 5 | 2016 | ISBN - 1-63102-466-3
European Article Number [EAN] - 978-1-63-102466-5
editor.ijrdtm@rtmonline.in | http://journal.rtmonline.in

Paper Id: **IJRDTM –0530136**

PROCESS OPTIMIZATION IN FERTILIZER MANUFACTURE INDUSTRY FOR ENVIRONMENTAL INTEGRATION

by

Arushi Gupta, Geeta Singh, Anunay Gour
Department of Environmental Engineering | arushigupta183@gmail.com | Delhi Technological University, Shahbad Daulatpur, Bawana Road, Delhi-110042

ABSTRACT

The growth of the fertilizer industry in the country all these years has been guided by the necessity of increasing production. This has led to serious environmental degradation of water resources, soil and air around these plants. The air emissions include nitrogen oxides, sulphur oxides, green house gases, waste water stream contains effluents like suspended solids, phosphates, fluorides etc, solid waste majorly phosphogypsum, contains trace metals and radionuclides. Worldwide the focus of pollution control in the fertilizer industry has shifted from end of pipe treatment to avoiding pollution, clean technology and sustainable development. Hence, there is a necessity that environmental considerations play a substantive role in the future development of the industry. Despite the importance and urgency of the problem, not much comprehensive work has so far been done in India on the whole issue with a view to develop a national level policy guidelines for the industry from the environmental angle. But this is the need of the hour. Minimization of the environmental damage is possible by adoption and implementation of cleaner production processes, appropriate treatment technologies, bulk utilization of solid waste and following the standard emission guidelines. This study is an attempt to fill up the above gap by addressing the issues of process optimization and suggesting techniques for environmental management.

Keywords: Fertilizer Industry, Environmental degradation, Air emissions, Waste water stream, Solid waste, Cleaner production processes, Treatment, Process optimization, Environmental management

INTRODUCTION

Rapid industrialization in India after the post independent era has often been associated with large scale ecological damage largely due to unscientific and unsystematic disposal of industrial effluents. Globally, fertilizer consumption has over the past few decades increasingly shifted towards developing countries. The main force responsible for the shift are the introduction of environmental legislation restricting use of fertilizer in many developed countries and a significant growth in fertilizer demand in developing regions as a result of an unprecedented growth in population particularly in Asia. In India, the number of fertilizer plants has increased many folds in last few decades. This has caused serious environmental problems due to the release of toxic contaminants into air, water and soil.

International Journal of Research & Development in Technology and Management Science –Kailash
Volume - 22| Issue 5 | 2016 | ISBN - 1-63102-466-3
European Article Number [EAN] - 978-1-63-102466-5
editor.ijrdtm@rtmonline.in | http://journal.rtmonline.in

Paper Id: **IJRDTM –0530136**

The objective of this literature review is to assess best optimization processes in the fertilizer industry in relation to their potential to mitigate effects of air pollution including green house gas emissions, waste water pollution, solid waste disposal, hazardous chemicals and noise pollution.

BACKGROUND

➢ FERTILIZER INDUSTRY IN INDIA

Indian Fertilizer Industry (2014-2015) is the second largest consumer of fertilizer in the World after China with 30 manufacturing units of urea with an installed capacity of 21.6 million tonnes and 12 units of DAP producing plants with a combined capacity of 8.3 million tonnes (Figure 1). India ranks 3rd in ammonia production and 2nd in urea in the world (Figure 2). Fertilizers can be grouped into:

- Nitrogenous eg; urea, ammonium sulphate, ammonium nitrate, ammonium chloride
- Phosphatic eg; superphosphates
- Complex eg; ammonium phosphate and ammonium sulphate-phosphate
- Pota

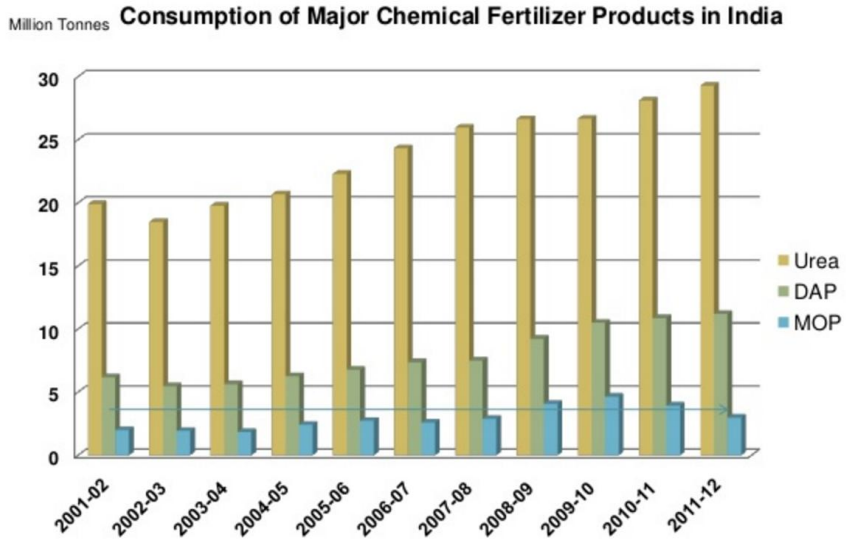


Figure 1. Consumption of Major Chemicals in India

International Journal of Research & Development in Technology and Management Science –Kailash
Volume - 22| Issue 5 | 2016 | ISBN - 1-63102-466-3
European Article Number [EAN] - 978-1-63-102466-5
editor.ijrdtm@rtmonline.in | http://journal.rtmonline.in

Paper Id: **IJRDTM –0530136**

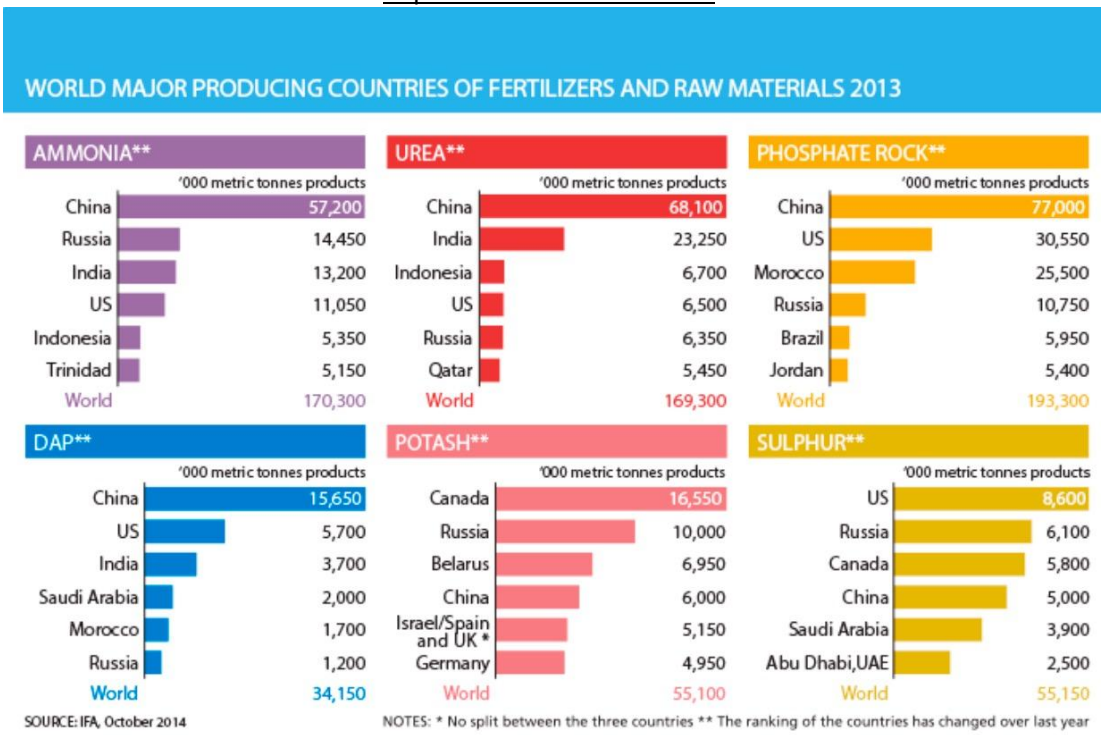


Figure 2. World Major Producing Countries of Fertilizers and Raw Materials (2013)

MANUFACTURING PROCESSES OF FERTILIZERS

➢ AMMONIA SYNTHESIS

Following process steps are proposed in the manufacturing of ammonia (Figure 3)

- Purification of Feedstock
- Primary, secondary and Heat Exchange Reforming
- Gas purification (Shift conversion and CO2 removal)
- Methanation and Syngas compression
- Ammonia Synthesis & Refrigeration
- Stripping of process Condensate

International Journal of Research & Development in Technology and Management Science –Kailash
Volume - 22| Issue 5 | 2016 | ISBN - 1-63102-466-3
European Article Number [EAN] - 978-1-63-102466-5
editor.ijrdtm@rtmonline.in | http://journal.rtmonline.in

Paper Id: **IJRDTM –0530136**

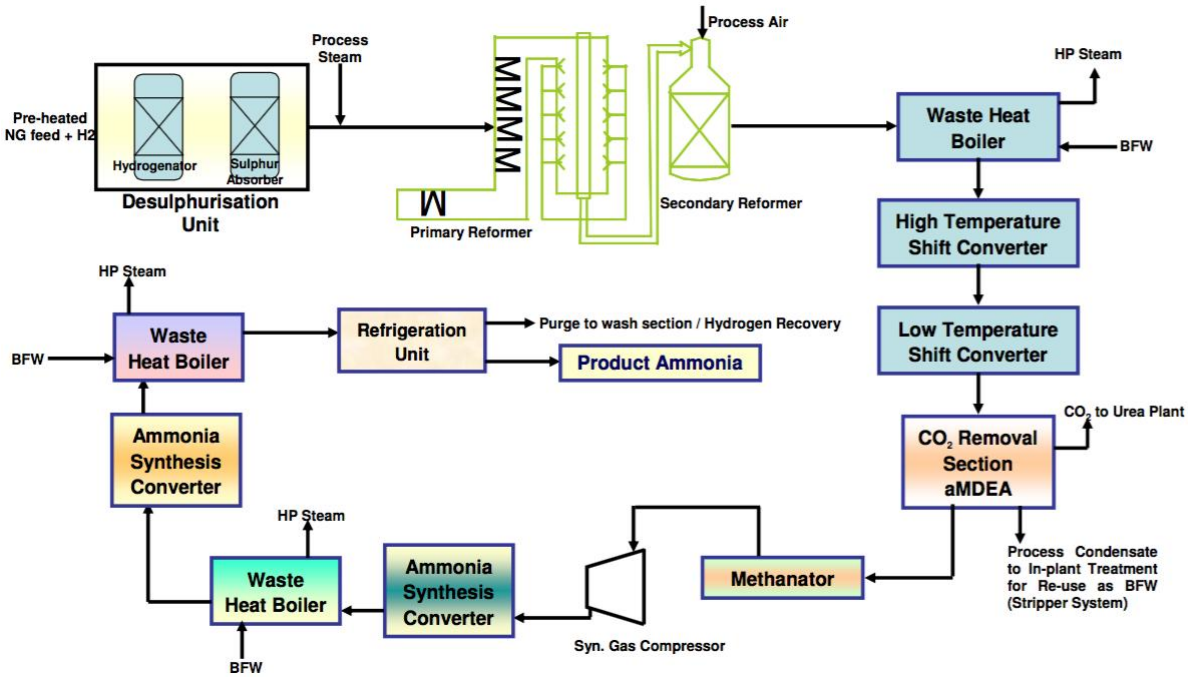


Figure 3. Ammonia Synthesis Flowchart

➢ UREA SYNTHESIS

Urea production process involves the following steps (Figure 4)

- Urea synthesis and high pressure recovery
- Urea purification and low pressure recovery
- Urea concentration
- Urea prilling
- Process condensate treatment

International Journal of Research & Development in Technology and Management Science –Kailash
Volume - 22| Issue 5 | 2016 | ISBN - 1-63102-466-3
European Article Number [EAN] - 978-1-63-102466-5
editor.ijrdtm@rtmonline.in | http://journal.rtmonline.in

Paper Id: **IJRDTM –0530136**

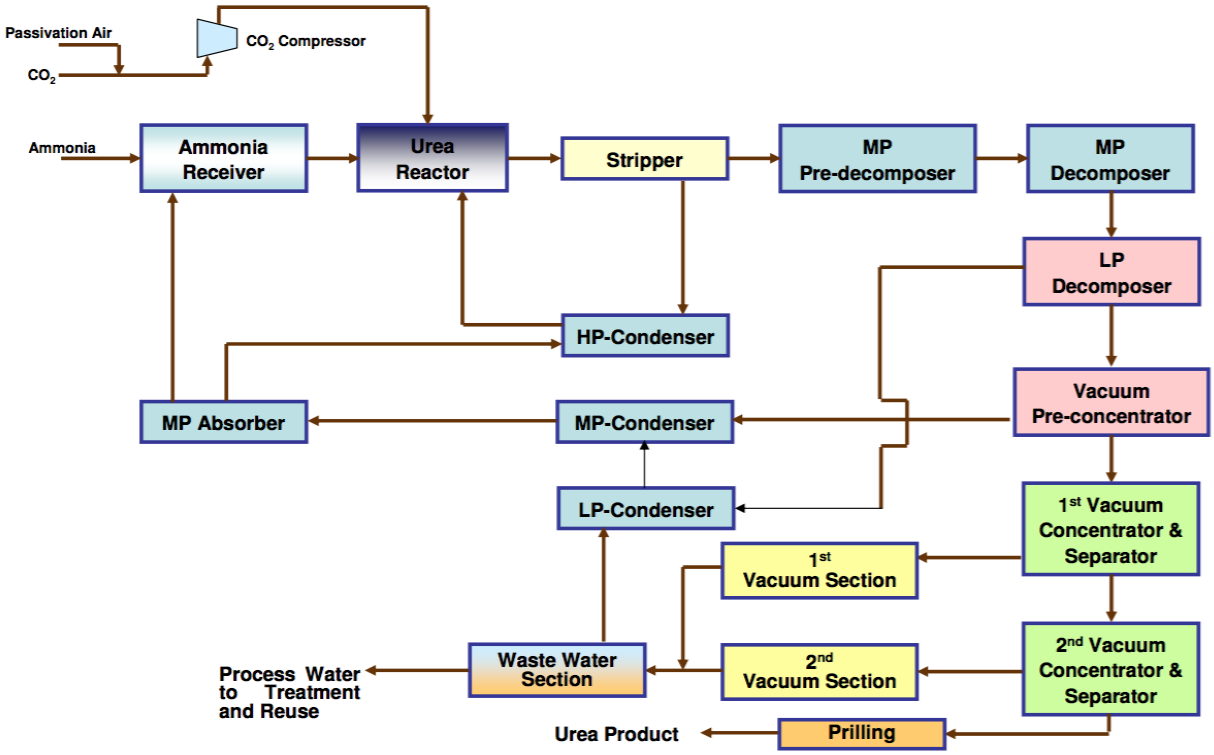


Figure 4. Urea Synthesis Flowchart

➢ PHOSPHORIC ACID SYNTHESIS

Phosphate rock, or fluorapatite, is reacted with sulphuric acid to form phosphoric acid. An important by product of this step is hydrofluoric acid, HF. It combines with silica to form fluosilicic acid, H2SiF6. Another by product is calcium sulphate sludge, which is used to form ammonium sulphate.

➢ AMMONIUM SULPHATE SYNTHESIS

Reaction between ammonia and sulphuric acid gives ammonium sulphate. Alternatively, calcium sulphate sludge from phosphoric acid plant can be reacted with ammonium carbonate to produce ammonium sulphate and calcium carbonate, which can be used in the manufacture of cement.

➢ DIAMMONIUM PHOSPHATE (DAP) SYNTHESIS

Phosphoric acid is neutralized with ammonia and the ammonium phosphate slurry so formed is granulated, or ammonium sulphate is added to the slurry before granulation to get ammonium sulphate phosphate.

International Journal of Research & Development in Technology and Management Science –Kailash
Volume - 22| Issue 5 | 2016 | ISBN - 1-63102-466-3
European Article Number [EAN] - 978-1-63-102466-5
editor.ijrdtm@rtmonline.in | http://journal.rtmonline.in

Paper Id: **IJRDTM –0530136**

FERTILIZER INDUSTRY EFFLUENTS AND THEIR SOURCES

Fertilizer plants contribute to atmospheric emission, effluent and solid waste generation. These environmental problems have repercussions at the local as well as global levels. Over the last 25 years considerable developments in technology has taken place in order to minimize the adverse environmental impacts. Even with the latest technology it has not been possible to fully ward off the ill effects arising out of the thermodynamic inefficiencies of the available systems and equipment. The environmental impact of a fertilizer plant depends on a wide variety of circumstances, including the nature of the plant, its design integrity, vintage, the processes and raw materials or feedstock which it uses, the location of the site, the nature of its surroundings, the regulations to which it must conform and the expertise of its operation and management network.

Table 1. Solid, Liquid and Gaseous Emissions from plants in Fertilizer Industry

PLANT	SOLID WASTE	LIQUID EFFLUENT	GASEOUS EMISSIONS
Ammonia	Spent catalysts Sludge from equipment Insulation debris Construction debris Oil sludge	Process condensate C02 removal solutions Cooling tower blowdown Boiler blowdown	Ammonia Carbon dioxide Furnace flue gas Vent gas
Urea	Nil	Process condensate Gland leakages from pumps Wash floorings	Prilling tower dust Ammonia
Sulphuric Acid	Sulphur sludge Spent catalysts Packing etc.	Water treatment effluents Acid leaks	Acid mists SO2/SO3 in stack
Phosphoric Acid	Gypsum Sludges Radioactivity	Plant washing Gypsum pond water Acid leaks	Fluorine Particulate matter
Nitric Acid	Spent catalysts	Plant washing	Nitrogen oxides Ammonia
Complex	Spillages Slurry from drainage/washing	Plant washing Plant leakages	Particulate matter Ammonia fumes
Ammonium Sulphate	Spillages Chalk slurry	Plant washing Plant leakages	Ammonia
Power generation	Oil sludge	Water treatment effluents Oil spillage	Sulphur dioxide in flue gas
Water treatment	Used resins Sludge from equipment	Regeneration effluents	Nil

International Journal of Research & Development in Technology and Management Science –Kailash
Volume - 22| Issue 5 | 2016 | ISBN - 1-63102-466-3
European Article Number [EAN] - 978-1-63-102466-5
editor.ijrdtm@rtmonline.in | http://journal.rtmonline.in

Paper Id: **IJRDTM –0530136**

OPTIMIZATION OF PROCESSES

- **AIR POLLUTION: GASEOUS EMISSIONS AND CONTROL SUUGESTIONS**
  - ✓ **AMMONIA PLANT**

Emissions from ammonia plants comprise of light hydrocarbons from storages, hydrogen, carbon dioxide, sulphur dioxide, ammonia, carbon monoxide and gaseous leak from flanges, stuffing boxes and dust and particulate matter from catalyst handling operations. Plant start-up may involve the flaring of synthesis gas, and some oxides of nitrogen emissions may also come. Typical ammonia process based on steam reforming generates around 2.2 tonne of carbon dioxide, and less than one kilogram of nitrogen oxides and 0.2 kilogram of sulphur dioxide per tonne of ammonia produced. In the partial oxidation process 2.7-2.8 tonnes of carbon dioxide, 1.8 kilogram of nitrogen oxides and 3 kilogram of sulphur dioxide are produced per tonne of ammonia.

Carbon dioxide (C02) is a greenhouse gas and contributes to global warming. The production of urea requires about 1.6 tonnes of CO2 per tonne of nitrogen. The fertilizer industry's share of the annual net addition of CO2 to the atmosphere resulting from human activities is estimated at 2%; and human activities account for only 7% of the quantity released annually by biological processes. Consequently, the share of fertilizer production in the total annual release of CO2 to the atmosphere is very small in the range of 0.1-0.2%. Nevertheless, the projected growth of fertilizer use makes it all the more desirable that the industry should keep CO2 emissions as low as possible. The fixation of by-product carbon dioxide as urea reduces the total carbon dioxide emissions considerably. Hence ammonia plants are most often associate with equivalent capacity urea plants also. Emissions also depend on the process and raw materials used as well as on the standards of operation and maintenance.

Steam injection and use of low NOx burners are control mechanisms adopted to reduce formation of nitrogen oxides. Usually the furnace is operated with excess air and hence the chances of formation of carbon monoxide (CO), usually a product of incomplete combustion, are remote.

Sulphur, an impurity invariably present in all petroleum fractions, gets converted to its compounds that are major sources of pollution during the manufacturing process. Natural gas, unlike other petroleum feedstock, contains only very small quantities of sulphur (up to 5 mglNm3) and is entirely removed by hydrogenation. In the case of naphtha the sulphur content in the range of 1000-1500 parts per million (ppm) and is usually gas or light hydrocarbons sulphur emissions are negligible. However, larger amounts of sulphur are present in heavy oils and coal. Partial oxidation processes extract up to 95% of sulphur in the elemental form in a Claus sulphur recovery unit. Depending on recovery equipment, up to 3 kilogram sulphur dioxide per tonne of ammonia could be emitted from coal and fuel oil based plants, compared with less than 0.01 kilogram in gas-based plants. Plants employing steam-reforming technology have lower emissions compared to partial oxidation processes. Removed by hydrofining or hydrodesulphurization process prior to reforming. There shall be no ammonia emission (odour concentration 18-35 mglNm3) from plants unless there is a leak or so.

International Journal of Research & Development in Technology and Management Science –Kailash
Volume - 22| Issue 5 | 2016 | ISBN - 1-63102-466-3
European Article Number [EAN] - 978-1-63-102466-5
editor.ijrdtm@rtmonline.in | http://journal.rtmonline.in

Paper Id: **IJRDTM –0530136**

All ammonia-bearing streams such as high-pressure loop purge gas from the synthesis unit etc. are scrubbed with water, ammonia is recovered and the rest is used as fuel in the reformer furnace. During plant start up and shutdown when nickel catalyst temperatures are in the range of lOO-150°C, in presence of carbon monoxide, there is a chance of formation of poisonous Nickel Carbonyl (NiC04) in the reformer. This situation is avoided by careful manipulation of the operating temperatures. Modern developments in gasification and ammonia process technology such as excess air reforming and auto thermal reforming provide significant reductions in emissions. Auto thermal reforming also reduces total energy consumption by necessitating (increased) power import and decreasing net heat loss.

- **UREA PLANT**

Urea plant capacities are normally commensurate with that of ammonia and carbon dioxide that are available from associated ammonia plants. Atmospheric emissions from this plant are mainly ammonia and urea dust arise out of the prilling or granulation process. The ammonia emissions are from leaks in the plant and degradation of urea to form biuret in the prilling tower. Much of the dust from prilling towers and granulators is caused by condensation products of urea vapours. Particulate emissions occur from seeding dust, undersize prills or granules, broken prills and also due to attrition. Prilling towers with natural draft may have less attrition and, hence, less dust than those with forced draft. Prilling tower, emissions range from 0.5 to 1 kilogram ammonia and 0.5-1.5 kilogram urea dust per tonne of product. With granulation, the granulator exit gas is scrubbed and losses can thereby limited to 0.25-0.8 kilogram of ammonia and 0.25-0.4 kilogram of urea dust per tonne. Without scrubbing, dust emission from granulators would be in the range of 5-30 kilogram per tonne or more, depending on granulation efficiency. In older plants, ammonia emitted from vents are typically be maintained within a range of 0.2-0.75 kilogram per tonne of urea, depending on the process and its operating efficiency, but in new plants this is reduced to as low as 0.06 kilogram per tonne.

- **NITRIC ACID PLANT**

The main atmospheric emissions from nitric acid plants are oxides of nitrogen (NOx)-nitrous oxide (N20), nitrogen peroxide (N02) and nitric oxide (NO). The concentration of these gases vary between 75 and 2000 ppmv depending on final acid concentration, pressure of the process, cooling temperatures, and degree of tail gas treatment available. Reduction in nitrogen oxides is usually achieved by absorption in cold dilute 25 to 30% nitric acid followed by stripping desorption and recycling the gas back to the process, acid or alkaline chemical absorption, adsorption on molecular sieves, catalytic reduction with natural gas or other hydrocarbon fuel or selective catalytic reduction with ammonia.

- **SO2 PLANT**

Atmospheric emissions from sulphuric acid plants consist of sulphur dioxide, sulphur trioxide, particulate matter and acid mist. Both are released with the waste gas from the final absorber tower. Acid mist can be effectively eliminated by equipment such as Brink filters or irrigated

International Journal of Research & Development in Technology and Management Science –Kailash
Volume - 22| Issue 5 | 2016 | ISBN - 1-63102-466-3
European Article Number [EAN] - 978-1-63-102466-5
editor.ijrdtm@rtmonline.in | http://journal.rtmonline.in

Paper Id: **IJRDTM –0530136**

candle filters. Sulphur trioxide emission being as low as 0.15 kilogram per tonne of sulphuric acid in new double conversion and double absorption (DCDA) plants where as it is usually around 0.6 kilogram per tonne in single contact plants. Sulphur dioxide emission is about 10-12 kilogram per tonne of sulphuric acid in single contact plants. and only 2-3 kilogram per tonne in double contact plants (UNEP, 1998). In plants where sulphur is burnt to produce S02 the only liquid effluent is generated from boiler blow-down and water treatment. In plants where S02 is received from pyrites roasting, effluent from gas cleaning operations also arise.

➢ CONTROL DEVICES

To control air emission, **electrostatic precipitators**, **scrubbers** for gaseous emissions, **cyclone dust collectors** can be installed and being operated efficiently. Adequate arrangement needs to be made for stack sampling and monitoring of pollutant level in flue gases. The stack emissions should always be well with-in the prescribed limits stipulated by State Pollution Control Board & MOEF. The ambient air quality monitoring stations should be installed at various locations in consultation with Pollution Control Board.

- ELECTROSTATIC PRECIPITATORS

The gas stream is passed between two electrodes, across which a high potential difference is maintained. Out of the two electrodes, one is the discharging and the other is the collecting electrode. Because of a high potential difference and the discharge system a powerful ionizing field is formed. Consequently. Ionization creates an active glow zone (blue electric discharge), called the 'corona' or 'corona glow'. ESP's have high efficiency approaching 99%.

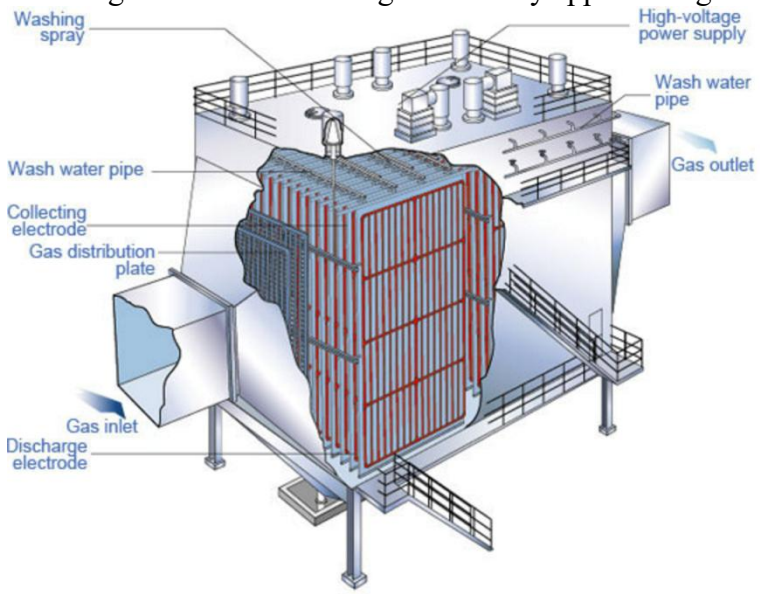


Figure 5. Electrostatic Precipitator

International Journal of Research & Development in Technology and Management Science –Kailash
Volume - 22| Issue 5 | 2016 | ISBN - 1-63102-466-3
European Article Number [EAN] - 978-1-63-102466-5
editor.ijrdtm@rtmonline.in | http://journal.rtmonline.in

Paper Id: **IJRDTM –0530136**

- CYCLONE

It is a structure without moving parts in which the velocity of an inlet gas stream is transformed into a confined vortex from which centrifugal forces tend to drive the suspended particles to the wall of the cyclone body.
It consists of a vertically placed cylinder which has an inverted cone attached to its base. The particulate laden gas stream centers tangentially at the inlet point into the cylinder. The outlet pipe for the purified gas is a central cylindrical opening at the top. The dust particles are collected at the bottom in a storage hopper. The gas path follows a double-vortex. First, the gas spirals downwards at the outer periphery of the cylindrical portion continues through the conical portion and reaches the bottom. The gas stream then moves upward in a narrower inner spiral concentric with the first and leaves through the outlet pipe. Due to the rapid spiraling movement of the gas, the dispersoids are projected towards the wall by the centrifugal force and then they drop by gravity to the bottom of the body, where they are collected in the storage hopper. High efficiency cyclones have a smaller body diameter to create greater separating forces.



Figure 6. Cyclone

- SCRUBBERS

To reduce the emission of Ammonia & Particulate Matter, adequate scrubbing system can be been installed. The un-reacted ammonia fumes and water vapor from the Pre-neutralizer and Granulator are fed to Fumes Scrubber where ammonia in the gas stream is scrubbed with scrubber liquor and the liquor is recycled back to the Pre-neutralizer. While all the dust generated from Dryer and Cooler and various other Material Handling equipment like Elevators, Conveyors, Pulverizes etc. are collected and passed through respective high efficiency Cyclones to separate the dust particles and the resultant gas is fed to the respective

International Journal of Research & Development in Technology and Management Science –Kailash
Volume - 22| Issue 5 | 2016 | ISBN - 1-63102-466-3
European Article Number [EAN] - 978-1-63-102466-5
editor.ijrdtm@rtmonline.in | http://journal.rtmonline.in

wet Scrubbers. The Fumes, Dust and Dryer scrubber are of venturi type followed by cyclonic type spray towers while cooler scrubber is only a spray tower. Each Scrubber is provided with a fan for creating the required draft. The scrubbed gasses are let out into the atmosphere through a common stack. Inclined venturi scrubber for granulator fumes and tail gas scrubber can be provided for additional scrubbing of Dryer and Fumes scrubber exhaust gases to achieve maximum recovery of ammonia and fertilizer dust before discharge to the stack.

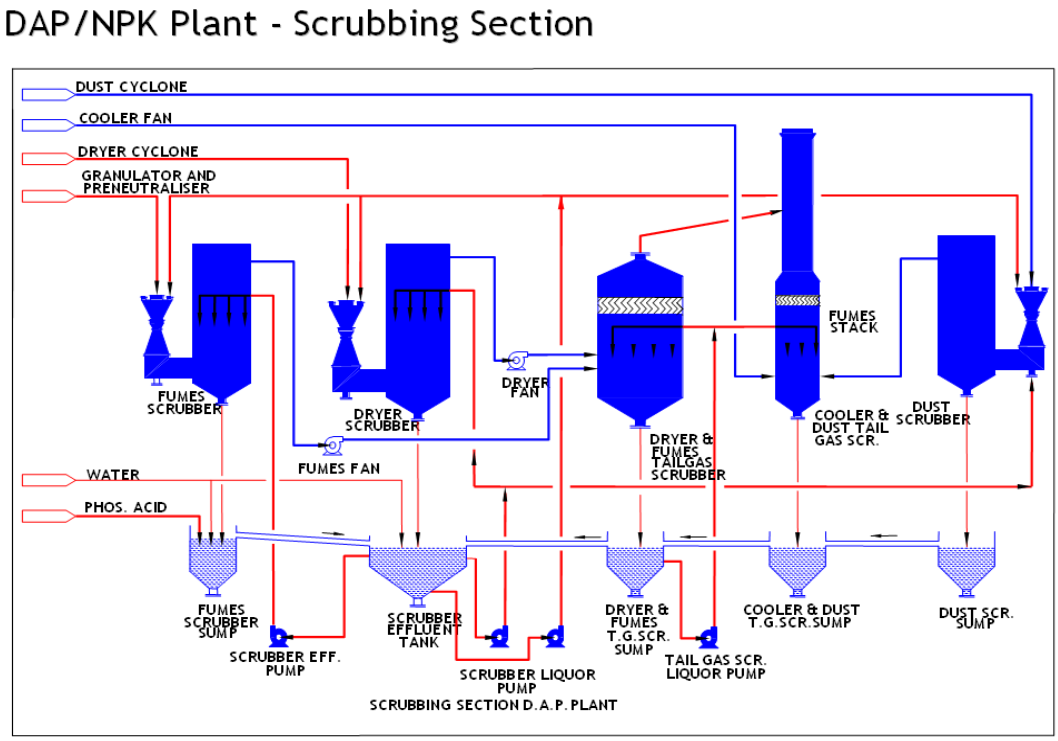


Figure 7. Scrubbing Section for DAP/NPK Plant

➢WATER POLLUTION: EFFLUENTS AND CONTROL SUUGESTIONS

Sources of waste water streams are

- Process water, final products
- Process intermediaries
- Oil bearing wastes from compressor house and boiler house
- Wash water from gas scrubbing towers
- Regeneration and rinse waters from demineralization plant
- Cooling tower and boiler blowdowns
- Phenols and cyanides, if ammonia is extracted from ammonical liquor of coke ovens

International Journal of Research & Development in Technology and Management Science –Kailash
Volume - 22| Issue 5 | 2016 | ISBN - 1-63102-466-3
European Article Number [EAN] - 978-1-63-102466-5
editor.ijrdtm@rtmonline.in | http://journal.rtmonline.in

Paper Id: **IJRDTM –0530136**

Table 2. AVERAGE COMPOSITION OF WASTE WATER STREAM

S.NO	ITEM OF ANALYSIS	VALUES (mg/l)
1	pH	7.5-9.5
2	Total Solids	5400
3	Ammonia Nitrogen	700
4	Urea Nitrogen	600
5	Phosphates	75
6	Fluorides	15
7	Arsenic	1.5

The levels of pollutants present in effluent can be reduced to acceptable level by adopting the following wastewater treatment schemes:

- Effluent treatment Plant
- Neutralization of waste water
- Sewage treatment plant.

➢ **AMMONIA PLANT**

Process condensate, from excess steam put to the primary reformer, is produced upon cooling the converted gas upstream of carbon dioxide removal unit and is a source of liquid effluent from the plant. Usually around one cubic metre of condensate per tonne of ammonia is generated and it contains up to 1000 ppm each of ammonia and methanol as pollutants. Most of this condensate can be recovered as steam and recycled by stripping with process steam feed to the primary reformer. The stripped condensate that contains not more than 50 ppm each of these pollutants can be further purified by ion exchange method and then used as boiler feed water. Similarly, ammonia from purge and flash gases from the synthesis loop are recovered by absorption in water followed by distillation in a closed loop. The lean gases from the stripper and purge recovery system are routed along with other off gases to the furnace.

➢ **UREA PLANT**

Blowdown from boilers, cooling tower and regeneration effluents from water conditioning plants also contribute to generation of wastewater. In addition to the above in the non-catalytic partial oxidation process, water containing suspended and dissolved impurities, soot and slag are produced, which necessitates treatment using mechanical, chemical and biological means.

International Journal of Research & Development in Technology and Management Science –Kailash
Volume - 22| Issue 5 | 2016 | ISBN - 1-63102-466-3
European Article Number [EAN] - 978-1-63-102466-5
editor.ijrdtm@rtmonline.in | http://journal.rtmonline.in

Paper Id: **IJRDTM –0530136**

Waste water from urea plants include the process condensate from the vacuum concentration stages (around 0.5 tonne per tonne urea) and the steam and turbine condensate (0.4 and 0.2 tonne per tonne urea respectively) and small quantities of oily water from equipment. The process condensate is normally treated and reused as boiler feed. Low-pressure steam so generated is used for process heating, in turbines, or exported to other plants. The waste-water normally contains about 2% ammonia, 4% carbon dioxide, and 1 % urea by weight and must therefore be treated in a thermal Hydrolyser-Stripper. The recovered gases are recycled to the synthesis section and the effluents now contain only around 0.0025 kg ammonia and 0.0005 kg urea per tonne of product. Alternatively the ammonia bearing effluents are also biologically treated, initially oxidizing to nitrate and then by de-nitrifying to nitrogen gas.

➢WAYS FOR EFFICIENT TREATMENT OF WASTE WATER STREAM

1. Efforts to reduce the consumption of water such as reuse of treated domestic sewage water in the area, rain water recharging well in the township with a storage pond to conserve rain water helps in reducing the salinity in the underground water table in the township and its neighboring areas. All the liquid effluents generated due to stoppage of plants, plant floor & equipment draining, washings etc if collected in a sump, can be recycled back to the process as it contains nutrients. Further, domestic sewage water generated in the factory premises can also be reused after treatment in domestic sewage treatment plant having facilities for secondary and tertiary treatment. All the solid wastes can be reclaimed and reused which includes sludge from sump and plant drain as it contains nutrients.

2. For efficient treatment, it is necessary to segregate the various waste streams and to treat them separately before they are mixed together for final treatment eg; carbon slurry waste which is generated during gasification of naptha by the steam reforming process, gas scrubber wastes containing monoethanolamine (MEA), arsenic, potassium carbonate and caustic, urea, ammonia and ammonium sulphate and phosphate bearing wastes, acid spillages, acidic and alkaline wastes from demineralization plant, oily wastes from equipments and cooling water and domestic sewage. These streams require individual treatment. The oily wastes should be passed through an oil water separator. Acidic wastes should be stored separately and mixed with the remaining wastes after ammonia removal. Wastes containing phosphates and fluorides should be separated from each other and should get treatment for reduction of phosphates and fluorides by lime and coagulant. Chemical precipitation reduces phosphates to 5mg/l and fluorides to 20 mg/l. Further biological treatment may take the form of trickling filter, activated sludge and its modifications, aerated lagoons and stabilization ponds.

3. Ammonia removal can be done by

   - air stripping- it involves raising the ph of the waste to 11.5 when ammonia is liberated as a gas. Vigorous agitation is required at this stage either with compressed air or by stripping towers fitted with fans. Compressed air agitation done for 3 hours at elevated ph effected 90.5% removal. Upto 98% removal can take place by using stripping towers filled with redwood slats and filled with air, provided enough air is supplied and the tower height is about 7 meters.

International Journal of Research & Development in Technology and Management Science –Kailash
Volume - 22| Issue 5 | 2016 | ISBN - 1-63102-466-3
European Article Number [EAN] - 978-1-63-102466-5
editor.ijrdtm@rtmonline.in | http://journal.rtmonline.in

Paper Id: **IJRDTM –0530136**

- steam stripping- it is economical if the ammonia concentration is 3-4% but the steam requirement is very high, of the order of 240 tonnes per hour, so this method is not economical.
- lagooning after ph adjustment- Lagooning after raising ph to 11 for a day can reduce ammonia by 44-61%.
- nitrification and denitrification- this process can be combined with carbonaceous BOD removal in the activated sludge process. But fertilizer wastes being deficit in carbon, a source of carbon is required for the success of tis process. Using a submerged fixed film reactor for nitrification of ammonia bearing waste water can be upto 4 times more efficient than the conventional trickling filter.

4. Conventional biological method of ammonia removal uses autotrophic nitrifying bacteria for nitrification and heterotrophic bacteria for denitrification. With a new process of anaerobic ammonium oxidation (ANAMMOX) the cost of bio treatment for ammonia removal will reduce substantially due to low oxygen requirement for nitrification and elimination of a carbon source for dentrification.

5. 1000 TPD unit produces ammonia and urea bearing waste-water of 10,000 m3 per day. Urea can be hydrolyzed to ammonia and carbon dioxide under high temperature and pressure, provided the waste water contains only urea and ammonia. Urea can be hydrolyzed under anaerobic conditions using a fixed film fixed bed (FFFB) reactor. This can handle about 2 times more urea than a continuous flow stirred tank (CFSTR) reactor.

6. A plant unit with zero liquid effluent can be designed through use of process condensate stripper and condensate polisher unit for recycling of process condensate.

7. The total liquid effluent generated from the water treatment plant and other plants should be segregated into two categories i.e. strong effluent and weak effluent and collected into respective strong effluent tank and bulk effluent tank. After confirming the permissible limit set by the state pollution control board, part of bulk effluent can be utilized for gardening within the plant premises, balance quantity is used for irrigation purpose by farmers of nearby villages. The strong effluent can be pumped to solar evaporation lagoons if available in the premises. To avoid the seepage of effluent to underground water, lagoons should be laminated with two layers of 100 micron thick black polythene sheet spread on the 30 mm thick and 20 mm thick plaster layer of bentonite, cement and local soil respectively. Also inspection wells should be made nearer to the lagoons to monitor seepage of the effluent into underground water.

Table 3: ANALYSIS OF WASTE WATER FROM PHOSPHATIC FERTILIZER PLANT

CHARCATERISTICS	PHOSPHORIC ACID PLANT (mg/l) except ph	DI-AMMONIUM PHOSPHATE PLANT (mg/l) except ph

International Journal of Research & Development in Technology and Management Science –Kailash
Volume - 22| Issue 5 | 2016 | ISBN - 1-63102-466-3
European Article Number [EAN] - 978-1-63-102466-5
editor.ijrdtm@rtmonline.in | http://journal.rtmonline.in

Paper Id: **IJRDTM –0530136**

pH	4.9	7.4
Dissolved Solids	16040	1340
Alkalinity (as CaC03)	-	275
Acidity (as CaCO3)	760	-
Free Ammonia	-	12
Fixed Ammonia	-	26
Phosphate (as PO4)	1800	-
Fluorides (as F)	200	-

➢ WATER CONSERVATION MEASURES

The liquid effluents generated from the various plants can be treated through deep hydrolyser, distillation column, stripper and ETP based on steam stripping, disc oil separator, Reverse Osmosis plant, pH neutralization, guard pond, etc. to ensure that the treated water quality conforms to the specification laid down by the designated authority. Non-Chromate cooling water system can be adopted to eliminate the generation of chromium (hazardous heavy metals).
The conservation of water, being precious resource, has always been given importance and following schemes can be adopted since inception to optimize the utilization of water and the entire effluent generated in the factory is recycled / reused after adequate treatment in plant process and irrigation of farm lands:

(1) Treatment and reuse of process condensate and turbine condensate

In Ammonia Plant, process condensate is treated in the stripper for removal of its ammonical content. Further it can be allowed to pass through a polisher unit to remove all dissolved salts contained in the process condensate. The polished condensate if pumped to plant can be reused as boiler feed water. Similarly, the turbine condensate of Ammonia Plant can be sent to condensate polisher unit of D.M. Plant for polishing in Ion Exchange units. The treated water can thus be recycled and reused as boiler feed water for steam generation.

(2) Reuse of Steam Condensate from Urea Plant

The steam condensate from surface condensate of turbo driven CO2 compressor system and from process of Urea can be recycled to steam generation plant as a make up to boiler feed water.

(3) Treatment and Reuse of waste water of Urea Plant (Deep Urea Hydrolyser)

International Journal of Research & Development in Technology and Management Science –Kailash
Volume - 22| Issue 5 | 2016 | ISBN - 1-63102-466-3
European Article Number [EAN] - 978-1-63-102466-5
editor.ijrdtm@rtmonline.in | http://journal.rtmonline.in

Paper Id: **IJRDTM –0530136**

In order to recover the valuable Urea and Ammonia from effluents and make the effluents reusable, the deep urea hydrolyser can be used.

(4) Treatment and reuse of Ammonical & Deoiled Effluent

Ammonical effluent and deoiled water from Ammonia and Urea Plant if treated in Ammonia stripper of effluent treatment plant, the treated effluent water can be recycled and reused in water softening plant.

(5) Total recycle of effluent through Reverse Osmosis effluent treatment plant

An effluent treatment cum recycle plant based on Reverse Osmosis Technology can be installed to treat the industrial liquid effluent e.g. regeneration effluent of D.M. Plant, cooling water blow down and surplus effluent water. The treated water can be reused in process as cooling water make-up.

EFFICIENT SOLID WASTE DISPOSAL STRATEGIES

Solid Waste Management: Domestic garbage generated from canteen and other areas of the plant should be collected and segregated. The reject paper bags and polythene bags should be stored in scrap yard and sold to outside party.

➢ AMMONIA PLANT

Spent catalysts and molecular sieves, used up resins, sludge from process vessels, packaging materials, insulation rejects etc., are sources of solid waste generated in modern ammonia plants. Usually eight or nine different catalysts are used in a steam-reforming based ammonia plant and most of these catalysts have an average useful life of around 2 to 6 years after which they are replaced. In the case of partial oxidation plants the number of catalysts used are only three or four. These catalysts contain heavy and toxic metals such as hexavalent chromium, nickel, zinc, iron, mineral supports etc., and hence cannot be disposed as landfills. Some of these spent catalysts are used for metal recovery. Additives used in the potassium carbonate solution used for absorption of carbon dioxide such as vanadium pentoxide, arsenic tri oxide, amines are also hazardous. Start up and shut downs cause majority of the process emissions from the ammonia plant. Reduction in start up time, recovery of vent gases as fuel and use of flare will reduce air pollution during start up and shut down. The economically achievable minimum emission levels vary among old and new plants. Assuming steady-state production, oxides of nitrogen can be limited to 0.45 kilogram nitrogen oxides per tonne of ammonia (75 ppmv or 150 mg/NmJ) in new plants, and about twice this in olden plants. Ammonia in wastewater can be reduced to 0.1 kilograms per tonne of ammonia produced. Spent catalysts can be limited to about 0.2 kilogram per tonne of ammonia. Environmental investment and operating costs vary according to emission standards or targets to be achieved, process design, integration with other facilities, raw materials, revamping requirements etc. The modem ammonia plant is characterized by large capacities and involves the storage, transport and handling of several hazardous and toxic materials in huge quantities. These involve petroleum feedstock and fuel, carbon monoxide, hydrogen, ammonia etc. that are hazardous. Hence it is

International Journal of Research & Development in Technology and Management Science –Kailash
Volume - 22| Issue 5 | 2016 | ISBN - 1-63102-466-3
European Article Number [EAN] - 978-1-63-102466-5
editor.ijrdtm@rtmonline.in | http://journal.rtmonline.in

Paper Id: **IJRDTM –0530136**

necessary that a comprehensive safety and risk analysis be carried out to operate and maintain these plants safely.

- **UREA PLANT**

  There are no solid wastes from urea plants except spillages of product and mechanical refuse which can be fully retrieved.

- **NITRIC ACID PLANT**

Spent catalysts and resins are major solid waste generated from nitric acid plants. The platinum/rhodium catalyst after use is usually returned to the manufacturer for recovery of precious metals. Spent resins are burned in kilns. Nitrous oxide (N20) emissions can be minimized by various means such as extended absorption in water to achieve a concentration of 100 ppmv. Alkaline absorption by treating the tail gas with sodium hydroxide solution produces nitrite solutions, which can be treated and safely disposed or sold. In non-selective catalytic reduction hydrogen or a hydrocarbon fuel is burned along with the tail gas over a platinum, rhodium or palladium catalyst to reduce nitrous oxide to nitric oxide. Tail gases may need to be pre-heated, and the use of hydrocarbon fuel release carbon monoxide and hydrocarbons in the atmosphere. In selective catalytic reduction ammonia is used to reduce nitrogen oxides to nitrogen over a catalyst such as vanadium pentoxide, platinum, iron/chromium oxides or zeolites. If there is some ammonia leakage, depending on catalyst efficiency, the tail gas must he kept above 100°C after expansion. On the other hand with ammonia addition and with a high efficiency catalyst, nitrogen oxides can be reduced to about 100 parts per million by volume (ppmv). Extended absorption and selective catalytic reduction are appropriate treatment techniques depending on their technical and economic feasibility. A Selective Catalytic Reduction (SCR) unit costs less than a new absorption tower, but the latter would have much lower associated running costs. With the above systems it is possible to achieve a reduction of nitrogen oxides to at least 150 ppmv (1.6 kilogram per tonne of 100% nitric acid), whilst the economic target for existing plant should be 400 ppmv (4.2 kilogram per tonne), except in the case of low pressure plants, where a realistic target would be 1000 ppmv (10.4 kilogram per tonne).

- ✓ **SULPHURIC ACID PLANT**

Solid wastes from these plants are spent catalyst and sulphur muck. Spent catalyst is returned to the catalyst supplier for recycling. Otherwise, solid wastes are usually disposed of by land filling, subject to screening for heavy metals.

- ❖ **HAZARDOUS CHEMICALS AND WASTE MANAGEMENT SUGGESTIONS**

Following practices can be used for proper management of hazardous chemicals and wastes:

- Filled containers with spent catalyst are taken to an isolated, covered designated area.
- The spent catalyst is stored in sealed drums and sold out to authorized parties for recycling and reuse.
- Proper training is being given and will continue to be provided to drivers for

International Journal of Research & Development in Technology and Management Science –Kailash
Volume - 22| Issue 5 | 2016 | ISBN - 1-63102-466-3
European Article Number [EAN] - 978-1-63-102466-5
editor.ijrdtm@rtmonline.in | http://journal.rtmonline.in

Paper Id: **IJRDTM –0530136**

transportation of hazardous chemicals, spill control and emergency actions.

- The storage conditions will be improved by taking necessary measures to reduce contamination.
- The personal protective equipment like hand gloves, PVC suit, safety goggles, dust mask and gumboots will be provided to the workers involved.

✓ NOISE LEVEL IN PLANT ATMOSPHERE AND ITS CONTROL

Noise sources in fertilizer plants are furnaces and fired heaters, burners, blowers and fans, air coolers, pumps, compressors, cooling tower fans. steam venting and let down, grinders, crushers, centrifuges, compressed air, vibration of equipment and pipelines. moving machinery. conveyors etc.

Insulating the source from the operators console is usually adopted as the basic strategy to combat sound pollution. Special refractory linings for furnaces, insulation, low noise burners, installation of silencers for fans, blowers, vent stacks etc. special noise attenuation for ducting and pipe work, control valves with special trims to reduce noise, low air velocity and low fin tip air coolers, special protective enclosures for machinery such as pumps. turbines. compressors etc., are the available techniques by which the impact of sound pollution in plants are reduced to an acceptable level.

A proper routine and preventive maintenance procedure for all the noise generating equipment should be implemented and followed up in consultation with the respective units, which will help to minimize noise levels within the plant area. The noise levels in the work area shall be maintained within standard prescribed for the work area as per CPCB. Personal protective equipment like earplugs, earmuffs etc. shall also be provided to the operators, workers and other personnel within the plant. Proper maintenance of machinery will be ensured to reduce noise level.

CONCLUSION

Pollution of air, water and land caused by emissions and effluents containing oxides of nitrogen, sulphur, carbon, ammonia, hydrogen sulphide, fluorine, greenhouse gases, acid mist, dust and particulates, radiation, phosphogypsum, heavy metals, toxic chemical, used catalysts, resins, chemical residues and spillages and waste oil and lubricants, chlorofluorocarbons, laboratory wastes, redundant equipment, mechanical refuse, plastics etc.. are the major environmental issues and concerns from the fertilizer industry. These concerns have been addressed in fertilizer production in such a way to keep the environmental impact of emissions and waste to a minimum by increasing the efficiency of production processes and adopting techniques of reducing pollution and through effective abatement. The extent of pollution and damage to the environment, arising out of the production processes varies with the different fertilizer materials and thus specific control strategies and optimization techniques have been suggested. With the currently available technologies, it is possible to control the impact of these concerns within an acceptable level.

This review suggests the following remedial measures:

International Journal of Research & Development in Technology and Management Science –Kailash
Volume - 22| Issue 5 | 2016 | ISBN - 1-63102-466-3
European Article Number [EAN] - 978-1-63-102466-5
editor.ijrdtm@rtmonline.in | http://journal.rtmonline.in

Paper Id: **IJRDTM –0530136**

1. Implementation of cleaner production processes
   Adoption of pollution prevention measures can yield both economic and environmental benefits. Gaseous emissions removal can be done by biohydrogenation and partial oxidation for sulphur removal, auto thermal reforming, adsorption for nitrogen oxides, double contact and double absorpotion process for sulphur oxide removal, segregation of various waste water streams, reduction, reuse and recycle of water, extended absorption and selective catalytic reduction for solid waste stabilization.

2. Treatment Technologies
   Gaseous emissions removal can be done by use of scrubbers, steam injection, NOx burners, cyclones, electrostatic precipitators, Brink filters and irrigated candle filters in sulphuric acid plant, ammonia removal by air stripping, steam stripping, lagooning after pH adjustment, nitrification and denitrification, noise control by use noise burners, installation of silencers for fans, blowers, special noise attenuation techniques etc.

3. Utilization of solid waste
   Opportunities to use phosphogypsum, the major kind of solid waste as a soil conditioner for alkali soil and soils deficient in sulphur should be explored. This will help in reducing volume of solid waste and save space for its disposal. Extended adsorption and selective catalytic reduction are appropriate techniques depending on their technical and economic feasibility.

4. Emission guidelines
   Well designed, well operated and well monitored pollution control systems help minimizing damages to the environment. The ideal air emission and effluent level should be achieved.

REFERENCES

[1]. Indian Fertilizer sector at a glance, krishijagran.com , Available at :http://www.krishijagran.com/corporate-watch/Industry-Profile/2014/12/Indian-Fertilizer-Sector-at-A-Glance, last access on 11 April 2016.
[2]. Priyanka Agarwal and Uma Melkania, Challenges & Innovations in Technology of Fertilizer Industry: NOx Abatement Techniques, International Journal of Innovation and Scientific Research, 2016, Vol. 20 No. 1, ISSN : 2351-8014.
[3]. ECElCHEM '78, Rational Use of Water and its Treatment in Chemical Industries, Economic Commission for Europe, New York, 1991.
[4]. Fertilizer Manual, UNIDO IFDC, Kluwer Academic Publishers, The Netherlands, 1998
[5]. MP Nair, Shodhganga , Fertilizer Manufacturing Processes and Its Environmental Problems 11_chapter 4.pdf
[6]. C.S.K. Mishra, Soumya Nayak, B.C. Guru and Monalisa Rath, Environmental Impact and Management of Wastes from Phosphate Fertilizer Plants, Journal of Industrial Pollution Control
[7]. Indian fertilizer Industry at a glance , Last access on 10 April 2016, Available at http://www.indianmirror.com/indian-industries/2015/fertilizer-2015.html

International Journal of Research & Development in Technology and Management Science –Kailash
Volume - 22| Issue 5 | 2016 | ISBN - 1-63102-466-3
European Article Number [EAN] - 978-1-63-102466-5
editor.ijrdtm@rtmonline.in | http://journal.rtmonline.in

Paper Id: **IJRDTM –0530136**

[8]. MP Nair , Shidhganga, Fertilizer Manufacturing Processes and Its Environmental Problems 8_chapter 1.pdf
[9]. Fertiliser Manual, UNIDOIIFDC, Kluwer Academic Publishers, The Netherlands 1998
[10]. Indian Farmers Fertilizer Corporation Limited website
[11]. Feasibility Report Indian Farmers Fertilizer Corporation Lmited Kalol – ESP_ 22.7.15_
[12]. M.N. Rao and H.V.N. Rao , Air Pollution, Tata McGraw-Hill education
[13]. Twigg M.V., Ed., Catalyst Handbook, Wolfe Publishing Ltd., UK, 1989, 2nd Edn
[14]. Josue Villesca, Vidya Bala, Alejandra Garcia Reactor Project: Ammonia Synthesis
[15]. UNEP, Mineral Fertiliser Production and the Environment, Technical Report No. 26, Part 1, United Nations Environment Progranune, Paris, France, 1998
[16]. James G.R. and Slack A.V., Ed., Ammonia, Part 1, Marce1 Decker, New York, 1973
[17]. F. No. J- 110011/60/2009-IA II (I) Government of India, Ministry of Environment and Forests (I.A. Division)
[18]. Zardy F., Technology for Existing Urea Plants Upgrading: High Efficiency Reactor Trays. FA! Symposium on Advances in Fertiliser Production Technology, New Delhi, 1995
[19]. N.K. Verma , Environmental Practices at Indian Farmers Fertilizer Corporation Limited
[20]. A.D. Patwardhan , Industrial waste water treatment, Ph1 Publications, 2013, 1st edition
[21]. Chemical Fertilizer Industry, Invest in India, Available at http://www.investinindia.com/industry/chemical-fertilizer/chemical-fertilizer-industry,last acce s s on 10 April 2016
[22]. The Hindu, Business Line, Ahmedabad, August 3,2011
[23]. Righi Serena, PatriziaLucialli and Luigi Bruzzi, Health and environmental impacts of a fertilizer plant- part 1: Assessment of radioactive pollution. J. Env. Radioactivity, 2005
[24]. MISHRA ET AL. Pandey, J. 2005. Evaluation of air pollution phytotoxicity downwind of a phosphate fertilizer factory in India. J. Env. Monitoring and Assessment. 100 (1-3) : 249-266. Pollution Prevention and Abatement Hand Book, (World Bank Group). 1998
[25]. Ana, Gree and Sridhar, M.K.C. 2005. Air pollution in a chemical fertilizer complexes in Nigeria: The impact on the health of the workers. J. Env. Health Res.
[26]. Urea Synthesis: A Status Report, Nitrogen, 186, British Sulphur Publishing, London, UK, 1990
[27]. LeBlanc, lR., Technical Aspects of Reducing Energy Consumption in New and Existing Ammonia Plants, Chemical Economy and Engineering Review, 1986, Vol.18, No.5
[28]. Strelzoff, SamueL Technology and Manufacture of Ammonia, Krieger Publishing Company, UK, 1981
[29]. Hodge C.A. and Popovici N.N., Ed. Pollution Control in Fertiliser Production, Marcel Dekker, New York, 1994
[30]. Czuppon T.A. and .Knez S.A., Emerging Technologies for the Ammonia Industry, Fertiliser Focus, Aug., 1991
[31]. Pagani G., Mariani L. and Cristaldini G., An Energy Efficient Urea Plant-The New Montedison IDR Process, F AI Seminar on Fertiliser Productivity and Advances in Technology, New Delhi, 1982
[32]. EFMA, BAT Booklet No. 5, Production of Urea and Urea Ammonium Nitrate, European Fertiliser Manufacturers' Association, Belgium, 1995

International Journal of Research & Development in Technology and Management Science –Kailash
Volume - 22| Issue 5 | 2016 | ISBN - 1-63102-466-3
European Article Number [EAN] - 978-1-63-102466-5
editor.ijrdtm@rtmonline.in | http://journal.rtmonline.in

[33]. EFMA, BAT Booklet No.3, Production of Sulphuric Acid, European Fertiliser Manufacturers' Association, Belgium, 1995
[34]. Duecker and West., Manufacture of Sulphuric Acid, Reinhold Publishing Company, New York, 1959.
[35]. Nebel R., Reduction of Nitrogen Losses in Plants for the Production of Ammonium Nitrate, Fertiliser News, Fertiliser Association of India, New Delhi, 1985
[36]. Pachayappan V., Indian Fertiliser Industry-Environmental Considerations, F AI Enviorunental Symposium 1980
[37]. Dave J.M., Environmental Pollution in Fertiliser Industry, FAI Group discussion. Ammoniacal Nitrogen Effluent in Fertiliser Industry, 1992
[38]. Gopinath N.D., Phosphoric Acid, A.V. Slack Ed., Marcel Dekker, New York, 1968
[39]. George K.C. and Gopinath N.D., Manufacture of Ammonium Sulphate, Conference on the Development of Fertiliser Industry in Asia and Far East, UN Economic Commission for Asia and Far East, Bombay, India, 1963
[40]. Vyas V.M., Environmental Management of Phosphatic Group of Plants-GSFC Ltd., India, Phosphate Fertilisers and the Environment, IFDC Workshop Proceedings, 1992
[41]. Isherwood K.F. Phosphate Industry and the Environment, Phosphate Fertilisers and the Environment,IFDC Workshop Proceedings, 1992
[42]. Haridasan, P.P., Paul, A.C. and Desai, M.Y.M. 2001. Natural radionuclides in the aquatic environment of a phosphogypsum disposal area. J. Env. Radioactivity.

Accepted Manuscript



Re-expression of cell cycle markers in aged neurons and muscles: Whether cells should divide or die?

Renu Sharma, Dhiraj Kumar, Niraj Kumar Jha, Saurabh Kumar Jha, Rashmi K Ambasta, Pravir Kumar

PII: S0925-4439(16)30228-9
DOI: doi:10.1016/j.bbadis.2016.09.010
Reference: BBADIS 64556

To appear in: *BBA - Molecular Basis of Disease*

Received date: 14 July 2016
Revised date: 1 September 2016
Accepted date: 13 September 2016

Please cite this article as: Renu Sharma, Dhiraj Kumar, Niraj Kumar Jha, Saurabh Kumar Jha, Rashmi K Ambasta, Pravir Kumar, Re-expression of cell cycle markers in aged neurons and muscles: Whether cells should divide or die?, *BBA - Molecular Basis of Disease* (2016), doi:10.1016/j.bbadis.2016.09.010

This is a PDF file of an unedited manuscript that has been accepted for publication. As a service to our customers we are providing this early version of the manuscript. The manuscript will undergo copyediting, typesetting, and review of the resulting proof before it is published in its final form. Please note that during the production process errors may be discovered which could affect the content, and all legal disclaimers that apply to the journal pertain.

ACCEPTED MANUSCRIPT

Invited review for BBA-Molecular Basis of Diseases

Re-expression of cell cycle markers in aged neurons and muscles: Whether cells should divide or die?

Renu Sharma[1], Dhiraj Kumar[1], Niraj Kumar Jha[1], Saurabh Kumar Jha[1], Rashmi K Ambasta[1] and Pravir Kumar[1, †]

[1]Molecular Neuroscience and Functional Genomics Laboratory, Delhi Technological University (Formerly DCE), Delhi 110042

[†]Author to whom correspondence should be addressed**:**
Dr. Pravir Kumar, PhD
Associate Professor
Department of Biotechnology
Delhi Technological University (Formerly Delhi college of engineering)
Room # FW4TF3, Mechanical Engineering Building
ShahbadDaulatpur, Bawana Road, Delhi 110042
Phone: +91- 9818898622; Email: pravirkumar@dce.edu; kpravir@gmail.com

ACCEPTED MANUSCRIPT

Abstract

Emerging evidence revealed that abrogated cell cycle entry into highly differentiated mature neurons and muscles is having detrimental consequences in response to cell cycle checkpoints disruption, altered signaling cascades, pathophysiological and external stimuli, for instance, Aβ, Parkin, p-tau, α-synuclein, impairment in TRK, Akt/GSK3β, MAPK/Hsp90, and oxidative stress. These factors, reinitiate undesired cell division by triggering new DNA synthesis, replication, and thus exquisitely forced mature cell to enter intoa disturbed and vulnerable state that often leads to death as reported in many neuro-and myodegenerative disorders. A pertinent question arises how to reverse this unwanted pathophysiological phenomenon is attributed to the usage of cell cycle inhibitors to prevent the degradation of crucial cell cycle arresting proteins, cyclin inhibitors, chaperones and E3 ligases. Herein, we identified the major culprits behind the forceful cell cycle re-entry, elucidated the cyclin re-expression based on disturbed signaling mechanisms in neuromuscular degeneration together with plausible therapeutic strategies.

ACCEPTED MANUSCRIPT

Invited review for BBA-Molecular Basis of Diseases

Key words: Post-mitotic cell division; signaling cascade; neuromuscular degeneration; cyclins; therapeutics

1. Introduction

The etiology of neuromuscular degeneration is characterized by the canonical deposition of non-functional/toxic proteins such as amyloid β, tau, parkin, α-synuclein, mutant huntingtin, and chronic inflammations in neuromuscular disorders (NMDs) including Alzheimer's disease (AD), Parkinson's disease (PD), Huntington's disease (HD), Inclusion body myositis (IBM) and Poly myositis (PM). The deposition of pathological proteins or inclusions create a physiological burden on cell that triggers multiple signaling cascades including mitogen-activated protein kinase (MAPK), c-Jun N-Terminal Kinases (JNK), Phosphatidylinositol 3-kinase/serine threonine kinase Akt/Glycogen synthase kinase 3 (PI3K/Akt/GSK3β), Notch and apoptotic signaling pathways. The consequent over expression of cell cycle markers have been observed with the symptoms of cell cycle re-entry (CCR) [1]. Moreover, the co-localisation of cell cycle markers with pathological proteins has reinforced the role of cell cycle machinery as a trigger to degeneration [2]. Further evidence suggests that re-expression of cell cycle markers occurs at prodromal stages before the appearance of pathological hallmarks in these neuromuscular disorders. A plethora of studies have demonstrated the involvement of oxidative stress, aging, mutation, mitochondrial dysfunction; ubiquitin proteasome system (UPS) shut down and loss of function of several protective proteins in the pathogenesis of these NMDs. For instance, prolonged activation or under the influence of acute insults such as DNA damage, oxidative stress, neurotrophic factor deprivation and altered micro RNA (miR) function; cell cycle machinery turns detrimental and drives the cascade of DNA synthesis and consequent neuronal

ACCEPTED MANUSCRIPT

death culminating into neurodegeneration [3]. Interestingly, numerous studies have established cell cycle re-entry as a true phenomenon in neurodegeneration with actual DNA synthesis and cannot be viewed as an epiphenomenon of other processes. Moreover, cell cycle markers' re-expression in terminally differentiated neurons is also reported to fulfill the physiological demands pertaining to synaptic plasticity, neuronal migration and maturation [4]. Importantly, current studies advocate that aberrant cell cycle re-entry is not a consequence, but rather a cause of neuromuscular degeneration, depicting the importance of targeting cell cycle re-entry as a therapeutic window for treating neuromuscular disorders. These days several compounds/biomolecules have been implicated for targeting cell cycle re-entry in neurons and muscles. Moreover, potential role of ubiquitin E3 ligases and heat shock proteins have also been demonstrated to revert the damaging effect caused by cell cycle re-entry in neuromuscular disorders.

2. Relevance of Cell cycle markers (Cyclins, CDKs, CDKIs) in maintaining Cell cycle homeostasis

The eukaryotic cell cycle is orchestrated machinery that accomplishes fundamental roles in cell replenishment such as DNA replication, cell growth, repair and birth of new daughter cells from the native mother cell. The coordination of the cell cycle requires complex interplay between the levels of different cyclins and cyclin dependent kinases (CDKs) at different checkpoints. For instance, Cyclin C/Cdk3 complex mark the transition of cells into G1 i.e. preparatory phase. Further, G1/S transition is controlled by the crucial action of cyclin D/Cdk4/6 and cyclin E/Cdk2 complex [5]. The DNA replication in S phase is triggered by the cyclin A/Cdk2 and Cyclin A/Cdk1 complex. Cell division in M phase is tightly regulated by the activity of cyclin

ACCEPTED MANUSCRIPT

B/Cdk1complex [6]. The integrity of the cell cycle is maintained by the timely degradation of cyclins and consequent inactivation of CDKs, which is brought about by a class of cyclin dependent kinase inhibitors (CDKIs). These CDKIs are categorized into Ink family and Cip/Kip family [7]. The Ink family is comprised of $p15^{Ink4b}$, $p16^{Ink4a}$, $p18^{Ink4c}$ and $p19^{Ink4d}$ that bind with Cdk4/6 and are known to inhibit its association with cyclin D, thereby promoting quiescent stage [8]. On contrary, members of Cip/Kip family comprised of $p21^{Cip1}$, $p27^{Kip1}$ and $p57^{Kip2}$ that bind and regulate specific Cyclin/Cdk complexes during different stages of cell cycle progression [9]. Additionally, activation of different signaling cascades tightly regulates the checkpoints, which are strategically distributed throughout the cell cycle. The checkpoints ensure the correct completion of previous phase before the beginning of new cell cycle phase, and ascertain the correction of any defect and provide protection against the transmittance into daughter cells by halting the cell cycle until the repair has been done or by alternatively triggering cell death pathways. For instance, the G1 phase is regulated by two checkpoints in its early and late phase to assess cell size and growth factors required for promotion to S phase [10]. While, the S phase is regulated by tumour suppressor gene p53 in response to DNA damage wherein the cell cycle is halted for repair or alternatively triggering apoptosis if the damage cannot be repaired [11]. Furthermore, the G2/M transition is tightly controlled by phosphorylation dynamics of Cdk1 where the activatory phosphorylation of Cdk1 is carried out by Cdk-activating kinase complex at Thr160/Thr161 while inhibitory phosphorylation is mediated by Myt1 and Wee1 kinase at Thr14 and Tyr15 respectively. These phosphorylation events can be reversed by the action of cell division cycle 25 (Cdc25) thereby tightly regulating Cdk1 activity [12]. In this way, cell cycle markers play a discrete role in the normal physiology of neuronal cells. However, post mitotic

ACCEPTED MANUSCRIPT

expression of these markers is responsible for the onset of cell cycle re-entry mediated neuromuscular dysfunction.

3. Causative agents that force cell cycle for re-entry into neurons and muscles

There are various factors that are responsible for triggering cell cycle re-entry in neurons and muscles, including environmental toxins, genetic factors, and other cellular stresses. These factors have different mechanistic approaches for eliciting cell cycle abnormalities in neurons and muscles that have been discussed below and elucidated in **Figure 1.**

PLEASE INSERT FIGURE 1 HERE

Figure 1: Triggering factors associated with the forceful cell cycle re-entries. Hypoxia and oxidative stress are two critical factors responsible for triggering CCR. Hypoxic exposure increases HIF-1α that causes up-regulation of growth factors and subsequent reduction of p27 expression. Reduced p27 expression and increased HIF-1α transactivation inducecyclin/Cdk complex thereby activating cell cycle progression. Further, ROS mediated oxidative stress could lead to aberrant CCR viz. several different pathways. First, ROS accumulation can result in cumulative DNA damage and consequent alteration in new DNA synthesis/replication, chromatin remodeling and transcriptional activation, signaling cascade activation and subsequent activation of cell cycle markers and thus CCR. Further, redox signaling activates pro-inflammatory cytokines (IL-1, IL-6, TNF-α) that triggers NF-κβ mediated arachidonic acid pathway metabolism and consequent CCR. In addition, ROS triggers Aβ mediated Tau phosphorylation and consequent dysfunction of ubiquitin-proteasome system and activation of mitogenic signaling pathways that also induce cell cycle progression. Hif1α-Hypoxia-inducible factor 1-alpha; Hif1β-Hypoxia-inducible factor 1-beta; CDK-Cyclin dependent Kinase; ROS-Reactive oxygen species; JNK-c-Jun N-terminal kinase; JAK/STAT-Janus kinase/signal transducers and activators of transcription; PI3K-Phosphoinositide 3-kinase; FOXO-Forkhead box protein; PL-Phospholipid; pRb-Phosphorylated retinoblastoma; IL-Interleukin; TNFα-Tumor necrosis factor-α; EETs-Epoxyeicosatrienoic acids; Cox-Cyclooxygenase.

3.1 Potential Cell cycle re-entry triggering factors

3.1.1 Environmental Factors

Recently, certain environmental factors have been identified, which contributed in the pathogenesis of several neuromuscular disorders. These environmental toxins comprised of heavy metals, pesticides and metal based nanoparticles, which are currently being studied for their role in CCR mediated neuromuscular degeneration. For instance, administration of methyl

ACCEPTED MANUSCRIPT

mercury (MeHg) is found to alter the expression of cell cycle regulators p16 and p21 in rat embryonic cortical neuronal stem cells. Moreover, compromised cell proliferation and a significant decrease in global DNA methylation were observed subsequent to MeHg treatment in NSCs, supporting the idea that its long-term exposure would lead to neurodevelopmental or neurodegenerative disorders [13]. Further, exposure to various other toxins likekainic acid, quinolinic acid and heavy metals, including cobalt, lead and iron was shown to be responsible for reactive gliosis. Accordingly, induced reactive gliotic changes led to cell cycle re-entry attempts in neurons [14]. Recently, fluoride and aluminium were found to disrupt neuronal morphology and cell cycle induced progressive cell death by triggering the activation of cell cycle markers and lysosomal proteins [15]. Additionally, a renal carcinogen OchratoxinA (OTA) induced cell cycle aberrations in renal tubular cells [16]. Moreover, environmental factors are found to exacerbate the neuromuscular degeneration in action with other triggering factors. There are numerous reports demonstrating the toxic effect of heavy metals, pesticides and nanoparticles in neurodegeneration, but very few showing the lethal effect of these toxins in the cell cycle re-entry mediated neuromuscular degeneration. Therefore, significant researches need to be carried out to determine the involvement of heavy metals and pesticides in cell cycle induction related neuromuscular toxicity.

3.1.2 Oxidative Stress

Oxidative stress is the most vulnerable and obvious cause for inducing cell cycle irregularities in post mitotic neurons and muscles reported till the date. Reactive oxygen species (ROS) generation is the prime factor responsible for causing oxidative stress, which in turn alters the

ACCEPTED MANUSCRIPT

components of mitogenic signaling cascade by activating various signaling molecules. For instance, MAPK, nuclear factor κB (NF-κB) and growth factor receptors are activated via ROS and initiate cell cycle re-entry in postmitotic neurons [17]. Interestingly, ROS also induced DNA damage; chromosomal breaks and base mis-incorporation in cell cycle events [18]. Moreover, ROS was also found to abort the activity of DNA repair proteins associated with the DNA replication process in AD. Numerous studies have reported ROS mediated unrepaired, oxidized nitrogenous bases and DNA strand breaks in post-mortem tissues of patients with different neuromuscular disorders [19]. Hypoxia has emerged as a critical player of cell cycle induction in neurons and muscles. Additionally, various studies have reported DNA replication in post-mitotic neurons upon exposure to hypoxia. Apart from DNA damage, oxidative stress is proposed to trigger cell cycle re-entry in response to UPS dysfunction [20]. However, UPS is evident to regulate the cell cycle in two disparate manner via degrading either cyclin D1 or Cdk inhibitors p21/p27 [18]. Likewise, altering the levels of HSPs including HSP 27, HSP 70 and HSP90, also trigger cell cycle re-entry via controlling different stages of the cell cycle. For instance, blocking of HSP90 action with geldanamycin, halted cell cycle at G0/G1 transition by obstructive action of HSP90-specific client proteins Cdc37 and FKBP52 [21]. Besides Kwon et al demonstrated the interaction between HSP70 and cyclin D or E1 in IBM and PM biopsy samples depicting their role in cell cycle progression [22]. Another study reported the association between Hsc70 and cyclin D1 to regulate its assembly with Cdk4 and Cip/Kip proteins and formation of a catalytically active complex [23]. Therefore, oxidative stress in concordance with cell cycle re-entry markers contributed significantly in the etiology of neuromuscular degeneration.

ACCEPTED MANUSCRIPT

3.1.3 Double stranded DNA break (DSB)

DSB accumulation and its attainment of non-repairable conformation is another crucial factor for initiating cell cycle re-entry in post-mitotic neurons [24]. DNA damage activates ataxia telangiectasia mutated (ATM), ataxia telangiectasia and Rad3-related (ATR) and E2F transcription factor 1 (E2F1), and other proteins, which regulate cell cycle; DNA damages repair, and apoptosis in post-mitotic neurons [25]. Chk1 and chk2 are the checkpoint kinases that are induced in response to DNA damage in the cell cycle. ATM is a well-known checkpoint in the cell cycle which regulates dsDNA break response in a p53 dependent manner and controls cell cycle arrest, apoptosis and mediates protection against oxidative stress [26]. Moreover, phosphorylated ATM has been shown to be elevated in cerebellar dentate neurons of AD patients when compared with age-matched controls [27]. Further, increased ATM expression accompanying down regulation of TP53-inducible glycolysis and apoptosis regulator (TIGAR) protein constituted a key feature of dementia associated with Alzheimer's disease. Furthermore, DSB mediated accumulation of functionally inactive monomers and dimers of TP53 have been reported in AD brain [28]. Likewise, E2F complexes are associated with histone-modifying enzymes, histone modifications, including histone acetylation and methylation, and therefore, essential for cell cycle re-entry that may play a regulatory role in DNA repair or apoptosis [25]. Moreover, evidence for DSB had also been reported in s-IBM muscles that resulted in muscle fiber maturation arrest [29]. Importantly, recent studies are going on to explore the relationship between DNA damage and cell cycle re-expression in different systems.

ACCEPTED MANUSCRIPT

3.1.4 Micro RNAs (miR)

miR has recently gained attention due to their strategic control of cell cycle regulation in post mitotic neurons. For instance, over-expression of miR26 has been reported to trigger aberrant cell cycle re-entry, DNA replication, and tau hyper phosphorylation in rat primary post mitotic neurons. Moreover, elevated level of miR-26b triggered the re-expression of cell cycle proteins cyclin E1, pRb, PCNA, Ki67 and BrdU in post-mitotic neurons [30]. Additionally, miR26b over-activation elicited Cdk5 mediated enhanced tau phosphorylation *in vitro* and *in*-vivo studies. It also attenuated the action of cell cycle inhibitors p15 and p27 [31]. In another study, increased miR-26b level induced cyclin E1 up-regulation and downregulated $p27^{kip1}$ expression mediated by Rb1/E2F protein complex, signifying its role in cell cycle regulation [30]. Further, genetic and epigenetic evidence revealed that NF-κB-regulated micro RNAs including miRNA-9, miRNA-125b, miRNA-146a and miRNA-155 are involved in the down regulation of small brain and retinal cell related family of target mRNAs causing complement factor H (CFH) deficiency leading to inflammatory neurodegeneration in AD and age-related macular degeneration (AMD) [32]. Likewise, disruption of miR34a and miR-132 has been linked with AD and other NDDs. For instance, Aβ mediated suppression of miR-34a resulted in unscheduled cell cycle re-entry and apoptosis via MEK-ERK pathway mediated degradation of tumor suppressor TAp73 in AD mouse model. Interestingly, numerous studies are evident for the over-expression of miRNAs in temporal cortex and hippocampus region of AD patients signifying that erroneous miRNA regulation is involved in the etiology of various NDDs [33]. Recently, altered miRNA expression has been observed in IBM, PM and other muscular dystrophies that are involved with myoblast

ACCEPTED MANUSCRIPT

differentiation and muscular regeneration [34]. However, few studies reported the role of microRNA in the cell cycle re-entry, but micro RNA research is still at preliminary stage.

3.1.5 Brain derived Neurotrophic Factor (BDNF)

BDNF is a member of neurotrophin family of growth factors that plays a crucial role in neuronal cell survival, growth and differentiation. It protects neurons against glutamate and oxidative stress, i.e. NMDA or H_2O_2 mediated toxicity, might be through inhibiting Ras-MAPK pathway. However, altered BDNF has been implicated in the cell cycle re-entry mediated pathogenesis of neuromuscular disorders during oxidative or excite toxic stress responses [35]. For instance, BDNF downregulatedcyclin B and Cdk1 levels (generally localized in NFTs in AD) in differentiating tetraploid neurons in the retina through TrkB neurotrophic receptor-mediated activity and thereby halted the cell cycle at G_2/M checkpoint. The inability of this complex to translocate into the nucleus likely played a role in blocking G_2/M transition [36] and abnormal tau phosphorylation, thereby contributing in the pathogenesis of AD [35]. Additionally, BDNF found to trigger inhibition of Cdk1 activity through phosphorylation of the site Tyr15, thereby halting G2/M transition in tetraploid neurons [36]. Another study identified that nerve growth factor (NGF) induces cell cycle re-entry through a novel, Cdk4/6-independent pathway, i.e. p^{38}/MAPK-Dependent E2F4 Phosphorylation mediated neurodegeneration [37]. The neurotrophin system also exhibits a role in myogenesis and regeneration in skeletal muscle biology. Moreover, differential study of BDNF receptors identified p75 neurotrophin receptor (p75NTR) to be predominantly expressed in human myocytes [38]. Presently, BDNF deprivation

ACCEPTED MANUSCRIPT

was well implicated in the cell cycle re-entry mediated pathogenesis in neurons, but its investigation in muscles is still desired.

3.2 Altered signaling cascades in aberrant cell cycle re-entry induced neuromuscular degeneration

Although there are several risks, factors identified to be involved in aberrant CCR but the demonstration of consequent alteration of signaling cascade is still at preliminary stage. However, a growing body of evidences have highlighted the involvement of multiple signaling pathways such as Notch, Wnt/β-catenin, Akt/GSK3β, P^{38}/MAPK and dyotic signaling in the biology of cell cycle re-entry **(Figure 2)**. For instance, treatment with kainic acid is reported to activate notch signaling that augmented the aberrant CCR via activation of CyclinD1-Rb-E2F1 axis. Moreover, this abundance of cyclin D1 expression was accomplished by Akt/GSK3β pathway in AD [39]. Similarly, elevated levels of β-catenin through wnt/β-catenin signaling in PS1 FAD brain has been found to accelerate CCR simply by upregulating cyclin D1 transcription [40]. Further, elevated cyclin D1 contributes towards the apoptotic response mediated neuronal cell death. Additionally, disturbed Cdk5 associated neurotrophic signals have also been reported to cause neuronal dysfunction. For instance, Cdk5 mediates phosphorylation of Ape1, MEF2D and GSk-3β and contribute in the pathophysiology of neuromuscular disorders [41]. Ape1 plays a crucial role in DNA repair mechanism while MEF2D, a pro-survival transcription factor assists in memory development [42]. Moreover, Cdk5 also inhibits protein phosphatase-1 (PP1) and promotes P^{38}/MAPK activity, which in turn leads to tau hyperphosphorylation and consequent microtubule dissociation [43]. Further, Cdk5 also involved with Parkin phosphorylation and glutamate or dopamine mediated neurotoxicity in PD and HD respectively [44]. Likewise, Cdk5

ACCEPTED MANUSCRIPT

is also responsible for altering Drp1 activity thereby increasing mitochondrial fission in HD. Besides, it is also reported to induce tau hyperphosphorylation and consequent increased Perikaryal inclusions of neuro-filaments (NF) in the SOD1 amyotrophic lateral sclerosis (ALS) mice model [45]. Furthermore, the increased expression of procaspase-3 and cleaved caspase-3 and 9 i.e. apoptotic signaling is observed in IBM/PM sample to be associated with Aβ accumulation. Since, accumulated Aβ in IBM/PM has evidenced to downregulate the Akt expression and subsequent alteration in G1/S phase transition thereby triggering aberrant CCR [22]. Recently, dyotic signaling has also been identified to be associated with CCR in post mitotic neuron. Since, this signaling trigger altered AβPP processing and neuronal hypertrophy in M phase of cell cycle, thus governing aberrant CCR in AD [40]. Moreover, recent studies are going on to identify the cell cycle markers associated signaling disturbances in post mitotic neurons and muscles to demonstrate the pathophysiology behind the cell cycle re-entry mediated neuromuscular degeneration. Such altered signaling associated with cell cycle markers in different neuromuscular disorders have been summarized in **Table 1**. Nevertheless, numerous signaling pathways are currently being explored in different models to unravel the complexity of cell cycle re-entry mechanisms in various NMDs.

PLEASE INSERT FIGURE 2 HERE

Figure 2: Disturbed signaling cascades associated with an aberrant cell cycle re-entry in neuromuscular degeneration. Multiple signaling pathways including Notch, Wnt/β-catenin, Akt/GSK3β, P^{38}/MAPK and dyotic signaling get affected in response to neurotophic signals, ROS production and neurotoxins attack and contribute towards the pathogenesis of neuromuscular disorders. ROS induced dyotic signaling alters AβPP processing and neuronal hypertrophy in M phase of cell cycle in post mitotic neurons. Neurotrophic signals mediated Cdk5 activation triggers neuronal dysfunction via phosphorylating Ape1, MEF2D and GSK-3β that govern the onset of NMDs. Further, Cdk5 also inhibits protein phosphatase-1 (PP1) and promotes P^{38}/MAPK activity, which in turn leads to tau hyperphosphorylation and consequent microtubule dissociation. In addition, it also directs Parkin's

ACCEPTED MANUSCRIPT

phosphorylation and glutamate or dopamine mediated neurotoxicity in PD and HD respectively. Similarly, altered Drp1 activity is also mediated via Cdk5 activity that augments mitochondrial fission in HD. Importantly, in case of ALS, mutant SOD1 impairs Cdk5 activity and subsequently causes tau hyper phosphorylation mediated Perikaryalneurofilaments (NF) accumulation. Further, neurotoxins induced Notch signaling causes aberrant CCR via activation of CyclinD1-Rb-E2F1 axis in AD. Similarly, increased levels of β-catenin viz. wnt/β-catenin pathway accelerate CCR via upregulating cyclin D1 transcription in PS1 FAD brain. Additionally, Aβ mediated increased expression of procaspase-3 and cleaved caspase-3 downregulatesAkt expression and subsequent alteration in G1/S phase transition i.e. CCR. Furthermore, EGFR mediated MK2 activation inhibits Cdc25B, which in turn promote Cdc2 and Cyclin B complex and cause neuronal dysfunction. ROS-Reactive oxygen species; Cdk5-Cyclin dependent kinase 5; GSK3β-Glycogen synthase kinase 3β; CREB-cAMP responsive element binding protein; PP1-Protein phosphatases 1; MEF2D-Pro-survival transcription factor; Ape1-Human AP-endonuclease 1; MK2-MAPK-activated protein kinase-2; NF-Neurofilaments; EGFR-Epidermal growth factor receptor; PS1-Presenilin 1.

Table 1: Consequences of altered cell signaling in the post mitotic cell division

4. Aberrant cell cycle re-entry in Neuromuscular Disorders

Scientists are investigating whether the re-expression of various cell cycle markers symbolizes an authentic cell cycle, or it is just a consequence of other pathological events. The growing evidence supports the notion that cyclin's re-expression is a true phenomenon representing actual re-activation of the cell cycle in post-mitotic neurons and muscles. However, cell cycle re-entry in terminally differentiated neurons and muscles is lethal and has been widely implicated in the pathogenesis of degenerative disorders like AD, PD, IBM/PM, HD and ALS **(Figure 3)**.

4.1 Alzheimer's Disease

Alzheimer's disease is the most common progressive neurodegenerative disorder, well characterized by the intracellular deposition of hyper-phosphorylated form of microtubule associated protein; Tau and extracellular aggregation of amyloid beta (Aβ) protein manifesting in neurofibrillary tangles (NFT) and senile plaques respectively. However, increasing evidencehas defined the role of cell cycle re-entry as one of the keys causal phenomenon in neuronal death

ACCEPTED MANUSCRIPT

associated pathogenesis of AD. Moreover, cell cycle aberrations are directly linked with the increase in pathological accumulation of Aβ and tau hyper-phosphorylation. Furthermore, cell cycle re-entry preceded NFT and senile plaque formation in AD and cell cycle markers were found to co-localize with NFTs, further reinforcing that cell cycle re-entry posits an early laid phenomenon in the pathogenesis of AD [24,63]. The cdc7 dependent phosphorylation of mini-chromosome maintenance protein 2 (Mcm2) at Ser40/41 has been reported in AD neuronal cytoplasm and NFTs, supporting the evidence of cell cycle re-entry in a DNA replication manner. However, it is interesting to note that the Mcm2 expression has not been reported in non-proliferating tissues, rather, its accumulation is observed in the cells re-entering G1 phase. Moreover, phosphorylated Mcm2 gets accumulated in the cytoplasm and is supposed to alter the minichromosome maintenance protein complex (MCM) to prevent cytokinesis in AD neurons [64]. Interestingly, mitotically active neuronal cells also trigger tau phosphorylation with the help of CDKs, which in turn stimulate the NFT formation. In a study of human tau expressing Drosophila model, Tau phosphorylation was carried out by Checkpoint kinase 1 & 2 (chk1/2) at Ser 262, which is an AD-related site [65]. In addition, Over-expressed chk2 mediated Ser 262 phosphorylation resulted in increased tau-led neurodegeneration [66]. Likewise, APP is also notably upregulated in response to mitogenic stimuli by cell cycle markers. The APP-BP1 adaptor protein, which plays an important role in APP cleavage, is a cell cycle protein involved in S-M phase transition. Augmented APP-BP1 level drives S phase mediated DNA replication in neurons accompanied by expression of cyclin B1 and cdc2 [67]. Similarly, *in-vitro* studies revealed that Presenilin 1 & 2 (PS1/PS2) over expression arrested the cycle in G1 phase while its knockdown promoted G1/S transition [40]. Further, transgenic mice studies with human APP

ACCEPTED MANUSCRIPT

mutant model (K670M/N671L), also corroborated the findings of upregulated G1/S cell cycle proteins like cyclin D1 and cyclinA in frontal cortical layers [68]. The cyclins re-expression intervened mitogenic signaling is thought to be induced by advanced glycation end products (AGEs) released from activated microglia and astroglia upon Aβ trigger. Further, in an apolipoprotein E-deficient mice model, AGEs deposition triggered cyclin D1 expression and consequent DNA replication through RAGE-ERK1/2 MAP Kinase Signaling Pathway [69]. Further, reports suggest that Aβ induced cell cycle re-entry in neurons can only be driven in the presence of tau phosphorylation carried out by non-receptor tyrosine kinase- fyn, cAMP-regulated protein kinase A and calcium-calmodulin kinase II at Y18, S409 and S416 sites respectively [70]. Moreover, it is also notable that Aβ is itself mitogenic *in-vitro,* thereby controlling the cell cycle events in AD. The evidence for Aβ induced cell cycle re-entry in post-mitotic neurons was marked by the re-expression of cyclin D1, PCNA and BrdU incorporation, evident of new DNA synthesis. Moreover, Aβ exerted a dose dependent effect on the expression of various cyclins. For instance, low Aβ triggered cyclin D1 expression, while high Aβ induced cyclin B1 [63]. Further, cell cycle reactivation is evident of non-homologous end joining (NHEJ) events in differentiated neurons. Recent studies demonstrated the elevated expression of cyclinD1, phosphorylated retinoblastoma protein (pRb), global cell cycle regulators such as Ki-67 and Mcm2 in relation with NHEJ response [24]. Cell cycle in AD is driven through G1/S phase, which is evident, by the increased level of cyclin E in different regions of the hippocampus in AD brains in comparison with age-matched controls. Moreover, upregulated cyclin E activity matched well with neuritic plaque burden in the neocortex region [46]. The affected neurons in AD also exhibit a crucial role of Cdk5 in cell cycle regulation. It has been

ACCEPTED MANUSCRIPT

demonstrated that nuclear Cdk5 plays a pivotal role in keeping neurons in the post-mitotic state as they mature while loss of nuclear Cdk5 leads to cell cycle entry [71]. Thus, increasing evidences confirm that Aβ and tau have a temporal relationship with the cell cycle re-entry and consequent neurodegeneration.

4.2 Parkinson's Disease

The signature, toxic accumulation of alpha-synuclein (α-syn) protein, characterizes the pathology of Parkinson's disease. The phenomenon of cell cycle re-entry has also been observed in PD. For instance, expression of E2F-1, pRb and proliferating cell nuclear antigen (PCNA), a marker of dividing cells has been evident in around 3-6% of substantia nigra pars compacta (SNpc) neurons in PD brains with respect to controls [55]. Moreover, neurons also showed aneuploidy of selected chromosomes signifying the involvement of DNA replication machinery. Further, the markers of G1/S phase; cyclin D and cyclin E were upregulated upon MPP^+ exposure in neuronal culture, suggesting the activation of Cdk4/6 and Cdk2 respectively. Moreover, experimental results suggest that Cdk2/cyclin E complex is more vulnerable than Cdk4/cyclin D or Cdk6/cyclin D complex [72]. Another study reported increased level of cyclin D in SNpc subsequent to rotenone administration in rats. Additionally, elevated levels of DNA polymerase β induced endoreplication were also found to be involved in the pathogenesis of PD [73]. Furthermore, microarray expression analysis revealed the association between cyclin-G-associated kinase (GAK) polymorphism rs1564282 and α-synuclein in post-mortem frontal cortex of PD brain [74]. The non-classical cell cycle protein Cdk5 possibly caused phosphorylation of Parkin, thereby reducing its E3 ligase activity and preventing the ubiquitination of toxic substrates. Moreover, several studies reported that Cdk5 also mediated

ACCEPTED MANUSCRIPT

MPTP induced neuronal cell death. Accordingly, MPTP induced activation of calpains, which triggered cleavage of p35 into p25 thereby inducing over-activation of Cdk5, which, in turn resulted in neuronal apoptosis. Furthermore, Cdk5 mediated higher levels of phosphorylated Peroxiredoxin-2 (Prx2), a neuronal antioxidant is observed in SNpc neurons in PD indicating its involvement in neuronal death [55]. This evidences suggested a potential connection between Cdk5 and cell cycle re-entry in PD. In addition, MPP induced ROS generation also triggered pRb dependent cell cycle reentry and subsequent ATM mediated DNA damage in animal models as well as in PD patients [75]. Thus, experimental studies strongly advocate the causal role of CCR in Parkinson's disease pathogenesis.

4.3 Inclusion Body Myositis and Polymyositis

IBM is the most common, progressive and debilitating, neuro inflammatory muscle fibre disease among the elderly that is primarily characterized by intra-muscular fibre aggregation of congophilic, misfolded/toxic multi-proteins and vacuolization [76]. Most importantly, IBM shows similar pathogenic manifestations as AD such as Aβ deposits, paired helical filaments containing hyperphosphorylated tau, aggregates of Aβ precursor protein (AβPP) and presenilin1 [77]. Similarly, the common morbid feature between IBM and PD has also been noticed including, enrichment of α-synuclein, Parkin and oxidized DJ-1 in muscle fibres. Such sharing of pathological features between AD, PD and IBM clearly points towards a common underlying switch to neuro-muscular degeneration marked by alteration of these proteins. However, PM has been much debated as to co-exist with IBM than as an independent phenomenon. PM is regarded as a T-cell mediated autoimmune disease typically manifesting as a painless, proximal myopathy [34]. The actual cause of occurrence and series of events leading to IBM/PM has not been fully

ACCEPTED MANUSCRIPT

understood as is the case with NDDs, though multiple factors, including toxic protein burden, UPS failure, aging and oxidative stress remained the common triggering mechanisms. Recently, Aβ induced aberrant CCR has been shown to be involved in the pathogenesis of IBM and PM. The markers of G1/S transition and proliferation, including cyclin D1, E, and Ki67 were also found to be up-regulated in both IBM and PM samples along with a parallel decrease in the level of cell cycle inhibitor p21. Further, cyclin D1 and E were shown to interact with HSP70 whose level was significantly increased in IBM and PM where heat shock proteins might be playing a role in stabilizing the cyclins [22]. Moreover, the level of various tau-phosphorylating cell cycle kinases including ERK, Cdk5 and GSK3β have been found to co-localize with inclusions containing hyper-phosphorylated tau in degenerating muscle fibres in IBM [78]. Further, co-localized ERK in tau containing paired helical filaments (PHFs) strongly suggested its role in directing tau hyper-phosphorylation led pathogenesis in IBM muscle fibres. Additionally, ERK activation was also proposed to contribute in the Activator protein 1 (AP-1) transcription factor mediated phosphorylation of AβPP gene thereby altering Aβ synthesis and processing. Furthermore, postsynaptic activation of ERK at neuromuscular junctions in normal muscles and at non-junctional regions in IBM muscle fibres provided evidence for its role in mediating junctional protein dynamics in health and disease respectively [79]. More evidence of cell cycle activation in IBM/PM has been provided by studies involving the action of NAD^+-dependent histone deacetylase (HDAC), Sirtuin 1 (Sirt1). Sirt1 was shown to promote cell cycle progression in adult skeletal muscle stem cells; muscle precursor cells (MPC) and are involved in the growth, repair and regeneration capability of adult skeletal muscle fibres. The over-expression of Sirt1, induced MPC proliferation through cell cycle activation in G1/S phase as

ACCEPTED MANUSCRIPT

evidenced by Rb phosphorylation and decreased expression of cell cycle inhibitor p21 & p27. Further, Sirt 1 induced cell cycle activation progressively into S phase and directed new DNA synthesis as indicated by the elevated level of PCNA and BrdU[80]. On contrary, the deacetylase activity of Sirt 1 is neuroprotective and its increased level has been shown to rescue neurons against Aβ induced toxicity through NF-κB inhibition or by inducing α-secretase in various models of tauopathies including AD and ALS [81]. However, the deacetylase activity and protein level of Sirt1 in the nucleus was found to be reduced in human sporadic IBM muscle fibres. Further, Sirt1 proteins are evident for forming cytoplasmic aggregates in response to ER stress. Moreover, increased AβPP and Aβ accumulation in IBM muscle fibres along with NF-κB activation is attributed to decreased Sirt 1 activity. Besides, upregulation of NF-κB was also reported in PM [82]. Taken together, muscular degeneration in IBM/PM seems to be a manifestation of aberrant CCR mediated cell death through DNA synthesis, as is the case with AD, PD and Poly Q diseases.

4.4. Other Neurodegenerative Disorders

Numerous studies on post-mortem brain revealed the pathological evidence of cell cycle re-entry in various other neurodegenerative disorders such as epilepsy, ALS, traumatic brain injury (TBI) and cerebral hypoxia-ischemia. The cell cycle re-entry was marked by the formation of cyclin D/Cdk4 complexes (G0/G1 transition) in these NDDs. Recent studies pointed towards oxidative stress as the main mechanism responsible for CCR. Experimental evidence suggests that oxidative stress mediated DNA damage activate ATM, which in turn activate the expression of E2F1 and consequent neuronal apoptosis. Furthermore, E2F-1 induced apoptosis may be p53-dependent or independent where multiple mitochondrial pathways might be activated including

ACCEPTED MANUSCRIPT

caspase dependent and independent signaling cascades. Similar evidence is observed in the western blot analysis of post-mortem brain samples in Huntington's patients [58]. Further, mHTT-perinuclear inclusions mediated cell cycle re-entry has been observed in primary cortical neurons of transgenic R6/2-J2 HD mice [83]. Another study reported an alteration in the ATF6α/Rheb pathway in HD patients triggering CCR [84]. Another finding identified the role of p25/Cdk5 in dopamine and glutamate neurotoxicity linked with HD [44]. Further, erroneous cell cycle entry and neuronal death has been demonstrated by kainic-acid induction through Notch dependent mechanism *in-vivo*. Additionally, they identified increased bioavailability of Cyclin D1 through Akt/GSK3β pathway and subsequent CCR mediated neurodegeneration via CyclinD1-Rb-E2F1 axis [39]. Recently, mutant cyclin F, a component of an E3 ubiquitin-protein ligase complex in neuronal cells has been detected through whole exome sequencing of ALS (Amyotrophic lateral sclerosis) and FTD (Frontotemporal dementia) patients. These mutants caused neuronal degeneration by altering ubiquitination process and precipitating ubiquitinatedproteins, including TDP-43 [85]. Previous reports on ALS also suggested the involvement of mutant SOD1 in Cdk5 mediated deregulation at G1-S checkpoint in neuronal death [86]. Since there is little evidence of cell cycle re-entry in other neurodegenerative disorders, further researches are required to demonstrate the involvement of cell cycle re-entry in traumatic brain injury (TBI), epilepsy and other neurodegenerative disorders of the CNS.

ACCEPTED MANUSCRIPT

Invited review for BBA-Molecular Basis of Diseases

PLEASE INSERT FIGURE 3 HERE

Figure 3: Cell cycle re-entry mechanisms in neuromuscular disorders. The pathogenesis of HD is mediated by altered activity of Cdk5, micro RNA-124 and mutant HTT, which triggers the activation of cyclins, disruption of nuclear membrane and thus subsequent CCR. While Neurotoxin (3NP) induced cyclin re-expression is also responsible for CCR in HD. Similarly, Aβ and Sirt-1induced re-activation of Cyclin D1, Cyclin E, Ki67, PCNA, Rb and reduced p27 level is responsible for CCR in case of IBM/PM. While in case of ALS, mutant SOD1 contributes towards CCR via induction of Cdk5 and reduction of p27. Similarly, microRNA-19 modulates the expression of CCR critical genes and thereby contributes towards CCR in ALS. Likewise, in case of AD, Aβ mediated Tau hyperphosphorylation triggers CCR and causes Cdk5 activation via NMDA induced Calmodulin activation. Further, MPTP activity that induced various factors such as Calpain and ATM, which triggers the cell cycle markers and contributes towards CCR mediated pathogenesis of PD. Additionally, Parkin and NOS also altered the activity of Cyclin E, p53 and α syn that triggers the apoptosis as well as impaired neuronal differentiation in PD progression via CCR. PHF-Paired helical filaments; Cdk-Cyclin dependent Kinase; miR-Micro RNA; 3NP-3-Nitropropionic acid; mtHTT-Mutant huntingtin; Sirt1-Sirtuin 1; PCNA-Proliferating cell nuclear antigen; mtSOD1-Mutant Superoxide dismutase1; Bcl2-B-cell lymphoma 2; PKA-Protein kinase A; CaMKII-Calmodulin-dependent protein kinase II; NMDA-N-methyl-D-aspartate receptor; CaM-Calmodulin; MPTP-1-methyl-4-phenyl-1,2,3,6-tetrahydropyridine; NOS-Nitric oxide synthase; MPP^+-1-methyl-4-phenylpyridinium; ATM-ataxia-telangiectasia mutated; Bax-Bcl-2-associated X protein; Rb-Retinoblastoma.

5. Post-mitotic cell division: Imperative or Impulsive?

Earlier neurons were believed to be 'truly' post-mitotic and thus being life-long arrested in the quiescent stage G_0. Paradoxically, mounting evidence suggested the exit of resting neurons, which actively participated in the untimely cell cycle re-entry upon receiving mitogenic stimuli, synthesized DNA and were subsequently crucified [64]. One of the possible explanations to the contradictory premise of 'permanent' post-mitotic neuronal state is to consider that neurons had to constantly suppress the urge of cell cycle reactivation in lieu of their healthy state or face the reverberation of death. For instance, Rb protein is one such cell cycle marker, which serves crucial function of life-long cell cycle suppression in adult neurons [87]. Another candidate ataxia-telangiectasia mutated (ATM) protein triggered checkpoints during the DNA damage response under physiological conditions and maintained neurons in quiescent stage in adult CNS [88]. Moreover, deregulation of ATM signaling is observed in at-risk neurons in AD brains.

ACCEPTED MANUSCRIPT

Likewise, Cdk5, a non-classical Cdk is found to ensure post-mitotic state of neurons by sequestering transcription factor E2F1 and thereby preventing its interaction with the activation subunit. While in response to the encountered neuronal stress, Cdk5 is translocated to the cytoplasm, thus relieving its cell cycle inhibition and inducing cell cycle re-entry. Further ATM, breakdown of Cdk5 also contributed to the pathogenesis of AD [71]. Similarly, the ubiquitin E3 ligase APC/Cdh1 also acted as the suppressor of a cell cycle in the adult brain [89].

However, increasing evidence showed the presence of different cell cycle markers in adult neurons, which was attributed to their requirement in neuronal maturation, migration and synaptic plasticity. Evidences also suggest that cell cycle activation is a crucial event for non-homologous end joining (NHEJ) repair for the double stranded breaks incorporated by excessive ROS under chronic inflammation. It has also been noticed that post mitotic neurons undergoing DNA repair did not enter S phase, but remain in G1 phase. While unconquerable DNA damage proceed towards G1/S transition evidenced by increased BrdU, CDK2 and cyclin E expression, subsequently leading to apoptosis. For instance, Rb protein served a key post-mitotic role in neuronal migration in conjunction with transcription factor E2F3 [90]. Further, ATM regulated synaptic functions, including Long-Term Potentiation and was involved in trafficking in adult neurons [89]. Another marker, cell-division cycle protein-20 (cdc20) subunit of ubiquitin E3 ligase APC/C induced NeuroD2 degradation found to promote presynaptic axonal differentiation. Further, cdc20 mediated CaMKIIβ driven retraction and pruning of dendrites. Likewise, Cdh1 modulated growth and patterning in axons, and its inhibition favoured axonal growth. Furthermore, p27 has been proposed to be a microtubule binding protein owing to its

ACCEPTED MANUSCRIPT

binding and disruption of Cofilin-actin complex upon Cdk5 phosphorylation, thereby promoting neuronal migration [91]. Similarly, p57 mediated cell cycle exit and promoted differentiation and maturation in post-mitotic neurons. Thus, the cell cycle machinery is 'repurposed' to serve important demands of the post-mitotic cells. Yet, such re-expression of cell cycle proteins under various stressors such as oxidative stress, DNA damage and neurotrophic factor deprivation forced mature neurons to re-enter the cell cycle and die at G_1/S transition before actual mitosis could begin. The DNA content and consequent cell death in at-risk neurons in AD has been proposed to corroborate with advancing disease stage. These neurons had diploid DNA content in early AD which shifted to hyperploid DNA in advanced stages of the disease. Additionally, the tetraploid neurons were positive for cyclin B1 which was indicative of re-entry into cell cycle. However, since neurons are mitotically incompetent, only about 2% of these completed DNA synthesis and had double DNA content. Moreover, majority of the tetraploid neurons remained arrested in S phase and at G2/M transition without completing DNA synthesis [92]. Further, these hyperploid neurons represented attenuated viability, breakdown of differentiation control and thus were selectively sacrificed during the progression of the disease [93,94]. Thus, aneuploidy marked an early signature of neuronal death in AD [95]. On the other hand, though a fraction of healthy neurons had more than double DNA content, these lacked the expression of cyclin B1 thus delineating their 'non-cycling' status. The tetraploid neurons in normal brains can be attributed to chromosomal missegregation during mitosis. Further, the constitutive expression of cyclin B1 in normal adult brains can be similarly attributed to extra-cell cycle roles pertaining to microtubule dynamics, neuronal plasticity, differentiation and tau phosphorylation [92]. Since, during normal development, tetraploid neurons are arrested at G_2/M and any attempt to go

ACCEPTED MANUSCRIPT

beyond this checkpoint induces apoptosis [96]. Therefore, it is not surprising that the affected neurons in AD completed S phase, arrested the cell cycle at G_2/M transition phase and remained in the tetraploid state for some years. These neurons never entered mitotic phase [40]. The evidence of failed mitosis was further agreed by shunted chromatin condensation and spindle formation. The role of various cell cycle markers including the evidence of DNA synthesis in CCR mediated NMD is outlined in **Table 2**. To sum up, erroneous cell cycle re-entry offers two choices to neurons; either they can divide and die in S phase or remain alive with double DNA content at G_2/M transition. Since neurons inherently lack mitotic competence, and no evidence of M phase entry has been reported in NDD, cell cycle re-entry in terminally, differentiated neurons drive them to death after successfully synthesizing new DNA. Thus, cell cycle re-entry into adult neurons constituted an early signature of neuromuscular degeneration and CNS injury.

Table 2. A consolidated list of various Cell cycle markers that actively participate in post mitotic neurons and related disorders as listed (shaded in grey); (–) indicates no reported action of that particular cell cycle markers

6 Therapeutic strategies for targeting cell cycle re-entry in Neuromuscular degeneration

The ectopic cell cycle re-entry causes abnormal cyclins and CDKs expression and alters the activity of various CDK inhibitors thereby contributing towards cellular imbalances. To target or reverse the chronic effects associated with cell cycle aberrancy in neuromuscular degeneration is a tedious task for neurobiologists. Till date, multiple targets and signaling pathways of the altered cell cycle have been reported that need to be addressed. In order to overcome such dyshomeostatis, numerous therapeutic strategies are currently being devised that slow down or attenuate the toxicity associated with the abnormal cell cycle re-entries in various neuromuscular

ACCEPTED MANUSCRIPT

disorders. One such strategy involves the implication of various CDK-inhibiting compounds for targeting NMDs. However, these days several compounds/biomolecules that possess anti-apoptotic, anti-proliferative and antioxidant properties have been shown to target various abnormally expressed CDKs and cyclins in NMDs. For instance, the protective role of Flavopiridol has been reported in neurodegenerative disorder like AD, PD and ALS. Flavopiridol is a semi-synthetic flavonoid that found to inhibit all CDKs and reduces cyclin D1 mRNA transcription by arresting G1 and G2/M phase transition of the cell cycle [106]. Similarly, Simvastatin (SIM) has found to inhibit the serum-mediated enhancement of cell proliferation in AD by blocking the events critical for G1/S transition. Further, it also induces a partial blockade of retinoblastoma (Rb) protein phosphorylation and is also responsible for inhibition of cyclin E/Cdk2 activity associated with increased levels of the CDK inhibitors p21(Cip1) and p27(kip1) [107]. Likewise, the protective role of Interleukin-1β (IL-1β) has also been identified in neurodegeneration through cell cycle arrest mechanism. It induced cell cycle arrest and apoptosis in neural precursor cells (NPCs) through an oxidative stress-dependent mechanism that resulted in p53-mediated induction of the CDK inhibitor p21 and the proapoptotic Bcl-2 family members Puma (p53-upregulated modulator of apoptosis) and Noxa[108]. Moreover, there are numerous other compounds identified so far that have been implicated for targeting aberrant CCR. The mechanism associated with therapeutic action of such compounds at different cell cycle check points are outlined in **Table 3**. Most of these biological compounds prevent the neurons and muscles from S phase entry and thereby provide protection against subsequent NMDs. Furthermore, these compounds have defined a beginning point for driving forward screening of potential therapeutic agents with desired pharmacological activity.

ACCEPTED MANUSCRIPT

Invited review for BBA-Molecular Basis of Diseases

Table 3: Different drugs and biomolecules to attenuate the cell cycle progression

6.1 Emerging therapies for preventing Cell cycle re-entry

Although, the important role of various bio-chemical compounds have been explored extensively to target altered cell cycle re-entry in neuromuscular disorders, yet, several new therapeutic strategies have been recently identified to target such alterations. Various studies have pointed towards the employment of UPS in the correction of CCR induced NMDs. The UPS plays a pivotal role in modulating cell cycle checkpoints, CDKs, transcription factors and other molecules critical for CCR. For instance, when a neuronal cell enters S phase, Cdk5 is transported to the cytoplasm, where it is ubiquitinated and rapidly degraded by the action of ubiquitin E3 ligase APC-Cdh1 complex. Further, APC-Cdh1 is responsible for degrading cyclin B1 where its accumulation was observed in the degenerating brain areas of AD patients [114]. Currently, p10, the N-terminal domain of p35, has also been shown the protective role against Cdk5/p25-induced toxicity in neurons [115]. Since, altered role of Cdk5 has been identified in disease pathology of NDDs. Further, it has been observed that raised expression of Skp1 protein corrects the malfunction of the E3 ligase SCF complex. Since, malfunction of the E3 ligase SCF complex subsequently results in dysregulation of cell cycle regulators of the G_1/S phase transition like cyclins, CDKs, and cell cycle inhibitors thereby leading to neurodegeneration [116]. Likewise, SCF complex controls the G1/S and G2/M transitions by maintaining the level of β-catenin, p21, p27 and cyclin E in HD. Another Ubiquitin E3 ligase, Parkin protected neurons against cyclin E accumulation by associating with a protein complex, including hSel-10 and Cullin-1 [117]. Importantly, molecular chaperones in general preserve intracellular protein homeostasis in cooperation with the UPS. Therefore, HSPs are also being induced upon the cell

ACCEPTED MANUSCRIPT

cycle trigger in neurons and muscles that regulate the G1 phase. For instance, increased expression of chaperone HSP70 along with cyclins E/D1 during cell cycle progression has been reported in both IBM and PM muscle and in AD brain. Moreover, the interaction between HSP70 and cyclins E/D1 has crucial importance during cell cycle progression in the inflammatory myopathies, probably controlling cyclin maturation or degradation. Similarly, elevated levels of HSP90 in human IBM and PM biopsy specimens have been reported as, presumably in a stress-protective role [22]. Further, targeting cell cycle proteins could be another potential therapeutic approach for treating NMDs. For instance, inhibition of Cdk4 prevents both inductions of Bim expression and thrombin-induced neuronal apoptosis. Since, exposure of neuronal cultures to thrombin causes induction of cell cycle proteins cyclin E and cyclin D1, at both mRNA and protein levels thereby triggering cell cycle re-entry [118].

Interestingly, abnormal activation of the MEK-ERK MAP kinase pathway could be a potential modulator for cell cycle proteins. For instance, aberrant activation of this signaling axis regulates Cyclin D1 expression and forces neurons into the S phase, leading to cell cycle-related neuronal apoptosis (CRNA) [119]. On contrary, Cyclin D1, in turn, prevents the activation of Cdk5 by its neuronal cyclin-like activator p35 and provides neuroprotection [120]. Similarly, ablating Notch signaling in neurons provides neuroprotection against kainic acid-induced neuronal death in AD. Since, kainic-acid treatment *in vivo* elicits erroneous CCR and neuronal death through a Notch-dependent mechanism, which further increases the bioavailability of CyclinD1 through Akt/GSK3β pathway, leading to aberrant CCR via activation of CyclinD1-Rb-E2F1 axis [39]. Furthermore, treatment with quercetin has currently reported to act as a disruptor of the β-catenin/TCF transcription complex and consequently, reduced cyclin D1 levels and reversed the cell cycle/cell death phenotype in the PS1 Familial Alzheimer's disease (FAD) brain [40].

ACCEPTED MANUSCRIPT

However, elevated expressions of β-catenin in the PS1 FAD brain accelerate CCR simply by increasing cyclin D1 transcription. Further, the induction of numerous cyclin-dependent kinase inhibitors, including, p16, p19, p21 and p27, have been reported as a protective molecule in AD. These inhibitors attenuate the phosphorylation activity of Cdk4 and Cdk6 thereby protecting neurons from apoptotic insults [121]. Currently, the regulatory role of Smad protein has been observed in AD brain via regulating the transcriptional activation of Cdk4. In the normal adult brain, Smad proteins are constitutively phosphorylated and predominantly localized in neuronal nuclei. Under neurodegenerative conditions such as AD, the subcellular localization of phosphorylated forms of Smad protein is heavily disturbed, lead to a loss of neuronal differentiation control and successive cell cycle re-entry [122]. Further, the involvement of histone deacetylases inhibitors such as suberoylanilidehydroxamic acid (SAHA) and sodium butyrate (NaB) and rapamycin, an inhibitor of mechanistic target of rapamycin (mTOR) has recently been reported to normalize the proliferation of PD lymphoblasts via preventing the over-expression of the cyclin D3/Cdk6/pRb signaling cascade. These drugs are having neuroprotective roles in both human neuroblastoma SH-SY5Y cells and primary rat mid-brain dopaminergic neuronal cultures toxicity induced by 6-hidroxydopamine [56]. Furthermore, humungous amount of researchers are still required in near future to explore the potential and probable therapies against cell cycle aberrancy to alleviate the disease atmosphere of neuromuscular disorders.

7. Conclusion

Re-expression of cell cycle markers in aged neurons and muscles is identified as an intriguing process for aggravating neuromuscular disorders. Earlier its re-expression was confounded by their multiplicity of functions in a *bonafide* mitotic process, but later it is reported to be showing partial mitotic cell division and subsequent cell death. The mechanism behind the cell cycle re-

ACCEPTED MANUSCRIPT

entry includes the homeostatic imbalances among the levels of different cyclins and Cycin dependent kinases. The cell cycle markers play a pertinent role in marking the cell for mitotic division or for controlling other functions like synapse regulation and damage repair. The recent research has identified the disturbances in multiple signaling cascades controlling the process of cell proliferation and apoptosis. Such CCR mediated disturbed signaling includes Notch, Wnt/β-catenin, Akt/GSK3β, P^{38}/MAPK and dyotic signaling pathways in post mitotic neurons and muscles. Moreover, numerous triggering factors forcing cell cycle re-entry has been identified, which includes, environmental factors like toxins, pesticides and metal based nanoparticles; oxidative stress, double-stranded DNA break (DSB), UPS dysfunctions, Micro RNAs, and deprivation of the brain derived neurotrophic factor (BDNF). Further, cell cycle aberrations have been widely studied in AD, while its investigation in other neurodegenerative disorders and muscular degenerative disorders like IBM and PM is still at preliminary stage. The upcoming research prospects are to device the potential methods for targeting the cyclin/CDKs dysregulation in neuromuscular degeneration. Currently, in order to target aberrant CCR or reverse the chronic effects of such abnormalities, numerous biomolecules and chaperones mediated therapeutic strategies have been adopted to obviate the disease symptoms. For instance, Flavopiridol, Roscovitine, and Olomoucineas CDKs inhibitor are used as a drug for the treatment of AD, PD, and ALS. Likewise, the potential protective role of numerous flavonoids such as Resveratrol, Apigenin and Epigallocatechin-gallate has also been observed for inducing cell cycle arrest at different checkpoints in AD, PD and HD. Moreover, numerous ubiquitin E3 ligases such as APC-Cdh1 complex has shown the protection against Cdk5/p25-induced toxicity in neurons via its proper ubiquitination and degradation. Similarly, HSP70 along with cyclins

ACCEPTED MANUSCRIPT

E/D1 during cell cycle progression in both IBM and PM muscle, AD brain has shown promising role in controlling cyclin maturation or degradation. Further, it is reasonable to proclaim that the current knowledge's on the involvement of aberrant CCR in the pathogenesis of NMDs are still at an elementary stage. However, in light of its substantial progression from both clinical research and therapeutic application perspectives, we look forward to major research efforts being drawn in this field and more approaches being formulated in the near future.

ACCEPTED MANUSCRIPT

ACCEPTED MANUSCRIPT

Invited review for BBA-Molecular Basis of Diseases

References

1. D. Zheng, G. Zhu, S. Liao, W. Yi, G Luo, J. He, Z. Pei, G. Li, Y. Zhou, Dysregulation of the PI3K/Aktsignaling pathway affects cell cycle and apoptosis of side population cells in nasopharyngeal carcinoma, Oncol Lett. 10 (2015) 182-188.
2. A. Thakur, S.L. Siedlak, S.L. James, Retinoblastoma protein phosphorylation at multiple sites is associated with neurofibrillary pathology in Alzheimer disease, Int J ClinExpPathol. 1 (2008) 134–46.
3. Y. Yang, E.J. Mufson, K. Herrup, Neuronal cell death is preceded by cell cycle events at all stages of Alzheimer's disease, J Neurosci. 23 (2003) 2557–2563.
4. S. Lim, P. Kaldis, Cdks, cyclins and CKIs: roles beyond cell cycle regulation, Development. 140 (2013) 3079-93.
5. M. Hengstschläger, K. Braun, T. Soucek, A. Miloloza, E. Hengstschläger-Ottnad, Cyclin-dependent kinases at the G1-S transition of the mammalian cell cycle, Mutat Res. 436 (1999) 1-9.
6. C. Bertoli, J.M. Skotheim, R.A. de Bruin, Control of cell cycle transcription during G1 and S phases, Nat Rev Mol Cell Biol. 14 (2013) 518-28.
7. Z. Ullah, C.Y. Lee, M.L. Depamphilis, Cip/Kip cyclin-dependent protein kinase inhibitors and the road to polyploidy, Cell Div. 4 (2009) 10.
8. J. Lin, S. Jinno, H. Okayama, Cdk6-cyclin D3 complex evades inhibition by inhibitor proteins and uniquely controls cell's proliferation competence, Oncogene. 20 (2001) 2000-9.

ACCEPTED MANUSCRIPT

9. N.G. Starostina, E.T. Kipreos, Multiple degradation pathways regulate versatile CIP/KIP CDK inhibitors, Trends Cell Biol. 22 (2012) 33-41.

10. D.A. Foster, P. Yellen, L. Xu, M. Saqcena, Regulation of G1 Cell Cycle Progression: Distinguishing the Restriction Point from a Nutrient-Sensing Cell Growth Checkpoint(s), Genes Cancer. 1 (2010) 1124-31.

11. A.M. Abreu Velez, M.S. Howard, Tumor-suppressor Genes, Cell Cycle Regulatory Checkpoints, and the Skin, N Am J Med Sci. 7 (2015) 176-88.

12. T.A. Potapova, J.R. Daum, K.S. Byrd, G.J. Gorbsky, Fine tuning the cell cycle: activation of the Cdk1 inhibitory phosphorylation pathway during mitotic exit, MolBiol Cell. 20 (2009) 1737-48.

13. R. Bose, N. Onishchenko, K. Edoff, A.M. Janson Lang, S. Ceccatelli, Inherited effects of low-dose exposure to methyl mercury in neural stem cells, Toxicol Sci. 130 (2012) 383-90.

14. L.H. Kerri, J. Damir, Cell Cycle, Neurological Disorders, and Reactive Gliosis, Springer. Book Part III (2006) 163-175.

15. I.D. Akinrinade, A.E. Memudu, O.M Ogundele, Fluoride and aluminium disturb neuronal morphology, transport functions, cholinesterase, lysosomal and cell cycle activities, Pathophysiology. 22 (2015) 105-15.

16. E. Taniai, A. Yafune, M. Nakajima, S.M. Hayashi, F. Nakane, M. Itahashi, M. Shibutani, Ochratoxin A induces karyomegaly and cell cycle aberrations in renal tubular cells without relation to induction of oxidative stress responses in rats, ToxicolLett. 224 (2014) 64-72.

17. J. Mizukami, G. Takaesu, H. Akatsuka, H. Sakurai, J. Ninomiya-Tsuji, K. Matsumoto, N. Sakurai, Receptor activator of NF-kappaB ligand (RANKL) activates TAK1 mitogen-

ACCEPTED MANUSCRIPT

activated protein kinase kinasekinase through a signaling complex containing RANK, TAB2, and TRAF6, Mol Cell Biol. 22 (2002) 992-1000.

18. I.I. Kruman, Why do neurons enter the cell cycle, Cell Cycle. 3 (2004), 769-73.
19. L.J. Martin, DNA damage and repair: relevance to mechanisms of neurodegeneration, J NeuropatholExp Neurol. 67 (2008) 377-87.
20. S. Fulda, A.M. Gorman, O. Hori, A. Samali, Cellular stress responses: cell survival and cell death, Int J Cell Biol. (2010) 214074.
21. Y. Miyata, Hsp90 inhibitor geldanamycin and its derivatives as novel cancer chemotherapeutic agents, Curr Pharm Des. 11 (2005) 1131-8.
22. B. Kwon, P. Kumar, H.K. Lee, L. Zeng, K. Walsh, Q. Fu, A. Barakat, H.W. Querfurth, Aberrant cell cycle re-entry in human and experimental inclusion body myositis and polymyositis, Hum Mol Genet. 23 (2014) 3681-94.
23. J.A. Diehl, W. Yang, R.A. Rimerman, H. Xiao, A. Emili, Hsc70 regulates accumulation of cyclin D1 and cyclin D1-dependent protein kinase, Mol Cell Biol. 23 (2003)1764-74.
24. L.A. van Leeuwen, J.J.M. Hoozemans, Physiological and pathophysiological functions of cell cycle proteins in post-mitotic neurons: implications for Alzheimer's disease, ActaNeuropathol. 129 (2015) 511-25.
25. P. Tokarz, K. Kaarniranta, J. Blasiak, Role of the Cell Cycle Re-Initiation in DNA Damage Response of Post-Mitotic Cells and Its Implication in the Pathogenesis of Neurodegenerative Diseases, Rejuvenation Res. 19 (2016) 131-9.
26. M. Huang, Z.H. Miao, H. Zhu, Y.J. Cai, W. Lu, J. Ding, Chk1 and Chk2 are differentially involved in homologous recombination repair and cell cycle arrest in response to DNA double-strand breaks induced by camptothecins, Mol Cancer Ther. 7 (2008) 1440-9.

ACCEPTED MANUSCRIPT

27. J. Chen, M.L. Cohen, A.J. Lerner, Y. Yang, K. Herrup, DNA damage and cell cycle events implicate cerebellar dentate nucleus neurons as targets of Alzheimer's disease, MolNeurodegener. 20 (2010) 5:60.

28. P. Katsel, W. Tan, P. Fam, D.P. Purohit, V. Haroutunian, Cell cycle checkpoint abnormalities during dementia: A plausible association with the loss of protection against oxidative stress in Alzheimer's disease corrected, PLoS One. 8 (2013) e68361.

29. D. Rossetto, A.W. Truman, S.J. Kron, J. Côté, Epigenetic modifications in double-strand break DNA damage signaling and repair, Clin Cancer Res. 16 (2010) 4543-52.

30. S. Absalon, D.M. Kochanek, V. Raghavan, A.M. Krichevsky, MiR-26b upregulated in Alzheimer's disease, activates cell cycle entry, tau-phosphorylation, and apoptosis in postmitotic neurons, J Neurosci. 33 (2013) 14645-59.

31. T. Kimura, K. Ishiguro, S. Hisanaga, Physiological and pathological phosphorylation of tau by Cdk5, Front MolNeurosci. 7 (2014) 65.

32. W.J. Lukiw, B. Surjyadipta, P. Dua, P.N. Alexandrov, Common micro RNAs (miRNAs) target complement factor H (CFH) regulation in Alzheimer's disease (AD) and in age-related macular degeneration (AMD), Int J BiochemMol Biol. 3 (2012) 105-16.

33. P.K. Modi, S Jaiswal, P. Sharma, Regulation of Neuronal Cell Cycle and Apoptosis by MicroRNA, Mol Cell Biol. 36 (2015) 84-94.

34. Y.B. Luo, F.L. Mastaglia, Dermatomyositis, polymyositis and immune-mediated necrotising myopathies, BiochimBiophysActa. 1852 (2015) 622-32.

35. N. Boutahar, E. Reynaud, F. Lassabliere, J. Borg, Brain-derived Neurotrophic factor inhibits cell cycle re-entry but not endoplasmic reticulum stress in cultured neurons following oxidative or excitotoxic stress, J Neurosci Res. 88 (2010) 2263-71.

ACCEPTED MANUSCRIPT

36. M.C. Ovejero-Benito, J.M. Frade, Brain-derived neurotrophic factor-dependent cdk1 inhibition prevents G2/M progression in differentiating tetraploid neurons, PLoS One. 8 (2013) e64890.

37. S.M. Morillo, E.P. Abanto, M.J. Román, J.M. Frade, Nerve growth factor-induced cell cycle re-entry in newborn neurons is triggered by p38MAPK-dependent E2F4 phosphorylation, Mol Cell Biol. 32 (2012) 2722-37.

38. E. Colombo, F. Bedogni, I. Lorenzetti, N. Landsberger, S.C. Previtali, C. Farina, Autocrine and immune cell-derived BDNF in human skeletal muscle: implications for myogenesis and tissue regeneration, J Pathol. 231 (2013) 190-8.

39. S. Marathe, S. Liu, E. Brai, M. Kaczarowski, L. Alberi, Notch signaling in response to excitotoxicity induces neurodegeneration via erroneous cell cycle re-entry, Cell Death Differ. 22 (2015) 1775-84.

40. A. Currais, T. Hortobágyi, S. Soriano, The neuronal cell cycle as a mechanism of pathogenesis in Alzheimer's disease, Aging (Albany NY). 1 (2009) 363-71.

41. J. Zhu, W. Li, Z. Mao, Cdk5: mediator of neuronal development, death and the response to DNA damage, Mech Ageing Dev. 132 (2011) 389-94.

42. M.R. Kelley, M.M. Georgiadis, M.L. Fishel, APE1/Ref-1 role in redox signaling: translational applications of targeting the redox function of the DNA repair/redox protein APE1/Ref-1, CurrMolPharmacol. 5 (2012) 36-53.

43. A. Mietelska-Porowska, U. Wasik, M. Goras, A. Filipek, G. Niewiadomska, Tau protein modifications and interactions: their role in function and dysfunction, Int J Mol Sci. 15 (2014) 4671-713.

ACCEPTED MANUSCRIPT

44. P. Paoletti, I. Vila, M. Rifé, J.M. Lizcano, J. Alberch, S. Ginés, Dopaminergic and glutamatergic signaling crosstalk in Huntington's disease neurodegeneration: the role of p25/cyclin-dependent kinase 5, J Neurosci. 28 (2008) 10090-101.

45. Q. Liu, F. Xie, A. Alvarado-Diaz, M.A. Smith, P.I. Moreira, X. Zhu, G. Perry, Neurofilamentopathy in neurodegenerative diseases, Open Neurol J. 5 (2011) 58-62.

46. D.J. Bonda, H.P. Lee, W. Kudo, X. Zhu, M.A. Smith, H.G. Lee, Pathological implications of cell cycle re-entry in Alzheimer disease, Expert Rev Mol Med. (2010) 12:e19.

47. T. Arendt, M. Holzer, U. Gärtner, Neuronal expression of cycline dependent kinase inhibitors of the INK4 family in Alzheimer's disease, J Neural Transm (Vienna). 105 (1998) 949-60.

48. X. Zhou, J. Jia, P53-mediated G(1)/S checkpoint dysfunction in lymphocytes from Alzheimer's disease patients, Neurosci Lett. 468 (2010) 320-5.

49. Z. Nagy, The dysregulation of the cell cycle and the diagnosis of Alzheimer's disease, BiochimBiophysActa. 1772 (2007) 402-8.

50. X. Zhu, A. McShea, P.L. Harris, A.K. Raina, R.J. Castellani, J.O. Funk, S. Shah, C. Bowen, R. Atwood, R. Bowser, L. Morelli, G. Perry, M.A. Smith, Elevated expression of a regulator of the G2/M phase of the cell cycle, neuronal CIP-1-associated regulator of cyclin B, in Alzheimer's disease, J Neurosci Res. 75 (2004) 698-703.

51. K.L. Jordan-Sciutto, L.M. Malaiyandi, R. Bowser, Altered distribution of cell cycle transcriptional regulators during Alzheimer disease, J NeuropatholExp Neurol. 61 (2002) 358-67.

ACCEPTED MANUSCRIPT

ACCEPTED MANUSCRIPT

52. X. Zhu, C.A. Rottkamp, A.K. Raina, G.J. Brewer, H.A. Ghanbari, H. Boux, M.A. Smith, Neuronal CDK7 in hippocampus is related to aging and Alzheimer disease, Neurobiol Aging. 21 (2000) 807-13.

53. K.L. Jordan-Sciutto, R. Dorsey, E.M. Chalovich, R.R. Hammond, C.L. Achim, Expression patterns of retinoblastoma protein in Parkinson disease, J NeuropatholExp Neurol. 62 (2003) 68-74.

54. K. Venderova, D.S. Park, Programmed cell death in Parkinson's disease, Cold Spring HarbPerspect, Med. 2 (2012) a009365.

55. O.A. Levy, C. Malagelada, L.A. Greene, Cell death pathways in Parkinson's disease: proximal triggers, distal effectors, and final steps, Apoptosis. 14 (2009) 478-500.

56. C. Alquézar, E. Barrio, N. Esteras, A. de la Encarnación, F. Bartolomé, J.A Molina, Á. Martín-Requero, Targeting cyclin D3/CDK6 activity for treatment of Parkinson's disease, J Neurochem. 133 (2015) 886-97.

57. A. Futatsugi, E. Utreras, P. Rudrabhatla, H. Jaffe, H.C. Pant, A.B. Kulkarni, Cyclin-dependent kinase 5 regulates E2F transcription factor through phosphorylation of Rb protein in neurons, Cell Cycle. 11 (2012) 1603-10.

58. C. Pelegrí, J. Duran-Vilaregut, J. del Valle, N. Crespo-Biel, I. Ferrer, M. Pallàs, A. Camins, J. Vilaplana, Cell cycle activation in striatal neurons from Huntington's disease patients and rats treated with 3-nitropropionic acid, Int J DevNeurosci. 26 (2008) 665-71.

59. M. Cherubini, M. Puigdellívol, J. Alberch, S Ginés, Cdk5-mediated mitochondrial fission: A key player in dopaminergic toxicity in Huntington's disease, BiochimBiophysActa. 1852 (2015) 2145-60.

ACCEPTED MANUSCRIPT

60. J. Chen, Z.F. Wang, Roles of cyclin-dependent kinase 5 in central nervous system development and neurodegenerative diseases, Sheng Li XueBao. 62 (2010) 295-308.

61. E. Das, N.R. Jana, N.P. Bhattacharyya, MicroRNA-124 targets CCNA2 and regulates cell cycle in STHdh (Q111)/Hdh (Q111) cells, BiochemBiophys Res Commun. 437 (2013) 217-24.

62. S. Ranganathan, R. Bowser, Alterations in G (1) to S phase cell-cycle regulators during amyotrophic lateral sclerosis, Am J Pathol. 162 (2003) 823-35.

63. S. Majd, A. Zarifkar, K. Rastegar, M.A. Takhshid, Different fibrillar Abeta 1-42 concentrations induce adult hippocampal neurons to reenter various phases of the cell cycle, Brain Res. 1218 (2008) 224-9.

64. D.J. Bonda, T.A. Evans, C. Santocanale, J.C. Llosá, J. Viña, V. Bajic, R.J. Castellani, S.L. Siedlak, G. Perry, M.A. Smith, H.G. Lee, Evidence for the progression through S-phase in the ectopic cell cycle re-entry of neurons in Alzheimer disease, Aging (Albany NY). 1 (2009) 382-8.

65. J. Mendoza, M. Sekiya, T. Taniguchi, K.M. Iijima, R. Wang, K. Ando, Global analysis of phosphorylation of tau by the checkpoint kinases Chk1 and Chk2 in vitro, J Proteome Res. 12 (2013) 2654-65.

66. Z. Liu, T. Li, P. Li, N. Wei, Z. Zhao, H. Liang, X. Ji, W. Chen, M. Xue, J. Wei, The Ambiguous Relationship of Oxidative Stress, Tau Hyperphosphorylation, and Autophagy Dysfunction in Alzheimer's Disease, Oxid Med Cell Longev. 2015 (2015) 352723.

67. Z. Liu, Y. Chen, R. Neve, H. Zheng, W. Griffin, S. Barger, R. Mrak, Cycle on Wheels: Is APP Key to the AppBp1 Pathway, Austin AlzheimersParkinsons Dis. 1 (2014) pii: id1008.

ACCEPTED MANUSCRIPT

68. W. Ouyang, Q. Ma, J. Li, D. Zhang, Z.G. Liu, A.K. Rustgi, C. Huang, Cyclin D1 induction through IkappaB kinase beta/nuclear factor-kappaB pathway is responsible for arsenite-induced increased cell cycle G1-S phase transition in human keratinocytes, Cancer Res. 65 (2005) 9287-93.

69. K. Bhaskar, N. Maphis, G. Xu, N.H. Varvel, O.N. Kokiko-Cochran, J.P. Weick, S.M. Staugaitis, A. Cardona, R.M. Ransohoff, K. Herrup, B.T. Lamb, Microglial derived tumor necrosis factor-α drives Alzheimer's disease-related neuronal cell cycle events, Neurobiol Dis. 62 (2014) 273-85.

70. M.E. Seward, E. Swanson, A. Norambuena, A. Reimann, J.N. Cochran, R. Li, E.D. Roberson, G.S. Bloom, Amyloid-β signals through tau to drive ectopic neuronal cell cycle re-entry in Alzheimer's disease, J Cell Sci. 126 (2013) 1278-86.

71. J. Zhang, S.A. Cicero, L. Wang, R.R. Romito-Digiacomo, Y. Yang, K. Herrup, Nuclear localization of Cdk5 is a key determinant in the postmitotic state of neurons, ProcNatlAcadSci U S A. 105 (2008) 8772-7.

72. S. Krantic, N. Mechawar, S. Reix, R. Quirion, Molecular basis of programmed cell death involved in neurodegeneration, Trends Neurosci. 28 (2005) 670-6.

73. H. Wang, Y. Chen, J. Chen, Z. Zhang, W. Lao, X. Li, J. Huang, T. Wang, Cell cycle regulation of DNA polymerase beta in rotenone-based Parkinson's disease models, PLoS One. 9 (2014) e109697.

74. A. Dumitriu, C.D. Pacheco, J.B. Wilk, K.E. Strathearn, J.C. Latourelle, S. Goldwurm, G. Pezzoli, J.C. Rochet, S. Lindquist, R.H. Myers, Cyclin-G-associated kinase modifies α-synuclein expression levels and toxicity in Parkinson's disease: results from the Gene PD Study, Hum Mol Genet. 20 (2011) 1478-87.

ACCEPTED MANUSCRIPT

75. A. Camins, J.G. Pizarro, D. Alvira, J. Gutierrez-Cuesta, A.V. de la Torre, J. Folch, F.X. Sureda, E. Verdaguer, F. Junyent, J. Jorda´n, I. Ferrer, M. Palla`s, Activation of ataxia telangiectasia muted under experimental models and human Parkinson's disease, Cell Mol Life Sci. 67 (2010) 3865–3882.

76. V. Askanas, W.K. Engel, A. Nogalska, Inclusion body myositis: a degenerative muscle disease associated with intra-muscle fiber multi-protein aggregates, proteasome inhibition, endoplasmic reticulum stress and decreased lysosomal degradation, Brain Pathol. 19 (2009) 493-506.

77. V. Askanas, W.K. Engel, Does overexpression of beta APP in aging muscle have a pathogenic role and a relevance to Alzheimer's disease? Clues from inclusion body myositis, cultured human muscle, and transgenic mice, Am J Pathol. 153 (1998) 1673-7.

78. V. Askanas, W.K. Engel, A. Nogalska, Sporadic inclusion-body myositis: A degenerative muscle disease associated with aging, impaired muscle protein homeostasis and abnormal mitophagy, BiochimBiophysActa. 1852 (2015) 633-43.

79. S. Pedrini, T.L. Carter, G. Prendergast, S. Petanceska, M.E. Ehrlich, S. Gandy, Modulation of statin-activated shedding of Alzheimer APP ectodomain by ROCK, PLoS Med. 2 (2005) e18.

80. C.R. Rathbone, F W. Booth, S.J. Lees, Sirt1 increases skeletal muscle precursor cell proliferation, Eur J Cell Biol. 88 (2009) 35-44.

81. A.Z. Herskovits, L. Guarente, SIRT1 in neurodevelopment and brain senescence, Neuron. 81 (2014) 471-83.

ACCEPTED MANUSCRIPT

82. A. Nogalska, C. D'Agostino, W.K. Engel, K.J. Davies, V. Askanas, Decreased SIRT1 deacetylase activity in sporadic inclusion-body myositis muscle fibers, Neurobiol, Aging. 31 (2010) 1637-48.

83. K.Y. Liu, Y.C. Shyu, B.A. Barbaro, Y.T. Lin, Y. Chern, L.M. Thompson, C.K. James Shen, J. L. Marsh, Disruption of the nuclear membrane by perinuclear inclusions of mutant huntingtin causes cell-cycle re-entry and striatal cell death in mouse and cell models of Huntington's disease, Hum Mol Genet. 24 (2015) 1602-16.

84. M.R. Fernandez-Fernandez, I. Ferrer, J.J. Lucas, Impaired ATF6α processing, decreased Rheb and neuronal cell cycle re-entry in Huntington's disease, Neurobiol Dis. 41 (2011) 23-32.

85. K.L. Williams, S. Topp, S. Yang, B. Smith, J.A. Fifita, S.T. Warraich, K.Y. Zhang, N. Farrawell, C. Vance, X. Hu, A. Chesi, C.S. Leblond, A. Lee, S.L. Rayner, V. Sundaramoorthy, C. Dobson-Stone, M.P. Molloy, M. van Blitterswijk, D.W. Dickson, R.C. Petersen, N.R. Graff-Radford, B.F. Boeve, M.E. Murray, C. Pottier, E. Don, C. Winnick, E.P. McCann, A. Hogan, H. Daoud, A. Levert, P.A. Dion, J. Mitsui, H. Ishiura, Y. Takahashi, J. Goto, J. Kost, C. Gellera, A.S. Gkazi, J. Miller, J. Stockton, W.S. Brooks, K. Boundy, M. Polak, J.L. Muñoz-Blanco, J. Esteban-Pérez, A. Rábano, O. Hardiman, K.E. Morrison, N. Ticozzi, V. Silani, J. de Belleroche, J.D. Glass, J.B. Kwok, G.J. Guillemin, R.S. Chung, S. Tsuji, R.H.Jr. Brown, A. García-Redondo, R. Rademakers, J.E. Landers, A.D. Gitler, G.A. Rouleau, N.J. Cole, J.J. Yerbury, J.D. Atkin, C.E. Shaw, G.A. Nicholson, I.P. Blair, CCNF mutations in amyotrophic lateral sclerosis and frontotemporal dementia, Nat Commun. 7 (2016) 11253.

ACCEPTED MANUSCRIPT

ACCEPTED MANUSCRIPT

86. M.D. Nguyen, M. Boudreau, J. Kriz, S. Couillard-Després, D.R. Kaplan, J.P. Julien, Cell cycle regulators in the neuronal death pathway of amyotrophic lateral sclerosis caused by mutant superoxide dismutase 1, J Neurosci. 23 (2003) 2131-40.

87. K. Herrup, Y. Yang, Cell cycle regulation in the post mitotic neuron: oxymoron or new biology, Nat Rev Neurosci. 8 (2007) 368-78.

88. W.C. Chou, L.Y. Hu, C.N. Hsiung, C.Y. Shen, Initiation of the ATM-Chk2 DNA damage response through the base excision repair pathway, Carcinogenesis. 36 (2015) 832-40.

89. J. Li, Y.R. Han, M.R. Plummer, K. Herrup, Cytoplasmic ATM in neurons modulates synaptic function, Curr Biol. 19 (2009) 2091-6.

90. M.G. Andrusiak, K.A. McClellan, D. Dugal-Tessier, L.M. Julian, S.P. Rodrigues, D.S. Park, T.E. Kennedy, R.S. Slack, Rb/E2F regulates expression of neogenin during neuronal migration, Mol Cell Biol. 31 (2011) 238-47.

91. T. Kawauchi, K. Chihama, Y. Nabeshima, M. Hoshino, Cdk5 phosphorylates and stabilizes p27kip1 contributing to actin organization and cortical neuronal migration, Nat Cell Biol. 8 (2006) 17-26.

92. B. Mosch, M. Morawski, A. Mittag, D. Lenz, A. Tarnok, T. Arendt, Aneuploidy and DNA replication in the normal human brain and Alzheimer's disease, J Neurosci. 27 (2007) 6859-67.

93. T. Arendt, M. K. Brückner, A. Lösch, Regional mosaic genomic heterogeneity in the elderly and in Alzheimer's disease as a correlate of neuronal vulnerability. Acta Neuropathol. 130 (2015) 501-10.

94. T. Arendt, M. K. Brückner, B. Mosch, A. Lösche, Selective cell death of hyperploids neurons in Alzheimer's disease. Am J Pathol. 177 (2010) 15-20.

ACCEPTED MANUSCRIPT

95. T. Arendt, Cell cycle activation and aneuploid neurons in Alzheimer's disease. Mol Neurobiol. 46 (2012) 125-35.

96. J.M. Frade, M.C. Ovejero-Benito, Neuronal cell cycle: the neuron itself and its circumstances, Cell Cycle. 14 (2015) 712-20.

97. U. Ueberham, A. Hessel, T. Arendt, Cyclin C expression is involved in the pathogenesis of Alzheimer's disease. Neurobiol Aging. 24 (2003) 427-35.

98. S. B. Wharton, G. H. Williams, K. Stoeber, C. H. Gelsthorpe, L. Baxter, A. L. Johnson, P. G. Ince, MRC-CFAS. Expression of Ki67, PCNA and the chromosome replication licensing protein Mcm2 in glial cells of the ageing human hippocampus increases with the burden of Alzheimer-type pathology. Neurosci Lett. 383 (2005) 33-8.

99. L. C. Chuang, L. K. Teixeira, J. A. Wohlschlegel, M. Henze, J. R. Yates, J. Méndez, S. I. Reed, Phosphorylation of Mcm2 by Cdc7 promotes pre-replication complex assembly during cell-cycle re-entry. Mol Cell. 35 (2009) 206-16.

100. H. G. Lee, G. Casadesus, X. Zhu, R. J. Castellani, A. McShea, G. Perry, R. B. Petersen, V. Bajic, M. A. Smith, Cell cycle re-entry mediated neurodegeneration and its treatment role in the pathogenesis of Alzheimer's disease. Neurochem Int. 54 (2009) 84-8.

101. J. G. Pizarro, F. Junyent, E. Verdaguer, J, Jordan, C. Beas-Zarate, M. Pallàs, A. Camins, J, Folch, Effects of MPP+ on the molecular pathways involved in cell cycle control in B65 neuroblastoma cells. Pharmacol Res. 61 (2010) 391-9.

102. X. F. Fei, Z. H. Qin, B. Xiang, L. Y. Li, F. Han, K. Fukunaga, Z. Q. Liang. Olomoucine inhibits cathepsin L nuclear translocation, activates autophagy and attenuates toxicity of 6-hydroxydopamine. Brain Res. 1264 (2009) 85-97.

ACCEPTED MANUSCRIPT

103. S. S. Lee, Y. M. Kim, E. Junn, G. Lee, K. H. Park, M. Tanaka, R. D. Ronchetti, M. M. Quezado, M. M. Mouradian, Cell cycle aberrations by alpha-synuclein over-expression and cyclin B immunoreactivity in Lewy bodies. Neurobiol Aging. 24 (2003) 687-96.

104. A. Appert-Collin, B. Hugel, R. Levy, N. Niederhoffer, G. Coupin, Y. Lombard, P. André, P. Poindron, J. P. Gies, Cyclin dependent kinase inhibitors prevent apoptosis of postmitotic mouse motoneurons. Life Sci. 79 (2006) 484-90.

105. Y. M. Jiang, M. Yamamoto, Y. Kobayashi, T. Yoshihara, Y. Liang, S. Terao, H. Takeuchi, S. Ishigaki, M. Katsuno, H. Adachi, J. Niwa, F. Tanaka, M. Doyu, M. Yoshida, Y. Hashizume, G. Sobue, Gene expression profile of spinal motor neurons in sporadic amyotrophic lateral sclerosis. Ann Neurol. 57 (2005) 236-51.

106. J. Wu, B.A. Stoica, A.I. Faden, Cell cycle activation and spinal cord injury, Neurotherapeutics. 8 (2011) 221-8.

107. S.G. Sala, U. Muñoz, F. Bartolomé, F. Bermejo, A. Martín-Requero, HMG-CoA reductase inhibitor simvastatin inhibits cell cycle progression at the G1/S checkpoint in immortalized lymphocytes from Alzheimer's disease patients independently of cholesterol-lowering effects, J PharmacolExpTher. 324 (2008) 352-9.

108. J. Guadagno, P. Swan, R. Shaikh, S.P. Cregan, Microglia-derived IL-1β triggers p53-mediated cell cycle arrest and apoptosis in neural precursor cells, Cell Death Dis. 6 (2015) e1779.

109. E. Tellone, A. Galtieri, A. Russo, B. Giardina, S. Ficarra, Resveratrol: A Focus on Several Neurodegenerative Diseases, Oxid Med Cell Longev. 2015 (2015) 392169.

ACCEPTED MANUSCRIPT

110. N.H. Varvel, K. Bhaskar, M.Z. Kounnas, S.L. Wagner, Y. Yang, B.T. Lamb, K. Herrup, NSAIDs prevent, but do not reverse, neuronal cell cycle re-entry in a mouse model of Alzheimer disease, J Clin Invest. 119 (2009) 3692-702.

111. N.S. Elsisi, S. Darling-Reed, E.Y. Lee, E.T. Oriaku, K.F. Soliman, Ibuprofen and apigenin induce apoptosis and cell cycle arrest in activated microglia, Neurosci Lett. 375 (2005) 91-6.

112. T. Liu, G. Perry, H.W. Chan, G. Verdile, R.N. Martins, M.A. Smith, C.S. Atwood, Amyloid-beta-induced toxicity of primary neurons is dependent upon differentiation-associated increases in tau and cyclin-dependent kinase 5 expression, J Neurochem. 88 (2004) 554-63.

113. M. Ahmed, P.M. Machado, A. Miller, C. Spicer, L. Herbelin, J. He, J. Noel, Y. Wang, A.L. McVey, M. Pasnoor, P. Gallagher, J. Statland, C.H. Lu, B. Kalmar, S. Brady, H. Sethi, G. Samandouras, M. Parton, J.L. Holton, A. Weston, L. Collinson, J.P. Taylor, G. Schiavo, M.G. Hanna, R.J. Barohn, M.M. Dimachkie, L. Greensmith, Targeting protein homeostasis in sporadic inclusion body myositis, SciTransl Med. 8 (2016) 331ra41.

114. M. Veas-Pérez de Tudela, C. Maestre, M. Delgado-Esteban, J.P. Bolaños, A. Almeida, Cdk5-mediated inhibition of APC/C-Cdh1 switches on the cyclin D1-Cdk4-pRb pathway causing aberrant S-phase entry of postmitotic neurons, Sci Rep. 5 (2015) 18180.

115. L. Zhang, W. Liu, K.K. Szumlinski, J. Lew, p10 the N-terminal domain of p35, protects against CDK5/p25-induced neurotoxicity, ProcNatlAcadSci U S A. 109 (2012) 20041-6.

116. T. Fishman-Jacob, L. Reznichenko, M.B. Youdim, S.A. Mandel, A sporadic Parkinson disease model via silencing of the ubiquitin-proteasome/E3 ligase component SKP1A, J Biol Chem. 284 (2009) 32835-45.

ACCEPTED MANUSCRIPT

117. R.J. Duronio, Y. Xiong, Signaling pathways that control cell proliferation, Cold Spring HarbPerspect Biol. 5 (2013) a008904.

118. H.V. Rao, L. Thirumangalakudi, P. Desmond, P. Grammas, Cyclin D1, cdk4, and Bim are involved in thrombin-induced apoptosis in cultured cortical neurons, J Neurochem. 101 (2007) 498-505.

119. T. Boutros, E. Chevet, P. Metrakos, Mitogen-activated protein (MAP) kinase/MAP kinase phosphatase regulation: roles in cell growth, death, and cancer, Pharmacol Rev. 60 (2008) 261-310.

120. K. Shah, D.K. Lahiri, Cdk5 activity in the brain - multiple paths of regulation, J Cell Sci. 127 (2014) 2391-400

121. B.B. McConnell, F.J. Gregory, F.J. Stott, E. Hara, G. Peters, Induced expression of p16(INK4a) inhibits both CDK4- and CDK2-associated kinase activity by reassortment of cyclin-CDK-inhibitor complexes, Mol Cell Biol. 19 (1999) 1981-9.

122. R. Von Bernhardi, F. Cornejo, G.E. Parada, J. Eugenín, Role of TGFβ signaling in the pathogenesis of Alzheimer's disease, Front Cell Neurosci. 9 (2015) 426.

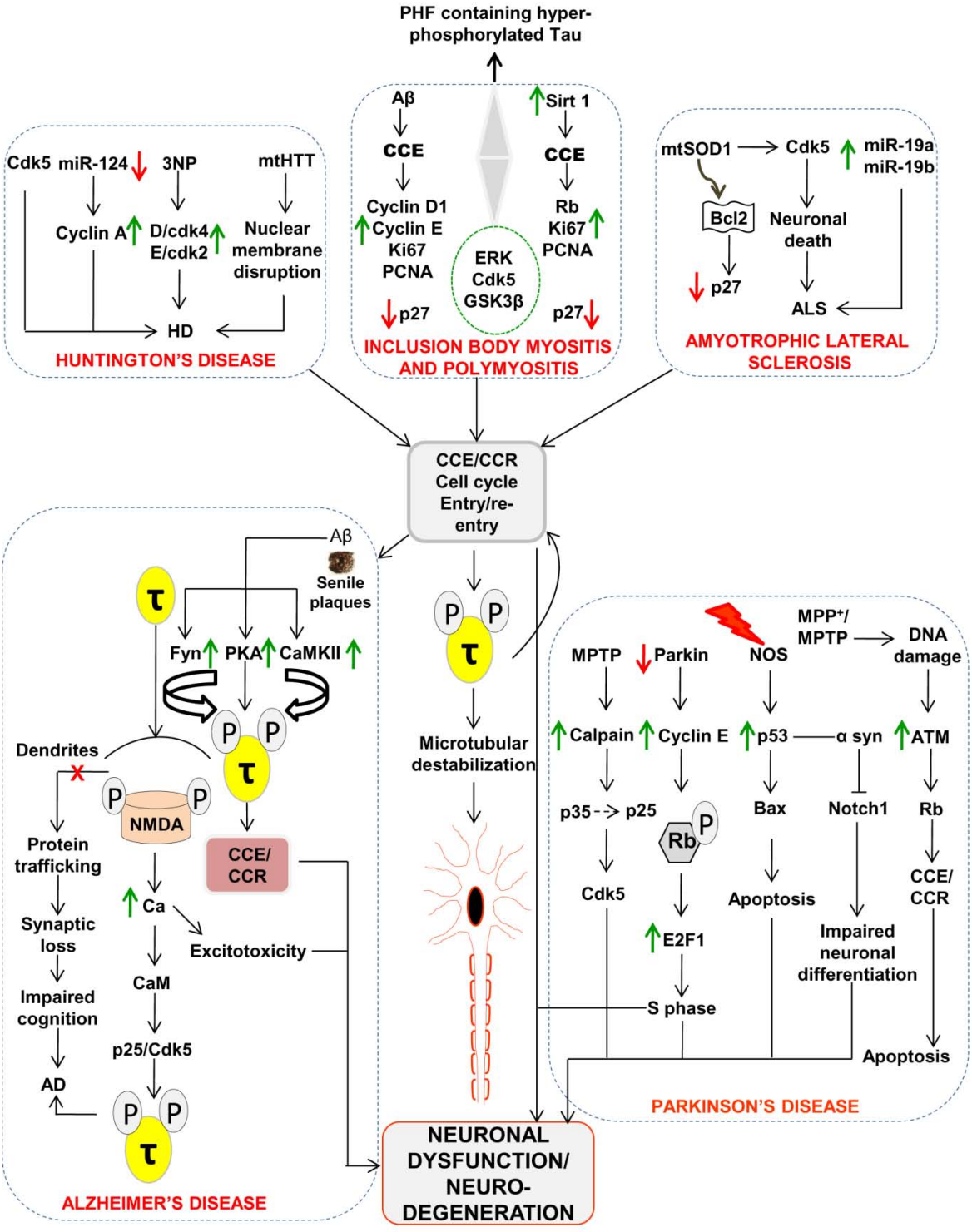
ACCEPTED MANUSCRIPT

ACCEPTED MANUSCRIPT

Invited review for BBA-Molecular Basis of Diseases

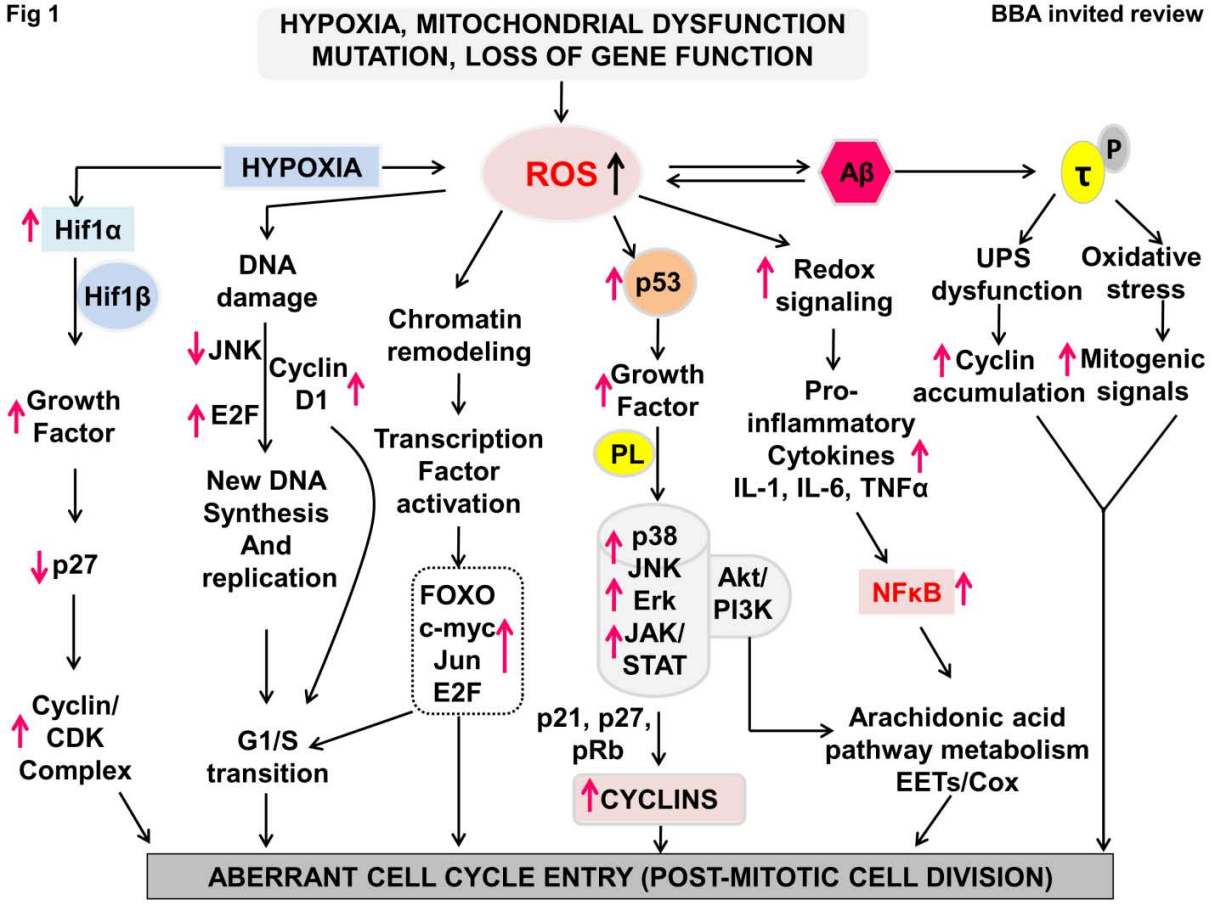
Sharma et al

Graphical Abstract



ACCEPTED MANUSCRIPT

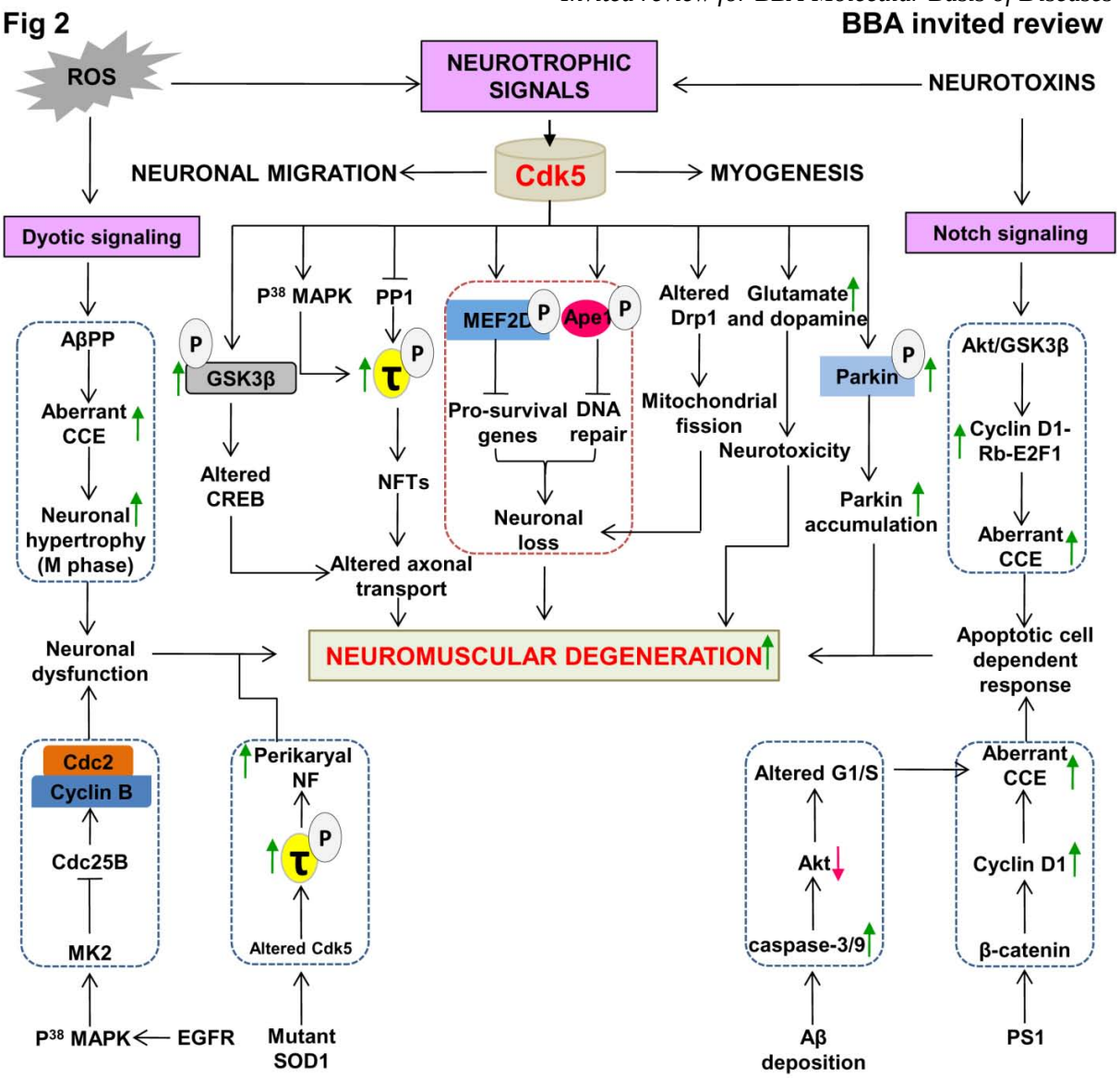
Fig 1



ACCE

ACCEPTED MANUSCRIPT

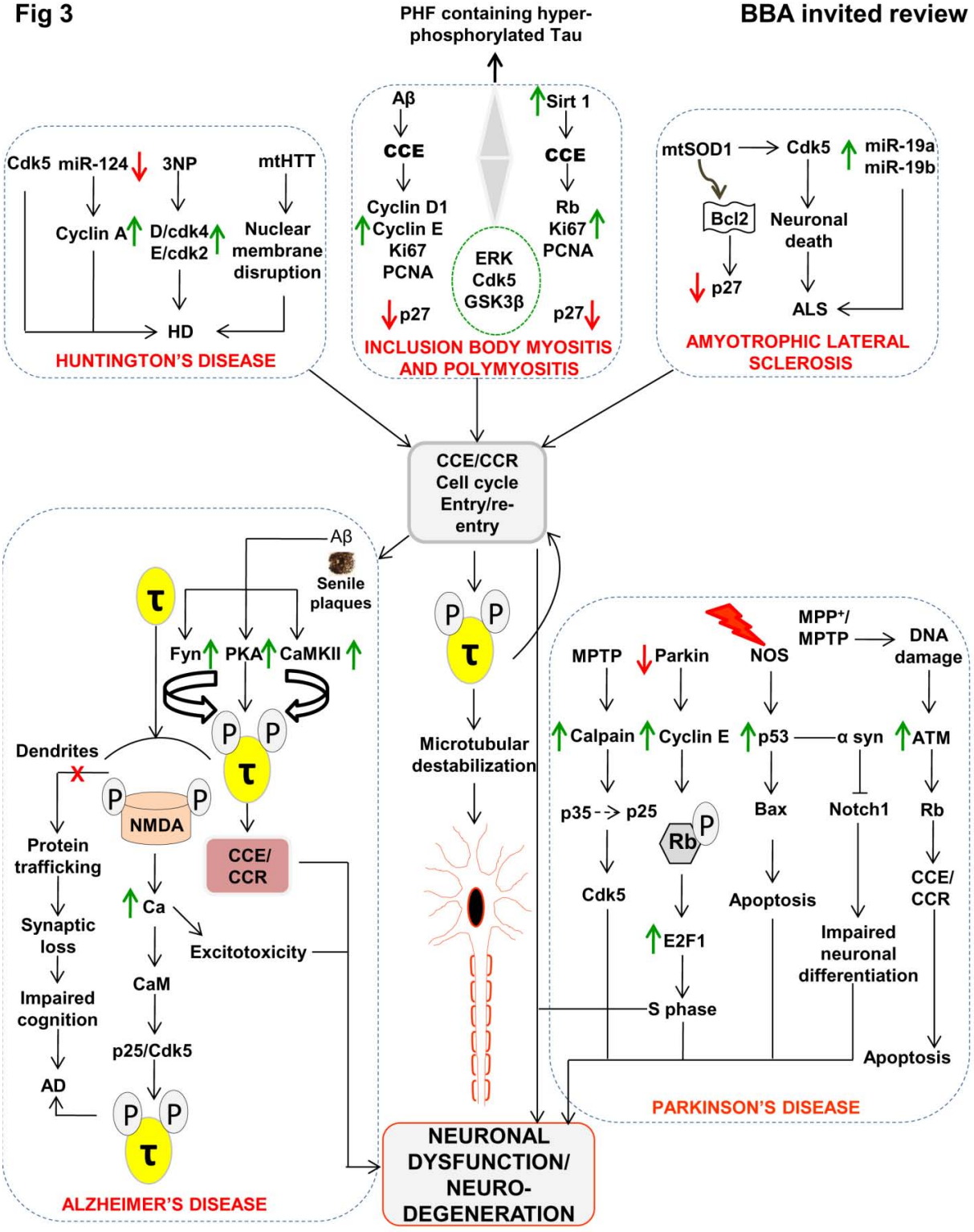
Fig 2



ACCEPTED MANUSCRIPT

Fig 3

BBA invited review



ACCEPTED MANUSCRIPT

Invited review for BBA-Molecular Basis of Diseases

TABLE 1: CONSEQUENCES OF ALTERED CELL SIGNALING IN THE POST MITOTIC CELL DIVISION

PRINCIPLE PHENOTYPE	SIGNALING CASCADES	CHECK POINTS	CYCLINS EXPRESSION	CDK/CDC/CDKI/TFS INVOLVED	REFERENCES
AD	MEK-ERK MAP pathway/p38 MAPK	G0 to G1 and G1/S phase	Cyclin D1 and Cyclin E1	Cdk4 and Ki67 (MKI67)	[46]
	Notch signaling and Akt/GSK3β pathway	G0 to G1 and G1/S phase	CyclinD1	Cdk4/Cdk6 and Rb-E2F1	[39]
	β-catenin/TCF transcription complex (Wnt signaling)	G1/S phase	Cyclin D1	Cdk4/Cdk6 and Rb-E2F1	[40]
	Not defined	G1/S transition and G2/M phase	Cyclin B, Cyclin C, cyclin D1 and Cyclin E	Cdk1, Cdk2, Cdk4/Cdk6, Cdk5, Cdk7, Cdk11, p15, p16, p18, p19, p21, p27, pRb/p107, Ki67, mpm-2, E2F-1, PCNA, MORF4-related transcription factor and p53	[47-52]
PD	Not defined	G1 to S phase	Cyclin D and Cyclin E	Cdk2, Cdk4, Rb-E2F1	[53]
	MEK-ERK MAP pathway/p38 MAPK	G0/G1 phase	Cyclin D3	Cdk5, Cdk6/pRb, p21, p25 and p35/p39, Prosurvival transcription factor MEF2D, E2F-1 and p53	[54-57]
HD	Not defined	G0/G1 phase and G1/S phase	Cyclin A2, Cyclin D1 and Cyclin E	Cdk2, Cdk4, Cdk5 and p25, E2F-1	[58-61]
ALS	Apoptotic signaling	G1 to S phase	Cyclin D1 and Cyclin F	Cdk4, Cdk5, Cdk6, p25, p35/p39 and pRb/p107, E2F-1	[62]
IBM/PM	Apoptotic signaling and Akt signaling	G1/S phase	Cyclins E and Cyclin D1	Cdk2, Cdk4, Cdk6, Ki-67, PCNA and p21	[22]

ACCEPTED MANUSCRIPT

ACCEPTED MANUSCRIPT

Invited review for BBA-Molecular Basis of Diseases

TABLE 2: A CONSOLIDATED LIST OF VARIOUS CELL CYCLE MARKERS THAT ACTIVELY PARTICIPATE IN POST MITOTIC NEURONS AND RELATED DISORDERS AS LISTED (SHADED IN GREY); (–) INDICATES NO REPORTED ACTION OF THAT PARTICULAR CELL CYCLE MARKERS

Cell cycle markers	AD	PD	HD	ALS	IBM/PM
Ki67		-	-	-	
BrdU		-	-		
PCNA			-	-	
Mcm2		-	-	-	-
Cyclin A	-				
Cyclin B	-		-	-	-
Cyclin C		-	-		-
Cyclin D					
Cyclin E					
Cyclin G	-		-		-
Cyclin F	-	-	-		-
References	[22,97-100]	[56,73,74,98,101-103]	[58-61]	[85,104,105]	[22]

AD- Alzheimer's disease; PD- Parkinson's disease; HD- Huntington's disease; ALS- Amyotrophic lateral sclerosis; IBM-inclusion body myositis; PM- Polymyositis.

ACCEPTED MANUSCRIPT

ACCEPTED MANUSCRIPT

Invited review for BBA-Molecular Basis of Diseases

TABLE 3: DIFFERENT DRUGS AND BIOMOLECULES TO ATTENUATE THE CELL CYCLE PROGRESSION

S.NO.	COMPOUNDS	INVOLVED CHECK POINTS	INVOLVED MECHANISMS	DISEASES	REFERENCES
1	Roscovitine	G1 and G2/M phases of cell cycle	Well-known purine analogue, responsible for suppressing the activation of both Cdk2 and Cdk5. Further, it also inhibits the activity of ERK1 and ERK2 signaling cascade at its higher concentration	AD, PD and ALS	[106]
2	Olomoucine	G1 and G2/M phases of cell cycle	Well-known purine analogue which modulates the activity of Cdk2 and Cdk5 by competitively binding the ATP-binding site. Moreover, neuronal cell death induced by p27 reduction is also inhibited by olomoucine administration	AD, PD and ALS	[106]
3	Resveratrol (RSV)	G_0/G_1 phase of cell cycle	It potentiates SIRT1 activity and induces an indirect inhibition of p53 that further inhibit the GSK3β and p53 interaction. Since, GSK3β overactivity leads to increased levels of plaques and tangles and p53 activity induces tau phosphorylation. Further, RSV also protects neuronal cells by toxic effects of mHtt, potentiating SIRT1 activity and inducing an indirect inhibition of p53	AD and HD	[109]
4	Ibuprofen	S phase of cell cycle	Non-steroidal anti-inflammatory drug Ibuprofen has been shown to abrogate the cell cycle arrest at S phase	AD and PD	[110,111]
5	Naproxen	G0/G1 phase of cell cycle	It blocks alterations in brain microglia as well as neuronal cell cycle events (CCEs) in the absence of detectable alterations in AβPP processing and Aβ metabolism	AD	[110]
6	Apigenin	G2/M phase of cell cycle	It induces cell cycle arrest preferentially in the G2/M phase	AD and PD	[111]
7	Epigallocatechin-gallate (EGCG)	G0-G1 phase of cell cycle	It is a natural product that has been shown to abrogate the cell cycle at the G0 to G1 phase in various tissues and is known as a cell cycle inhibitor	AD	[46]
8	Tamoxifen	G0-G1 phase of cell cycle	It is a well-tolerated anti-proliferative cancer drug that has been reported to abrogate the cell cycle progression from G0 to G1 in various tissues	AD	[46]
9	Butyrolactone I	G1-S phase of cell cycle	A Cdk5 inhibitor, provides protection against Aβ toxicity in SEK1-AL-expressing cells, advocating that Cdk5 and JNK activation independently contributed to this toxicity	AD	[112]
10	Arimoclomol	Not defined	It upregulates the HSP70 expression therefore it might be used as a potential molecule to treat IBM. Since, the interaction between HSP70 and cyclins E/D1 has crucial importance during cell cycle progression in the inflammatory myopathies, probably controlling cyclin maturation or degradation	IBM	[113]

ACCEPTED MANUSCRIPT

Invited review for BBA-Molecular Basis of Diseases

HIGHLIGHTS

Cyclin/CDKs mediated cell cycle homeostasis and re-expression of cyclins in response to stress.

Potential triggering factors that force mature neuron and muscles to re-enter into cell division post mitotically

Altered signal transduction cascade, which causes disruption in cell cycle homeostasis.

Postmitotic cell division in the progression of AD, PD, HD, ALS and IBM diseases.

Therapeutic strategies using cell cycle inhibitors, chaperones, UbE3 ligase for the reversal of aberrant cell cycle entry.

ACCEPTED MANUSCRIPT

Physics Letters A ••• (••••) •••–•••

Contents lists available at ScienceDirect

Physics Letters A

www.elsevier.com/locate/pla

Signature of triply excited Li-like V states in ion–solid collisions

Gaurav Sharma [a], K. Haris [b], G. Singh [a], B. Kumar [c], S. Karmakar [d], N.K. Puri [a], Adya P. Mishra [e], Pravin Kumar [f], T. Nandi [f]

[a] Delhi Technological University, DTU, Delhi 110042, India
[b] Dept. of Physics, Aligarh Muslim University, Aligarh 2022002, India
[c] Jai Prakash Vishsvidyalaya, Chapra, Bihar 841301, India
[d] Lalbaba College, 117 G.T. Road, Belur Math, Howrah 711202, India
[e] Atomic and Molecular Physics Division, Bhabha Atomic Research Centre, Trombay, Mumbai 400 085, India
[f] Inter University Accelerator Centre, IUAC, New Delhi 110067, India

ARTICLE INFO

Article history:
Received 31 May 2016
Received in revised form 12 August 2016
Accepted 13 August 2016
Available online xxxx
Communicated by V.A. Markel

Keywords:
Beam-foil interaction
Triply excited states
Autoionizing Rydberg states
Double autoionization

ABSTRACT

The transitions originating from triply excited, doubly autoionizing states of Li-like V formed in beam foil experiments detected within a set of blended spectroscopic profiles have been assigned tentatively by the Hartree–Fock calculations including relativistic corrections and multi-configuration interactions as perturbations. The x-ray decay channels from the triply excited states such as $3p^3\ ^4S$, $2p^2np\ ^4S$ ($n \sim 12$) through radiative transitions to the ground state via two or more steps have been observed.

© 2016 Elsevier B.V. All rights reserved.

UNCORRECTED PROOF

1. Introduction

The simplest four-body Coulomb interactions are studied by the atomic Li and Li-like ions. These systems exhibit distinct electron–electron correlation effects when all three electrons are excited forming the triply-excited states. These states mostly lie above the second ionization limit, and decay normally via autoionization. Sometimes the triply excited states is formed with such total spin, parity and angular momentum that it cannot find any suitable lower states to autoionize and thus the states remain metastable against autoionization. Thus, even though the $2p^3\ ^4S^\circ$ state lies above the second ionization limit, the dominant decay is the radiative dipole allowed transition to the $1s2p^2\ ^4P$ state in Li-like ions [1]. Nevertheless, the other states of $2p^3$ such as $2p^3\ ^2D^\circ$, $^2P^\circ$ are autoionization allowed; and besides the single autoionization, the double autoionization becomes possible. Consequently, a double autoionizing level can decay either by one-step double autoionization or two-step sequential single-autoionization. Recently, both types of autoionization processes have been observed experimentally in Li atom [2,3]. The one-step double autoionization channel is usually much slower compared to two-step sequential single-autoionization and thereby it is rare. Whatsoever, the theoretical study of triply excited, and the double autoionizing states is challenging as the absolute ionization strengths are difficult to predict [4].

Various techniques such as the beam–foil spectroscopy [5–10], the electron and the photon impact [1,11,12] and the theoretical investigations [13–15] are available to study the above mentioned exotic atomic systems for the understanding of the triply excited systems. The impact of highly charged ions which can lead to a different excitation mechanism in this exotic systems is not studied in great detail [1,16–18]. The interactions between the highly charged ions and the solid surfaces [18,19] yields to the hollow states like the triply excited states in Li-like ions. Sometimes this interaction allow one of the excited electron in the triply excited states lie in the high orbit and they can be named as the triply excited Rydberg states or the double-autoionizing Rydberg states. Nevertheless, the impact of fast energetic ions with the solid surface is necessary to create varieties of the triply excited Li-like states in high Z systems.

Resolving the triply excited states from other excited states of the projectile ions is necessary for absolute intensity measurements and hence determination of the branching ratios. Very often the lifetime of triply excited states in highly charged ions is small and thus comparable to that for the singly and doubly excited states, which makes the measurement more challenging. Therefore, the standard beam–foil time-of-flight technique; has remained limited to the Li-like carbon [5–10,12] for studying the

E-mail addresses: nanditapan@gmail.com, nandi@iuac.res.in (T. Nandi).

http://dx.doi.org/10.1016/j.physleta.2016.08.026
0375-9601/© 2016 Elsevier B.V. All rights reserved.

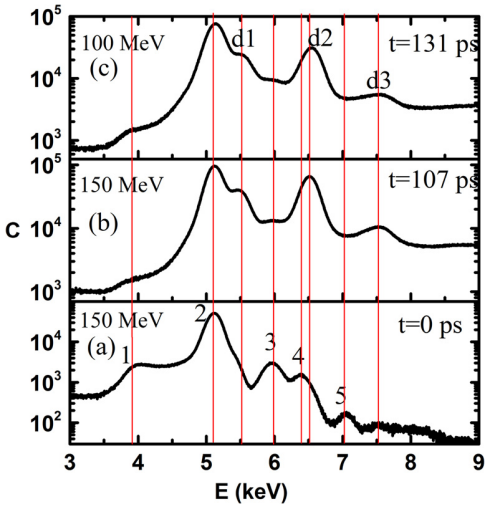


Fig. 1. X-ray spectra recorded after an energetic beam of V^{11+} emerges out of 80 μg/cm^2 thick carbon foil: (a) Prompt x-ray spectrum with the beam energy 150 MeV, (b) and (c) represent the delayed spectra at the beam energy 150 and 100 MeV, respectively.

four body systems. The radiative transitions from the triply excited states in the heavier systems in the beam–foil interactions can be recorded, in principle, with a suitable technique. We have made use of the high-efficiency solid-state detector to record the prompt and the delayed x-ray spectra from the double autoionizing states of Li-like V ions, provided they are metastable against autoionization. Otherwise, they follow two-step single autoionization and no x-ray emissions are possible. The observed blended profiles are assigned tentatively by the Hartree–Fock calculations using the COWAN code [20], where single configuration calculation approach is used and both, relativistic corrections and configuration interactions, are treated as perturbations. In this paper, we discuss a sort of the evidence for several double autoionizing states as well as double-autoionizing Rydberg states of Li-like V decaying through the radiative channels.

2. Experimental details

The experiments were performed using the 15 UD tandem Pelletron accelerator at IUAC, New Delhi, India. A beam of $^{51}_{23}V^{11+}$, having energy of 100 and 150 MeV was passed through 80 μg/cm^2 thick carbon foil to produce the excited states in highly charged ions. The targets were placed in a small vacuum chamber maintained at a pressure better than 1×10^{-6} Torr. The carbon foil was mounted on either surface of an aluminum ladder so that the distance between two positions remained to be 2.55 mm. A germanium ultralow energy detector (GUL0035, Canberra Inc., with 25 μm thick beryllium entrance window, resolution ~150 eV at 5.9 keV), was placed in perpendicular geometry at 50 mm away from the beam axis in such a way that it views the beam just after the back surface of the foil holder. Thus, when the foil is mounted on the front surface of the holder, the x-ray spectra are recorded at delay times about 100–140 ps depending upon the beam energy. Whereas if it is mounted on back side of the holder, the recorded spectra corresponds to time $t \to 0$ with respect to the center of the collimator placed in front of the detector. The observed x-ray spectra were calibrated with a ^{241}Am source.

3. Results and discussion

The prompt and the delayed x-ray spectra of the foil excited $^{51}_{23}V^{11+}$ ions are shown in Fig. 1. The spectrum taken at $t \to 0$ differs from the delayed spectra. The most prominent line appears at 5.12 keV. A few lines in the prompt spectra disappear either completely or decrease in intensity with the delay. Besides, we see a peculiar structure in delayed spectra. Certain peaks become more prominent with the delay such as the lines at 5.4, 6.5, and 7.5 keV marked as d1, d2, and d3. Such kind of features has been observed recently with H-like ions of projectile [21–23] and projectile-like ions [24] owing to the formation of circular Rydberg states. The excited states corresponding to the maximum orbital quantum number (l_{max}) as well as magnetic quantum numbers ($|m|$) for a particular principal quantum number (n) satisfying the relation $l_{max} = |m| = n - 1$ have exactly a circular path and are called the circular Rydberg states [25], which decay via the resonance state through the cascading chain leading to the E2 transitions. Therefore, the delayed transitions observed in present study are expected to originate from the circular Rydberg states. The circular Rydberg states can be observed either through the resonances appearing on the lifetime decay curve of a certain metastable state [22] or the current technique involving the prompt and the delayed measurements. If the time-of-flight is selective, the resonance will be missing in the measurement and one measures only the decay of the metastable level [26].

The lines in prompt spectra which disappear or decay with the delay are labeled as 1, 2, 3, 4 and 5. The transitions assigned to these lines are given in Table 1. The peak energies of the lines observed in all the three spectra of Fig. 1 as given in Table 1 are the average value with the error of ~ ±50 eV. The most prominent line observed at 5.12 keV belongs to the K_α-lines in the V^{q+} ions, where q is the charge state of the outgoing ions. The equilibrium charge state distribution of the V ions can be estimated from the code ETACHA [27]. The charge state fractions obtained for 17+ to 23+ states producing with the impact of the 100 MeV V^{11+} beam are 14, 25, 28, 18, 5, 0.17, and 0.0017%, respectively. Whereas, the same for the 150 MeV V^{11+} projectiles are 2, 10, 25, 35, 22, 2, and 0.067%, respectively. Since, the peak remains to be most prominent even with the delays, the line must be arising predominantly from the forbidden transitions including $1s2p\ ^3P_2–1s^2\ ^1S_0$ in He-like V and the $1s2s2p\ ^4P_{5/2}–1s^22s\ ^2S_{1/2}$ line in Li-like V ion [28]. Though the energy of the transition $1s2s\ ^3S_1–1s^2\ ^1S_0$ in He-like V lies within the peak profile, but its presence can be ignored due to its low transition probability (6.07×10^7/sec) compared to the other two lines (see Table 1). One point is worth noting here that the $1s2s2p\ ^4P_{5/2}$ level lies above the first ionization potential, and thereby it may decay to all the $1s^2ns\ ^2S_{1/2}$ levels for $n = 2, 3, 4, 5$, etc. The broad structure observed around 4 keV (line 1) corresponds to the transitions $1s2s2p\ ^4P_{5/2}–1s^2ns\ ^2S_{1/2}$ ($n = 3–5$). The individual lines are quite close to each other, but the calculated transition probability of the peak (shown in Table 1) suggests a bit higher intensity for the $1s2s2p\ ^4P_{5/2}–1s^23s\ ^2S_{1/2}$ transition. The contribution from the transitions $1s2s2p\ ^4P_{3/2,1/2}–1s^2ns\ ^2S_{1/2}$ ($n = 3–5$) comes at $t \to 0$ and also in the delayed spectra due to their long lifetime (123 ± 13 ps [28]) as seen in Fig. 1. Further, the He-like transitions $1s4p–2s^2$ and $2p^2–1s5s$ lie at this energy domain and hence the contribution arising from them cannot be fully ruled out. In addition, the β transition of the line $1s2s2p\ ^4P_{5/2}–1s^2ns\ ^2S_{1/2}$ i.e., $1s2s3p\ ^4P_{5/2}–1s^22s\ ^2S_{1/2}$ corresponds to the observed line at 5.99 keV (line 3) due to its quite close energy and a large lifetime 389 ps. Since this line almost disappears with the delay, it must be predominantly originating from a much faster transition such as $1s3p^2\ ^2S–1s^23p\ ^2P$. The energy of the transition (6.10 keV) is quite close to the measured value and the upper level lifetime is also as short as 9.4 fs. Though $1s3p^2\ ^2P$, ^2D, $^4P–1s^23p\ ^2P$ and $1s3p\ ^3P_{1,2}–1s^2\ ^1S_0$ lines are also close to this energy, but their lifetimes are 44 ps, 38 ps, 0.2 ps, and 0.23 ps, respectively. The line remains present with the delay and thus, the contribution from these transition as well as $1s2s3p\ ^4P_{5/2}–1s^2ns\ ^2S_{1/2}$ can-

UNCORRECTED PROOF

Please cite this article in press as: G. Sharma et al., Signature of triply excited Li-like V states in ion–solid collisions, Phys. Lett. A (2016), http://dx.doi.org/10.1016/j.physleta.2016.08.026

Table 1
Transitions observed in Fig. 1 are assigned. All the transitions belong to H- to Li-like vanadium.

Peak obs.	E (keV)	Assignment	Decay type	Energy (keV)	A_{ki} (s^{-1})	Ion species
		$1s2s2p\ ^4P_{5/2}–1s^25s\ ^2S_{1/2}$	M2	3.818$^+$	1.17e+09^a	Li-like V
1	4.00	$1s2s2p\ ^4P_{5/2}–1s^24s\ ^2S_{1/2}$	M2	3.958$^+$	1.41e+09^a	Li-like V
		$1s2s2p\ ^4P_{5/2}–1s^23s\ ^2S_{1/2}$	M2	4.261$^+$	2.03e+09^a	Li-like V
2	5.12	$1s2p\ ^3P_2–1s^2\ ^1S_0$	M2	5.19$^+$	2.43e+09$^+$	He-like V
		$1s2s2p\ ^4P_{5/2}–1s^22s\ ^2S_{1/2}$	M2	5.14$^+$	5.20e+09$^\$$	Li-like V
		$1s2p^2\ ^2P_{3/2}–1s^22p\ ^2P_{3/2}$	E1	5.16*	3.90e+14*	Li-like V
3	5.99	$1s3p^2\ ^2S_{1/2}–1s^23p\ ^2P_{3/2,1/2}$	E1	6.09*	1.10e+12*	Li-like V
		$1s3p\ ^1P_1–1s\ ^2S_0$	E1	6.11$^+$	7.68e+13$^+$	He-like V
		$1s2s3p\ ^4P_{5/2}–1s^22s\ ^2S_{1/2}$	M2	5.99$^+$	1.12e+10$^\$$	Li-like V
		$1s3p^2\ ^2P–1s^23p\ ^2P$	E1	6.10*	5.03e+13*	Li-like V
		$1s3p^2\ ^2D–1s^23p\ ^2P$	E1	6.10*	3.54e+13*	Li-like V
		$1s3p^2\ ^4P–1s^23p\ ^2P$	E1	6.09*	9.38E + 11*	Li-like V
	4.82	$1s2s3p\ ^4P_{5/2}–1s^24s\ S_{1/2}$	M2	4.81$^+$	3.72e+09$^\$$	Li-like V
	4.67	$1s2s3p\ ^4P_{5/2}–1s^25s\ ^2S_{1/2}$	M2	4.66$^+$	3.18e+09$^\$$	Li-like V
4	6.38	$2p^23p\ ^4S–1s2p^2\ ^4P$	E1	6.34*	4.82e+13*	Li-like V
		$3p^3\ ^4S–1s3p^2\ ^4P$	E1	6.39*	4.33e+13*	Li-like V
		$2s^23p^2P–1s2s^2\ ^2S$	E1	6.30*	4.02e+13*	Li-like V
		$2p3d\ ^1P–1s2p\ ^1D$	E2	6.39*	5.97e+11*	He-like V
	6.45	$1s4p\ ^1P–1s^2\ ^1S$	E1	6.44$^+$	3.11e+13$^+$	He-like V
5	7.02	$2p^212p\ ^4S–1s2p^2\ ^4P$	E1	6.97*	7.01e+11*	Li-like V
d1	5.40	$2s\ ^2S_{1/2}–1s\ ^2S_{1/2}$	M1	5.43$^+$	1.32e+09$^\&$	H-like V
		$2p\ ^2P_{3/2,\,1/2}–1s\ ^2S_{1/2}$	E1	5.44$^+$	1.83e+14$^+$	H-like V
		$2p^2\ ^3P_1–1s2p\ ^3P_2$	E1	5.41^{1*}	1.42e+14$^+$	He-like V
		$2p^3–1s2p^2$	E1	5.37*	6.92e+13*	Li-like V
d2	6.51	$2s\ ^2S_{1/2}–1s\ ^2S_{1/2}$	M1	6.42$^+$	2.27e+09$^\&$	H-like Mn
		$2p\ ^2P_{3/2,\,1/2}–1s\ ^2S_{1/2}$	E1	6.44$^+$	2.52e+14$^+$	H-like Mn
d3	7.50	$2s\ ^2S_{1/2}–1s\ ^2S_{1/2}$	M1	7.50$^+$	3.74e+09$^\&$	H-like Co
		$2p\ ^2P_{3/2,\,1/2}–1s\ ^2S_{1/2}$	E1	7.50$^+$	3.43e+14$^+$	H-like Co

'*' represents Cowan calculations, '+' for NIST values [31], the values marked as '$' are from [24], '&' are from [30] and '$' values are scaled. Peaks 4 and 5 are assigned with only the terms.

not be ruled out. Further, the $1s2s3p\ ^4P_{5/2}–1s^2ns\ ^2S_{1/2}$ ($n = 4$–5) transitions (see Table 1 for the line energies) yields a plateau-like structure as seen between the line 1 and line 2 in Fig. 1(a). With the delay as shown in Fig. 1 (b)–(c), the intensity of $1s2s3p\ ^4P_{5/2}–1s^2ns\ ^2S_{1/2}$ ($n = 4$–5, lifetime = 389 ps) lines is higher than that of the lines $1s2s2p\ ^4P_{5/2}–1s^2ns\ ^2S_{1/2}$ ($n = 4$–5, lifetime = 123 ps) due to difference in the lifetimes. We note here that the triply excited states in the Li-like ions such as $np^3\ ^4S°$ are forbidden to decaying straightway to the ground state, they ought to decay in steps, in particular, the $3p^3\ ^4S°$ systems require three steps. Two of them lie in the x-ray region and the third in the VUV. Hence, the second step of the decay of the $3p^3\ ^4S°$ level as shown in Fig. 3 is the line $1s3p^2\ ^2S–1s^23p\ ^2P°$ observed at 6.1 keV.

The line 4 at 6.4 keV can be fitted with the two peaks appearing at 6.38 and 6.45 keV as shown in Fig. 2(top). Interestingly, both the peaks disappear with the delay and instead, a new peak appears at 6.5 keV designated as d2 line. The beam energy used in the experiment surpasses the Coulomb barrier energy, and therefore, the projectile like ions [24] can be produced from the α and 2α transfer reactions of the binary system [29] containing the ^{12}C target atom and the ^{51}V projectile ions. Consequently, we ought to see the transitions from ^{55}Mn and ^{59}Co ions. Accordingly, the lines d2 and d3 are assigned to the $2p\ ^2P_{3/2,\,1/2}–1s\ ^2S_{1/2}$ transition in H-like ^{55}Mn and ^{59}Co, respectively (Table 1). Although these E2 transitions are fast decaying, they are still observed at the delays because of the circular Rydberg states cascading through the yrast chain [21,22,24]. Since the $2p\ ^2P_{3/2,\,1/2}–1s^2S_{1/2}$ transitions from the circular Rydberg states evolve with the delay, a little intensity contribution in the spectra at $t = 0$ must be due to the M1 transition $2s\ ^2S_{1/2}–1s\ ^2S_{1/2}$. The M1 line energies [30] are very close to the E2 lines [31] as given in Table 1.

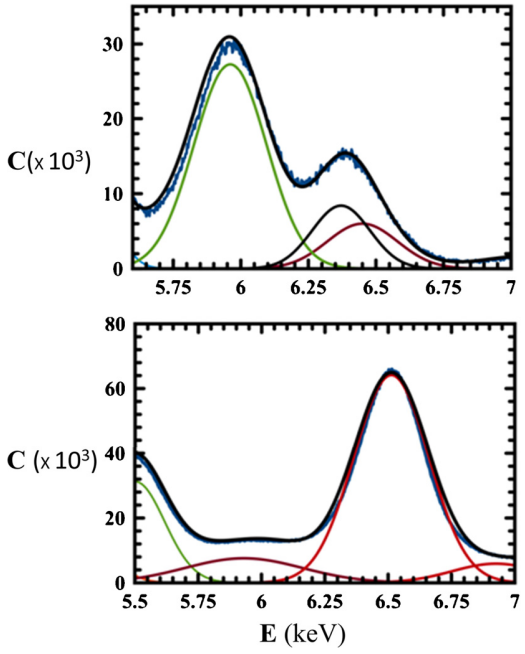


Fig. 2. Prompt and delayed spectra: The peak around 6.4 keV in prompt spectrum fits with two peaks at 6.45 and 6.51 keV (top), whereas the peak with the delayed spectrum fits with a single peak at 6.5 keV (bottom).

Note that the x-ray intensity ratio for the target like ions to the target atoms is measured as high as 10% for ^{180}Hf, ^{181}Ta, ^{186}W, $^{185,187}Re$, $^{194,198}Pt$, ^{197}Au, $^{203,205}Tl$, ^{208}Pb, $^{209}Bi(^{6,7}Li, xn)$ reactions

Please cite this article in press as: G. Sharma et al., Signature of triply excited Li-like V states in ion–solid collisions, Phys. Lett. A (2016), http://dx.doi.org/10.1016/j.physleta.2016.08.026

UNCORRECTED PROOF

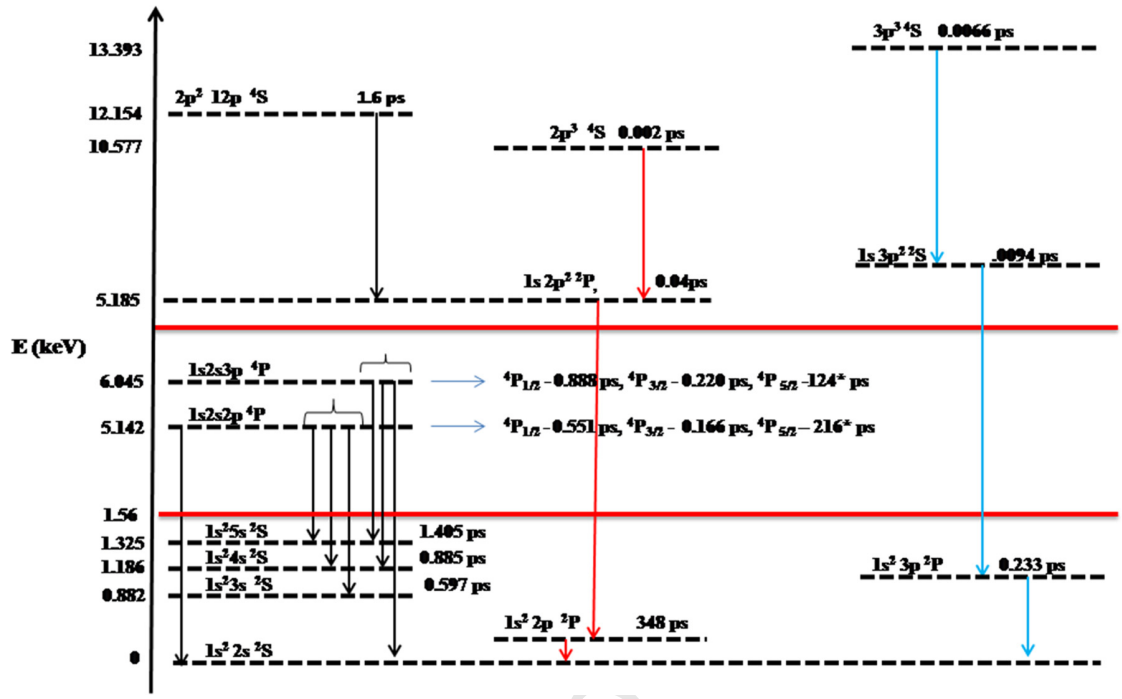


Fig. 3. The schematic of the transitions observed. The vertically downward arrows show the radiative transitions in Li-like V. Red horizontal lines are the ionization potentials. (* scaled values). (For interpretation of the references to color in this figure legend, the reader is referred to the web version of this article.)

[32]. This intensity ratio depends on the system, which is ~1% in the present experiment where heavy ions are irradiated on the light target.

The line 4 cannot be assigned to any previously known transitions in any ionic states of the vanadium. Thus, the theoretical energy structures of the He and the Li-like V ions have been calculated using the COWAN configuration interaction code [20]. The states $1s^2$, $1snl$ ($n = 2$–9), $1snd$ ($n = 3$–11), $1sng$ ($n = 5$–9), $2p^2$, $3d^2$, $2snl$ ($n = 3$–5), $2snd$ ($n = 3, 4$), $2pnp$ ($n = 3, 4$) and 2p4f in even parity system and $1snp$ ($n = 2$–11), $1snf$ ($n = 4$–11), $2snp$ ($n = 3, 4$), 2s4f, $2pns$ ($n = 3, 4$) and $2pnd$ ($n = 3, 4$) in odd parity system are included for the He-like V. Whereas, the calculations for the Li-like V include the configurations $1s^2ns$ ($n = 2$–6), $1s^2nd$ ($n = 3$–7), $1snp^2$ ($n = 2, 3$), $1sns^2$ ($n = 2, 3$), $1s2sns$ ($n = 3$–5), $1s2snd$ ($n = 3, 4$) and $2s3p^2$, $2s^23d$, $2s^23s$ in the even parity set, and the odd parity set contains $1s^2np$ ($n = 2$–7), $1s^2nf$ ($n = 4$–8), $1s2snp$ ($n = 3, 4, 5$), $2p3p^2$, np^3 ($n = 3$–4), $2s^2np$ ($n = 2, 3$), $2s^24f$ and $2p^2np$ ($n = 3$–12) configurations. With thorough analysis, we assign the line 4 to the transitions $2p^23p\ ^4S$–$1s2p^2\ ^4P$, $3p^3\ ^4S$–$1s3p^2\ ^4P$, $2s^23p\ ^2P$–$1s2s^2\ ^2S$, and $2p3d\ ^1P$–$1s2p\ ^1D$. The level $2p^23p\ ^4S_{3/2}$ lies above the second ionization limit, but its autoionization probability (~10^7/sec) is about six orders of magnitude smaller than the radiative rate (~10^{13}/sec). The $3p^3\ ^4S$ state is metastable against the autoionization and thus, cannot decay radiatively to the ground state. It has to stabilize through a few steps as shown in Fig. 3. The $3p^3\ ^4S$–$1s3p^2\ ^4P$ transition at 6.38 keV and the $1s3p^2\ ^2S_{1/2}$–$1s^23p\ ^2P_{3/2,\,1/2}$ transition at 5.99 keV are supposed to be the first and the second steps of the decay of the $3p^3\ ^4S$ level. Further, the 2p3d ^1P–1s2p ^1D transition is another possibility of the blended profile as 2p3d ^1P state is a fluorescence active doubly excited state [33,34].

The $3p^3\ ^4S$ state has been populated in the present experiment, naturally the $2p^3\ ^4S$ state is expected to be produced too. Indeed, the first two steps of the decay of the $2p^3\ ^4S$ state as shown in Fig. 3 may have been observed through the transitions $2p^3\ ^4S$–$1s2p^2\ ^4P$ as a member of blended line d1 at 5.4 keV appearing at $t \to 0$ and certainly disappearing with delay due to its small lifetime of 2 fs (see Fig. 3). However, exactly at this x-ray energy the E1 transition $^2P_{3/2,\,1/2}$–1s $^2S_{1/2}$ in the H-like V appears with the delay as it is originated from the circular Rydberg states cascading through yrast chain. Hence, the intensity at 5.4 keV is seen as a hump at $t \to 0$ and it becomes more prominent with the delays. The second component of the state $2p^3\ ^4S$ decaying through the $1s2p^2\ ^4P$–$1s^22p\ ^2P$ transition at 5.15 keV is blended with line 2 (5.12 keV).

The line 5 appearing at 7.0 keV is assigned to the transitions $2p^2np\ ^4S_{3/2}$–$1s2p^2\ ^4P_{5/2,\,3/2,\,1/2}$; where n can be a certain value close to 12 as the transition energies are around 7 keV for $n \geq 12$. Though these transitions are also above the second ionization limit like line 4, it should be present in the prompt spectra clearly, and should disappear totally in the delayed spectra. The clear disappearance of the line with the delays suggests the presence of the only allowed transitions at 7.0 keV. The disappearance can be confirmed by the much higher radiative decay rate (7.10^{12}/sec) of these transitions than their autoionization rates (~10^5/sec). Further, we note that the line energy for 7p–1s is also around 7.0 keV, however the transitions np–1s, for $n = 3$–6 have not been observed in the spectra and therefore, the existence of such transition must be ruled out.

The beam–foil method is known to excite the exotic states in the excited ions. It is, therefore, possible to have two K-shell vacancies in a system; for example, two-electron–one-photon transitions [35–37]. In the current experiment, we do get certain indication of such transitions; however, the low statistics forbid discussing on them here.

4. Conclusion

The four-body problem has been studied through the triply excited states of Li-like V ions. These states lie above the second ionization limit. Besides the single autoionization, the double autoionization is also possible. However, the set of quantum numbers for some states makes them metastable against autoionization. Such states decaying through radiative transitions have been stud-

Please cite this article in press as: G. Sharma et al., Signature of triply excited Li-like V states in ion–solid collisions, Phys. Lett. A (2016), http://dx.doi.org/10.1016/j.physleta.2016.08.026

ied by the prompt and the delayed x-ray spectroscopy as well as the theoretical calculations of the transition energies and the relative decay rates using the COWAN code [20]. We have obtained the signature of the double autoionizing states and the double autoionizing Rydberg states, such as $3p^3\ ^4S$ and $2p^2\ np^4S$ ($n \sim 12$), in Li-like V ions. These states are identified through radiative transitions to the ground state via two or more steps.

Acknowledgements

We are thankful to the Pelletron staff at IUAC for providing stable beam during the experiment. Help from P. Sharma during analysis is acknowledged. G. Sharma is thankful to University Grant Commission for financial supports. We also acknowledge DST, India for funding the project No. SP/S2/LOP-0006/2011.

References

[1] L.B. Madsen, J. Phys. B, At. Mol. Opt. Phys. 36 (2003) R223–R278.
[2] R. Wehlitz, M.-T. Huang, K.A. Berrington, S. Nakazaki, Y. Azuma, Phys. Rev. A 60 (1999) R17–R20.
[3] Y. Azuma, F. Koike, J.W. Cooper, T. Nagata, G. Kutluk, E. Shigemasa, R. Wehlitz, I.A. Sellin, Phys. Rev. Lett. 79 (1997) 2419–2422.
[4] M.S. Pindzola, F. Robicheaux, J. Colgan, Phys. Rev. A 72 (2005) 022709.
[5] E.J. Knystautas, J. Phys. B, At. Mol. Opt. Phys. 25 (1992) L395–L399.
[6] S. Mannervik, R.T. Short, D. Sonnek, E. Trabert, G. Moller, V. Lodwig, P.H. Heckmann, J.H. Blanke, K. Brand, Phys. Rev. A 39 (1989) 3964.
[7] E.J. Knystautas, Phys. Rev. Lett. 69 (1992) 2635.
[8] R. Bruch, G. Paul, J. Andra, L. Lipsky, Phys. Rev. A 12 (1975) 1808.
[9] M. Rodbro, R. Bruch, P. Bisgaard, J. Phys. B, At. Mol. Phys. 12 (1979) 2413.
[10] M. Agentoft, T. Andersen, K.T. Chung, J. Phys. B, At. Mol. Phys. 17 (1984) L433–L438.
[11] A. Muller, G. Hofmann, B. Weissbecker, M. Stenke, K. Tinschert, M. Wagner, E. Salzborn, Phys. Rev. Lett. 63 (1989) 758–761.
[12] L.M. Kiernan, E.T. Kennedy, J.-P. Mosnier, J.T. Costello, B.F. Sonntag, Phys. Rev. Lett. 72 (1994) 2359.
[13] M. Ahmed, L. Lipsky, Phys. Rev. A 12 (1975) 1176–1196.
[14] N.A. Piangos, C.A. Nicolaides, Phys. Rev. A 48 (1993) 4142.
[15] X. Yang, C.G. Bao, C.D. Lin, Phys. Rev. Lett. 76 (1996) 3096.
[16] E.T. Kennedy, Phys. Scr. T95 (2001) 32–44.
[17] N. Vaeck, J.E. Hansen, P. Palmeri, P. Quinet, N. Zitane, M. Godefroid, S. Fritzsche, N. Kylstra, Phys. Scr. (T95) (2001) 68–75.
[18] H. Winter, F. Aumayr, J. Phys. B, At. Mol. Opt. Phys. 32 (1999) R39–R65.
[19] G. Verbockhaven, J.E. Hansen, Phys. Rev. Lett. 84 (2000) 2810–2813.
[20] R.D. Cowan, The Theory of Atomic Structure and Spectra, University of California Press, Berkeley, CA, and Cowan code package for Windows by A. Kramida, available from http://das101.isan.troitsl.ru/COWAN, 1982.
[21] T. Nandi, Astrophys. J. 673 (2008) L103–L106.
[22] A.P. Mishra, T. Nandi, B.N. Jagatap, J. Quant. Spectrosc. Radiat. Transf. 120 (2013) 114–119.
[23] N.N. Nedeljković, S.M.D. Galijaš, M.A. Mirković, J. Quant. Spectrosc. Radiat. Transf. 134 (2014) 46–54.
[24] T. Nandi, J. Phys. B, At. Mol. Opt. Phys. 42 (2009) 125201.
[25] J.N. Tan, S.M. Brewer, N.D. Guise, Phys. Scr. T 144 (2011) 014009.
[26] T. Nandi, B.P. Mohanty, J. Phys. B, At. Mol. Opt. Phys. 42 (2009) 225402.
[27] J.P. Rozet, C. Stephan, D. Vemhet, Nucl. Instrum. Methods B 107 (1996) 67–70.
[28] T. Nandi, P. Marketos, P. Joshi, R.P. Singh, C.P. Safvan, P. Verma, A. Mandal, A. Roy, R.K. Bhowmik, Phys. Rev. A 66 (2002) 052510.
[29] P. Sharma, T. Nandi, in: Proceedings of the DAE Symp. on Nucl. Phys., vol. 59, 2014, pp. 460–461.
[30] F.A. Parpia, W.R. Johnson, Phys. Rev. A 26 (1982) 1142–1145.
[31] NIST atomic spectra database, http://www.nist.gov/pml/data/asd.cfm.
[32] H.J. Karwowski, S.E. Vigdor, W.W. Jacobs, S. Kailas, P.P. Singh, F. Soga, T.G. Throwe, T.E. Ward, D.L. Wark, J. Wiggins, Phys. Rev. C 25 (1982) 1355–1378.
[33] S. Kasthurirangan, J.K. Saha, A.N. Agnihotri, S. Bhattacharyya, D. Misra, A. Kumar, P.K. Mukherjee, J.P. Santos, A.M. Costa, P. Indelicato, T.K. Mukherjee, L.C. Tribedi, Phys. Rev. Lett. 111 (2013) 243201.
[34] J.K. Saha, S. Bhattacharyya, P.K. Mukherjee, T.K. Mukherjee, Chem. Phys. Lett. 517 (2011) 223–226.
[35] C. Stoller, W. Wolfli, G. Bonani, M. Stockli, M. Suter, Phys. Rev. A 15 (1977) 990.
[36] J. Auerhammer, H. Genz, A. Kumar, A. Richter, Phys. Rev. A 38 (1988) 688–694.
[37] T.K. Mukherjee, P.K. Mukherjee, Z. Phys. D 42 (1997) 29–31.

UNCORRECTED PROOF

Electrical Power and Energy Systems 85 (2017) 87–96

Contents lists available at ScienceDirect

Electrical Power and Energy Systems

journal homepage: www.elsevier.com/locate/ijepes

Two degrees of freedom dc voltage controller of grid interfaced PV system with optimized gains

Ravi Nath Tripathi *, Tsuyoshi Hanamoto

Graduate School of Life Science and Systems Engineering, Kyushu Institute of Technology, Kitakyushu 808-0196, Japan

ARTICLE INFO

Article history:
Received 14 January 2016
Received in revised form 5 July 2016
Accepted 14 August 2016

Keywords:
Iterative tuning
dc voltage controller
Photovoltaic (PV)
Particle swarm optimization

ABSTRACT

This paper proposes the application of fictitious reference iterative tuning (FRIT) method to optimize the gains of dc voltage controller of grid connected photo-voltaic (PV) system. It may be difficult to achieve good control of dc voltage using conventional PI controller having only one-degree-of-freedom (1-DOF) due to the trade-off between overshoot (in step response) and disturbance response. In this paper, the optimal control of dc voltage is proposed with improved disturbance response by implementing 2-DOF PI controller structure. FRIT method has been programmed in MATLAB based upon the particle swarm optimization (PSO) algorithm. The fundamental idea related to FRIT method is the extraction of input and output data, reference model setting and range of controller gains. The performance of dc voltage control for the optimized 2-DOF PI controller is also compared with the fuzzy logic controller (FLC) response.

© 2016 Elsevier Ltd. All rights reserved.

1. Introduction

The use of renewable energy sources have been motivated to use as distributed energy source for the generation of environmental friendly energy. In the distributed energy source, photovoltaic (PV), wind, biomass, tidal and geothermal are getting attention in the last decades. The technological advancement and research leads to the more feasible and cheaper production of renewable energy but still it is costlier in comparison to conventional sources of energy [1,2]. The PV system is extensively popular due to wide range of power application and received much attention as distributed generating (DG) source in grid connected mode to cater energy demand problem with inherent propoerty of energy storage [3–7]. The PV power generating system as a DG in grid connected mode having better control operation to operate at maximum power point (MPP) which will help to evacuate maximum generated power and controlled by grid following power export control technique [2–6]. The power electronics interface is essential for interfacing of PV system as a DG to grid and it can be implemented using direct/indirect current controlled pulse width modulated (PWM) voltage source inverters (VSI) [2–11]. VSI as a power electronics interface supports to implement the grid interfacing and power conversion [12].

The capacitor dc voltage of VSI in a grid connected PV system can be regulated using various types of controllers like proportional plus integral type controller (PI/PID), Fuzzy-PI, fuzzy logic controller (FLC) etc. [2–15]. Generally, PI/PID controller is extensively used as single input-output system for dc voltage control and for process control in industrial applications due to ease of implementation. The conventional PI control structure deals with the limitation to obtain the optimal response for the system. So, the 2-DOF PI/PID control structure has been proposed and utilized under various control schemes for different type of application with significant advantage over 1-DOF PI control [16–20]. The DOF of a control system defines the number of independent closed loops in the control configuration [21–23]. The 2-DOF control structure can be design in various control configuration as feedforward, feedback, set point filter etc. [21–25].

The PI/PID control structure is designed to obtain the stability and good control with better transient responses. The performance of the designed control structure is dependent upon the controller gains. So, the gains of the controller need to be appropriately tuned and various tuning methods have been proposed and discussed like as iterative feedback tuning (IFT), virtual reference feedback tuning (VRFT) and fictitious reference iterative tuning (FRIT) by several researchers in [26–30]. These direct design approach only requires the input and output data of the controlled system and received significant attention. The IFT tuning requires the multiple experiment data for iterative tuning so as to achieve the desired optimal response while VRFT required only one-shot experimental

* Corresponding author.
E-mail address: ravi1989tripathi@gmail.com (R.N. Tripathi).

http://dx.doi.org/10.1016/j.ijepes.2016.08.006
0142-0615/© 2016 Elsevier Ltd. All rights reserved.

data. FRIT is also used only one-shot experimental data for the optimal controller gain tuning. So, these tuning methods helps to achieve the optimal controller gains without any requirement of system/plant model information based upon the one-shot closed loop experimental data. The basic difference between VRFT and FRIT is that in case of the VRFT minimization of function emphasizes on the input while FRIT emphasizes on the output. So, the FRIT method may be more advantageous and establishing better understanding in practical sense. FRIT method implementation and approach is better for 1-DOF as well as 2-DOF controller in comparison to VRFT [29–33].

FRIT method was modified, studied and analyzed for different application and optimal performances in [28–35]. It can be implemented as both online and offline system for controller tuning. The FRIT method deals with the disadvantage that it may results in local minimum for PI/PID controller tuning due to the non-linear and non-convex problem consideration. So, the FRIT method should be combined with an optimization technique to mitigate the local minimum solution for non-linear and non-convex optimization problems.

The DOF based control with optimal tuning methods of controller gains was widely applied and implemented specially in motor control application and process industry. Sometime, numerical examples are considered to show the effectiveness of DOF controllers and tuning method. This is the first time that the optimal tuning method and DOF based controller is used for dc voltage control. In this paper, the application of 2-DOF controller is proposed for the dc voltage regulation of VSI. The data driven tuning method FRIT is used for optimal tuning of dc voltage controller of grid connected PV system. FRIT is implemented based upon the particle swarm optimization (PSO) algorithm to prevent the problem of local minimum solution. The proposed 2-DOF PI control configuration is implemented to mitigate the overshoot in the response of conventional PI control as well as to achieve the fast transient response using optimal controller gains. FRIT is used as off-line tuning method and tune the controller gains by minimizing performance index error function based upon the fictitious reference signal. The performance of the proposed controller is investigated for step response as wells as under varied ir-radiance as system response affected due to change in ir-radiance and transient response.

The paper is organized as follows. In Section 2, the DOF based controller configuration and design is considered. In Section 3 the optimization problem of FRIT method is considered and implementation in combination with PSO is explained with step by step procedure considered for 2-DOF PI controller. In Section 4 FLC is considered and membership function for dc voltage control is shown. In Section 5 the control algorithm of dc voltage control with VSI is considered. In Section 6 the performance of controllers have been discussed and analyzed considering disturbance in reference dc voltage. In Section 7 concluding remarks have been given for the paper.

2. dc voltage PI controller

The conventional PI control structure in Fig. 1 consists of controller and plant/system transfer function block where, $P(s)$: PI controller ($k_p + k_i/s$) and $G(s)$: transfer function of the plant/system. The 1-DOF PI controller may not achieve very satisfactory response considering multi-objective view point of the system control and therefore 2-DOF controller have natural advantage over conventional PI controller [21]. In this paper, the 2-DOF PI control has been instrumented first time for dc voltage control.

The number of independent closed loops in control structure decides the DOF of the system control and considered as

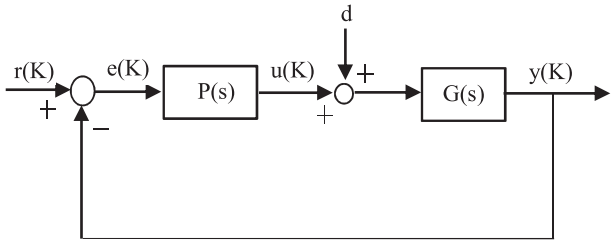


Fig. 1. Generalized 1-DOF PI controller configuration.

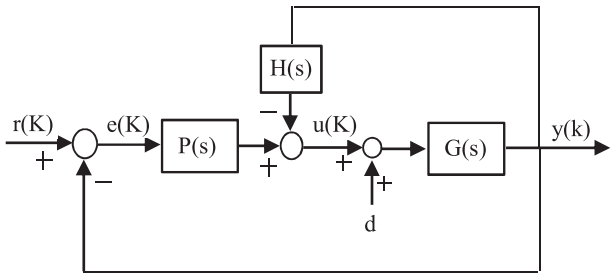


Fig. 2. Generalized 2-DOF FB type PI controller configuration.

two-input and one output system. The 2-DOF controller designed and discussed in [16,21] with various configuration stated as feed-forward type(FF), feedback type (FB), filter type, filter and preceded derivative type and component separated type depending upon the application and objective of system control. The 2-DOF feedback compensating (2-DOF FB) controller in Fig. 2 is implemented for dc voltage regulation. The 2-DOF PI control configuration used for dc voltage control consists of proportional gain (K_p) and integral gain (K_i) same as conventional PI controller and additional feedback proportional gain (K_{pfb}) as a feedback compensation. So, it is having two proportional control gain and one integral control gain and can be represented as PI-P (2-DOF PI) controller. The reference input signal (r) and controller output signal (y) are the input signal and the modified output signal (u) output signal. The closed loop transfer function of conventional PI control structure in Fig. 1, from reference input r to controlled output y and from disturbance d to y are given respectively as

$$M_{r1}(s) = \frac{G(s)P(s)}{1 + G(s)P(s)} \tag{1}$$

$$M_{d1}(s) = \frac{G(s)}{1 + G(s)P(s)} \tag{2}$$

The transfer function shown in Eqs. (1) and (2) is having only one tuning element as $P(s)$ for optimal system performance. As it includes only one tuning element it can-not be tuned independently. The closed loop transfer function of 2-DOF FB control structure in Fig. 2 from reference input r to controlled output y and from disturbance d to y are given respectively as

$$M_{r2}(s) = \frac{G(s)P(s)H(s)}{1 + G(s)H(s)(P(s) + 1)} \tag{3}$$

$$M_{d2}(s) = \frac{G(s)}{1 + G(s)(P(s) + H(s))} \tag{4}$$

Here, the transfer function shown in Eqs. (3) and (4) having two tuning element as $P(s)$ and $H(s)$. It helps to achieve the optimal performance for the system with feedback compensating terms.

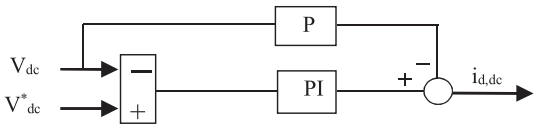


Fig. 3. 2-DOF controller configuration for dc link voltage control of grid connected PV system.

The controller system is analyzed for the step change in r and response of the y and termed as reference point (set point) response. The generalized 2-DOF control configuration shown in the form of dc voltage control in Fig. 3. The reference dc voltage (V^*_{dc}) is the reference input signal (r) and measure dc voltage (V_{dc}) which have to be regulated to reference level is considered as output for dc voltage control scheme. The 1-DOF and 2-DOF controller response for dc voltage control have been analyzed for the step change in V^*_{dc}.

3. Fictitious Reference Iterative Tuning (FRIT)

The performance of the controller is dependent upon gains so the parameter tuning is one of the significant consideration for better performance. FRIT is data-driven parameter tuning method so it only requires one shot input and output data. Using this input and output data it is possible to optimize the controller parameter without any mathematical model of the system.

3.1. Reference signal generation

The reference signal is generated by using the input and output data for initial parameter k_0 of controller. The k_0 was obtained using trial and error method and represented as $[k_{p0}, k_{int0}]^T$. The one shot data as: intermediate output u_0 as input data and controlled output y_0 as output data. The reference signal generation for conventional PI control and 2-DOF PI control can be computed as.

3.1.1. For 1-DOF PI controller

The fictitious reference signal can be computed using Eq. (1) based upon the system configuration in Fig. 1. The mathematical evaluation of reference signal for conventional 1-DOF PI controller is as follows

$$\tilde{r}(k) = P(s,k)^{-1}u_0 + y_0 \tag{5}$$

$$= e_0 + y_0 \tag{6}$$

e_0 is the error in between r and y_0 for the initial response and data obtained using initial controller gains k_0. The data set (u_0, y_0) is obtained using k_0.

3.1.2. For 2-DOF PI controller

The fictitious reference signal computation can be modified for 2-DOF FB controller in Fig. 2. The reference signal for 2-DOF FB control configuration can be computed by using transfer function from r to y in Eq. (3) as

$$(\tilde{r}(k,k_{fb}) - y_0)P(s,k) - H(s,k_{fb})y_0 = u_0 \tag{7}$$

$$\Rightarrow \tilde{r}(k,k_{fb}) - y_0 = (u_0 + y_0 H(s,k_{fb}))P(s,k)^{-1} \tag{8}$$

$$\Rightarrow \tilde{r}(k,k_{fb}) = (u_0 + H(s,k_{fb})y_0)P(s,k)^{-1} + y_0 \tag{9}$$

where,

$$k = [k_p, k_{int}]^T \tag{10}$$

$$P(s,k) = k_p + \frac{k_{int}}{s} \tag{11}$$

$$H(s,k_{fb}) = C_{fb}(s,k) = k_{pfb} \tag{12}$$

k_{fb} is the feedback controller gain, k_{pfb} is the proportional gain of feedback controller and initial controller gain for FB is k_{fb0}. The data set (u_0, y_0) for reference signal computation was obtained by performing one-shot simulation/experiment using P(s, k_0) and C_{fb} (s, k_{fb0}) with the initial parameter k_0 and k_{pfb0}.

3.2. Optimization function and reference model

The optimization of controller parameter can be achieved by minimizing the optimization function/performance index function. The optimization function is designed based upon the response obtained using fictitious reference signal and reference model and the primary response of the controller for the trial and error gain.The controller parameters/gains $k - k_{fb}$ have to be tuned and optimized in such a way that the optimization function should be minimized. The performance index optimization function is represented as mathematical equation and based upon system configuration in Fig. 4. As the FRIT method does not require any mathematical or dynamical model of the system so a reference model is to be assumed as transfer function. The generalized transfer function for reference model setting is shown as

$$M(s) = \frac{1}{(Ts+1)^n}e^{-\tau s} \tag{13}$$

where, T is time constant and τ is dead time. In this paper, the reference model setting $T = 0.0005$, $\tau = 0$ is been used and $n = 2$. The controlled output y_0 generated using initial parameters is compared with the output generated using fictitious reference signal and reference model to obtain the optimized controller parameters so that closed loop response of the system should follow the presumed ideal response of reference model. The optimization function based on the initial data set can be defined as

$$\tilde{e} = y_0 - M(s)\tilde{r} \tag{14}$$

$$I = \sum(\tilde{e})^2 \tag{15}$$

In the FRIT method, fictitious reference signal generated by Eqs. (6) and (9) is utilized to generate objective function for optimization and the optimization function is defined considering the system configuration in Fig. 4 given as

$$\tilde{e}(k,k_{fb}) = y_0 - \tilde{y} \tag{16}$$

$$\Rightarrow \tilde{e}(k,k_{fb}) = y_0 - M(s)\tilde{r}(k,k_{fb}) \tag{17}$$

$$\tilde{I}(k,k_{fb}) = \sum(\tilde{e}(k,k_{fb}))^2 \tag{18}$$

So, the objective function for optimization of gain parameters is to minimize the performance index error function of Eq. (18). It can be represented as mathematical function of controller gains

$$(k,k_{fb})_{opt.} = argmin\tilde{I}(k,k_{fb}) \tag{19}$$

3.3. PSO based FRIT

The optimization algorithm is essential to implement FRIT method so that local minimum solution can be avoided from the

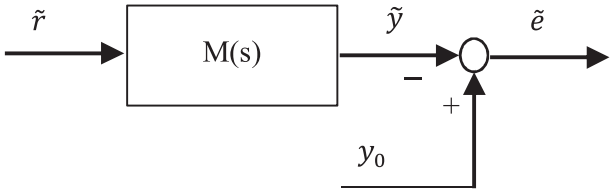


Fig. 4. System configuration for performance index function.

FRIT method. The PSO based FRIT (PSO-FRIT) is proposed for the computation of optimized controller parameters of 2-DOF PI configuration used for dc voltage control. So, an objective function is required as an optimization problem to achieve optimized controller gains. The optimization method is based upon the behavior of particle to imitate the potential solution of neighboring particle which is related to the neighborhood best/local best and its own achieved solution which is related to the person best solution.

3.3.1. Generalized PSO

PSO method search the possible potential solutions as a swarm of particles which move in virtual space. So, it is a stochastic approach and swarm population based search method considering the behavior of bird flocks. The position and velocity vector is associated with each particle and updated at each iteration. So, the position of a particle is dependent upon the personal best (p_{best}) and neighborhood best which leads to the global best (g_{best}). Therefore, the particle velocity can be modified as follows

$$\rho_i^{\alpha+1} = \phi\rho_i^{\alpha} + c_1 w_1 (p_{best} - x_i^{\alpha}) + c_2 w_2 (g_{best} - x_i^{\alpha}) \tag{20}$$

The velocity of particle updated considering following three terms

(1) Acceleration coefficient/cognitive component (c_1), which is related to the personal best solution (p_{best}) of each particle.
(2) Acceleration coefficient/social component (c_2), which relates with the best position of particle in whole solution and termed as global best solution (g_{best}).
(3) An inertia weight (ϕ), which controls the velocity of particle. The value of w_1 and w_2 should be decided in between 0 and 1. The position of each particle is modified based upon the changes in velocity of each particle. The position update shown as

$$x_i^{\alpha+1} = x_i^{\alpha} + \rho_i^{\alpha+1} \tag{21}$$

3.3.2. PSO-FRIT

The general PSO method can be modified for the FRIT method implementation. The position of particle is defined as the controller gain parameter and update of the velocity represents the perturbation in controller gains. So, the position update of each particle in Eq. (21) is modified for controller parameter as follows

$$k_i^{\alpha+1} = k_i^{\alpha} + \rho_i^{\alpha+1} \tag{22}$$

The controller gain parameter update in Eq. (22) is adjusted for 2-DOF PI controller gains (k_p, k_{int} and k_{pfb}) as

$$k_{p,i}^{\alpha+1} = k_{p,i}^{\alpha} + \rho_{p,i}^{\alpha+1} \tag{23}$$

$$k_{p,int}^{\alpha+1} = k_{p,int}^{\alpha} + \rho_{p,int}^{\alpha+1} \tag{24}$$

$$k_{pfb,int}^{\alpha+1} = k_{pfb,int}^{\alpha} + \rho_{pfb,int}^{\alpha+1} \tag{25}$$

The PSO application for FRIT method is illustrated in the following steps:

Step 1: The number of particles (N) based solution vector of controller parameter is defined as follows

$$k = [k_1 k_2 k_3 \ldots k_j] \tag{26}$$

$$j = 1, 2, 3, \ldots, N \tag{27}$$

The solution vector of controller parameter will be applicable to the all the three gains (k_p, k_{int} and k_{pfb}) of 2-DOF PI controller. The position of each particle with random controller gains is initialized considering range constraint for gains based upon the earlier experience of trial and error method.

$$k_i(0) = [k_{p,i}(0), k_{int,i}(0)] \qquad (for\ PI) \tag{28}$$

$$k_i(0) = [k_{p,i}(0), k_{int,i}(0), k_{pfb,i}(0)] \qquad (for\ PI - P) \tag{29}$$

$$k_{imax} \geqslant k_i \geqslant k_{imin} \tag{30}$$

The velocity of the particle is also initialized and range constraint is applied too for proper convergence.

$$\rho_i(0) = [\rho_{p,i}(0), \rho_{int,i}(0), \rho_{pfb,i}(0)] \tag{31}$$

$$\rho_{imax} \geqslant \rho_i \geqslant \rho_{imin} \tag{32}$$

The pbest and gbest of the particle i and swarm population is also initialized.

Step 2: The one-shot data (input u_0, output y_0) is collected using initial parameters k_0 obtained by trial and error method. The fictitious reference signal generated using the u_0 and y_0 will be adjusted and updated for each particle. So, the performance index is also adjusted related to the reference signal and error signal for each particle. The updated equation for reference, error and performance are

$$\tilde{r}(k_i) = P(s, k_i)^{-1} u_0 + y_0 \tag{33}$$

$$\tilde{e}(k_i) = y_0 - M(s)\tilde{r}(k_i) \tag{34}$$

$$\widetilde{I}(k_i) = \sum (\tilde{e}(k_i))^2 \tag{35}$$

$$\tilde{r}(k_i, k_{fbi}) = (u_0 + y_0 H(s, k_{fbi}))P(s, k_i)^{-1} + y_0 \tag{36}$$

$$\tilde{e}(k_i, k_{fbi}) = y_0 - M(s)\tilde{r}(k_i, k_{fbi}) \tag{37}$$

$$\widetilde{I}(k_i) = \sum (\tilde{e}(k_i, k_{fbi}))^2 \tag{38}$$

Reference, error and performance index equation for 1-DOF PI and 2-DOF PI controller is shown from Eqs. (33)–(35) and from Eqs. (36)–(38) respectively. So, the objective function of PSO-FRIT method for 2-DOF PI is Eq. (39) can be represented as

$$(k_i, k_{fbi})_{opt.} = argmin\widetilde{I}(k_i, k_{fbi}) \tag{39}$$

Objective function of eq. is evaluated based upon the pbest of each particle and personal best position is updated for iteration. if

$$p_{besti} \leqslant l_{besti} \tag{40}$$

then

$$l_{besti} = p_{besti} \tag{41}$$

and

$$k_{localbest} = k_i \tag{42}$$

Step 3: The global best position is updated based upon the personal best of each particle. if

$$p_{besti} \leqslant g_{besti} \tag{43}$$

then

$$g_{besti} = p_{besti} \tag{44}$$

and

$$k_{globalbest} = k_i \tag{45}$$

Step 4: The velocity and position of particle has been updated as according to eq. to eq.

$$\rho_i^{\alpha+1} = \phi\rho_i^{\alpha} + c_1 w_1 (p_{best} - k_i^{\alpha}) + c_2 w_2 (g_{best} - k_i^{\alpha}) \tag{46}$$

The iteration is repeated until the good fitness value is not achieved considering the constraint of number of iterations as

$$\alpha = \alpha_{max} \tag{47}$$

4. Fuzzy Logic Controller (FLC)

The outer voltage control loop may consist of different type of controllers along with power compensation control. Fuzzy logic controller (FLC) is used to regulate the dc link voltage to reference level and the performance of FLC is compared with the non-optimized and optimized 1-DOF PI and 2-DOF PI controller response. The control configuration of FLC in Fig. 5 used for the dc link voltage control. The error in between the reference value and output value (E) of dc link voltage and change in error (CE) are the input quantities to the FLC and output would be the equivalent current quantity for the voltage as the current control algorithm is applied to the system. The inputs of FLC can be represented as

$$E(K) = V^*_{dc}(K) - V_{dc}(K) \tag{48}$$

$$CE = E(k) - E(K-1) \tag{49}$$

The fuzzy rule base in Table 1 is implemented for FLC. The membership function of E is implemented with five fuzzy levels.

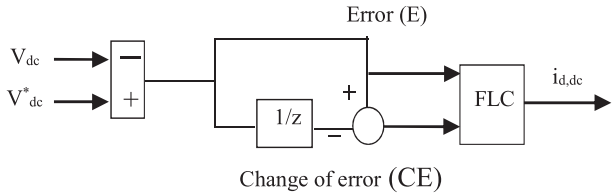


Fig. 5. System configuration of FLC for dc voltage control.

Table 1
Controller gains.

E/CE	NM	NS	ZE	PS	PM
NM	NM	NM	NM	NS	ZE
NS	NM	NS	NS	ZE	PS
ZE	NM	NS	ZE	PS	PM
PS	NS	ZE	PS	PM	PM
PM	ZE	PS	PM	PM	PM

The five fuzzy levels of FLC membership function are: NM (Negative Medium), NS (Negative Small), ZE (Zero), PS (Positive Small), PM (Positive Medium). The membership function for output of the FLC is having same number of fuzzy levels and adjusted as according to desired response.

5. Control algorithm

The grid interfaced PV system in Fig. 6 consists of LCL filter and isolation transformer. The power control strategy in Fig. 7 is implemented based upon the generation of in-phase and quadrature templates responsible for frequency synchronization and generation of reference current for active and reactive power.

5.1. dc link control

The dc voltage of grid connected PV system is regulated by processing error through dedicated controller. The error is defined by mathematical equation as

$$E(K) = V^*_{dc}(K) - V_{dc}(K) \tag{50}$$

where $V^*_{dc}(K)$ and measured voltage $V_{dc}(K)$ of dc link The output quantity after the PI control is current as current control method have been used which is considered in terms of losses. So, the active power component of current required to compensate the losses and regulate the dc link voltage to the reference level and can be computation as:

(a) The dedicated 1-DOF PI controller regulates the dc bus voltage to desired reference level & provides the active power component of current for dc link ($i_{d,dc}$) to compensate losses. The value of output current quantity after the PI controller needed compensate the losses can be computed as

$$i_{d,dc}(K) = i_{d,dc}(K-1) + K_{pd}(v_{de}(K) - v_{de}(K-1)) + K_{id}(v_{de}(K)) \tag{51}$$

k_p and k_{int} are proportional and integral gain of the PI controller. $I_{d,dc}(K)$ and $I_{d,dc}(K-1)$ are the loss component of current at Kth and $K-1$th sampling.

(b) The dedicated 2-DOF PI controller is replaced by PI-P controller for regulation of the dc bus voltage to desired reference level by feeding losses of VSC. The equation for the value of output current quantity Eq. (51) is modified as

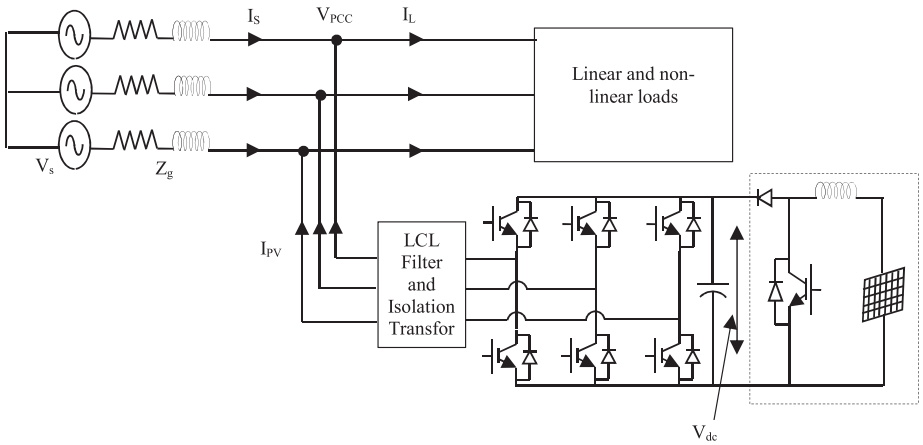


Fig. 6. Grid interfaced PV system.

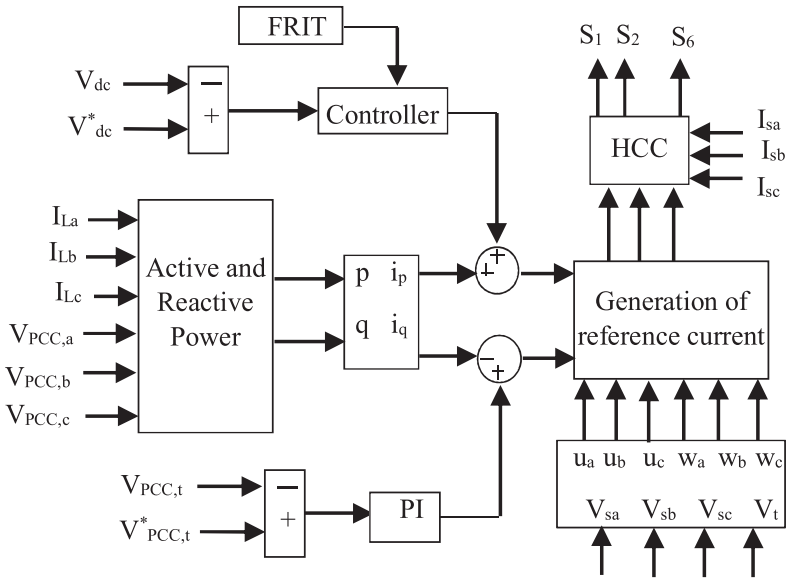


Fig. 7. Power Balance Theory (PBT) based control strategy.

$$i_{d,dc}(K) = i_{d,dc}(K-1) + K_{pd1}(v_{de}(K) - v_{de}(K-1)) + K_{id}(v_{de}(K)) - K_{pd2}(v_{de}(K)) \quad (52)$$

k_p, k_{int} and k_{pfb} are proportional, integral gain and proportional gain of the PI-P controller. $I_{d,dc}(K)$ and $I_{d,dc}(K-1)$ are the loss component of current at Kth and $K-1$th sampling.

5.2. Reference current generation

Unit templates are generated based upon their phase orientation in reference to the grid voltage. The in-phase templates are generated as [4]

$$u_{sa} = \frac{V_{sa}}{V_t}, \quad u_{sb} = \frac{V_{sb}}{V_t}, \quad u_{sc} = \frac{V_{sc}}{V_t} \quad (53)$$

where u_{sa}, u_{sb} and u_{sc} are the in-phase templates of phase a, b and c respectively. V_t is amplitude of three phase point of common coupling (PCC) voltage and calculated as

$$V_{PCC,t} = \left(\frac{2}{3}\right)^{\frac{1}{2}} (v_{sa}^2 + v_{sb}^2 + v_{sc}^2) \quad (54)$$

The equivalent active component of current can be compute by using the Eq. (55)

$$i_{Lp} = \frac{2}{3}\frac{p_L}{V_t} \quad (55)$$

Therefore, the reference current generated for d component/ active power current of grid current is given as

$$i_{Lp}^* = i_p + i_{d,dc} \quad (56)$$

Active power components of reference grid currents are

$$I_{spa}^* = I_{Lp}^* * u_{sa}, I_{spb}^* = I_{Lp}^* * u_{sb}, I_{spc}^* = I_{Lp}^* * u_{sc} \quad (57)$$

6. Result and discussion

The grid connected PV system is modeled and simulated in the MATLAB-Simulink environment. The system response for the initial controller gains can be improved using an optimized tuning method. The input u_k and output y_k data were collected for the FRIT method. The u_k and y_k has been extracted using the proportional and integral gains obtained through trial and error method. Extracted data has been utilized to search the optimum gains through PSO-FRIT programmed in MATLAB-mfile. The response of conventional PI controller (optimized and non-optimized) is investigated and compared with PI-P controller (optimized and non-optimized). The dc voltage regulation of grid connected PV system is further compared between 2-DOF PI-P control and FLC. The transient response during grid coupling of PV system as well as under the disturbance is investigated and discussed considering simulation results for 1-DOF and 2-DOF PI control. The simulation data of the system are collected for dc voltage response and plotted using MS-excel.

In the experimental system, when the switching devices of VSI were not controlled through PWM signals the dc link voltage of the VSI system is charged up to a certain voltage level depending upon the grid voltage rating through anti-parallel diodes of VSI. The switching of VSI is delayed to show the charging of dc link capacitor and therefore performance of dc voltage regulation to desired reference level is illustrated when PWM signals are applied to VSI. The results are discussed and analyzed considering following cases.

6.1. 1-DOF and 2-DOF PI control response

6.1.1. Non-optimized response

The additional proportional controller in 2-DOF PI control is designed as feedback compensation as shown in Figs. 2 and 3 by breaking the proportional gain of 1-DOF PI controller into two parts. The response of the non-optimized traditional PI and PI-P controller has been illustrated in Fig. 8. The traditional PI controller is having overshoot with slow response. The objective to design and implement 2-DOF FB PI control is to minimize the overshoot by maintaining similar or better response time. In Fig. 8, it is showing improved transient response having no overshoot as well as settling time is also maintained.

6.1.2. Optimized response

The optimized and non-optimized response of traditional dc voltage PI control can be observed in Figs. 8 and 9 respectively. The dc voltage control response is improved for optimized gains showing fast response and reduced overshoot. Non-optimized response settled at $t = 0.11$ s while optimized response settled at

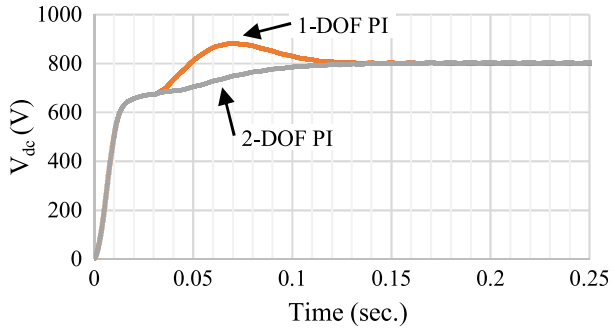


Fig. 8. Performance of non-optimized dc voltage controller.

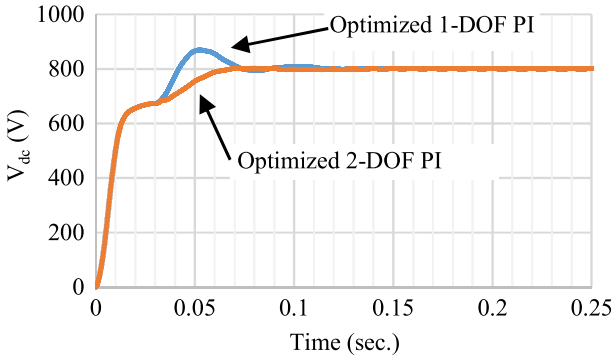


Fig. 9. Performance of optimized dc voltage controller.

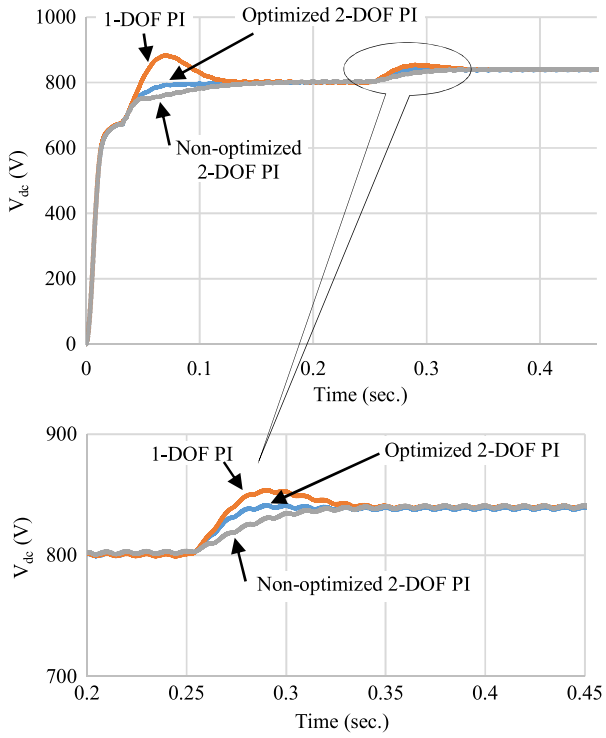


Fig. 10. Transient response of dc voltage controller for grid coupling of PV system and perturbation in reference dc voltage.

Table 2
1-DOF controller gains.

1-DOF PI (trial and error)	$K_p = 0.3$, $K_i = 8$
1-DOF PI (optmized)	$K_p = 0.77957$, $K_i = 29.1989$

Table 3
2-DOF controller gains.

2-DOF PI (trial and error)	$K_{p1} = 0.24$, $K_i = 12.5$, $K_{p2} = 0.04$
2-DOF PI (optmized)	$K_{p1} = 0.49$, $K_i = 28$, $K_{p2} = 0.09$

$t = 0.07$ s. The peak overshoot is reduced from V_{dc} (overshoot) = 882.79 V under non-optimized control to 865.94 V under optimized control. The optimized and non-optimized controller gains for conventional PI controller are given in Table 2.

Optimized response of dc voltage control for 1-DOF and 2-DOF PI controller is compared as in Fig. 9. The fast response have been obtained using optimized gains for both the controllers (PI and PI-P). But, the response of optimized 1-DOF PI is having overshoot and settled at $t = .07$ s. The optimized 2-DOF PI response is not having any overshoot and also the response is even little faster. PI-P controller response for optimized gains showing improved transient response with no overshoot as well as fast response and settling time. The optimized and non-optimized response of PI-P controller settled at $t = 0.065$ s and $t = 0.1$ s respectively.

6.2. Disturbance in reference dc voltage

The transient response of the controllers has been analyzed under the disturbance in reference dc voltage. The reference dc voltage ($V*_{dc}$) is altered from 800 V to 840 V (5% of reference dc voltage) through unit step signal. The response of non-optimized 1-DOF PI and 2-DOF PI is illustrated under the condition of disturbance in reference dc voltage as in Fig. 10. The response of 2-DOF controller is better in comparison to 1-DOF controller under the disturbance too. The optimized 2-DOF PI transient response is having no overshoot under disturbance occurred at as well as showing fast response in comparison to non-optimized 2-DOF and 1-DOF controller. The controller gains for optimized and non-optimized 2-DOF PI controller configuration is given in Table 3.

6.3. Varied Ir-radiance

The performance of the PV system is usually affected due to the change in ir-radiance level. Therefore, the performance of the control should be investigated under the disturbance caused due to change in ir-radiance. Fig. 11 shows the dc voltage response for optimized and non-optimized control of 1-DOF and 2-DOF

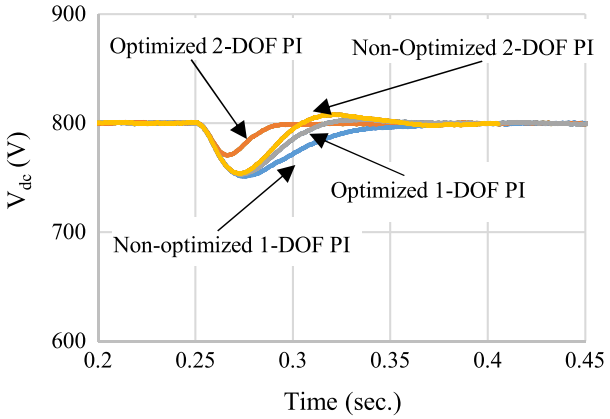


Fig. 11. dc voltage controller response under disturbance due to ir-radiance.

controller under the disturbance due to change in ir-radiance. One of the most critical case of change in ir-radiance is considered to test the performance of the controller. The ir-radiance is changed from 1000 W/m^2 to 0 W/m^2 at $t = 0.25$ s. and dc voltage get disturbed. The controller tries to regulate the dc voltage to its reference level quickly. Optimized 2-DOF PI control is showing best performance with better dynamic response and having low undershoot under this condition.

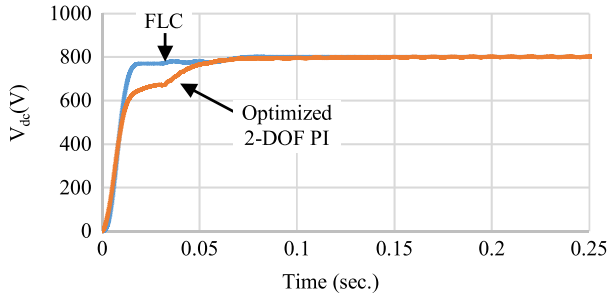


Fig. 12. Comparison of response for FLC and optimized PI controller.

6.4. FLC and optimized PI controller response

The FLC transient response of dc voltage control has been illustrated in Fig. 12. The FLC response is having very fast response but reached to the reference dc voltage at $t = 0.075$ s. and not having overshoot in the response. The FLC response have been compare with the optimized PI controller (2-DOF) response as illustrated in Fig. 12. The optimized 2-DOF PI controller showing quickest response as dc voltage is been regulated at $t = 0.06$ s in comparison to FLC and optimized traditional PI with time $t = 0.075$ and 0.07 s respectively. And, the 2-DOF PI is showing no overshoot in transient response.

In respect of showing transient response for regulation of dc voltage, the source current performance have been also analyzed during transient. The source current in Figs. 13 and 14 for the

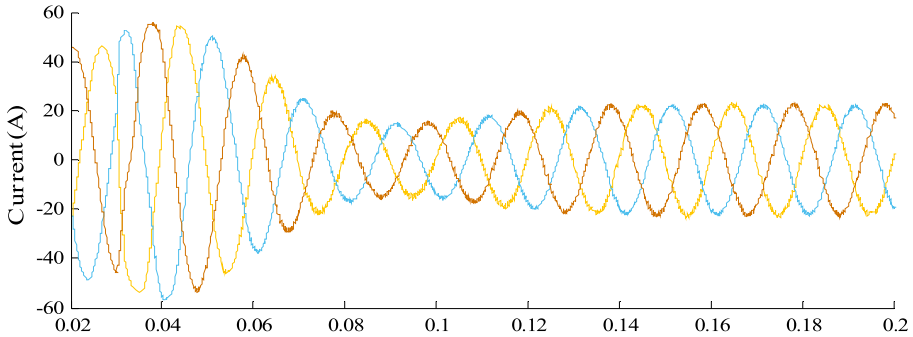


Fig. 13. Grid current response for 1-DOF PI controller in respect to dc voltage regulation.

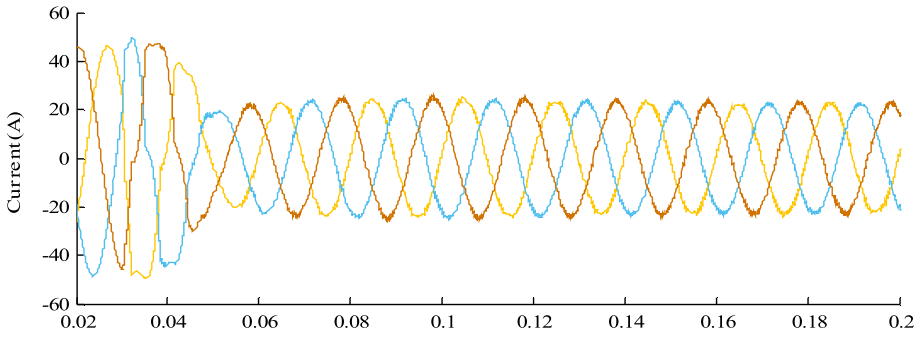


Fig. 14. Grid current response for 2-DOF PI controller in respect to dc voltage regulation.

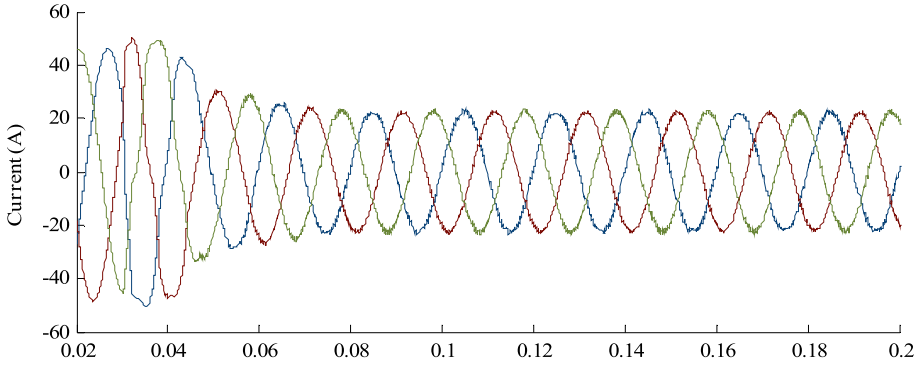


Fig. 15. Grid current response for optimized 2-DOF PI controller in respect to dc voltage regulation.

Table 4
Parameter of electrical utility grid system.

Line impedance (Z_g)	$R_s = 0.05$ ohm, $L_s = 1$ mH
Grid voltage (V_g)	$V_{LL} = 415$ V
LCL filter	$L_i = 1.4$ mH, $L_g = 1.4$ mH, $C_f = 5$ μF, $R_d = 20$ ohm
dc link voltage (V_{dc})	$V_{dc} = 800$ V
dc link capacitance (C_d)	$C_d = 1500$ μF
Base impedance (Z_b)	$Z_b = 17.22$
Frequency (f)	$f = 50$ Hz
Switching frequency (f_s)	$f_s = 10$ kHz

1-DOF PI and 2-DOF PI-P controller (non-optimized) respectively during interconnection of PV system to grid. The source current reaches to steady state at $t = 0.115$ s for the conventional 1-DOF PI control and at $t = 0.08$ s for non-optimized PI-P control. So, the source current transient response is also improved as the dc voltage regulation response is improved and reaches to steady state smoothly without overshoot under PI-P control. The source current for optimized 2-DOF PI-P control is illustrated in Fig. 15 and it is showing very smooth and fast response in comparison to non-optimized 1-DOF and 2-DOF controllers. The parameters of the considered grid connected PV system have been summarized in Table 4.

7. Conclusion

The 2-DOF PI-P controller configuration is proposed and implemented for dc voltage control of connected PV system. The dc voltage response of conventional PI control and proposed 2-DOF control is investigated and the performance of proposed controller found satisfactory as compared to conventional control. The controller gain parameters are optimally tuned using data-driven tuning method. Data driven FRIT method is programmed based upon PSO algorithm to overcome the drawback of tuning method. The optimized PI-P controller showing fast and smooth response in comparison to non-optimized PI-P and traditional PI control during grid coupling of PV system. As well as, the proposed optimally tuned controller is also effective under step change in reference dc voltage (step response) and disturbance due to varied irradiance of PV system. The grid current performance is also investigated during integration of PV system and better response is achieved corresponding to significantly improved dc voltage regulation.

References

[1] Yang Bo, Li Wuhua, Zhao Yi, He Xiangning. Design and analysis of a grid-connected photovoltaic power system. IEEE Trans Power Electron 2010;25(4):992–1000.
[2] Azmi SA, Adam GP, Ahmed KH, Finney SJ. Grid interfacing of multimegawatt of photovoltaic inverters. IEEE Trans Power Electron 2013;28(June):2770–84.
[3] Al Fadil H, Giri F, Guerrero JM. Grid-connected of photovoltaic module using nonlinear control. In: IEEE international symposium on power electronics for distributed generation systems (PEDG), Aalborg, Denmark, June 25–28. p. 119–24.
[4] Tripathi Ravi Nath, Singh Alka. Design and control of grid interconnected solar photovoltaic (SPV) system with improvement in power quality. In: Fifth international conference on power and energy systems (ICPS), Kathmandu, Nepal, Oct. 28–30.
[5] Koutroulis Eftichios, Blaabjerg Frede. Design optimization of transformerless grid-connected PV inverters including reliability. IEEE Trans Power Electron 2013;28(1):325–35.
[6] Katiraei Farid, Iravani Reza, Hatziargyriou Nikos, Dimeas Aris. Microgrid management control and operation aspect of microgrids. IEEE Power Energy Mag 2008(May/June).
[7] German solar energy society. Planning and installing photovoltaic systems - a guide for installers, architects and engineers. Earthscan, 2nd ed.; Reprint 2006.
[8] Yang Yongheng, Wang Huai, Zhao Yi, Blaabjerg F. Reactive power injection strategies for single-phase photovoltaic systems considering grid requirements. IEEE Trans Indus Appl 2014;50(6):4065–76.
[9] Terzic B, Majic Goran, Slautez Alojz. Stability analysis of three-phase PWM converter with LCL filter by means of nonlinear model. Automatika 2010;51(3):221–32.
[10] Tripathi Ravi Nath, Singh Alka, Hanamoto Tsuyoshi. Design and control of LCL filter interfaced grid connected solar photovotaic (SPV) system using power balance theory. Int J Electr Power Energy Syst (IJEPES) 2015;69:264–72.
[11] Kazmierkowski MP, Malesani L. Current control techniques for three phase voltage-source PWM converters: a survey. IEEE Trans Indus Electron 1998;45(5):691–703.
[12] Vasquez Juan C, Mastromauro RA, Guerrero Joseph M, Liserre Marco. Voltage support provided by a droop-controlled multigunctional inverter. IEEE Trans Indus Electron 2009;56(11):4510–9.
[13] Louzazni M, Aroudam E. Control and Stabilization of three-phase grid connected photovoltaics using PID-fuzzy logic. In: IEEE international conference on intelligent energy and power systems (IEPS). p. 279–84.
[14] Gia Minh Thao Nguyen, Uchida K. Control the photovoltaic grid connected system using fuzzy logic and backstepping approach. In: 9th Asian control conference (ASCC).
[15] Luo An, Tang Ci, Shuai Z, Tang Jie, Xu Xian Yong, Chen Dong. Fuzzy-PI based direct output-voltage control strategy for the STATCOM used in utility distribution systems. IEEE Trans Indus Electron 2009;56:2401–11.
[16] Miklosovic Robert, Gao Zhiqiang. A robust two-degree-of-freedom control design technique and its practical application. In: IEEE industry application conference, Oct. 3–7.
[17] Lai Yen-Shin, Chang Ye-Then, Kuo Chun-Ting. Robust control of digital controlled buck converter based upon two-degree-of-freedom controller. IECON, Glendale, AZ; 2010.
[18] Hanif Moin, Khadikar Vinod, Xiao Weidong, Kirtley Jr James L. Two degrees of freedom active damping technique for LCL filter-based grid connected PV systems. IEEE Trans Indus Electron 2014;61:2795–803.
[19] Nemati Hosein, Bagheri Peyman. A new approach to tune the two-degree-of-freedom (2DOF). In: IEEE international symposium on computer-aided control system design, Yokohama, Japan, Sep. 8–10.
[20] Dash P, Saikia Chandra, Sinha N. AGC of a multi-area system using firefly optimized two degree of freedom PID controller. In: Power and energy systems conference, Bangalore.
[21] Araki Mituhiko, Taguchi Hidefumi. Two-degree-of-freedom (2-DoF) PID controller systems. Int J Control Autom Syst 2003;1(4):401–11.
[22] Bagheri Peyman, Nemati Hosein. Novel tuning strategy for two-degree-of-freedom (2DOF) Pi controllers. In: 18th IFAC world congress, Milano, Italy, Aug. 28-Sep. 02.
[23] Horowitz IM. Synthesis of feedback systems. Academic Press; 1963.
[24] Alfaro VM, Vilanova R, Arrieta O. Robust tuning of two-degree-of-freedom (2-DoF) PI/PID based cascaded control systems. J Process Control 2009;19(10):1658–70.
[25] Tripathi Ravi N, Hanamoto Tsuyoshi. 2-DOF based novel controller design for dc voltage regulation of LCL interfaced three phase grid connected solar PV system. IFEEC, Taipei, Taiwan; 2015.
[26] Hjalmarsson H, Gevers M, Gunnarsson S, Lequin O. Iterative feedback tuning: theory and applications. IEEE Control Syst Mag 1998;18(4):26–41.
[27] Campi MC, Lecchini A, Saversi SM. Virtual reference feedback tuning: a direct method for design of feedback controllers. Automatica 2002;38(8):1337–46.
[28] Lecchini A, Campi MC, Saversi SM. Virtual reference feedback tuning for two degree of freedom controllers. Int J Adaptive Control Signal Process 2002;16(5):355–71.
[29] Souma S, Kaneko O, Fujii T. A new method of controller parameter tuning based on input-output data, fictitious reference iterative tuning (frit). In: Proceedings of IFAC workshop on adaptation and learning on control and signal processing (ALCOSP).
[30] Tripathi Ravi N, Hanamoto Tsuyoshi. FRIT based optimized PI tuning for dc link voltage control of grid connected solar PV system. IECON, Yokohama, Japan; 2015.
[31] Kaneko Osamu, Souma Shotaro, Fuji Takao. A fictitious reference iterative tuning (frit) in the two degree of freedom scheme and its application to closed loop system identification. Trans Soc Instrum Control Eng 2006;42(1):17–25.
[32] Masuda Shiro. A direct PID gains tuning method for dc motor control using an input-output data generated by disturbance response. In: IEEE international conference on control application (CCA), Senver, USA, Sep. 28–30.
[33] Kaneko O, Yamashina Y, Yamamoto S. Fictitious reference tuning of the feed-forward controller in a two-degree-of-freedom control system. SICE J Control Measure Syst Integr 2011;4:55–62.
[34] Wakasa Y, Tanaka K, Nishimura Y. Online controller tuning via FRIT and recursive least-squares. In: IFAC conference on advance in PID control, Brescia (Italy), March 28–30.
[35] Tripathi Ravi Nath, Hanamoto Tsuyoshi. Novel controller design for dc link voltage control of grid connected PV system and optimized PI response analysis with improved transients. ISGT-Asia, Bangkok, Thailand; 2015.

Ravi Nath Tripathi received his B.Tech (Electrical and Electronics) degree in 2011 from Graphic Era Institute of Technology (GEIT), India and M.Tech (Power Systems) degree in 2013 from Delhi Technological University (formerly Delhi College of Engineering), Delhi, India. He is currently working as doctoral student at the Hanamoto Laboratory, LSSE, Kyushu Institute of Technology, Japan. His current research is design, modeling and optimization of grid connected PV system.

Tsuyoshi Hanamoto was born in 1961. He received an M.S degree from Kyushu Institute of Technology, Japan, in 1986 and then joined Kobe Works of Kobe Steel, Ltd. In 1990, he joined the Center for Cooperative Research of Kyushu Institute of Technology. From 1997 to 2000 he was with Department of Electrical Engineering and since April 2000, he has been with the Graduate School of Life Science and Systems Engineering, Kyushu Institute of Technology, where he is presently a Professor. His research interests include motor control and power electronics.